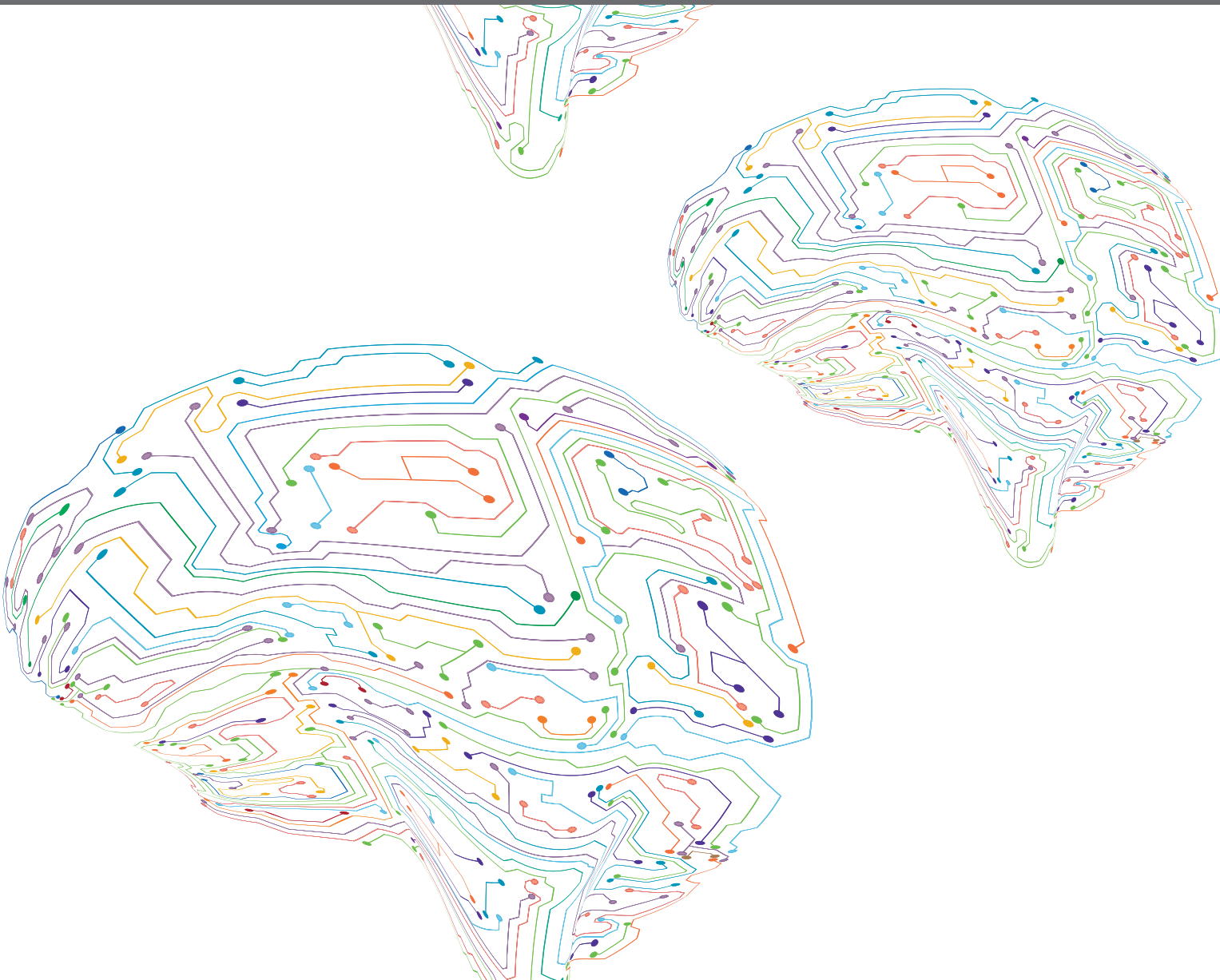


FRONTIERS IN NEURAL CIRCUITS - EDITORS' PICK 2021

EDITED BY: Edward S. Ruthazer and Takao K. Hensch
PUBLISHED IN: Frontiers in Neural Circuits





frontiers

Frontiers eBook Copyright Statement

The copyright in the text of individual articles in this eBook is the property of their respective authors or their respective institutions or funders. The copyright in graphics and images within each article may be subject to copyright of other parties. In both cases this is subject to a license granted to Frontiers.

The compilation of articles constituting this eBook is the property of Frontiers.

Each article within this eBook, and the eBook itself, are published under the most recent version of the Creative Commons CC-BY licence.

The version current at the date of publication of this eBook is CC-BY 4.0. If the CC-BY licence is updated, the licence granted by Frontiers is automatically updated to the new version.

When exercising any right under the CC-BY licence, Frontiers must be attributed as the original publisher of the article or eBook, as applicable.

Authors have the responsibility of ensuring that any graphics or other materials which are the property of others may be included in the CC-BY licence, but this should be checked before relying on the CC-BY licence to reproduce those materials. Any copyright notices relating to those materials must be complied with.

Copyright and source acknowledgement notices may not be removed and must be displayed in any copy, derivative work or partial copy which includes the elements in question.

All copyright, and all rights therein, are protected by national and international copyright laws. The above represents a summary only. For further information please read Frontiers' Conditions for Website Use and Copyright Statement, and the applicable CC-BY licence.

ISSN 1664-8714

ISBN 978-2-88971-643-2

DOI 10.3389/978-2-88971-643-2

About Frontiers

Frontiers is more than just an open-access publisher of scholarly articles: it is a pioneering approach to the world of academia, radically improving the way scholarly research is managed. The grand vision of Frontiers is a world where all people have an equal opportunity to seek, share and generate knowledge. Frontiers provides immediate and permanent online open access to all its publications, but this alone is not enough to realize our grand goals.

Frontiers Journal Series

The Frontiers Journal Series is a multi-tier and interdisciplinary set of open-access, online journals, promising a paradigm shift from the current review, selection and dissemination processes in academic publishing. All Frontiers journals are driven by researchers for researchers; therefore, they constitute a service to the scholarly community. At the same time, the Frontiers Journal Series operates on a revolutionary invention, the tiered publishing system, initially addressing specific communities of scholars, and gradually climbing up to broader public understanding, thus serving the interests of the lay society, too.

Dedication to Quality

Each Frontiers article is a landmark of the highest quality, thanks to genuinely collaborative interactions between authors and review editors, who include some of the world's best academicians. Research must be certified by peers before entering a stream of knowledge that may eventually reach the public - and shape society; therefore, Frontiers only applies the most rigorous and unbiased reviews.

Frontiers revolutionizes research publishing by freely delivering the most outstanding research, evaluated with no bias from both the academic and social point of view. By applying the most advanced information technologies, Frontiers is catapulting scholarly publishing into a new generation.

What are Frontiers Research Topics?

Frontiers Research Topics are very popular trademarks of the Frontiers Journals Series: they are collections of at least ten articles, all centered on a particular subject. With their unique mix of varied contributions from Original Research to Review Articles, Frontiers Research Topics unify the most influential researchers, the latest key findings and historical advances in a hot research area! Find out more on how to host your own Frontiers Research Topic or contribute to one as an author by contacting the Frontiers Editorial Office: frontiersin.org/about/contact

FRONTIERS IN NEURAL CIRCUITS - EDITORS' PICK 2021

Topic Editors:

Edward S. Ruthazer, McGill University, Canada

Takao K. Hensch, Harvard University, United States

Citation: Ruthazer, E. S., Hensch, T. K., eds. (2021). Frontiers in Neural Circuits - Editors' Pick 2021. Lausanne: Frontiers Media SA.
doi: 10.3389/978-2-88971-643-2

Table of Contents

- 04 *A Computational Model of Loss of Dopaminergic Cells in Parkinson's Disease Due to Glutamate-Induced Excitotoxicity***
Vignayanandam Ravindernath Muddapu, Alekhya Mandali,
V. Srinivasa Chakravarthy and Srikanth Ramaswamy
- 30 *Cellular, Synaptic and Network Effects of Acetylcholine in the Neocortex***
Cristina Colangelo, Polina Shichkova, Daniel Keller, Henry Markram and
Srikanth Ramaswamy
- 57 *A Novel Type of Neuron Within the Dorsal Striatum***
Miaomiao Mao, Aditya Nair and George J. Augustine
- 75 *Neural Correlates of Anesthesia in Newborn Mice and Humans***
Mattia Chini, Sabine Gretenkord, Johanna K. Kostka, Jastyn A. Pöpplau,
Laura Cornelissen, Charles B. Berde, Ileana L. Hanganu-Opatz and
Sebastian H. Bitzenhofer
- 88 *Microglia Regulate Pruning of Specialized Synapses in the Auditory Brainstem***
Giedre Milinkeviciute, Caden M. Henningfield, Michael A. Muniak,
Sima M. Chokr, Kim N. Green and Karina S. Cramer
- 107 *Spontaneous Activity Patterns are Altered in the Developing Visual Cortex of the Fmr1 Knockout Mouse***
Juliette E. Cheyne, Nawal Zabouri, David Baddeley and Christian Lohmann
- 115 *Multiplex Neural Circuit Tracing With G-Deleted Rabies Viral Vectors***
Toshiaki Suzuki, Nao Morimoto, Akinori Akaike and Fumitaka Osakada
- 138 *Structural Neural Connectivity Analysis in Zebrafish With Restricted Anterograde Transneuronal Viral Labeling and Quantitative Brain Mapping***
Manxiu Ma, Stanislav Kler and Y. Albert Pan
- 156 *Neural Correlates of Learning Pure Tones or Natural Sounds in the Auditory Cortex***
Ido Maor, Ravid Shwartz-Ziv, Libi Feigin, Yishai Elyada, Haim Sompolinsky
and Adi Mizrahi
- 177 *Common Principles in Functional Organization of VIP/Calretinin Cell-Driven Disinhibitory Circuits Across Cortical Areas***
Alexandre Guet-McCreight, Frances K. Skinner and Lisa Topolnik



A Computational Model of Loss of Dopaminergic Cells in Parkinson's Disease Due to Glutamate-Induced Excitotoxicity

Vignayanandam Ravindernath Muddapu¹, Alekhya Mandali², V. Srinivasa Chakravarthy^{1*} and Srikanth Ramaswamy³

¹ Computational Neuroscience Lab, Department of Biotechnology, Bhupat and Jyoti Mehta School of Biosciences, IIT-Madras, Chennai, India, ² Department of Psychiatry, Behavioural and Clinical Neuroscience Institute, University of Cambridge, Cambridge, United Kingdom, ³ Blue Brain Project, Brain and Mind Institute, EPFL, Geneva, Switzerland

OPEN ACCESS

Edited by:

Edward A. Fon,
Montreal Neurological Institute and
Hospital, McGill University, Canada

Reviewed by:

Bratislav Mistic,
McGill University, Canada
James Mac Shine,
The University of Sydney, Australia

*Correspondence:

V. Srinivasa Chakravarthy
schakra@iitm.ac.in

Received: 14 September 2018

Accepted: 05 February 2019

Published: 25 February 2019

Citation:

Muddapu VR, Mandali A,
Chakravarthy VS and Ramaswamy S
(2019) A Computational Model of
Loss of Dopaminergic Cells in
Parkinson's Disease Due to
Glutamate-Induced Excitotoxicity.
Front. Neural Circuits 13:11.
doi: 10.3389/fncir.2019.00011

Parkinson's disease (PD) is a neurodegenerative disease associated with progressive and inexorable loss of dopaminergic cells in Substantia Nigra pars compacta (SNc). Although many mechanisms have been suggested, a decisive root cause of this cell loss is unknown. A couple of the proposed mechanisms, however, show potential for the development of a novel line of PD therapeutics. One of these mechanisms is the peculiar metabolic vulnerability of SNc cells compared to other dopaminergic clusters; the other is the SubThalamic Nucleus (STN)-induced excitotoxicity in SNc. To investigate the latter hypothesis computationally, we developed a spiking neuron network-model of SNc-STN-GPe system. In the model, prolonged stimulation of SNc cells by an overactive STN leads to an increase in 'stress' variable; when the stress in a SNc neuron exceeds a stress threshold, the neuron dies. The model shows that the interaction between SNc and STN involves a positive-feedback due to which, an initial loss of SNc cells that crosses a threshold causes a runaway-effect, leading to an inexorable loss of SNc cells, strongly resembling the process of neurodegeneration. The model further suggests a link between the two aforementioned mechanisms of SNc cell loss. Our simulation results show that the excitotoxic cause of SNc cell loss might initiate by weak-excitotoxicity mediated by energy deficit, followed by strong-excitotoxicity, mediated by a disinhibited STN. A variety of conventional therapies were simulated to test their efficacy in slowing down SNc cell loss. Among them, glutamate inhibition, dopamine restoration, subthalamotomy and deep brain stimulation showed superior neuroprotective-effects in the proposed model.

Keywords: Parkinson's disease, excitotoxicity, deep brain stimulation, Izhikevich neuron model, Substantia Nigra pars compacta, SubThalamic Nucleus, Globus Pallidus externa, metabolic disorders

1. INTRODUCTION

There is a long tradition of investigation into the etiology and pathogenesis of Parkinson's Disease (PD) that seeks to link molecular (pesticides, oxidative stress, protein dysfunction etc.) (Hwang, 2013; Ortiz et al., 2016; Chiti and Dobson, 2017; Anselmi et al., 2018; Stykel et al., 2018) and subcellular (mitochondrial dysfunction etc.) (Henchcliffe and Beal, 2008; Reeve et al., 2018; Tsai et al., 2018) factors with the disease development. However, recent years see the emergence of two

novel lines of investigation into PD pathogenesis. These approaches, that aim to understand the PD pathology at the cellular and network level, mark a significant deviation from the traditional approaches (Rodriguez et al., 1998; Pissadaki and Bolam, 2013; Pacelli et al., 2015; Chakravarthy and Moustafa, 2018).

The first approach believes the primary factor that causes the degeneration of dopaminergic neurons of Substantia Nigra pars compacta (SNc) is its high metabolic requirements. SNc neurons are one of the most vulnerable and energy consuming neuronal clusters, due to their structural and functional properties. Here, we have listed down some of the plausible factors which make SNc cells to be most susceptible.

- **Complex axonal arbors:** Large axonal arborisation which requires large amounts of energy to drive currents along these axons (Bolam and Pissadaki, 2012; Pissadaki and Bolam, 2013).
- **Reactive neurotransmitter:** When a reactive neurotransmitter like dopamine is present in excess, it would readily oxidizes with proteins, nucleic acids and lipids (Sulzer, 2007) eventually leading to neurodegeneration. One of the mechanisms for sequestration of excess cytosolic dopamine is packing of dopamine into synaptic vesicles through vesicular monoamine transporter-2 (VMAT-2) using H^+ concentration gradient which is maintained by H^+ -ATPase. In addition to that, in the case of substantia nigra, the expression of VMAT2 is lower than in the ventral tegmental area (Liang et al., 2004; Mosharov et al., 2009) which likely causes dopamine-mediated oxidative stress in SNc cells.
- **Auto-rhythmicity:** Uses L-type calcium channels for maintaining the pace-making type of firing which in turn requires higher amounts of energy to maintain calcium homeostasis (Surmeier et al., 2017) and lower expression of calcium-binding proteins (lower capacity of calcium buffering mechanism) adds additional burden on the cell's metabolic activity (German et al., 1992).
- **NMDA synaptic activation:** Due to pacemaker type of firing, magnesium blockage of NMDA receptors is ineffective, resulting in substantial NMDA receptor currents even with weak glutamatergic inputs resulting in additional burden to maintain calcium homeostasis; the resulting energy deficiency leads to excitotoxicity (Rodriguez et al., 1998; Surmeier et al., 2010).
- **Prone to neuroinflammation:** Astrocytes play a modulatory role in microglial activation (McGeer and McGeer, 2008; Glass et al., 2010; Rocha et al., 2012) and any miscommunication between them results in neuroinflammation which eventually leads to neurodegeneration (Waak et al., 2009; Booth et al., 2017). The risk of inflammation in SNc neurons is high due to the small proportion of astrocytes regulating the huge population of microglia in this region (Lawson et al., 1990; Whitton, 2007; Mena and García de Yébenes, 2008). It has been reported that neuromelanin can induce microglial activation (Zecca et al., 2008; Zhang et al., 2011). SNc neurons are more susceptible to neuro-melanin induced inflammation compared to VTA neurons due to their high neuro-melanin

biosynthesis as a result of underexpression of VMAT2 (Peter et al., 1995; Liang et al., 2004).

- **Weak microvasculature:** SNc neurons are more prone to environmental toxins due to weak surrounding cerebral microvasculature (Rite et al., 2007).

Since the metabolic demands of SNc neurons are particularly high when compared to any other neuronal types (Sulzer, 2007) including neurons of other dopaminergic systems (Bolam and Pissadaki, 2012; Pacelli et al., 2015; Giguère et al., 2018), any sustained insufficiency in the supply of energy can result in cellular degeneration, characteristic of PD (Mergenthaler et al., 2013).

According to the second approach, the overactivity of SubThlamic Nucleus (STN) in PD causes excessive release of glutamate to the SNc, which in turns causes degeneration of SNc neurons by glutamate excitotoxicity (Rodriguez et al., 1998). The above two approaches are interrelated and not entirely independent as one form of excitotoxicity - the 'weak excitotoxicity' - is thought to have its roots in impaired cellular metabolism (Albin and Greenamyre, 1992). Therefore, the insight behind these new lines of investigation is the mismatch in energy supply and demand which could be a primary factor underlying neurodegeneration in PD. Such a mismatch is more likely to take place in special nuclei like SNc due to their peculiar metabolic vulnerability (Bolam and Pissadaki, 2012; Pissadaki and Bolam, 2013; Sulzer and Surmeier, 2013; Pacelli et al., 2015; Surmeier et al., 2017; Giguère et al., 2018). Similar ideas have been proffered to account for other forms of neurodegenerative diseases such as Huntington's disease, Alzheimer's disease, and amyotrophic lateral sclerosis (Beal et al., 1993; Johri and Beal, 2012; Gao et al., 2017).

If metabolic factors are indeed the underlying reason behind PD pathogenesis, it is a hypothesis that deserves closer attention and merits a substantial investment of time and effort for an in-depth study. This is because any positive proof regarding the role of metabolic factors puts an entirely new spin on PD research. Several researchers proposed that systems-level energy imbalance probably a principal cause of PD (Wellstead and Cloutier, 2011; Bolam and Pissadaki, 2012; Pacelli et al., 2015). Unlike current therapeutic approaches that manage the symptoms rather than provide a cure, the new approach can in principle point to a more lasting solution. If inefficient energy delivery or energy transformation mechanisms are the reason behind degenerative cell death, relieving the metabolic load on the vulnerable neuronal clusters, by intervening through current clinically approved therapeutics (such as brain stimulation and pharmacology) could prove to be effective treatments (Adhihetty and Beal, 2008; Spieles-Engemann et al., 2010; Seidl and Potashkin, 2011; Musacchio et al., 2017).

In this paper, with the help of computational models, we investigate the hypothesis that the cellular energy deficiency in SNc could be the primary cause of SNc cell loss in PD. *The higher metabolic demand of SNc cells due to their unique molecular characteristics, complex morphologies, and other energy-demanding features perhaps make them more vulnerable to energy deficit.* Therefore, prolonged energy deprivation or

insufficiency in such cells creates metabolic stress, eventually leading to neurodegeneration. If we can aim to reduce the metabolic stress on SNc cells, we can delay the progression of cell loss in PD.

In the proposed modeling study, we focus on excitotoxicity in SNc caused by STN which is precipitated by energy deficiency (Greene and Greenamyre, 1996) and exploring simulated therapeutic strategies for slowing down SNc cell loss. With the help of computational models of neurovascular coupling, our group had earlier explored the effect of rhythms of energy delivery from the cerebrovascular system on neural function (Gandrakota et al., 2010; Chander and Chakravarthy, 2012; Chhabria and Chakravarthy, 2016; Philips et al., 2016). Recently, we proposed a preliminary computational spiking network model of STN-mediated excitotoxicity in SNc with a slightly abstract treatment of apoptosis (Muddapu and Chakravarthy, 2017). Building on the previous version of the model, we have improved the excitotoxicity model by incorporating more biologically plausible dopamine plasticity and also explored the therapeutic strategies to slow down or halt the SNc cell loss.

2. MATERIALS AND METHODS

All the nuclei were modeled as Izhikevich 2D neurons (**Figure 1**). All the simulations were performed by numerical integration using MATLAB (RRID:SCR_001622) with a time step (dt) of 0.1 s. The average time for 50-s simulation was around 10 h, and it reduced to 5 h when ran on GPU card (Nvidia Quadro K620).

2.1. Izhikevich Neuron Model

Computational neuroscientists are often required to select the level at which a given model of interest must cast, i.e., biophysical-level, conductance-based modeling level, spiking neuron-level or rate-coded level. Biophysical models capture a more biologically detailed dynamics but are computationally expensive whereas rate-coded, point-neuron models are computationally inexpensive but possess less biologically detailed dynamics. To overcome this predicament, Izhikevich

(2003) developed spiking neuron models that are comparatively computationally inexpensive yet capture various neuronal dynamics. The proposed model of excitotoxicity consists of SNc, STN, and Globus Pallidus externa (GPe) modeled using Izhikevich neuron models arranged in a 2D lattice (**Figure 1**). The population sizes of these nuclei in the model were selected based on the neuronal numbers of these nuclei in rat basal ganglia (Oorschot, 1996). The Izhikevich parameters for STN and GPe were adapted from Michmizos and Nikita (2011) and Mandali et al. (2015) and the parameters for SNc were adapted from Cullen and Wong-Lin (2015). The firing rates of these neuronal types were tuned to match the published data (Modolo et al., 2007; Tripathy et al., 2014) by varying the external bias current (I_{ij}^x). All parameters values are given in the **Table 1**. The Izhikevich model consists of two variables, one for membrane potential (v^x) and the other one for membrane recovery variable (u^x).

$$\frac{dv_{ij}^x}{dt} = 0.04(v_{ij}^x)^2 + 5v_{ij}^x + 140 - u_{ij}^x + I_{ij}^x + I_{ij}^{syn} \quad (1)$$

$$\frac{du_{ij}^x}{dt} = a(bv_{ij}^x - u_{ij}^x) \quad (2)$$

$$\text{if } v_{ij}^x \geq v_{peak} \begin{cases} v_{ij}^x \leftarrow c \\ u_{ij}^x \leftarrow u_{ij}^x + d \end{cases} \quad (3)$$

where, v_{ij}^x , u_{ij}^x , I_{ij}^{syn} , and I_{ij}^x are the membrane potential, the membrane recovery variable, the total amount synaptic current received and the external current applied to neuron x at location (i, j) , respectively, v_{peak} is the maximum membrane voltage set to neuron (+30 mV) with x being GPe or SNc or STN neuron.

2.2. Synaptic Connections

The presence of excitatory synaptic connectivity from STN to SNc was observed from anatomical and electrophysiology studies (Kita and Kitai, 1987; Smith and Grace, 1992; Hamani et al., 2004, 2017) and these connections might take part in controlling the bursting activity of SNc (Smith and Grace 1992). The sizes (number of neurons) of SNc (8×8), STN (32×32) and GPe (32×32) nuclei in the model were selected such that they match the proportions as observed in the rat basal ganglia (Oorschot, 1996). We also modeled convergent projections from STN to SNc as per anatomical observations (Oorschot, 1996). Similarly, the synaptic connectivity between GPe and STN was considered one-to-one as in Dovzhenok and Rubchinsky (2012) and Mandali et al. (2015). The equations used to model synaptic connectivity are

$$\tau_{Recep} * \frac{dh_{ij}^{x \rightarrow y}}{dt} = -h_{ij}^{x \rightarrow y} + S_{ij}^x(t) \quad (4)$$

$$I_{ij}^{x \rightarrow y}(t) = W_{x \rightarrow y} * h_{ij}^{x \rightarrow y}(t) * (E_{Recep} - V_{ij}^y(t)) \quad (5)$$

The NMDA currents are regulated by voltage-dependent magnesium channel (Jahr and Stevens, 1990) which was modeled as,

$$B_{ij}(v_{ij}) = \frac{1}{1 + (\frac{Mg^{2+}}{3.57}) * e^{-0.062 * V_{ij}^y(t)}} \quad (6)$$

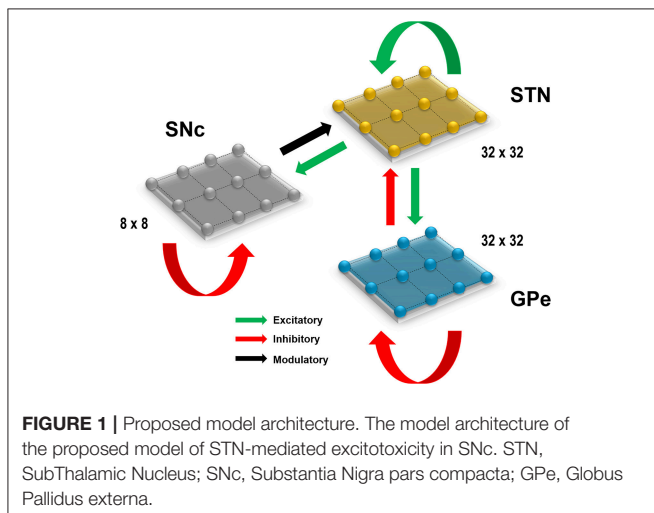


TABLE 1 | Parameter values used in the proposed model.

Parameter(s)	STN	SNc	GPe
Izhikevich parameters (a, b, c, d)	a = 0.005, b = 0.265, c = -65, d = 1.5	a = 0.0025, b = 0.2, c = -55, d = 2	a = 0.1, b = 0.2, c = -65, d = 2
External current (I^x)	$I^{STN} = 3$	$I^{SNc} = 9$	$I^{GPe} = 4.25$
Number of laterals ($nlat_x$)	$nlat_{STN} = 11$	$nlat_{SNc} = 5$	$nlat_{GPe} = 15$
Radius of Gaussian laterals (R_x)	$R_{STN} = 1.4$	$R_{SNc} = 1.6$	$R_{GPe} = 1.6$
Synaptic strength within laterals (A_x)	$A_{STN} = 1.3$	$A_{SNc} = 0.1$	$A_{GPe} = 0.1$
Time decay constant for AMPA (τ_{AMPA})	6 ms	6 ms	6 ms
Time decay constant for NMDA (τ_{NMDA})	160 ms	160 ms	160 ms
Time decay constant for GABA (τ_{GABA})	4 ms	4 ms	4 ms
Synaptic potential of AMPA receptor (E_{AMPA})	0 mV	0 mV	0 mV
Synaptic potential of NMDA receptor (E_{NMDA})	0 mV	0 mV	0 mV
Synaptic potential of GABA receptor (E_{GABA})	-60 mV	-60 mV	-60 mV
Effect on the post-synaptic current ($cd2$)	0.1	0.1	0.1
Concentration of Magnesium (Mg^{2+})	1 nM	1 nM	1 nM

ms, milliseconds; mV, millivolts; nM, nanomolar.

where, S_{ij}^x is the spiking activity of neuron x at time t , τ_{Recep} is the decay constant for synaptic receptor, $h_{ij}^{x \rightarrow y}$ is the gating variable for the synaptic current from x to y , $W_{x \rightarrow y}$ is the synaptic weight from neuron x to y , Mg^{2+} is the magnesium ion concentration, V_{ij}^y is the membrane potential of the neuron y for the neuron at the location (i, j) and E_{Recep} is the receptor associated synaptic potential (Recep = NMDA/AMPA/GABA). The time constants of NMDA, AMPA, and GABA in GPe, SNc, and STN were chosen from Götz et al. (1997) are given in the **Table 1**.

2.3. Lateral Connections

Lateral connections are similar to collaterals of a neuron, and here it is defined as connections within each neuronal population. Earlier studies show the presence of lateral connections in STN (Kita et al., 1983) and GPe (Kita and Kita, 1994). In the case of SNc, the GABAergic interneurons were observed and their control of SNc activity revealed by immunohistochemistry studies (Hebb and Robertson, 1999; Tepper and Lee, 2007). To simplify the model, the GABAergic interneurons were replaced by GABAergic lateral connections in SNc population. Experimental studies show that synaptic current from lateral connections follows Gaussian distribution (Lukasiewicz and Werblin, 1990) that is, nearby neurons will have more influence than distant neurons. The lateral connections in various modules in the current network (STN, GPe, and SNc) were modeled as Gaussian neighborhoods (Mandali et al., 2015) and the parameters used are given in the **Table 1**. Each neuron receives synaptic input from a set number of neighboring neurons located in a 2D grid of size $n \times n$.

$$w_{ij,pq}^{m \rightarrow m} = A_m * e^{\frac{-d_{ij,pq}^2}{R_m^2}} \quad (7)$$

$$d_{ij,pq}^2 = (i - p)^2 + (j - q)^2 \quad (8)$$

where, $w_{ij,pq}^{m \rightarrow m}$ is the lateral connection weight of neuron type m at location (i, j) , $d_{ij,pq}^2$ is the distance from center neuron (p, q) , R_m is the variance of Gaussian, A_m is the strength of lateral synapse, m = GPe or SNc or STN.

2.4. Effect of DA on Synaptic Plasticity

Several experimental studies demonstrate dopamine-dependent synaptic plasticity in STN (Hassani et al., 1997; Magill et al., 2001; Yang et al., 2016) and GPe (Magill et al., 2001; Mamad et al., 2015). Experimental observations show an increase in synchrony in STN (Bergman et al., 1994, 1998) and GPe populations (Bergman et al., 1998) at low DA levels. The effect of low DA was implemented in the model by increasing in lateral connections strength in STN population as in Hansel et al. (1995) and similarly decrease in lateral connections strength in GPe as in Wang and Rinzel (1993). Similarly, SNc populations also showed an increase in synchrony at low DA levels (Hebb and Robertson, 1999; Vandecasteele et al., 2005; Tepper and Lee, 2007; Ford, 2014) which was modeled similarly to the model of DA-modulated GPe.

We modeled DA effect on the network as follows: as DA level increases, the strength of the lateral connections in STN decreases whereas, in GPe and SNc, lateral connection weights become stronger. As the lateral connection weights directly controls the amount of synaptic current each neuron receives. All the neurons in STN population will tend to fire together as the lateral connection weights increases (due to excitatory synapses). However, in the case of SNc and GPe it is contrary, that is, all the neurons will not tend to fire together as the lateral connection weights increases (due to inhibitory synapses). Lateral strength was modulated

by DA as follows,

$$A_{STN} = s_{STN}^{max} * e^{(-cd_{stn} * DA_s(t))} \quad (9)$$

$$A_{GPe} = s_{GPe}^{max} * e^{(cd_{gpe} * DA_s(t))} \quad (10)$$

$$A_{SNc} = s_{SNc}^{max} * e^{(cd_{snc} * DA_s(t))} \quad (11)$$

where, s_{STN}^{max} , s_{GPe}^{max} , and s_{SNc}^{max} are strength of the lateral connections at the basal spontaneous activity of the population without any external influence in STN, GPe, and SNc, respectively. cd_{stn} , cd_{gpe} , and cd_{snc} were the factors by which dopamine affects the lateral connections in STN, GPe, and SNc populations, respectively, $DA_s(t)$ is the instantaneous dopamine level which is the spatial average activity of all the neurons in SNc.

According to experimental studies, DA causes post-synaptic effects on afferent currents in GPe and STN (Shen and Johnson, 2000; Smith and Kieval, 2000; Magill et al., 2001; Cragg et al., 2004; Fan et al., 2012). DA causes post-synaptic effects on afferent currents in SNc through somatodendritic DA receptors (Jang et al., 2011; Courtney et al., 2012; Ford, 2014). Thus, we included a factor ($cd2$), which regulates the effect of DA on synaptic currents of GPe, SNc, and STN. As observed in Kreiss et al. (1997), as DA level increases, the regulated current decreases as follows:

$$W_{x \rightarrow y} = (1 - cd2 * DA_s(t)) * w_{x \rightarrow y} \quad (12)$$

where, $W_{x \rightarrow y}$ is the synaptic weight ($STN \rightarrow GPe$, $GPe \rightarrow STN$, $STN \rightarrow STN$, $GPe \rightarrow GPe$, $STN \rightarrow SNc$, $SNc \rightarrow SNc$), ($cd2$) is the parameter that affects the post-synaptic current, $DA_s(t)$ is the instantaneous dopamine level which is the spatial average activity of all the neurons in SNc.

2.5. Total Synaptic Current Received by Each Neuron

STN:

The total synaptic current received by a STN neuron at lattice position (i, j) is the summation of lateral glutamatergic input from other STN neurons considering both NMDA and AMPA currents and the GABAergic input from the GPe neurons.

$$I_{ij}^{STNsyn} = I_{ij}^{NMDAat} + I_{ij}^{AMPAat} + I_{ij}^{GABA \rightarrow STN} \quad (13)$$

where, I_{ij}^{NMDAat} and I_{ij}^{AMPAat} are the lateral glutamatergic current from other STN neurons considering both NMDA and AMPA receptors, respectively, $I_{ij}^{GABA \rightarrow STN}$ is the GABAergic current from GPe neuron.

GPe:

The total synaptic current received by a GPe neuron at lattice position (i, j) is the summation of the lateral GABAergic current from other GPe neurons and the glutamatergic input from the STN neurons considering both NMDA and AMPA currents.

$$I_{ij}^{GPesyn} = I_{ij}^{GABAat} + I_{ij}^{NMDA \rightarrow GPe} + I_{ij}^{AMPA \rightarrow GPe} \quad (14)$$

where, I_{ij}^{GABAat} is the lateral GABAergic current from other GPe neurons, $I_{ij}^{NMDA \rightarrow GPe}$ and $I_{ij}^{AMPA \rightarrow GPe}$ are the glutamatergic current from STN neuron considering both NMDA and AMPA receptors, respectively.

SNc:

The total synaptic current received by a SNc neuron at lattice position (i, j) is the summation of the lateral GABAergic current from other SNc neurons and the glutamatergic input from the STN neurons considering both NMDA and AMPA currents.

$$I_{ij}^{SNcsyn} = I_{ij}^{GABAat} + I_{ij}^{NMDA \rightarrow SNc} + I_{ij}^{AMPA \rightarrow SNc} \quad (15)$$

where, I_{ij}^{GABAat} is the lateral GABAergic current from other SNc neurons, $I_{ij}^{NMDA \rightarrow SNc}$ and $I_{ij}^{AMPA \rightarrow SNc}$ are the glutamatergic current from STN neuron considering both NMDA and AMPA receptors, respectively.

2.6. Neurodegeneration

According to Rodriguez et al. (1998), dopamine deficiency in SNc leads to disinhibition and overactivity of the STN, which in turn causes excitotoxic damage to its target structures, including SNc itself. In order to simulate the SNc excitotoxicity induced by STN, we incorporate a mechanism of programmed cell death, whereby an SNc cell under high stress kills itself. The stress on a given SNc cell was calculated based on the firing history of the cell - higher firing activity causes higher stress.

The stress of each SNc neuron at lattice position (i, j) at time t due to excess firing is calculated as,

$$\tau_{stress} * \frac{dQ_{ij}^x}{dt} = -Q_{ij}^x + r_{ij}^x(t) \quad (16)$$

where, $r_{ij}^x(t)$ is instantaneous mean firing rate of a SNc neuron at lattice position (i, j) at time t , calculated with a fixed sliding window Δt (1 s) (Dayan and Abbott, 2005) as,

$$r_{ij}^x(t) = \frac{1}{\Delta t} \int_{t-\Delta t}^t d\tau \rho(\tau) \quad (17)$$

and,

$$\rho(\tau) = \sum_{i=1}^n \delta(t - t_i) \quad (18)$$

Sequence of spike timing: $t_i = 1, 2, 3 \dots n$

If stress variable (Q_{ij}^x) of a SNc neuron at lattice position (i, j) crosses certain threshold (S_{thres}) then that particular SNc neuron will be eliminated (Iglesias and Villa, 2008).

$$\text{if } Q_{ij}^x(t) > S_{thres}, \quad \text{then } v_{ij}^x(t) = 0 \quad (19)$$

2.6.1. Estimating Rate of Degeneration

For a given course of SNc cell loss, the half-life is the time taken for half of the SNc cells to be lost ($t_{1/2}$). The following equation was used to estimate the number of

SNC cells ($N_{sc}(t)$) for a given course that survived after a given time t .

$$N_{sc}(t) = N_{sc}^0 * e^{-\lambda t} \quad (20)$$

where, λ is the rate of degeneration (sec^{-1}), N_{sc}^0 is the number of surviving SNC cells at $t = 0$.

To estimate the rate of degeneration λ from a given course of SNC cell loss, the following equation was used,

$$\lambda = \frac{\ln 2}{t_{1/2}} \quad (21)$$

The instantaneous rate of degeneration $\lambda(t)$ was calculated by the following equation,

$$\lambda(t) = \frac{\ln(N_{sc}(t)) - \ln(N_{sc}(t-1))}{t - (t-1)} \quad (22)$$

2.7. Neuroprotective Strategies

Pharmacological or surgical therapies that abolish the pathological oscillations in STN or block the receptors on SNC can be neuroprotective and might slow down the progression of SNC cell loss (Rodriguez et al., 1998).

2.7.1. Glutamate Inhibition Therapy

Glutamate drug therapy can have neuroprotective effect on SNC in two ways (1) Inactivation of NMDA (N-methyl-D-aspartate), AMPA (2-amino-3-(5-methyl-3-oxo-1,2-oxazole-4-yl) propanoic acid) or excitatory metabotropic glutamate (Group-I - mGluR1/5) receptors (mGluR) by glutamate antagonists, and (2) Activation of metabotropic glutamate (Group-II/III - mGluR2,3/4,6,7,8) receptors by glutamate agonists. NMDA antagonist MK-801 showed reduction of SNC cell loss in the neurotoxic rats (Turski et al., 1991; Zuddas et al., 1992b; Brouillet and Beal, 1993; Blandini, 2001; Armentero et al., 2006) and primates (Zuddas et al., 1992a,b). AMPA antagonists such as NBQX (Merino et al., 1999), LY-503430 (Murray et al., 2003) and LY-404187 (O'Neill et al., 2004) exhibited neuroprotection of SNC cells in the neurotoxic animal models. mGluR-5 antagonist MPEP and MTEP showed neuroprotection in 6-OHDA lesioned rats (Armentero et al., 2006; Hsieh et al., 2012; Ferrigno et al., 2015; Fuzzati-Armentero et al., 2015) and MPTP-treated primates (Masilamoni et al., 2011), respectively. Broad-spectrum group II (Murray et al., 2002; Battaglia et al., 2003; Vernon et al., 2005) and group III (Vernon et al., 2005; Austin et al., 2010) agonists showed neuroprotection in neurotoxic rats. Selective mGluR2/3 agonist 2R,4R APDC (Chan et al., 2010) and mGluR4 agonist VU0155041 (Betts et al., 2012) significantly attenuated SNC cell loss in 6-OHDA lesioned rats.

The glutamate drug therapy was implemented in the proposed excitotoxicity model by the following criterion,

$$W_{STN \rightarrow SNC}(N_{sc}, t) = \begin{cases} W_{STN \rightarrow SNC}^0, & N_{sc}(t) > N_i \\ W_{STN \rightarrow SNC}^0 * \delta_{GI}, & N_{sc}(t) \leq N_i \end{cases} \quad (23)$$

where, $W_{STN \rightarrow SNC}(N_{sc}, t)$ is the instantaneous change in synaptic weight of STN to SNC based on the number of surviving SNC neurons at time t $N_{sc}(t)$ is the instantaneous number of surviving SNC neurons, $W_{STN \rightarrow SNC}^0$ is the basal connection strength of STN to SNC, δ_{GI} is the proportion of glutamate inhibition, N_i is the number representing SNC cell loss ($i = 25\% \mid 50\% \mid 75\%$) at which therapeutic intervention was employed. In the present study, we have considered 25% (cells lost = 16), 50% (cells lost = 32) and 75% (cells lost = 48) SNC cell loss as early, intermediate and late stages of disease progression, respectively.

2.7.2. Dopamine Restoration Therapy

The neuroprotective effects of DA agonists therapy are thought to be due to one or more of the following mechanisms: (1) L-DOPA sparing, (2) Autoreceptor effects, (3) Antioxidant effects, (4) Antiapoptotic effects, and (5) Amelioration of STN-mediated excitotoxicity (Olanow et al., 1998; Grandas, 2000; Schapira, 2003; Zhang and Tan, 2016). In the present study, we focus on the amelioration of STN-mediated excitotoxicity. DA agonists can restore the dopaminergic tone in the dopamine-denervated brain, which results in increased inhibition in STN, thereby diminishing STN-induced excitotoxicity on SNC neurons (Olanow et al., 1998; Schapira and Olanow, 2003; Piccini and Pavese, 2006; Vaarmann et al., 2013).

The dopamine agonist therapy was implemented in the proposed excitotoxicity model by the following criterion,

$$DA(N_{sc}, t) = \begin{cases} DA_s(t), & N_{sc}(t) > N_i \\ DA_s(t) + \delta_{DAA}, & N_{sc}(t) \leq N_i \end{cases} \quad (24)$$

where, $DA(N_{sc}, t)$ is the instantaneous change in dopamine level based on the number of surviving SNC neurons at time t $N_{sc}(t)$ is the instantaneous number of surviving SNC neurons, $DA_s(t)$ is the instantaneous dopamine signal from the SNC neurons, δ_{DAA} is the proportion of dopamine content restoration, N_i is the number representing SNC cell loss at which therapeutic intervention was employed.

2.7.3. Subthalamotomy

Subthalamotomy is still quite a common treatment amongst patients in advanced stages of PD where patients stop responding to L-DOPA (wearing-off) or chronic L-DOPA therapy results in motor complications such as L-DOPA Induced Dyskinesias (LID) (Alvarez et al., 2009; Obeso et al., 2017). It was reported that STN lesioning exhibits neuroprotective effect which acts as an antiglutamatergic effect in neurotoxic animal models (Piallat et al., 1996; Chen et al., 2000; Carvalho and Nikkhah, 2001; Paul et al., 2004; Wallace et al., 2007; Jourdain et al., 2014).

STN ablation was implemented in the proposed excitotoxicity model by the following criterion,

$$\text{if } N_{sc}(t) \leq N_i, \quad \text{then } v_{ij}^{STN}(P_{les}, t) = 0 \quad (25)$$

where, P_{les} is the lesion percentage of STN which is selected from the following range: [5, 10, 20, 40, 60, 80, 100], $N_{sc}(t)$ is the instantaneous number of surviving SNC neurons, N_i is the number representing SNC cell loss at which therapeutic intervention was employed.

2.7.4. Deep Brain Stimulation (DBS) in STN

DBS therapy is preferred over ablation therapy of STN due to the potentially irreversible damage to the stimulated brain region in ablation therapy. It has been reported that long-term stimulation (DBS) of STN results in the slowdown of the progression of SNc cell loss in animal models (Benazzouz et al., 2000; Maesawa et al., 2004; Temel et al., 2006; Wallace et al., 2007; Spieles-Engemann et al., 2010; Musacchio et al., 2017).

The DBS electrical stimulation was given in the form of current or voltage pulses to the target neuronal tissue (Cogan, 2008). The effect of DBS therapy was modeled as external stimulation current given to the entire or part of the STN module in the form of Gaussian distribution (Rubin and Terman, 2004; Hauptmann and Tass, 2007; Foutz and McIntyre, 2010; Mandali and Chakravarthy, 2016). The DBS parameters such as amplitude (A_{DBS}), frequency ($f_{DBS} = \frac{1}{T_{DBS}}$) and pulse width (δ_{DBS}) were adjusted by using clinical settings as a constraint (Moro et al., 2002; Garcia et al., 2005), in order to reduce the synchrony in STN population along with the minimal rise in the firing rate. In addition to exploring DBS parameters, a range of stimulus waveforms (such as rectangular monophasic (MP) and biphasic (BP) current pulses) and different types of stimulation configurations (such as single contact point (SCP), four contact points (FCP) and multiple contact points (MCP)) were also implemented (Figure 2) (Cogan, 2008; Lee et al., 2016).

In the present study, the current pulses which given to neuronal network are in the form of monophasic and biphasic waveforms. The monophasic current pulse (P_{MP}) was generated as the following,

$$P_{MP}(t) = \begin{cases} A_{DBS}, & t_k \leq t < t_k + \delta_{DBS} \\ 0, & \text{else} \end{cases} \quad (26)$$

where, t_k are the onset times of the current pulses, A_{DBS} is the amplitude of the current pulse, δ_{DBS} is the current pulse width.

The biphasic current pulse (P_{BP}) was generated as the following,

$$P_{BP}(t) = \begin{cases} A_{DBS}, & t_k \leq t < t_k + \frac{\delta_{DBS}}{2} \\ -A_{DBS}, & t_k + \frac{\delta_{DBS}}{2} \leq t < t_k + \delta_{DBS} \\ 0, & \text{else} \end{cases} \quad (27)$$

where, t_k are the onset times of the current pulses, A_{DBS} is the amplitude of the current pulse, δ_{DBS} is the current pulse width.

The influence of stimulation on a particular neuron will depend on the position of the stimulation electrode in the neuronal network (Cogan, 2008). The effect of stimulation will decay as the distance between electrode position (i_c, j_c) and neuronal position (i, j) increased which was modeled as a Gaussian neighborhood (Mandali and Chakravarthy, 2016). We have assumed that the center of the electrode to be the mean of the Gaussian which coincides with the lattice position (i_c, j_c) and the spread of stimulus current was controlled by the width

of the Gaussian (σ).

$$I_{ij}^{DBS-STN}(t) = \sum_{\beta=1}^{N_{cp}^x} \mathcal{M}_{\beta}(t) * P_y(t) * e^{-\frac{[(i-i_c)^2 + (j-j_c)^2]}{\sigma_{DBS-STN}^2}} \quad (28)$$

where, $I_{ij}^{DBS-STN}(t)$ is the DBS current received by STN neuron at position (i, j) considering lattice position (i_c, j_c) as the electrode contact point at time t , $\mathcal{M}_{\beta}(t)$ is the indicator function which controls the activation of stimulation site β , N_{cp}^x is the number of activated stimulation contact points for different stimulation configurations $x = [SCP, FCP, MCP]$ ($N_{cp}^{SCP} = 1$, $N_{cp}^{FCP} = 4$, $N_{cp}^{MCP} = \text{Number of neurons in simulated network} - 1024$), $P_y(t)$ is the current pulse at time t for $y = [MP, BP]$, $\sigma_{DBS-STN}$ is used to control the spread of stimulus current in STN network.

DBS was implemented in the proposed excitotoxicity model by the following criterion,

$$I_{ij}^{DBS-STN}(N_{sc}, t) = \begin{cases} 0, & N_{sc}(t) > N_i \\ I_{ij}^{DBS-STN}(t), & N_{sc}(t) \leq N_i \end{cases} \quad (29)$$

where, $I_{ij}^{DBS-STN}(t)$ is the instantaneous change in the stimulation current to STN neuron at position (i, j) based on the number of surviving SNc neurons at time t , $N_{sc}(t)$ is the instantaneous number of surviving SNc neurons, N_i is the number representing SNc cell loss at which therapeutic intervention was employed.

2.7.5. Antidromic Activation

The mechanism of how DBS alleviates advanced PD symptoms is not precise. One of the theories behind the therapeutic effect of DBS is activation of afferent connections of STN which results in antidromic activation of cortical, GPi or GPe neurons (Lee et al., 2004; McIntyre et al., 2004; Hammond et al., 2008; Montgomery and Gale, 2008; Kang and Lowery, 2014; Chiken and Nambu, 2015). In our study, we implemented the antidromic activation of GPe during DBS therapy. Antidromic activation was implemented similarly to Mandali and Chakravarthy (2016), where a percentage of DBS current given to STN neurons were given directly to GPe neurons. Similar to DBS applied to STN, external stimulation current was given to GPe neuron in the form of Gaussian distribution. The specifications of antidromic activation were described by the following equation,

$$I_{ij}^{DBS-GPe}(t) = \sum_{\beta=1}^{N_{cp}^x} \mathcal{M}_{\beta}(t) * P_y(t) * e^{-\frac{[(i-i_c)^2 + (j-j_c)^2]}{\sigma_{DBS-GPe}^2}} \quad (30)$$

where, $I_{ij}^{DBS-GPe}(t)$ is the DBS current received by GPe neuron at position (i, j) considering lattice position (i_c, j_c) as the electrode contact point, $\mathcal{M}_{\beta}(t)$ is the indicator function which controls the activation of stimulation site β , N_{cp}^x is the number of activated stimulation contact points for different stimulation configurations $x = [SCP, FCP, MCP]$ ($N_{cp}^{SCP} = 1$, $N_{cp}^{FCP} = 4$, $N_{cp}^{MCP} = \text{Number of neurons in simulated network} - 1024$), $P_y(t)$ is the current pulse at time t for $y = [MP, BP]$, $A_{DBS-GPe}$ is the portion of DBS current pulse amplitude given as antidromic activation to

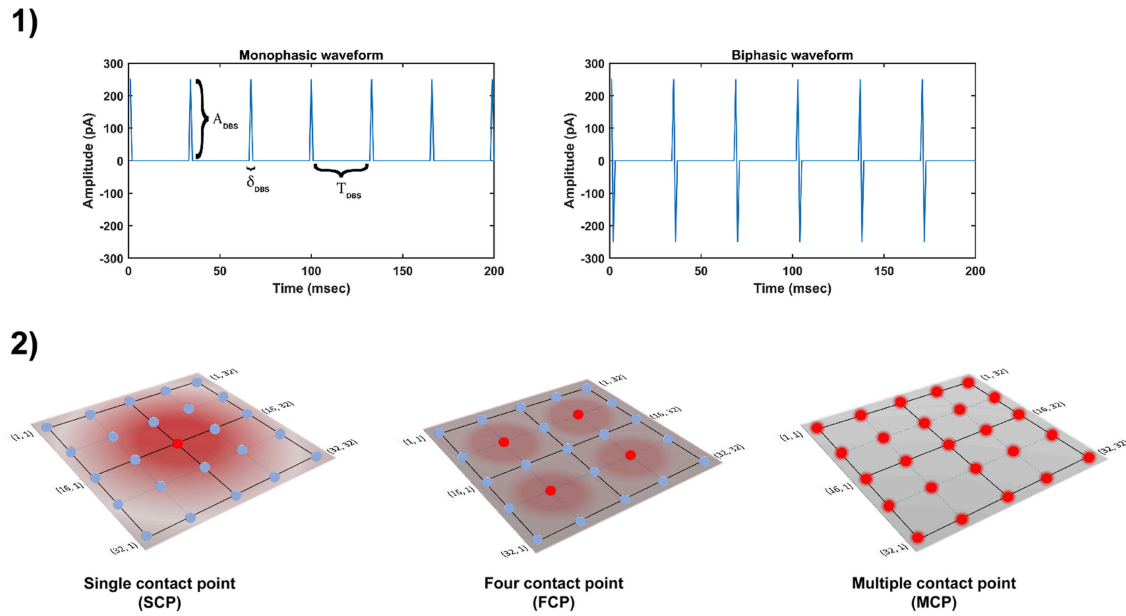


FIGURE 2 | Different DBS protocol used in the study. **(1)** DBS stimulation waveforms. **(2)** DBS stimulation configurations. DBS, Deep Brain Stimulation; A_{DBS} , Amplitude of DBS current pulse; δ_{DBS} , Pulse width of DBS current pulse; $T_{DBS}(1/f_{DBS})$, frequency of DBS current pulse; SCP, Single Contact Point; FCP, Four Contact Point; MCP, Multiple Contact Point.

GPe neurons, $\sigma_{DBS-GPe}$ is used to control the spread of stimulus current in GPe ensemble.

The DBS therapy with antidromic activation was implemented in the proposed excitotoxicity model by the following criterion,

$$I_{ij}^{DBS-STN}(N_{sc}, t) = \begin{cases} 0, & N_{sc}(t) > N_i \\ I_{ij}^{DBS-STN-AA}(t), & N_{sc}(t) \leq N_i \end{cases} \quad (31)$$

$$I_{ij}^{DBS-GPe}(N_{sc}, t) = \begin{cases} 0, & N_{sc}(t) > N_i \\ I_{ij}^{DBS-GPe}(t), & N_{sc}(t) \leq N_i \end{cases} \quad (32)$$

where, $I_{ij}^{DBS-STN-AA}(t)$ is the DBS current received by STN neuron at position (i, j) considering lattice position (i_c, j_c) as the electrode contact point with antidromic activation ($A_{DBS-GPe} = Per_{AA} * A_{DBS-STN}$; $A'_{DBS-STN} = (1 - Per_{AA}) * A_{DBS-STN}$), Per_{AA} is the proportion of $A_{DBS-STN}$ applied as $A_{DBS-GPe}$, $A'_{DBS-STN}$ is the portion of DBS current pulse amplitude given to STN neurons during antidromic activation, $N_{sc}(t)$ is the instantaneous number of surviving SNc neurons, N_i is the number representing SNc cell loss at which therapeutic intervention was employed.

2.7.6. STN Axonal & Synaptic Failures

In-vitro recordings observed depression in the synapse of STN neurons with SNc and is believed to be due to the delivery of continuous high-frequency stimulation pulses (Ledonne et al., 2012). This synaptic depression caused by increased STN activity during DBS arises due to an amalgamation of axonal and synaptic failures in the STN (Shen and Johnson, 2008; Ammari et al., 2011;

Moran et al., 2011, 2012; Zheng et al., 2011; Carron et al., 2013; Rosenbaum et al., 2014).

The effect of synaptic depression due to DBS of the STN was implemented by the following criterion,

$$W_{STN \rightarrow SNc}(s_{DBS}, t) = \begin{cases} W_{STN \rightarrow SNc}, & s_{DBS} = OFF \\ W_{STN \rightarrow SNc} * W_{ASF}(Per_{ASF}), & s_{DBS} = ON \end{cases} \quad (33)$$

where, $W_{STN \rightarrow SNc}(s_{DBS}, t)$ is the instantaneous change in synaptic weight of STN to SNc based $s_{DBS} = \{ON, OFF\}$, s_{DBS} is DBS stimulation, W_{ASF} is the weight matrix based on the percentage of axonal and synaptic failures (Per_{ASF}).

$$W_{STN \rightarrow GPe}(s_{DBS}, t) = \begin{cases} W_{STN \rightarrow GPe}, & s_{DBS} = OFF \\ W_{STN \rightarrow GPe} * W_{ASF}(Per_{ASF}), & s_{DBS} = ON \end{cases} \quad (34)$$

where, $W_{STN \rightarrow GPe}(s_{DBS}, t)$ is the instantaneous change in synaptic weight of STN to GPe based $s_{DBS} = \{ON, OFF\}$, s_{DBS} is DBS stimulation, W_{ASF} is the weight matrix based on the percentage of axonal and synaptic failures (Per_{ASF}).

2.8. Network Analysis

We analyzed the dynamics of the network (STN-GPe-SNc) by firing frequency (Dayan and Abbott, 2005), network synchrony (Pinsky and Rinzel, 1995) and bursting measures (van Elburg and van Ooyen, 2004). The equations used to compute these measures are described below.

2.8.1. Frequency of Firing

The spike-count firing rate is the measure of the number of action potentials for a given duration of time (Dayan and Abbott, 2005). The instantaneous mean firing rate ($r_{ij}^x(t)$) of a neuron at lattice position (i, j) at time t was calculated with a fixed sliding window Δt (0.1 s) which is similarly to Equations (17), (18). The mean firing rate of the population of neurons is simply the average of instantaneous mean firing rate across the number of neurons and the simulation time.

2.8.2. Synchronization

Neuronal synchronization is the measure of synchronicity (high synchrony - almost all neurons firing at once, low synchrony - least number of neurons firing at once) in the population of neurons within a network (Golomb, 2007). We had quantified the synchrony in the population of neurons at time t by following equation (Pinsky and Rinzel, 1995),

$$R_x(t) = \frac{1}{N * e^{i*\theta(t)}} \sum_{j=1}^N e^{i*\phi_j(t)} \quad (35)$$

$$\phi_j(t) = 2 * \pi * \frac{(T_{j,k} - t_{j,k})}{t_{j,k+1} - t_{j,k}} \quad (36)$$

where, $R_x(t)$ is the instantaneous synchronization measure ($0 \leq R_x(t) \leq 1$), x being GPe or SNc or STN neuron, N is the number of neurons in the network, $\theta(t)$ is the instantaneous average phase of neurons, $\phi_j(t)$ is the instantaneous phase of j th neuron, $t_{j,k}$ and $t_{j,k+1}$ are the spike times of k th and $(k+1)$ th spike of j th neuron, respectively, $T_{j,k} \in [t_{j,k}, t_{j,k+1}]$.

2.8.3. Bursting

If a neuron fires repeatedly with discrete groups of spikes, this dynamic state is termed as burst. Between two bursts, there is a period of quiescence where there will be no spikes. Burst can have two (doublet), three (triplet), four (quadruplet) or many spikes in it (Izhikevich, 2006). We had quantified the bursting of a neuron at lattice position (i, j) across time by following equation (van Elburg and van Ooyen, 2004),

$$B_{i,j} = \frac{2 * Var(t_{i,j,k+1} - t_{i,j,k}) - Var(t_{i,j,k+2} - t_{i,j,k})}{2 * E^2(t_{i,j,k+1} - t_{i,j,k})} \quad (37)$$

where, $B_{i,j}$ is the measure of bursting of a neuron at lattice position (i, j) , Var is the variance of the spike times, E is the expected value (mean) of the spike times, $t_{i,j,k}$, $t_{i,j,k+1}$ and $t_{i,j,k+2}$ are the spike times of k th, $(k+1)$ th and $(k+2)$ th spike of a neuron at lattice position (i, j) , respectively.

3. RESULTS

We have investigated the Izhikevich parameters of STN, SNc and GPe which were chosen from the literature (Michmizos and Nikita, 2011; Cullen and Wong-Lin, 2015; Mandali et al., 2015) for their characteristic firing pattern and other biological properties (Figure 3-1). We then extensively studied the effect

of lateral connections in the network of neurons (Figure 3-2). Next, we have explored the effect of dopamine on the network of GPe, SNc, and STN neurons and compared with published data (Figure 4).

Then, we showed the results of the proposed excitotoxicity model which exhibits STN-mediated excitotoxicity in SNc (Figures 5, 6) and studied their sensitivity to parameter uncertainty (Figure 7). Finally, we have explored current therapeutics such as glutamate inhibition (Figure 8), dopamine restoration (Figure 9), subthalamotomy (Figure 10) and deep brain stimulation (Figures 11, 12) which might have a neuroprotective effect on the progression of SNc cell loss.

3.1. Characteristic Firing of Different Neuronal Types

The firing response of a single neuron to different external current input was characterized for the three different neuronal types involved in the excitotoxicity model (Figure 3-1). In the proposed model, we adjusted I_{ij}^x and other parameters of the Izhikevich model such that the basal firing frequencies of the different neuronal types match with experimental data (Modolo et al., 2007; Tripathy et al., 2014). The adjusted values can be seen in the Table 1.

The SNc neurons experimentally exhibit two distinct firing patterns: low-frequency irregular tonic or background firing (3–8 Hz) and high-frequency regular phasic or burst firing (~20 Hz) (Grace and Bunney, 1984a,b). The Izhikevich parameters which were chosen for SNc neurons configured the model to exhibit both types of firing patterns. Other properties such as doublet-spikes which were occasionally observed experimentally (Grace and Bunney, 1983) were also exhibited (Figure 3-1A). In the present model, SNc neuron basal firing rate were required to be ~4 Hz which is in the range of 3–8 Hz observed experimentally (Grace and Bunney, 1984a). Similar to SNc, STN neurons also exhibit tonic pacemaking firing and phasic high-frequency bursting (Beurrier et al., 1999; Allers et al., 2003). The basal firing rate of STN neurons was required to be ~13 Hz which is in the range of 6–30 Hz observed experimentally (Allers et al., 2003; Lindahl et al., 2013). The STN neurons also exhibit characteristic inhibitory rebound which was observed experimentally (Figure 3-1B) (Hamani et al., 2004; Johnson, 2008). Unlike SNc and STN, GPe neurons exhibit high-frequency tonic firing which was interpreted by bursts and pauses (Kita and Kita, 2011; Hegeman et al., 2016). The Izhikevich parameters which were chosen for GPe neurons were able to exhibit high-frequency firing without any bursts (Figure 3-1C). The basal firing rate of GPe neurons was required to be ~30 Hz which is in the range of 17–52 Hz observed experimentally (Lindahl et al., 2013).

3.2. Behavior Regimes With Varying Collateral Strength and Radius

We now study the network dynamics of each of the three neuronal types in a 2D array with lateral connections. The effect of network structural properties such as the strength and

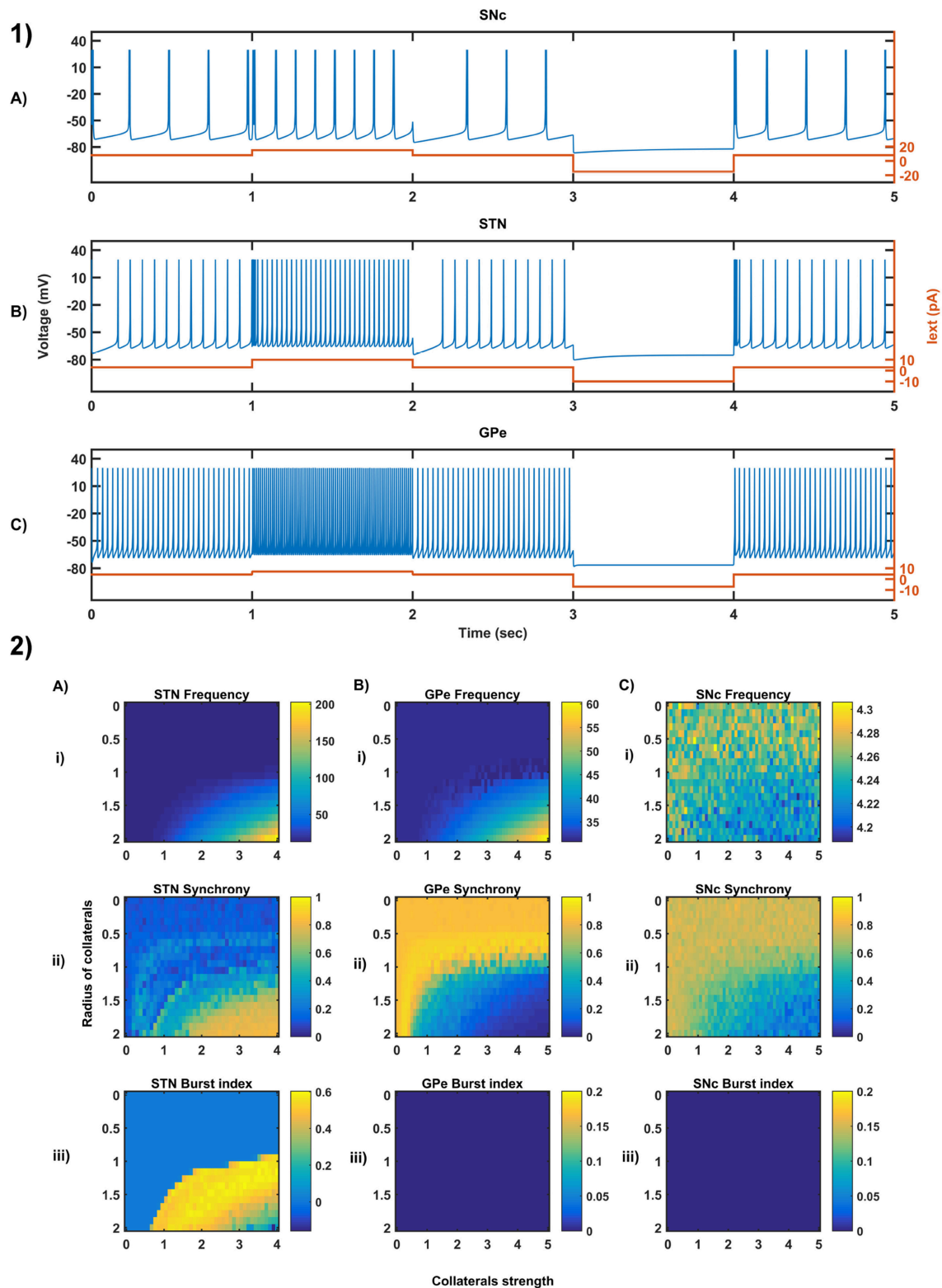


FIGURE 3 | Characteristic behavior in the single-neuron and the population of neurons of different neuronal types. **(1)** Characteristics firing patterns of SNc **(A)**, STN **(B)**, and GPe **(C)** for varying external currents (orange line - current in picoAmpere (pA)). **(2)** The response of STN **(A)**, GPe **(B)**, and SNc **(C)** populations for varying lateral connection strength (A_x) and radius (R_x) at the level of network properties [Frequency **(i)**, Synchrony **(ii)**, Burst Index **(iii)**]. I_{ext} , External current applied; STN, SubThalamic Nucleus; SNc, Substantia Nigra pars compacta; GPe, Globus Pallidus externa.

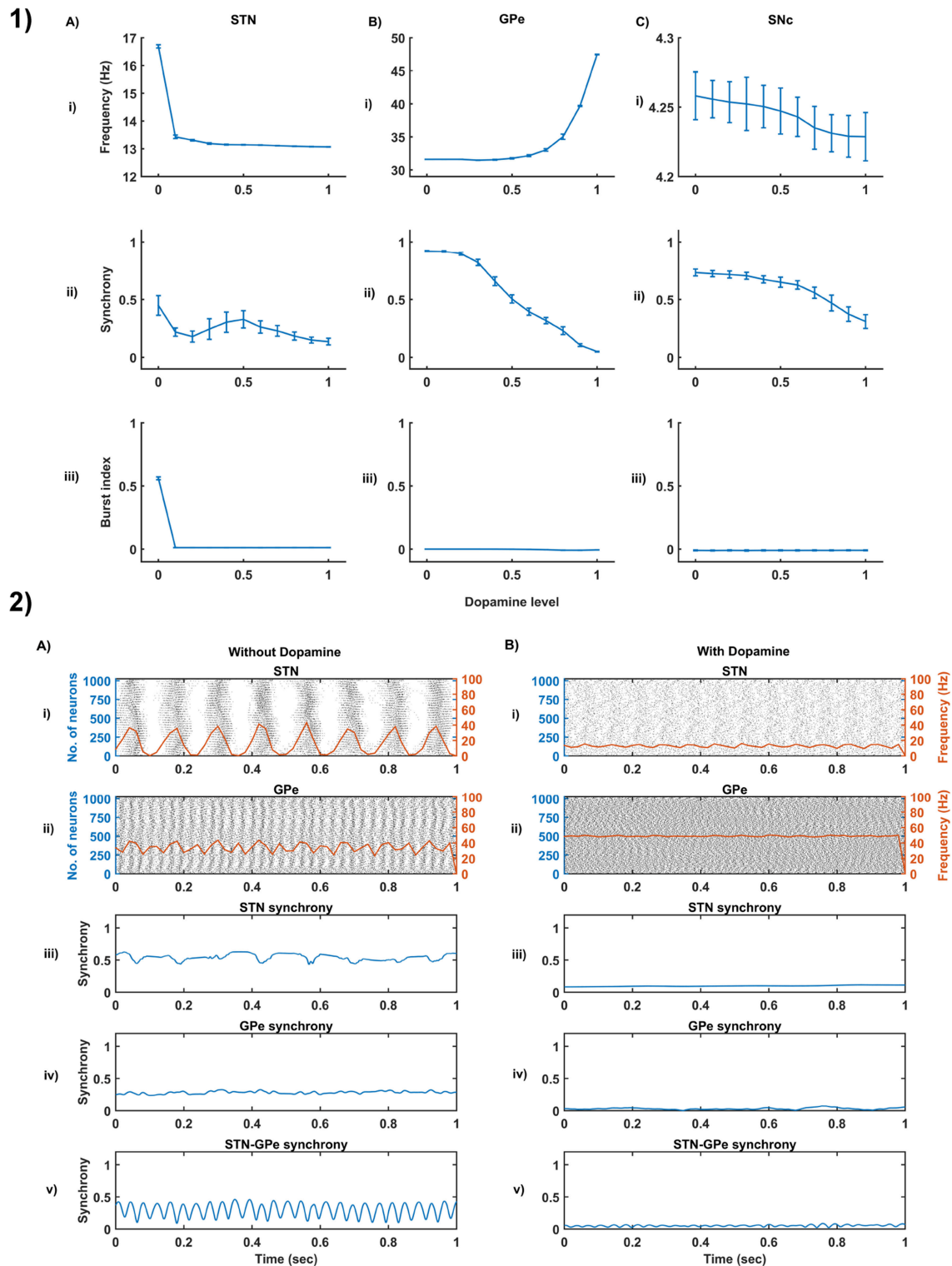


FIGURE 4 | Dopamine effect on the basal activity of different neuronal types. **(1)** The response of STN **(A)**, GPe **(B)**, and SNc **(C)** populations for varying dopamine levels at the level of network properties [Frequency **(i)**, Synchrony **(ii)**, and Burst Index **(iii)**]. **(2)** The response of STN-GPe network without **(A)** & with **(B)** dopamine - Raster plots of STN **(i)** & GPe **(ii)** populations overlaid with spike-count firing rate (orange line), Synchrony plots of STN **(iii)**, GPe **(iv)**, and combined STN-GPe **(v)**. STN, SubThalamic Nucleus; SNc, Substantia Nigra pars compacta; GPe, Globus Pallidus externa.

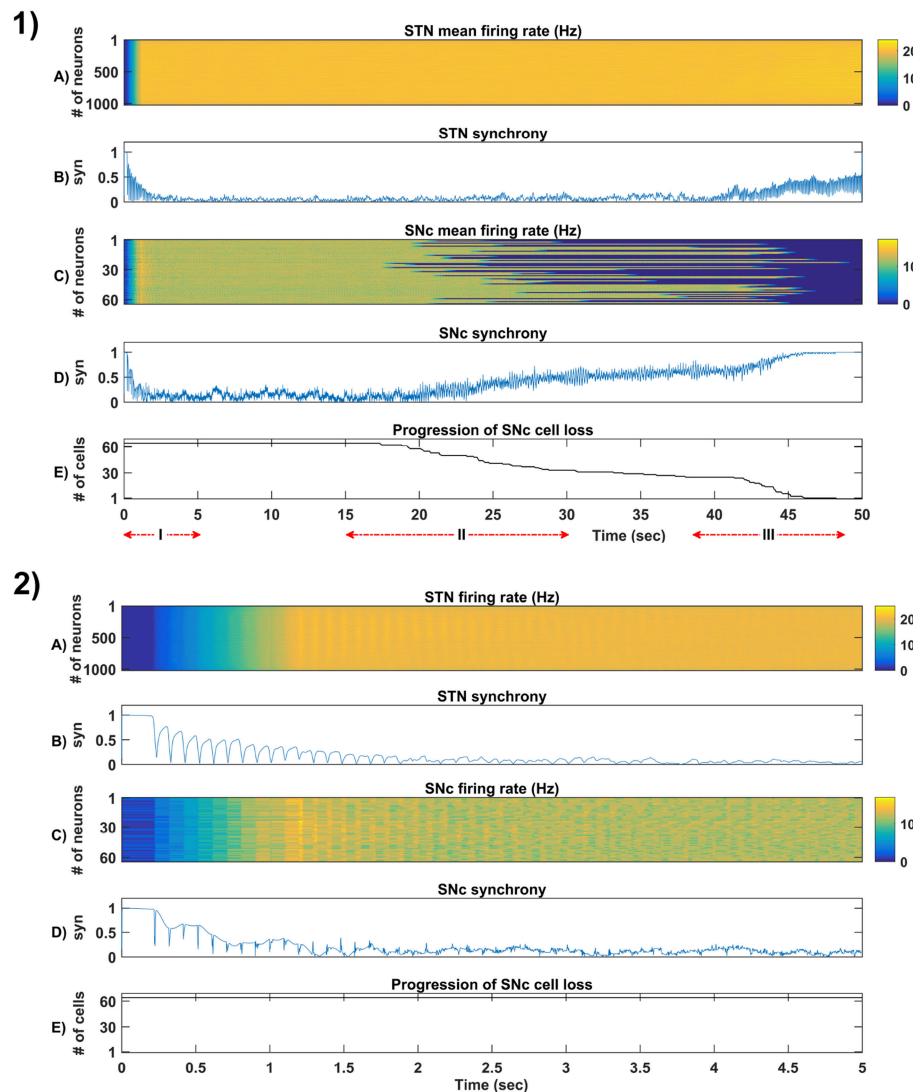


FIGURE 5 | Simulation plots of whole and step-wise mechanism (I) of the proposed excitotoxicity model. **(1)** Whole 50 sec simulation plots of the proposed excitotoxicity model. **(2)** Part-I of **(1)** Simulation plots of STN-SNc loop dynamics - Mean firing rate (1 s) of STN **(A)** & SNc **(C)**, Synchrony (syn) of STN **(B)** & SNc **(D)**, Progression of SNc cell loss **(E)**. STN, SubThalamic Nucleus; SNc, Substantia Nigra pars compacta; GPe, Globus Pallidus externa.

neighborhood size of the lateral connections on the network functional properties such as average firing rate, network synchrony, and burst index was studied (Figure 3-2). The suitable values of lateral connection strength and radius for each neuronal type were chosen in correlation with experimental data (Humphries et al., 2006; Tepper and Lee, 2007). The selected values can be seen in the Table 1. As specified above, I_{ij}^x , A_x and R_x was adjusted such that the basal population activity correlated well with the experimental data (Humphries et al., 2006; Tepper and Lee, 2007).

The network dynamics of STN plays a vital role in the proposed model of excitotoxicity, in this scenario we have studied the role of lateral connections in regulating STN network properties. The basal STN population activity without lateral connections showed regular spiking without any bursting type

of behavior. Contrarily, the basal STN population activity with lateral connections showed the bursting type of activity (not shown here).

3.3. Dopamine Effect on the Basal Activity of Different Neuronal Populations

From the simulated results, it is clear that as DA level increases the mean firing rate decreases in STN, increases in GPe and decreases in SNc (Figure 4-1). The network synchrony decreases in all neuronal populations as DA levels increases. However, in the case of STN, the decrease is not monotonic (Figure 4-1Aii) where high synchrony was observed at moderate levels of DA, with synchrony falling on either side. This high synchronicity at moderate levels of DA is a result of the change in firing pattern from asynchronous bursting to synchronous spiking

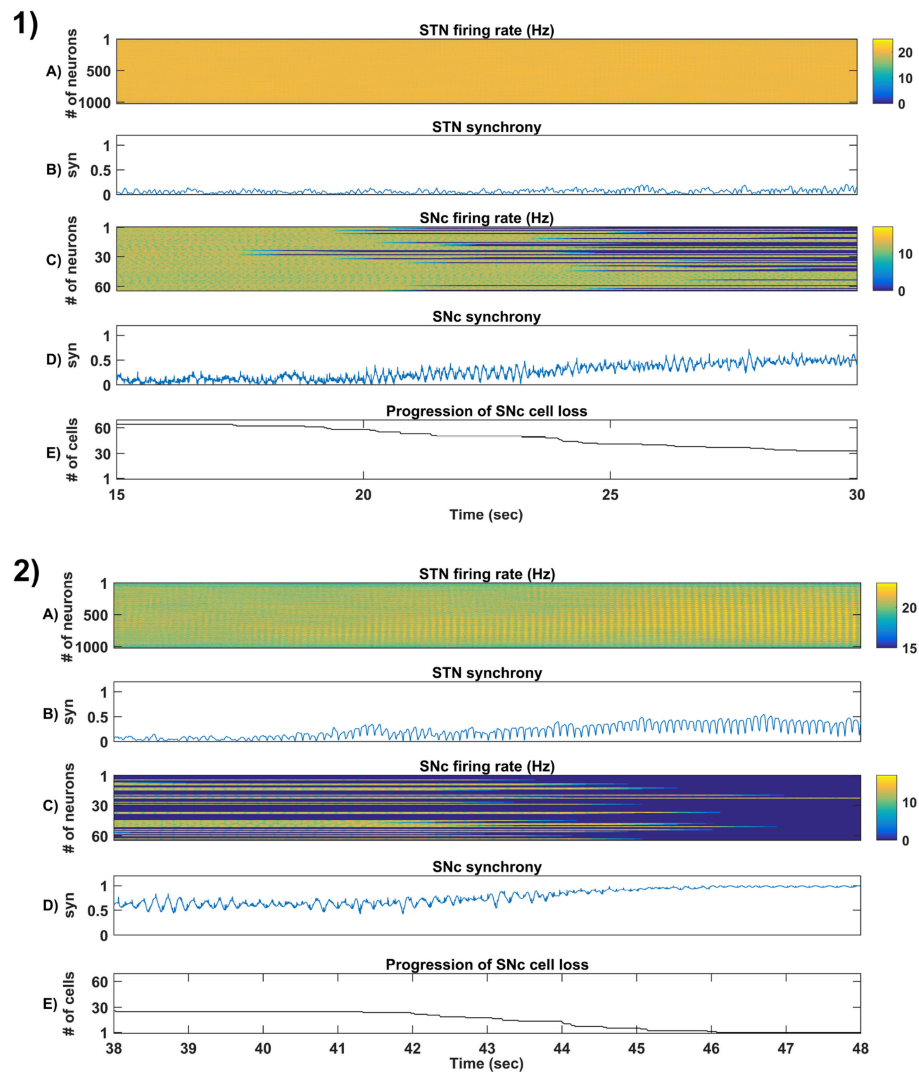


FIGURE 6 | Simulation plots of step-wise mechanisms (II, III) of the proposed excitotoxicity model. **(1)** Part-II of (**Figure 5-1**) Stress-induced neurodegeneration in SNc. **(2)** Part-III of (**Figure 5-1**) STN-mediated runaway effect of neurodegeneration in SNc - Mean firing rate (1 s) of STN (**A**) & SNc (**C**), Synchrony (syn) of STN (**B**) & SNc (**D**), Progression of SNc cell loss (**E**). STN, SubThalamic Nucleus; SNc, Substantia Nigra pars compacta; GPe, Globus Pallidus externa.

which can be correlated with burst index (**Figure 4-1Aiii**) in STN population. In the dopamine-depleted condition, STN shows the bursting type of firing pattern which was exhibited by our model consistent with published studies (Vila et al., 2000; Ammari et al., 2011; Park et al., 2015). The following trend of STN activity was observed when DA level increases from 0 to 1: synchronous bursting, asynchronous bursting, synchronous spiking and asynchronous spiking. At very low DA levels (0–0.1), the STN exhibits regular bursting (**Figure 4-1Aiii**) with high synchrony (**Figure 4-1Aii**). At low DA levels (0.1–0.3), the STN exhibits an irregular mixed mode of bursting and singlet-spiking with low synchrony (**Figure 4-1Aii**). At moderate DA levels (0.3–0.7), the STN exhibits regular singlet-spiking (**Figure 4-1Aiii**) with high synchrony (**Figure 4-1Aii**). Moreover, at high DA levels (0.7–1), the STN exhibits irregular singlet-spiking with low synchrony (**Figure 4-1Aii**).

STN-GPe dynamics is known to play an important role in PD pathological oscillations that are thought to be strongly related to the cardinal symptoms of PD (Bergman et al., 1994; Brown, 2003; Litvak et al., 2011; Park et al., 2011). Numerous computational models were developed to explain the pathological oscillations in STN-GPe (Terman et al., 2002; Pavlides et al., 2015; Shouno et al., 2017). The connectivity pattern between STN and GPe was explored by using a conductance-based model (Terman et al., 2002) which exhibited different rhythmic behaviors. In our model, the connectivity pattern between STN and GPe was considered to be dopamine-dependent (Cragg et al., 2004; Mandali et al., 2015) and spontaneous activity of the STN-GPe network was studied with no external input current. Under normal DA conditions, low synchrony and minimal oscillations were exhibited by the STN-GPe network (**Figure 4-2B**) (Kang and Lowery, 2013).

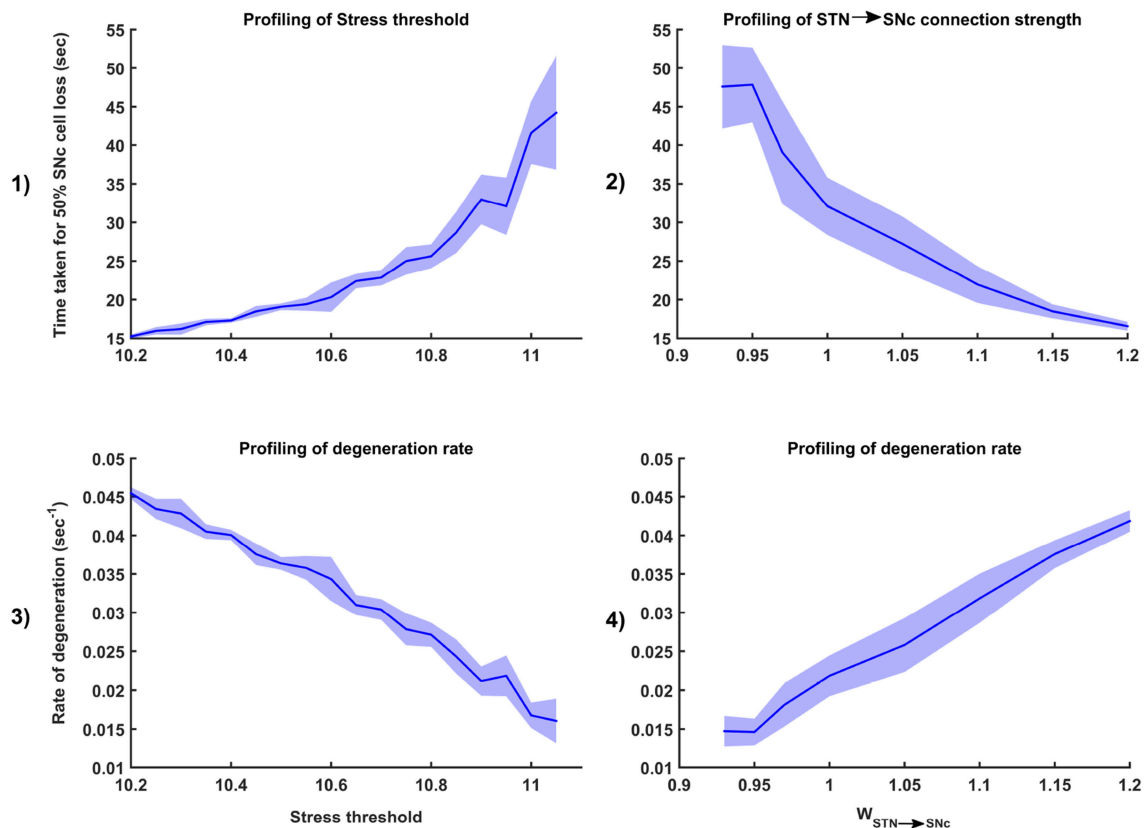


FIGURE 7 | Sensitivity of the proposed model toward parameter uncertainty. Time taken for 50% SNc cell loss for varying stress threshold (Q_{thres}) (1) and connection strength from STN→SNc ($W_{STN \rightarrow SNc}$) (2). Rate of degeneration (λ) for varying stress threshold (Q_{thres}) (3) and connection strength from STN→SNc ($W_{STN \rightarrow SNc}$) (4). STN, SubThalamic Nucleus; SNc, Substantia Nigra pars compacta.

It was reported that dopamine-depleted condition results in pathological oscillations in STN characterized by high synchrony and beta range oscillations (Brown et al., 2001; Weinberger et al., 2006; Park et al., 2010, 2011; Lintas et al., 2012; Kang and Lowery, 2013; Pavlides et al., 2015). In our model during dopamine-depleted conditions, high synchrony and the higher rate of oscillations were exhibited in the STN-GPe network, and beta range oscillations were also observed in STN population (Figure 4-2A).

3.4. STN-Induced Excitotoxicity in SNc

The proposed excitotoxicity model was able to exhibit STN-mediated excitotoxicity in SNc which was precipitated by energy deficiency (Albin and Greenamyre, 1992; Beal et al., 1993; Greene and Greenamyre, 1996; Rodriguez et al., 1998; Blandini, 2001, 2010; Ambrosi et al., 2014) (Figures 5, 6). For a more detailed explanation of the excitotoxicity results obtained, we have sub-divided 50 s simulation into three parts - (I) STN-SNc loop dynamics (normal condition), (II) Stress-induced neurodegeneration in SNc (pre-symptomatic PD condition), and (III) STN-mediated runaway effect of neurodegeneration in SNc (symptomatic PD condition).

3.4.1. (I) STN-SNc Loop Dynamics

In the first part of the simulation, connectivity between STN and SNc were introduced at $t = 0$, and the model exhibited decreased synchrony in STN and SNc over time (Figure 5-2B). The results showed the pivotal role of dopamine in modulating STN activity (Cragg et al., 2004; Lintas et al., 2012; Yang et al., 2016). The excitatory drive from STN to SNc results in decreased synchrony in SNc due to increased inhibitory drive from lateral connections (Figure 5-2D). During this whole process, the stress threshold ($Q_{thres} = 11.3$) was fixed, and there was no SNc cell loss due to stress (Figure 5-2E).

3.4.2. (II) Stress-Induced Neurodegeneration in SNc

In the second part of the simulation, stress threshold was slightly reduced from $Q_{thres} = 11.3$ to $Q_{thres} = 10.8$ at $t = 10$ s to replicate PD-like condition in the model where stress-induced neurodegeneration gets initiated. The model exhibited stress-induced neurodegeneration in SNc where SNc cells start dying when stress variable (Q_{ij}^x) exceeds the stress threshold (Q_{thres}) which acts like an apoptotic threshold (Figure 6-1E). It was observed that there was no increased synchrony in the STN population as a result of SNc cell loss (Figure 6-1B). However, there was increased synchrony

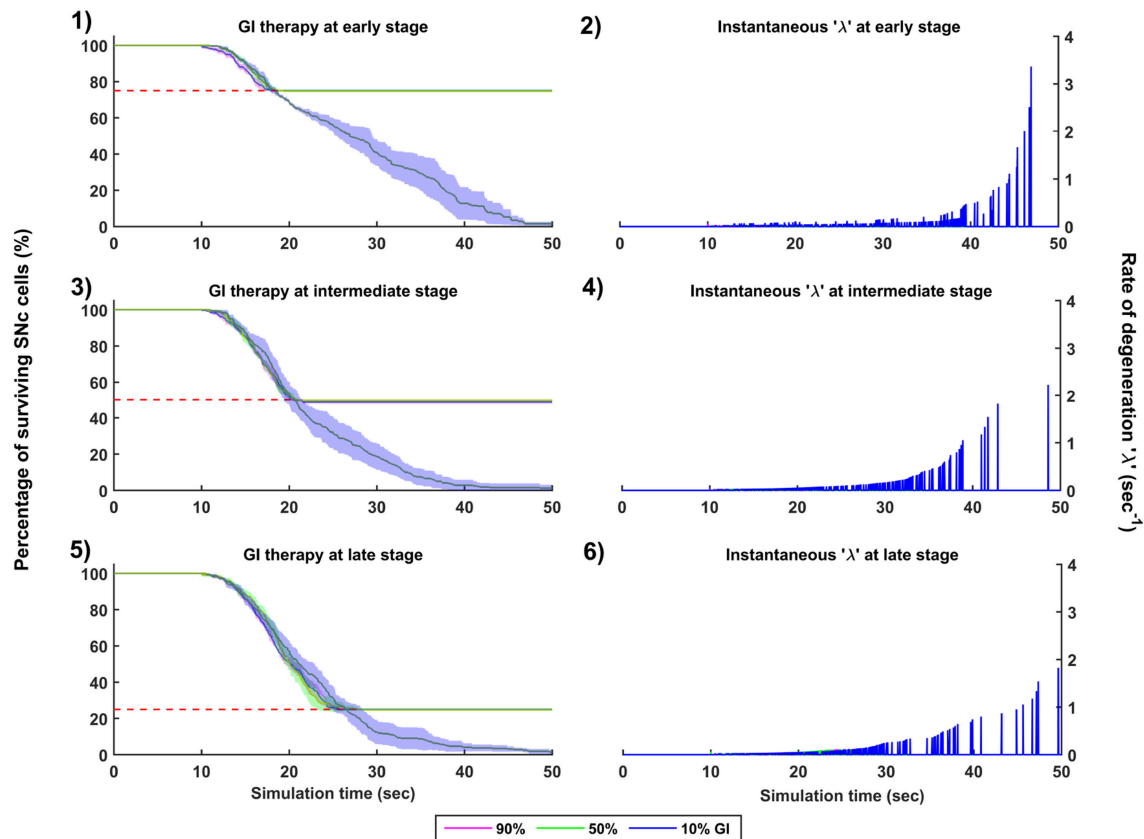


FIGURE 8 | Simulation plots for Glutamate Inhibition (GI) therapy. Progression of SNc cell loss for 90, 50, and 10% GI at early (25%) (1), intermediate (50%) (3) and late (75%) (5) stages of SNc cell loss. Instantaneous rate of degeneration (λ) for 90, 50, and 10% GI at early (25%) (2), intermediate (50%) (4) and late (75%) (6) stages of SNc cell loss. SNc, Substantia Nigra pars compacta.

in the SNc population (Figure 6-1D) which might be due to reduced inhibitory drive from lateral connections as a result of SNc cell loss.

3.4.3. (III) STN-Mediated Runaway Effect of Neurodegeneration in SNc

In the third part of the simulation, no parameters were changed, but after $t = 40$ s, there was a rise in STN synchrony as a result of stress-induced SNc cell loss (Figure 6-2). A substantial amount of SNc cell loss (more than 50%) resulted in increased synchrony (Figure 6-2B) and firing rates (Figure 6-2A) of the STN population. As the STN synchrony increased, runaway effect kicks in where increased STN excitatory drive to SNc cells result in hastening the stress-induced neurodegeneration of remaining SNc cells (Figure 6-2E).

3.5. Sensitivity of Excitotoxicity Model Toward Parameter Uncertainty

To check the sensitivity of excitotoxicity model for different parametric values, we have considered two factors which can maximally influence the output results. Firstly, stress threshold (Q_{thres}) which is analogous to the apoptotic

threshold and is assumed to be dependent on the amount of available energy to the cell (Albin and Greenamyre, 1992; Greene and Greenamyre, 1996). Secondly, the synaptic weight between STN and SNc ($W_{STN \rightarrow SNc}$) which is analogous to synaptic modification and is assumed to be modulated by the excitatory drive from STN to SNc (Hasselmo, 1994, 1997).

3.5.1. Stress Threshold (Q_{thres})

Simulation results showed that the time taken for 50% SNc cell loss ($t_{1/2}$) increases as the stress threshold increases (Figure 7-1). The rate of degeneration or degeneration constant (λ) is the ratio of the number of SNc cells that degenerate in a given period of time compared with the total number of SNc cells present at the beginning of that period. The rate of degeneration (λ) decreases as the stress threshold increases (Figure 7-3). These results show the importance of stress threshold in regulating excitotoxic damage to SNc and also support the idea of “weak excitotoxicity hypothesis” where SNc cells showed increased susceptibility to glutamate due to impaired cellular energy metabolism (Albin and Greenamyre, 1992; Greene and Greenamyre, 1996).

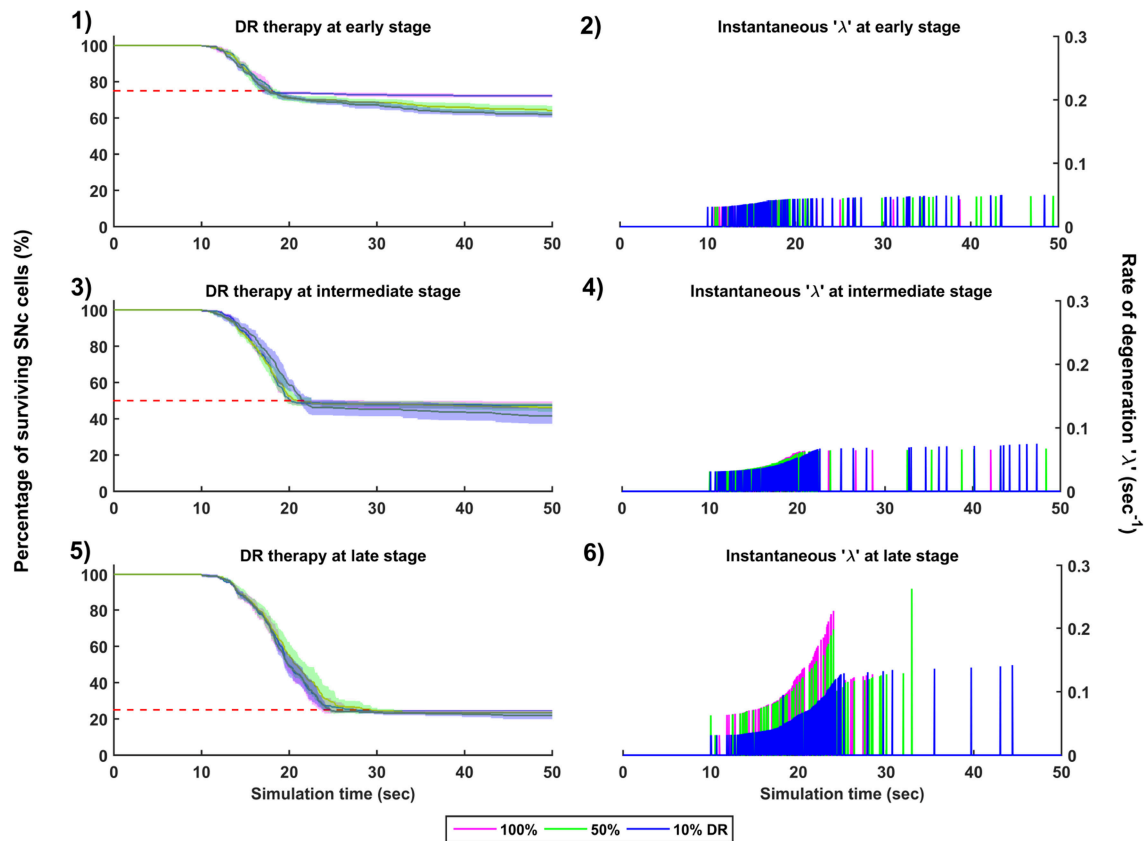


FIGURE 9 | Simulation plots for Dopamine Restoration (DR) therapy. Progression of SNc cell loss for 100, 50, and 10% DR at early (25%) (1), intermediate (50%) (3) and late (75%) (5) stages of SNc cell loss. Instantaneous rate of degeneration (λ) for 100, 50, and 10% DR at early (25%) (2), intermediate (50%) (4) and late (75%) (6) stages of SNc cell loss. SNc, Substantia Nigra pars compacta.

3.5.2. STN-SNc Synaptic Weight ($W_{STN \rightarrow SNc}$)

Simulation results showed that time taken for 50% SNc cell loss ($t_{1/2}$) decreases as the STN-SNc synaptic weight increases (Figure 7-2). The rate of degeneration (λ) increases as the STN-SNc synaptic weight increases (Figure 7-4). These results show the extent of STN influence in the causation of excitotoxicity in SNc. They also support the notion that STN-mediated excitotoxicity might play a major role in SNc cell loss in PD condition (Rodriguez et al., 1998; Blandini, 2001, 2010; Ambrosi et al., 2014).

3.6. Strategies for Neuroprotection of SNc

We now extend the proposed excitotoxic model to study the effect of various therapeutic interventions on the progression of SNc cell loss. The following three types of interventions which were simulated: (1) drugs, (2) surgical interventions, and (3) Deep Brain Stimulation (DBS).

3.6.1. Glutamate Inhibition Therapy

The effect of glutamate agonists and antagonists on the progression of SNc cell loss was implemented in the manner specified in the methods section. The onset of glutamate therapy at different stages of SNc cell loss showed that cell loss was

delayed or halted (Figure 8). For the glutamate therapy which is initiated at 25, 50, and 75% SNc cell loss, the progression of SNc cell loss was halted when the percentage of glutamate inhibition administrated was above 50%. As the glutamate dosage increases the progression of SNc cell loss delays and after a particular dosage of glutamate inhibitors the SNc cell loss halts. There was no change in the course of SNc cell loss for low levels of glutamate inhibition (Figures 8-1, 8-3, 8-5). The peak of the instantaneous rate of degeneration decreases as the therapeutic intervention is delayed in the case of 10% glutamate inhibition (Figures 8-2, 8-4, 8-6).

3.6.2. Dopamine Restoration Therapy

The effect of dopamine agonists on the progression of SNc cell loss was also implemented in the manner specified in the methods section. The onset of dopamine agonist therapy at different stages of SNc cell loss showed that the progression of cell loss was only delayed (Figure 9). For the dopamine agonists therapy which is initiated at 25, 50, and 75% SNc cell loss, the progression of SNc cell loss was delayed when the percentage of dopamine restoration was a mere 10%. The neuroprotective effect of dopamine agonist therapy is dependent on the level of restoration of dopamine tone on the STN.

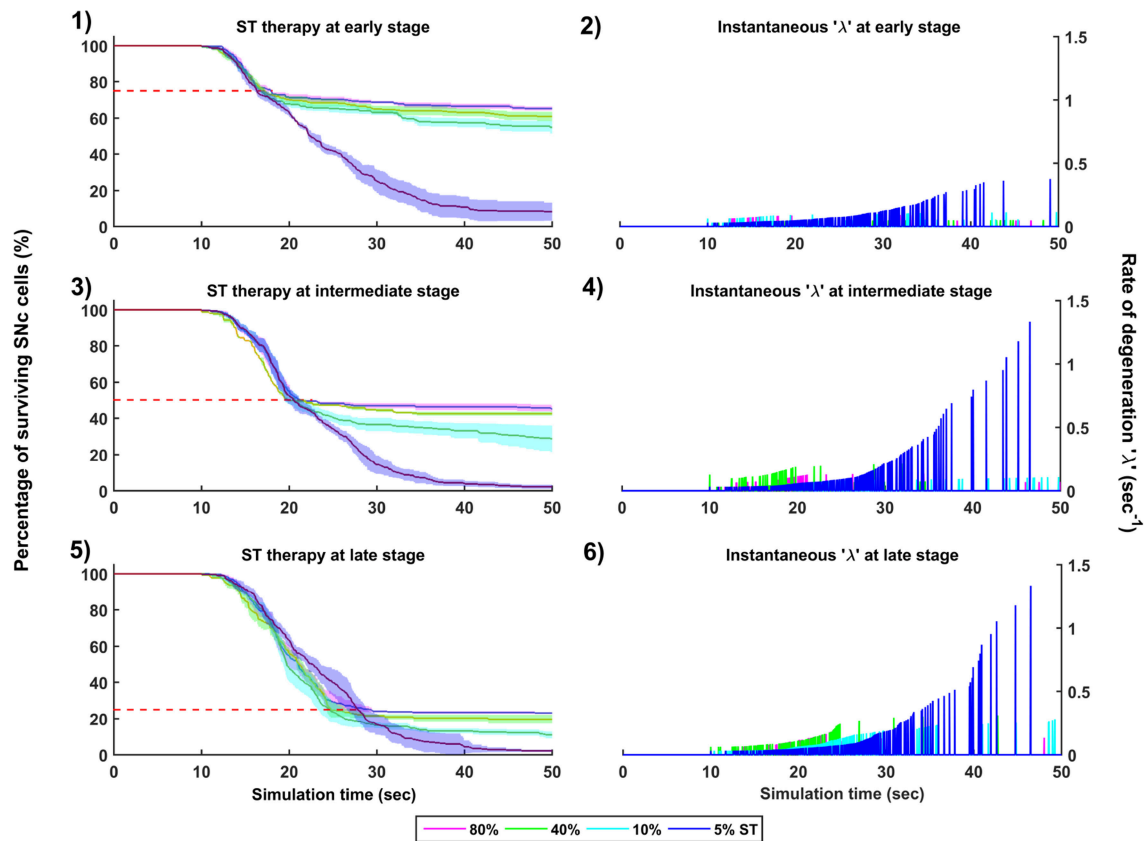


FIGURE 10 | Simulation plots for Subthalamic Tomotomy (ST) therapy. Progression of SNc cell loss for 80, 40, 10, and 5% ST at early (25%) (1), intermediate (50%) (3) and late (75%) (5) stages of SNc cell loss. Instantaneous rate of degeneration (λ) for 80, 40, 10, and 5% ST at early (25%) (2), intermediate (50%) (4) and late (75%) (6) stages of SNc cell loss. SNc, Substantia Nigra pars compacta.

In other words, as the dopamine content in STN increases, the progression of SNc cell loss delays. Unlike glutamate inhibition, the progression of SNc cell loss was not halted even at 100% dopamine restored in all the case of intervention (Figures 9-1, 9-3, 9-5). The dopamine restoration therapy did not have much effect on the instantaneous rate of degeneration (Figures 9-2, 9-4, 9-6).

3.6.3. Subthalamotomy

The effect of subthalamotomy on the progression of SNc cell loss was implemented in a way described in the methods section. The onset of STN ablation therapy at different stages of SNc cell loss showed that progression of cell loss was delayed or halted (Figure 10). The neuroprotective effect of subthalamotomy is dependent on the proportion of lesioning of STN population. In other words, as the proportion of STN lesioning increases the progression of SNc cell loss delays and halts only when almost all of the STN population is lesioned (Figures 10-1, 10-3, 10-5). The progression of SNc cell loss is halted only at 100% STN lesioning in all cases of intervention (not shown here). However, as the proportion of STN lesioning decreases, the rate of degeneration increases. Similarly to dopamine restoration therapy, subthalamotomy also did not

have much effect on the instantaneous rate of degeneration (Figures 10-2, 10-4, 10-6).

3.6.4. Deep Brain Stimulation of STN

The effect of deep brain stimulation on the progression of SNc cell loss was implemented in the way described in the methods section. Along with the stimulation of STN, the inhibitory drive to STN through the afferent connections as result of antidromic activation of the GPe population and the synaptic depression in STN as result of increased axonal and synaptic failures in STN were incorporated in the model.

As specified earlier, different stimulation configurations and stimulus waveforms were implemented while exploring the optimal DBS parameters for therapeutic benefits. The STN population response for different types of DBS protocol was simulated. To study the neuroprotective effect, stimulation parameters which reduce the STN overactivity (Meissner et al., 2005) during dopamine depletion condition were chosen (Table 2). The biphasic stimulus pulse shows more therapeutic benefits than monophasic stimulus pulse; biphasic current alleviates the STN pathological activity without increasing the firing rate of STN population as a whole. The four-contact point type of stimulation configuration required lesser stimulus

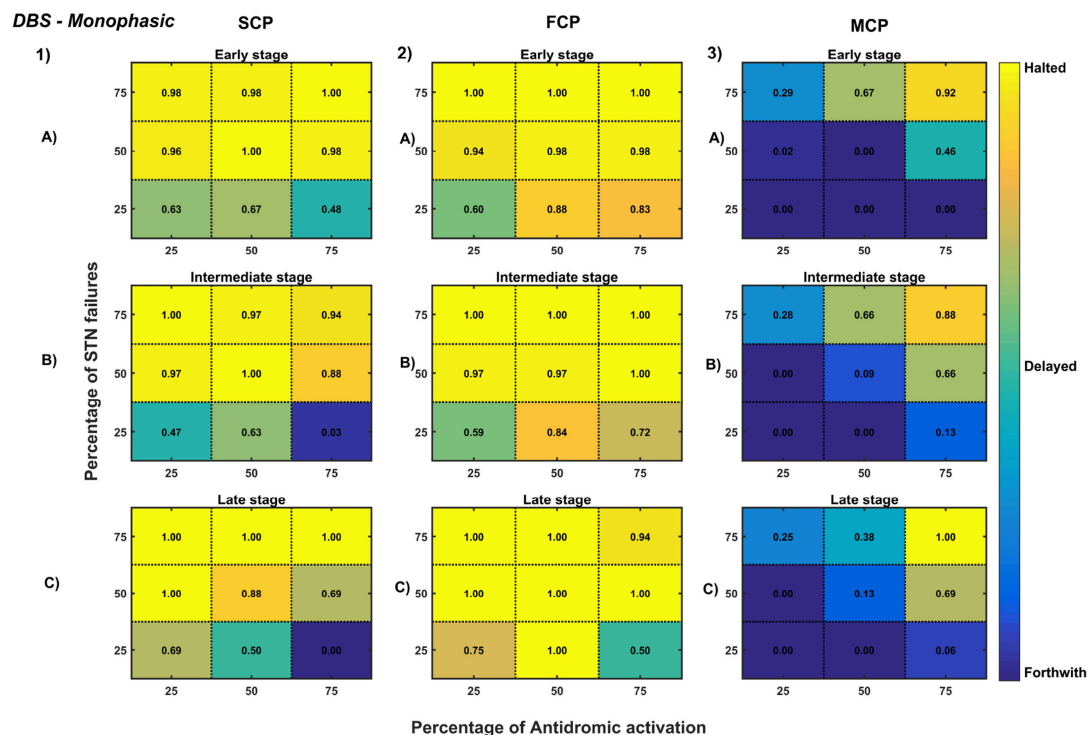


FIGURE 11 | Simulation plots for Monophasic DBS therapy. Profiling of monophasic stimulus waveform for different stimulation configuration in order to achieve the maximal neuroprotective effect of DBS. Confusion matrices for SCP (1), FCP (2), and MCP (3) configurations showing survival ratios of SNc cells for different percentage activation of antidromic activation and STN axonal & synaptic failures at early (25%) (A), intermediate (50%) (B) and late (75%) (C) stages of SNc cell loss. Ratios around 0 is indicated as forthwith (indigo), ratios around 0.5 is indicated as delayed (light green), and ratios around 1 is indicated as halted (yellow). DBS, Deep Brain Stimulation; SNc, Substantia Nigra pars compacta; STN, SubThalamic Nucleus; SCP, Single Contact Point; FCP, Four Contact Point; MCP, Multiple Contact Point.

amplitude for producing the same effect when compared with the other two configurations. From these studies, we can say that four-contact point configuration with biphasic stimulus pulse gives maximum therapeutic benefits from the neuroprotective point of view.

To understand the neuroprotective therapeutic mechanism of DBS in PD (Benazzouz et al., 2000; Maesawa et al., 2004; Wallace et al., 2007; Spieles-Engemann et al., 2010; Musacchio et al., 2017), we have investigated some of the prominent hypotheses regarding the therapeutic effect of DBS viz., (1) excitation hypothesis, (2) inhibition hypothesis and most recent one (3) disruptive hypothesis (McIntyre et al., 2004; Chiken and Nambu, 2015).

The excitation hypothesis was implemented by direct stimulation of the STN population in the proposed excitotoxicity model. The simulation results show that DBS to STN diminishes the pathological synchronized activity but in turn increases the firing rate of the STN population which was not apt for neuroprotection. Next, we have implemented the inhibition hypothesis where antidromic activation of GPe neurons during STN-DBS is highlighted, thereby increasing the inhibitory drive to STN (Mandali and Chakravarthy, 2016). In this scenario also, the inhibitory drive from GPe was not sufficient

to produce comprehensive neuroprotection (Figures 11, 12). On average FCP stimulus configuration produced better neuroprotective effect compared to other two configurations in both monophasic and biphasic current (Figures 11-2, 12-2). Moreover, MCP stimulus configuration results in worsening the disease progression by hastening the SNc cell loss in monophasic stimulus (Figure 11-3), but in biphasic stimulus, neuroprotection increased with higher levels of antidromic activation in all stages of therapeutic intervention (Figure 12-3).

Finally, the disruptive hypothesis was implemented by increasing the proportion of axonal and synaptic failures in STN population (Rosenbaum et al., 2014). From simulation results, it was observed that the progression of SNc cell loss was delayed or halted as the percentage of STN axonal and synaptic failures increased (Figures 11, 12). On average FCP stimulus configuration produced better neuroprotective effect compared to other two configurations in both monophasic and biphasic currents (Figures 11-2, 12-2). For the higher percentage of STN axonal and synaptic failures also, the neuroprotective effect was not pronounced in monophasic MCP DBS setting (Figure 11-3), but in biphasic MCP DBS setting neuroprotection increased with the higher percentage of STN axonal and synaptic failures (Figure 12-3).

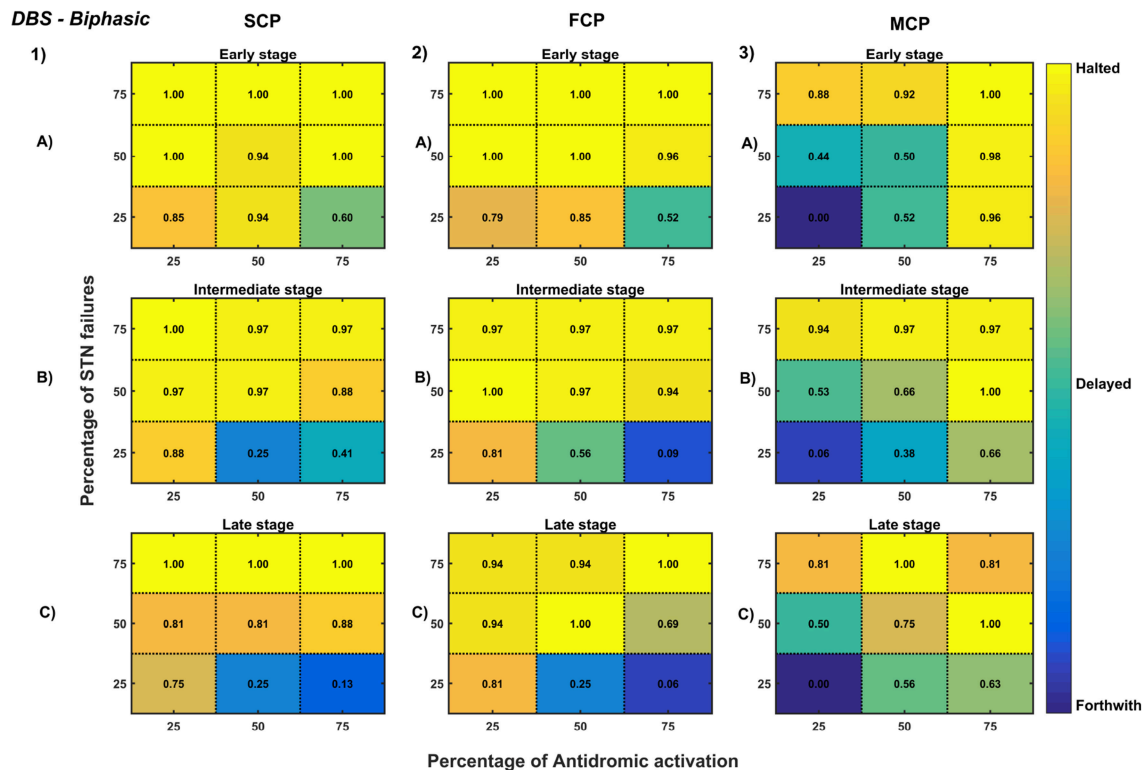


FIGURE 12 | Simulation plots for Biphasic DBS therapy. Profiling of biphasic stimulus waveform for different stimulation configuration in order to achieve the maximal neuroprotective effect of DBS. Confusion matrices for SCP (1), FCP (2), and MCP (3) configurations showing survival ratios of SNc cells for different percentage activation of antidromic activation and STN axonal & synaptic failures at early (25%) (A), intermediate (50%) (B) and late (75%) (C) stages of SNc cell loss. Ratios around 0 is indicated as forthwith (indigo), ratios around 0.5 is indicated as delayed (light green), and ratios around 1 is indicated as halted (yellow). DBS, Deep Brain Stimulation; SNc, Substantia Nigra pars compacta; STN, SubThalamic Nucleus; SCP, Single Contact Point; FCP, Four Contact Point; MCP, Multiple Contact Point.

4. DISCUSSION

4.1. Excitotoxicity Model

The goal of this work was to develop a model which investigates the role of excitotoxicity in SNc cell loss, where excitotoxicity was caused by STN and precipitated by energy deficiency. The study suggests that excitotoxicity in SNc is initially driven by an energy deficit which leads to an initial dopamine reduction as a result of SNc cell loss. This initial dopamine reduction causes disinhibition of STN which in turns leads to excitotoxic damage due to excessive release of glutamate to its target nuclei including SNc (Rodriguez et al., 1998). The excitotoxicity which was driven by energy deficit, termed as “weak excitotoxicity,” results in increased vulnerability of SNc neurons to even physiological concentration of glutamate. The excitotoxicity which was driven by overactive excitatory STN neurons termed as “strong excitotoxicity” results in overactivation of glutamatergic receptors on SNc neurons (Albin and Greenamyre, 1992). In summary, it appears that the excitotoxic cause of SNc cell loss in PD might be initiated by weak excitotoxicity mediated by energy deficit, and followed by strong excitotoxicity, mediated by disinhibited STN.

The results from the proposed model reinforce the role of STN in regulating SNc cell loss (Hamani et al., 2004, 2017). The

model results show that although cell loss was observed, there was no increased synchrony in the STN population which is a pathological marker of the PD condition (Lintas et al., 2012). Thus, the SNc cell loss and STN synchrony have a threshold-like relation where there is an increased STN synchrony only after substantial SNc cell loss. The initial SNc cell loss leads to further activation of STN by disinhibition, which in turn further activates SNc compensating for the dopamine loss, acting as a pre-symptomatic compensatory mechanism (Bezard et al., 2003). It was reported that the onset of PD symptoms occurs only after there is more than 50% SNc cell loss (Bezard et al., 2001). This was observed in our simulation results also where only at around 50–70% SNc cell loss there is an increased STN synchrony. As a result of substantial SNc cell loss, decreased dopamine causes disinhibition of STN which in turn overactivates STN, eventually producing a runaway effect that causes an unstoppable SNc cell loss due to excitotoxic damage (Rodriguez et al., 1998). The threshold-like behavior of SNc cell loss and STN synchrony might also be facilitated by the inhibitory drive from GPe to STN: the proliferation of GPe-STN synapses (Fan et al., 2012) also acts as a presymptomatic compensatory mechanism. It was also reported that lesioning of GPe caused progressive SNc cell loss by increasing STN activity (Wright et al., 2002) and lesioning of STN proved to be neuroprotective (Wright and Arbuthnott, 2007).

To summarize, up to a point of stress threshold, SNc cells can survive indefinitely; but if, for any reason, there is loss of cells in SNc, and the SNc cell count falls below a threshold, from that point onwards, the aforementioned runaway effect kicks in leading to a progressive and irrevocable cell loss. Such cell loss is strongly reminiscent of cell loss due to neurodegeneration.

4.2. Neuroprotective Strategies

A variety of conventional therapies are simulated in the model to test their efficacy in slowing down or arresting SNc cell loss. Among the current therapeutics, glutamate inhibition, dopamine restoration, subthalamotomy and deep brain stimulation showed superior neuroprotective effects in the proposed model. Glutamate inhibition and subthalamotomy were successful in delaying or arresting the SNc cell loss by inhibiting the excitatory drive from STN to SNc (Lee et al., 2003; Wallace et al., 2007; Austin et al., 2010), and in case of dopamine restoration it is by replenishing the dopamine tone to the STN which in turn restores inhibition on itself (Olanow et al., 1998; Vaarmann et al., 2013), thereby diminishing STN-mediated excitotoxicity in SNc. The neuroprotective effect of glutamate inhibition, dopamine restoration and subthalamotomy was dependent on the dosage of glutamate inhibitors, the extent of dopamine restored and proportion of STN lesioned, respectively. As the disease progresses, the effect of glutamate inhibition on the rate of degeneration increased but in the case of dopamine restoration and subthalamotomy, it was decreased. In the late stages of disease progression, our computational study indicates that the neuroprotective effect of glutamate inhibition is more prominent than dopamine restoration and subthalamotomy.

From our study, it can be said that subthalamotomy mostly delays the SNc cell loss but very rarely halts it. This phenomenon was not much evident in the late stages of disease progression in the model which is consistent with the standard clinical understanding that the neuroprotective effect of subthalamotomy in advanced PD is not quite successful (Guridi and Obeso, 2015). Early treatment with subthalamotomy in PD can have a neuroprotective effect (Guridi et al., 2016) a trend that was reflected in our computational study. Another factor underlying the neuroprotective effect of subthalamotomy during the early stage

of PD is the involvement of presymptomatic compensation mechanisms (Bezard et al., 2003). One of the compensatory mechanisms is the increased activity of STN before any significant striatal dopamine loss which leads to excess excitatory drive from STN to the remaining SNc cells to restore the dopamine loss due to initial cell loss (Bezard et al., 1999). This excess excitatory drive from STN eventually leads to excitotoxicity in SNc neurons. To overcome this excitotoxicity, subthalamotomy had to be applied very early after diagnosis of PD to have any neuroprotective effect (Guridi et al., 2016).

In our modeling study, we have explored various aspects of DBS protocol from stimulus waveforms to stimulus configurations and other DBS parameters. From the simulation results, it can be suggested that biphasic stimulus waveform with four-contact point stimulation configuration showed maximal neuroprotective effect since biphasic stimulus guarantees charge-balance in the stimulated neuronal tissue (Hofmann et al., 2011) and DBS parameters were given in the **Table 2**.

It has been reported that long-term stimulation (DBS) of STN results in the slowdown of the SNc cell loss in animal models (Maesawa et al., 2004; Temel et al., 2006; Wallace et al., 2007; Spieles-Engemann et al., 2010; Musacchio et al., 2017), but the mechanism behind the neuroprotective benefits of DBS is not elucidated. To understand the neuroprotective effect of DBS in PD, we have investigated three prominent hypotheses viz., excitation, inhibition and disruptive actions of DBS (Chicken and Nambu, 2015). In the excitation hypothesis, only DBS was applied which results in increased firing rate in STN and leads to more excitatory drive to SNc which eventually kills the SNc cells due to stress. Therefore, considering only the excitation hypothesis cannot explain the neuroprotective effect of DBS. Next, inhibition hypothesis was implemented where antidromic activation of GPe result in the increased inhibitory drive to STN (Mandali and Chakravarthy, 2016). In this scenario also, the neuroprotective effect of DBS could not be comprehensively explained. Finally, the disruptive hypothesis was implemented by increasing the axonal and synaptic failures in STN population during DBS therapy (Rosenbaum et al., 2014). From simulation results, it was observed that the progression of SNc cell loss kept on delaying as the percentage of STN axonal and synaptic failure increased. Therefore, it can be inferred that DBS blocks the propagation of

TABLE 2 | DBS parameter values obtained from the preliminary studies.

Parameter(s)	SCP	FCP	MCP
DBS frequency (f_{DBS}) in Hz	130	130	130
Monophasic pulse width (δ_{DBS}) in ms	100	100	100
Biphasic pulse width (δ_{DBS}) in ms	200	200	200
Monophasic DBS amplitude (A_{DBS}) in pA	650	650	650
Biphasic DBS amplitude (A_{DBS}) in pA	1,000	1,000	1,000
Spread of the current (σ_{DBS})	5	2	0
Electrode contact point(s)	(16, 16)	(8, 8)(8, 24)(24, 8)(24, 24)	Many

Hz, Hertz; ms, milliseconds; pA, picoamperes.

pathological oscillations occurring in STN to other nuclei; in other words DBS disrupts the information transfer through the stimulation site, producing neuroprotection effect in SNc (Ledonne et al., 2012).

4.3. Limitations and Future Directions

Though the model captures the exciting results of excitotoxicity, it is not without limitations. The timescales which are represented in the results of the proposed model are not realistic, as the neurodegeneration which occurs over the years in PD was exhibited in a few tens of seconds in the model. This limitation is inevitable due to the practical challenges faced by computer simulations since it is impractical to simulate the model for months and years. The difficulty arises due to the fact that the simulation must span widely separated time scales - sub-millisecond time scales to describe spiking activity and years to describe neurodegenerative processes.

The major inputs to the SNc neurons come from the striatum which was not included in the model. As our objective was to investigate the extent of STN-mediated excitotoxicity in SNc, we avoided any other structures which can influence this phenomenon at present.

In the proposed model, the variability of stress threshold, which is analogous to an apoptotic threshold (that can be broadly associated with the available energy represented as (ATP/ADP) ratio), is sensitive enough to alter the model results is a constant parameter. In order to achieve variability in this parameter, astrocytic and vascular network-level models can be introduced. With the astrocyte layer introduced, the effect of astrocytes on the therapeutic effect of DBS can be explored (Fenoy et al., 2014).

In the future, we plan to simulate the SNc activity using a detailed biophysical model to study the dynamics at the molecular level and also to investigate the cellular pathways

related to PD pathology. We would like to include Spike-timing-dependent plasticity (STDP) learning in STN population for the long-term effect of DBS (Ebert et al., 2014).

Our hypothesis behind this whole study is to understand the pathogenesis of PD as cellular energy deficiency in SNc as a cause. As Wellstead and Cloutier pointed out (Wellstead and Cloutier, 2011), PD should be understood by placing the failure of brain energy delivery mechanisms in the center as a core pathological process, with other manifestations of pathology as deriving from that core process (see the Figure 12 in Wellstead, 2010).

CODE ACCESSIBILITY

The code of the proposed excitotoxicity model is available on ModelDB server (McDougal et al., 2017), and access code will be provided on request. (<https://senselab.med.yale.edu/modeldb/enterCode.cshtml?model=244384>).

AUTHOR CONTRIBUTIONS

VM and VC: conceived, developed the model and prepared the manuscript. AM: conceived and developed the model. SR: prepared the manuscript.

ACKNOWLEDGMENTS

We would like to acknowledge Dr. Vignesh Muralidharan for his intense discussion in the model development. We would also like to acknowledge P. G. Senapathy Center for computing Resource, IIT-Madras for computing facilities. The pre-print version of the manuscript was released by bioRxiv (Muddapu et al., 2018) for feedback from fellow neuroscientists.

REFERENCES

- Adhihetty, P. J., and Beal, M. F. (2008). Creatine and its potential therapeutic value for targeting cellular energy impairment in neurodegenerative diseases. *NeuroMol. Med.* 10, 275–290. doi: 10.1007/s12017-008-8053-y
- Albin, R. L., and Greenamyre, J. T. (1992). Alternative excitotoxic hypotheses. *Neurology* 42, 733–738. doi: 10.1212/WNL.42.4.733
- Allers, K. A., Walters, J. R., and Kreiss, D. S. (2003). "Neuronal firing patterns in the subthalamic nucleus," in *The Basal Ganglia V*, eds A. M. Graybiel, M. R. Delong, and S. T. Kitai (Boston, MA: Springer), 245–254.
- Alvarez, L., Macias, R., Pavón, N., López, G., Rodríguez-Oroz, M. C., Rodríguez, R., et al. (2009). Therapeutic efficacy of unilateral subthalamotomy in Parkinson's disease: results in 89 patients followed for up to 36 months. *J. Neurol. Neurosurg. Psychiatry* 80, 979–985. doi: 10.1136/jnnp.2008.154948
- Ambrosi, G., Cerri, S., and Blandini, F. (2014). A further update on the role of excitotoxicity in the pathogenesis of Parkinson's disease. *J. Neural Transm.* 121, 849–859. doi: 10.1007/s00702-013-1149-z
- Ammari, R., Bioulac, B., Garcia, L., and Hammond, C. (2011). The subthalamic nucleus becomes a generator of bursts in the dopamine-depleted state. Its high frequency stimulation dramatically weakens transmission to the globus pallidus. *Front. Syst. Neurosci.* 5:43. doi: 10.3389/fnsys.2011.00043
- Anselmi, L., Bove, C., Coleman, F. H., Le, K., Subramanian, M. P., Venkiteswaran, K., et al. (2018). Ingestion of subthreshold doses of environmental toxins induces ascending Parkinsonism in the rat. *NPJ Parkinson's Dis.* 4:30. doi: 10.1038/s41531-018-0066-0
- Armentero, M.-T., Fancellu, R., Nappi, G., Bramanti, P., and Blandini, F. (2006). Prolonged blockade of NMDA or mGluR5 glutamate receptors reduces nigrostriatal degeneration while inducing selective metabolic changes in the basal ganglia circuitry in a rodent model of Parkinson's disease. *Neurobiol. Dis.* 22, 1–9. doi: 10.1016/j.nbd.2005.09.010
- Austin, P. J., Betts, M. J., Broadstock, M., O'Neill, M. J., Mitchell, S. N., and Duty, S. (2010). Symptomatic and neuroprotective effects following activation of nigral group III metabotropic glutamate receptors in rodent models of Parkinson's disease. *Brit. J. Pharmacol.* 160, 1741–1753. doi: 10.1111/j.1476-5381.2010.00820.x
- Battaglia, G., Busceti, C. L., Pontarelli, F., Biagioni, F., Fornai, F., Paparelli, A., et al. (2003). Protective role of group-II metabotropic glutamate receptors against nigro-striatal degeneration induced by 1-methyl-4-phenyl-1,2,3,6-tetrahydropyridine in mice. *Neuropharmacology* 45, 155–166. doi: 10.1016/S0028-3908(03)00146-1
- Beal, M., Hyman, B. T., and Korosetz, W. (1993). Do defects in mitochondrial energy metabolism underlie the pathology of neurodegenerative diseases? *Trends Neurosci.* 16, 125–131. doi: 10.1016/0166-2236(93)90117-5
- Benazzouz, A., Piallat, B., Ni, Z. G., Koudsie, A., Pollak, P., and Benabid, A. L. (2000). Implication of the subthalamic nucleus in the pathophysiology and pathogenesis of Parkinson's disease. *Cell Transpl.* 9, 215–221. doi: 10.1177/096368970000900207

- Bergman, H., Feingold, A., Nini, A., Raz, A., Slovin, H., Abeles, M., et al. (1998). Physiological aspects of information processing in the basal ganglia of normal and parkinsonian primates. *Trends Neurosci.* 21, 32–38. doi: 10.1016/S0166-2236(97)01151-X
- Bergman, H., Wichmann, T., Karmon, B., and DeLong, M. R. (1994). The primate subthalamic nucleus. II. Neuronal activity in the MPTP model of parkinsonism. *J. Neurophysiol.* 72, 507–520. doi: 10.1152/jn.1994.72.2.507
- Betts, M. J., O'Neill, M. J., and Duty, S. (2012). Allosteric modulation of the group III mGlu4 receptor provides functional neuroprotection in the 6-hydroxydopamine rat model of Parkinson's disease. *Brit. J. Pharmacol.* 166, 2317–2330. doi: 10.1111/j.1476-5381.2012.01943.x
- Beurrier, C., Congar, P., Bioulac, B., and Hammond, C. (1999). Subthalamic nucleus neurons switch from single-spike activity to burst-firing mode. *J. Neurosci.* 19, 599–609. doi: 10.1523/JNEUROSCI.19-02-00599.1999
- Bezard, E., Boraud, T., Bioulac, B., and Gross, C. E. (1999). Involvement of the subthalamic nucleus in glutamatergic compensatory mechanisms. *Eur. J. Neurosci.* 11, 2167–2170. doi: 10.1046/j.1460-9568.1999.00627.x
- Bezard, E., Dovero, S., Prunier, C., Ravenscroft, P., Chalon, S., Guilloteau, D., et al. (2001). Relationship between the appearance of symptoms and the level of nigrostriatal degeneration in a progressive 1-methyl-4-phenyl-1,2,3,6-tetrahydropyridine-lesioned macaque model of Parkinson's disease. *J. Neurosci.* 21, 6853–6861. doi: 10.1523/JNEUROSCI.21-17-06853.2001
- Bezard, E., Gross, C. E., and Brotchie, J. M. (2003). Presymptomatic compensation in Parkinson's disease is not dopamine-mediated. *Trends Neurosci.* 26, 215–221. doi: 10.1016/S0166-2236(03)00038-9
- Blandini, F. (2001). The role of the subthalamic nucleus in the pathophysiology of Parkinson's disease. *Funct. Neurol.* 16(4 Suppl):99–106.
- Blandini, F. (2010). An update on the potential role of excitotoxicity in the pathogenesis of Parkinson's disease. *Funct. Neurol.* 25, 65–71.
- Bolam, J. P., and Pissadaki, E. K. (2012). Living on the edge with too many mouths to feed: why dopamine neurons die. *Move. Disord.* 27, 1478–1483. doi: 10.1002/mds.25135
- Booth, H. D. E., Hirst, W. D., and Wade-Martins, R. (2017). The role of astrocyte dysfunction in Parkinson's disease pathogenesis. *Trends Neurosci.* 40, 358–370. doi: 10.1016/j.tins.2017.04.001
- Brouillet, E., and Beal, M. F. (1993). NMDA antagonists partially protect against MPTP induced neurotoxicity in mice. *Neuroreport* 4, 387–390. doi: 10.1097/00001756-199304000-00011
- Brown, P. (2003). Oscillatory nature of human basal ganglia activity: relationship to the pathophysiology of Parkinson's disease. *Mov. Disord.* 18, 357–363. doi: 10.1002/mds.10358
- Brown, P., Oliviero, A., Mazzone, P., Insola, A., Ttonali, P., and Di Lazzaro, V. (2001). Dopamine dependency of oscillations between subthalamic nucleus and pallidum in Parkinson's disease. *J. Neurosci.* 21, 1033–1038. doi: 10.1523/JNEUROSCI.21-03-01033.2001
- Carron, R., Chaillet, A., Filipchuk, A., Pasillas-Lépine, W., and Hammond, C. (2013). Closing the loop of deep brain stimulation. *Front. Syst. Neurosci.* 7:112. doi: 10.3389/fnsys.2013.00112
- Carvalho, G. A., and Nikkhah, G. (2001). Subthalamic nucleus lesions are neuroprotective against terminal 6-OHDA-induced striatal lesions and restore postural balancing reactions. *Exp. Neurol.* 171, 405–417. doi: 10.1006/exnr.2001.7742
- Chakravarthy, V. S., and Moustafa, A. A. (2018). *Computational Neuroscience Models of the Basal Ganglia, volume 15 of Cognitive Science and Technology*. Singapore: Springer.
- Chan, H., Paur, H., Vernon, A. C., Zabarsky, V., Datla, K. P., Croucher, M. J., et al. (2010). Neuroprotection and functional recovery associated with decreased microglial activation following selective activation of mGluR2/3 receptors in a rodent model of Parkinson's disease. *Parkinson's Dis.* 2010, 1–12. doi: 10.4061/2010/190450
- Chander, B. S., and Chakravarthy, V. S. (2012). A computational model of neuro-glio-vascular loop interactions. *PLoS ONE* 7:e48802. doi: 10.1371/journal.pone.0048802
- Chen, L., Liu, Z., Tian, Z., Wang, Y., and Li, S. (2000). Prevention of neurotoxin damage of 6-OHDA to dopaminergic nigral neuron by subthalamic nucleus lesions. *Stereot. Funct. Neurosurg.* 75, 66–75. doi: 10.1159/000048385
- Chhabria, K., and Chakravarthy, V. S. (2016). Low-dimensional models of "Neuro-Glio-Vascular Unit" for describing neural dynamics under normal and energy-starved conditions. *Front. Neurol.* 7:24. doi: 10.3389/fneur.2016.00024
- Chiken, S., and Nambu, A. (2015). Mechanism of deep brain stimulation: inhibition, excitation, or disruption? *Neuroscientist* 22, 313–322. doi: 10.1177/1073858415581986
- Chiti, F., and Dobson, C. M. (2017). Protein misfolding, amyloid formation, and human disease: a summary of progress over the last decade. *Annu. Rev. Biochem.* 86, 27–68. doi: 10.1146/annurev-biochem-061516-045115
- Cogan, S. F. (2008). Neural stimulation and recording electrodes. *Annu. Rev. Biomed. Eng.* 10, 275–309. doi: 10.1146/annurev.bioeng.10.061807.160518
- Courtney, N. A., Mamaligas, A. A., and Ford, C. P. (2012). Species differences in somatodendritic dopamine transmission determine D2-autoreceptor-mediated inhibition of ventral tegmental area neuron firing. *J. Neurosci.* 32, 13520–13528. doi: 10.1523/JNEUROSCI.2745-12.2012
- Cragg, S. J., Baufreton, J., Xue, Y., Bolam, J. P., and Bevan, M. D. (2004). Synaptic release of dopamine in the subthalamic nucleus. *Eur. J. Neurosci.* 20, 1788–1802. doi: 10.1111/j.1460-9568.2004.03629.x
- Cullen, M., and Wong-Lin, K. (2015). Integrated dopaminergic neuronal model with reduced intracellular processes and inhibitory autoreceptors. *IET Syst. Biol.* 9, 245–258. doi: 10.1049/iet-syb.2015.0018
- Dayan, P., and Abbott, L. F. (2005). *Theoretical Neuroscience: Computational And Mathematical Modeling of Neural Systems*. Cambridge: Computational Neuroscience, Massachusetts Institute of Technology Press.
- Dovzhenok, A., and Rubchinsky, L. L. (2012). On the origin of tremor in Parkinson's disease. *PLoS ONE* 7:e41598. doi: 10.1371/journal.pone.0041598
- Ebert, M., Hauptmann, C., and Tass, P. A. (2014). Coordinated reset stimulation in a large-scale model of the STN-GPe circuit. *Front. Comput. Neurosci.* 8:154. doi: 10.3389/fncom.2014.00154
- Fan, K. Y., Baufreton, J., Surmeier, D. J., Chan, C. S., and Bevan, M. D. (2012). Proliferation of external globus pallidus-subthalamic nucleus synapses following degeneration of midbrain dopamine neurons. *J. Neurosci.* 32, 13718–13728. doi: 10.1523/JNEUROSCI.5750-11.2012
- Fenoy, A. J., Goetz, L., Chabardès, S., and Xia, Y. (2014). Deep brain stimulation: are astrocytes a key driver behind the scene? *CNS Neurosci. Therapeut.* 20, 191–201. doi: 10.1111/cns.12223
- Ferrigno, A., Vairetti, M., Ambrosi, G., Rizzo, V., Richelmi, P., Blandini, F., et al. (2015). Selective blockade of mGlu5 metabotropic glutamate receptors is protective against hepatic mitochondrial dysfunction in 6-OHDA lesioned Parkinsonian rats. *Clin. Exp. Pharmacol. Physiol.* 42, 695–703. doi: 10.1111/1440-1681.12410
- Ford, C. P. (2014). The role of D2-autoreceptors in regulating dopamine neuron activity and transmission. *Neuroscience* 282, 13–22. doi: 10.1016/j.neuroscience.2014.01.025
- Foutz, T. J., and McIntyre, C. C. (2010). Evaluation of novel stimulus waveforms for deep brain stimulation. *J. Neural Eng.* 7:066008. doi: 10.1088/1741-2560/7/6/066008
- Fuzzati-Armentero, M.-T., Cerri, S., Levandis, G., Ambrosi, G., Montepeloso, E., Antoninetti, G., et al. (2015). Dual target strategy: combining distinct non-dopaminergic treatments reduces neuronal cell loss and synergistically modulates L-DOPA-induced rotational behavior in a rodent model of Parkinson's disease. *J. Neurochem.* 134, 740–747. doi: 10.1111/jnc.13162
- Gandrakota, R., Chakravarthy, V. S., and Pradhan, R. K. (2010). A model of indispensability of a large glial layer in cerebrovascular circulation. *Neural Comput.* 22, 949–968. doi: 10.1162/neco.2009.01-09-945
- Gao, J., Wang, L., Liu, J., Xie, F., Su, B., and Wang, X. (2017). Abnormalities of mitochondrial dynamics in neurodegenerative diseases. *Antioxidants* 6:25. doi: 10.3390/antiox6020025
- Garcia, L., D'Alessandro, G., Bioulac, B., and Hammond, C. (2005). High-frequency stimulation in Parkinson's disease: more or less? *Trends Neurosci.* 28, 209–216. doi: 10.1016/j.tins.2005.02.005
- German, D. C., Manaye, K. F., Sonsalla, P. K., and Brooks, B. a. (1992). Midbrain dopaminergic cell loss in Parkinson's disease and MPTP-induced parkinsonism: sparing of calbindin-D28k-containing cells. *Ann. N. Y. Acad. Sci.* 648, 42–62. doi: 10.1111/j.1749-6632.1992.tb24523.x
- Giguère, N., Burke Nanni, S., and Trudeau, L.-E. (2018). On cell loss and selective vulnerability of neuronal populations in Parkinson's disease. *Front. Neurol.* 9:455. doi: 10.3389/fneur.2018.00455

- Glass, C. K., Saijo, K., Winner, B., Marchetto, M. C., and Gage, F. H. (2010). Mechanisms underlying inflammation in neurodegeneration. *Cell* 140, 918–934. doi: 10.1016/j.cell.2010.02.016
- Golomb, D. (2007). Neuronal synchrony measures. *Scholarpedia* 2:1347. doi: 10.4249/scholarpedia.1347
- Götz, T., Kraushaar, U., Geiger, J., Lübke, J., Berger, T., and Jonas, P. (1997). Functional properties of AMPA and NMDA receptors expressed in identified types of basal ganglia neurons. *J. Neurosci.* 17, 204–15. doi: 10.1523/JNEUROSCI.17-01-00204.1997
- Grace, A. A., and Bunney, B. S. (1983). Intracellular and extracellular electrophysiology of nigral dopaminergic neurons. 1. Identification and characterization. *Neuroscience* 10, 301–315. doi: 10.1016/0306-4522(83)90135-5
- Grace, A. A., and Bunney, B. S. (1984a). The control of firing pattern in nigral dopamine neurons: burst firing. *J. Neurosci.* 4, 2877–2890. doi: 10.1523/JNEUROSCI.04-11-02877.1984
- Grace, A. A., and Bunney, B. S. (1984b). The control of firing pattern in nigral dopamine neurons: single spike firing. *J. Neurosci.* 4, 2866–2876. doi: 10.1523/JNEUROSCI.04-11-02866.1984
- Grandas, F. (2000). The putative neuroprotective role of dopamine agonists in Parkinson's disease. *Neurotox. Res.* 2, 205–213. doi: 10.1007/BF03033794
- Greene, J. G., and Greenamyre, J. T. (1996). Bioenergetics and glutamate excitotoxicity. *Prog. Neurobiol.* 48, 613–634. doi: 10.1016/0301-0082(96)00006-8
- Guridi, J., Marigil, M., Becerra, V., and Parras, O. (2016). [Neuroprotective subthalamotomy in Parkinson's disease. The role of magnetic resonance-guided focused ultrasound in early surgery]. *Neurocirugía (Asturias, Spain)* 27, 285–290.
- Guridi, J., and Obeso, J. A. (2015). Letter to the editor: Parkinson's disease and early subthalamotomy. *J. Neurosurg.* 122, 980–981. doi: 10.3171/2014.8.JNS141799
- Hamani, C., Florence, G., Heinsen, H., Plantinga, B. R., Temel, Y., Uludag, K., et al. (2017). Subthalamic nucleus deep brain stimulation: basic concepts and novel perspectives. *Eneuro* 4:ENEURO.0140–17.2017. doi: 10.1523/ENEURO.0140-17.2017
- Hamani, C., Saint-Cyr, J. A., Fraser, J., Kaplitt, M., and Lozano, A. M. (2004). The subthalamic nucleus in the context of movement disorders. *Brain* 127, 4–20. doi: 10.1093/brain/awh029
- Hammond, C., Ammari, R., Bioulac, B., and Garcia, L. (2008). Latest view on the mechanism of action of deep brain stimulation. *Move. Disord.* 23, 2111–2121. doi: 10.1002/mds.22120
- Hansel, D., Mato, G., and Meunier, C. (1995). Synchrony in excitatory neural networks. *Neural Comput.* 7, 307–337. doi: 10.1162/neco.1995.7.2.307
- Hassani, O. K., François, C., Yelnik, J., and Féger, J. (1997). Evidence for a dopaminergic innervation of the subthalamic nucleus in the rat. *Brain Res.* 749, 88–94. doi: 10.1016/S0006-8993(96)01167-5
- Hasselmo, M. E. (1994). Runaway synaptic modification in models of cortex: implications for Alzheimer's disease. *Neural Netw.* 7, 13–40. doi: 10.1016/0893-6080(94)90053-1
- Hasselmo, M. E. (1997). A computational model of the progression of Alzheimer's disease. *M.D. Computing* 14, 181–191.
- Hauptmann, C., and Tass, P. A. (2007). Therapeutic rewiring by means of desynchronizing brain stimulation. *BioSystems* 89, 173–181. doi: 10.1016/j.biosystems.2006.04.015
- Hebb, M. O., and Robertson, H. A. (1999). Identification of a subpopulation of substantia nigra pars compacta ??-aminobutyric acid neurons that is regulated by basal ganglia activity. *J. Compar. Neurol.* 416, 30–44.
- Hegeman, D. J., Hong, E. S., Hernández, V. M., and Chan, C. S. (2016). The external globus pallidus: progress and perspectives. *Eur. J. Neurosci.* 43, 1239–1265. doi: 10.1111/ejn.13196
- Henchcliffe, C., and Beal, M. F. (2008). Mitochondrial biology and oxidative stress in Parkinson disease pathogenesis. *Nat. Clin. Pract. Neurol.* 4, 600–609. doi: 10.1038/ncpneu0924
- Hofmann, L., Ebert, M., Tass, P. A., and Hauptmann, C. (2011). Modified pulse shapes for effective neural stimulation. *Front. Neuroeng.* 4:9. doi: 10.3389/fneng.2011.00009
- Hsieh, M. H., Ho, S. C., Yeh, K. Y., Pawlak, C. R., Chang, H. M., Ho, Y. J., et al. (2012). Blockade of metabotropic glutamate receptors inhibits cognition and neurodegeneration in an MPTP-induced Parkinson's disease rat model. *Pharmacol. Biochem. Behav.* 102, 64–71. doi: 10.1016/j.pbb.2012.03.022
- Humphries, M. D., Stewart, R. D., and Gurney, K. N. (2006). A physiologically plausible model of action selection and oscillatory activity in the basal ganglia. *J. Neurosci.* 26, 12921–12942. doi: 10.1523/JNEUROSCI.3486-06.2006
- Hwang, O. (2013). Role of oxidative stress in Parkinson's disease. *Exp. Neurobiol.* 22:11. doi: 10.5607/en.2013.22.1.11
- Iglesias, J., and Villa, A. E. P. (2008). Emergence of preferred firing sequences in large spiking neural networks during simulated neuronal development. *Int. J. Neural Syst.* 18, 267–277. doi: 10.1142/S0129065708001580
- Izhikevich, E. (2003). Simple model of spiking neurons. *IEEE Trans. Neural Netw.* 14, 1569–1572. doi: 10.1109/TNN.2003.820440
- Izhikevich, E. M. (2006). Bursting. *Scholarpedia* 1:1300. doi: 10.4249/scholarpedia.1300
- Jahr, C. E., and Stevens, C. F. (1990). Voltage dependence of NMDA-activated macroscopic conductances predicted by single-channel kinetics. *J. Neurosci.* 10, 3178–3182. doi: 10.1523/JNEUROSCI.10-09-03178.1990
- Jang, J. Y., Jang, M., Kim, S. H., Um, K. B., Kang, Y. K., Kim, H. J., et al. (2011). Regulation of dopaminergic neuron firing by heterogeneous dopamine autoreceptors in the substantia nigra pars compacta. *J. Neurochem.* 116, 966–974. doi: 10.1111/j.1471-4159.2010.07107.x
- Johnson, S. W. (2008). Rebound bursts following inhibition: how dopamine modifies firing pattern in subthalamic neurons. *J. Physiol.* 586, 2033. doi: 10.1113/jphysiol.2008.153643
- Johri, A., and Beal, M. F. (2012). Mitochondrial dysfunction in neurodegenerative diseases. *J. Pharmacol. Exp. Therapeut.* 342, 619–630. doi: 10.1124/jpet.112.192138
- Jourdain, V. A., Schechtman, G., and Di Paolo, T. (2014). Subthalamotomy in the treatment of Parkinson's disease: clinical aspects and mechanisms of action. *J. Neurosurg.* 120, 140–151. doi: 10.3171/2013.10.JNS13332
- Kang, G., and Lowery, M. M. (2013). Interaction of oscillations, and their suppression via deep brain stimulation, in a model of the cortico-basal ganglia network. *IEEE Trans. Neural Syst. Rehabil. Eng.* 21, 244–253. doi: 10.1109/TNSRE.2013.2241791
- Kang, G., and Lowery, M. M. (2014). Effects of antidromic and orthodromic activation of STN afferent axons during DBS in Parkinson's disease: a simulation study. *Front. Comput. Neurosci.* 8:32. doi: 10.3389/fncom.2014.00032
- Kita, H., Chang, H. T., and Kitai, S. T. (1983). The morphology of intracellularly labeled rat subthalamic neurons: a light microscopic analysis. *J. Compar. Neurol.* 215, 245–57. doi: 10.1002/cne.902150302
- Kita, H., and Kita, S. T. (1994). The morphology of globus pallidus projection neurons in the rat: an intracellular staining study. *Brain Res.* 636, 308–319. doi: 10.1016/0006-8993(94)91030-8
- Kita, H., and Kita, T. (2011). Role of striatum in the pause and burst generation in the globus pallidus of 6-OHDA-treated rats. *Front. Syst. Neurosci.* 5:42. doi: 10.3389/fnsys.2011.00042
- Kita, H., and Kitai, S. T. (1987). Efferent projections of the subthalamic nucleus in the rat: light and electron microscopic analysis with the PHA-L method. *J. Compar. Neurol.* 260, 435–452. doi: 10.1002/cne.902600309
- Kreiss, D. S., Mastropietro, C. W., Rawji, S. S., and Walters, J. R. (1997). The response of subthalamic nucleus neurons to dopamine receptor stimulation in a rodent model of Parkinson's disease. *J. Neurosci.* 17, 6807–6819. doi: 10.1523/JNEUROSCI.17-17-06807.1997
- Lawson, L. J., Perry, V. H., Dri, P., and Gordon, S. (1990). Heterogeneity in the distribution and morphology of microglia in the normal adult mouse brain. *Neuroscience* 39, 151–170. doi: 10.1016/0306-4522(90)90229-W
- Ledonne, A., Mango, D., Bernardi, G., Berretta, N., and Mercuri, N. B. (2012). A continuous high frequency stimulation of the subthalamic nucleus determines a suppression of excitatory synaptic transmission in nigral dopaminergic neurons recorded *in vitro*. *Exp. Neurol.* 233, 292–302. doi: 10.1016/j.expneurol.2011.10.018
- Lee, H. H., Yang, L. L., Wang, C. C., Hu, S. Y., Chang, S. F., and Lee, Y. H. (2003). Differential effects of natural polyphenols on neuronal survival in primary cultured central neurons against glutamate- and glucose deprivation-induced neuronal death. *Brain Res.* 986, 103–113. doi: 10.1016/S0006-8993(03)03197-4

- Lee, K. H., Chang, S.-Y., Roberts, D. W., and Kim, U. (2004). Neurotransmitter release from high-frequency stimulation of the subthalamic nucleus. *J. Neurosurg.* 101, 511–517. doi: 10.3171/jns.2004.101.3.0511
- Lee, K. H., Duffy, P. S., and Bieber, A. J. (2016). *Deep Brain Stimulation: Indications and Applications*. Singapore: Pan Stanford Publishing.
- Liang, C.-L., Nelson, O., Yazdani, U., Pasbakhsh, P., and German, D. C. (2004). Inverse relationship between the contents of neuromelanin pigment and the vesicular monoamine transporter-2: human midbrain dopamine neurons. *J. Compar. Neurol.* 473, 97–106. doi: 10.1002/cne.20098
- Lindahl, M., Kamali Sarvestani, I., Ekeberg, O., and Kotaleski, J. H. (2013). Signal enhancement in the output stage of the basal ganglia by synaptic short-term plasticity in the direct, indirect, and hyperdirect pathways. *Front. Comput. Neurosci.* 7:76. doi: 10.3389/fncom.2013.00076
- Lintas, A., Silkis, I. G., Albéri, L., and Villa, A. E. (2012). Dopamine deficiency increases synchronized activity in the rat subthalamic nucleus. *Brain Res.* 1434, 142–151. doi: 10.1016/j.brainres.2011.09.005
- Litvak, V., Jha, A., Eusebio, A., Oostenveld, R., Foltyni, T., Limousin, P., et al. (2011). Resting oscillatory cortico-subthalamic connectivity in patients with Parkinson's disease. *Brain* 134, 359–374. doi: 10.1093/brain/awq332
- Lukasiewicz, P. D., and Werblin, F. S. (1990). The spatial distribution of excitatory and inhibitory inputs to ganglion cell dendrites in the tiger salamander retina. *J. Neurosci.* 10, 210–221. doi: 10.1523/JNEUROSCI.10-01-00210.1990
- Maesawa, S., Kaneoke, Y., Kajita, Y., Usui, N., Misawa, N., Nakayama, A., et al. (2004). Long-term stimulation of the subthalamic nucleus in hemiparkinsonian rats: neuroprotection of dopaminergic neurons. *J. Neurosurg.* 100, 679–687. doi: 10.3171/jns.2004.100.4.0679
- Magill, P. J., Bolam, J. P., and Bevan, M. D. (2001). Dopamine regulates the impact of the cerebral cortex on the subthalamic nucleus-globus pallidus network. *Neuroscience* 106, 313–330. doi: 10.1016/S0306-4522(01)00281-0
- Mamad, O., Delaville, C., Benjelloun, W., and Benazzouz, A. (2015). Dopaminergic control of the globus pallidus through activation of D2 receptors and its impact on the electrical activity of subthalamic nucleus and substantia nigra reticulata neurons. *PLoS ONE* 10:e0119152. doi: 10.1371/journal.pone.0119152
- Mandali, A., and Chakravarthy, V. S. (2016). Probing the role of medication, DBS electrode position, and antidromic activation on impulsivity using a computational model of basal ganglia. *Front. Hum. Neurosci.* 10:450. doi: 10.3389/fnhum.2016.00450
- Mandali, A., Rengaswamy, M., Chakravarthy, V. S., and Moustafa, A. A. (2015). A spiking Basal Ganglia model of synchrony, exploration and decision making. *Front. Neurosci.* 9:191. doi: 10.3389/fnins.2015.00191
- Masilamoni, G. J., Bogenpohl, J. W., Alagille, D., Delevich, K., Tamagnan, G., Votaw, J. R., et al. (2011). Metabotropic glutamate receptor 5 antagonist protects dopaminergic and noradrenergic neurons from degeneration in MPTP-treated monkeys. *Brain* 134, 2057–2073. doi: 10.1093/brain/awr137
- McDougal, R. A., Morse, T. M., Carnevale, T., Marengo, L., Wang, R., Migliore, M., et al. (2017). Twenty years of ModelDB and beyond: building essential modeling tools for the future of neuroscience. *J. Comput. Neurosci.* 42, 1–10. doi: 10.1007/s10827-016-0623-7
- McGeer, P. L., and McGeer, E. G. (2008). Glial reactions in Parkinson's disease. *Mov. Disord.* 23, 474–483. doi: 10.1002/mds.21751
- McIntyre, C. C., Mori, S., Sherman, D. L., Thakor, N. V., and Vitek, J. L. (2004). Electric field and stimulating influence generated by deep brain stimulation of the subthalamic nucleus. *Clin. Neurophysiol.* 115, 589–595. doi: 10.1016/j.clinph.2003.10.033
- Meissner, W., Leblois, A., Hansel, D., Bioulac, B., Gross, C. E., Benazzouz, A., et al. (2005). Subthalamic high frequency stimulation resets subthalamic firing and reduces abnormal oscillations. *Brain* 128, 2372–2382. doi: 10.1093/brain/awh616
- Mena, M. A., and García de Yébenes, J. (2008). Glial cells as players in parkinsonism: the "good," the "bad," and the "mysterious" glia. *Neuroscientist* 14, 544–560. doi: 10.1177/1073858408322839
- Mergenthaler, P., Lindauer, U., Dienel, G. A., and Meisel, A. (2013). Sugar for the brain: the role of glucose in physiological and pathological brain function. *Trends Neurosci.* 36, 587–597. doi: 10.1016/j.tins.2013.07.001
- Merino, M., Vizuete, M. L., Cano, J., and Machado, A. (1999). The non-NMDA glutamate receptor antagonists 6-cyano-7-nitroquinoxaline-2,3-dione and 2,3-dihydroxy-6-nitro-7-sulfamoylbenzo(f)quinoxaline, but not NMDA antagonists, block the intrastratial neurotoxic effect of MPP+. *J. Neurochem.* 73, 750–757. doi: 10.1046/j.1471-4159.1999.0730750.x
- Michmizos, K. P., and Nikita, K. S. (2011). "Addition of deep brain stimulation signal to a local field potential driven Izhikevich model masks the pathological firing pattern of an STN neuron," in *Conference proceedings : ... Annual International Conference of the IEEE Engineering in Medicine and Biology Society. IEEE Engineering in Medicine and Biology Society. Annual Conference* (Boston, MA), 7290–7293. doi: 10.1109/IEMBS.2011.6091700
- Modolo, J., Mosekilde, E., and Beuter, A. (2007). New insights offered by a computational model of deep brain stimulation. *J. Physiol. Paris* 101, 56–63. doi: 10.1016/j.jphysparis.2007.10.007
- Montgomery, E. B., and Gale, J. T. (2008). Mechanisms of action of deep brain stimulation (DBS). *Neurosci. Biobehav. Rev.* 32, 388–407. doi: 10.1016/j.neubiorev.2007.06.003
- Moran, A., Stein, E., Tischler, H., and Bar-Gad, I. (2012). Decoupling neuronal oscillations during subthalamic nucleus stimulation in the parkinsonian primate. *Neurobiol. Dis.* 45, 583–590. doi: 10.1016/j.nbd.2011.09.016
- Moran, A., Stein, E., Tischler, H., Belevsky, K., and Bar-Gad, I. (2011). Dynamic stereotypic responses of basal ganglia neurons to subthalamic nucleus high-frequency stimulation in the Parkinsonian primate. *Front. Syst. Neurosci.* 5:21. doi: 10.3389/fnsys.2011.00021
- Moro, E., Esselink, R. J., Xie, J., Hommel, M., Benabid, A. L., and Pollak, P. (2002). The impact on Parkinson's disease of electrical parameter settings in STN stimulation. *Neurology* 59, 706–713. doi: 10.1212/WNL.59.5.706
- Mosharov, E. V., Larsen, K. E., Kanter, E., Phillips, K. A., Wilson, K., Schmitz, Y., et al. (2009). Interplay between cytosolic dopamine, calcium, and alpha-synuclein causes selective death of substantia nigra neurons. *Neuron* 62, 218–229. doi: 10.1016/j.neuron.2009.01.033
- Muddapu, V. R., and Chakravarthy, S. V. (2017). Programmed cell death in substantia nigra due to subthalamic nucleus-mediated excitotoxicity: a computational model of Parkinsonian neurodegeneration. *BMC Neurosci.* 18:59. doi: 10.1186/s12868-017-0371-2
- Muddapu, V. R., Mandali, A., Chakravarthy, S. V., and Ramaswamy, S. (2018). A computational model of loss of dopaminergic cells in Parkinson's disease due to glutamate-induced excitotoxicity. *bioRxiv*, 1–69. doi: 10.1101/385138
- Murray, T. K., Messenger, M. J., Ward, M. A., Woodhouse, S., Osborne, D. J., Duty, S., et al. (2002). Evaluation of the mGluR2/3 agonist LY379268 in rodent models of Parkinson's disease. *Pharmacol. Biochem. Behav.* 73, 455–466. doi: 10.1016/S0091-3057(02)00842-0
- Murray, T. K., Whalley, K., Robinson, C. S., Ward, M. A., Hicks, C. A., Lodge, D., et al. (2003). LY503430, a novel alpha-amino-3-hydroxy-5-methylisoxazole-4-propionic acid receptor potentiator with functional, neuroprotective and neurotrophic effects in rodent models of Parkinson's disease. *J. Pharmacol. Exp. Ther.* 306, 752–762. doi: 10.1124/jpet.103.049445
- Musacchio, T., Rebenstorff, M., Fluri, F., Brotchie, J. M., Volkman, J., Koprich, J. B., et al. (2017). Subthalamic nucleus deep brain stimulation is neuroprotective in the A53T α -synuclein Parkinson's disease rat model. *Ann. Neurol.* 81, 825–836. doi: 10.1002/ana.24947
- Obeso, I., Casabona, E., Rodríguez-Rojas, R., Bringas, M. L., Macías, R., Pavón, N., et al. (2017). Unilateral subthalamotomy in Parkinson's disease: cognitive, psychiatric and neuroimaging changes. *Cortex* 94, 39–48. doi: 10.1016/j.cortex.2017.06.006
- Olanow, C. W., Jenner, P., and Brooks, D. (1998). Dopamine agonists and neuroprotection in Parkinson's disease. *Ann. Neurol.* 44(Suppl 1):S167–S174. doi: 10.1002/ana.410440725
- O'Neill, M. J., Murray, T. K., Whalley, K., Ward, M. A., Hicks, C. A., Woodhouse, S., et al. (2004). Neurotrophic actions of the novel AMPA receptor potentiator, LY404187, in rodent models of Parkinson's disease. *Eur. J. Pharmacol.* 486, 163–174. doi: 10.1016/j.ejphar.2003.12.023
- Oorschot, D. E. (1996). Total number of neurons in the neostriatal, pallidal, subthalamic, and substantia nigral nuclei of the rat basal ganglia: a stereological study using the cavalieri and optical disector methods. *J. Compar. Neurol.* 366, 580–599.
- Ortiz, G. G., Pacheco-Moisés, F. P., Mireles-Ramírez, M. A., Flores-Alvarado, L. J., González-Usigli, H., Sánchez-López, A. L., et al. (2016). "Oxidative stress and Parkinson's disease: effects on environmental toxicology," in *Free Radicals and Diseases*, ed R. Ahmad (Rijeka: InTech), 183–209.

- Pacelli, C., Giguère, N., Bourque, M.-J., Lévesque, M., Slack, R. S., and Trudeau, L.-É. (2015). Elevated mitochondrial bioenergetics and axonal arborization size are key contributors to the vulnerability of dopamine neurons. *Curr. Biol.* 25, 2349–2360. doi: 10.1016/j.cub.2015.07.050
- Park, C., Worth, R. M., and Rubchinsky, L. L. (2010). Fine temporal structure of beta oscillations synchronization in subthalamic nucleus in Parkinson's disease. *J. Neurophysiol.* 103, 2707–2716. doi: 10.1152/jn.00724.2009
- Park, C., Worth, R. M., and Rubchinsky, L. L. (2011). Neural dynamics in Parkinsonian brain: the boundary between synchronized and nonsynchronized dynamics. *Phys. Rev. E* 83, 1–4. doi: 10.1103/PhysRevE.83.042901
- Park, S. E., Song, K.-i., Suh, J.-k. F., and Youn, I. (2015). "Characteristics of the neuronal firing patterns in the subthalamic nucleus with graded dopaminergic cell loss in the nigrostriatal pathway," in *Conference proceedings: ... Annual International Conference of the IEEE Engineering in Medicine and Biology Society. IEEE Engineering in Medicine and Biology Society. Annual Conference (Milan)*, 2510–2513.
- Paul, G., Meissner, W., Rein, S., Harnack, D., Winter, C., Hosmann, K., et al. (2004). Ablation of the subthalamic nucleus protects dopaminergic phenotype but not cell survival in a rat model of Parkinson's disease. *Exp. Neurol.* 185, 272–280. doi: 10.1016/S0014-4886(03)00363-7
- Pavlidis, A., Hogan, S. J., and Bogacz, R. (2015). Computational models describing possible mechanisms for generation of excessive beta oscillations in Parkinson's disease. *PLoS Comput. Biol.* 11:e1004609. doi: 10.1371/journal.pcbi.1004609
- Peter, D., Liu, Y., Sternini, C., de Giorgio, R., Brecha, N., and Edwards, R. (1995). Differential expression of two vesicular monoamine transporters. *J. Neurosci.* 15, 6179–6188. doi: 10.1523/JNEUROSCI.15-09-06179.1995
- Philips, R. T., Chhabria, K., and Chakravarthy, V. S. (2016). Vascular dynamics aid a coupled neurovascular network learn sparse independent features: a computational model. *Front. Neural Circuits* 10:7. doi: 10.3389/fncir.2016.00007
- Piallat, B., Benazzouz, A., and Benabid, A. L. (1996). Subthalamic nucleus lesion in rats prevents dopaminergic nigral neuron degeneration after striatal 6-OHDA injection: behavioural and immunohistochemical studies. *Eur. J. Neurosci.* 8, 1408–1414. doi: 10.1111/j.1460-9568.1996.tb01603.x
- Piccini, P., and Pavese, N. (2006). State-of-the-art Therapeutic Strategies in Parkinson's Disease. *Eur. Neurol. Rev.* 6, 20–25. doi: 10.17925/ENR.2006.00.01.1a
- Pinsky, P. F., and Rinzel, J. (1995). Synchrony measures for biological neural networks. *Biol. Cybern.* 73, 129–137. doi: 10.1007/BF00204051
- Pissadaki, E. K., and Bolam, J. P. (2013). The energy cost of action potential propagation in dopamine neurons: clues to susceptibility in Parkinson's disease. *Front. Comput. Neurosci.* 7:13. doi: 10.3389/fncom.2013.00013
- Reeve, A. K., Grady, J. P., Cosgrave, E. M., Bennison, E., Chen, C., Hepplewhite, P. D., et al. (2018). Mitochondrial dysfunction within the synapses of substantia nigra neurons in Parkinson's disease. *NPJ Parkinson's Dis.* 4:9. doi: 10.1038/s41531-018-0044-6
- Rite, I., Machado, A., Cano, J., and Venero, J. L. (2007). Blood-brain barrier disruption induces *in vivo* degeneration of nigral dopaminergic neurons. *J. Neurochem.* 101, 1567–1582. doi: 10.1111/j.1471-4159.2007.04567.x
- Rocha, S. M., Cristovão, A. C., Campos, F. L., Fonseca, C. P., and Baltazar, G. (2012). Astrocyte-derived GDNF is a potent inhibitor of microglial activation. *Neurobiol. Dis.* 47, 407–415. doi: 10.1016/j.nbd.2012.04.014
- Rodriguez, M. C., Obeso, J. A., and Olanow, C. W. (1998). Subthalamic nucleus-mediated excitotoxicity in Parkinson's disease: a target for neuroprotection. *Ann. Neurol.* 44(3 Suppl 1):S175–88. doi: 10.1002/ana.410440726
- Rosenbaum, R., Zimnik, A., Zheng, F., Turner, R. S., Alzheimer, C., Doiron, B., et al. (2014). Axonal and synaptic failure suppress the transfer of firing rate oscillations, synchrony and information during high frequency deep brain stimulation. *Neurobiol. Dis.* 62, 86–99. doi: 10.1016/j.nbd.2013.09.006
- Rubin, J. E., and Terman, D. (2004). High frequency stimulation of the subthalamic nucleus eliminates pathological thalamic rhythmicity in a computational model. *J. Comput. Neurosci.* 16, 211–235. doi: 10.1023/B:JCNS.0000025686.47117.67
- Schapira, A. (2003). Neuroprotection in PD - A role for dopamine agonists? *Neurology* 61(6 Suppl.):S34–S42. doi: 10.1212/WNL.61.6_suppl_3.S34
- Schapira, A. H. V., and Olanow, C. W. (2003). Rationale for the use of dopamine agonists as neuroprotective agents in Parkinson's disease. *Ann. Neurol.* 53(Suppl. 3):S149–S157. discussion: S157–S159. doi: 10.1002/ana.10514
- Seidl, S. E., and Potashkin, J. A. (2011). The promise of neuroprotective agents in Parkinson's disease. *Front. Neurol.* 2:68. doi: 10.3389/fneur.2011.00068
- Shen, K. Z., and Johnson, S. W. (2000). Presynaptic dopamine D2 and muscarine M3 receptors inhibit excitatory and inhibitory transmission to rat subthalamic neurones *in vitro*. *J. Physiol.* 525(Pt 2):331–341. doi: 10.1111/j.1469-7793.2000.00331.x
- Shen, K. Z., and Johnson, S. W. (2008). Complex EPSCs evoked in substantia nigra reticulata neurons are disrupted by repetitive stimulation of the subthalamic nucleus. *Synapse* 62, 237–242. doi: 10.1002/syn.20488
- Shouno, O., Tachibana, Y., Nambu, A., and Doya, K. (2017). Computational model of recurrent subthalamo-pallidal circuit for generation of Parkinsonian oscillations. *Front. Neuroanat.* 11:21. doi: 10.3389/fnana.2017.00021
- Smith, I. D., and Grace, A. A. (1992). Role of the subthalamic nucleus in the regulation of nigral dopamine neuron activity. *Synapse (New York, N.Y.)* 12, 287–303. doi: 10.1002/syn.890120406
- Smith, Y., and Kiehl, J. Z. (2000). Anatomy of the dopamine system in the basal ganglia. *Trends Neurosci.* 23(10 Suppl):S28–S33. doi: 10.1016/S1471-1931(00)00023-9
- Spieles-Engemann, A. L., Behbehani, M. M., Collier, T. J., Wohlgenant, S. L., Steece-Collier, K., Paumier, K., et al. (2010). Stimulation of the rat subthalamic nucleus is neuroprotective following significant nigral dopamine neuron loss. *Neurobiol. Dis.* 39, 105–115. doi: 10.1016/j.nbd.2010.03.009
- Stykel, M. G., Humphries, K., Kirby, M. P., Czaniecki, C., Wang, T., Ryan, T., et al. (2018). Nitration of microtubules blocks axonal mitochondrial transport in a human pluripotent stem cell model of Parkinson's disease. *FASEB J.* 32, 5350–5364. doi: 10.1096/fj.201700759RR
- Sulzer, D. (2007). Multiple hit hypotheses for dopamine neuron loss in Parkinson's disease. *Trends Neurosci.* 30, 244–250. doi: 10.1016/j.tins.2007.03.009
- Sulzer, D., and Surmeier, D. J. (2013). Neuronal vulnerability, pathogenesis, and Parkinson's disease. *Move. Disord.* 28, 41–50. doi: 10.1002/mds.25095
- Surmeier, D. J., Guzman, J. N., Sanchez-Padilla, J., and Goldberg, J. A. (2010). What causes the death of dopaminergic neurons in Parkinson's disease? *Prog. Brain Res.* 183, 59–77. doi: 10.1016/S0079-6123(10)83004-3
- Surmeier, D. J., Obeso, J. A., and Halliday, G. M. (2017). Selective neuronal vulnerability in Parkinson disease. *Nat. Rev. Neurosci.* 18, 101–113. doi: 10.1038/nrn.2016.178
- Temel, Y., Visser-Vandewalle, V., Kaplan, S., Kozan, R., Daemen, M. A. R. C., Blokland, A., et al. (2006). Protection of nigral cell death by bilateral subthalamic nucleus stimulation. *Brain Res.* 1120, 100–105. doi: 10.1016/j.brainres.2006.08.082
- Tepper, J. M., and Lee, C. R. (2007). GABAergic control of substantia nigra dopaminergic neurons. *Prog. Brain Res.* 160, 189–208. doi: 10.1016/S0079-6123(06)60011-3
- Terman, D., Rubin, J. E., Yew, A. C., and Wilson, C. J. (2002). Activity patterns in a model for the subthalamopallidal network of the basal ganglia. *J. Neurosci.* 22, 2963–2976. doi: 10.1523/JNEUROSCI.22-07-02963.2002
- Tripathy, S. J., Savitskaya, J., Burton, S. D., Urban, N. N., and Gerkin, R. C. (2014). NeuroElectro: a window to the world's neuron electrophysiology data. *Front. Neuroinform.* 8:40. doi: 10.3389/fninf.2014.00040
- Tsai, P.-I., Lin, C.-H., Hsieh, C.-H., Papakyriakos, A. M., Kim, M. J., Napolioni, V., et al. (2018). PINK1 phosphorylates MIC60/mitofilin to control structural plasticity of mitochondrial cristae junctions. *Mol. Cell* 69, 744–756.e6. doi: 10.1016/j.molcel.2018.01.026
- Turski, L., Bressler, K., Jürgen Rettig, K., Löschmann, P.-A., and Wachtel, H. (1991). Protection of substantia nigra from MPP+ neurotoxicity by N-methyl-D-aspartate antagonists. *Nature* 349, 414–418. doi: 10.1038/349414a0
- Vaarmann, A., Kovac, S., Holmström, K. M., Gandhi, S., and Abramov, A. Y. (2013). Dopamine protects neurons against glutamate-induced excitotoxicity. *Cell Death Dis.* 4:e455. doi: 10.1038/cddis.2012.194
- van Elburg, R. A., and van Ooyen, A. (2004). A new measure for bursting. *Neurocomputing* 58–60, 497–502. doi: 10.1016/j.neucom.2004.01.086
- Vandecasteele, M., Glowinski, J., and Venance, L. (2005). Electrical Synapses between dopaminergic neurons of the substantia nigra pars compacta. *J. Neurosci.* 25, 291–298. doi: 10.1523/JNEUROSCI.4167-04.2005
- Vernon, A. C., Palmer, S., Datla, K. P., Zbarsky, V., Croucher, M. J., and Dexter, D. T. (2005). Neuroprotective effects of metabotropic glutamate receptor ligands in a 6-hydroxydopamine rodent model of Parkinson's disease. *Eur. J. Neurosci.* 22, 1799–1806. doi: 10.1111/j.1460-9568.2005.04362.x

- Vila, M., Périer, C., Féger, J., Yelnik, J., Faucheux, B., Ruberg, M., et al. (2000). Evolution of changes in neuronal activity in the subthalamic nucleus of rats with unilateral lesion of the substantia nigra assessed by metabolic and electrophysiological measurements. *Eur. J. Neurosci.* 12, 337–344. doi: 10.1046/j.1460-9568.2000.00901.x
- Waak, J., Weber, S. S., Waldenmaier, A., Görner, K., Alunni-Fabroni, M., Schell, H., et al. (2009). Regulation of astrocyte inflammatory responses by the Parkinson's disease-associated gene DJ-1. *FASEB J.* 23, 2478–2489. doi: 10.1096/fj.08-125153
- Wallace, B. A., Ashkan, K., Heise, C. E., Foote, K. D., Torres, N., Mitrofanis, J., et al. (2007). Survival of midbrain dopaminergic cells after lesion or deep brain stimulation of the subthalamic nucleus in MPTP-treated monkeys. *Brain* 130, 2129–2145. doi: 10.1093/brain/awm137
- Wang, X. J., and Rinzel, J. (1993). Spindle rhythmicity in the reticularis thalami nucleus: synchronization among mutually inhibitory neurons. *Neuroscience* 53, 899–904. doi: 10.1016/0306-4522(93)90474-T
- Weinberger, M., Mahant, N., Hutchison, W. D., Lozano, A. M., Moro, E., Hodaie, M., et al. (2006). Beta oscillatory activity in the subthalamic nucleus and its relation to dopaminergic response in Parkinson's disease. *J. Neurophysiol.* 96, 3248–3256. doi: 10.1152/jn.00697.2006
- Wellstead, P. (2010). Systems biology and the spirit of tustin. *IEEE Control Syst.* 30, 57–102. doi: 10.1109/MCS.2009.934989
- Wellstead, P., and Cloutier, M. (2011). An energy systems approach to Parkinson's disease. *Wiley Interdiscip. Rev.* 3, 1–6. doi: 10.1002/wsbm.107
- Whitton, P. S. (2007). Inflammation as a causative factor in the aetiology of Parkinson's disease. *Brit. J. Pharmacol.* 150, 963–976. doi: 10.1038/sj.bjp.0707167
- Wright, A. K., and Arbuthnott, G. W. (2007). The influence of the subthalamic nucleus upon the damage to the dopamine system following lesions of globus pallidus in rats. *Eur. J. Neurosci.* 26, 642–648. doi: 10.1111/j.1460-9568.2007.05706.x
- Wright, A. K., McLaughlin, K. E., Atherton, J. F., Norrie, L., and Arbuthnott, G. W. (2002). "Lesions of the rat globus pallidus, which increase subthalamic nucleus activity, cause dopamine cell death," in *The Basal Ganglia VII*, eds L. F. B. Nicholson and R. L. M. Faull (Boston, MA: Springer), 457–464.
- Yang, C., Yan, Z., Zhao, B., Wang, J., Gao, G., Zhu, J., and Wang, W. (2016). D2 dopamine receptors modulate neuronal resonance in subthalamic nucleus and cortical high-voltage spindles through HCN channels. *Neuropharmacology* 105, 258–269. doi: 10.1016/j.neuropharm.2016.01.026
- Zecca, L., Wilms, H., Geick, S., Claasen, J.-H., Brandenburg, L.-O., Holzknecht, C., et al. (2008). Human neuromelanin induces neuroinflammation and neurodegeneration in the rat substantia nigra: implications for Parkinson's disease. *Acta Neuropathol.* 116, 47–55. doi: 10.1007/s00401-008-0361-7
- Zhang, J., and Tan, L. C.-S. (2016). Revisiting the medical management of Parkinson's disease: levodopa versus dopamine agonist. *Curr. Neuropharmacol.* 14, 356–363. doi: 10.2174/1570159X14666151208114634
- Zhang, W., Phillips, K., Wielgus, A. R., Liu, J., Albertini, A., Zucca, F. A., et al. (2011). Neuromelanin activates microglia and induces degeneration of dopaminergic neurons: implications for progression of Parkinson's disease. *Neurotox. Res.* 19, 63–72. doi: 10.1007/s12640-009-9140-z
- Zheng, F., Lammert, K., Nixdorf-Bergweiler, B. E., Steigerwald, F., Volkman, J., and Alzheimer, C. (2011). Axonal failure during high frequency stimulation of rat subthalamic nucleus. *J. Physiol.* 589, 2781–2793. doi: 10.1113/jphysiol.2011.205807
- Zuddas, A., Oberto, G., Vaglini, F., Fascetti, F., Fornai, F., and Corsini, G. U. (1992a). MK-801 Prevents 1-Methyl-4-Phenyl-1,2,3,6-Tetrahydropyridine-Induced Parkinsonism in Primates. *J. Neurochem.* 59, 733–739. doi: 10.1111/j.1471-4159.1992.tb09429.x
- Zuddas, A., Vaglini, F., Fornai, F., Fascetti, F., Saginario, A., and Corsini, G. U. (1992b). Pharmacologic modulation of MPTP toxicity: MK 801 in prevention of dopaminergic cell death in monkeys and mice. *Ann. N.Y. Acad. Sci.* 648, 268–271. doi: 10.1111/j.1749-6632.1992.tb24553.x

Conflict of Interest Statement: The authors declare that the research was conducted in the absence of any commercial or financial relationships that could be construed as a potential conflict of interest.

Copyright © 2019 Muddapu, Mandal, Chakravarthy and Ramaswamy. This is an open-access article distributed under the terms of the Creative Commons Attribution License (CC BY). The use, distribution or reproduction in other forums is permitted, provided the original author(s) and the copyright owner(s) are credited and that the original publication in this journal is cited, in accordance with accepted academic practice. No use, distribution or reproduction is permitted which does not comply with these terms.



Cellular, Synaptic and Network Effects of Acetylcholine in the Neocortex

Cristina Colangelo*, Polina Shichkova, Daniel Keller, Henry Markram and Srikanth Ramaswamy*

Blue Brain Project, Ecole Polytechnique Fédérale de Lausanne (EPFL), Geneva, Switzerland

OPEN ACCESS

Edited by:

Robert C. Froemke,
New York University, United States

Reviewed by:

Heiko J. Luhmann,
Johannes Gutenberg University
Mainz, Germany
Gilad Silberberg,
Karolinska Institute (KI), Sweden

*Correspondence:

Cristina Colangelo
cristina.colangelo@epfl.ch
Srikanth Ramaswamy
srikanth.ramaswamy@epfl.ch

Received: 28 January 2019

Accepted: 22 March 2019

Published: 12 April 2019

Citation:

Colangelo C, Shichkova P, Keller D,
Markram H and Ramaswamy S
(2019) Cellular, Synaptic and Network
Effects of Acetylcholine in
the Neocortex.
Front. Neural Circuits 13:24.
doi: 10.3389/fncir.2019.00024

The neocortex is densely innervated by basal forebrain (BF) cholinergic neurons. Long-range axons of cholinergic neurons regulate higher-order cognitive function and dysfunction in the neocortex by releasing acetylcholine (ACh). ACh release dynamically reconfigures neocortical microcircuitry through differential spatiotemporal actions on cell-types and their synaptic connections. At the cellular level, ACh release controls neuronal excitability and firing rate, by hyperpolarizing or depolarizing target neurons. At the synaptic level, ACh impacts transmission dynamics not only by altering the presynaptic probability of release, but also the magnitude of the postsynaptic response. Despite the crucial role of ACh release in physiology and pathophysiology, a comprehensive understanding of the way it regulates the activity of diverse neocortical cell-types and synaptic connections has remained elusive. This review aims to summarize the state-of-the-art anatomical and physiological data to develop a functional map of the cellular, synaptic and microcircuit effects of ACh in the neocortex of rodents and non-human primates, and to serve as a quantitative reference for those intending to build data-driven computational models on the role of ACh in governing brain states.

Keywords: neuromodulation, acetylcholine, ACh receptors, neocortex, cellular excitability, synaptic transmission, network activity

INTRODUCTION

The cholinergic system is one of the most well-studied neuromodulatory systems, and perhaps phylogenetically the oldest. Acetylcholine (ACh) is found in both vertebrates and invertebrates and together with adrenaline and noradrenaline (NA), it acts as one of the main effectors of the autonomic nervous system. In the central nervous system (CNS), ACh impacts cellular and synaptic physiology and may switch network dynamics resulting in behavioral transitions such as from sleep to wakefulness, distraction to attention, and learning and recall (Hasselmo and Sarter, 2011; Lee and Dan, 2012).

Cholinergic effects have been studied for more than a century. In 1869, Schmiedeberg and Koppe (1869) demonstrated how extracts of a common mushroom, *Amanita muscaria*, could slow, and at a higher concentration arrest the beat of the frog heart. They purified the extract and named it muscarine. This substance, when applied to the brain and spinal cord was able to produce flaccidity and weaken the peripheral reflexes. However, the pharmacology of the nitrite ester of choline was different in that it had considerable nicotinic activity (nicotine is the major alkaloid of tobacco, first isolated by Posselt and Reiman from *Nicotiniana tabacum* leaves in 1828; Koukouli et al., 2017).

In 1921 experimental proof was obtained for ACh's role as a chemical transmitter at the cardiac vagal endings. The active substance was initially named "vagusstoff" by Otto Loewi in 1921 (Loewi, 1924). Sir Henry Dale further described that muscarinic responses were antagonized by atropine, whereas the nicotine actions were antagonized by curare (Dale, 1914).

It has long been known that ACh is also present at the level of the CNS, however, it was not until 1953 that evidence of the release of ACh in the brain was provided (Eccles et al., 1953). Prior to this discovery, it was known that anti-cholinergic drugs could influence learning and memory—pharmacological activation of muscarinic ACh receptors (mAChRs) was known to produce delirium symptoms, while receptor blockade generates severe anterograde amnesia. Moreover, the dementia of Alzheimer's and Parkinson's diseases has been associated with the loss of cortical cholinergic innervation (Little et al., 1998; Giacobini, 2003; Sabri et al., 2008; Hasselmo and Sarter, 2011), and chronic administration of nicotine reverses hypofrontality in animal models of addiction and schizophrenia (Koukoulis et al., 2017).

Classical notions sustain the view that the central cholinergic system works by a diffuse release of ACh across the cortex, activating its receptors globally and producing slow responses. While this view might be applicable to long-lasting behavioral phenomena, such as cortical arousal, it does not explain the modulation of processes that happen on a much faster scale, such as sensory gating, or plasticity (Muñoz and Rudy, 2014). ACh release in the neocortex originates from neurons distributed within the basal forebrain (BF) nuclei, including the medial septum, the vertical and horizontal diagonal band of Broca, the substantia innominata, and the nucleus basalis of Meynert (NBM). Release occurs through topographical projections, and all the projections arise from six groups of choline acetyltransferase (ChAT)-positive neurons in the BF (Ch1–Ch4) and brainstem (Ch5–Ch6; Wevers, 2011). The innervation sparsely reaches all cortical layers, but layer 5 is more heavily innervated, particularly in the motor and sensory areas; cholinergic pathways often provide *en passant* innervation (Dani and Bertrand, 2007) to the neocortex. Additionally, ACh-releasing cells are found in cortical layer 2/3. These cells exhibit a bipolar morphology, stain positive for calretinin (CR) and vasoactive intestinal peptide (VIP), and are GABAergic (von Engelhardt et al., 2007; Granger et al., 2018).

The function of a neuromodulatory system is largely defined by the anatomy of its projections. Projections from the BF selectively control cortical activity and target neocortical regions more specifically than previously assumed (Hasselmo and Sarter, 2011; Muñoz and Rudy, 2014; Obermayer et al., 2017). Recent evidence suggests that a roughly topographical organizational scheme exists in the rostro-caudal sequence of neurons of the BF (Zaborszky et al., 2015) and that specific BF nuclei innervate specific cortical areas, as opposed to what happens with noradrenergic fibers originating from the locus coeruleus (Chaves-Coira et al., 2016; Kim et al., 2016). Cholinergic fibers can take one of four different routes to cortical structures: the septal pathway (which projects mainly to the hippocampal cortex) the medial pathway, the lateral

pathway, or the internal capsule projection (which preferentially project to the neocortex; Poorthuis et al., 2014). Cholinergic terminals that reach the neocortex, mainly *via* layer 1 or layer 6 (Obermayer et al., 2017), can either exert a spread out control of cortical activity and regulate processes such as the transition from sleep to wakefulness and arousal, or contact a restricted number of cortical elements and have cell-type specific effects; here contextual cholinergic signals act in concert with local processing of sensory inputs in order to guide behavior.

The aim of this review is to bring together current knowledge of cholinergic modulation in the neocortex and to identify the gaps to propose future directions to advance the field of neuromodulation. Here, we summarize existing literature on ACh release in the neocortex of rodents and non-human primates, specifically focusing on how ACh-induced effects on the diversity of cell-types and synapses shape the emergence of network states and review theories that bridge the modulation of local circuit properties and the consequent reconfiguration of cortical states. Data-driven computational models allow predictions on the potential role of ACh in reconfiguring neocortical states (Ramaswamy et al., 2018). Therefore, this review reconciles the minimal, although sparse, datasets required to build a multi-scale computational model of the neocortical cholinergic system.

VOLUME vs. SYNAPTIC TRANSMISSION

A major factor that determines the spatiotemporal precision of ACh action is the transmission mode at cholinergic terminals. Cholinergic cortical signaling has historically been considered a slow and diffuse process, which was established upon examination of the functional organization of cholinergic projections and was mainly based on reports indicating a nearly complete absence of classical synapses at the level of cholinergic terminals (Muñoz and Rudy, 2014). Before optogenetic techniques were available, cholinergic pathways could not be activated in a selective manner, and thus evidence of the existence of fast cholinergic synaptic transmission was lacking, although some proof of fast nicotinic responses was already available from hippocampal recordings (Kalmbach et al., 2012; Obermayer et al., 2017).

In the cerebral cortex, cholinergic fibers are distributed in an intricate network with a characteristic laminar pattern. They have a higher density in the deeper layers. Cholinergic innervation reflects the classic organizational scheme of information processing systems (Kennedy and Bullier, 1985), with a higher number of projections being present in higher-order areas. Presumed cholinergic release sites have been ultra-structurally inspected and the subtle presence of synapse-like contacts has indeed been revealed; however, a relatively large number of these small varicosities, which are often associated with accumulated synaptic vesicles, do not seem to effectively establish synaptic contact with neighboring neurons, or exhibit only a few morphologically identifiable synapses. Furthermore, the scarceness of astrocytic processes in the immediate vicinity of ChAT-immuno-reactive axons (when compared to

glutamatergic terminals) may also allow greater diffusion of ACh within the extracellular space (Aoki and Kabak, 1992). Thus, relatively low concentrations of ACh will reach locations that are distant from the release site. This produces volume transmission or bulk release: neuromodulators slowly diffuse in a wide cortical area and bind to a large pool of extra-synaptic receptors (Dani and Bertrand, 2007).

Many studies (Umbriaco et al., 1994; Descarries and Mechawar, 2000; Sarter et al., 2009; Yamasaki et al., 2010) conducted in the neocortex have suggested that ACh acts preferentially non-synaptically; however, central cholinergic synapses had already been observed in the early '90s. Actual synapses were found on cholinergic varicosities in the cingulate cortex of the rat (Umbriaco et al., 1994), and in macaque more than 40 percent of cholinergic varicosities contained synaptic specializations (Mrzijek et al., 1995). Later, Turrini et al. (2001) provide definitive evidence that suggests that synaptic mechanisms of cholinergic transmission not only exist but prevail in the rat neocortex. Ultrastructural observations that most (66%) cholinergic boutons—as revealed by IR assays for the specific cholinergic marker, vesicular ACh transporter (vAChT)—establish classical synapses in layer 5 of the rat parietal cortex. By applying an improved fixation protocol and by using an antibody for vAChT, Turrini et al. (2001) demonstrated that cholinergic boutons predominantly established symmetric synapses on layer 5 dendritic shafts. The authors also found that immuno-stained varicosities occasionally established asymmetric contacts, but always on dendritic spines.

Another study probed the molecular-anatomical relationship between detectable cholinergic varicosities and the most abundant receptor subtype in the cortex—the muscarinic receptor subtype M1 (Yamasaki et al., 2010). This study established that in the mouse neocortex M1 can be found almost exclusively on the extra-synaptic membrane of pyramidal cells (PCs). Here, they observed that M1 distribution is far denser than the putative cholinergic release sites and that it does not show any apposition pattern to the varicosities, nor to the cytomatrix active zone proteins that are normally found at glutamatergic terminals. Hence, M1's function in cortical PCs may be to sense ambient ACh released from cholinergic terminals at variable distances, and the main modality through which it is recruited is likely to be volume transmission. These approaches not only contribute to building a more refined knowledge of the subcellular localization of receptor subtypes but also provide a method to qualitatively discriminate between two major modes of transmission. Because of a substantial difference in the distribution pattern of cholinergic receptors across species, it is very likely that experiments performed in different species will yield conflicting results. For instance, even though a low incidence of classical synapses was reported for the rodent brain, a much higher proportion of cholinergic synapses was found in primates (Smiley et al., 1997). In the human cerebral cortex, the same authors found that up to 67% of all cholinergic varicosities established synaptic contacts, suggesting that ACh signaling in humans is mostly mediated by point-to-point synaptic transmission; this mechanism appears to prevail

in the primate brain, but whether the same can be said for rodents is still a matter of open debate.

Cholinergic innervation from the BF is more specific than previously considered; ACh can control cortical activity on a fine spatial scale as well. Indeed, these findings agree with the evidence of ACh signaling occurring through direct fast point-to-point synaptic transmission brought about by the application of optogenetic tools (Kalmbach et al., 2012). Overall, it is not completely clear yet whether one mode of cholinergic transmission prevails over the other. Instead, a growing body of evidence suggests that volume and synaptic transmission may be complementary mechanisms by which ACh modulates cortical function (Sarter et al., 2009). While bulk release is thought to cause a more tonic change in extracellular ACh concentration, in the scale of seconds and minutes, and is mainly mediated by activation of extra-synaptic receptors, ACh release occurring at junctional sites would have a more circumscribed influence, with the modulation of circuit activity being restricted to the contacted cortical elements and to a much more delimited spatiotemporal scale (Muñoz and Rudy, 2014). Taken together, evidence shows that ACh modulates microcircuit activity with different modalities, ranging from synaptic release to volume transmission, and exerts its effects by modifying membrane excitability or synaptic activity.

Instead of trying to proclaim one modality over the other, future research should address the issue of whether they can occur simultaneously and have a differential impact on the temporal aspects of the response. Traditional bath application of agonists results in broad spatial and temporal activation that might not reflect the accuracy of endogenous ACh release (Urban-Ciecko et al., 2018). It is thus of crucial importance to determine whether the different ways in which cholinergic agonists are experimentally applied reflect different transmission modalities, and how faithfully stimulation protocols replicate physiological conditions. In the future, ACh application should be standardized according to precisely obtained dose-response and sensitization kinetics curves, and ascending concentrations should be used in order to detect eventual dose-dependent responses. Furthermore, it would be of outstanding interest to better understand how ACh release obtained by optogenetic stimulation of cholinergic afferents compares against bath application of cholinergic agonists. In a recent study, optogenetic recruitment of cholinergic fibers was performed in parallel with 1 mM ACh bath-application to detect changes in Martinotti cells (MCs) activity: the two techniques yielded very similar results (Obermayer et al., 2018). Perhaps the high concentration of ACh used in this case is comparable with a more physiological activation of the cholinergic system. Further clarification is required on the matter, and future studies should, therefore, consider this issue and design their experiments accordingly.

Cholinergic projections are likely to be arranged according to a modular pattern, with isolated bands of neighboring ChAT⁺ cells in the BF having defined cortical targets that are, in turn, functionally associated. When retrograde dyes are injected in distant cortical areas, labeled regions of cholinergic cells in the BF still largely overlap, even though the innervated

cortical space is quite restricted (Muñoz and Rudy, 2014). Furthermore, Zaborszky et al. (2015) assert that the degree of overlap of labeled neuronal locations within the BF is positively correlated to the connection strength between the different injected cortical regions. Such an organization could induce widespread modulation even when the system is only focally activated (Muñoz and Rudy, 2014). Nevertheless, the response to neuromodulatory inputs is determined by the interplay of multiple factors, such as post-synaptic target, receptor type and subunit composition, subcellular localization of the receptors and their sensitivity. This way, a diffusely-organized projection system can fine-tune microcircuit activity. The cholinergic projection system should be viewed as a highly dynamic structure, able to propagate inputs either selectively or diffusely, switching from one modality to another, depending on the needs.

The next section aims to unravel the contribution of each subtype of cholinergic receptor to microcircuit modulation and attempts to determine the physiological relevance of their compartmentalized distribution and differential activation.

CHOLINERGIC RECEPTORS

Even though the differential pharmacological effects had already been characterized, it was not until the early 1950s that the idea of “receptors” as the binding site for ACh was firmly established by Eccles et al. (1953). Cholinergic receptors are composed of two classes of transmembrane macromolecular complexes, the muscarinic and the nicotinic receptor families, each of which is further divided into subclasses. The occurrence of many ACh receptor subtypes and their differential dendritic, somatic, axonal, and synaptic localization contribute to the varied roles that these receptors play in the CNS. Cholinergic receptors have been found on axons originating from thalamic, cortical or basalo-cortical fibers as well as on cortical pyramidal excitatory neurons and inhibitory GABAergic interneurons (Groleau et al., 2015). The precise layer-wise distribution of cholinergic terminals, the identification of cell-types that actually express cholinergic receptors, and the subcellular localization of these receptors are described in the following sections.

MUSCARINIC RECEPTORS

Cholinergic synapses throughout the CNS are composed of muscarinic receptors (mAChRs), which can be further differentiated into subtypes that are encoded by a single gene (Venter et al., 1988; Van der Zee and Luiten, 1999). Five genetically defined and pharmacologically characterized (M1 to M5) mAChR subtypes have been identified in the CNS with high levels of expression in subcortical structures and the cerebral cortex (Wevers, 2011). Immunocytochemical approaches have identified different levels of expression of mAChRs throughout the cerebral cortex. These studies have detected moderate levels of mAChRs in the frontal cortex, parietal cortex, temporal cortex, entorhinal cortex, occipital cortex, insular and cingulate cortex, with the highest values for

the temporal and occipital cortex. M1 receptors are the most abundantly expressed among all subtypes of mAChRs (Wevers, 2011). The density of cholinergic terminals in the rat neocortex differs between the six layers and depends on the cortical region studied (Eckenstein et al., 1988; Lysakowski et al., 1989). The pattern of cellular staining for mAChRs in the neocortex is characterized by a clear laminar distribution: in most of the cortical mantle, especially in neocortical areas, predominantly layer 5 PCs (L5PCs) show strong immunoreactivity across mammals such as the mouse, golden hamster, rat, cat, and human (Van der Zee and Luiten, 1999).

The density of each mAChR subtype differs throughout the brain with M1 being the most abundantly expressed and M5 the least (Alger et al., 2014). In the hippocampus and neocortex, M1 is present at high levels, M3 is moderately represented (though generally low elsewhere) and M4 is present in high density, as almost anywhere else in the brain, even though its concentration is considerably lower than M1. M2 instead, is found at very low densities, and this class of receptors seems to be distributed according to a precise pattern. M2 receptors frequently reside on presynaptic axonal terminals, whereas M1 receptors are often located on somato-dendritic regions of neurons. The M5 subtype is believed to play an important role in cortical perfusion, and it is mainly expressed on endothelial cells of the cerebral vascular system (Elhousseiny and Hamel, 2000; Gericke et al., 2011) even though recent evidence suggests that the M3 subtype is also involved in this kind of process (Zuccolo et al., 2017). In the rodent visual cortex, the subtypes M1 and M2 predominate, while in primates the subtypes M1, M2 and M4 prevail. Besides a few regional variations, highest labeling densities have been observed in the superficial layers of most cortical areas for both M1 and M2 (Wevers, 2011).

Most cholinergic receptors are metabotropic and mediate slow responses, which are typically associated with volume transmission. In the neonatal and adult cortices of rodents and primates, M1–M5 subtypes of mAChRs occur in both pre-synaptic and post-synaptic positions (Mrzljak et al., 1993; Groleau et al., 2015). All mAChRs are transmembrane macromolecular complexes that are coupled to membrane-embedded G-proteins of different kinds; g-proteins act as intracellular effectors and initiate signaling cascades that ultimately have an effect on intracellular processes, leading to the opening or closing of some ion channel, or to the production of long-term modifications of genetic activity and protein expression. Different mAChRs are coupled to specific G-proteins. The pre-synaptic mAChRs M2 and M4 preferentially couple to G_i and G_o proteins that generally have inhibitory effects on voltage-activated calcium channels or extend the opening of potassium channels. The resulting decrease in c-AMP signaling suppresses neurotransmitter release (Groleau et al., 2015). M1, M3 and M5 subtypes are preferentially coupled to G_q and G_{11} proteins and are mainly located post-synaptically. Their activation seems to trigger membrane depolarization and increases the input-resistance of the cell membrane. M1-like (M1-M3-M5) receptors are known to potentiate NMDA currents and also influence and modulate voltage-dependent calcium currents, mostly by upregulating phospholipase C

(PLC) signaling and inositol triphosphate (IP₃) turnover. One major effect that can be attributed to M1-type receptors is the inhibition of potassium currents, including the I_m and the I_{AHP} (both medium and slow rate). However, M1-type receptors can also potentiate cationic currents like the I_h and the TRP currents, and the I_{cat} (Teles-Grilo Ruivo and Mellor, 2013). For a more detailed description of the effects of ACh on various currents and their associated intracellular signaling pathways, we direct the reader to the section “Subcellular Nicotinic and Muscarinic Pathways” of this review.

PRE-SYNAPTIC LOCALIZATION

What anatomical and functional evidence exists on the distribution of mAChRs in the neocortex? Muscarinic cholinergic activity influences sensory processing by facilitating or depressing neuronal responses to specific stimuli, and by modulating connections strength and neural synchronization: this results in the fine-tuning of cellular and network properties during developmental processes, the execution of attention tasks and perceptual learning (Groleau et al., 2015). These effects can largely be attributed to M1 and M2 subtypes, which appear to be highly prevalent in the neocortex. The presence of M1 and M2 mAChRs on PC somata and apical dendrites in non-human primates is well established, but M2 receptors are also found on excitatory and inhibitory axons in the primate neocortex (Mrzljak et al., 1993). Disney et al. (2006) report that M1 and M2 receptor labeling can be observed, but is quite weak in axons and terminals in the macaque visual cortex, whereas mAChRs are mostly expressed at the level of the soma of GABAergic neurons and in the dendritic compartments of glutamatergic cells.

Among the presynaptic receptors in the rodent and human visual cortex, M2 is very abundant while M4 is less prevalent (Groleau et al., 2015). M2 and M4 are mostly found at the presynaptic terminals; activation of these receptor subtypes causes membrane hyperpolarization and conveys a self-inhibitory signal. Thus, extracellular levels of ACh are regulated by means of negative feedback. In the rat's primary visual cortex (V1) M2 is mainly found at the level of cholinergic terminals in layer 4 and layer 5. Being the main inhibitory auto-receptor, it contributes to the suppression of presynaptic ACh release (Mrzljak et al., 1993).

It is not yet clear whether the presence of M2-like subtypes at the level of the presynaptic terminal is a distinctive feature of cholinergic axons innervating the neocortex. Conflicting results emerge when looking at rodent studies, while experiments done on non-human primates and cats corroborate M2 receptors as the main auto-receptors localized on BF cholinergic axons. Subsequent research should, therefore, address this issue and determine the extent to which presynaptic M2-like receptors account for negative feedback *via* auto-inhibition, since this type of self-regulatory process is crucial for the fine-tuning of the response. Moreover, given that BF fibers originating from distinct neuron clusters differentially innervate separate cortical areas (Zaborszky et al., 2015; Chaves-Coira et al., 2016; Kim et al., 2016), discrepancies should be expected

when assessing receptor subtype distributions across neocortical regions. Estimation of the physiological presynaptic distribution profile of inhibitory auto-receptors in the rodent sensory cortex is of key importance to understanding the system's self-calibrating features. A systematic anatomical profiling of receptor expression should be performed in the rodent models, and quantitative comparisons should be made across sensory areas.

POST-SYNAPTIC LOCALIZATION

Neocortical PCs and inhibitory interneurons are strongly innervated by cholinergic axons, with L5PCs being the most densely innervated cells; however, numerous immuno-reactive interneurons can be found in all layers, but most frequently in layer 2/3 and layer 5. Here, the mAChR positive interneurons are intermingled with labeled PCs, but in general, the immunostaining of interneurons is less dense than that of the PCs (Van der Zee and Luiten, 1999). While mAChRs are more easily found in the dendritic compartments of PCs, their expression profile throughout the diversity of inhibitory interneurons is quite homogeneous, as these receptors are detected in proximity of the somatic compartment (Disney et al., 2006). mAChRs are expressed by different types of interneurons. In macaque, M2 receptors are found in 31% of PV neurons, 23% of CB neurons, and 25% of CR neurons. 87% of PV⁺ neurons, 60% of CB⁺ neurons and 40% of CR⁺ neurons however, express M1-type mAChRs. The M1 subtype is found across the cortical mantle on the cell bodies and dendrites of post-synaptic PCs, and it appears to be present mainly in layers 2/3 and 6, but it can be found across all cortical layers. In macaque V1, M1 is mostly expressed on GABAergic interneurons, but it is also found on cortico-cortical fibers (Mrzljak et al., 1993; Groleau et al., 2015). M1 immuno-reactivity is also observable in interneurons of the rat neocortex (Levey et al., 1991), although other studies have pointed to a low expression of M1 in primary sensory cortices of rats, such as S1 and V1. Some found M1 expression on PV⁺ neurons to be low or even undetectable in mice neocortex (Yamasaki et al., 2010). The significant difference in expression between rodents and primates could be explained by the fact that M1 receptors are much more associated to the extra-synaptic membrane compartments and are usually activated by volume transmission. Given that the BF cholinergic projection system is scaled-up in primates relative to rodents, there could be a more widespread distribution of M1 receptors throughout cortical interneurons. M1 immuno-reactivity is also detected at the synaptic level, in both inhibitory and excitatory synapses across cortical layers, but more frequently on asymmetric synapses, and here, preferentially on dendritic spines, as opposed to symmetric synapses where M1 is found mostly on dendritic shafts (Mrzljak et al., 1993). This preferential distribution perspective is challenged though, by experimental evidence that cholinergic boutons form synapses mainly with dendritic shafts, much fewer with dendritic spines and only occasionally on neuronal somata (Beaulieu and Somogyi, 1991; Mrzljak et al., 1993; Umbriaco et al., 1994). However, in mice, the highest density of M1 immuno-particles is observed in small-caliber

oblique dendrites (smaller than $0.66\ \mu\text{m}$ in diameter) of PCs (Yamasaki et al., 2010).

In L5PCs, M2 mAChRs are mainly localized postsynaptically, where they bring about a decrease in excitatory conductances, but M2 and M4 receptors are also present on the cell bodies of GABAergic interneurons in layers 2/3 and 4; here, M2 activation inhibits GABA release. The M3 subtype is localized postsynaptically in rodent inhibitory neurons and dendrites, where it enhances inhibitory transmission (Mrzljak et al., 1993; Groleau et al., 2015). Finally, M4 mAChRs are expressed in cortical excitatory neurons, in particular, in layer 4 spiny stellate neurons (L4SS) across different neocortical regions—S1, V1, and prefrontal cortex (PFC)—where they generate a persistent

hyperpolarizing response (Radnikow and Feldmeyer, 2018). Perhaps the presence of M4 mAChRs is a marker to tell apart layer 4 from other layers.

Cholinergic inputs to the cortex generate different responses depending on which receptor is recruited: while M1-like (M1–M3–M5) receptors activation generally leads to an increase in postsynaptic conductance, M2-like receptors (M2–M4) have the opposite tendency to decrease synaptic transmission, by regulating presynaptic ACh release or by directly hyperpolarizing the post-synaptic membrane. mAChRs thus seem to be distributed both at the presynaptic and the postsynaptic level, and the resulting effect depends mostly on which subtype is activated. A detailed understanding of the cellular localization

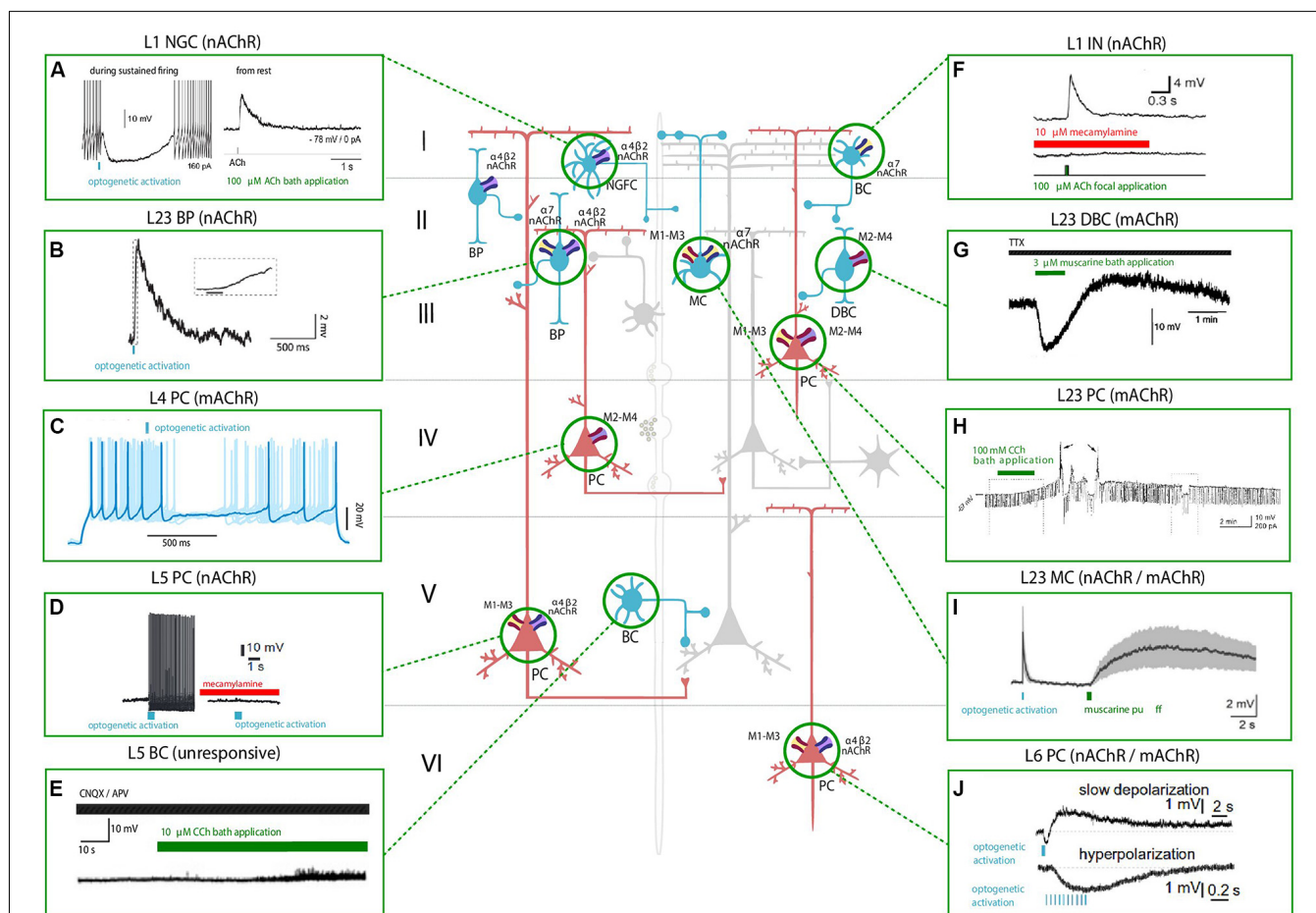


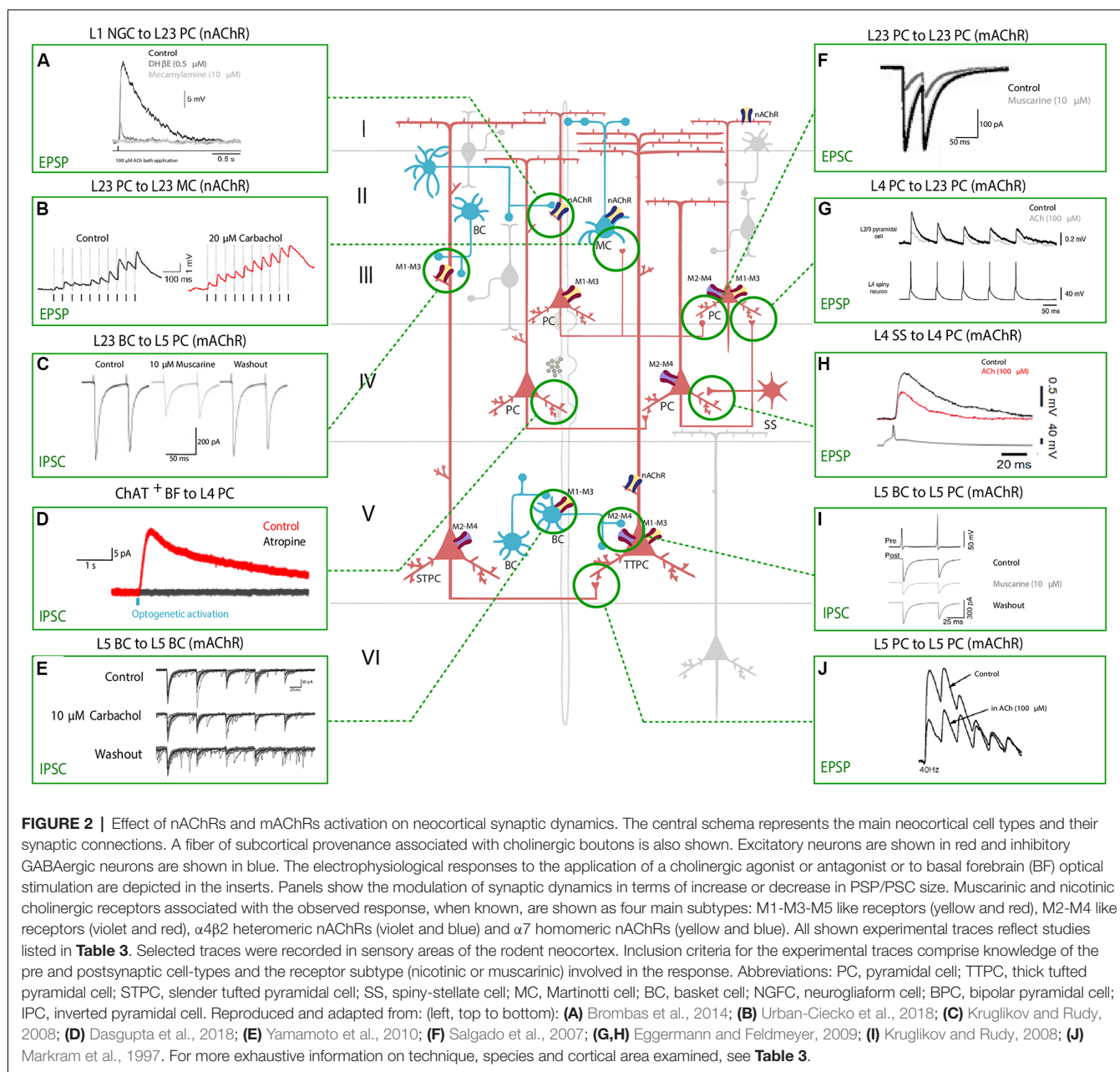
FIGURE 1 | Effect of nicotinic acetylcholine receptors (nAChRs) and muscarinic ACh receptors (mAChRs) activation on the membrane potential of various neocortical cell types. The central schema represents the main cell types in the neocortex. Excitatory neurons are shown in red and inhibitory GABAergic neurons are shown in blue. The electrophysiological responses to the optogenetic activation of cholinergic fibers (in light blue) or the application of a cholinergic agonist (shown in green) or antagonist (shown in red) of each cell type are depicted in the inserts. Timing of cholinergic manipulation is shown as a vertical or horizontal bar. Muscarinic and nicotinic cholinergic receptors associated with the observed response, when known, are shown as four main subtypes: M1–M3–M5 like receptors (yellow and red), M2–M4 like receptors (violet and red), $\alpha 4\beta 2$ heteromeric nAChRs (violet and blue) and $\alpha 7$ homomeric nAChRs (yellow and blue). All shown experimental traces reflect studies listed in **Tables 1, 2**. Selected traces were recorded in sensory areas of the rodent neocortex. Inclusion criteria for the experimental traces comprise knowledge of the cell-types and the receptor subtype (nicotinic or muscarinic) involved in the electrophysiological response. Abbreviations: PC, pyramidal cell; SS, spiny-stellate cell; IN, interneuron; MC, Martinotti cell; BC, basket cell; DBC, double-bouquet cell; NGFC, neurogliaform cell; BPC, bipolar cell. Reproduced and adapted from: (left, top to bottom): (A) Brombas et al., 2014; (B) Arroyo et al., 2012; (C) Dasgupta et al., 2018; (D) Hedrick and Waters, 2015; (E) Kawaguchi, 1997 (Right, top to bottom): (F) Gullledge et al., 2007; (G) Kawaguchi, 1997; (H) Shalinsky et al., 2002; (I) Dasgupta et al., 2018; (J) Hedrick and Waters, 2015. For more exhaustive information on agonist concentration, species and cortical area examined, see **Tables 1, 2**.

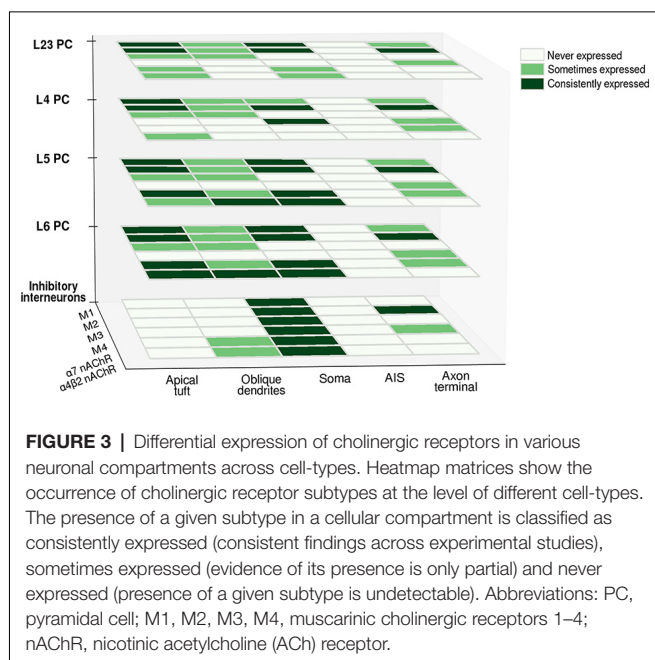
of each receptor subtype for every cell-type is still lacking; some generalizations can be made (as can be seen in **Figure 3**), but in order to precisely understand how neuromodulatory signals affect neural computation, a detailed knowledge of the amount and distribution of receptor subtypes at the level of each compartment is essential. Furthermore, it is of vital importance to gather this information for each neocortical cell-type. Neuromodulatory inputs very likely affect each cell-type differently, unlocking the possibility of fine-tuning the response and allowing delicate recalibration based on contextual information processing. This is most likely achieved by differentially distributing receptors along cellular compartments, thus creating modulatory micro-domains.

REGULATION OF NEURONAL AND SYNAPTIC PHYSIOLOGY

ACh can either increase or decrease neurotransmitter release probability, consistent with its role as a neuromodulator rather than a transmitter, and the effect on synaptic release probability depends on the identity of the pre and postsynaptic partners. Cell-types in the neocortex are differentially regulated by ACh, and the effects of cholinergic release include modulation of membrane properties (**Figure 1**) and synaptic dynamics (**Figure 2**).

The effects of ACh on neocortical PCs have been thoroughly investigated, and many studies (Gil et al., 1997;





Disney et al., 2007) have come to the conclusion that besides generating direct PC depolarization, cholinergic modulation has an overall effect of increasing the signal to noise ratio

(SNR) of incoming thalamic inputs. ACh seems to play a role in enhancing circuit responses to relevant stimuli, providing a mechanism to regulate sensory processing during learning and attention.

The involvement of mAChRs in the depolarizing response of PCs to BF cholinergic inputs has been established by numerous studies (McCormick and Prince, 1985; Delmas and Brown, 2005; Gullledge and Stuart, 2005; Carr and Surmeier, 2007; Zhang and Séguéla, 2010), which report that muscarinic activation in PCs leads to an initial SK-mediated hyperpolarization, followed by a more sustained and slow depolarization (Table 1, Figure 1). Interestingly, the same biphasic response can be induced by bath perfusion of muscarinic agonists in hippocampal interneurons (Heys and Hasselmo, 2012; Heys et al., 2012). The mechanism by which this depolarization emerges has not been fully clarified yet, but some authors suggest the suppression of muscarinic-sensitive and voltage-dependent K^+ conductance termed the M current (I_m) or the activation of a non-specific cationic current both support the observed depolarization (McCormick and Prince, 1985; Krnjević, 2004).

In L5PCs, transient activation of M1-type mAChRs induces calcium release from IP_3 -sensitive intracellular calcium stores and subsequent activation of an apamin-sensitive, SK-type calcium-activated potassium conductance (Gullledge et al., 2007). Conversely, M4-mediated activation of a potassium conductance (K_{ir3}) in L4SS generates a persistent membrane

TABLE 1 | Effect of muscarinic acetylcholine receptors (mAChRs) activation on membrane potential in various neocortical cell types.

Cell type	Receptor	Effect	Area	Technique—Reference
L5 PC	M1 (soma)	Transient hyperpolarization	Rat PMC/V1/PFC	Optogenetics (Hedrick and Waters, 2015)
	M1 (soma)	Slow depolarization	Rat PMC/V1/PFC	1. Optogenetics (Hedrick and Waters, 2015)
	M1 (soma)	Hyperpolarization	Rat SSC	2. Somatic puff 100 μ M ACh/CCh (Gullledge and Stuart, 2005)
	M1 (soma)	Depolarization	Rat mPFC	3. 100 μ M ACh focally applied (Gullledge et al., 2007)
L23 PC	Muscarinic	Depolarization	Rat SSC	100 μ M ACh focally applied (Gullledge et al., 2007)
	Muscarinic	Prolonged depolarization	Rat EC layer II	30 μ M muscarine or oxotremorine bath application (Haj-Dahmane and Andrade, 1996)
	M2–M4	Hyperpolarization	Mouse SSC (p12–p16)	<i>In vivo</i> 2-photon imaging (Alitto and Dan, 2013)
L4 PC	M2–M4	Persistent hyperpolarization	Mouse SSC	100 mM CCh bath application (Shalinsky et al., 2002)
L4 SS	M4 (soma)	Persistent hyperpolarization	Optogenetics (Dasgupta et al., 2018)	100 μ M ACh, puff (Eggermann and Feldmeyer, 2009)
L1 BC	Muscarinic	Depolarization	100 μ M ACh, puff (Eggermann and Feldmeyer, 2009)	1. 100 μ M ACh focally applied (Gullledge et al., 2007)
L1 DBC	Muscarinic	Depolarization	Mouse V1	<i>In vivo</i> 2-photon imaging (Alitto and Dan, 2013)
L23 DBC	M2	1. Hyperpolarization	1. Mouse V1	1. <i>In vivo</i> 2-photon imaging (Alitto and Dan, 2013)
		2. Hyperpolarization + slow depolarization	2. Rat PFC	2. 10 μ M CCh or 3 μ M muscarine bath application (Kawaguchi, 1997)
L23 MC	M1–M3	Depolarization	1. Rat SSC	1. 100 μ M ACh focally applied (Gullledge et al., 2007)
			2. Rat PFC	2. 10 μ M CCh or 3 μ M muscarine bath application (Kawaguchi, 1997)
L23 BC	Muscarinic	Depolarization	Mouse SSC	1. Muñoz et al. (2017; M1–M3 KO lines)
		Not responsive (NR)	Mouse V1	2. Optogenetics (Dasgupta et al., 2018)
L5 BC	Muscarinic	NR	1. Rat SSC	1 μ M/10 mM ACh application (Chen et al., 2015)
L5 MC		NR/slight depolarization	2. Rat PFC	1. 100 μ M ACh focally applied (Gullledge et al., 2007)
			Rat SSC	2. 10 μ M CCh or 3 μ M muscarine bath application (Kawaguchi, 1997)
				100 μ M ACh focally applied (Gullledge et al., 2007)

The table links the distribution and localization (when known, in brackets) of muscarinic receptors across neocortical cell types, with respect to cortical layers, with the effect of their activation. The effect of receptor activation is represented in terms of variation of membrane potential. Age of the specimen is given in brackets, when known. When biphasic effects occur, they are listed as multiple effects. Inclusion criteria for the listed studies comprise: (1) recordings performed in the rodent neocortex; (2) knowledge of the morphological type involved; and (3) knowledge of the receptor subtype involved in the response. Abbreviations: PC, pyramidal cell; SS, spiny-stellate cell; IN, interneuron; MC, Martinotti cell; BC, basket cell; DBC, double-bouquet cell; NGFC, neurogliaform cell; BPC, bipolar cell; NBC, nest basket cell; RS, regular spiking. PMC, primary motor cortex; V1, primary visual area; PFC, prefrontal cortex; mPFC, medial prefrontal cortex; EC, entorhinal cortex; SSC, somatosensory cortex; ACh, acetylcholine; CCh, carbachol.

hyperpolarization and induces suppression of neurotransmitter release (Table 1, Figure 1). The observed hyperpolarizing response is supported by a decrease in presynaptic calcium conductance, at synapses between L4PCs and also at synapses between L4PCs and L23PCs (see Table 3, Figure 2; Eggermann and Feldmeyer, 2009). Focal application of ACh onto the soma of L5PCs evokes a biphasic response in which a transient membrane hyperpolarization precedes a slower and longer-lasting depolarization. Pharmacological evidence suggests that this effect is mediated by M1 receptors. Compared with the pressure application of ACh, activation of cholinergic synapses with brief bursts provides relatively weak activation of mAChRs that often fails to affect the somatic membrane potential at rest (Hedrick and Waters, 2015). One possible interpretation of these results might be that synaptically released ACh activates first nAChRs and usually fails to activate mAChRs, whereas pressure ejection onto the soma recruits primarily mAChRs.

Muscarinic activation modulates K^+ conductances (McCormick, 1992), but the reversal potential for K^+ is approximately -90 mV: mAChR activation, therefore, exerts

a little effect at resting membrane potential. However, when a neuron is depolarized, the observable mAChR-mediated hyperpolarization and subsequent depolarization are larger. The reported biphasic effect affects both cortico-pontine (CPn) and commissural (COM) pyramidal neurons; however, COM neurons show a more pronounced inhibitory phase, while CPn neurons have a larger and longer-lasting depolarizing phase (Baker et al., 2018). While these effects have been characterized thoroughly in deep-layers PCs, others report that ACh has limited ability to inhibit superficial PCs *via* changes in membrane potential (Gulledge et al., 2007).

Cortical inhibitory interneurons are, as well as PCs, a prominent target of cholinergic neuromodulation. The ways in which ACh modulates the dynamics of local interneurons have not been completely clarified yet, because the effects of BF cholinergic stimulation and bath application of cholinergic agonists (Table 1) strongly depend on the inhibitory cell-type.

Exogenous application is unlikely to mimic accurately the spatiotemporal profile of ACh release from cholinergic axons, and furthermore, there seems to be no agreement within

TABLE 2 | Effect of nAChRs activation on membrane potential in various neocortical cell types.

Cell type	Receptor	Effect	Area	Technique—Reference
L5 PC	$\alpha_4\beta_2$ (soma and main dendrite)	Medium depolarization	Mouse PMC/V1/PFC	Optogenetics (Hedrick and Waters, 2015)
	$\alpha_4 \alpha_5$	Depolarization Persistent spiking (starting from subthreshold)	Mouse PMC/V1/PFC	Optogenetics (Hedrick and Waters, 2015)
L6 PC	$\alpha_4 \alpha_5$ (soma and main dendrite)	Depolarization	Mouse PMC/V1/PFC	Optogenetics (Hedrick and Waters, 2015)
	$\alpha_4\beta_2$	Depolarization	Rat PFC (p7–p27)	Kassam et al. (2008; bath application of $10 \mu\text{M}$ ACh to 1 mM)
L1 NGFC	Nicotinic (non- α_7)	Depolarization (from RP) Suppression of activity (from subthreshold)	Rat SSC	Ionophoretic application or bath application of $100 \mu\text{M}$ ACh (Brombas et al., 2014)
L1 BC	Nicotinic	Suppression of activity (at low levels of cortical desynchronization)	Mouse V1	<i>In vivo</i> 2-photon imaging (Alitto and Dan, 2013)
L1 INs	Nicotinic	Fast depolarization (from RP)	Rat SSC	$100 \mu\text{M}$ ACh focally applied (Christophe et al., 2002) and (Gulledge et al., 2007)
NBC	Nicotinic	Depolarization	Rat SSC	$100 \mu\text{M}$ ACh focally applied (Gulledge et al., 2007)
BPC	Nicotinic	Depolarization	Rat SSC	$100 \mu\text{M}$ ACh focally applied (Gulledge et al., 2007)
DBC	Nicotinic	Depolarization	Rat PFC	$10 \mu\text{M}$ CCh or $3 \mu\text{M}$ muscarine bath application (Kawaguchi, 1997)
L23 MC	Nicotinic	Depolarization	Mouse V1	$1 \mu\text{M}/10 \text{ mM}$ ACh application (Chen et al., 2015)
	Nicotinic	Depolarization	Rat SSC	Optogenetics (Dasgupta et al., 2018)
	$\alpha_4\beta_2$	Depolarization	Mouse S1 and mPFC	Optogenetics or 1 mM ACh bath-application (Obermayer et al., 2018)
L23 BC	Nicotinic	Some are depolarized Some are hyperpolarized	Mouse V1	<i>In vivo</i> 2-photon imaging (Alitto and Dan, 2013)
L23 CHAT ⁺ BPC	$\alpha_4\beta_2$	Depolarization	Mouse SSC (P20–P40)	Optogenetics (Arroyo et al., 2012)
L23 BPC	$\alpha_4\beta_2$ and α_7	Depolarization	Mouse and rat SSC	Optogenetics (Arroyo et al., 2012) and (Dasgupta et al., 2018); $100 \mu\text{M}$ ACh focally applied (Gulledge et al., 2007)
L5 MC	$\alpha_4\beta_2$	Depolarization	Mouse S1 and mPFC	Optogenetics or 1 mM ACh bath-application (Obermayer et al., 2018)

The table links the distribution and localization (when known, in brackets) of nicotinic receptors across neocortical cell types, with respect to cortical layers, with the effect of their activation. The effect of receptor activation is represented in terms of variation of membrane potential. Age of the specimen is given in brackets, when known. When biphasic effects occur, they are listed as multiple effects. Inclusion criteria for the listed studies comprise: (1) recordings performed in the rodent neocortex, (2) knowledge of the morphological type involved and (3) knowledge of the receptor subtype involved in the response. Abbreviations: PC, pyramidal cell; SS, spiny-stellate cell; IN, interneuron; MC, Martinotti cell; BC, basket cell; DBC, double-bouquet cell; NGFC, neurogliaform cell; BPC, bipolar cell; NBC, nest basket cell; RS, regular spiking. PMC, primary motor cortex; V1, primary visual area; PFC, prefrontal cortex; SSC, somatosensory cortex; ACh, acetylcholine; CCh, carbachol; RP, resting potential; NR, not responsive.

TABLE 3 | Cholinergic mediated modulation of neocortical synaptic dynamics.

Connection type	Receptor	Effect	Area	Technique—Reference
L5 PC-L5 PC	Muscarinic	Reduction in depression rate of consecutive EPSPs	Rat SSC	Bath application of 50 μ M ACh (Tsodyks and Markram, 1997)
	M1 (perisomatic)	Enhancement of EPSCs	Rat SSC (p14–p16)	1–10 μ M ACh local puff (Nuñez et al., 2012)
	M2 (basal dendrites)	Reduction of IPSCs	Rat SSC (p14–p16)	50–100 μ M ACh local puff (Nuñez et al., 2012)
	Nicotinic	Increase in EPSPs	Rat SSC (p14–p16)	1–10 μ M ACh local puff (Nuñez et al., 2012)
L5 PC-L5 MC	Nicotinic heteromeric	Decrease in onset delay, increase in time course; no change in EPSP size	Mouse S1 and mPFC	Optogenetics or 1 mM ACh bath-application (Obermayer et al., 2018)
		Reduction in first EPSP amplitude	Rat SSC	Bath application of 100 μ M ACh (Eggermann and Feldmeyer, 2009)
L4 PC-L4 PC	M4	Reduction in first EPSP amplitude	Rat SSC	Bath application of 100 μ M ACh (Eggermann and Feldmeyer, 2009)
L4 SS-L4 SS	M4	Reduction in EPSC amplitude	Rat A1 (p21–p28)	Bath application of 10 μ M oxotremorine or muscarine (Atzori et al., 2005)
L23 PC-L23 PC	M1/M3	Reduction in EPSP amplitude	Rat PFC	Iontophoretic application of 0.05 M muscarine (Vidal and Changeux, 1993)
	Muscarinic (apical dendrite)	Increase in EPSPs	Rat PFC	Iontophoretic application of 0.05 M muscarine (Vidal and Changeux, 1993)
TC fibers-L4 PC	Nicotinic	Increase in EPSP depression rate	Rats and mice TC slice (p21–p28)	Bath application of 5–10 μ M muscarine (Gil et al., 1997)
CHAT ⁺ fibers—L4 PC	Muscarinic	IPSC	Mouse TC slice (p12–p16)	Optogenetic activation (Dasgupta et al., 2018)
L23 PC-L23 MC	Nicotinic	Increase in EPSPs	Mouse SSC	Bath application of 20 μ M CCh (Urban-Ciecko et al., 2018) and optogenetics
		No change in EPSP size	Mouse S1 and mPFC	Optogenetics or 1 mM ACh bath-application (Obermayer et al., 2018)
L1 NGF-L23 PC	Nicotinic heteromeric	Connection is silenced (L23 PC is disinhibited)	Rat SSC (p24–p31)	Iontophoretic application or bath application of 100 μ M ACh (Brombas et al., 2014)
	Nicotinic (non α 7)	Connection is silenced	Rat SSC (p24–p31)	Iontophoretic application or bath application of 100 μ M ACh (Brombas et al., 2014)
L23 BC-L5 PC	Muscarinic	Reduction in IPSPs amplitudes (connection is silenced)	Mouse SSC	Bath application of 10 μ M muscarine (Kruglikov and Rudy, 2008)
L5 BC-L5 PC	M2/M4	Reduction in u-IPSC amplitude	Mouse SSC	Bath application of 10 μ M muscarine (Kruglikov and Rudy, 2008)
	Muscarinic	Reduction in u-IPSC amplitude	Rat insular cortex	Bath application of 10 μ M CCh (Yamamoto et al., 2010)
L5 MC-L5 PC	Nicotinic heteromeric	Decrease in onset delay, no change in IPSP size	Mouse S1 and mPFC	Optogenetics or 1 mM ACh bath-application (Obermayer et al., 2018)
		Increase in IPSP size	Mouse A1	Bath application of 10 μ M CCh (Hilischer et al., 2017)
L5 BC-L5 BC	Muscarinic	Decrease in IPSCs amplitudes	Rat insular cortex	Bath application of 10 μ M CCh (Yamamoto et al., 2010)
L5 RS IN-L5 PC	Muscarinic	Decrease in IPSCs amplitudes	Rat insular cortex	Bath application of 10 μ M CCh (Yamamoto et al., 2010)
L5 BC-L5 RS IN	Muscarinic	Increase in first IPSCs amplitudes	Rat insular cortex	Bath application of 10 μ M CCh (Yamamoto et al., 2010)
L5 RS IN-L5 RS IN	Muscarinic	Increase in first IPSCs amplitudes	Rat insular cortex	Bath application of 10 μ M CCh (Yamamoto et al., 2010)

The table links the distribution and localization (when known, in brackets) of nicotinic and muscarinic receptors across neocortical cell types, with respect to cortical layers, with the effect of their activation on synaptic dynamics. Effect is represented in terms of increase or decrease in PSP/IPSC size. Age of the specimen is given in brackets, when known. Inclusion criteria for the listed studies comprise: (1) recordings performed in the rodent neocortex; (2) knowledge of the pre and post synaptic morphological types involved; and (3) knowledge of the receptor subtype involved. Abbreviations: PC, pyramidal cell; SS, spiny-stellate cell; IN, interneuron; MC, Martinotti cell; BC, basket cell; DBC, double-bouquet cell; NGFC, neurogliaform cell; BPC, bipolar cell; NBC, nest basket cell; RS, regular spiking; A1, primary auditory area; PFC, prefrontal cortex; SSC, somatosensory cortex; TC thalamo-cortical; ACh, acetylcholine; CCh, carbachol; EPSP, excitatory post-synaptic potential; IPSP, inhibitory post-synaptic current; EPSC, excitatory post-synaptic current; IPSC, inhibitory post-synaptic current.

the neuroscientific community on which concentration of cholinergic agonists should be used to promote activation of the cholinergic receptors. The applied dose ranges from 10 to 100 micromolar across different experimental groups, and in other cases, it even spans the millimolar range. These discrepancies arise from the fact that to measure the physiological extracellular concentration of ACh is experimentally challenging, because of the prompt intervention of hydrolases in the synaptic cleft. Application of acetylcholinesterase inhibitors cannot be avoided, making it extremely difficult to detect physiological levels of ACh in the extracellular space. Moreover, while mAChR agonists have been extensively used and are known to generate a multitude of responses in cortical neurons, much fewer studies (Hedrick and Waters, 2015; Dasgupta et al., 2018) have discerned muscarinic responses evoked by endogenous ACh release (see Figures 1, 2).

Cholecystokinin-immunoreactive (CCK) cells are affected heterogeneously by cholinergic agonists depending on their sizes. For example, small CCK cells are promptly depolarized by cholinergic inputs, while bigger CCK cells show a biphasic response comprising an initial hyperpolarization and a subsequent depolarization similarly to PCs (Kawaguchi, 1997). There is a general consensus (Gulledge et al., 2007; Kruglikov and Rudy, 2008; Poorthuis et al., 2013) that cholinergic modulation of fast-spiking PV positive (PV⁺) interneurons does not produce any effect on membrane excitability (Table 1). However, evidence also shows the opposite. For example, Alitto and Dan (2013) report in their review that PV⁺ interneurons are depolarized *via* muscarinic activation, but when mAChRs are blocked by antagonist application, the excitation is converted to inhibition; in turn inhibition of PV⁺ cells is converted to excitation when nAChRs are blocked, suggesting that excitation and inhibition compete in the same population of PV⁺ interneurons through the activity of the different receptors.

The subpopulation of dendrite-targeting interneurons, that is identified as somatostatin (Sst) expressing (Sst⁺) interneurons (MCs), can be depolarized by activation of mAChRs (Fanselow et al., 2008). However, some studies report that only very few Sst⁺ interneurons display excitation or inhibition in response to BF stimulation and that the inhibitory cells displaying the strongest excitation by ACh are L1 and VIP⁺ interneurons. Recent findings outlined by Muñoz et al. (2017) challenge these results. In their study, they claim that cholinergic modulation of Sst⁺ interneurons *via* M1 and/or M3 mAChRs provides a major excitatory drive to these cells during whisking activity.

VIP expressing interneurons are highly responsive to cholinergic inputs and show a mixed activation profile that is partially blocked by both nicotinic and muscarinic receptor antagonists (Kawaguchi and Kubota, 1997).

In summary, muscarinic activation has differential effects on membrane potential, based on which subtypes are expressed in a specific cell-type and in cellular compartments. These heterogeneous responses might play different roles in neocortical information processing: the initial hyperpolarizing phase observed in PCs and some CCK⁺ cells could be used to push the cell away from threshold, while the subsequent depolarization selectively augments inputs that are strong enough to reach

threshold, therefore increasing the SNR, and at the same time promoting synchronization of neural activity. At the same time, the presynaptic inhibition of excitatory feedback could serve as a mechanism to prevent interference during the encoding of new stimuli and reduce top-down influences on perceptive processes. In addition, muscarinic receptors contribute to the generation of the gamma rhythm by inducing synchronized oscillations in both excitatory and inhibitory neurons (Heys et al., 2012).

Another class of receptors contributes to cholinergic signaling in the neocortex. Nicotinic receptors exert fast cortical actions, playing a key role in many cognitive processes (Dani and Bertrand, 2007), as described in the following section (Dani and Bertrand, 2007).

NICOTINIC RECEPTORS

ACh is primarily regarded as a neuromodulator rather than a neurotransmitter in the CNS because its physiological effects have a latency of onset of tens of milliseconds to minutes (Van der Zee and Luiten, 1999). This great variability in the response of cortical neurons to ACh stimulation originates from the fact that there are two main types of ACh receptor proteins. Neuronal nicotinic receptors (nAChRs) are ionotropic receptors which are composed of combinations of twelve different nAChR subunits: $\alpha 2$ to $\alpha 10$ and $\beta 2$, $\beta 3$, $\beta 4$. Each receptor is made of five subunits. It is generally assumed that nicotinic actions are fast and precise; however, the depolarization rate produced by the opening of the nicotinic channel can vary depending on the specific subunit composition. Because mAChR signaling acts through G-proteins, mAChR signaling might be expected to be slower than ionic nAChR signaling. However, homomeric ($\alpha 7$) nAChRs can also mediate slow responses, and the time course of muscarinic action may also vary widely, depending on the signal pathways involved (Muñoz and Rudy, 2014).

The nicotinic branch of the AChR family can be further divided into at least two classes, based on the affinity that their binding sites have for nicotine itself or the snake toxin α -bungarotoxin. At their simplest neuronal nAChRs are homomeric (constituted from five identical subunits) while the more complex forms are heteromeric, composed of at least one α and one β subtype. Binding studies using [³H]-nicotine have shown that high-affinity nAChR binding sites are very common for the human cerebral cortex, while autoradiographic labeling of nAChRs shows an inhomogeneous distribution over architectonically identified cortical areas of the rat brain, with highest concentrations in the medial PFC (mPFC) and generally frontal areas.

As for mAChRs, the expression of different subunit combinations varies across layers and across cortical areas. Given the involvement of the nicotinic system in the treatment of tobacco addiction, many studies have been performed in the human brain. Most data on the distribution of nAChRs has been obtained from human autopsy tissue homogenates using techniques such as ligand binding, RT-PCR, immunoprecipitation, and Western blot.

Currently-available nAChR agonists and antagonists used for receptor auto-radiography are not subtype specific, although

they act on nAChR subtypes with a distinct profile: labeling experiments carried out with different probes revealed that nAChRs are widely expressed in the cortex, both at the level of gray and white matter; many fibers show immunoreactivity at the neuropil level (Schröder, 1992). Five α subunits (3–7) and three β subunits (2–4) are expressed in the human brain. The expression of $\alpha 4$ and $\beta 2$ subunits in the frontal cortex, parietal cortex, and temporal cortex shows a characteristic laminar distribution. Higher receptor binding is observed in layers 1, 3 and 5. These results are in agreement with the observed distribution of $\alpha 3$ and $\alpha 4$ mRNAs that are mostly found in PCs of layer 2/3 and layer 5 of the frontal cortex (Wevers, 2011). However, other studies report that the $\alpha 3$ mRNA is exclusively expressed in layer 4, while $\alpha 4$ subunit is moderately expressed in all layers (Radnikow and Feldmeyer, 2018). The $\alpha 7$ subunit is found mostly in layer 1–3 and 5 and is virtually absent in layer 4, while $\alpha 4$ and $\beta 2$ immunoreactive fibers were observed in layer 4 of the PFC (Sparks et al., 2018). The $\alpha 2$ subunit is a characteristic feature of L5MCs that project to layer 1 and specifically target L5TTPCs (Hilscher et al., 2017). The detection of nicotinic subunits is possible because of the existence of specific antisubunit-antibodies and the introduction of nAChR subunit-Cre mouse lines. Nevertheless, nicotinic receptors are made up of multiple subunits and are either homomeric or heteromeric. The most abundant receptor subtypes in the neocortex are the homomeric receptor $\alpha 7$ and the heteromeric $\alpha 4\beta 2$ channel (which is often associated with the regulatory subunit $\alpha 5$; Radnikow and Feldmeyer, 2018). Nicotinic receptors can be activated both *via* volume transmission and fast synaptic activity (Dani and Bertrand, 2007; Hedrick and Waters, 2015; Hay et al., 2016).

PRE-SYNAPTIC LOCALIZATION

None of the studies mentioned above investigates the precise cellular localization of cholinergic receptors, which is crucial in determining the outcome of the response. This is especially true for nAChRs, because their activation directly leads to a cation influx into the cell, and immediately results in a voltage change in the underlying compartment.

nAChRs are expressed on glutamatergic inputs to layer 5, mostly contacting layer 5 interneurons and L5/L6 PCs. L5PCs and L6PCs are modulated by $\alpha 7$ and $\beta 2$ nAChRs, respectively, while L23PCs and glutamatergic inputs to these cells do not contain nAChRs. Interneurons across layers contain mixed combinations of nAChRs (Poorthuis et al., 2013). Some subtypes, such as $\alpha 7$ homomeric receptors, are preponderantly expressed in presynaptic areas, whereas heteromeric receptors are more expressed on cell bodies and main dendrites (Bertrand, 2010). Cholinergic axons that diffusely innervate the cortex are thought to make *en passant* connections in the area of the main dendrite of the PCs from layer 5 and VI, therefore causing a volume release of ACh. Pre-synaptically, nAChRs generally increase the release of GABA and glutamate (Dani and Bertrand, 2007). However, both nAChR and mAChRs can reduce EPSPs by acting pre-synaptically (Levy et al., 2006).

POST-SYNAPTIC LOCALIZATION

The distribution of nAChRs at the light and electron microscopic level was studied in the human cerebral cortex using anti-nAChR monoclonal antibody (mAb) WF-6, which is not subunit selective (Schröder et al., 1990): nAChR immunoreactivity revealed a pattern for the frontal and temporal cortex that was very similar to that obtained with the auto-radiography. In the frontal cortex, *in situ* hybridization techniques display numerous labeled neurons, mostly PCs bearing the $\alpha 7$ mRNA in the cell body and in the apical dendrite. In the motor cortex, many PCs showed signals in the proximal part of their apical dendrite.

As reported by Schröder et al. (1989) and Schröder (1992) nAChR localization is predominant in L23 and L5 PCs; a few nAChR-expressing fusiform cells can be detected in layer 4 and VI. Many PCs show nAChRs on basal dendrites that originate in layer 5, cross the superficial layers of the cortex perpendicular to the pial surface, and branch between layers 1 and 2. Immuno-precipitate is detectable both in cell bodies and in their apical dendrites, in branches of various diameters, and in the PSD of synaptic junctions. In a double-labeling approach conducted in the temporal cortex, it was further demonstrated that PV⁺ interneurons express $\alpha 4$ and $\alpha 7$ subunit protein (Wevers, 2011). Double-labeling studies have shown that at least 30% of cortical neurons contain both nAChR and mAChR proteins, the majority of these being PCs. In the human cortex, nicotinic immuno-staining in individual neurons appears generally comparable to that seen in the rodent model (Schröder et al., 1989; Schröder, 1992): as in the rat occipital cortex, nAChRs can be detected on the cell bodies and dendrites of L23 and L5 PCs.

Most studies agree that nAChRs are preferentially found in infragranular layers, mostly at the level of L5 and L6PCs, but also at the level of inhibitory interneurons; CB-immunoreactive neurons, as well as PV⁺ neurons all express nAChRs, while that is not true for CR-ir neurons (Coppola and Disney, 2018); furthermore, nAChRs are expressed at the level of layer 2/3 as well, both in PC bodies and in the apical dendrites of deeper-layer placed cells. However, only a small subset of layer 2/3 excitatory neurons and no layer 4 neurons express nAChRs; layer 6 expression profile can be set apart from the rest, given that these neurons predominantly express the slowly desensitizing heteromeric $\alpha 4\beta 2$ channel (Radnikow and Feldmeyer, 2018).

The distribution of nAChRs and the subunits combination, therefore, depends on cell-types, laminar position and on the cortical area studied, similarly to mAChRs; nowadays the possibility of systematically studying the distribution profile of cholinergic receptors has greatly increased, due to the advancement in the production of anti-subunit-specific-antisera and to the development of better immunoprecipitation and ligand binding techniques. Such studies exist and are quite informative as regards, for instance, the striatum (Zoli et al., 2002), but a comprehensive and detailed investigation of the expression of subunits in the neocortex is still lacking. Nicotinic activation prevalently modulates the excitability of deep cortical layers: in the next section, we move on and

explore the contribution of nicotinic stimulation to local circuit properties and examine studies that investigated the involvement of the nicotinic system in the modulation of neocortical activity.

REGULATION OF NEURONAL AND SYNAPTIC PHYSIOLOGY

Even though nAChRs are predominantly expressed pre-synaptically, where their activation modulates neurotransmitter release through calcium influx or terminal depolarization (Nashmi and Lester, 2006), there is evidence that nAChRs may also influence post-synaptic signaling and that these effects vary based on the subcellular localization of the receptor (**Tables 2, 3**). nAChRs expressed on distal dendrites are thought to cause the generation of fast excitatory post-synaptic potentials since activation of nAChRs on distal apical dendrites promotes PC depolarization and leads to an increase in action potential firing. On the contrary, activation of nAChRs on the proximal apical dendrites (closer to the cell body) reduces membrane impedance and shunts signal incoming from the apical tuft: when the nAChRs opens, the membrane resistance of the PC decreases and signals incoming from the apical dendrites get attenuated (Dani and Bertrand, 2007).

Optogenetic activation of cortical cholinergic input generates an increase in membrane excitability (**Table 2**) mediated by nAChRs and promotes spiking in L5PCs (Hedrick and Waters, 2015). When the stimulation is paired with additional depolarization, spiking activity becomes persistent and can be blocked by BAPTA application, suggesting that the observed depolarization is mediated by intracellular Ca^{++} transients. As suggested by kinetic analysis it is likely that non- $\alpha 7$ nAChRs determine this response. The depolarizing response spans all layers, but occurs with laminar and regional differences; additionally, the effect of the depolarization can be moderate and transitory or pronounced and persistent depending on the cell membrane potential. Although the modulatory effect was found to be stronger in deeper layers, the authors report that it was similar in M1, V1 and prefrontal (PF) cortices. The preferential modulation of deep neocortical layers is likely to influence the flow of excitation occurring throughout the neocortex that originates in layer 4 and then propagates to the superficial layers, whose role is to modify the output of layer 5. Altogether this study showed that nAChR activation increases the excitability of neocortical PCs; in the light of previous evidence that $\alpha 4$ and $\alpha 5$ subunits are highly expressed in layer 6 (Tribollet et al., 2004), and nAChR-mediated responses in layer 6 of the PFC have already been reported by many studies (Kassam et al., 2008; Bailey et al., 2010; Poorthuis et al., 2013), the authors suggest that the presence of $\alpha 4$ and $\alpha 5$ -mediated PSPs could be a characteristic feature of L6PCs across neocortical regions (see **Table 2, Figure 1**).

Pyramidal-to-PCs connections in layer 5 can be potentiated by using a spike-timing-dependent-plasticity (STDP) protocol. Bath-application of 10 μM (or 300 nM) nicotine impairs L5PC to L5PC potentiation and favors the induction of LTD. When monitoring spontaneous synaptic events, application of nicotine

increases the frequency and amplitude of sEPSCs. Evoked excitatory post-synaptic currents (EPSCs) behave differently and are reduced in amplitude by nicotine. However, puffing nicotine directly on PCs fails to elicit an inward current, and application of gabazine prevents the de-potentialization. Therefore, the effects of nicotine on L5PC to L5PC synapses should be attributed to an enhancement of GABAergic transmission, rather than the direct activation of a PCs (Couey et al., 2007).

nAChRs are known to be distributed throughout the dendritic trees of cortical PCs (van der Zee et al., 1992), but a comprehensive mapping of cholinergic synapses apposition remains elusive. To provide concomitant information on receptor localization while recording electrical responses more researchers should apply the strategy used by Hedrick and Waters (2015), who measured nicotinic PSPs during restricted illumination of the slice: illumination of the tuft dendrites failed to evoke a nicotinic PSP at the soma and therefore the authors concluded that nAChRs that contribute to the somatic depolarization are likely to be within 300 μm of the soma and many are probably located in the proximal 50 μm of the apical and basal arbor. This technique sheds light on the compartmental origin of the observed response and it is immensely useful to causally link the distribution of cholinergic receptors and their physiological role. A subsequent investigation should combine this strategy with pharmacological inactivation of specific receptor subunits and provide further proof that PCs responses to cholinergic inputs in different layers are mediated by specific receptor subunits and that their distribution profile is greatly involved in determining the outcome of neural computations.

Although nAChRs are mainly found on PCs, there is extensive evidence that nAChRs are expressed on the membrane of cortical interneurons (**Table 2**), such as MC, chandelier cells (ChCs) and basket cells (BCs), where they contribute to the modulation of GABAergic signaling (Couey et al., 2007; Wevers, 2011). The subpopulation of serotonin receptor 5-HT 3aR expressing GABAergic interneurons is depolarized by ACh *via* nAChRs (Gulledge et al., 2007; Poorthuis et al., 2013); this embryologically distinguished subpopulation, that accounts for about 30% of the total number of cortical inhibitory interneurons, is heterogeneous and includes all the VIP $^{+}$ interneurons, as well as the VIP $^{-}$ neurogliaform cells (NGCs; Rudy et al., 2011). VIP $^{+}$ interneurons show a mixed activation profile in which both nicotinic and muscarinic receptors are involved (**Figure 1**; Kawaguchi, 1997).

Prominent nAChRs expression is a hallmark of layer 1 inhibitory interneurons both in rodents and humans (Letzkus et al., 2011; Alitto and Dan, 2013) and endogenous cholinergic release is known to rapidly recruit this receptor subpopulation during locomotion and attentive processes. These fast, nicotinic responses are mediated by $\alpha 7$ and $\beta 2$ containing receptors (Poorthuis et al., 2018). When at rest, all layer 1 interneurons are depolarized *via* nicotinic activation (**Figure 1, Table 2**); however, when these interneurons are engaged in repetitive firing, ACh inhibits the activity of L1 NGCs (Brombas et al., 2014). Conversely, single bouquet cells (SBCs) are activated by ACh in the regime of repetitive firing (Jiang et al., 2013). Layer

1 interneurons responses are abolished by application of nAChR antagonists (**Figure 1**; Christophe et al., 2002).

ACh enhances the activation of neocortical deep-layers PCs by ascending thalamic inputs *via* mAChR-mediated depolarization and subsequent enhanced glutamate release from thalamocortical terminals in layer 4 (Gil et al., 1997; Metherate and Hsieh, 2004; Disney et al., 2007), but it also releases inhibition on superficial layers PCs. There is extensive evidence that ACh mediates activation of layer 1 and layer 2/3 non-fast spiking PV⁻ cortical interneurons *via* non- $\alpha 7$ nAChRs. These interneurons, in turn, inhibit MCs and BCs that directly target PCs: nAChR-mediated inhibition of superficial interneurons reduces inhibition of superficial PCs (Gulledge et al., 2007; Arroyo et al., 2012; Brombas et al., 2014). Photostimulation of ChAT⁺ neurons in the BF evokes a prolonged disynaptic inhibition in PCs; pharmacological manipulation of the response suggests that it is supported by non- $\alpha 7$ mediated excitation of specific interneurons subtypes. This finding indicates that nicotinic cholinergic input originating from BF fibers is also comprised of a slow component. The observed delayed barrage of inhibitory post-synaptic current (IPSC) in L23PCs exhibits a long latency (of about 26 ms) characteristic of dysynaptic inhibition. Layer 1 and layer 2/3 inhibitory interneurons, and in particular in late-spiking cells and L23 ChAT⁺ bipolar cells are responsible for this phenomenon (Arroyo et al., 2012). In agreement with previous reports (Poorthuis et al., 2014) fast-spiking cells such as BCs and ChCs do not exhibit EPSPs in response to optogenetic stimulation of ChAT⁺ BF neurons, but rather respond similarly to PCs and are swamped by an IPSC barrage as well. While layer 1 and layer 2/3 late spiking cells (LS) exhibit both a fast and a slow response, L23 ChAT bipolar cells display only a slow response. This study demonstrates that the fast and slow components are mediated by $\alpha 7$ receptors and non- $\alpha 7$ receptors, respectively, and that non- $\alpha 7$ receptor-mediated excitation elicits action potentials in cortical interneurons that in turn produce a delayed and prolonged wave of inhibition in L23PCs and FS cells. One proposed explanation for the slow response is that it may arise from a cholinergic bulk transmission and that it may sustain the high metabolic demand of processes such as attention and memory (Cauli et al., 2004). Cortical ChAT⁺/VIP⁺ interneurons have been shown to dilate local microvasculature to increase blood supply during periods of elevated neuronal activity (Kocharyan et al., 2008) during the execution of memory and attention tasks, following electrical BF stimulation. The fast component of the cholinergic response may also be implicated in the emergence of a broader phenomenon like synchronized neuronal activity; it has been shown that LS cells are connected *via* gap junctions, and this fast response may thus play a fundamental role in the emergence of network oscillations that sustain plasticity and attention mechanisms.

Couey et al. (2007) realized that the effect of nicotine on L5PC to L5PC connections is mostly due to an enhancement of GABAergic transmission, and they decided to dissect the effects of nicotine on three different interneurons types. First, they looked at the activity of FS cells in layer 5, and observed no effect when adding nicotine to the bath; later they stained the cells for certain neuropeptides and several nAChR subunits and found an

extremely low amount of mRNA coding for nicotinic subunits in FS cells, which might explain their unresponsiveness. Once again, another piece of evidence emerges confirming that (putative) BCs have a tendency not to respond to the application of cholinergic agonists. The authors identified another type of interneuron as a regular-spiking-non-PC (RSNPC), and observed a fast inward current after application of nicotine. LTS cells (putative MC) showed an even bigger inward current response; in both cell-types the most abundantly stained nicotinic subunit was $\alpha 4$, but $\beta 2$ and $\alpha 7$ were also present. In this study, nicotine application increases the frequency and amplitude of spontaneous EPSCs in putative BCs and MCs; as for putative ChC (RSNP) a decrease in the frequency, but not the amplitude of sEPSCs can be observed (Couey et al., 2007).

Pyramidal to SST⁺ interneurons neocortical connections are relatively weak, but local excitatory input to SST neurons is selectively enhanced during cholinergic modulation of network activity. In a recent 2018 study, it was shown that endogenous ACh release activates presynaptic nAChRs and boosts glutamatergic input in a target-cell specific manner (Urban-Ciecko et al., 2018). Thus, there is evidence that local excitatory input to SST neurons is selectively enhanced during nicotinic modulation of network activity (**Table 2**, **Figure 2**). In a recent study by Obermayer et al. (2018) examined PC-MC-PC disynaptic connections in both layer 2/3 and layer 5 and found that the typical delayed disynaptic inhibitory response in the post-synaptic PC is faster and stronger when cholinergic inputs are activated optogenetically, or by means of 1 mM ACh bath application. When looking at the activity of a single MC, they observed that ACh inputs lead to a significant decrease of the onset delay of AP firing and increases the number of APs fired in MCs, which can account for the earlier onset and prolonged duration of disynaptic inhibition. This effect was abolished by application of 10 μ M DH β E demonstrating that it is mediated by heteromeric nicotinic receptors (**Table 2**, **Figure 2**). However, when they recorded from synaptically connected PC-MC pairs during concurrent activation of cholinergic fibers, they could only observe an increase in the membrane depolarization level, but not in EPSP sizes. The same effect was found in MC-PC connections, and this as well was confirmed to be nicotinic in nature, contradicting the result obtained by Urban-Ciecko and others and others. The setups of the two experiments are comparable: both studies were performed in the adult mouse somatosensory cortex. However, the first remarkable difference lies in the nature of the cholinergic input used in the two experiments: while Obermayer et al. (2018) used bath-application of 1 mM ACh and optogenetic activation, Urban-Ciecko et al. (2018) decided to record activity in the presence of 20 μ M CCh, a non-hydrolyzable analogue of ACh. Not only the two concentrations differ by two orders of magnitude, but the two cholinergic agonists work in fundamentally different ways. While ACh is almost immediately hydrolyzed by the cholinesterase in the synaptic cleft (within a few milliseconds), carbachol has a much more prolonged effect (Katz and Miledi, 1973). Nevertheless, the results obtained by bath-application of ACh are in agreement with the results achieved by optogenetic activation of the cholinergic system,

which is supposed to be a more physiological way of stimulating cholinergic release (Obermayer et al., 2018).

Interestingly, optogenetic activation of cholinergic inputs did not affect the typical fast disynaptic post-PC response mediated by BCs, which provides yet another example of how BCs tend to be unresponsive to cholinergic release in both layer 2/3 and layer 5, or more generally show a more heterogeneous response profile to ACh inputs (Obermayer et al., 2018). This could be explained by the lack of a precise morphological identification of various subtypes of BCs, which could express cholinergic receptors in different subcellular locations or in a different amount, and therefore show differential responses to ACh inputs. These findings indicate that subcortical neuromodulatory projections recruit nicotinic receptors to alter network function through increased inhibition and provide a potential mechanism by which attention controls the gain of local circuits.

NICOTINIC AND MUSCARINIC KINETICS

What are the receptor affinities to various agonists and can this be related to the actual amount of nicotinic modulation? The relative activation of receptors vs. the concentration of agonist has been measured (Table 4).

Muscarine reversibly reduces Ca^{2+} currents in a dose-dependent manner. The modulation is rapid, with an onset time constant of 1.2 s. A slowly developing component of the modulation also is observed, with a time constant of 17 s. Under elevated Ca^{2+} conditions, the fast component is due to a reduction in both N- and P-type calcium currents, whereas the slow component involves L-type current (Stewart et al., 1999). Receptor properties such as conductance, open time, and sensitivity to ACh depend on the nicotinic subunit composition (Table 4). ($\alpha 4$) $2(\beta 2)$ 3 nAChRs are sensitive to micromolar scale changes, while ($\alpha 7$) 5 receptors have a half-maximal sensitivity of more than a hundred micromolar. Extracellular choline is normally 3–5 μM but can attain 20 μM in some pathological cases. However, ACh reaches the millimolar range at the site of release (Alkondon and Albuquerque, 2004). Responses mediated by $\alpha 7$ nAChRs are short-lasting, whereas those mediated by $\alpha 4\beta 2$ nAChRs are long-lasting. This is because the mean open time of $\alpha 7$ nAChRs is shorter than that of $\alpha 4\beta 2$ nAChRs. Also, $\alpha 7$ nAChRs desensitize much faster than $\alpha 4\beta 2$ nAChRs (Alkondon et al., 1999).

An interesting hypothesis was put forward by Albuquerque et al. (2000). $\alpha 7$ but not $\alpha 4\beta 2$ nAChRs can be fully activated by choline (Nguyen et al., 1995; Alkondon et al., 1999). Choline and acetate are the products of hydrolyzation of synaptically released ACh by ACh-esterase in the synaptic cleft. This process occurs quickly, but reuptake of choline into presynaptic terminals is slow. Therefore, the ACh concentration in the synaptic cleft should decay rapidly, with only low levels of diffusing ACh reaching peri-synaptic sites. But choline levels should rapidly rise in the synaptic cleft with high levels of diffusing choline reaching peri-synaptic sites. This implies that extrasynaptically located $\alpha 4\beta 2$ nAChRs (i.e., the high affinity nAChRs) could be activated by diffusing, low levels of ACh, extrasynaptically located while low-affinity $\alpha 7$ nAChRs may be activated by diffusing choline.

TABLE 4 | Nicotinic homomeric and heteromeric receptors kinetics.

Receptor type	Single channel conductance	Open time	P_{Omax}	EC50 for ACh or nicotine	Kinetics
Nicotinic heteromeric ($\alpha 3$) $2(\beta 4)$ 3	29 pS	0.71 \pm 0.14 and 3.5 \pm 0.4 ms		EC50 ACh 1.70–1.83 μM for ACh EC50 Nicotine 2.91 μM	Fast: 40–121 ms; slow: 274–1039 ms (Figl and Cohen, 2000)
Nicotinic heteromeric ($\alpha 3$) $2(\beta 4)$ 3	29 pS (Stetzer et al., 1996), 18.2 \pm 0.46 (Rovira et al., 1998)	147 ms (Stetzer et al., 1996)		IO50 Nicotine 2.92 μM (Kuryatov et al., 2011) EC50 ACh 115–122 μM EC50 Nicotine 4.64 IO50 Nicotine 16.7 μM (Kuryatov et al., 2011)	
($\alpha 3\beta 2$) $2\alpha 5$				High affinity is 1.6 μM , low affinity is 62 μM (Buisson and Bertrand, 2001)	Fast 4–6 ms; slow 30–53 ms (Figl and Cohen, 2000)
($\alpha 3\beta 4$) $2\alpha 5$			0.8 (Li and Steinbach, 2010)	EC50 for ACh in activating $\alpha 7$ is 3 μM (Albuquerque et al., 2000) EC50 ACh 1.44–1.64 μM for variants tested EC50 Nicotine 0.62 μM	
Nicotinic heteromeric ($\alpha 4\beta 2$) $2\alpha 5$	31.3 pS, 40.5 pS (high state) and 21.9 pS (low; Hales et al., 2006)	207 \pm 38 ms (Hsiao et al., 2008)		Choline: EC50 1.6 mM; IC50 37 μM (Alkondon and Albuquerque, 2004). 200 μM ACh (Buisson and Bertrand, 2001). EC50 for ACh in activating $\alpha 7$ 130 μM (Albuquerque et al., 2000)	
Nicotinic homomeric ($\alpha 7$) 5	82.9 pS (Albuquerque et al., 2000)	108 μs and 92.7 μs for channels activated by 11 and 10 mM ACh, respectively (Albuquerque et al., 2000)			

The table lists properties of nicotinic homomeric and heteromeric receptors (single-channel conductance, open time and open probability and EC50 and kinetics).

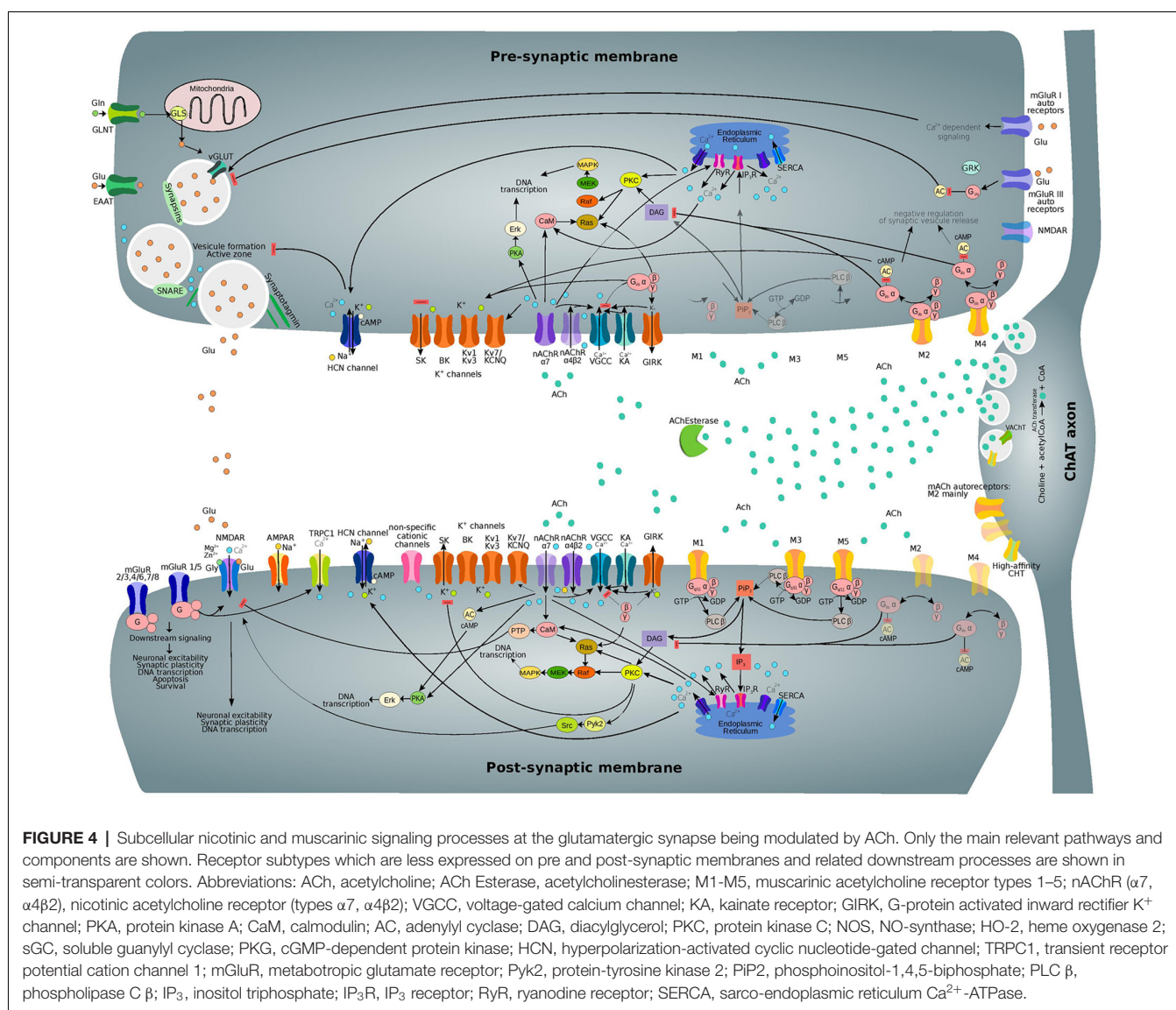
Thus, $\alpha 7$ and $\alpha 4\beta 2$ nAChRs might exhibit differential control (Albuquerque et al., 2000).

SUBCELLULAR NICOTINIC AND MUSCARINIC PATHWAYS

ACh affects membrane conductance through several subcellular pathways, as illustrated in **Figure 4**, leading to both hyperpolarizing and depolarizing effects (**Tables 1, 2**). ACh can act on both pre and post-synaptic membranes, binding to muscarinic and nicotinic receptors. The interplay among intracellular pathways leads to a dynamically changing outcome, such as the transient hyperpolarization and following long-term depolarization resulting from the binding of ACh to M1 mAChR (Dasari et al., 2017). When ACh interacts with M1, the exchange of coupled GDP for GTP produces the dissociation of the G-protein complex from the receptor. The released α subunit of the Gq protein then activates

the enzyme phospholipase C (PLC β) which hydrolyzes phosphatidyl-inositol 4,5 biphosphate (PIP₂), leading to its dissociation from the membrane and the subsequent formation of diacylglycerol (DAG) and IP₃. IP₃ initiates calcium ions release from the endoplasmic reticulum (ER), serving as a trigger for this process. Refilling of the ER with Ca²⁺ ions is then obtained by the activity of the sarco-ER Ca²⁺-ATPase (SERCA). Extracellular calcium ions are therefore crucial for the maintenance of calcium cycling. M1 activation facilitates voltage-dependent refilling of calcium stores by promoting excitation. Thus, fine-tuned calcium dynamics govern complex reciprocal relations among many different proteins contributing to changes in membrane potential. Ultimately, changes in K⁺, Ca²⁺-activated K⁺-currents and non-specific cationic currents support a shift from transient hyperpolarization to a sustained excitation.

Meanwhile, DAG together with Ca²⁺ ions activate kinases such as protein kinase C (PKC), causing multiple downstream



effects. PKC controls the function of many proteins including members of both pre and post-synaptic membranes. PKC is also involved in synaptic plasticity regulation and causes the internalization of AMPARs and NMDARs, leading to LTD phenomena (Callender and Newton, 2017).

PKC can also phosphorylate metabotropic glutamate receptor 5 (mGluR5; Hwang et al., 2005) as well as many other proteins. Moreover, PKC activates heme-oxygenase 2 (HO-2; Artinian et al., 2001) and inhibits NO-synthase (NOS), interfering with the calcium/calmodulin activation of NOS enzyme (Borda et al., 1998). These effects contribute to the downstream processes involving carbon monoxide (CO) and nitric oxide (NO) as interacting messengers (Mathes and Thompson, 1996; Artinian et al., 2001). Long-term effects of PKC activation include changes in DNA transcription that are mediated by MAPK/Erk signaling. Furthermore, there is recent evidence for the direct interaction of M3 mAChR with PLC β , which increases signaling efficiency (Kan et al., 2014).

The downstream signaling pathways of M3 and M5 receptors overlap with that of M1, and therefore they are grouped as M1-like receptors; similarly, M2-type mAChRs comprise both M2 and M4 receptors. Binding of ACh to M2-type mAChRs results in the inhibition of adenylyl cyclase (AC) by the α subunit of $G_{i/o}$ protein and in the subsequent reduction of cAMP levels (Muñoz and Rudy, 2014). However, there are some differences between the G_i and G_o mechanisms of AC regulation (Jiang and Bajpayee, 2009). The $\beta\gamma$ -complex of the dissociated G-protein can activate the G-protein activated inward rectifier K^+ channels (GIRK) and inhibit voltage-gated calcium channels (VGCCs). Moreover, G_o proteins can also regulate Na^+ channels (Jiang and Bajpayee, 2009). Particular effects of M1 and M2 receptors on different ion channels have been already summarized by Thiele et al. (2012).

A significant increase in intracellular calcium concentration comes from the direct flow of ions due to the permeability of nAChRs to Ca^{2+} . However, nAChR activation also leads to the activation of VGCC and subsequent Ca^{2+} influx. (Dajas-Bailador and Wonnacott, 2004; Shen and Yakel, 2009). Moreover, functional cross-talk among presynaptic nAChRs has been shown to affect signal transduction (Marchi and Grilli, 2010). Therefore, the action of one receptor might depend on the function of co-existing receptor subtypes in the same cell. The interaction between presynaptic nicotinic receptors with other ionotropic or metabotropic receptors serves the purpose of producing an integrated response.

TRANSCRIPTOME CELL-SPECIFIC PREDICTION OF CHOLINERGIC RECEPTORS

In recent years, a wealth of transcriptomic data from the mouse brain has become available (Saunders et al., 2018; Zeisel et al., 2018). Many different cell types may exist; one study found 565 different cell groups, for example (Saunders et al., 2018). Since a standard classification of cortical cell types is still

emerging, most articles employ different approaches to arrive at cell type specific transcriptomes.

We examined a representative data set from the somatosensory cortex in order to interpret possible cell-specific differences in cholinergic receptor expression (Figure 5). We chose this data set since excitatory cell types are mapped to layer-specific types, allowing the easiest comparison with the types referenced in this review. In this dataset, normalized expression of M1 receptors is highest in L4 PCs. There is a strong expression of M2 in deep layer neurons, particularly in layer 5a. M3 is highly expressed in layer 2/3 and layer 5a, while M4 is highest in layer 4. $\alpha 3$ nAChR subunits are highest in layer 4, but also in the deep layers. β subunit expression is highest in layer 6 and layer 6a neurons. Inhibitory interneuron expression of cholinergic receptors is definitely cell-type specific, though heterologous. PV cells express more nAChR $\alpha 3$ than do somatostatin-expressing interneurons (Figure 5B). Somatostatin expression is best correlated with M2 expression and nicotinic β subunit expression and negatively correlated with M1 expression (Figure 5C). VIP and Htr3a expression is correlated with nAChR $\alpha 3$, nAChR $\alpha 4$, and nAChR $\alpha 5$. Furthermore, ChAT expression is correlated with M1 expression. In layer 5a, the effects of the predominantly-expressed nAChR and mAChRs seemed to be synergistic.

We also examined an additional dataset for frontal cortex (Figure 5E; Saunders et al., 2018). M5 is expressed in a subset of interneurons, including some cholinergic and MCs. The nicotinic receptor ChRNA5 is expressed in a subset of deep PCs. ChRNA6 is most expressed in a particular type of layer 5 PC. This dataset illustrates that the degree of sub-classification of PCs is likely to be important. For example, there are many subtypes of L5PCs, which have different cholinergic receptor expression. Both datasets showed consistency in M3 expression in L2/3 and L5a PCs but not L4 and L5 PCs.

In addition to cell-type specific correlation, nAChR genes that encode heteromeric α/β subunits are well correlated among themselves (Zoli et al., 2015; Saunders et al., 2018). The genes encoding the α subunits correlate well with the corresponding β subunit.

Cholinergic neurons can be identified by cluster analysis (Zeisel et al., 2018). In particular, separate types have been identified in the red nucleus and habenular nucleus of the thalamus (ibid). ACh often is released in neurons releasing other neurotransmitters (Zeisel et al., 2018). In the habenular nucleus, the glutamate transporter Slc17a6, in cholinergic cells, suggesting co-release of glutamate and ACh (Mancarci et al., 2017). In the ventral midbrain, a neuron type that was both dopaminergic and cholinergic was identified (Zeisel et al., 2018). Many forebrain cholinergic neurons also are GABAergic (Mancarci et al., 2017), consistent with the co-release of these two substances (Saunders et al., 2015).

GLOBAL NETWORK EFFECT AND MODULATION OF BRAIN STATES

The transition between different brain states that occurs whenever an organism switches from one behavioral state to

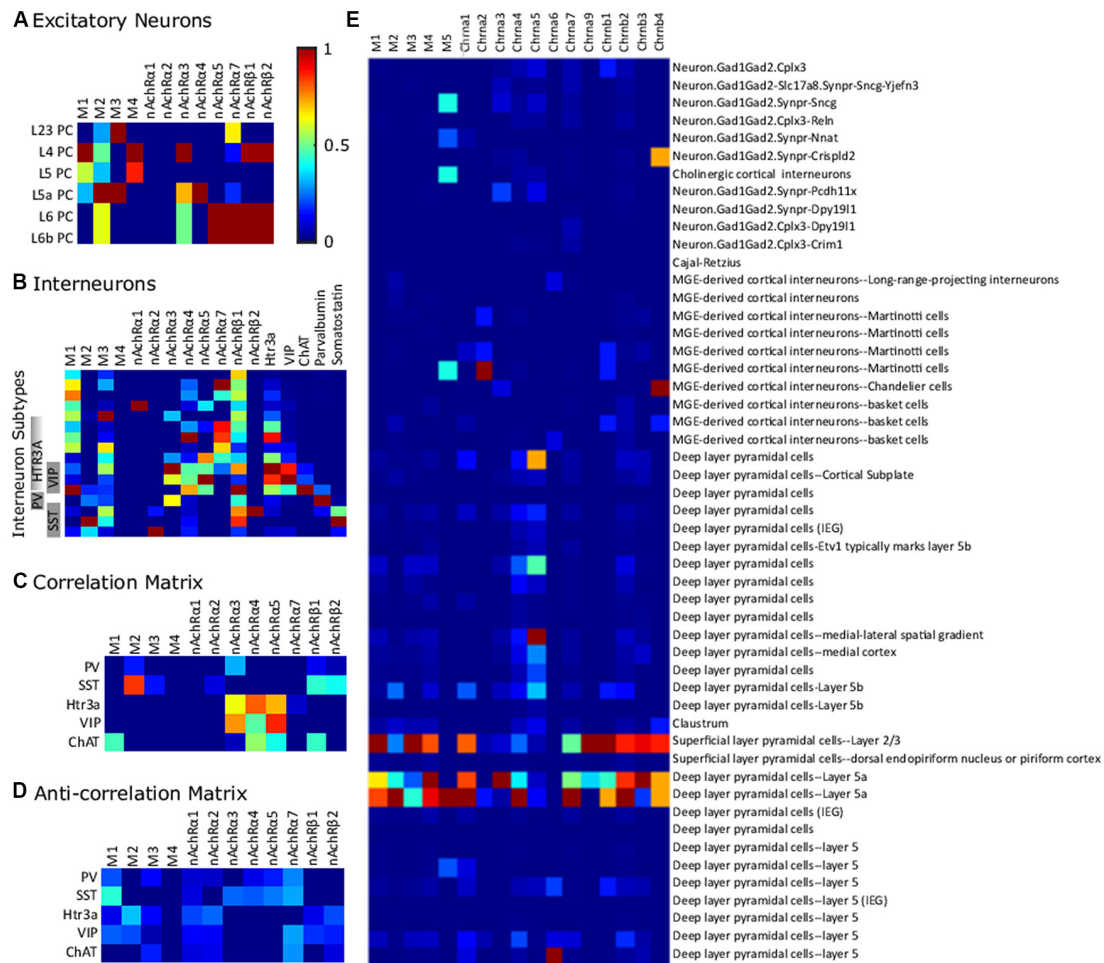


FIGURE 5 | Differential expression of cholinergic receptors in transcriptome-derived cell types. **(A)** Excitatory cell types. **(B)** Interneurons in somatosensory cortex. Gene expression is normalized to a maximum of 1 on a gene-by-gene basis. **(C)** Correlation matrix (positive values of correlation matrix Pearson correlation coefficient matrix). **(D)** Anti-correlation matrix (negative values of correlation matrix). The data is from Zeisel et al. (2018) and was collected with high-throughput single-cell RNA sequencing, a method which counts individual RNA molecules. Abbreviations: PV, parvalbumin; SST, somatostatin; VIP, vasointestinal peptide; ChAT, choline acetyltransferase. **(E)** Expression of ACh receptor genes across the Frontal cortex cell-clusters identified in Saunders et al. (2018). The data was collected using Drop-seq (a method which allows the use of older animals and elimination of certain technical artifacts) to profile the RNA expression of individual cells. Semi-supervised independent component analysis was used to group cells into the sub-clusters using network-based clustering (ibid). Expression levels were normalized to the highest expression across all the selected genes. In this data set, receptor expression was particularly high in L23 and L5a PCs.

another is associated with changes in the overall pattern of neural activity, which can be captured with EEG or LFP recordings. The pattern of EEG activity can change dramatically with the behavioral state of the animal (Lee and Dan, 2012), as can be seen in the transition from slow-wave sleep to wakefulness (or from deep sleep to REM sleep), when the EEG pattern shifts from large and synchronous waves of neural activity to a more desynchronized and short-amplitude wave pattern (Berger, 1929). Ensemble neuronal activity undergoes impressive changes during behavioral state transitions, and different brain states have been associated with different brain functions; definitive evidence for these functions although, is still lacking, and the mechanism by which these transitions are achieved in the cortical network is not yet understood. Many authors have proposed that the switch between cortical states may be driven by the

action of neuromodulators like ACh (Lee and Dan, 2012). However, precisely how these neuromodulators influence global cortical processing by locally targeting specific cells is largely an unsolved mystery.

BASAL FOREBRAIN MODULATION OF BRAIN STATES

A large body of evidence suggests that the BF, a complex and heterogeneous structure classically defined by the presence of clusters of cholinergic neurons, is crucial for the maintenance of the sleep/wake cycle and for processes that underlie arousal and attentional modulation, but it is unclear which BF neurons promote each brain state and how they interact with each other to regulate transitions between states (Anacleit et al., 2015). Already

since 1930, it was known that BF lesions could cause severe insomnia (Saper et al., 2001); however, this evidence has been an object of constant challenge over the years, and the attempts to replicate this experiment would yield different results. Finally, Szymusiak and McGinty (1986) observed that sleep-active cells were confined to the ventral BF in the cat (the horizontal limb of the diagonal bands of Broca, substantia innominata, entopeduncular nucleus and ventral globus pallidus) and that these areas partially overlap with those where chemical and electrical stimulations evoke sleep, and where lesions suppress sleep. The sleep-active cells were thus considered optimal candidates for mediating some of the sleep-promoting functions attributed to the BF (Szymusiak and McGinty, 1986).

Many BF neurons are active during wake and during REM sleep (Lee and Dan, 2012), and specific lesions reduce wakefulness, in agreement with the finding that BF lesions cause significant increases in delta waves occurrence during wakefulness, and that BF stimulation induces cortical desynchronization of EEG or LFP signals, accompanied by a decrease in correlated spiking. Furthermore, the BF receives inputs from the LDT and PPT pontine nuclei; cholinergic neurons that can be found at the level of the LDT nucleus exhibit an increase in firing rate during cortical activation, just before the transition from slow-wave sleep frequencies to faster frequencies (Saper et al., 2010).

Therefore, it seems reasonable to hypothesize the existence of functionally diverse neurons in the BF: according to Duque et al. (2000), BF cells that exhibit different wake/sleep activity pattern, also express different molecular markers (Zaborszky and Duque, 2000). There are three major neuronal types in the BF: cholinergic, glutamatergic and GABAergic cells (Anacleit et al., 2015; Xu et al., 2015). There might be extensive local synaptic interactions among BF neurons mediating local reciprocal inhibition between GABAergic neurons and sleep-active and wake-active cholinergic neurons. The well-known flip-flop circuit for sleep/wake cycle control (Saper et al., 2010) could, therefore, comprise multiple loops and switches. However, some findings suggest that BF GABAergic neurons provide major contributions to wakefulness, while cholinergic and glutamatergic neurons appear to play a lesser role; chemogenetic activation of GABAergic neurons promotes wake and high-frequency EEG activity, whereas cholinergic or glutamatergic activation have a destabilizing effect on slow-wave-sleep (SWS), but has no effect on total wake (Anacleit et al., 2015).

Cholinergic neurons residing in the BF can be divided into two subpopulations, that might be involved in different functions: an early-spiking population may reflect phasic changes in cortical ACh release associated with attention, while the late-spiking group could be more suited for the maintenance of the cholinergic tone during general cortical arousal (Unal et al., 2012).

MULTI-TRANSMITTER NEURONS: ACh AND GABA CO-TRANSMISSION

Nevertheless, functional co-transmission of ACh and GABA seems to be a common feature of nearly all

forebrain ACh-producing neurons (Henny and Jones, 2008; Granger et al., 2016). BF inputs to the neocortex are therefore not only constituted of different fibers, but also use a mixture of functionally diverse neurotransmitters (Kalmbach et al., 2012). This opens the question of whether there is a substantial difference between the cholinergic modulation and the BF modulation of neocortical activity. The contribution of GABA needs to be considered when studying the functional impact of ACh-producing neurons: electrical stimulation of BF fibers might evoke markedly different responses than optogenetically-evoked selective cholinergic release.

Does the co-release happen in a target-specific modality, at different terminals branching from the same axon, or is the release site the same for both transmitters? And if so, how does GABA affect the ongoing cholinergic modulation? Release of an excitatory (ACh) and inhibitory (GABA) neurotransmitter by the same axons seems to be functionally antagonistic. However, both transmitters could act in parallel, depending on the mode of co-transmission (Granger et al., 2016). If both ACh and GABA are released simultaneously onto the same post-synaptic cells, then GABA may act to shunt the (supposed) excitation generated by ACh. Otherwise, they could target different postsynaptic cells, such that GABA inhibits one cell population while ACh excites another. Given previous experimental results showing that GABA release from VIP interneurons shunts activity of Sst⁺ interneurons, but not other VIP interneurons, it is thought that VIP/ChAT cortical interneurons may release ACh and GABA onto different post-synaptic targets, perhaps from separate synaptic vesicle populations (Granger et al., 2016). Indeed, a recent analysis of the molecular composition of the pre-synaptic terminals of cortical VIP/ChAT interneurons revealed that ACh and GABA vesicles are confined to separate boutons. At the post-synaptic level, the subset of GABAergic boutons seems to contact prevalently other inhibitory interneurons, while ACh boutons target mostly L1 interneurons and other VIP/ChAT cortical interneurons. Here, ACh evokes EPSCs that are mediated by nicotinic receptors (Granger et al., 2018). Another recent study conducted in the mPFC confirms that only 10%–20% of post-synaptic targets of VIP/ChAT cortical interneurons are contacted by both cholinergic and GABAergic inputs (Obermayer et al., 2018); here they report that VIP/ChAT neurons directly excite interneurons in layers 1–3 as well as PCs in L2/3 and L6 by fast nicotinic transmission.

Immunolabeling studies (Beaulieu and Somogyi, 1991) have shown substantial co-labeling of presynaptic cholinergic terminals for both GABA and ChAT in the neocortex, but more studies should address the functional consequences of the synaptic co-release of these neurotransmitters and try to dissect the differential impact of each transmitter on postsynaptic cells excitability. Analysing the co-localization of post-synaptic receptors or scaffolding proteins could also allow the identification of individual synapses that are sensitive to both ACh and GABA. These possibilities should be addressed systematically in order to precisely understand the contribution of each neurotransmitter to cortical processing.

ACh INVOLVEMENT IN NEUROPLASTICITY

Apart from the fine-tuning of sleep/wake transitions, cholinergic neuromodulation is tightly implicated in regulating selective attention to a given sensory stimulus by altering the activity of the sensory cortex that perceives that modality (Kim et al., 2016). ACh is known to be especially involved in cortical arousal (Saper et al., 2010) and in the state-dependent modulation of cortical activity; cholinergic neurons are active during locomotion (Buzsáki et al., 1988) and during transition to the attentive state (Kim et al., 2016). Studies have shown that the occurrence of relevant sensory events evokes a transient increase in ACh concentration in the rat PFC (Hasselmo and Sarter, 2011). Conversely, activating cholinergic transmission in the PFC determines an improvement in subject's performance during sustained attention tasks (Saper et al., 2010). It is, therefore, reasonable to hypothesize that ACh can induce long-lasting changes in neuronal excitability, and indeed this was demonstrated. Pioneering experiments showing that ablation of noradrenergic and cholinergic innervation in the striate cortex substantially impairs ocular dominance plasticity in kittens (Bear and Singer, 1986) opened the way for subsequent studies on the involvement of ACh in cortical plasticity. Some showed that when a tone is paired with NBM stimulation or ACh application, auditory cortex receptive fields change and prolonged enhanced responses to the paired frequency can be observed (Metherate and Weinberger, 1990; Rasmusson, 2000). Others discovered that co-application of muscarinic agonists with glutamate induces a prolonged increase in response to glutamate in somatosensory cortical neurons (Sugihara et al., 2016), and that these effects concern as well the somatosensory cortex and the primary visual area V1. According to Metherate and Weinberger (1990), the potentiation can be blocked by cortical application of atropine, but others (Sugihara et al., 2016) report that cholinergic antagonists cannot reverse the prolonged changes, thereby confirming that ACh is necessary for the induction, but not the maintenance of these modifications. ACh seems to act more as an instructive, rather than a permissive signal (Lin et al., 2015).

ACh is as well involved in the generation of LTD at synapses between cortical pyramidal neurons and striatal medium spiny neurons through disinhibition of Ca_v channels. Here, the activation of D_2 receptors reduces basal ACh release from cholinergic striatal interneurons and lowers M_1 receptor tone in medium spiny neurons, which leads to enhanced opening of intraspine $\text{Ca}_v1.3$ Ca^{2+} channels in response to synaptic depolarization. The calcium transient results in enhanced production of endocannabinoids (ECs) such as 2-arachidonoylglycerol, and activation of presynaptic CB_1 receptors that reduce glutamate release (Wang et al., 2006).

Furthermore, the role of several neuromodulatory systems in STDP induction (Pawlak et al., 2010) has been studied across multiple brain areas. While dopamine (DA) and NA modulation of STDP has been mostly investigated in subcortical areas, ACh's role in STDP induction has been extensively researched in neocortical sensory areas and in the PFC. In mouse mPFC,

nicotine application increases the threshold for STDP in L5PCs by reducing their dendritic calcium signals. This effect, however, is due to an enhancement in GABAergic transmission in various types of interneurons in the PFC network, that express multiple types of nAChRs (Couey et al., 2007), and not to a direct nicotinic action on PCs.

Taken together, evidence suggests that cholinergic inputs to the cortex incoming from the BF should be viewed more as teaching, rather than motivational signals. Overall, activation of the cholinergic system controls the shift from a correlated or synchronized state, to a decorrelated or desynchronized state and results in an enhancement of cortical information processing (Lee and Dan, 2012). However, exactly how the detection of relevant stimuli is enhanced and which are the mechanisms at the basis of this ACh-induced desynchronization are still a matter of open debate.

ACh ENHANCEMENT OF SENSORY PROCESSING

NBM stimulation has a differential effect on spontaneous and sensory-evoked activity. In a recent study, Meir et al. (2018) showed that NBM stimulation desynchronizes cortical LFP and increases the SNR of sensory-evoked responses while suppressing ongoing spontaneous synaptic activity. The authors recorded spontaneous PSPs occurring in L4 and showed that following NBM stimulation the frequency and amplitude of sPSPs were decreased. Moreover, the mean membrane voltage of the response became more hyperpolarized, and trial-to-trial variability was decreased, both during spontaneous and evoked activity. However, sensory stimulation did not change the amplitude of the response, whereas it caused a prominent reduction in the noise amplitude, therefore changing the SNR of the sensory response. By analyzing the coupling of Vm and LFP signals, they also showed that cholinergic activation largely reduced fluctuations in the membrane potential and caused a decorrelation in network activity.

Chen et al. (2015) were able to identify a defined microcircuit in the superficial layers of mouse V1 that supports ACh driven desynchronization. The authors measured the activity of different inhibitory interneurons while optogenetically stimulating superficial cholinergic axons, and found that cholinergic inputs facilitate Sst^+ interneurons, which in turn inhibit PV^+ interneurons and PCs. Optogenetic inhibition of Sst^+ neurons blocks desynchronization, whereas direct activation of Sst^+ neurons is sufficient to induce desynchronization (Chen et al., 2015). The observed desynchronization in cortical activity may explain the role of ACh in mediating transitions between phases of the sleep-wake cycle, but it fails to explain how ACh enhances sensory processing. A large body of evidence suggests that ACh enhances sensory inputs while simultaneously suppressing intrinsic cortical activation (Kimura et al., 1999; Disney et al., 2007; Newman et al., 2012), but a detailed understanding of this process is currently lacking. ACh's role may substantially differ across sensory areas and affect different tuning properties.

Nucleus basalis activation affects sensory responses to natural stimuli of a population of cortical neurons. Before BF stimulation, multi-unit activity (MUA) in the rat's V1 is highly correlated but poorly time-locked to the stimulus; after BF stimulation it becomes less correlated but more time-locked to the sensory event. NBM stimulation also decreases single-unit activity (SU) correlation (between cells correlation) and increases response reliability (between trials correlation coefficient) but does not induce any significant change in receptive field size, orientation tuning nor direction selectivity. Atropine application decreases NBM induced decorrelation, indicating that mAChRs support this effect (Goard and Dan, 2009). After NBM stimulation a shift in the firing modality of the LGN resembling that found at the level of the thalamus can be observed, namely a transition from burst to tonic mode (Bazhenov et al., 2002; Castro-Alamancos and Gulati, 2014). A similar study (Thiele et al., 2012) was conducted in the extrastriate cortex of the macaque and yielded opposing results: at the level of the middle temporal (MT) area it revealed how other tuning properties, like orientation and direction discriminability, are also affected by cholinergic modulation; in this case, ACh had little effect on response reliability, though it is still not clear whether these differences are attributable to differences existing between rodents and primates or to functional differences between sensory areas. In an effort to clarify the precise role of neocortical cholinergic modulation, Disney et al. (2007) concentrated on the role of nAChRs in a well-studied cortical model system, the V1 of the macaque monkey. Here they showed *in vivo* that nicotine reliably enhances the gain of responses to visual stimuli in layer 4c, but not in other layers. Having found $\beta 2$ -nAChR in a pre-synaptic position at the level of thalamo-cortical synapses on PV⁺ interneurons, they prove that nicotine enhances detection of visual stimuli through enhanced TC transmission. These findings confirm that cholinergic activation causes an increase in cortical sensory responses through enhancement of thalamic synaptic transmission and suppression of intracortical inputs. A systematic effort to extend these results to other sensory areas is therefore needed in order to decipher whether the mechanism supporting cholinergic modulation is common throughout all cortical areas or if different tuning properties are affected each time.

ACh MODULATION OF THalamo-CORTICAL TRANSMISSION

Castro-Alamancos and Gulati recorded, multi-electrode activity (MUA) and field potential from adult rat barrel cortex following multi-whisker stimulation at 0.2 Hz, while increasing concentrations of carbachol or other drugs were applied by means of micro-dialysis. The authors found that the application of 50 μ M carbachol, but not norepinephrine, can stop the emergence of the 10–15 Hz oscillations that are observed during baseline recordings and that in the presence of atropine these oscillations are even enhanced (Castro-Alamancos and Gulati, 2014). The effect of carbachol on barrel cortex LFP is thus congruent with the traditionally termed desynchronization

for doses higher than 50 μ M (Moruzzi and Magoun, 1949; Steriade et al., 1993). A low tone of cholinergic activation (0.5–1 μ M) however, reinforces the deactivated cortical state by enhancing synchronous slow oscillations. A very high tone of cholinergic activation (250–2,500 μ M) leads to a significant increase in tonic firing, without altering the overall firing rate. An interesting follow-up to this experiment would be to check whether the same effect can be observed in the whole somatosensory region, and across other sensory cortices. The group then tried to decipher whether cholinergic activation would also modulate thalamocortical activity: by recording from the VPM, they found that cholinergic cortical activation suppresses burst-firing in the thalamus and changes neuronal firing to a tonic mode. This result is fairly consistent with the outcome predicted by the model of thalamo-cortical slow-wave sleep oscillations and transition to activated states generated by Bazhenov et al. (2002). Here, the increase in ACh activity was modeled by the reduction of a K⁺ leak current in pyramidal and thalamo-cortical cells and resulted in the abolishment of the hyperpolarizing phase of network activity and a consequent increase in the input/resistance relationship, accompanied by a switch to the tonic firing (15–20 Hz) modality. The transition from bursting to tonic firing thus seems to be a characteristic feature of relay diencephalic structures like the thalamus and the meta-thalamus.

Enhanced thalamo-cortical transmission seems to be a constant finding across a vast number of articles and reviews (Bazhenov et al., 2002; Disney et al., 2007; Hasselmo and Sarter, 2011) with the aim of revealing the mechanisms by which cholinergic neuromodulation operates. Next studies in this field should, therefore, consider the possibility that cholinergic inputs reach the cortex not only through direct BF projections but also exploiting the thalamo-cortical loop.

Voltage-sensitive dye imaging revealed that ACh application to the neocortex, upon stimulation of layer 2/3, suppresses the spread of excitation to nearby areas. Thus, ACh seems to play an important role in coding sensory stimuli by enhancing thalamocortical inputs, but at the same time, by suppressing intracortical interactions (Kimura et al., 1999).

One of the proposed models for the cholinergic mediated shift from default mode to detection mode suggests that ACh acts to enhance the glutamatergic representation of thalamic input through stimulation of nAChRs, while suppressing the cortical spread of associational input through activation of mAChRs (Hasselmo and Sarter, 2011). Minces et al. (2017) recently evaluated the effect of increases in cortical ACh following optogenetic BF stimulation on the correlation structure of the visual network and found that transient cholinergic release in the cortex decreases the slope between signal and noise correlations. The authors propose that this mechanism acts to increase the encoding capacity of the network.

Another article evaluated the impact of ACh on local circuit activation and found that cholinergic inputs exclude unreliable neurons from contributing to circuit activity while conserving neurons that were active in response to thalamic activity and showed strong correlations. Moreover, weak functional connections were pruned, thus yielding a more

modular and hierarchical circuit structure. Once again, these results highlight how ACh is able to reorganize the circuit function in a way that promotes the discriminability of thalamic inputs at the expense of weak pairwise relationships (Runfeldt et al., 2014).

SENSORY MODALITY-SPECIFIC INFORMATION PROCESSING AND ACh

Many studies (Disney et al., 2007; Minces et al., 2017) have focused on trying to understand the role played by ACh in improving stimuli detection or modifying receptor fields size in the visual cortex. While many of them have been done in primates, others have privileged the somatosensory areas and highlight the involvement of the cholinergic system in the regulation of sensory cortical processing in rodents as well, supporting the idea that cholinergic modulation of cortical microcircuits is functionally equivalent across brain areas and model organisms, even though a canonical and anatomically equivalent system is not strictly identifiable (Coppola and Disney, 2018).

The finding that distinct neuronal clusters in the BF project selectively to specific sensory areas (Kim et al., 2016) and that cholinergic inputs to sensory cortices are spatially segregated supports the idea that cholinergic release improves sensory discrimination in a modality-selective manner and with a high degree of specificity. The authors mapped BF projections to different sensory areas and found retrobead-labeled neurons from three different sensory cortices within the BF, with a clear distinction between the clusters of cells: neurons in the HDB project preferentially to V1, the posterior part of NBM projects to A1, while the aNBM preferentially projects to S1. These results were further confirmed by another experiment in which the authors optogenetically activated cholinergic neurons in the BF subnuclei and successfully induced modality-selective desynchronization in specific sensory cortices.

A similar experiment was performed by Chaves-Coira et al. (2016), who also used retrograde anatomical procedures to demonstrate the existence of specific neuronal groups in the BF implicated in the modulation of specific sensory cortices. However, here the authors found that most of the neurons located in the HDB projected to the S1 cortex, suggesting that this area is specialized in the sensory processing of tactile stimuli, and the NBM was found to have a similar number of cells projecting to S1 as to A1. Furthermore, optogenetic HDB stimulation induced a larger facilitation of tactile evoked potentials in S1 than auditory evoked potentials in A1, while optogenetic stimulation of the NBM facilitated either tactile or auditory evoked potentials equally. These results suggest that cholinergic projections to the cortex are organized into spatially segregated pools of neurons that modulate specific cortical areas; although, additional research will be needed in order to provide a clear and definitive picture of the topographical organization of the projections arising from the BF region and innervating the cortex. Despite the many attempts to clarify this issue, it remains unclear whether there exist distinct neuronal populations in the HDB, or whether

the differences observed in the outcomes of the experiments mentioned above are due to discrepancies existing in the transgenic mouse lines used or to the slightly different techniques that were employed.

ACh is thus involved both in the bottom-up attentional process that leads to a general and whole-state arousal of the cortex and in the top-down modifications of circuit activity that occur during detection of behaviorally relevant sensory stimuli. Cognitive functions of cholinergic projection systems vary according to the brain area that is being modulated. Cholinergic modulation may act as a common mechanism to improve sensory encoding in several brain areas.

SUMMARY AND OUTLOOK

ACh release in the neocortex controls transitions between brain states, such as attention, memory and wakefulness, and can occur through volume or synaptic transmission. However, it is not clear yet whether one modality prevails upon the other or if they are complementary mechanisms. Further studies are needed to establish correlations between the distribution profile of the receptor subtypes, the relative proximity and density of cholinergic varicosities to assess differences between the two modalities. Moreover, as results could vastly vary across species, a systematic effort is crucial to be able to compare quantitative measurements.

The expression of muscarinic and nicotinic cholinergic receptors—the two main types—varies according to the cell-type and the pattern of receptor localization varies across cortical layers. A detailed knowledge of the subcellular localization of cholinergic receptors is, however, currently lacking. The detection of cholinergic structures such as the receptor protein has become easier with the advent of polyclonal antibodies targeting different subtypes. Future investigations should, therefore, converge on systematically measuring the amount of each receptor subtype across cellular compartments.

In this review, we have endeavored to determine, in a quantitative manner, the cellular and synaptic effects of ACh release in the neocortex. While the cholinergic modulation of excitatory PCs has been extensively researched, its effect on inhibitory interneurons is still largely unknown. For example, the effect of ACh on BCs (fast-spiking, PV⁺ interneurons) remains unclear. This could be due to the lack of a thorough classification of diverse morphological types of BCs where a differential distribution of cholinergic receptors could modulate divergent cellular and synaptic effects. Furthermore, it is not clear whether bath-application of cholinergic agonists is comparable to a physiological activation of the cholinergic system. Applied concentrations of cholinergic agonists vary substantially (up to three orders of magnitude) across electrophysiological studies, which seldom use more than one concentration. To obtain carefully designed dose-response curves of the effects of cholinergic agonists is paramount to dissect the consequences of physiological ACh release in the neocortex. The advent of optogenetics holds promise in designing physiological protocols of ACh release. Future experiments should not only merely

employ traditional bath-application of cholinergic agonists but also exploit optogenetics to reconcile how doses of agonists directly map to effects of endogenous, physiological release of ACh.

The effects of ACh on synaptic connections can vary drastically according to the identity of the presynaptic terminal and its postsynaptic partner. Additionally, the magnitude of the postsynaptic response also depends on the receptor subtype being activated. Therefore, there is a clear requirement for systematic investigations of the effects of ACh on different synapse-types, combined with knowledge of implicated cell-types and receptor subtypes to unravel the effects of ACh release on neocortical synaptic transmission.

ACh is involved in the induction of synaptic plasticity mechanisms, which could support its role in cortical learning and memory. In addition, ACh enhances sensory processing by affecting receptor fields size and tuning properties. It is not clear, however, if the effects of ACh are modality-specific or can be generalized to all sensory processing, nor exactly which tuning properties are affected. Many studies point to a role of ACh in increasing the SNR of a sensory response, and others describe how ACh suppresses cortico-cortical interactions in favor of thalamic transmission. Therefore, further clarification is required on the matter. Moreover, special attention must be paid in integrating data from primates and rodents: neuromodulatory systems are commonly the object of evolutionary modifications, even though they might maintain some functional similarity throughout species.

The mechanisms of ACh-induced changes in the physiology of neocortical neurons and their synapses, and how these changes shape the emergence of global network states still remains elusive. The impact of ACh on global cortical computations sustains cognitive functions such as attention, learning and memory, which are characterized by desynchronized network

activity. Cholinergic inputs mainly originate in the BF, a structure comprising distinct multi-transmitter neuronal populations. The functional relevance of neuronal subpopulations in the BF and the co-release of two potentially antagonistic transmitters to the desynchronization of cortical activity is unknown. Furthermore, recent work identifies that a sub-population of VIP⁺ cortical interneurons co-release ACh and GABA with potentially differing functions across species. Future research should, therefore, focus on dissecting the impact of each transmitter on cellular excitability. In addition, analyzing the co-localization of post-synaptic receptors could also allow the identification of individual synapses that are sensitive to multiple neurotransmitters. All these possibilities should be addressed systematically in order to precisely understand the contribution of each neurotransmitter to ACh-induced effects on the emergence of cortical network states in health and disease.

AUTHOR CONTRIBUTIONS

CC, DK, PS and SR wrote the manuscript and drafted the figures and tables. SR, DK and HM reviewed and edited the manuscript and the figures. SR conceived the idea and supervised the study.

FUNDING

This work was supported by funding from the ETH Domain for the Blue Brain Project (BBP).

ACKNOWLEDGMENTS

We thank Dr Natali Barros-Zulaica and Taylor H. Newton for useful discussions.

REFERENCES

- Albuquerque, E. X., Pereira, E. F., Mike, A., Eisenberg, H. M., Maelicke, A., and Alkondon, M. (2000). Neuronal nicotinic receptors in synaptic functions in humans and rats: physiological and clinical relevance. *Behav. Brain Res.* 113, 131–141. doi: 10.1016/S0166-4328(00)00208-4
- Alger, B. E., Nagode, D. A., and Tang, A.-H. (2014). Muscarinic cholinergic receptors modulate inhibitory synaptic rhythms in hippocampus and neocortex. *Front. Synaptic Neurosci.* 6:18. doi: 10.3389/fnsyn.2014.00018
- Alitto, H. J., and Dan, Y. (2013). Cell-type-specific modulation of neocortical activity by basal forebrain input. *Front. Syst. Neurosci.* 6:79. doi: 10.3389/fnsys.2012.00079
- Alkondon, M., and Albuquerque, E. X. (2004). The nicotinic acetylcholine receptor subtypes and their function in the hippocampus and cerebral cortex. *Prog. Brain Res.* 145, 109–120. doi: 10.1016/S0079-6123(03)45007-3
- Alkondon, M., Pereira, E. F., Eisenberg, H. M., and Albuquerque, E. X. (1999). Choline and selective antagonists identify two subtypes of nicotinic acetylcholine receptors that modulate GABA release from CA1 interneurons in rat hippocampal slices. *J. Neurosci.* 19, 2693–2705. doi: 10.1523/JNEUROSCI.19-07-02693.1999
- Anacleit, C., Pedersen, N. P., Ferrari, L. L., Venner, A., Bass, C. E., Arrigoni, E., et al. (2015). Basal forebrain control of wakefulness and cortical rhythms. *Nat. Commun.* 6:8744. doi: 10.1038/ncomms9744
- Aoki, C., and Kabak, S. (1992). Cholinergic terminals in the cat visual cortex: ultrastructural basis for interaction with glutamate-immunoreactive neurons and other cells. *Vis. Neurosci.* 8, 177–191. doi: 10.1017/S095252380002832
- Arroyo, S., Bennett, C., Aziz, D., Brown, S. P., and Hestrin, S. (2012). Prolonged disinaptic inhibition in the cortex mediated by slow, non- $\alpha 7$ nicotinic excitation of a specific subset of cortical interneurons. *J. Neurosci.* 32, 3859–3864. doi: 10.1523/JNEUROSCI.0115-12.2012
- Artinian, L. R., Ding, J. M., and Gillette, M. U. (2001). Carbon monoxide and nitric oxide: interacting messengers in muscarinic signaling to the brain's circadian clock. *Exp. Neurol.* 171, 293–300. doi: 10.1006/exnr.2001.7781
- Atzori, M., Kanold, P. O., Pineda, J. C., Flores-Hernandez, J., and Paz, R. D. (2005). Dopamine prevents muscarinic-induced decrease of glutamate release in the auditory cortex. *Neuroscience* 134, 1153–1165. doi: 10.1016/j.neuroscience.2005.05.005
- Bailey, C. D. C., De Biasi, M., Fletcher, P. J., and Lambe, E. K. (2010). The nicotinic acetylcholine receptor $\alpha 5$ subunit plays a key role in attention circuitry and accuracy. *J. Neurosci.* 30, 9241–9252. doi: 10.1523/JNEUROSCI.2258-10.2010
- Baker, A. L., O'Toole, R. J., and Gullledge, A. T. (2018). Preferential cholinergic excitation of corticopontine neurons. *J. Physiol.* 596, 1659–1679. doi: 10.1111/jp275194
- Bazhenov, M., Timofeev, I., Steriade, M., and Sejnowski, T. J. (2002). Model of thalamocortical slow-wave sleep oscillations and transitions to activated states. *J. Neurosci.* 22, 8691–8704. doi: 10.1523/JNEUROSCI.22-19-08691.2002
- Bear, M. F., and Singer, W. (1986). Modulation of visual cortical plasticity by acetylcholine and noradrenaline. *Nature* 320, 172–176. doi: 10.1038/320172a0

- Beaulieu, C., and Somogyi, P. (1991). Enrichment of cholinergic synaptic terminals on GABAergic neurons and coexistence of immunoreactive GABA and choline acetyltransferase in the same synaptic terminals in the striate cortex of the cat. *J. Comp. Neurol.* 304, 666–680. doi: 10.1002/cne.903040412
- Berger, H. (1929). Über das elektroencephalogramm des menschen. *Arch. Für Psychiatr. Nervenkrankh.* 87, 527–570. doi: 10.1007/BF01797193
- Bertrand, D. (2010). Neurocircuitry of the nicotinic cholinergic system. *Dialogues Clin. Neurosci.* 12, 463–470.
- Borda, T., Genaro, A., Sterin-Borda, L., and Cremaschi, G. (1998). Involvement of endogenous nitric oxide signalling system in brain muscarinic acetylcholine receptor activation. *J. Neural Transm.* 105, 193–204. doi: 10.1007/s007020050048
- Brombas, A., Fletcher, L. N., and Williams, S. R. (2014). Activity-dependent modulation of layer 1 inhibitory neocortical circuits by acetylcholine. *J. Neurosci.* 34, 1932–1941. doi: 10.1523/JNEUROSCI.4470-13.2014
- Buisson, B., and Bertrand, D. (2001). Chronic exposure to nicotine upregulates the human $\alpha 4\beta 2$ nicotinic acetylcholine receptor function. *J. Neurosci.* 21, 1819–1829. doi: 10.1523/JNEUROSCI.21-06-01819.2001
- Buzsaki, G., Bickford, R. G., Ponomareff, G., Thal, L. J., Mandel, R., and Gage, F. H. (1988). Nucleus basalis and thalamic control of neocortical activity in the freely moving rat. *J. Neurosci.* 8, 4007–4026. doi: 10.1523/JNEUROSCI.08-11-0407.1988
- Callender, J. A., and Newton, A. C. (2017). Conventional protein kinase C in the brain: 40 years later. *Neuronal Signal.* 1:NS20160005. doi: 10.1042/ns20160005
- Carr, D. B., and Surmeier, D. J. (2007). M1 muscarinic receptor modulation of Kir2 channels enhances temporal summation of excitatory synaptic potentials in prefrontal cortex pyramidal neurons. *J. Neurophysiol.* 97, 3432–3438. doi: 10.1152/jn.00828.2006
- Castro-Alamancos, M. A., and Gulati, T. (2014). Neuromodulators produce distinct activated states in neocortex. *J. Neurosci.* 34, 12353–12367. doi: 10.1523/JNEUROSCI.1858-14.2014
- Cauli, B., Tong, X.-K., Rancillac, A., Serluca, N., Lambolze, B., Rossier, J., et al. (2004). Cortical GABA interneurons in neurovascular coupling: relays for subcortical vasoactive pathways. *J. Neurosci.* 24, 8940–8949. doi: 10.1523/JNEUROSCI.3065-04.2004
- Chaves-Coira, I., Barros-Zulaica, N., Rodrigo-Angulo, M., and Núñez, Á. (2016). Modulation of specific sensory cortical areas by segregated basal forebrain cholinergic neurons demonstrated by neuronal tracing and optogenetic stimulation in mice. *Front. Neural Circuits* 10:28. doi: 10.3389/fncir.2016.00028
- Chen, N., Sugihara, H., and Sur, M. (2015). An acetylcholine-activated microcircuit drives temporal dynamics of cortical activity. *Nat. Neurosci.* 18, 892–902. doi: 10.1038/nn.4002
- Christophe, E., Roebuck, A., Staiger, J. F., Lavery, D. J., Charkpak, S., and Audinat, E. (2002). Two types of nicotinic receptors mediate an excitation of neocortical layer I interneurons. *J. Neurophysiol.* 88, 1318–1327. doi: 10.1152/jn.2002.88.3.1318
- Coppola, J. J., and Disney, A. A. (2018). Is there a canonical cortical circuit for the cholinergic system? Anatomical differences across common model systems. *Front. Neural Circuits* 12:8. doi: 10.3389/fncir.2018.00008
- Couey, J. J., Meredith, R. M., Spijker, S., Poorthuis, R. B., Smit, A. B., Brussaard, A. B., et al. (2007). Distributed network actions by nicotine increase the threshold for spike-timing-dependent plasticity in prefrontal cortex. *Neuron* 54, 73–87. doi: 10.1016/j.neuron.2007.03.006
- Dajas-Bailador, F., and Wonnacott, S. (2004). Nicotinic acetylcholine receptors and the regulation of neuronal signalling. *Trends Pharmacol. Sci.* 25, 317–324. doi: 10.1016/s0165-6147(04)00118-x
- Dale, H. H. (1914). The action of certain esters and ethers of choline and their relation to muscarine. *J. Pharmacol. Exp. Ther.* 6, 147–190.
- Dani, J. A., and Bertrand, D. (2007). Nicotinic acetylcholine receptors and nicotinic cholinergic mechanisms of the central nervous system. *Annu. Rev. Pharmacol. Toxicol.* 47, 699–729. doi: 10.1146/annurev.pharmtox.47.120505.105214
- Dasari, S., Hill, C., and Gullledge, A. T. (2017). A unifying hypothesis for M1 muscarinic receptor signalling in pyramidal neurons. *J. Physiol.* 595, 1711–1723. doi: 10.1113/jp273627
- Dasgupta, R., Seibt, F., and Beierlein, M. (2018). Synaptic release of acetylcholine rapidly suppresses cortical activity by recruiting muscarinic receptors in layer 4. *J. Neurosci.* 38, 5338–5350. doi: 10.1523/JNEUROSCI.0566-18.2018
- Delmas, P., and Brown, D. A. (2005). Pathways modulating neural KCNQ/M (Kv7) potassium channels. *Nat. Rev. Neurosci.* 6, 850–862. doi: 10.1038/nrn1785
- Descarries, L., and Mechawar, N. (2000). “Ultrastructural evidence for diffuse transmission by monoamine and acetylcholine neurons of the central nervous system,” in *Progress in Brain Research* eds L. F. Agnati, K. Fuxe, C. Nicholson and Syková E (Amsterdam: Elsevier), 27–47.
- Disney, A. A., Aoki, C., and Hawken, M. J. (2007). Gain modulation by nicotine in macaque V1. *Neuron* 56, 701–713. doi: 10.1016/j.neuron.2007.09.034
- Disney, A. A., Domakonda, K. V., and Aoki, C. (2006). Differential expression of muscarinic acetylcholine receptors across excitatory and inhibitory cells in visual cortical areas V1 and V2 of the macaque monkey. *J. Comp. Neurol.* 499, 49–63. doi: 10.1002/cne.21096
- Duque, A., Balatoni, B., Detari, L., and Zaborszky, L. (2000). EEG correlation of the discharge properties of identified neurons in the basal forebrain. *J. Neurophysiol.* 84, 1627–1635. doi: 10.1152/jn.2000.84.3.1627
- Eccles, J. C., Fatt, P., and Koketsu, K. (1953). Cholinergic and inhibitory synapses in a central nervous pathway. *Aust. J. Sci.* 16, 50–54.
- Eckenstein, F. P., Baughman, R. W., and Quinn, J. (1988). An anatomical study of cholinergic innervation in rat cerebral cortex. *Neuroscience* 25, 457–474. doi: 10.1016/0306-4522(88)90251-5
- Eggermann, E., and Feldmeyer, D. (2009). Cholinergic filtering in the recurrent excitatory microcircuit of cortical layer 4. *Proc. Natl. Acad. Sci. U S A* 106, 11753–11758. doi: 10.1073/pnas.0810062106
- Elhussainy, A., and Hamel, E. (2000). Muscarinic—but not nicotinic—acetylcholine receptors mediate a nitric oxide-dependent dilation in brain cortical arterioles: a possible role for the M5 receptor subtype. *J. Cereb. Blood Flow Metab.* 20, 298–305. doi: 10.1097/00004647-200002000-00011
- Fanselow, E. E., Richardson, K. A., and Connors, B. W. (2008). Selective, state-dependent activation of somatostatin-expressing inhibitory interneurons in mouse neocortex. *J. Neurophysiol.* 100, 2640–2652. doi: 10.1152/jn.90691.2008
- Figl, A., and Cohen, B. N. (2000). The subunit dominates the relaxation kinetics of heteromeric neuronal nicotinic receptors. *J. Physiol.* 524, 685–699. doi: 10.1111/j.1469-7793.2000.00685.x
- Gericke, A., Sniatecki, J. J., Mayer, V. G. A., Goloborodko, E., Patzak, A., Wess, J., et al. (2011). Role of M1, M3, and M5 muscarinic acetylcholine receptors in cholinergic dilation of small arteries studied with gene-targeted mice. *Am. J. Physiol. Heart Circ. Physiol.* 300, H1602–H1608. doi: 10.1152/ajpheart.00982.2010
- Giacobini, E. (2003). Cholinergic function and Alzheimer’s disease. *Int. J. Geriatr. Psychiatry* 18, S1–S5. doi: 10.1002/gps.935
- Gil, Z., Connors, B. W., and Amitai, Y. (1997). Differential regulation of neocortical synapses by neuromodulators and activity. *Neuron* 19, 679–686. doi: 10.1016/s0896-6273(00)80380-3
- Goard, M., and Dan, Y. (2009). Basal forebrain activation enhances cortical coding of natural scenes. *Nat. Neurosci.* 12, 1444–1449. doi: 10.1038/nn.2402
- Granger, A. J., Mulder, N., Saunders, A., and Sabatini, B. L. (2016). Cotransmission of acetylcholine and GABA. *Neuropharmacology* 100, 40–46. doi: 10.1016/j.neuropharm.2015.07.031
- Granger, A. J., Wang, W., Robertson, K., El-Rifai, M., Zanello, A., Bistrong, K., et al. (2018). Target-specific co-transmission of acetylcholine and GABA from a subset of cortical VIP⁺ interneurons. *BioRxiv*:69064 [preprint]. doi: 10.1101/469064
- Groleau, M., Kang, J. I., Huppé-Gourgues, F., and Vaucher, E. (2015). Distribution and effects of the muscarinic receptor subtypes in the primary visual cortex. *Front. Synaptic Neurosci.* 7:10. doi: 10.3389/fnsyn.2015.00010
- Gulledge, A. T., Park, S. B., Kawaguchi, Y., and Stuart, G. J. (2007). Heterogeneity of phasic cholinergic signaling in neocortical neurons. *J. Neurophysiol.* 97, 2215–2229. doi: 10.1152/jn.00493.2006
- Gulledge, A. T., and Stuart, G. J. (2005). Cholinergic inhibition of neocortical pyramidal neurons. *J. Neurosci.* 25, 10308–10320. doi: 10.1523/JNEUROSCI.2697-05.2005

- Haj-Dahmane, S., and Andrade, R. (1996). Muscarinic activation of a voltage-dependent cation nonselective current in rat association cortex. *J. Neurosci.* 16, 3848–3861. doi: 10.1523/JNEUROSCI.16-12-03848.1996
- Hales, T. G., Dunlop, J. I., Deeb, T. Z., Carland, J. E., Kelley, S. P., Lambert, J. J., et al. (2006). Common determinants of single channel conductance within the large cytoplasmic loop of 5-hydroxytryptamine type 3 and $\alpha 4\beta 2$ nicotinic acetylcholine receptors. *J. Biol. Chem.* 281, 8062–8071. doi: 10.1074/jbc.M513222200
- Hasselmo, M. E., and Sarter, M. (2011). Modes and models of forebrain cholinergic neuromodulation of cognition. *Neuropsychopharmacology* 36, 52–73. doi: 10.1038/npp.2010.104
- Hay, Y. A., Lambolez, B., and Tricoire, L. (2016). Nicotinic transmission onto layer 6 cortical neurons relies on synaptic activation of non- $\alpha 7$ receptors. *Cereb. Cortex* 26, 2549–2562. doi: 10.1093/cercor/bhv085
- Hedrick, T., and Waters, J. (2015). Acetylcholine excites neocortical pyramidal neurons via nicotinic receptors. *J. Neurophysiol.* 113, 2195–2209. doi: 10.1152/jn.00716.2014
- Henny, P., and Jones, B. E. (2008). Projections from basal forebrain to prefrontal cortex comprise cholinergic, GABAergic and glutamatergic inputs to pyramidal cells or interneurons. *Eur. J. Neurosci.* 27, 654–670. doi: 10.1111/j.1460-9568.2008.06029.x
- Heys, J. G., and Hasselmo, M. E. (2012). Neuromodulation of I_h in layer II medial entorhinal cortex stellate cells: a voltage-clamp study. *J. Neurosci.* 32, 9066–9072. doi: 10.1523/JNEUROSCI.0868-12.2012
- Heys, J. G., Schultheiss, N. W., Shay, C. F., Tsuno, Y., and Hasselmo, M. E. (2012). Effects of acetylcholine on neuronal properties in entorhinal cortex. *Front. Behav. Neurosci.* 6:32. doi: 10.3389/fnbeh.2012.00032
- Hilscher, M. M., Leão, R. N., Edwards, S. J., Leão, K. E., and Kullander, K. (2017). ChR2-martinotti cells synchronize layer 5 type a pyramidal cells via rebound excitation. *PLoS Biol.* 15:e2001392. doi: 10.1371/journal.pbio.2001392
- Hsiao, B., Mihalak, K. B., Magleby, K. L., and Luetje, C. W. (2008). Zinc potentiates neuronal nicotinic receptors by increasing burst duration. *J. Neurophysiol.* 99, 999–1007. doi: 10.1152/jn.01040.2007
- Hwang, J.-I., Kim, H. S., Lee, J. R., Kim, E., Ryu, S. H., and Suh, P.-G. (2005). The interaction of phospholipase C- $\beta 3$ with Shank2 regulates mGluR-mediated calcium signal. *J. Biol. Chem.* 280, 12467–12473. doi: 10.1074/jbc.M410740200
- Jiang, M., and Bajpayee, N. S. (2009). Molecular mechanisms of go signaling. *Neurosignals* 17, 23–41. doi: 10.1159/000186688
- Jiang, X., Wang, G., Lee, A. J., Stornetta, R. L., and Zhu, J. J. (2013). The organization of two new cortical interneuronal circuits. *Nat. Neurosci.* 16, 210–218. doi: 10.1038/nn.3305
- Kalmbach, A., Hedrick, T., and Waters, J. (2012). Selective optogenetic stimulation of cholinergic axons in neocortex. *J. Neurophysiol.* 107, 2008–2019. doi: 10.1152/jn.00870.2011
- Kan, W., Adjobo-Hermans, M., Burroughs, M., Faibis, G., Malik, S., Tall, G. G., et al. (2014). M3 muscarinic receptor interaction with phospholipase C $\beta 3$ determines its signaling efficiency. *J. Biol. Chem.* 289, 11206–11218. doi: 10.1074/jbc.M113.538546
- Kassam, S. M., Herman, P. M., Goodfellow, N. M., Alves, N. C., and Lambe, E. K. (2008). Developmental excitation of corticothalamic neurons by nicotinic acetylcholine receptors. *J. Neurosci.* 28, 8756–8764. doi: 10.1523/JNEUROSCI.2645-08.2008
- Katz, B., and Miledi, R. (1973). The binding of acetylcholine to receptors and its removal from the synaptic cleft. *J. Physiol.* 231, 549–574. doi: 10.1113/jphysiol.1973.sp010248
- Kawaguchi, Y. (1997). Selective cholinergic modulation of cortical GABAergic cell subtypes. *J. Neurophysiol.* 78, 1743–1747. doi: 10.1152/jn.1997.78.3.1743
- Kawaguchi, Y., and Kubota, Y. (1997). GABAergic cell subtypes and their synaptic connections in rat frontal cortex. *Cereb. Cortex* 7, 476–486. doi: 10.1093/cercor/7.6.476
- Kennedy, H., and Bullier, J. (1985). A double-labeling investigation of the afferent connectivity to cortical areas V1 and V2 of the macaque monkey. *J. Neurosci.* 5, 2815–2830. doi: 10.1523/JNEUROSCI.05-10-02815.1985
- Kim, J.-H., Jung, A.-H., Jeong, D., Choi, I., Kim, K., Shin, S., et al. (2016). Selectivity of neuromodulatory projections from the basal forebrain and locus ceruleus to primary sensory cortices. *J. Neurosci.* 36, 5314–5327. doi: 10.1523/JNEUROSCI.4333-15.2016
- Kimura, F., Fukuda, M., and Tsumoto, T. (1999). Acetylcholine suppresses the spread of excitation in the visual cortex revealed by optical recording: possible differential effect depending on the source of input. *Eur. J. Neurosci.* 11, 3597–3609. doi: 10.1046/j.1460-9568.1999.00779.x
- Kocharyan, A., Fernandes, P., Tong, X.-K., Vaucher, E., and Hamel, E. (2008). Specific subtypes of cortical GABA interneurons contribute to the neurovascular coupling response to basal forebrain stimulation. *J. Cereb. Blood Flow Metab.* 28, 221–231. doi: 10.1038/sj.jcbfm.9600558
- Koukoulis, F., Rooy, M., Tziotis, D., Sailor, K. A., O'Neill, H. C., Levenga, J., et al. (2017). Nicotine reverses hypofrontality in animal models of addiction and schizophrenia. *Nat. Med.* 23, 347–354. doi: 10.1038/nm.4274
- Krnjević, K. (2004). Synaptic mechanisms modulated by acetylcholine in cerebral cortex. *Prog. Brain Res.* 145, 81–93. doi: 10.1016/s0079-6123(03)45005-x
- Kruglikov, I., and Rudy, B. (2008). Perisomatic GABA release and thalamocortical integration onto neocortical excitatory cells are regulated by neuromodulators. *Neuron* 58, 911–924. doi: 10.1016/j.neuron.2008.04.024
- Kuryatov, A., Berrettini, W., and Lindstrom, J. (2011). Acetylcholine receptor (AChR) $\alpha 5$ subunit variant associated with risk for nicotine dependence and lung cancer reduces ($\alpha 4\beta 2$) $\alpha 5$ AChR function. *Mol. Pharmacol.* 79, 119–125. doi: 10.1124/mol.110.066357
- Lee, S.-H., and Dan, Y. (2012). Neuromodulation of brain states. *Neuron* 76, 209–222. doi: 10.1016/j.neuron.2012.09.012
- Letzkus, J. J., Wolff, S. B. E., Meyer, E. M. M., Tovote, P., Courtin, J., Herry, C., et al. (2011). A disinhibitory microcircuit for associative fear learning in the auditory cortex. *Nature* 480, 331–335. doi: 10.1038/nature10674
- Levey, A. I., Kitt, C. A., Simonds, W. F., Price, D. L., and Brann, M. R. (1991). Identification and localization of muscarinic acetylcholine receptor proteins in brain with subtype-specific antibodies. *J. Neurosci.* 11, 3218–3226. doi: 10.1523/JNEUROSCI.11-10-03218.1991
- Levy, R. B., Reyes, A. D., and Aoki, C. (2006). Nicotinic and muscarinic reduction of unitary excitatory postsynaptic potentials in sensory cortex; dual intracellular recording *in vitro*. *J. Neurophysiol.* 95, 2155–2166. doi: 10.1152/jn.00603.2005
- Li, P., and Steinbach, J. H. (2010). The neuronal nicotinic $\alpha 4\beta 2$ receptor has a high maximal probability of being open. *Br. J. Pharmacol.* 160, 1906–1915. doi: 10.1111/j.1476-5381.2010.00761.x
- Lin, S.-C., Brown, R. E., Shuler, M. G. H., Petersen, C. C. H., and Kepecs, A. (2015). Optogenetic dissection of the basal forebrain neuromodulatory control of cortical activation, plasticity, and cognition. *J. Neurosci.* 35, 13896–13903. doi: 10.1523/JNEUROSCI.2590-15.2015
- Little, J. T., Johnson, D. N., Minichiello, M., Weingartner, H., and Sunderland, T. (1998). Combined nicotinic and muscarinic blockade in elderly normal volunteers: cognitive, behavioral, and physiologic responses. *Neuropsychopharmacology* 19, 60–69. doi: 10.1016/s0893-133x(98)00002-5
- Loewi, O. (1924). Über humorale Übertragbarkeit der Herznervenzirkung: V. Mitteilung. Die Übertragbarkeit der negativ chrono- und dromotropen Vaguswirkung. *Pflüg. Arch. Für Gesamte Physiol. Menschen Tiere* 204, 629–640.
- Lysakowski, A., Wainer, B. H., Bruce, G., and Hersh, L. B. (1989). An atlas of the regional and laminar distribution of choline acetyltransferase immunoreactivity in rat cerebral cortex. *Neuroscience* 28, 291–336. doi: 10.1016/0306-4522(89)90180-2
- Mancarci, B. O., Toker, L., Tripathy, S. J., Li, B., Rocco, B., Sibille, E., et al. (2017). Cross-laboratory analysis of brain cell type transcriptomes with applications to interpretation of bulk tissue data. *eNeuro* 4:ENEURO.0212–17.2017. doi: 10.1523/eneuro.0212-17.2017
- Marchi, M., and Grilli, M. (2010). Presynaptic nicotinic receptors modulating neurotransmitter release in the central nervous system: functional interactions with other coexisting receptors. *Prog. Neurobiol.* 92, 105–111. doi: 10.1016/j.pneurobio.2010.06.004
- Markram, H., Lübke, J., Frotscher, M., Roth, A., and Sakmann, B. (1997). Physiology and anatomy of synaptic connections between thick tufted pyramidal neurones in the developing rat neocortex. *J. Physiol.* 500, 409–440. doi: 10.1113/jphysiol.1997.sp022031
- Mathes, C., and Thompson, S. H. (1996). The nitric oxide/cGMP pathway couples muscarinic receptors to the activation of Ca^{2+} influx. *J. Neurosci.* 16, 1702–1709. doi: 10.1523/JNEUROSCI.16-05-01702.1996
- McCormick, D. A. (1992). Cellular mechanisms underlying cholinergic and noradrenergic modulation of neuronal firing mode in the cat and guinea

- pig dorsal lateral geniculate nucleus. *J. Neurosci.* 12, 278–289. doi: 10.1523/JNEUROSCI.12-01-00278.1992
- McCormick, D. A., and Prince, D. A. (1985). Two types of muscarinic response to acetylcholine in mammalian cortical neurons. *Proc. Natl. Acad. Sci. U S A* 82, 6344–6348. doi: 10.1073/pnas.82.18.6344
- Meir, I., Katz, Y., and Lampl, I. (2018). Membrane potential correlates of network decorrelation and improved SNR by cholinergic activation in the somatosensory cortex. *J. Neurosci.* 38, 10692–10708. doi: 10.1523/JNEUROSCI.1159-18.2018
- Metherate, R., and Hsieh, C. Y. (2004). Synaptic mechanisms and cholinergic regulation in auditory cortex. *Prog. Brain Res.* 145, 143–156. doi: 10.1016/s0079-6123(03)45010-3
- Metherate, R., and Weinberger, N. M. (1990). Cholinergic modulation of responses to single tones produces tone-specific receptive field alterations in cat auditory cortex. *Synapse* 6, 133–145. doi: 10.1002/syn.890060204
- Mincses, V., Pinto, L., Dan, Y., and Chiba, A. A. (2017). Cholinergic shaping of neural correlations. *Proc. Natl. Acad. Sci. U S A* 114, 5725–5730. doi: 10.1073/pnas.1621493114
- Moruzzi, G., and Magoun, H. W. (1949). Brain stem reticular formation and activation of the EEG. *Electroencephalogr. Clin. Neurophysiol.* 1, 455–473. doi: 10.1016/0013-4694(49)90066-8
- Mrzjak, L., Papp, M., Laranth, C., and Goldman-Rakic, P. S. (1995). Cholinergic synaptic circuitry in the macaque prefrontal cortex. *J. Comp. Neurol.* 357, 603–617. doi: 10.1002/cne.903570409
- Mrzjak, L., Levey, A. I., and Goldman-Rakic, P. S. (1993). Association of m1 and m2 muscarinic receptor proteins with asymmetric synapses in the primate cerebral cortex: morphological evidence for cholinergic modulation of excitatory neurotransmission. *Proc. Natl. Acad. Sci. U S A* 90, 5194–5198. doi: 10.1073/pnas.90.11.5194
- Muñoz, W., and Rudy, B. (2014). Spatiotemporal specificity in cholinergic control of neocortical function. *Curr. Opin. Neurobiol.* 26, 149–160. doi: 10.1016/j.conb.2014.02.015
- Muñoz, W., Tremblay, R., Levenstein, D., and Rudy, B. (2017). Layer-specific modulation of neocortical dendritic inhibition during active wakefulness. *Science* 355, 954–959. doi: 10.1126/science.aag2599
- Nashmi, R., and Lester, H. A. (2006). CNS localization of neuronal nicotinic receptors. *J. Mol. Neurosci.* 30, 181–184. doi: 10.1385/jmn:30:1:181
- Newman, E. L., Gupta, K., Climer, J. R., Monaghan, C. K., and Hasselmo, M. E. (2012). Cholinergic modulation of cognitive processing: insights drawn from computational models. *Front. Behav. Neurosci.* 6:24. doi: 10.3389/fnbeh.2012.00024
- Nguyen, Q., Sapp, D. W., Van Ness, P. C., and Olsen, R. W. (1995). Modulation of GABA_A receptor binding in human brain by neuroactive steroids: species and brain regional differences. *Synapse* 19, 77–87. doi: 10.1002/syn.890190203
- Núñez, A., Domínguez, S., Buño, W., and Fernández de Sevilla, D. (2012). Cholinergic-mediated response enhancement in barrel cortex layer V pyramidal neurons. *J. Neurophysiol.* 108, 1656–1668. doi: 10.1152/jn.00156.2012
- Obermayer, J., Heistek, T. S., Kerkhofs, A., Goriounova, N. A., Kroon, T., Baayen, J. C., et al. (2018). Lateral inhibition by Martinotti interneurons is facilitated by cholinergic inputs in human and mouse neocortex. *Nat. Commun.* 9:4101. doi: 10.1038/s41467-018-06628-w
- Obermayer, J., Verhoog, M. B., Luchicchi, A., and Mansvelder, H. D. (2017). Cholinergic modulation of cortical microcircuits is layer-specific: evidence from rodent, monkey and human brain. *Front. Neural Circuits* 11:100. doi: 10.3389/fncir.2017.00100
- Pawlak, V., Wickens, J. R., Kirkwood, A., and Kerr, J. N. (2010). Timing is not everything: neuromodulation opens the STDP gate. *Front. Synaptic Neurosci.* 2:146. doi: 10.3389/fnsyn.2010.00146
- Poorthuis, R. B., Bloem, B., Schak, B., Wester, J., de Kock, C. P. J., and Mansvelder, H. D. (2013). Layer-specific modulation of the prefrontal cortex by nicotinic acetylcholine receptors. *Cereb. Cortex* 23, 148–161. doi: 10.1093/cercor/bhr390
- Poorthuis, R. B., Enke, L., and Letzkus, J. J. (2014). Cholinergic circuit modulation through differential recruitment of neocortical interneuron types during behaviour. *J. Physiol.* 592, 4155–4164. doi: 10.1113/jphysiol.2014.273862
- Poorthuis, R. B., Muhammad, K., Wang, M., Verhoog, M. B., Junek, S., Wrana, A., et al. (2018). Rapid neuromodulation of layer 1 interneurons in human neocortex. *Cell Rep.* 23, 951–958. doi: 10.1016/j.celrep.2018.03.111
- Radnikow, G., and Feldmeyer, D. (2018). Layer- and cell type-specific modulation of excitatory neuronal activity in the neocortex. *Front. Neuroanat.* 12:1. doi: 10.3389/fnana.2018.00001
- Ramaswamy, S., Colangelo, C., and Markram, H. (2018). Data-driven modeling of cholinergic modulation of neural microcircuits: bridging neurons, synapses and network activity. *Front. Neural Circuits* 12:77. doi: 10.3389/fncir.2018.00077
- Rasmusson, D. (2000). The role of acetylcholine in cortical synaptic plasticity. *Behav. Brain Res.* 115, 205–218. doi: 10.1016/s0166-4328(00)00259-x
- Rovira, J. C., Ballesta, J. J., Vicente-Agulló, F., Campos-Caro, A., Criado, M., Sala, F., et al. (1998). A residue in the middle of the M2–M3 loop of the beta4 subunit specifically affects gating of neuronal nicotinic receptors. *FEBS Lett.* 433, 89–92. doi: 10.1016/s0014-5793(98)00889-8
- Rudy, B., Fishell, G., Lee, S., and Hjerling-Leffler, J. (2011). Three groups of interneurons account for nearly 100% of neocortical GABAergic neurons. *Dev. Neurobiol.* 71, 45–61. doi: 10.1002/dneu.20853
- Runfeldt, M. J., Sadovsky, A. J., and MacLean, J. N. (2014). Acetylcholine functionally reorganizes neocortical microcircuits. *J. Neurophysiol.* 112, 1205–1216. doi: 10.1152/jn.00071.2014
- Sabri, O., Kendziorra, K., Wolf, H., Gertz, H.-J., and Brust, P. (2008). Acetylcholine receptors in dementia and mild cognitive impairment. *Eur. J. Nucl. Med. Mol. Imaging* 35, S30–S45. doi: 10.1007/s00259-007-0701-1
- Salgado, H., Bellay, T., Nichols, J. A., Bose, M., Martinolich, L., Perrotti, L., et al. (2007). Muscarinic M₂ and M₁ receptors reduce GABA release by Ca²⁺ channel modulation through activation of PI₃K/Ca²⁺-independent and PLC/Ca²⁺-dependent PKC. *J. Neurophysiol.* 98, 952–965. doi: 10.1152/jn.00060.2007
- Saper, C. B., Chou, T. C., and Scammell, T. E. (2001). The sleep switch: hypothalamic control of sleep and wakefulness. *Trends Neurosci.* 24, 726–731. doi: 10.1016/s0166-2236(00)02002-6
- Saper, C. B., Fuller, P. M., Pedersen, N. P., Lu, J., and Scammell, T. E. (2010). Sleep state switching. *Neuron* 68, 1023–1042. doi: 10.1016/j.neuron.2010.11.032
- Sarter, M., Parikh, V., and Howe, W. M. (2009). Phasic acetylcholine release and the volume transmission hypothesis: time to move on. *Nat. Rev. Neurosci.* 10, 383–390. doi: 10.1038/nrn2635
- Saunders, A., Granger, A. J., and Sabatini, B. L. (2015). Corelease of acetylcholine and GABA from cholinergic forebrain neurons. *Elife* 4:e06412. doi: 10.7554/elife.06412
- Saunders, A., Macosko, E. Z., Wysoker, A., Goldman, M., Krienen, F. M., de Rivera, H., et al. (2018). Molecular diversity and specializations among the cells of the adult mouse brain. *Cell* 174, 1015.e16–1030.e16. doi: 10.1016/j.cell.2018.07.028
- Schmiedeberg, O., and Koppe, R. (1869). *Das Muscarin. Das Giftige Alkaloid des Fliegenpilzes*. Leipzig: Vogel.
- Schröder, H. (1992). Immunohistochemistry of cholinergic receptors. *Anat. Embryol.* 186, 407–429. doi: 10.1007/bf00185457
- Schröder, H., Zilles, K., Luiten, P. G. M., and Strosberg, A. (1990). Immunocytochemical visualization of muscarinic cholinergic receptors in the human cerebral cortex. *Brain Res.* 514, 249–258. doi: 10.1016/0006-8993(90)91420-1
- Schröder, H., Zilles, K., Maelicke, A., and Hajós, F. (1989). Immunohisto- and cytochemical localization of cortical nicotinic cholinergic receptors in rat and man. *Brain Res.* 502, 287–295. doi: 10.1016/0006-8993(89)90624-0
- Shalinsky, M. H., Magistretti, J., Ma, L., and Alonso, A. A. (2002). Muscarinic activation of a cation current and associated current noise in entorhinal-cortex layer-II neurons. *J. Neurophysiol.* 88, 1197–1211. doi: 10.1152/jn.2002.88.3.1197
- Shen, J., and Yakel, J. L. (2009). Nicotinic acetylcholine receptor-mediated calcium signaling in the nervous system. *Acta Pharmacol. Sin.* 30, 673–680. doi: 10.1038/aps.2009.64
- Smiley, J. F., Morrell, F., and Mesulam, M. M. (1997). Cholinergic synapses in human cerebral cortex: an ultrastructural study in serial sections. *Exp. Neurol.* 144, 361–368. doi: 10.1006/exnr.1997.6413
- Sparks, D. W., Tian, M. K., Sargin, D., Venkatesan, S., Intson, K., and Lambe, E. K. (2018). Opposing cholinergic and serotonergic modulation of layer 6 in prefrontal cortex. *Front. Neural Circuits* 11:107. doi: 10.3389/fncir.2017.00107

- Steriade, M., Amzica, F., and Nunez, A. (1993). Cholinergic and noradrenergic modulation of the slow (approximately 0.3 Hz) oscillation in neocortical cells. *J. Neurophysiol.* 70, 1385–1400. doi: 10.1152/jn.1993.70.4.1385
- Stetzer, E., Ebbinghaus, U., Storch, A., Poteur, L., Schratzenholz, A., Kramer, G., et al. (1996). Stable expression in HEK-293 cells of the rat $\alpha 3/\beta 4$ subtype of neuronal nicotinic acetylcholine receptor. *FEBS Lett.* 397, 39–44. doi: 10.1016/s0014-5793(96)01115-5
- Stewart, A. E., Yan, Z., Surmeier, D. J., and Foehring, R. C. (1999). Muscarinic modulates Ca^{2+} channel currents in rat sensorimotor pyramidal cells via two distinct pathways. *J. Neurophysiol.* 81, 72–84. doi: 10.1152/jn.1999.81.1.72
- Sugihara, H., Chen, N., and Sur, M. (2016). Cell-specific modulation of plasticity and cortical state by cholinergic inputs to the visual cortex. *J. Physiol. Paris* 110, 37–43. doi: 10.1016/j.jphysparis.2016.11.004
- Szymusiak, R., and McGinty, D. (1986). Sleep suppression following kainic acid-induced lesions of the basal forebrain. *Exp. Neurol.* 94, 598–614. doi: 10.1016/0014-4886(86)90240-2
- Teles-Grilo Ruivo, L. M., and Mellor, J. R. (2013). Cholinergic modulation of hippocampal network function. *Front. Synaptic Neurosci.* 5:2. doi: 10.3389/fnsyn.2013.00002
- Thiele, A., Herrero, J. L., Distler, C., and Hoffmann, K.-P. (2012). Contribution of cholinergic and GABAergic mechanisms to direction tuning, discriminability, response reliability and neuronal rate correlations in macaque middle temporal area. *J. Neurosci.* 32, 16602–16615. doi: 10.1523/JNEUROSCI.0554-12.2012
- Tribollet, E., Bertrand, D., Marguerat, A., and Ragenbass, M. (2004). Comparative distribution of nicotinic receptor subtypes during development, adulthood and aging: an autoradiographic study in the rat brain. *Neuroscience* 124, 405–420. doi: 10.1016/j.neuroscience.2003.09.028
- Tsodyks, M. V., and Markram, H. (1997). The neural code between neocortical pyramidal neurons depends on neurotransmitter release probability. *Proc. Natl. Acad. Sci. U S A* 94, 719–723. doi: 10.1073/pnas.94.2.719
- Turrini, P., Casu, M. A., Wong, T. P., De Koninck, Y., Ribeiro-da-Silva, A., and Cuello, A. C. (2001). Cholinergic nerve terminals establish classical synapses in the rat cerebral cortex: synaptic pattern and age-related atrophy. *Neuroscience* 105, 277–285. doi: 10.1016/s0306-4522(01)00172-5
- Umbriaco, D., Watkins, K. C., Descarries, L., Cozzari, C., and Hartman, B. K. (1994). Ultrastructural and morphometric features of the acetylcholine innervation in adult rat parietal cortex: an electron microscopic study in serial sections. *J. Comp. Neurol.* 348, 351–373. doi: 10.1002/cne.903480304
- Unal, C. T., Golowasch, J. P., and Zaborszky, L. (2012). Adult mouse basal forebrain harbors two distinct cholinergic populations defined by their electrophysiology. *Front. Behav. Neurosci.* 6:21. doi: 10.3389/fnbeh.2012.00021
- Urban-Ciecko, J., Jouhanneau, J.-S., Myal, S. E., Poulet, J. F. A., and Barth, A. L. (2018). Precisely timed nicotinic activation drives SST inhibition in neocortical circuits. *Neuron* 97, 611–625.e5. doi: 10.1016/j.neuron.2018.01.037
- Van der Zee, E. A., and Luiten, P. G. (1999). Muscarinic acetylcholine receptors in the hippocampus, neocortex and amygdala: a review of immunocytochemical localization in relation to learning and memory. *Prog. Neurobiol.* 58, 409–471. doi: 10.1016/s0301-0082(98)00092-6
- van der Zee, E. A., Streefland, C., Strosberg, A. D., Schröder, H., and Luiten, P. G. (1992). Visualization of cholinergic neurons in the rat neocortex: colocalization of muscarinic and nicotinic acetylcholine receptors. *Mol. Brain Res.* 14, 326–336. doi: 10.1016/0169-328x(92)90100-p
- Venter, J. C., di Porzio, U., Robinson, D. A., Shreeve, S. M., Lai, J., Kerlavage, A. R., et al. (1988). Evolution of neurotransmitter receptor systems. *Prog. Neurobiol.* 30, 105–169. doi: 10.1016/0301-0082(88)90004-4
- Vidal, C., and Changeux, J.-P. (1993). Nicotinic and muscarinic modulations of excitatory synaptic transmission in the rat prefrontal cortex in vitro. *Neuroscience* 56, 23–32. doi: 10.1016/0306-4522(93)90558-w
- von Engelhardt, J., Eliava, M., Meyer, A. H., Rozov, A., and Monyer, H. (2007). Functional characterization of intrinsic cholinergic interneurons in the cortex. *J. Neurosci.* 27, 5633–5642. doi: 10.1523/JNEUROSCI.4647-06.2007
- Wang, Z., Kai, L., Day, M., Ronesi, J., Yin, H. H., Ding, J., et al. (2006). Dopaminergic control of corticostriatal long-term synaptic depression in medium spiny neurons is mediated by cholinergic interneurons. *Neuron* 50, 443–452. doi: 10.1016/j.neuron.2006.04.010
- Wevers, A. (2011). Localisation of pre- and postsynaptic cholinergic markers in the human brain. *Behav. Brain Res.* 221, 341–355. doi: 10.1016/j.bbr.2010.02.025
- Xu, M., Chung, S., Zhang, S., Zhong, P., Ma, C., Chang, W.-C., et al. (2015). Basal forebrain circuit for sleep-wake control. *Nat. Neurosci.* 18, 1641–1647. doi: 10.1038/nn.4143
- Yamamoto, K., Koyanagi, Y., Koshikawa, N., and Kobayashi, M. (2010). Postsynaptic cell type-dependent cholinergic regulation of GABAergic synaptic transmission in rat insular cortex. *J. Neurophysiol.* 104, 1933–1945. doi: 10.1152/jn.00438.2010
- Yamasaki, M., Matsui, M., and Watanabe, M. (2010). Preferential localization of muscarinic M1 receptor on dendritic shaft and spine of cortical pyramidal cells and its anatomical evidence for volume transmission. *J. Neurosci.* 30, 4408–4418. doi: 10.1523/JNEUROSCI.5719-09.2010
- Zaborszky, L., and Duque, A. (2000). Local synaptic connections of basal forebrain neurons. *Behav. Brain Res.* 115, 143–158. doi: 10.1016/s0166-4328(00)00255-2
- Zaborszky, L., Duque, A., Gielow, M., Gombkoto, P., Nadasy, Z., and Somogyi, J. (2015). “Organization of the basal forebrain cholinergic projection system,” in *The Rat Nervous System*, ed. G. Paxinos (Amsterdam: Elsevier Inc.), 491–507.
- Zeisel, A., Hochgerner, H., Lönnerberg, P., Johnsson, A., Memic, F., van der Zwan, J., et al. (2018). Molecular architecture of the mouse nervous system. *Cell* 174, 999–1014.e22. doi: 10.1016/j.cell.2018.06.021
- Zhang, Z., and Séguéla, P. (2010). Metabotropic induction of persistent activity in layers II/III of anterior cingulate cortex. *Cereb. Cortex* 20, 2948–2957. doi: 10.1093/cercor/bhq043
- Zoli, M., Moretti, M., Zanardi, A., McIntosh, J. M., Clementi, F., and Gotti, C. (2002). Identification of the nicotinic receptor subtypes expressed on dopaminergic terminals in the rat striatum. *J. Neurosci.* 22, 8785–8789. doi: 10.1523/jneurosci.22-20-08785.2002
- Zoli, M., Pistillo, F., and Gotti, C. (2015). Diversity of native nicotinic receptor subtypes in mammalian brain. *Neuropharmacology* 96, 302–311. doi: 10.1016/j.neuropharm.2014.11.003
- Zuccolo, E., Lim, D., Kheder, D. A., Perna, A., Catarsi, P., Botta, L., et al. (2017). Acetylcholine induces intracellular Ca^{2+} oscillations and nitric oxide release in mouse brain endothelial cells. *Cell Calcium* 66, 33–47. doi: 10.1016/j.ceca.2017.06.003

Conflict of Interest Statement: The authors declare that the research was conducted in the absence of any commercial or financial relationships that could be construed as a potential conflict of interest.

Copyright © 2019 Colangelo, Shichkova, Keller, Markram and Ramaswamy. This is an open-access article distributed under the terms of the Creative Commons Attribution License (CC BY). The use, distribution or reproduction in other forums is permitted, provided the original author(s) and the copyright owner(s) are credited and that the original publication in this journal is cited, in accordance with accepted academic practice. No use, distribution or reproduction is permitted which does not comply with these terms.



A Novel Type of Neuron Within the Dorsal Striatum

Miaomiao Mao^{1,2†}, Aditya Nair^{1,2,3,4} and George J. Augustine^{1,2*}

¹Lee Kong Chian School of Medicine, Nanyang Technological University, Singapore, Singapore, ²Institute of Molecular and Cell Biology, Singapore, Singapore, ³Life Sciences Programme, Faculty of Science, National University of Singapore, Singapore, Singapore, ⁴Singapore Bioimaging Consortium, Agency of Science, Technology and Research, Singapore, Singapore

OPEN ACCESS

Edited by:

Deborah Baro,
Georgia State University,
United States

Reviewed by:

Matthew S. Grubb,
King's College London,
United Kingdom
Helen S. Bateup,
Harvard Medical School,
United States
Osvaldo Ibáñez-Sandoval,
Universidad Autónoma de San Luis
Potosi, Mexico

*Correspondence:

George J. Augustine
George.Augustine@ntu.edu.sg

†Present address:

Miaomiao Mao,
The Florey Institute of Neuroscience
and Mental Health, Parkville, VIC,
Australia

Received: 11 October 2018

Accepted: 12 April 2019

Published: 21 May 2019

Citation:

Mao M, Nair A and Augustine GJ
(2019) A Novel Type of Neuron Within
the Dorsal Striatum.
Front. Neural Circuits 13:32.
doi: 10.3389/fncir.2019.00032

The striatum is predominantly composed of medium spiny projection neurons, with the remaining neurons consisting of several types of interneurons. Among the interneurons are a group of cells that express tyrosine hydroxylase (TH). Although the intrinsic electrical properties of these TH-expressing interneurons have been characterized, there is no agreement on the number of TH-expressing cell types and their electrical properties. Here, we have used transgenic mice in which YFP-tagged channelrhodopsin-2 (ChR2) was expressed in potential TH-expressing cells in a Cre-dependent manner. We found that the YFP⁺ neurons in the striatum were heterogeneous in their intrinsic electrical properties; unbiased clustering indicated that there are three main neuronal subtypes. One population of neurons had aspiny dendrites with high-frequency action potential (AP) firing and plateau potentials, resembling the TH interneurons (THIN) described previously. A second, very small population of labeled neurons resembled medium-sized spiny neurons (MSN). The third population of neurons had dendrites with an intermediate density of spines, showed substantial AP adaptation and generated prolonged spikes. This type of striatal neuron has not been previously identified in the adult mouse and we have named it the Frequency-Adapting Neuron with Spines (FANS). Because of their distinctive properties, FANS may play a unique role in striatal information processing.

Keywords: interneurons, neuron diversity, dorsal striatum, tyrosine hydroxylase, intrinsic electrical properties, neuron classification

INTRODUCTION

The striatum is a major component of the basal ganglia circuit and is involved in a number of functions such as motor planning, motivation and reward perception. Medium-sized spiny neurons (MSN) are the most abundant cell type in the striatum and constitute about 95% of all striatal neurons in rodents (Graveland and DiFiglia, 1985; Kreitzer, 2009). MSN are GABAergic and are the only known projection neurons of the striatum. The remaining striatal neurons are made up of several kinds of interneurons that differ in their neurochemical and electrophysiological characteristics: (1) fast-spiking (FS) parvalbumin (PV)-expressing GABAergic interneurons; (2) low-threshold Ca²⁺ spiking (LTS) somatostatin (SOM)/neuropeptide Y (NPY)/nitric oxide synthase (NOS)-expressing GABAergic interneurons; and (3) spontaneously active cholinergic interneurons. In addition,

calretinin-expressing GABAergic interneurons have also been observed in immunohistochemical studies but their electrophysiological properties are unknown (Rymar et al., 2004; Tepper et al., 2010). More recently, the use of transgenic mice expressing neuron-specific markers has revealed still other types of striatal interneurons. These include a NPY-expressing interneuron that differs from the NPY-LTS cell (Ibáñez-Sandoval et al., 2011; Assous et al., 2017), as well as a heterogeneous population of interneurons that express 5HT3a receptors (Faust et al., 2015, 2016; Muñoz-Manchado et al., 2016).

An additional population of tyrosine hydroxylase (TH)-immunoreactive (TH⁺) interneurons has been found in the striatum of several species, including primates (Dubach et al., 1987), rat (Tashiro et al., 1989), mouse (Mao et al., 2001) and human (Ikemoto et al., 1997; Cossette et al., 2005). These neurons are up-regulated after denervation of dopaminergic input from the midbrain (Nakahara et al., 2001; Tandé et al., 2006; Darmopil et al., 2008) and their morphology, electrophysiological properties and distribution have been characterized (Ibáñez-Sandoval et al., 2010; Masuda et al., 2011; Ünal et al., 2011). These characterizations have yielded somewhat inconsistent conclusions; specifically, it is currently unclear whether there are two (Masuda et al., 2011) or four (Ibáñez-Sandoval et al., 2010) subtypes of TH-expressing neurons.

Here, we have extended the genetic approach to characterize striatal neurons in transgenic mice in which YFP-tagged Channelrhodopsin-2 (ChR2) expression was driven by Cre expression in a TH-Cre mouse line. We found that YFP⁺ striatal neurons were quite heterogeneous in their intrinsic electrical properties and could be sorted, by an unsupervised clustering method, into three main groups. More than 20% of the neurons resembled the TH-expressing interneurons (THIN) described previously (Ibáñez-Sandoval et al., 2010), while a small fraction of neurons closely resembled typical MSN. A third group of cells had unique electrophysiological properties that did not resemble those of THIN, MSN, or any other striatal cell that has previously been described. These cells showed substantial action potential (AP) adaptation, generated prolonged spikes in response to depolarizing currents and possessed dendrites with an intermediate density of spines. We have named these novel neurons Frequency-Adapting Neurons with Spines (FANS) and here we compare the properties of FANS to those of the other YFP⁺ cells within the dorsal striatum in our transgenic mice.

MATERIALS AND METHODS

Animals

Transgenic mice expressing ChR2 fused to YFP in TH-Cre expressing neurons were generated by mating a line of TH-Cre transgenic mice (Lindeberg et al., 2004) with another line (Ai32) expressing YFP-tagged ChR2 behind a floxed stop cassette (Madisen et al., 2012). Both mouse lines were obtained from Jackson Labs. All mice used in the experiments were of either sex and age 6–14 weeks; all animal procedures were approved by the Institutional Animal Care and Use Committee of Biopolis.

Preparation of Brain Slices

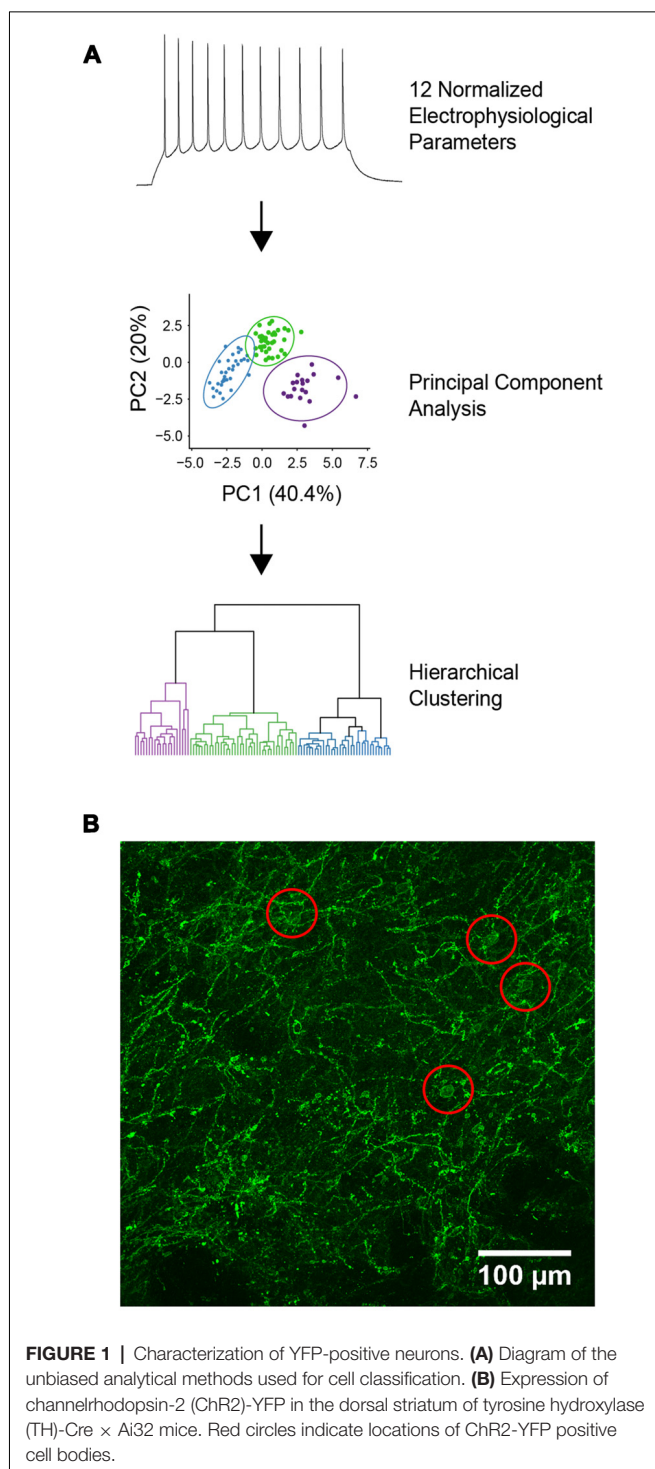
Mice were anesthetized with isoflurane and euthanized *via* decapitation. Brains were removed quickly and placed in carbogen-saturated ice-cold cutting solution containing the following (in mM): 250 sucrose, 26 NaHCO₃, 10 glucose, 2.5 KCl, 1.25 NaH₂PO₄·H₂O, 3 myoinositol, 2 sodium pyruvate, 4 MgCl₂, 0.1 CaCl₂, 0.5 ascorbic acid and 1 kynurenic acid. 300 μm thick parasagittal slices containing the dorsal striatum were cut with a vibratome and then transferred to a recovery chamber containing carbogen-saturated artificial cerebrospinal fluid (ACSF) of the following composition (in mM): 126 NaCl, 24 NaHCO₃, 10 glucose, 2.5 KCl, 1 NaH₂PO₄·H₂O, 2 MgCl₂, 2 CaCl₂, 0.4 ascorbic acid. The brain slices were incubated at 34°C for 1 h before being returned to room temperature for recording in ACSF.

Electrophysiology

ChR2-YFP expressing cells in the dorsal striatum were visualized using a 25× objective (NA = 1.05) on an Olympus FV-1000 two-photon microscope. Neurons expressing ChR2-YFP were activated by blue light (BP470-495 excitation filter, Olympus) from a Mercury arc lamp. The duration of the light flashes was controlled by an electronic shutter (Uniblitz Model T132, Vincent Associates). Whole-cell patch clamp recordings were made using a MultiClamp 700B amplifier (Molecular Devices) and were performed under visual guidance. Recording pipettes (6–8 MΩ resistance) were filled with an internal solution containing (in mM, unless otherwise stated): 130 potassium gluconate, 10 KOH, 2.5 MgCl₂, 10 HEPES, 4 Na₂ATP, 0.4 Na₃GTP, 5 EGTA, 5 disodium phosphocreatine, 0.025 Alexa fluor 594 (Invitrogen) and 0.2% (w/v) neurobiotin (Vector Labs). All reagents were obtained from Sigma-Aldrich unless otherwise indicated. Series resistance and whole-cell compensation were performed immediately after establishing the whole-cell recording configuration, while bridge balance was performed in current-clamp mode. Recordings with series resistance greater than 25 MΩ, resting membrane potential (RMP) more depolarized than −50 mV or fluctuations greater than 10% were excluded from analysis. Electrophysiological data were acquired with a Digidata 1330a interface and pClamp 10.4 software (both from Molecular Devices); data were analyzed using Clampfit 10.4 (Molecular Devices), OriginPro (OriginLab) and/or GraphPad Prism 7 (GraphPad). Numerical values presented here indicate mean ± SEM. Liquid-liquid junction potentials were estimated from the compositions of ionic species in the external and internal solutions, using the junction potential calculator in pClamp; membrane potentials stated in this paper include this correction.

Electrophysiological Classification of Neuron Types

To identify functionally related YFP⁺ neurons, intrinsic electrical properties were recorded from each cell and unsupervised hierarchical clustering was used to cluster these data (Figure 1A). A total of 12 electrical properties (Table 1) were determined from responses to a series of 1 s long current steps, ranging from −200 pA to 200 pA. Input resistance was calculated



after constructing a current-voltage relationship from responses to hyperpolarizing current pulses. These responses were also used to determine other passive properties, such as membrane time constant, voltage sag during hyperpolarization, and input conductance. Responses to depolarizing current pulses were used to determine active properties, such as threshold current for evoking an AP, AP amplitude, after-hyperpolarization (AHP)

TABLE 1 | Electrophysiological properties used for unbiased classification of YFP-positive neurons.

Property	Description
C_m (pF)	Membrane capacitance measured after whole-cell configuration was achieved.
R_{in} ($M\Omega$)	Slope of linear fit between current-voltage response curve.
RMP (mV)	Y-intercept of linear fit between current-voltage response curve.
Sag amplitude (mV)	Difference between most hyperpolarized voltage and steady-state voltage, measured in response to hyperpolarizations to approximately -100 mV.
AHP (mV)	Difference in voltage from AP threshold to maximum negative deflection during repolarization.
AP amplitude (mV)	Difference between AP threshold and peak amplitude of 1st AP.
AP frequency adaptation	Ratio between instantaneous frequencies of the first two APs and last three APs.
AP amplitude adaptation	Ratio between amplitudes of first and last AP during AP train.
AP Half-width (ms)	Time difference between rising phase and decaying phase of AP at half-maximum amplitude.
Decay rate of AP (mV/ms)	Maximum rate of rise of membrane voltage during AP rising phase.
Rise rate of AP (mV/ms)	Maximum rate of rise of membrane voltage during AP falling phase.
Current threshold (pA)	Smallest current that evoked at least one AP.

amplitude, duration (half-width), and maximum rise and fall rates of APs. AP adaptation properties were measured from responses to the smallest current step that elicited at least 10 AP. These properties were extracted from raw data using custom scripts written in Matlab (Mathworks).

From the 12 intrinsic properties, data dimensionality was reduced using principal component (PC) analysis. PCs were calculated using singular value decomposition, performed using the *pcaMethods* package in the R programming language (Stacklies et al., 2007; R Core Team, 2013). The first three PCs, which accounted for 69.2% of the total variance in the data, were used for unsupervised agglomerative hierarchical clustering using Euclidean distance as a measure of linkage distance. Ward's (1963) minimum variance was used to combine clusters, which reduced the total within-cluster variance. This was implemented using the online webtool Clustvis, which uses R packages such as *pheatmap*, *FactoMineR* and *ggplot2* internally to generate dendrograms of the hierarchically clustered data (Metsalu and Vilo, 2015). The optimal number of clusters was determined using silhouette analysis which measures the quality of clustering by calculating the separation between identified clusters (Rousseeuw, 1987). Silhouette analysis was performed using the cluster package in R with Euclidean distance used for calculating silhouette width (Maechler et al., 2018). To visualize the identified clusters, a dendrogram was constructed where the horizontal lines represent joined clusters. Radar plots were generated in R using the packages *ggplot2* and *radarchart* after normalizing population feature means to ranges of 0–1.

Immunohistochemistry and Imaging

Following electrical recordings, neurobiotin-filled cells were visualized by fixing brain slices in 4% paraformaldehyde overnight at 4°C followed by permeabilization in phosphate-buffered saline containing 0.25% Triton X-100 (PBST) for 1 h at room temperature. Slices were then incubated in streptavidin-Alexa 633 (1:1,000 diluted in PBST) for 48 h at 4°C before washing in PBST three times for 20 min each. Brain slices were mounted on glass slides and imaged using the same microscope system described above. A Z-stack of images was obtained for each labeled cell and cell morphology was digitally reconstructed as described below. Maximum projection images of such reconstructions are shown here unless otherwise stated.

To analyze and compare the morphology of neurobiotin-labeled neurons, cells were digitally reconstructed using AdReconstructor, a software suite for reconstruction of neuronal morphology (Nair et al., 2018). This program first applies pre-processing algorithms to remove common sources of noise, such as non-specific background staining and neurobiotin leakage. Cells were then reconstructed using the All Path Pruning algorithms developed by Xiao and Peng (2013) and post-processing measures were applied to ensure accuracy of reconstructions. The automated traces obtained in the open source SWC format were then quantified using L-Measure to obtain parameters such as surface area against path distance and spine density (Scorcioni et al., 2008). Sholl analysis was performed to analyze dendritic branching using the Simple Neurite Tracer plugin in ImageJ (Ferreira, 2016).

ChR2-YFP expressing cells in the dorsal striatum were also visualized by immunolabeling, using an anti-YFP/GFP antibody. The dendrites of YFP⁺ cells were dispersed throughout the dorsal striatum and the somata of these cells seemed to be evenly dispersed throughout the striatum (**Figure 1B**). Brain slices were fixed in 4% paraformaldehyde overnight at 4°C followed by permeabilization and blocking of the endogenous epitopes by applying 10% normal goat serum in PBST for 1 h at room temperature. Chicken anti-GFP antibody (Abcam) was applied at 1:1,000 in PBST for 48 h at 4°C and then washed three times in PBST for 20 min each. Goat anti-chicken Alexa 488 secondary antibody was applied at 1:500 in PBST for 2 h at room temperature followed by washing three times in PBST for 20 min each. All antibodies were obtained from Life Technologies unless otherwise stated. All image processing and analyses were carried out using FIJI, except those used for morphological reconstruction as described above.

Morphological Classification of Neuron Types

To determine the relationship between electrophysiologically-defined cell types and their morphological properties, we also performed unsupervised hierarchical clustering of morphological features extracted from digital reconstructions of 15 neurobiotin-labeled neurons. The morphological properties

extracted were based on definitions used in Scorcioni et al. (2008) and Gouwens et al. (2018), and are described in detail in **Table 2**. A total of 23 properties were extracted from digital reconstructions saved in the open source SWC format using the “compute global feature” plugin in Vaa3D (Peng et al., 2014). Dimensionality reduction was then performed using PC analysis, calculated using singular value decomposition and implemented using `pcaMethods` in R (Stacklies et al., 2007). Agglomerative hierarchical clustering was then performed on the first three PCs which account for 69.7% of the total variance in the dataset using the online tool Clustvis with correlation as a distance measure and Ward’s distances as a clustering method (Metsalu and Vilo, 2015). To identify the optimal number of clusters, silhouette analysis was again used—using Euclidean distance to calculate silhouette width—and implemented using the `cluster` package in R (Maechler et al., 2018). Radar plots were created in R using the packages `ggplot2` and `radarchart` after normalizing population means to a range of 0–1.

RESULTS

Three Types of YFP⁺ Striatal Neurons

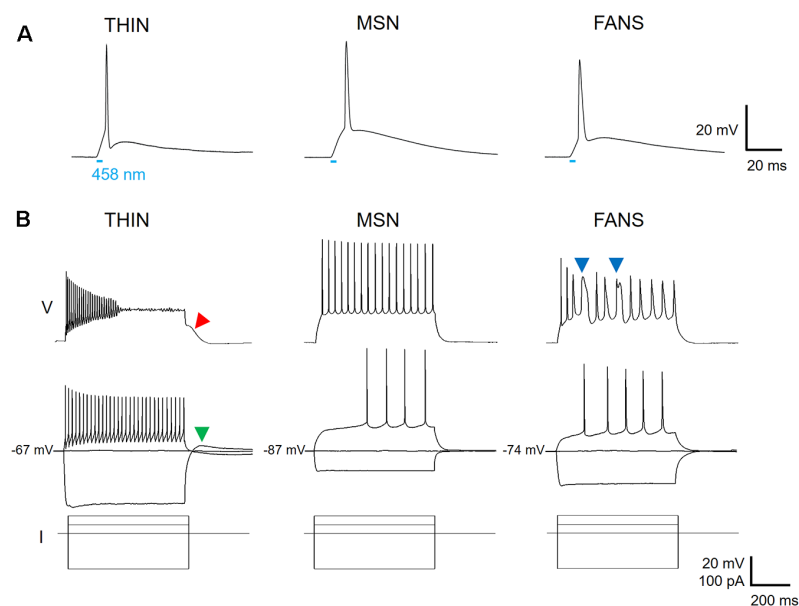
In an attempt to identify TH-expressing neurons in the striatum, we used double-transgenic mice with ChR2 expression driven by the TH promoter. Positive striatal cells could be identified, in live brain slices prepared from these mice, by the fluorescence of YFP fused to the ChR2. Expression of ChR2 was confirmed by the APs that were evoked when brief (5 ms duration) laser light flashes (458 nm; 0.006–0.018 mW) were used to activate the ChR2 (**Figure 2A**). Due to the possibility of ectopic expression of ChR2-YFP in neurons that do not express TH in adulthood (Lammel et al., 2015; Stuber et al., 2015), we do not assume that neurons expressing ChR2-YFP actually express TH and instead will conservatively refer to these cells as YFP⁺ neurons.

Applying depolarizing and hyperpolarizing current pulses to such YFP⁺ cells revealed a diversity of cellular responses (**Figure 2B**). Unsupervised hierarchical clustering of these cell responses, based on the 12 intrinsic electrical properties listed in **Table 1**, revealed that there were three different populations of YFP⁺ cells (**Figure 3A**). Comparing AP half-width, AP amplitude adaptation during prolonged depolarizations, and cell input resistance also showed a clear separation into the same three cell types identified by the clustering approach (**Figure 3B**). Indeed, all 12 intrinsic electrical properties considered differed significantly between the three different types of neurons (**Figure 3C**).

One type of cell resembled the THIN described previously (Ibáñez-Sandoval et al., 2010); these cells exhibited high input resistance and prominent voltage sag during responses to hyperpolarizing currents (**Figure 2B**, left and **Figure 3C**). THIN often exhibited a rebound depolarization following a hyperpolarizing current pulse (**Figure 2B**, green arrowhead), which sometimes evoked rebound APs. Large depolarizing

TABLE 2 | Morphological properties used for unbiased classification of YFP-positive neurons.

Property	Description
Number of nodes	The total number of nodes in the given digital reconstruction. A node in a reconstruction represents a single sample point of the neuron defined by its X, Y and Z coordinates, a radius, and its connectivity to other nodes in the neuron.
Soma surface area (μm^2)	The surface of the spherical node representing the soma in the digital reconstruction.
Number of stems	The number of nodes attached to the soma.
Number of bifurcations	The number of points which have two daughter nodes for the given reconstruction.
Number of branches	The number of compartments that lie between two branching points or between one branching point and a termination point in the given reconstruction.
Number of tips	The number of terminal tips for the given input neuron.
Neuronal height (μm)	Height is the difference of minimum and maximum y-values after eliminating the outer points on either end by using the 95% approximation of the y-values of the given reconstruction.
Neuronal width (μm)	Width is the difference of minimum and maximum x-values after eliminating the outer points on either end by using the 95% approximation of the x-values of the given reconstruction.
Neuronal depth (μm)	Depth is the difference of minimum and maximum z-values after eliminating the outer points on either end by using the 95% approximation of the z-values of the given reconstruction.
Average diameter (thickness; μm)	The average diameter of all compartments of the neuron.
Total length (μm)	The total length of the neuron is computed as the sum of distances between two connected nodes for all branches.
Total volume (μm^3)	The total volume of the entire neuron.
Maximum Euclidean distance to root (μm)	The maximum Euclidean distance of all nodes. Euclidean distance is the straight line distance from the soma to the node.
Maximum path distance to root (μm)	The maximum path distance of all nodes. The path distance is the sum of lengths of all connected nodes from the soma, ending with that node.
Maximum branch order	The maximum order of the branch. A branch's order is defined with respect to the soma where the soma has a branch order = 0 and ever bifurcation has an increasing branch order.
Average contraction	The average ratio between Euclidean distance of a branch and its path length.
Average fragmentation	The average number of compartments that constitute a branch between two bifurcation points or between a bifurcation point and a terminal tip.
Average parent-daughter ratio	The average ratio between the diameter of a daughter branch and its parent branch
Average local amplitude angle (degrees)	The average angle between the first two compartments at a bifurcation
Average remote amplitude Angle (degrees)	The average angle between two bifurcation points or between bifurcation point and terminal point or between two terminal points.
Intersection at 30 μm	The number of Sholl plot intersections at a distance of 30 μm from the soma.
Intersection at 50 μm	The number of Sholl plot intersections at a distance of 50 μm from the soma.
Spine density (μm^{-1})	Total number of spines in all branches of a given neuron

**FIGURE 2 |** Three types of ChR2-YFP expressing cell in the dorsal striatum. **(A)** Action potentials could be evoked in response to a 5 ms laser light flash (458 nm, at bar), confirming expression of ChR2 in the three cell types. **(B)** Voltage responses to hyperpolarizing and depolarizing current pulses reveal different firing patterns for the three cell types (top two rows, current pulses shown at bottom).

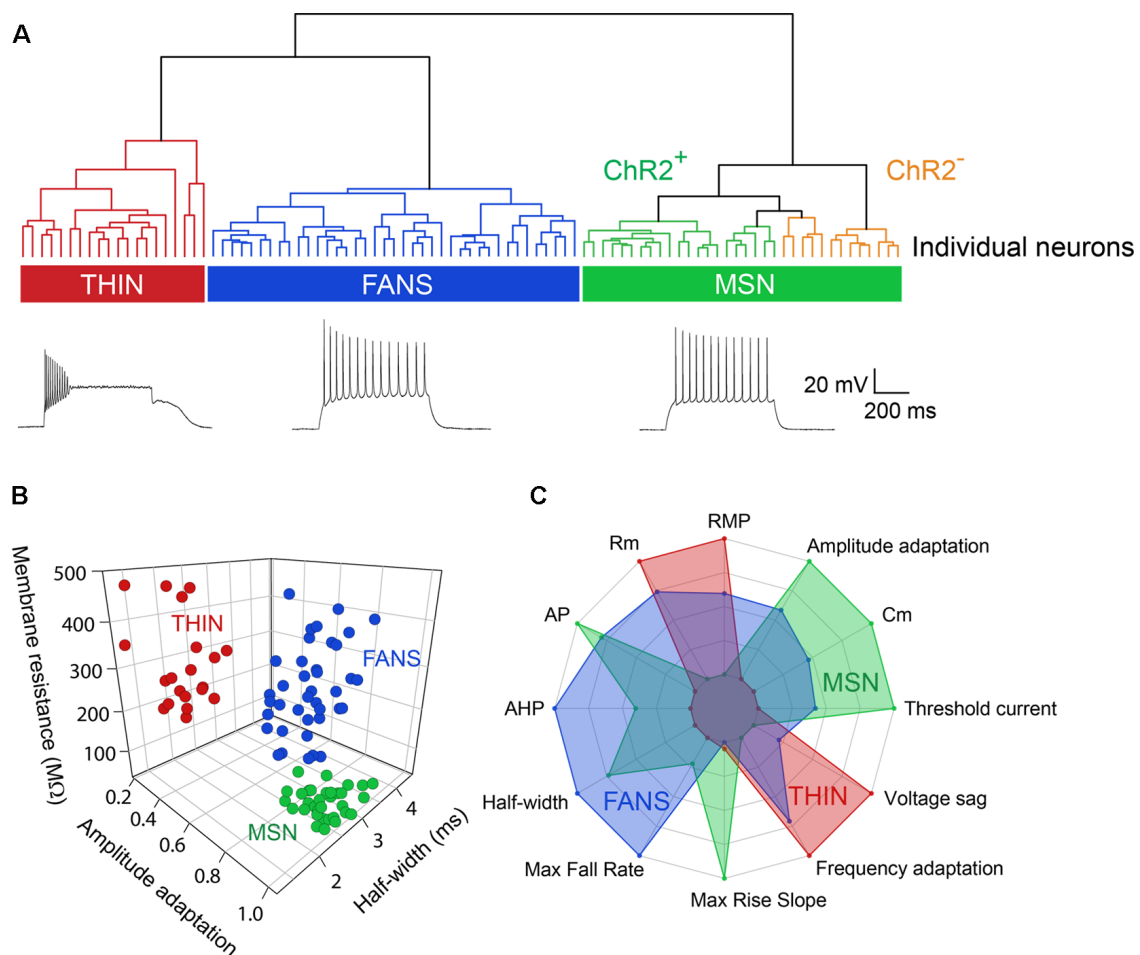


FIGURE 3 | Unbiased hierarchical analysis revealed significant differences between the three types of YFP⁺ neurons. **(A)** A dendrogram showing the unbiased classification of the three types of YFP⁺ neurons (top) and spiking pattern of a representative cell from each type (bottom). **(B)** 3D scatter plots showing the clustering of the three YFP⁺ cell types. **(C)** Radar plots revealing substantial differences between the three cell types, with indicated properties displayed using normalized population means in the range of 0–1.

current pulses often evoked damped voltage oscillations during such depolarizations, as well as a plateau potential following the end of depolarization (**Figure 2B**, red arrow). Four subtypes of THIN, with subtle differences in their electrophysiological properties, have been reported (Ibáñez-Sandoval et al., 2010), and these are evident in the subclusters of THIN shown in **Figure 3A**. To simplify our analyses, we have grouped together recordings made from all of these THIN subtypes.

Unexpectedly, a small proportion of the YFP⁺ cells unambiguously exhibited the intrinsic electrical properties of MSN, specifically low input resistance and delayed spiking with depolarization (**Figure 2B**, middle and **Figure 3C**). While these cells exhibited some small differences in population means when compared to ChR2[−] MSN, such as their higher RMP and input resistance, as well as smaller AP and AHP amplitudes (see **Figure 4**), overall in our analysis they clustered together with MSN that did not express ChR2 (**Figure 3A**). This indicates that the two populations of MSN are much

more similar to each other than they are to the other YFP⁺ cell types.

In addition, a third population of cells displayed properties distinct from those of any striatal cell described previously. These cells were characterized by intrinsic electrical properties that were intermediate between those of THIN and MSN (**Figures 3B,C**). Although their responses to small depolarizing currents were more similar to those of MSN than THIN (**Figure 2B**, right), they exhibited significantly more AP adaptation during prolonged depolarizations (see **Figures 6–8** below). Further, in response to large depolarizations, these cells exhibited APs that broadened substantially, often yielding plateau potentials (**Figure 2B**, blue arrows). As will be established in more detail below, these cells are unique in their properties, most notably their large range of AP frequency adaptation (see **Figure 6**) and the presence of spines on their dendrites (see **Figure 9**). We have therefore named these cells Frequency-Adapting Neurons with Spines (FANS).

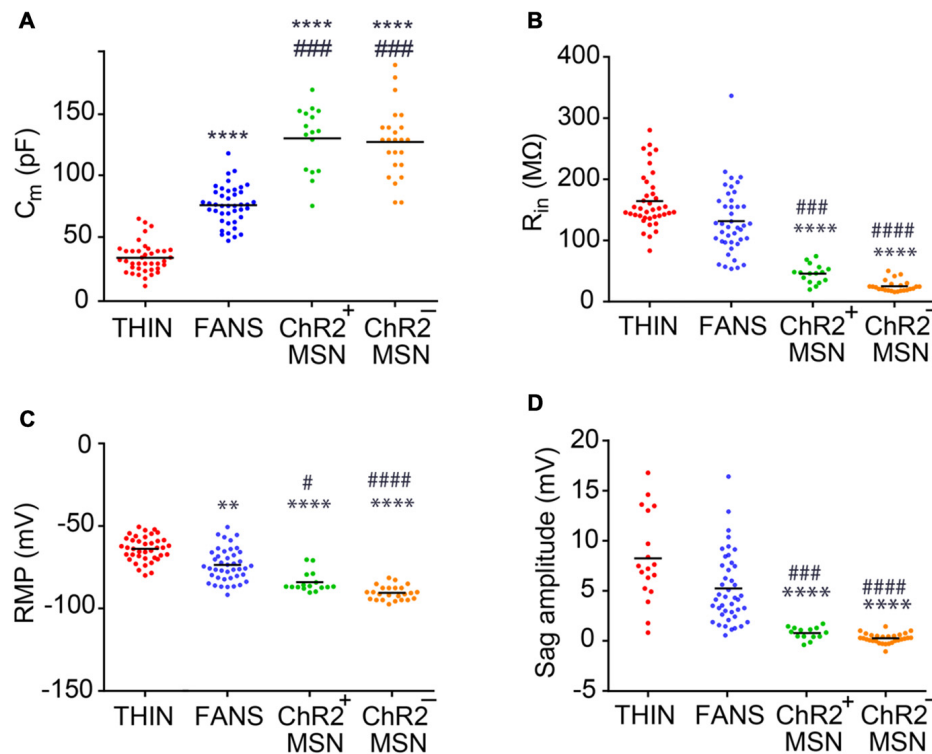


FIGURE 4 | Passive electrical properties of the YFP⁺ neurons in the dorsal striatum. **(A)** Membrane capacitance. **(B)** Input resistance. **(C)** Resting membrane potential (RMP). **(D)** Amplitude of voltage sag during responses to hyperpolarizing current. One-way ANOVA with Dunn's multiple comparison test; # $p < 0.05$, ** $p < 0.01$, *** $p < 0.001$, ****/#### $p < 0.0001$, where * and # indicate comparisons with THIN and FANS, respectively. Each horizontal line indicates mean value.

Intrinsic Electrical Properties of Three YFP⁺ Cell Types

We characterized the three types of YFP⁺ neurons more extensively by comparing their passive electrical properties (Figure 4). We first measured the apparent membrane capacitance (C_m), which is proportional to cell surface area and, hence, the overall size of the cell. The C_m of the three YFP⁺ cell types were significantly different from each other (Figure 4A; one-way ANOVA, $p < 0.0001$; Dunn's multiple comparison test), with THIN being smallest, followed by FANS and MSN. The C_m of YFP⁺ MSN was very similar to that of YFP⁻ MSN. As expected, cell input resistance—which is inversely related to surface area—followed the reverse order, with THIN and FANS significantly different from MSN but not from each other (Figure 4B; $p < 0.0001$; one-way ANOVA with Dunn's multiple comparison test). Again, there were no significant differences between the input resistances of MSN that did or did not express ChR2-YFP.

Striatal MSN are characterized by hyperpolarized RMPs and this was evident both in MSN that did or did not express ChR2-YFP (Figure 4C). In contrast, THIN and FANS had RMPs that were significantly more depolarized than those of MSN ($p < 0.0001$; one-way ANOVA with Dunn's multiple comparison test). In addition, the amplitude of the depolarizing sag in membrane potential in response to hyperpolarizing current

pulses—when measured at similar membrane potentials to take into account differences in input resistance (see Figure 2A, left)—was largest in THIN (Ibáñez-Sandoval et al., 2010) while FANS had an intermediate degree of sag and MSN exhibited the smallest amount of sag (Figure 4D; $p < 0.0001$; one-way ANOVA with Tukey's multiple comparison test). In summary, the passive electrical characteristics (and amount of depolarizing sag) of THIN, FANS and MSN were distinctively different from each other.

We next compared the waveforms of APs evoked in the three types of YFP⁺ cells in response to depolarizing current pulses (Figure 5A). FANS had the broadest APs (Figure 5A, left), measured as their width at half-maximum amplitude, while THIN had the narrowest APs (Figure 5B; $p < 0.0001$; one-way ANOVA with Holm-Sidak's multiple comparison test). The reverse was true for the AHP that followed the APs (Figure 5A, right): AHP magnitudes were greatest for THIN while FANS and MSN were similar (Figure 5C; $p < 0.0001$; one-way ANOVA with Holm-Sidak's multiple comparison test). Peak AP amplitude, measured for the first AP evoked during a depolarizing current pulse, was largest for FANS and smallest for THIN (Figure 5A, left); the APs of MSN were similar in amplitude to those of FANS (Figure 5D; $p = 0.0002$; one-way ANOVA with Holm-Sidak's multiple comparison test).

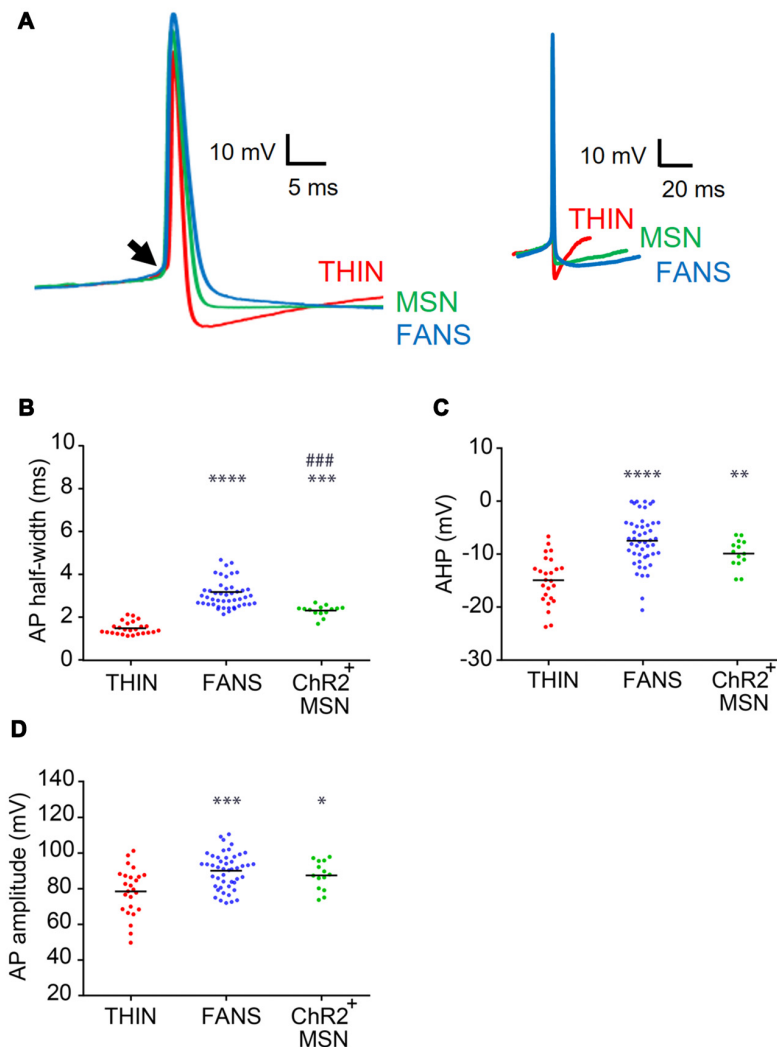


FIGURE 5 | AP characteristics of YFP⁺ neurons in the dorsal striatum. **(A)** Representative APs recorded from each cell type, shown at fast (left) and slow (right) time scales. Arrow indicates the point of inflection of APs, which was used as the reference point when measuring the amplitudes of APs and their after-hyperpolarizations (AHPs). **(B)** AP duration as measured at half-width. **(C)** AHP amplitude. **(D)** AP peak amplitude. One-way ANOVA with Holm-Sidak's multiple comparisons; * $p < 0.05$, ** $p < 0.01$, *** $p < 0.001$, **** $p < 0.0001$, where * and # indicate comparisons with THIN and FANS, respectively. Each horizontal line indicates mean value.

Action Potential Adaptation During Sustained Depolarization

During trains of APs, AP properties dynamically changed due to adaptation (**Figure 6A**). We quantitatively compared AP adaptation in response to sustained depolarizations (1 s duration) of all three types of YFP⁺ striatal cells. Because adaptation properties vary with the degree of depolarization, we measured adaptation in different cells at a standard criterion current level of 50 pA above the minimum current required to evoke a single AP.

Frequency Adaptation

The frequency of APs declined during sustained depolarizations (**Figure 6A**). Plots of normalized AP instantaneous frequency (IF), defined as the inverse of the interval between successive APs, illustrate the differences in the AP frequency adaptation

properties of these three cell types (**Figure 6B**). While both FANS and THIN showed substantial AP frequency adaptation, evident as a progressive decline in IF during a train of APs, MSN exhibited less frequency adaptation. The degree of decline during these trains was quantified by the ratio of IF of APs measured at the beginning and end of the depolarizing current pulse (**Figure 6C**). MSN showed significantly less AP frequency adaptation in comparison to THIN or FANS ($p < 0.0001$; one-way ANOVA with Dunn's multiple comparison test).

In most THIN and FANS, the time course of the decline in AP frequency during adaptation could be described by a double exponential function, with a fast initial phase followed by a second, more gradual component (**Figure 6D**). When a plateau potential occurred in FANS, AP frequency adaptation was interrupted and appeared to reset. For this reason, responses

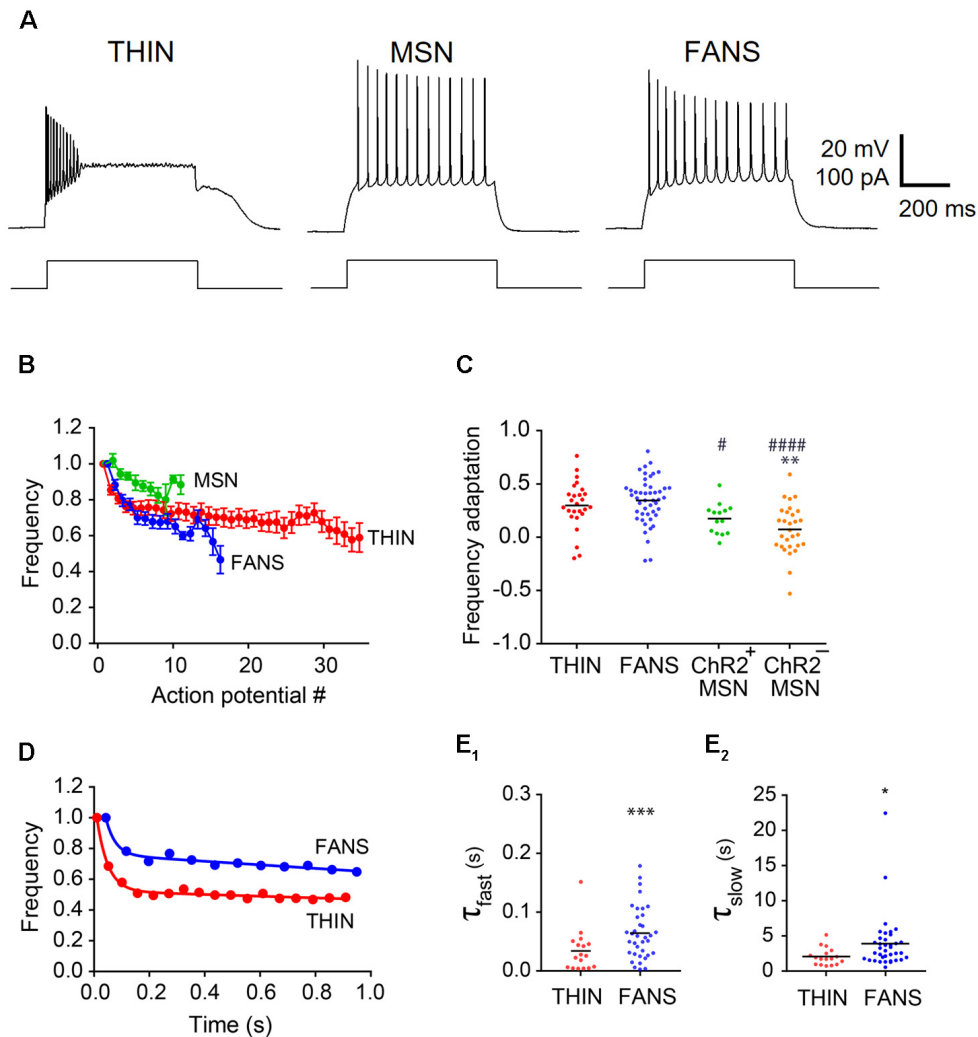


FIGURE 6 | Adaptation of AP frequency in YFP⁺ neurons. **(A)** Representative traces of APs evoked by 1 s current pulses. **(B)** Normalized mean instantaneous frequency (IF); error bars indicate SEM. **(C)** Frequency adaptation calculated as (1-last AP/first AP). One-way ANOVA with Dunn's multiple comparisons; $^{*}/\#p < 0.05$, $^{**}p < 0.01$ and $^{****}p < 0.0001$, where * and $^{\#}$ indicate comparisons with THIN and FANS, respectively. **(D)** Normalized IF vs. time plots fitted by two-component exponential curve from representative THIN and FANS neurons. **(E)** Exponential fit time constants (τ) of the fast (**E1**) and slow (**E2**) components of THIN and FANS calculated for IF (unpaired t -tests; $^{***}p < 0.001$; $^{****}p < 0.0001$). Each horizontal line indicates mean value.

that included plateau potentials were excluded from our analysis. MSN were also excluded, because they exhibited relatively little AP frequency adaptation. The mean time constants of both the fast and slow components for the remaining FANS were significantly larger than those of THIN, indicating slower frequency adaptation in FANS (Figures 6E1,E2; $p < 0.001$, unpaired t -test).

Amplitude Adaptation

In all three cell types, the peak amplitudes of APs also progressively decreased during prolonged depolarization (Figures 6A, 7A). The kinetics of this adaptation of AP amplitude is illustrated for all three cell types in Figure 7B. By calculating the ratio of the amplitudes of the last and first

APs, we could compare the amount of this adaptation of AP amplitude across the three cell types (Figure 7C). THIN exhibited the greatest amount of AP amplitude adaptation, while MSN had the least (Figure 7C; $p < 0.0001$; one-way ANOVA with Dunn's multiple comparison test). For all three cell types, AP amplitude adaptation followed a bi-exponential time course (Figure 7D). Calculation of the time constants for these exponential functions indicated that the initial rate of adaptation was similar in THIN and FANS, while MSN had significantly slower adaptation (Figure 7E1; $p < 0.0001$, one-way ANOVA with Tukey's multiple comparison test). The three cell types showed no significant differences in the kinetics of the slow phase of amplitude adaptation, although there was a tendency for THIN to have slightly faster adaptation than

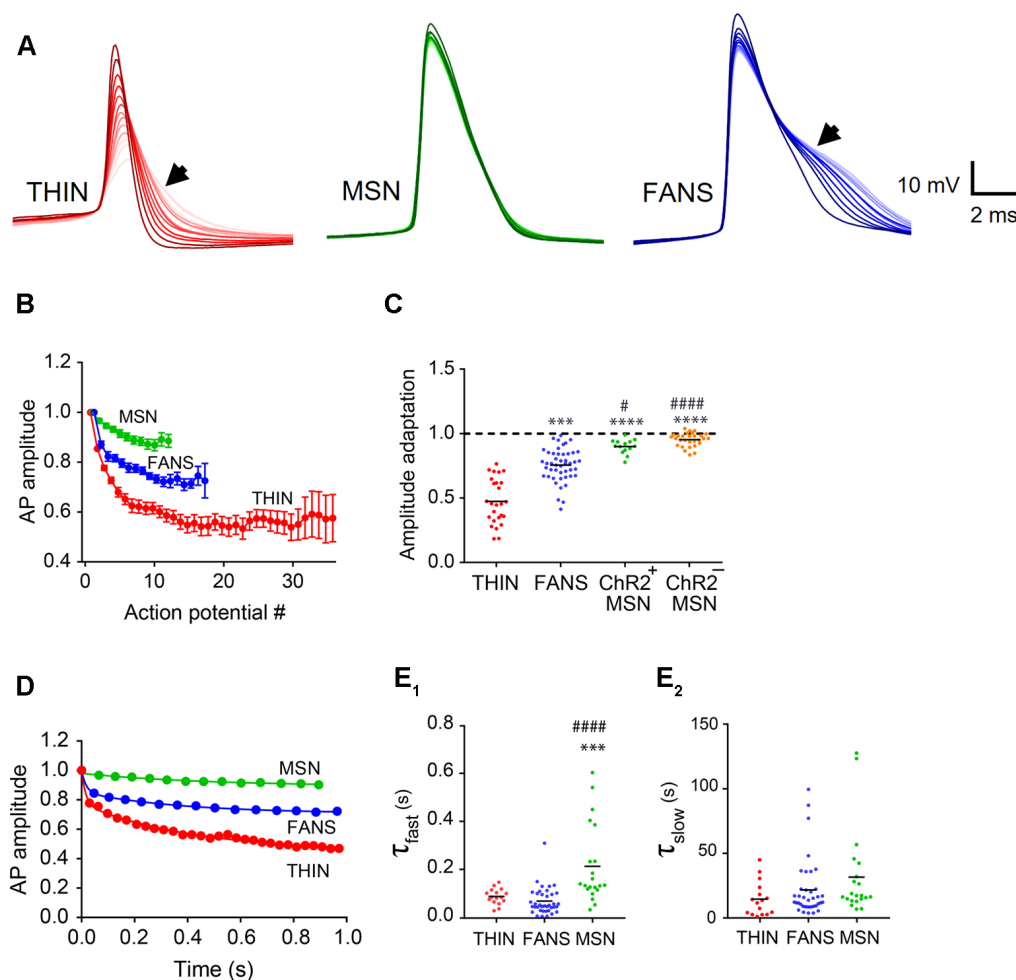


FIGURE 7 | AP amplitude adaptation in YFP⁺ neurons of the dorsal striatum. **(A)** Representative traces of APs. Dark to light colors indicate AP progression. Arrows indicate AP broadening evident in THIN and FANS. **(B)** Normalized mean AP peak amplitude, mean ± SEM. **(C)** AP amplitude change calculated as the ratio of last AP/first AP. One-way ANOVA with Dunn's multiple comparisons; # $p < 0.05$, *** $p < 0.001$ and ****/##### $p < 0.0001$, where * and # indicate comparisons with THIN and FANS, respectively. **(D)** Normalized amplitude vs. time plots fitted by two-phase exponential curve from representative cells. **(E)** Exponential fit time constants (τ) of the fast (**E₁**) and slow (**E₂**) components of THIN, FANS and ChR2⁺MSN calculated for AP amplitude (one-way ANOVA with Tukey's multiple comparisons; *** $p < 0.001$, ##### $p < 0.0001$). Each horizontal line indicates mean value.

FANS and for FANS to be slightly faster than MSN (Figure 7E2; $p = 0.1158$, one-way ANOVA).

AP Broadening

During prolonged depolarizations, AP duration also progressively broadened in both FANS and THIN (Figure 7A, black arrows). Two temporal patterns for AP broadening were observed for different THIN: accelerating (positive curvature; Figure 8A1) or decelerating (negative curvature; Figure 8A2) changes in the rate of adaptation, indicated by the slopes of the plots. FANS also tended to exhibit decelerating broadening of APs (Figure 8B). The degree of AP broadening measured at half-width was on average larger for THIN than for FANS (Figure 8C). In contrast, MSN exhibited little, if any, AP broadening ($p < 0.0001$; one-way ANOVA with Dunn's multiple comparison test). Due to the difference in the kinetics of AP

broadening in THIN, only THIN with negative curvature were compared with FANS. In these cells, the time course of AP broadening could be described by single exponential functions. The rate of adaptation of AP duration in THIN was slower than in FANS, as demonstrated by the larger time constants for AP broadening in THIN (Figure 8D; unpaired t -test, $p = 0.0009$).

In summary, FANS exhibit distinctive electrophysiological properties that are uniquely different from the properties of both THIN and MSN (Table 3). Therefore, FANS appear to be a novel, previously unrecognized cell type within the striatum.

Unique Morphology of FANS

To examine their morphology, YFP⁺ neurons also were filled with neurobiotin during whole-cell patch clamp recordings (Figure 9, left). Neurobiotin-filled neurons were then fixed,

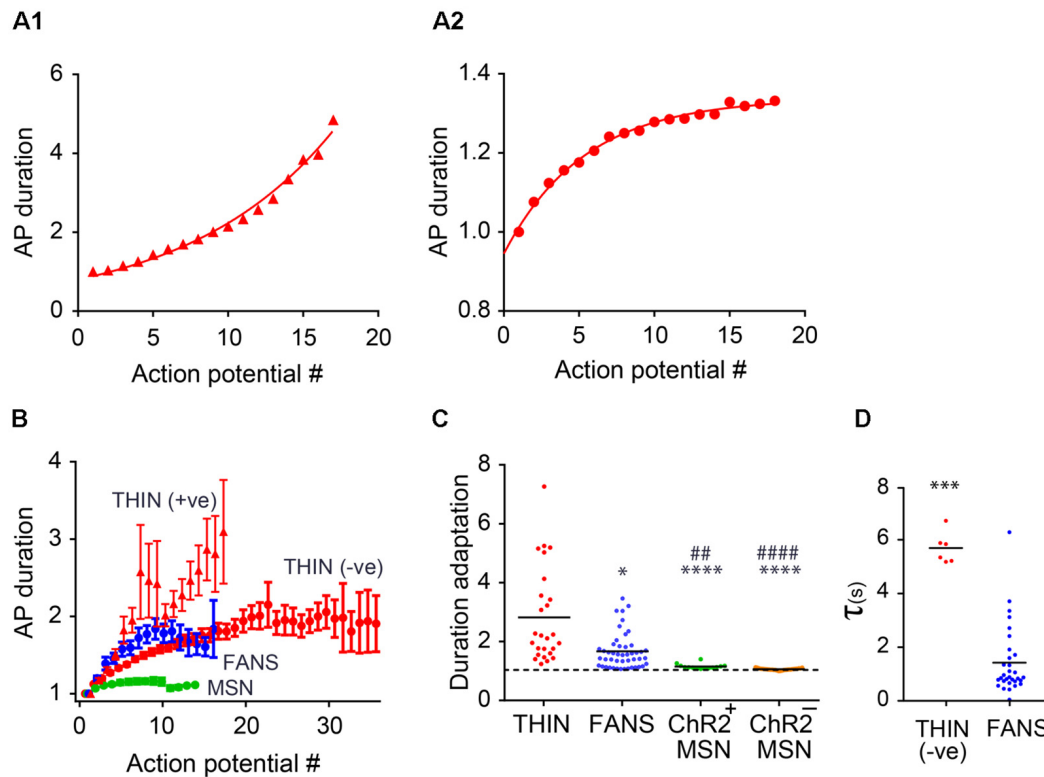


FIGURE 8 | AP duration adaptation in YFP⁺ neurons in the dorsal striatum. **(A)** Changes in AP duration (measured at half-width) from a representative THIN showing positive **(A1)** and negative **(A2)** curvatures. **(B)** Normalized mean AP duration, mean \pm SEM. **(C)** AP duration adaptation calculated as the ratio of last AP/first AP. One-way ANOVA with Dunn's multiple comparisons; * $p < 0.05$, ** $p < 0.01$ and ****/##### $p < 0.0001$, where * and # indicate comparisons with THIN and FANS, respectively. **(D)** Time constants (τ) of AP broadening for THIN and FANS (unpaired t -test; *** $p = 0.0009$). Each horizontal line indicates mean value.

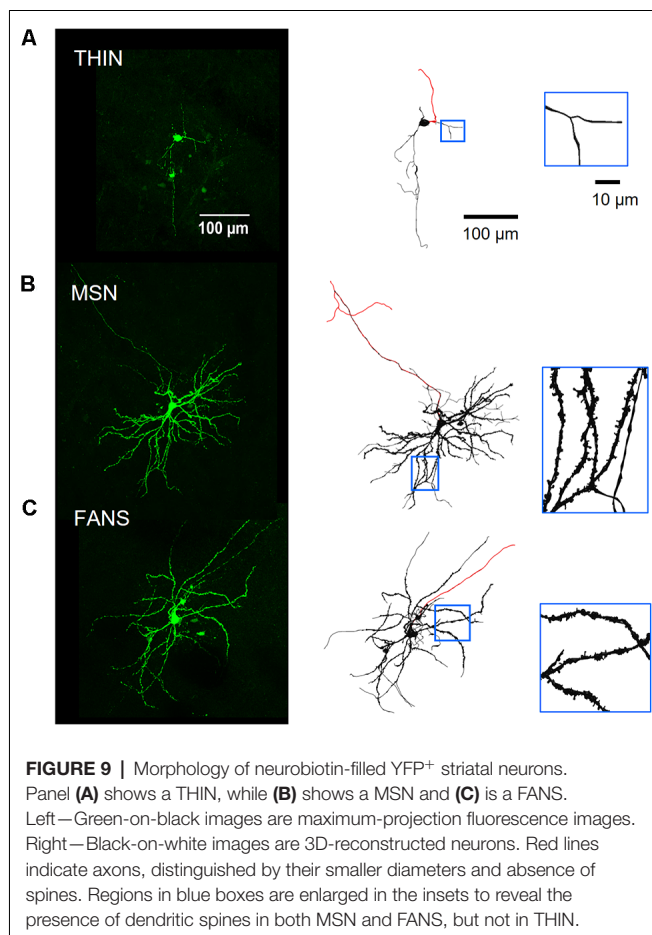
TABLE 3 | Electrical and morphological properties of TH interneuron (THIN), frequency-adapting neurons with spines (FANS) and medium-sized spiny neuron (MSN).

Property	THIN	FANS	MSN (ChR2 ⁺)	MSN (ChR2 ⁻)
C_m (pF)	34.7 ± 2.0	76.6 ± 2.4	131 ± 6.5	128 ± 5.7
R_{in} (M Ω)	328 ± 14.5	262 ± 17.0	90.8 ± 7.6	49.6 ± 3.8
RMP (mV)	-63.9 ± 1.2	-73.6 ± 1.5	-84.1 ± 1.5	-90.6 ± 0.9
Sag amplitude (mV)	4.4 ± 0.8	1.5 ± 0.2	0.5 ± 0.1	0.4 ± 0.1
AP duration (ms)	1.47 ± 0.06	3.20 ± 0.14	2.34 ± 0.07	
AHP (mV)	-14.9 ± 0.9	-7.4 ± 0.7	-10.0 ± 0.7	
AP amplitude (mV)	78.7 ± 2.6	90.2 ± 1.5	87.6 ± 2.1	
AP frequency adaptation	0.30 ± 0.04	0.34 ± 0.03	0.18 ± 0.04	0.08 ± 0.04
AP duration adaptation	2.82 ± 0.31	1.68 ± 0.09	1.14 ± 0.02	1.01 ± 0.01
AP amplitude adaptation	0.47 ± 0.03	0.76 ± 0.02	0.90 ± 0.01	0.95 ± 0.01
Soma diameter (μ m)	13.7 ± 0.5	15.5 ± 0.8	13.8 ± 1.0	
No. primary dendrites	3.3 ± 0.3	3.9 ± 0.3	5.5 ± 0.2	
Spine density (μ m ⁻¹)	0	0.52 ± 0.04	0.57 ± 0.06	

Values indicate mean \pm SEM.

processed and imaged on a two-photon microscope. Stacks of cell images obtained at different z-axis planes were then digitally reconstructed in an automated fashion to obtain bias-free representations of neuronal morphology (Figure 9, right; see “Materials and Methods” section). THIN had somata that were medium-sized ($13.7 \pm 0.5 \mu$ m, long axis diameter) and oval or round in shape (Figure 9A). The primary and secondary dendrites of THIN appeared to branch sparsely

and were often varicose; most notably, their dendrites lacked spines (Figure 9A, inset). These morphological features are very similar to those previously reported for THIN (Ibáñez-Sandoval et al., 2010). The morphology of YFP⁺ MSN also resembled typical MSN (Gertler et al., 2008; Kreitzer, 2009): they had medium-sized somata ($13.8 \pm 1.0 \mu$ m, long axis diameter) and dendrites that branched extensively and were densely covered with spines (Figure 9B). Occasionally the main



axon of these cells could be observed for a sufficient length to visualize its projection towards the posterior of the brain. The morphology of FANS was different from that of THIN or MSN: the dendrites of FANS were also covered with spines, similar to MSN, but their dendritic branching was much less extensive (Figure 9C). The somata of FANS were also medium-sized ($15.5 \pm 0.8 \mu\text{m}$, long axis diameter) and were mostly oval in shape.

Several of the morphological properties of the three types of YFP⁺ neurons are quantified in Figure 10. All three cell types had similar-sized soma (Figure 10A; $p = 0.25$, one-way ANOVA with Dunn's multiple comparison test). MSN had significantly more primary dendrites than either FANS or THIN (Figure 10B; $p = 0.0031$, one-way ANOVA with Dunn's multiple comparison test). MSN also had the highest density of dendritic spines, as revealed by a 3D analysis of spine density from the reconstructed neurons (Figure 10C). FANS had a lower density of spines compared to MSN, while THIN had no spines ($p \leq 0.001$, one-way ANOVA with Tukey's multiple comparison test). Our measured values of spine density for MSN are similar to those previously reported (Shen et al., 2008).

Dendritic branching in the three types of cells first was compared by a two-dimensional analysis described by Sholl (1953). This analysis revealed that dendritic branching was

greatest in MSN and least in THIN (Figure 10D). Although the extent of branching was similar in MSN and FANS within the first $10 \mu\text{m}$ from their somata, MSN branched more extensively at $20\text{--}130 \mu\text{m}$ from their somata (Figure 10D; $p < 0.05$; multiple t -tests). As an alternative way to compare dendritic branching in the three cell types, a three-dimensional variant of the Sholl analysis was also performed (Scorcioni et al., 2008). This analysis measured neurite surface area as a function of path distance from the cell body and captured the spatial extent of the neuron in three-dimensions, as opposed to the planar projections used in the Sholl (1953) analysis. Furthermore, measurement of surface area increases the functional relevance of the analysis because surface area should be more proportional to the number of synapses. This analysis (Figure 10E) revealed the same differences between the MSN and FANS that were evident in the Sholl (1953) analysis (Figure 10D), with MSN having the most dendritic branching, THIN having the least and FANS exhibiting branching intermediate between MSN and THIN over the first $100 \mu\text{m}$ from the cell body ($p < 0.05$, multiple t -tests).

To systematically examine the relationship between the morphological properties of the three types of YFP⁺ neurons, we extracted 23 features from digital reconstructions of these neurons and then performed an unsupervised clustering analysis. FANS clustered separately from both THINs and MSNs in our analysis (Figure 11A); remarkably, although the intrinsic electrical properties of these neurons were not considered in the morphological clustering analysis of Figure 11A, the clustering nonetheless completely segregated the neurons in a way that was consistent with the distinctive electrical properties of these neurons. This indicates that FANS represent a unique cell type both in regard to their morphological properties and their intrinsic electrical properties. Comparing dendritic branching within the first $50 \mu\text{m}$ from the soma, total length and spine density also showed a clear separation into the same three cell types identified by electrophysiology (Figure 11B). In fact, 11 of the morphological properties that we considered differed considerably between the three different types of YFP⁺ neurons, with a fairly consistent trend that MSNs possessed the highest means for each of these features, followed by FANS and then THIN (Figure 11C).

Heterogeneity of FANS

Although FANS were distinctly different from THIN and MSN in regard to their intrinsic electrical properties and morphology, there was considerable heterogeneity between individual FANS. FANS were diverse both in terms of their dendritic field orientation and in their AP firing patterns. For example, their dendritic fields could be oriented along the long axis of the cell body, towards one side of the cell body, or could radiate in numerous directions around the soma (Figure 12).

Hierarchical clustering, based on intrinsic electrical properties, revealed three subtypes of FANS (Figure 13A). We refer to these as Types I, II and III. The three subtypes of FANS showed differences in their AP amplitude, RMP and amount of AP amplitude adaptation (Figure 13B). These FANS subtypes also showed differences in most of the 12 properties used for classification (Figure 13C and

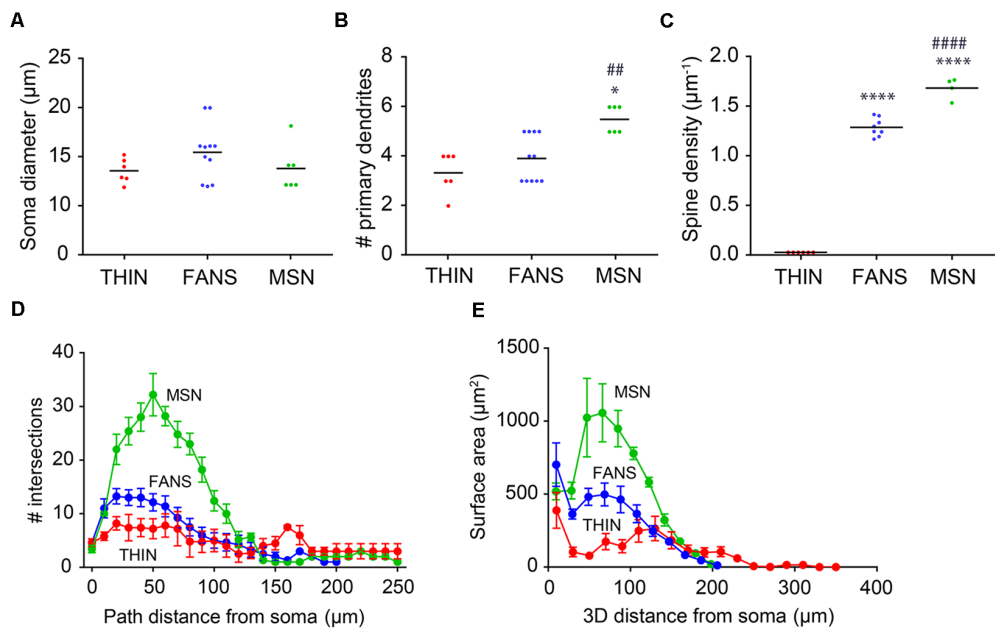


FIGURE 10 | Morphological analysis of YFP⁺ striatal neurons. **(A)** Soma diameter (one-way ANOVA, $p = 0.2458$; Dunn's multiple comparisons). **(B)** Number of primary dendrites (one-way ANOVA, $p = 0.0031$; Dunn's multiple comparisons; * $p < 0.05$ to THIN, ** $p < 0.01$ to FANS). **(C)** Spine density (one-way ANOVA, $p < 0.0001$; Tukey's multiple comparisons; **** $p < 0.0001$ to THIN, ##### $p < 0.0001$ to FANS). **(D)** Sholl analysis indicating dendritic arborization, with points indicating means and error bars indicating \pm SEM. **(E)** Surface area vs. path distance plot to indicate dendritic branching, with points indicating means and error bars indicating \pm SEM.

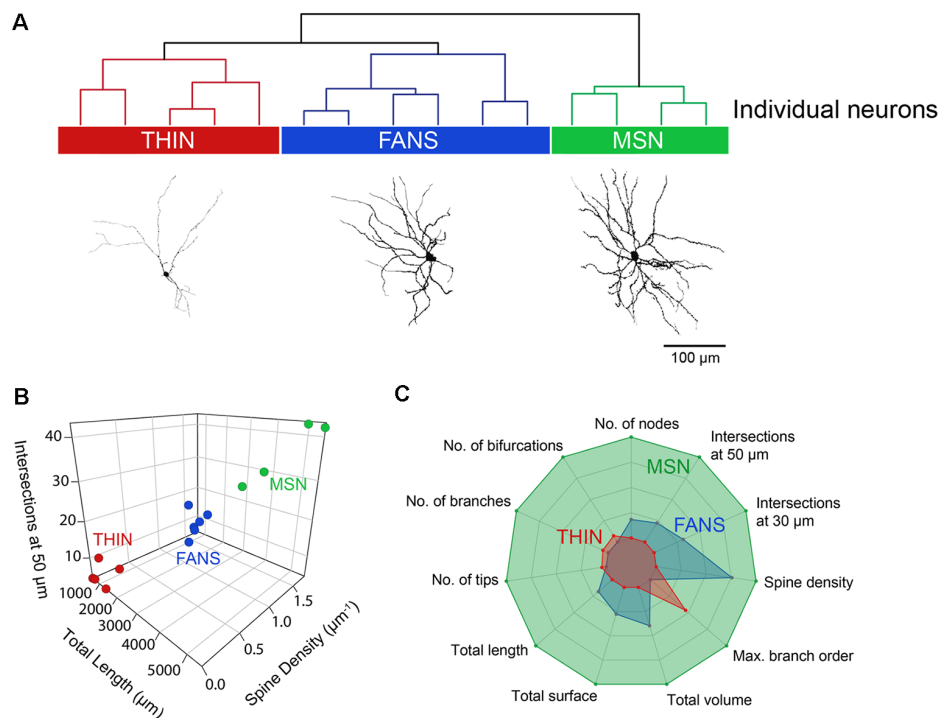


FIGURE 11 | Unsupervised hierarchical clustering of morphology recapitulates electrophysiologically defined cell types. **(A)** A dendrogram showing the unbiased classification of the three types of YFP⁺ neurons (top) and digital reconstruction of a representative cell from each type (bottom). **(B)** 3D scatter plots showing the clustering of the three YFP⁺ cell types. **(C)** Radar plots revealing substantial differences between the three cell types, calculated using normalized population means in the range of 0–1.

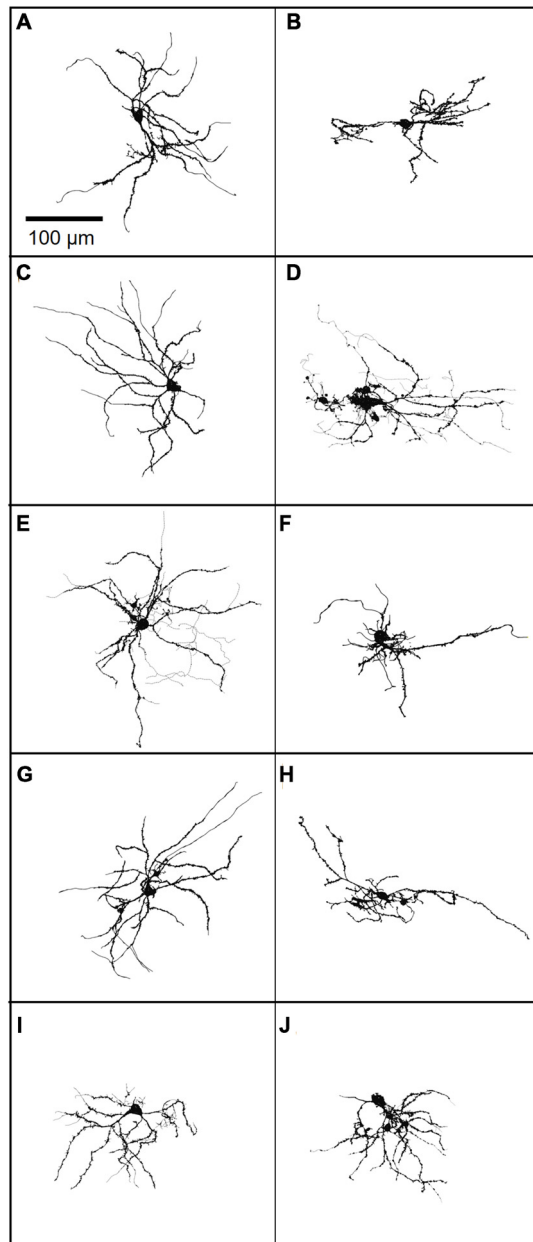


FIGURE 12 | (A–J) A gallery of 10 neurobiotin-filled FANS showing their diverse morphology. Light lines indicate axons, wherever traceable; dark lines indicate dendrites.

Table 4). The temporal patterns of AP firing varied between the different classes of FANS, with depolarization-induced plateau potential present mostly in Type III FANS. Due to the relatively small number of FANS successfully filled with neurobiotin, it is not yet clear whether the differences in morphology and intrinsic electrical properties of FANS are correlated. However, based on an analysis of the 10 neurobiotin-filled FANS shown in **Figure 12**, it appeared that Type II FANS had less dendritic arborization than the other two FANS subtypes (**Figure 13A**, bottom).

DISCUSSION

Here, we describe a heterogeneous population of YFP⁺ neurons in the striatum of transgenic mice with ChR2-YFP expression driven by the TH promoter.

Heterogeneity of YFP⁺ Striatal Neurons

Three main subtypes of YFP⁺ striatal neurons were found with distinct morphological and electrophysiological properties (**Figures 2, 3; Table 3**). One subtype resembled the THIN described previously (Ibáñez-Sandoval et al., 2010), confirming the existence of these cells *via* a different genetic targeting strategy. Most THIN we examined were of the Type I or III described previously (Ibáñez-Sandoval et al., 2010). In fact, these two THIN subtypes are very similar to each other in terms of their firing patterns; they mainly differ in their RMP and input resistances. A second, small proportion of neurons resembled MSN. While this could arise from ectopic expression of Cre recombinase, as has been previously reported in some TH-Cre lines (Lammel et al., 2015; Stuber et al., 2015), it is also possible that these MSN might express TH at some point during their development. A third distinct population of YFP⁺ striatal neurons has not been observed previously in mature animals; these neurons have morphological and electrophysiological properties that uniquely distinguish them from all other YFP-expressing neurons (**Figure 3**). We have named these cells FANS. FANS have passive membrane properties (C_m , R_{in} , RMP and sag amplitude) that are intermediate between THIN and MSN (**Figure 4**) and their AHPs are longest lasting and smallest in amplitude (**Figure 5**). Similar to THIN, FANS show substantial adaptation of AP frequency, duration and peak amplitudes during AP trains, but differ from THIN in the amount or rate of adaptation (**Figures 6–8**). Morphologically, FANS have dendritic spines; while MSN are the only striatal neurons previously described to have dendritic spines, our quantitative analysis indicates that FANS spine density and dendritic branching are significantly lower than that of MSN (**Figures 9–11**). Finally, FANS may represent a heterogeneous population because they have diverse morphological and electrophysiological properties (**Figures 12, 13**).

Unique Properties of FANS

Our discovery of FANS is surprising because they were not reported in previous descriptions of THIN in TH-EGFP mice (Grace and Bunney, 1983; Ibáñez-Sandoval et al., 2010; Ünal et al., 2011, 2015) or in TH-Cre mice with virally expressed ChR2-EYFP (Xenias et al., 2015). The reason why FANS were not observed previously is unknown but could be related to their relatively low numbers and the absence of specific markers to identify them. In addition, transgene expression patterns may differ with the same promoter due to positional effect variegation. Finally, it could be that TH-expressing cells could have been underreported in previous experiments; for example, in the experiments of Xenias et al. (2015), not all dopamine-expressing neurons in the midbrain expressed EYFP. The electrophysiological properties of FANS are somewhat similar, but not identical, to those of the type A TH-expressing

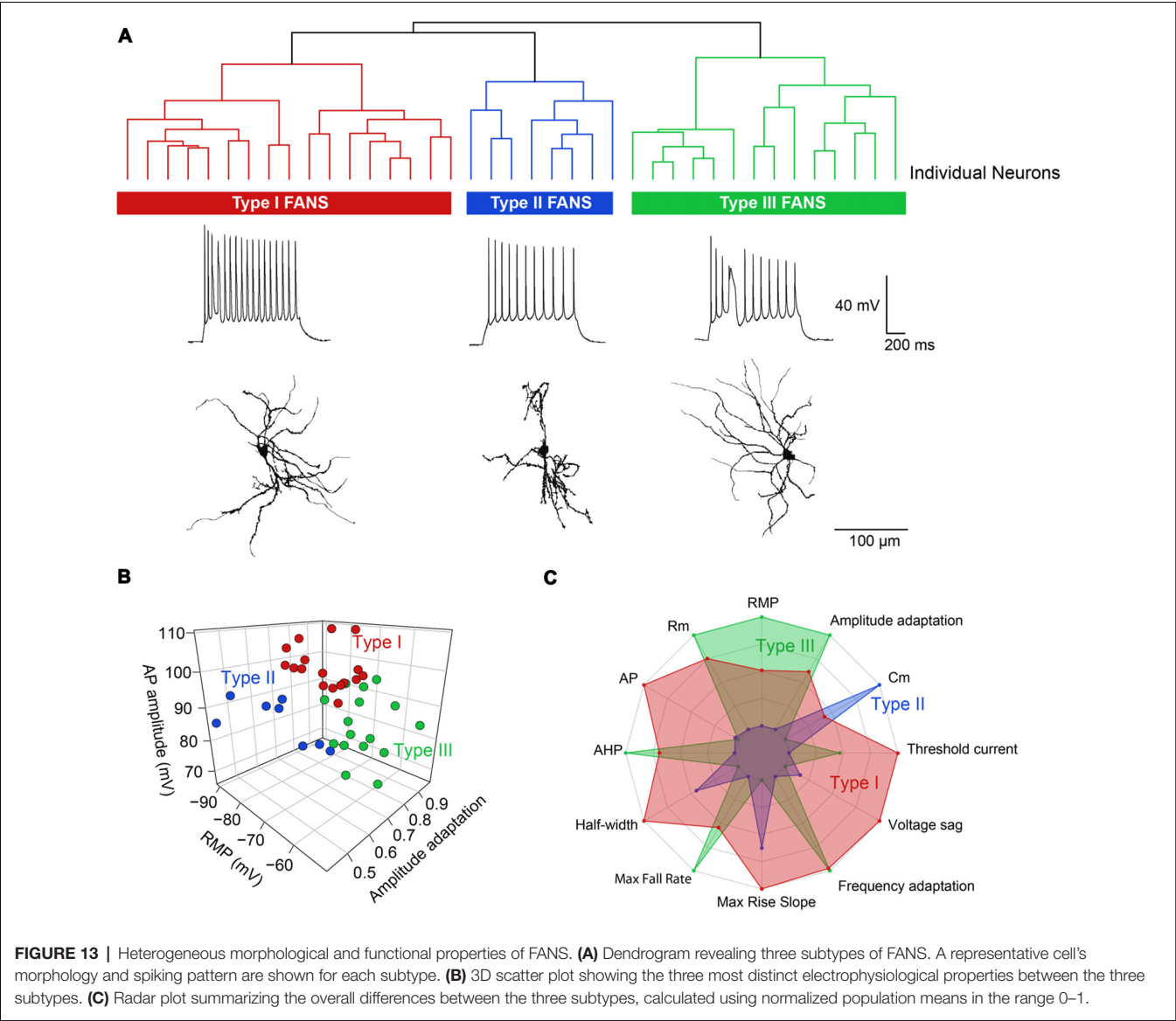


TABLE 4 | Electrical properties of Type I, II and III FANS.

Property	Type I	Type II	Type III
C _m (pF)	76.8 ± 3.4	81.7 ± 7.0	73.3 ± 3.1
R _{in} (MΩ)	275 ± 21	164 ± 18	312 ± 29
RMP (mV)	−74.0 ± 1.7	−82.1 ± 2.3	−66.2 ± 2.1
Sag amplitude (mV)	1.8 ± 0.5	1.4 ± 0.3	1.3 ± 0.1
AP duration (ms)	3.3 ± 0.1	3.0 ± 0.2	2.8 ± 0.1
AHP (mV)	−3.7 ± 0.6	−5.1 ± 1.7	−3.1 ± 0.9
AP amplitude (mV)	100 ± 1.3	83.6 ± 2.9	83.1 ± 2.1
Maximum AP frequency adaptation (Hz)	45.8 ± 6.3	26.6 ± 14	46.3 ± 6.7
AP amplitude adaptation	0.75 ± 0.02	0.63 ± 0.04	0.82 ± 0.02
Current threshold (pA)	43.5 ± 2.5	27.5 ± 6.4	35.0 ± 4.6

Values indicate mean ± SEM.

striatal neurons described in neonatal mouse striatum by Masuda et al. (2011). Likewise, THIN are similar to what these authors call type B neurons. Thus, it is possible that these two types of TH-expressing neurons in neonatal striatum

are the developmental precursors of FANS and THIN in the adult.

FANS are not a subtype of THIN, because their firing patterns do not resemble any previously described THIN

subtypes. In addition, FANS have dendrites with a high density of spines, while THIN are largely aspiny; only a very small proportion of Type I THIN reportedly have spine-like appendages and the density of these structures still is much lower than the density of dendritic spines we observed in FANS (Ibáñez-Sandoval et al., 2010).

Two lines of evidence clearly indicate that FANS also are not MSN. First, none of the 12 electrophysiological and 11 morphological properties of FANS clustered with MSN in our unbiased clustering analyses (see **Figures 3** and **11**). Second, we did not encounter any FANS amongst non-YFP⁺ neurons of the striatum; most non-YFP⁺ neurons we examined were MSN while we occasionally encountered PV and cholinergic interneurons. With MSN making up ~95% of the total striatal population, we would expect to see FANS relatively frequently among non-YFP⁺ neurons if they are indeed a subtype of MSN. Finally, in contrast to the axons of MSN, we never observed the axons of FANS projecting out of the striatum. Therefore, we are confident that FANS are distinctly different from MSN.

FANS are also unlikely to be the other types of striatal interneurons that have been previously identified (see Tepper et al., 2010 for a review of striatal interneurons). For example, FANS do not exhibit the rapid APs that characterize PV interneurons. They also lack the low-threshold calcium spikes observed in SOM/NPY/NOS-positive interneurons and have much lower input resistance than these interneurons. Further, cholinergic interneurons have very large cell bodies, tend to fire spontaneous APs and have prominent hyperpolarization-induced sag, all properties that differ from those of FANS. Most importantly, unlike striatal interneurons, FANS have spines. We therefore conclude that FANS are a unique type of striatal neuron.

The plateau spikes generated in FANS in response to large depolarizing currents resemble the complex spikes seen in cerebellar Purkinje cells and cartwheel cells of the dorsal cochlear nucleus, two electrical signals that arise from activation of voltage-dependent calcium channels (Llinás and Sugimori, 1980; Kim and Trussell, 2007; Portfors and Roberts, 2007). Based on these similarities, we speculate that the depolarization-induced plateau spikes, as well as the other distinctive intrinsic properties, may allow FANS to provide input with a unique temporal structure in comparison to other striatal neurons. In addition, because FANS have dendritic spines, it is likely that they receive glutamatergic input from the cortex and/or dopaminergic input from the midbrain; both of these types of input contact dendritic spines on MSN (Freund et al., 1984; Dubé et al., 1988).

Several questions remain regarding the identity of FANS in the striatum. First, although we used TH-Cre mice as a tool for genetic access to FANS, it is not clear whether or not FANS express TH. It is possible that FANS do express TH at some time during their development or FANS may not express TH at all; as mentioned above, ectopic expression has been reported in TH-Cre mouse lines (Lammel et al., 2015; Stuber et al., 2015). Future work will be needed to understand

why Cre (and ChR2-YFP) is expressed in FANS in our mice. Second, it is not known what neurotransmitter(s) FANS use. For the case of GABAergic THIN, despite the expression of TH these neurons are not dopaminergic because they do not release dopamine and lack other molecular components required for dopamine synthesis, such as L-amino acid decarboxylase, dopamine transporter and vesicular monoamine transporter-2 (Xenias et al., 2015). Third, it is unclear whether FANS are projection neurons or interneurons. For the 10 FANS we successfully labeled with neurobiotin (**Figure 12**), axonal arborizations were visible and observed to ramify locally; they were never observed to send long-distance projections beyond their dendritic fields (see **Figures 12D,E**). This observation suggests that FANS, like THIN (Ibáñez-Sandoval et al., 2010), are likely to be interneurons.

CONCLUSIONS

We have discovered FANS, a novel type of neuron in the mouse dorsal striatum. The unique electrical and morphological properties of these neurons add a novel cellular element to striatal local circuitry; future work will be needed to determine the functions of these cells.

ETHICS STATEMENT

All mice used in the experiments were 6–14 weeks old of either sex and all procedures were approved by the Institutional Animal Care and Use Committee of Biopolis, Agency of Science and Technology, Singapore.

AUTHOR CONTRIBUTIONS

MM and GA designed the experiments. MM performed the experiments. MM and AN analyzed the data. MM, AN and GA wrote the article.

FUNDING

This work was supported by research grants (MOE2015-T2-2-095 and MOE2017-T3-1-002) from the Singapore Ministry of Education and by a National Science Scholarship from the Agency of Science, Technology and Research, Singapore.

ACKNOWLEDGMENTS

We thank P. Teo, J. Tan, K. Chung, and S. Kay for technical assistance, M. Fukuda for assistance with instrumentation, M. Graf for advice on immunohistochemistry and helpful discussions and G. Silberberg for comments on our manuscript.

REFERENCES

- Assous, M., Kaminer, J., Shah, F., Garg, A., Koós, T., and Tepper, J. M. (2017). Differential processing of thalamic information via distinct striatal interneuron circuits. *Nat. Commun.* 8:15860. doi: 10.1038/ncomms15860
- Cossette, M., Lévesque, D., and Parent, A. (2005). Neurochemical characterization of dopaminergic neurons in human striatum. *Parkinsonism Relat. Disord.* 11, 277–286. doi: 10.1016/j.parkreldis.2005.02.008
- Darmopil, S., Muñetón-Gómez, V. C., de Ceballos, M. L., Bernson, M., and Moratalla, R. (2008). Tyrosine hydroxylase cells appearing in the mouse striatum after dopamine denervation are likely to be projection neurones regulated by l-dopa. *Eur. J. Neurosci.* 27, 580–592. doi: 10.1111/j.1460-9568.2008.06040.x
- Dubach, M., Schmidt, R., Kunkel, D., Bowden, D. M., Martin, R., and German, D. C. (1987). Primate neostriatal neurons containing tyrosine hydroxylase: immunohistochemical evidence. *Neurosci. Lett.* 75, 205–210. doi: 10.1016/0304-3940(87)90298-9
- Dubé, L., Smith, A. D., and Bolam, J. P. (1988). Identification of synaptic terminals of thalamic or cortical origin in contact with distinct medium-size spiny neurons in the rat neostriatum. *J. Comp. Neurol.* 267, 455–471. doi: 10.1002/cne.902670402
- Faust, T. W., Assous, M., Shah, F., Tepper, J. M., and Koós, T. (2015). Novel fast adapting interneurons mediate cholinergic-induced fast gabaa ipscs in striatal spiny neurons. *Eur. J. Neurosci.* 42, 1764–1774. doi: 10.1111/ejn.12915
- Faust, T. W., Assous, M., Tepper, J. M., and Koós, T. (2016). Neostriatal gabaergic interneurons mediate cholinergic inhibition of spiny projection neurons. *J. Neurosci.* 36, 9505–9511. doi: 10.1523/JNEUROSCI.0466-16.2016
- Ferreira, T. (2016). Sholl Analysis. *Development* 3, 4.
- Freund, T. F., Powell, J. F., and Smith, A. D. (1984). Tyrosine hydroxylase-immunoreactive boutons in synaptic contact with identified striatonigral neurons, with particular reference to dendritic spines. *Neuroscience* 13, 1189–1215. doi: 10.1016/0306-4522(84)90294-x
- Gertler, T. S., Chan, C. S., and Surmeier, D. J. (2008). Dichotomous anatomical properties of adult striatal medium spiny neurons. *J. Neurosci.* 28, 10814–10824. doi: 10.1523/JNEUROSCI.2660-08.2008
- Gouwens, N. W., Sorensen, S. A., Berg, J., Lee, C., Jarsky, T., Ting, J., et al. (2018). Classification of electrophysiological and morphological types in mouse visual cortex. *bioRxiv* 368456
- Grace, A., and Bunney, B. (1983). Intracellular and extracellular electrophysiology of nigral dopaminergic neurons—I. Identification and characterization. *Neuroscience* 10, 301–315. doi: 10.1016/0306-4522(83)90135-5
- Graveland, G. A., and DiFiglia, M. (1985). The frequency and distribution of medium-sized neurons with indented nuclei in the primate and rodent neostriatum. *Brain Res.* 327, 307–311. doi: 10.1016/0006-8993(85)91524-0
- Ibáñez-Sandoval, O., Tecuapetla, F., Unal, B., Shah, F., Koós, T., and Tepper, J. M. (2010). Electrophysiological and morphological characteristics and synaptic connectivity of tyrosine hydroxylase-expressing neurons in adult mouse striatum. *J. Neurosci.* 30, 6999–7016. doi: 10.1523/JNEUROSCI.5996-09.2010
- Ibáñez-Sandoval, O., Tecuapetla, F., Unal, B., Shah, F., Koós, T., and Tepper, J. M. (2011). A novel functionally distinct subtype of striatal neuropeptide y interneuron. *J. Neurosci.* 31, 16757–16769. doi: 10.1523/JNEUROSCI.2628-11.2011
- Ikemoto, K., Kitahama, K., Juvet, A., Arai, R., Nishimura, A., Nishi, K., et al. (1997). Demonstration of l-dopa decarboxylating neurons specific to human striatum. *Neurosci. Lett.* 232, 111–114. doi: 10.1016/s0304-3940(97)00587-9
- Kim, Y., and Trussell, L. O. (2007). Ion channels generating complex spikes in cartwheel cells of the dorsal cochlear nucleus. *J. Neurophysiol.* 97, 1705–1725. doi: 10.1152/jn.00536.2006
- Kreitzer, A. C. (2009). Physiology and pharmacology of striatal neurons. *Annu. Rev. Neurosci.* 32, 127–147. doi: 10.1146/annurev.neuro.051508.135422
- Lammel, S., Steinberg, E., Földy, C., Wall, N., Beier, K., Luo, L., et al. (2015). Diversity of transgenic mouse models for selective targeting of midbrain dopamine neurons. *Neuron* 85, 429–438. doi: 10.1016/j.neuron.2014.12.036
- Lindeberg, J., Usoskin, D., Bengtsson, H., Gustafsson, A., Kylberg, A., Söderström, S., et al. (2004). Transgenic expression of cre recombinase from the tyrosine hydroxylase locus. *Genesis* 40, 67–73. doi: 10.1002/gene.20065
- Llinás, R., and Sugimori, M. (1980). Electrophysiological properties of *in vitro* purkinje cell somata in mammalian cerebellar slices. *J. Physiol.* 305, 171–195. doi: 10.1113/jphysiol.1980.sp013357
- Madisen, L., Mao, T., Koch, H., Zhuo, J. M., Berenyi, A., Fujisawa, S., et al. (2012). A toolbox of cre-dependent optogenetic transgenic mice for light-induced activation and silencing. *Nat. Neurosci.* 15, 793–802. doi: 10.1038/nn.3078
- Maechler, M., Rousseeuw, P., Struyf, A., Hubert, M., and Hornik, K. (2018). Cluster: Cluster analysis basics and extensions. *R package version 2.0*. 5.
- Mao, L., Lau, Y. S., Petroske, E., and Wang, J. Q. (2001). Propound astrogenesis in the striatum of adult mice following nigrostriatal dopaminergic lesion by repeated mptp administration. *Dev. Brain Res.* 131, 57–65. doi: 10.1016/s0165-3806(01)00260-7
- Masuda, M., Miura, M., Inoue, R., Imanishi, M., Saino-Saito, S., Takada, M., et al. (2011). Postnatal development of tyrosine hydroxylase mrna-expressing neurons in mouse neostriatum. *Eur. J. Neurosci.* 34, 1355–1367. doi: 10.1111/j.1460-9568.2011.07873.x
- Metsalu, T., and Vilo, J. (2015). Clustvis: a web tool for visualizing clustering of multivariate data using principal component analysis and heatmap. *Nucleic Acids Res.* 43, W566–W570. doi: 10.1093/nar/gkv468
- Muñoz-Manchado, A., Foldi, C., Szydlowski, S., Sjulson, L., Farries, M., Wilson, C., et al. (2016). Novel striatal gabaergic interneuron populations labeled in the 5ht3aegfp mouse. *Cereb. Cortex* 26, 96–105. doi: 10.1093/cercor/bhu179
- Nair, A., Silberberg, G., and Lim, K. L. (2018). AdReconstructor: a software suite for automated reconstruction of neuronal morphology [Software]. doi: 10.5281/zenodo.2648332
- Nakahara, T., Yamamoto, T., Endo, K., and Kayama, H. (2001). Neuronal ectopic expression of tyrosine hydroxylase in the mouse striatum by combined administration of 1-methyl-4-phenyl-1,2,3,6-tetrahydropyridine and 3-nitropropionic acid. *Neuroscience* 108, 601–610. doi: 10.1016/s0306-4522(01)00441-9
- Peng, H., Bria, A., Zhou, Z., Iannello, G., and Long, F. (2014). Extensible visualization and analysis for multidimensional images using vaa3d. *Nat. Protoc.* 9, 193–208. doi: 10.1038/nprot.2014.011
- Portfors, C. V., and Roberts, P. D. (2007). Temporal and frequency characteristics of cartwheel cells in the dorsal cochlear nucleus of the awake mouse. *J. Neurophysiol.* 98, 744–756. doi: 10.1152/jn.01356.2006
- R Core Team. (2013). *R: A Language and Environment for Statistical Computing*. R Foundation for Statistical Computing. Vienna Available online at: <http://www.R-project.org/>. Accessed August 10, 2018.
- Rousseeuw, P. J. (1987). Silhouettes: a graphical aid to the interpretation and validation of cluster analysis. *J. Comput. Appl. Math.* 20, 53–65. doi: 10.1016/0377-0427(87)90125-7
- Rymar, V. V., Sasseville, R., Luk, K. C., and Sadikot, A. F. (2004). Neurogenesis and stereological morphometry of calretinin-immunoreactive gabaergic interneurons of the neostriatum. *J. Comp. Neurol.* 469, 325–339. doi: 10.1002/cne.11008
- Scorcioni, R., Polavaram, S., and Ascoli, G. A. (2008). L-measure: a web-accessible tool for the analysis, comparison and search of digital reconstructions of neuronal morphologies. *Nat. Protoc.* 3, 866–876. doi: 10.1038/nprot.2008.51
- Shen, H., Sesack, S. R., Toda, S., and Kalivas, P. W. (2008). Automated quantification of dendritic spine density and spine head diameter in medium spiny neurons of the nucleus accumbens. *Brain Struct. Funct.* 213, 149–157. doi: 10.1007/s00429-008-0184-2
- Sholl, D. A. (1953). Dendritic organization in the neurons of the visual and motor cortices of the cat. *J. Anat.* 87, 387–406.
- Stacklies, W., Redestig, H., Scholz, M., Walther, D., and Selbig, J. (2007). Pcamethods—a bioconductor package providing pca methods for incomplete data. *Bioinformatics* 23, 1164–1167. doi: 10.1093/bioinformatics/btm069
- Stuber, G., Stamatakis, A., and Kantak, P. (2015). Considerations when using cre-driver rodent lines for studying ventral tegmental area circuitry. *Neuron* 85, 439–445. doi: 10.1016/j.neuron.2014.12.034
- Tandé, D., Höglinger, G., Debeir, T., Freundlieb, N., Hirsch, E. C., and François, C. (2006). New striatal dopamine neurons in mptp-treated macaques result from a phenotypic shift and not neurogenesis. *Brain* 129, 1194–1200. doi: 10.1093/brain/awl041
- Tashiro, Y., Sugimoto, T., Hattori, T., Uemura, Y., Nagatsu, I., Kikuchi, H., et al. (1989). Tyrosine hydroxylase-like immunoreactive neurons in the striatum of the rat. *Neurosci. Lett.* 97, 6–10. doi: 10.1016/0304-3940(89)90130-4

- Tepper, J., Tecuapetla, F., Koós, T., and Ibáñez-Sandoval, O. (2010). Heterogeneity and diversity of striatal gabaergic interneurons. *Front. Neuroanat.* 4:150. doi: 10.3389/fnana.2010.00150
- Ünal, B., Ibáñez-Sandoval, O., Shah, F., Abercrombie, E. D., and Tepper, J. M. (2011). Distribution of tyrosine hydroxylase-expressing interneurons with respect to anatomical organization of the neostriatum. *Front. Syst. Neurosci.* 5:41. doi: 10.3389/fnsys.2011.00041
- Ünal, B., Shah, F., Kothari, J., and Tepper, J. M. (2015). Anatomical and electrophysiological changes in striatal th interneurons after loss of the nigrostriatal dopaminergic pathway. *Brain Struct. Funct.* 220, 331–349. doi: 10.1007/s00429-013-0658-8
- Ward, Jr., J. H. (1963). Hierarchical grouping to optimize an objective function. *J. Am. Stat. Assoc.* 58, 236–244. doi: 10.1080/01621459.1963.10500845
- Xenias, H. S., Ibáñez-Sandoval, O., Koós, T., and Tepper, J. M. (2015). Are striatal tyrosine hydroxylase interneurons dopaminergic? *J. Neurosci.* 35, 6584–6599. doi: 10.1523/JNEUROSCI.0195-15.2015
- Xiao, H., and Peng, H. (2013). APP2: automatic tracing of 3D neuron morphology based on hierarchical pruning of a gray-weighted image distance-tree. *Bioinformatics* 29, 1448–1454. doi: 10.1093/bioinformatics/btt170

Conflict of Interest Statement: The authors declare that the research was conducted in the absence of any commercial or financial relationships that could be construed as a potential conflict of interest.

Copyright © 2019 Mao, Nair and Augustine. This is an open-access article distributed under the terms of the Creative Commons Attribution License (CC BY). The use, distribution or reproduction in other forums is permitted, provided the original author(s) and the copyright owner(s) are credited and that the original publication in this journal is cited, in accordance with accepted academic practice. No use, distribution or reproduction is permitted which does not comply with these terms.



Neural Correlates of Anesthesia in Newborn Mice and Humans

Mattia Chini¹, Sabine Gretenkord¹, Johanna K. Kostka¹, Jastyn A. Pöpplau¹, Laura Cornelissen^{2,3}, Charles B. Berde^{2,3}, Ileana L. Hanganu-Opatz^{1*†} and Sebastian H. Bitzenhofer^{1*†‡}

¹Developmental Neurophysiology, Institute of Neuroanatomy, University Medical Center Hamburg-Eppendorf, Hamburg, Germany, ²Department of Anesthesiology, Critical Care and Pain Medicine, Boston Children's Hospital, Boston, MA, United States, ³Department of Anesthesia, Harvard Medical School, Boston, MA, United States

OPEN ACCESS

Edited by:

Tommaso Pizzorusso,
University of Florence, Italy

Reviewed by:

Paola Binda,
University of Pisa, Italy
Laura Baroncelli,
Italian National Research Council
(CNR), Italy

*Correspondence:

Ileana L. Hanganu-Opatz
hangop@zmnh.uni-hamburg.de
Sebastian H. Bitzenhofer
sbitzenhofer@ucsd.edu

[†]These authors have contributed
equally to this work

*Present address:

Sebastian H. Bitzenhofer,
Center for Neural Circuits and
Behavior, Department of
Neurosciences, University of
California, San Diego, La Jolla, CA,
United States

Received: 31 January 2019

Accepted: 03 May 2019

Published: 22 May 2019

Citation:

Chini M, Gretenkord S, Kostka JK, Pöpplau JA, Cornelissen L, Berde CB, Hanganu-Opatz IL and Bitzenhofer SH (2019) Neural Correlates of Anesthesia in Newborn Mice and Humans. *Front. Neural Circuits* 13:38. doi: 10.3389/fncir.2019.00038

Monitoring the hypnotic component of anesthesia during surgeries is critical to prevent intraoperative awareness and reduce adverse side effects. For this purpose, electroencephalographic (EEG) methods complementing measures of autonomic functions and behavioral responses are in use in clinical practice. However, in human neonates and infants existing methods may be unreliable and the correlation between brain activity and anesthetic depth is still poorly understood. Here, we characterized the effects of different anesthetics on brain activity in neonatal mice and developed machine learning approaches to identify electrophysiological features predicting inspired or end-tidal anesthetic concentration as a proxy for anesthetic depth. We show that similar features from EEG recordings can be applied to predict anesthetic concentration in neonatal mice and humans. These results might support a novel strategy to monitor anesthetic depth in human newborns.

Keywords: development, anesthesia, LFP, EEG, mouse, human, machine learning, network dynamics

INTRODUCTION

Reliable monitoring of anesthesia depth is critical during surgery. It allows for loss of consciousness, analgesia and immobility without incurring the risk of side effects and complications due to anesthetic misdosing. Typically used measures to monitor anesthesia depth are inspired and end-tidal anesthetic concentrations as well as physiologic parameters, including respiratory rate and depth (in the absence of neuromuscular blockade or controlled ventilation), heart rate, blood pressure, and responses to noxious stimuli (Punjasawadwong et al., 2014). These measures all respond to spinal and brainstem reflexes and are not specific for arousal or cortical responses to noxious events.

Anesthesia-induced changes in brain activity can be measured with electroencephalographic (EEG) recordings. Specific algorithms have been developed to predict anesthesia depth in adults (Glass et al., 1997; Prichep et al., 2004; Kreuzer, 2017). The most commonly used of such methods, the Bispectral Index, has been shown to significantly reduce intraoperative awareness, amount of anesthetic used, recovery time and post-anesthesia care unit stay in a recent Cochrane meta-analysis (Punjasawadwong et al., 2014), but see (Kalkman et al., 2011; Hajat et al., 2017). However, evidence of similar benefits in infants and younger children is sparse, as recently shown (Cornelissen et al., 2015, 2017, 2018a). EEG in anesthetized infants changes dramatically depending on postnatal age. Slow oscillations are present from birth on, whereas theta and alpha oscillations

occur 3 months after birth, but lack the frontal dominance typically seen in adults (Davidson et al., 2005; Lo et al., 2009; Hayashi et al., 2012; Cornelissen et al., 2015; Koch et al., 2017).

EEG recordings mainly monitor neocortical activity. Converging evidence from animal and human studies has shown that most anesthetics slow EEG oscillations (Alkire et al., 2008; Chauvette et al., 2011; Purdon et al., 2015). While power at high frequency oscillations is reduced (>40 Hz), power at slower frequencies (<15 Hz) is enhanced (Purdon et al., 2015). The computations underlying proprietary indexes such as the Bispectral index or Narcotrend are thought to take advantage of these phenomena (Kertai et al., 2012). However, in preterm and term neonates for the first weeks of life, EEG during sleep-wake cycles is weakly correlated with behavioral states and shows characteristic bursts or spontaneous activity transients (Milh et al., 2007; O'Toole et al., 2016). Anesthesia-induced theta and alpha oscillations have been reported to emerge around 3–4 months of age, albeit with less frontal predominance than in older children and adults (Cornelissen et al., 2015, 2018a). Moreover, high concentrations/doses of anesthetics have been reported to depress brain activity and enhance signal discontinuity in both human and rodent neonates (Chang et al., 2016; Cornelissen et al., 2017; Stolwijk et al., 2017). However, to our knowledge, a comprehensive algorithmic approach identifying EEG parameters that robustly correlate with anesthetic depth during early postnatal development is still lacking.

Here, we developed a novel strategy to model anesthesia depth by using common electrophysiological features that correlate with inhaled anesthetic concentrations during early development of mice and humans at similar stage of brain development. We performed intracranial electrophysiological recordings to study the temporal and dose-dependent dynamics of brain activity in neonatal mice [postnatal day (P) 8–10] during bolus urethane administration, and during dose-titrated isoflurane general anesthesia, respectively. Dominant local field potential (LFP) features of anesthetic state were identified and used to develop a machine-learning algorithm that distinguishes non-anesthetized from deeply anesthetized states and predicts anesthetic concentration as a proxy for anesthetic depth. Using a similar approach, we used multielectrode EEG recordings to study the dose-dependent dynamics of brain activity in a secondary analysis of a combined new and previously reported data set (Cornelissen et al., 2018a) of human infants 0–6 months of age during induction, maintenance and emergence from general anesthesia (sevoflurane, isoflurane, or desflurane) administered for routine surgical care. Dominant EEG features of anesthetic state were identified and used to develop a machine-learning algorithm to predict end-tidal volume anesthetic concentration (an indirect measure of anesthetic concentration in the brain, and anesthetic depth).

MATERIALS AND METHODS

Animals

All experiments were performed in compliance with the German laws and the guidelines of the European Community for the

use of animals in research and were approved by the local ethical committee (G132/12, G17/015, N18/015). Experiments were carried out on C57Bl/6J mice of both sexes. Timed-pregnant mice from the animal facility of the University Medical Center Hamburg-Eppendorf were housed individually at a 12 h light/12 h dark cycle, with *ad libitum* access to water and food. Day of birth was considered P0.

In vivo Electrophysiology in Neonatal Mice

Multisite extracellular recordings were performed in the prefrontal cortex (PFC) and HP, or lateral entorhinal cortex (LEC) and olfactory bulb (OB) of P8–10 mice. Pups were on a heating blanket during the entire procedure. Under isoflurane anesthesia (induction: 5%; maintenance: 2.5%), craniotomies were performed above PFC (0.5 mm anterior to Bregma, 0.1–0.5 mm right to Bregma) and HP (3.5 mm posterior to Bregma, 3.5 mm right to Bregma), or LEC (0 mm anterior to lambda, 6.5 mm right to lambda) and OB (0.5–0.8 mm anterior from the frontonasal suture, 0.5 mm right from internasal suture). Pups were head-fixed into a stereotaxic apparatus using two plastic bars mounted on the nasal and occipital bones with dental cement. Multisite electrodes (NeuroNexus, MI, USA) were inserted into PFC (four-shank, A4x4 recording sites, 100 μ m spacing, 2.0 mm deep) and HP (one-shank, A1x16 recording sites, 50 μ m spacing, 1.6 mm deep, 20° angle from the vertical plane), or LEC (one-shank, A1x16 recording sites, 100 μ m spacing, 2 mm deep, 10° angle from the vertical plane) and OB (one-shank, A1x16 recording sites, 50 μ m spacing, 1.4–1.8 mm deep). A silver wire was inserted into the cerebellum and served as ground and reference electrode. Pups were allowed to recover for 30 min prior to recordings. Extracellular signals were band-pass filtered (0.1–9,000 Hz) and digitized (32 kHz) with a multichannel extracellular amplifier (Digital Lynx SX, Neuralynx, Bozeman, MO, USA).

In vivo Electrophysiology in Juvenile Mice

Multisite extracellular recordings were performed in the PFC of P24–39 mice. Under isoflurane anesthesia (induction: 5%; maintenance: 2.5%), a metal head-post (Luigs and Neumann) was attached to the skull with dental cement and 2-mm craniotomies were performed above PFC (0.5–2.0 mm anterior to Bregma, 0.1–0.5 mm right to Bregma) and protected by a customized synthetic window. A silver wire was implanted in the cerebellum as ground and reference electrode. Surgery was performed at least 5 days before recordings. After recovery mice were trained to run on a custom-made spinning-disc. For recordings, craniotomies were uncovered and multisite electrodes (NeuroNexus, MI, USA) were inserted into PFC (one-shank, A1x16 recording sites, 50 μ m spacing, 2.0 mm deep). Extracellular signals were band-pass filtered (0.1–9,000 Hz) and digitized (32 kHz) with a multichannel extracellular amplifier (Digital Lynx SX, Neuralynx, Bozeman, MO, USA).

Recordings Under Urethane

Activity was recorded for 15 min without anesthesia before intraperitoneally injecting urethane (1 mg/g body weight; Sigma-Aldrich, St. Louis, MO, USA). Activity was recorded for further 45 min. Animals were transcardially perfused after recordings,

brains were sectioned coronally, and wide field images were acquired to verify recording electrode positions.

Recordings Under Isoflurane

Mouth piece of an isoflurane evaporator (Harvard Apparatus, Holliston, MA, USA) was placed in front of the pups in the recording setup until animals accustomed to it. Activity was recorded for 15 min 0% isoflurane, but with the evaporator running (1.4 l/min). Afterward, isoflurane was added to the airflow and increased every 15 min (1%, 2%, 3%). Animals were transcardially perfused after recordings, brains were sectioned coronally, and wide field images were acquired to verify recording electrode positions.

Electroencephalographic Recordings in Human Neonates and Young Infants

Neonates and infants who were scheduled for an elective surgical procedure were recruited from the pre-operative clinic at Boston Children's Hospital from 12/2012 to 08/2018 (under Institutional Review Board P-3544, with written informed consent obtained from parents/legal guardians). Subjects required surgery below the neck, were clinically stable on the day of study and American Society of Anesthesiologists' physical status I or II. Exclusion criteria were born with congenital malformations or other genetic conditions thought to influence brain development, diagnosed with a neurological or cardiovascular disorder, or born at <32 weeks post-menstrual age. Datasets from previously published work ($n = 25$; Cornelissen et al., 2018a) and new subjects ($n = 10$) were included in the analysis. Data are presented from 35 subjects aged 0–6 months.

Anesthetic Management

Each patient received anesthesia induced with sevoflurane (32 subjects), isoflurane (two subjects) or desflurane (one subject) alone or a combination of one of the previous and nitrous oxide. Epochs used for analysis were comprised of sevoflurane, isoflurane or desflurane administration with air and oxygen, titrated to clinical signs; end-tidal anesthetic concentration was adjusted per the anesthetist's impression of clinical need, not a pre-set end-tidal anesthetic concentration.

EEG Recording

EEG data were acquired using an EEG cap (WaveGuard EEG cap, Advanced NeuroTechnology, Netherlands). Thirty-three- or 41-recording electrodes were positioned per the modified international 10/20 electrode placement system. Reference and ground electrodes were located at Fz and AFz respectively. EEG activity from 0.1 to 500 Hz was recorded with an Xtek EEG recording system (EMU40EX, Natus Medical Inc., Canada). Signals were digitized at a sampling rate of 1,024 Hz and a resolution of 16-bit. The EEG recording was started prior to anesthetic induction to capture the loss of consciousness and stopped once the participant reached the Post-Anesthesia Recovery to capture recovery of consciousness. For some infants, the EEG recording was started after anesthetic induction.

Clinical Data Collection

Demographics and clinical information were collected from the electronic medical records and from the in-house Anesthesia

Information Management System (AIMS; **Supplementary Table S1**). None of the pathologies causing the need of surgery presented a risk for brain maturation. End-tidal sevoflurane, oxygen, and nitrous oxide concentrations were downloaded from the anesthetic monitoring device (Dräger Apollo, Dräger Medical Inc., Telford, PA, USA) to a recording computer in real-time using ixTrend software (ixcellence, Germany). Signals were recorded at a 1 Hz sampling rate.

Data Analysis

In vivo data were analyzed with custom-written algorithms in the Matlab environment. Data were processed as following: band-pass filtered (500–5,000 Hz) to analyze multi-unit activity (MUA) and band-pass filtered (2–100 Hz) using a third-order Butterworth filter before downsampling to analyze LFP. Filtering procedures were performed in a phase preserving manner.

Multi-Unit Activity

MUA was detected as the peak of negative deflections exceeding five times the standard deviation of the filtered signal and having a prominence larger than half the peak itself. Firing rates were computed by dividing the total number of spikes by the duration of the analyzed time window.

Detection of Oscillatory Activity

Discontinuous active periods were detected with a modified version of a previously developed algorithm for unsupervised analysis of neonatal oscillations (Cichon et al., 2014). Briefly, deflections of the root mean square of band-pass filtered signals (1–100 Hz) exceeding a variance-depending threshold were considered as network oscillations. The threshold was determined by a Gaussian fit to the values ranging from 0 to the global maximum of the root-mean-square histogram. If two oscillations occurred within 200 ms of each other they were considered as one. Only oscillations lasting >1 s were included, and their occurrence, duration and amplitude were computed.

Power Spectral Density

For power spectral density analysis, 1 s-long windows of full signal or network oscillations were concatenated, and the power was calculated using Welch's method with non-overlapping windows.

Imaginary Coherence

The imaginary part of coherence, which is insensitive to volume-conduction-based effects (Nolte et al., 2004), was calculated by taking the absolute value of the imaginary component of the normalized cross-spectrum.

Pairwise Phase Consistency

Pairwise phase consistency (PPC) was computed as previously described (Vinck et al., 2010). Briefly, the phase in the band of interest was extracted using Hilbert transform and the mean of the cosine of the absolute angular distance among all pairs of phases was calculated.

1/f Slope

1/f slope was computed as previously described (Gao et al., 2017). We used robust linear regression (MATLAB function *robustfit*)

to find the best fit over 20–40 Hz frequency range of the power spectral density, in 1-min bins.

Sample Entropy

Sample Entropy was computed using the SampEn function (MATLAB File Exchange) in 1.5 s windows and in 2 Hz frequency bins. Tolerance was set to $0.2 \times \text{std}(\text{signal})$, and tau to 1.

EEG Data Analysis

EEG signal was visually inspected to detect and reject channels with low signal to noise ratio and re-referenced to a common average reference. The signal was automatically scored in 5 s epochs, and channels in which signal was significantly contaminated by artifacts (patient handling, surgical electrocautery etc.) were discarded. Epochs were rejected if signal was saturated due to electrocautery, signal exceeded $150 \mu\text{V}$, or the median signal across all EEG channels exceeds $30 \mu\text{V}$ (Supplementary Figure S5). Minutes containing more than 10 s of contaminated signal were removed from further analysis. On average $14 \pm 9\%$ (median \pm median absolute deviation) of the signal was discarded. To compute EEG amplitude, we smoothed the absolute value of the signal, using a moving average filter with a window of 1,024 points (1 s). If more than one volatile anesthetic was used, we retained only epochs in which the main anesthetic was used in isolation. Subjects with epidural anesthesia halfway through the surgery ($n = 2$ subjects), or with less than 20 min of artifact-free signal ($n = 5$ subjects) were excluded from further analysis.

Feature Engineering

Features to predict anesthetic concentration in neonatal mice were calculated in 1-min bins. LFP power in the 1–100 Hz range in 10 Hz bins, the percentage of active periods, median length and number of oscillations, median and maximum signal amplitude were computed. All features were computed for both PFC and HP and were normalized to their median value in the non-anesthetized 15 min of recordings. Features to predict anesthetic concentration in human infants were also calculated in 1-min bins. The median amplitude of the smoothed EEG signal and the percentage of the EEG envelope that fell into each amplitude quartile was computed. Amplitude quartiles were computed on the entire EEG trace, averaged over channels. All features were calculated for unfiltered signal, and in the 1–50 Hz range in 5 Hz bins, averaged over channels. Features were normalized to their median value in the non-anesthetized portion of the recording, or lowest anesthetic concentration, if no artifact-free minute was available.

Regressors

Machine-learning analyses were performed using Python (Python Software Foundation, NH, USA) in the Spyder (Pierre Raybaut, The Spyder Development Team) development environment. Model training and performance evaluation were carried out using the scikit-learn toolbox. The set was iteratively ($n = 100$) divided between a training (2/3 of the set) and a cross-validation (1/3) set. Hyper-parameter of the model was tuned on the training set, which was further split using the standard

three-fold cross-validation split implemented by the function “GridSearchCV,” to which a “pipeline” object was passed. The “pipeline” object was built using the “Pipeline” function, and concatenating quantile transformation of the input features (“Quantile Transformer,” tuning the number of quantiles), feature selection (“Select Percentile,” using mutual information and tuning the percentage of features to select) and Radial Basis Function (RBF) kernel support-vector classification/regression (tuning the regularization parameters C and epsilon (regression only), and the kernel coefficient gamma). The classifier input was fed to the regressor as an additional feature. Performance assessment was then computed on the cross-validation set. Regressor decision space was reduced and plotted with t-sne. The decision space was approximated by imposing a Voronoi tessellation on the 2d plot, using k-nearest regression on the t-sne coordinates (Migut et al., 2015).

Statistics

Statistical analyses were performed using R Statistical Software (Foundation for Statistical Computing, Austria). Data were tested for significant differences ($*p < 0.05$, $**p < 0.01$ and $***p < 0.001$) using non-parametric one- and two-way repeated-measures ANOVA (ARTool R package) with Bonferroni corrected *post hoc* analysis (emmeans R package). Correlations were computed using Spearman’s rank correlation coefficient (ρ). No statistical measures were used to estimate the sample size since the effect size was unknown. For the main experimental results, more information about tests used, values and parameters are provided in the supplementary material (Supplementary Table S2).

Data Availability

Electrophysiological data for hippocampus and prefrontal cortex mouse recordings, under both urethane and isoflurane condition, is available at the following open-access repository: https://web.gin.g-node.org/mchini/Neural_correlates_of_anesthesia_in_newborn_mice_and_humans.

RESULTS

Anesthesia Affects the Occurrence but Not the Spectral and Temporal Structure of Oscillatory Events in Neonatal Mice

We monitored the impact of anesthesia on immature brain activity in several cortical areas [PFC, hippocampus (HP), and LEC] as well as in a sensory area OB. For this, multi-site extracellular recordings of LFP and MUA were performed from P8 to 10 mice before and for 45 min after induction of anesthesia by intraperitoneal urethane injection (Figure 1A), an anesthetic commonly used in rodents (Khazipov et al., 2004; Colonnese and Khazipov, 2010).

The recorded network activity had a highly fragmented structure (defined as discontinuous activity) in all investigated areas (PFC, HP, LEC and OB). The full signal (i.e., entire LFP trace) consisted of transient episodes of oscillatory discharges with mixed frequencies (from here referred to as “active periods”), alternating with periods of relative electrical silence

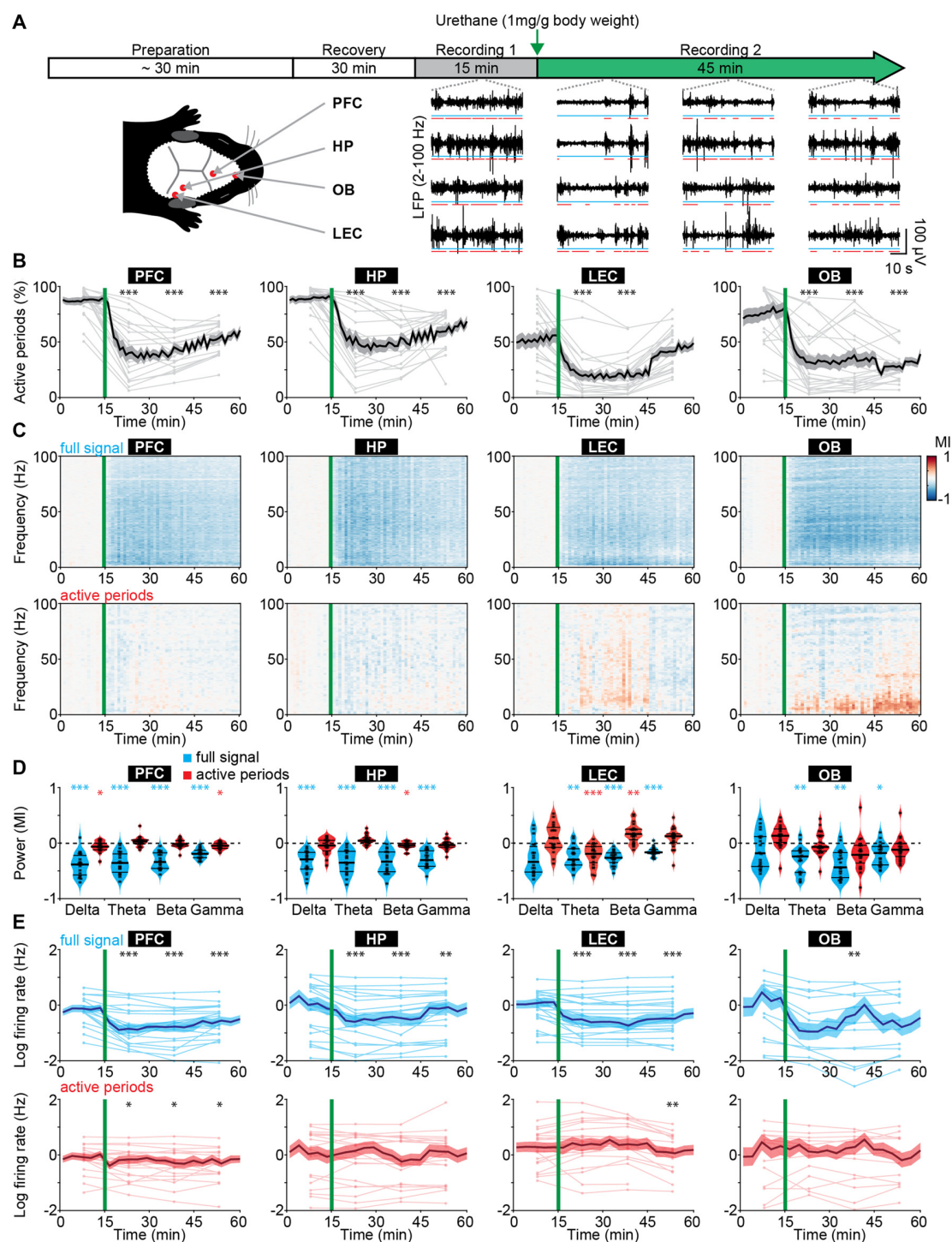


FIGURE 1 | Frequency-unspecific dampening of neuronal activity during urethane anesthesia in neonatal mice. **(A)** Schematic representation of experimental paradigm and recording sites as well as characteristic local field potential (LFP) recordings of discontinuous activity in the prefrontal cortex (PFC), HP, lateral entorhinal cortex (LEC), and olfactory bulb (OB) of neonatal mice (P8–10) during non-anesthetized and urethane-anesthetized state. Time windows of active periods are marked by red lines. **(B)** Line plots displaying the relative occurrence of active periods normalized to total recording time in PFC, HP, OB and LEC before and after urethane injection. **(C)** Color-coded MI of power spectra for full signal (top) and active periods (bottom) recorded in PFC, HP, LEC and OB of neonatal mice before and after urethane injection. **(D)** Violin plots displaying the MI of power in delta (2–4 Hz), theta-alpha (4–12 Hz), beta (12–30 Hz) and gamma (30–100 Hz) frequency bands for full signal (blue) and active periods (red) recorded in the PFC, HP, LEC and OB. **(E)** Line plots displaying multi-unit activity (MUA) rates during full signal (blue) and active periods (red). In **(B,C,E)** green lines correspond to the time point of urethane injection.

and suppressed activity (from here referred to as “silent periods”; **Figure 1A**; Khazipov et al., 2004; Hanganu et al., 2006; Brockmann et al., 2011; Bitzenhofer et al., 2017; Gretenkord et al., 2019). The prevalence of active periods decreased rapidly and robustly over time in all investigated brain areas upon urethane injection (**Figure 1B**). The most prominent reduction was observed 5–15 min after urethane injection. A partial recovery towards baseline levels during the following 30 min was detected in cortical areas, and to a lesser extent in OB (**Figure 1B**). The temporal sequence of events likely reflects the pharmacokinetics of urethane and is line with the previously reported quick onset (few minutes) and long-lasting effects of urethane anesthesia (2–4 h; Huh and Cho, 2013).

The anesthesia-induced reduced occurrence of active periods was reflected in a broadband (1–100 Hz) decrease in oscillatory power shown as modulation index (MI) defined as $(\text{power}_{\text{post}} - \text{power}_{\text{pre}})/(\text{power}_{\text{post}} + \text{power}_{\text{pre}})$. In contrast, power spectra during active periods were largely unaffected (**Figure 1C**). Of note, for OB, delta and theta power during active periods increased over time after urethane injection and might be related to an observed augmentation of respiration amplitude. Spectral properties of full signal and active periods were quantified for delta (2–4 Hz), theta-alpha (4–12 Hz), beta (12–30 Hz) and gamma (30–100 Hz) frequency bands for the first 15 min post urethane administration, the time window of strongest reduction of active periods. In contrast to the significant reduction of full signal power in all frequency bands, the power during active periods was only marginally affected by anesthesia (**Figure 1D**). Thus, urethane anesthesia affected network activity in the immature rodent brain predominantly by decreasing the amount of active periods without perturbing the frequency structure of active periods. This is in stark contrast with the well-characterized switch from a low-amplitude high-frequency regime to a high-amplitude low-frequency regime of electrical activity that has been reported for the adult rodent and human brain (Voss and Sleight, 2007; Alkire et al., 2008).

Anesthesia was shown to induce alterations of long-range network interactions in adult rodents (Bettinardi et al., 2015) and humans (Ferrarelli et al., 2010; Lewis et al., 2012; Sarasso et al., 2015). We examined whether similar alterations are present in the immature mouse brain. Simultaneous recordings of HP and PFC, as well as OB and LEC were analyzed to assess the effects of anesthesia on long-range functional coupling. We previously showed that at the end of the first postnatal week hippocampal theta bursts drive the oscillatory entrainment of local circuits in the PFC, whereas discontinuous activity in OB controls the network activity in LEC (Brockmann et al., 2011; Ahlbeck et al., 2018; Gretenkord et al., 2019). Urethane did not modify these interactions. The synchrony within networks quantified by HP-PFC and OB-LEC coherence was similar during baseline (no urethane anesthesia) and in the presence of urethane (**Supplementary Figure S1A**). These data indicate that the core features of long-range functional coupling are retained under anesthesia in neonatal mice.

Anesthesia modified neuronal firing in all investigated areas. Firing rates in PFC, HP, LEC and OB decreased after urethane

injection and only partially recovered during the following 45 min (**Figure 1E**). However, firing rates during active periods were only marginally affected. To examine whether the timing of neuronal firing to the phase of oscillatory activity was altered by anesthesia, we calculated PPC, a firing rate-independent measure of spike-LFP phase locking (Vinck et al., 2010). All four brain regions showed similar frequency-resolved phase locking profiles before and after urethane injection (**Supplementary Figures S1B,C**).

Anesthetics have been shown to alter the excitation/inhibition balance in the adult brain through their action on specific ion channels involved in synaptic transmission (Gao et al., 2017). Such alteration is usually monitored by changes in the 1/f slope of power spectral density. Further, signal complexity and information content measured by sample entropy have been correlated with behavioral states of adults, such as consciousness, sleep/wake states and anesthesia (Liang et al., 2015; Liu et al., 2018). For neonatal mice, we observed similar values of 1/f slope and sample entropy before and during urethane anesthesia (**Supplementary Figures S1D–F**), suggesting that urethane does not perturb cortical excitation/inhibition balance and signal complexity at this early age. The findings provide additional evidence to the hypothesis that anesthesia has unique effects on the immature brain.

To add additional evidence for this hypothesis, we extended the time window of investigation and performed extracellular recordings from the PFC of juvenile mice (P24–39). At this age oscillatory activity is continuous, thus a distinction between active and inactive periods is not possible. In contrast to the frequency-unspecific reduction of active periods in neonates, urethane anesthesia increased the oscillatory power in the delta frequency band and suppressed power in beta and gamma frequency bands (**Supplementary Figure S2**), confirming the anesthetic effects in the adult brain (Alkire et al., 2008; Chauvette et al., 2011; Purdon et al., 2015).

Taken together, these results indicate that urethane anesthesia dampened neonatal brain activity mainly by augmenting the discontinuity of network activity, i.e., reducing the proportion of time the brain spent in active periods. However, the active periods were largely unaffected in their temporal structure and firing dynamics. In contrast, urethane anesthesia in older mice led to frequency-specific changes. Thus, urethane anesthesia differently impacts neonatal and adult brain activity in mice.

Suppression of Active Periods Predicts Anesthetic Concentration in Neonatal Mice

To test whether the effects of urethane on neonatal brain activity generalize to other anesthetics, we performed LFP and MUA recordings from HP and PFC of P8–10 mice at increasing doses of isoflurane-induced anesthesia (0, 1, 2 and 3%; 15 min per concentration; **Figure 2A**). Urethane hyperpolarizes neurons by potentiating a resting potassium conductance (Pagliardini et al., 2013), whereas most other anesthetics, such as isoflurane and sevoflurane, mainly act by potentiating GABA_A receptor-mediated transmission (Franks, 2006). Isoflurane reduced the incidence of active periods in a dose-dependent manner (**Figure 2B**). Accordingly, the broadband reduction of LFP power

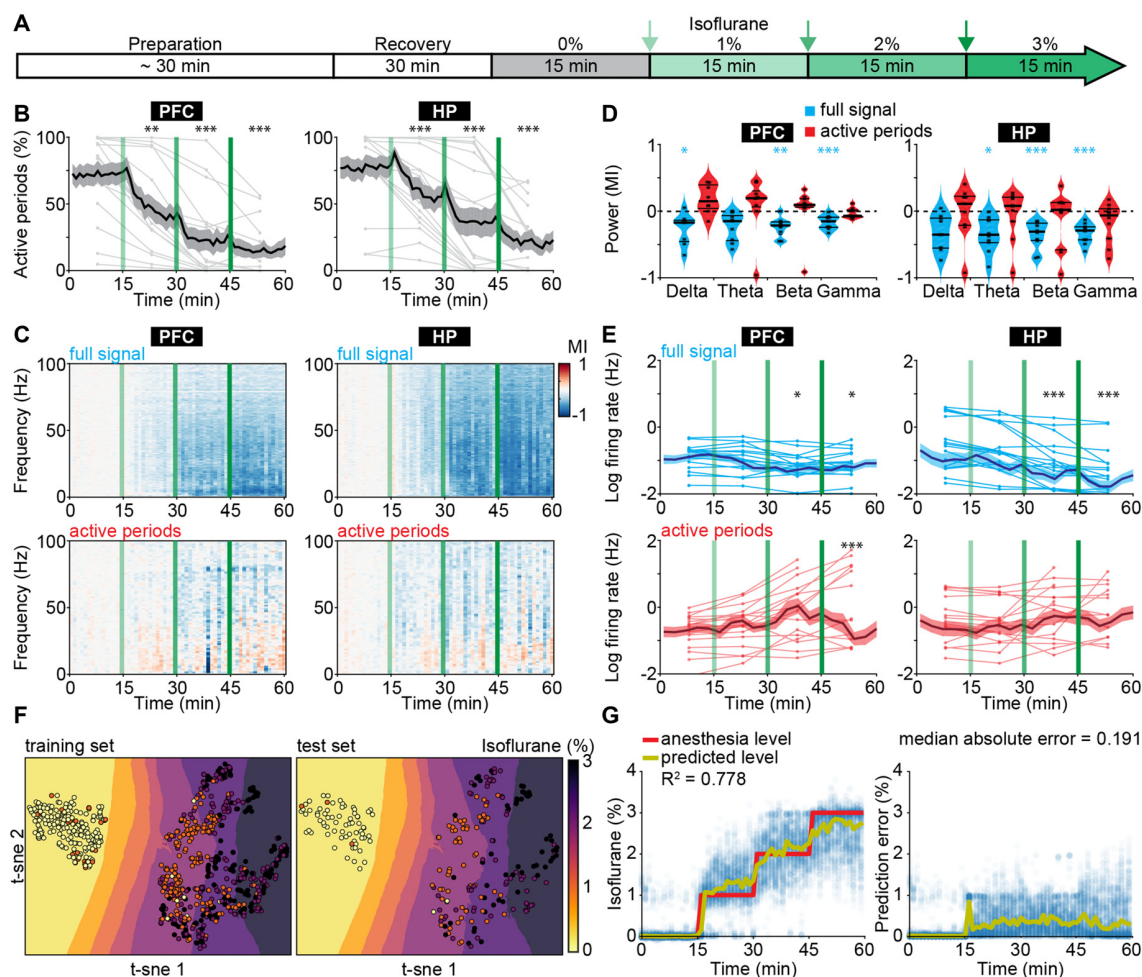


FIGURE 2 | Suppression of active periods in relationship with the depth of isoflurane anesthesia in neonatal mice. **(A)** Schematic representation of experimental protocol for LFP recordings without anesthesia and during increasing levels of isoflurane anesthesia in neonatal mice (P8–10). **(B)** Line plots displaying the relative occurrence of active periods in PFC and HP during increasing levels of isoflurane anesthesia. **(C)** Color-coded MI of power spectra for full signal (top) and active periods (bottom) during increasing levels of isoflurane anesthesia. **(D)** Violin plots displaying the MI of power in delta (2–4 Hz), theta (4–12 Hz), beta (12–30 Hz) and gamma (30–100 Hz) frequency bands for full signal (blue) and active periods (red). **(E)** Line plots displaying MUA firing rates during full signal (blue) and active periods (red). In **(B,C,E)** green lines correspond to the time points of increasing isoflurane anesthesia. **(F)** Visualization of anesthesia depth prediction by t-sne plots. Background color codes for predicted anesthesia depth, while the color of the dots represents the actual anesthesia level in the training (left) and test set (right). **(G)** Scatter plots displaying anesthesia depth predictions with support vector regression (left) and absolute errors between anesthesia depth prediction and actual anesthesia depth (right).

was also dependent on isoflurane concentration (**Figures 2C,D**). Power spectra of active periods remained largely unaffected in the presence of isoflurane, similarly to the urethane effects (**Figures 2C,D**). MUA rates during active periods in PFC and HP were hardly modified in the presence of isoflurane, yet the overall firing decreased corresponding to the reduced occurrence of active periods (**Figure 2E**). Together, these findings identify the suppression of active periods as the main effect of bolus urethane injection and isoflurane anesthesia in the neonatal mouse brain.

The development-specific response of the immature brain to anesthesia might represent the main obstacle when trying to predict anesthesia depth in infants using algorithms based on the mature brain activity of adults. Therefore, we next aimed to use electrophysiological properties specific for anesthetized

neonatal mice to predict the concentration of administered isoflurane. We used support vector regression (**Supplementary Figure S3**), with the following input features: median amplitude of broadband LFP, percent of time spent in active periods, and spectral power from 1 to 100 Hz in 10 Hz bins for both hippocampal and prefrontal activity. An additional feature was the output of a support vector classifier that received the same features as for the support vector regression, and that was designed to predict whether the animal was under anesthesia or not. The algorithm accurately predicted anesthesia depth across all levels of isoflurane concentration (**Figures 2F,G**). Estimation of information content of the different features identified the median amplitude of broadband LFP as the most informative feature (**Supplementary Figure S4A**). As the power of active

periods was only marginally affected by anesthesia, this feature mainly mirrors the suppression of active periods. Interestingly, the algorithm was also able to distinguish non-anesthetized from anesthetized recordings from neonatal mice under urethane, even though it had not been exposed to this dataset during training (**Supplementary Figure S4B**).

Thus, features of electrophysiological activity that capture the particularities of immature neuronal networks can predict anesthetic concentration in neonatal mice. The generalization of the classifier to a different anesthetic indicates that it can identify general anesthesia-related features of brain activity in neonatal mice.

Frequency-Unspecific Suppression of Activity in Anesthetized Human Neonates and Young Infants

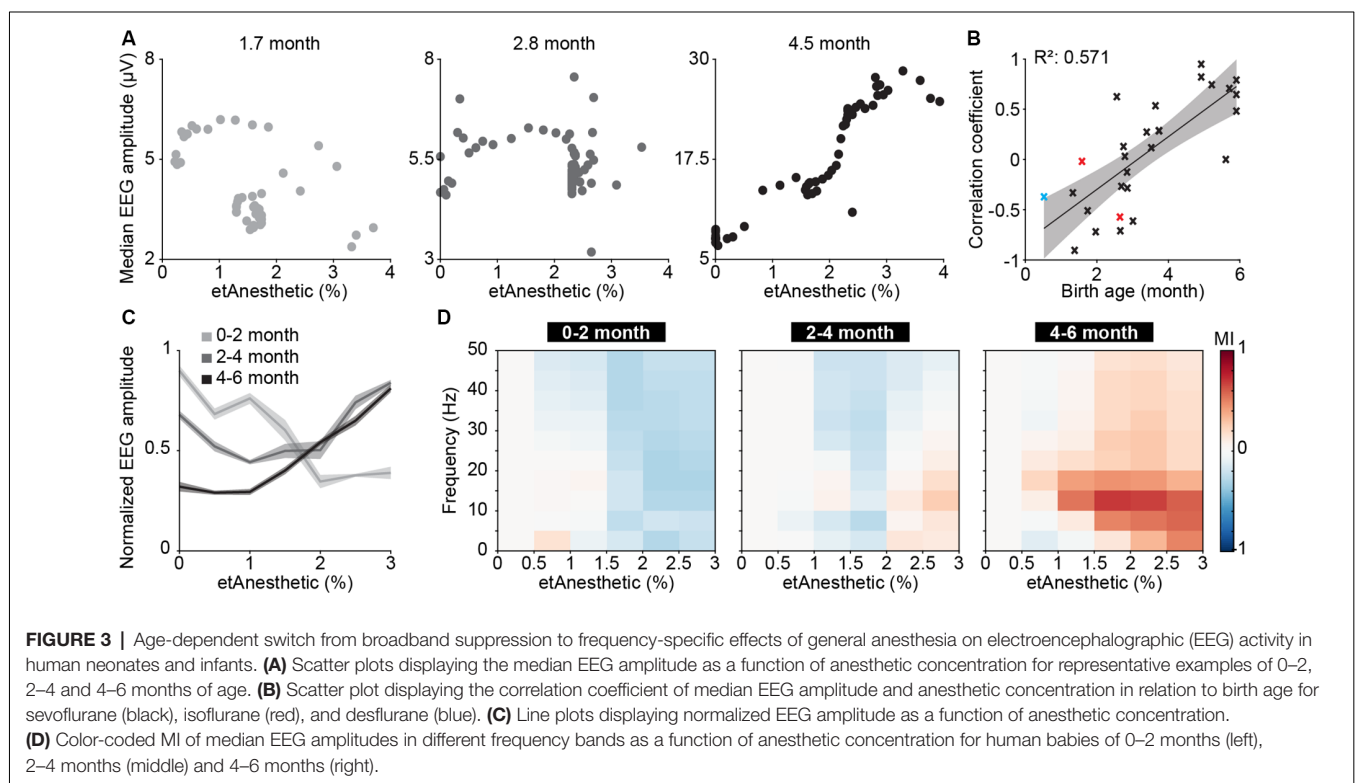
To test if human neonates and infants, similarly to mice, respond to anesthesia with a broadband decrease of periods of oscillatory activity, we examined EEG recordings from humans aged 0–6 months postnatal age, who received general anesthesia with volatile anesthetics (sevoflurane 32 subjects, isoflurane two subjects, desflurane one subject) for surgery (**Supplementary Table S1**).

In neonatal mice, the median LFP amplitude of broadband activity was identified as the most informative feature to predict anesthetic depth. We, therefore, applied the same data analysis approach to human EEG data (**Supplementary Figure S5**). We found the median amplitude of broadband EEG activity

(averaged across all recording electrodes across the scalp) was negatively correlated with end-tidal anesthetic concentration (etAnesthetic) in human neonates from birth until 2 months postnatal age (**Figures 3A,B**). For older human infants, the correlation of the median EEG amplitude with the anesthetic concentration switched to a positive correlation, in agreement with adult human data (Hagihira, 2015). This relationship was even stronger using expected birth age, corrected for conceptional age (**Supplementary Figure S6A**). This switch from negative to positive correlation was also visible in the normalized median EEG amplitude when averaged for age-grouped babies (0–2, 2–4, 4–6 months; **Figure 3C**).

Quantification of median EEG amplitude across frequencies revealed a broadband suppression of EEG activity in human neonates of 0–2 months (**Figure 3D**). In contrast, the relationship between activity amplitude and etAnesthetic indicated frequency-specificity in human infants of 2–4 and 4–6 months, as previously reported (Cornelissen et al., 2017). Frontal activity has been shown to be particularly sensitive to age-varying anesthesia-related effects in human neonates (Cornelissen et al., 2015). Analysis of only frontal electrodes (Fp1, Fp2, F3, F4, F7, F8, Fpz) showed the same age-dependent anesthesia-induced changes as analysis of full scalp electrodes (**Supplementary Figures S6B–D**).

Thus, analogous to what we found in neonatal mice, general anesthesia in human infants younger than 2 months suppressed neuronal population activity, as reported previously (Cornelissen et al., 2015), while at older age anesthesia induced frequency-specific effects.



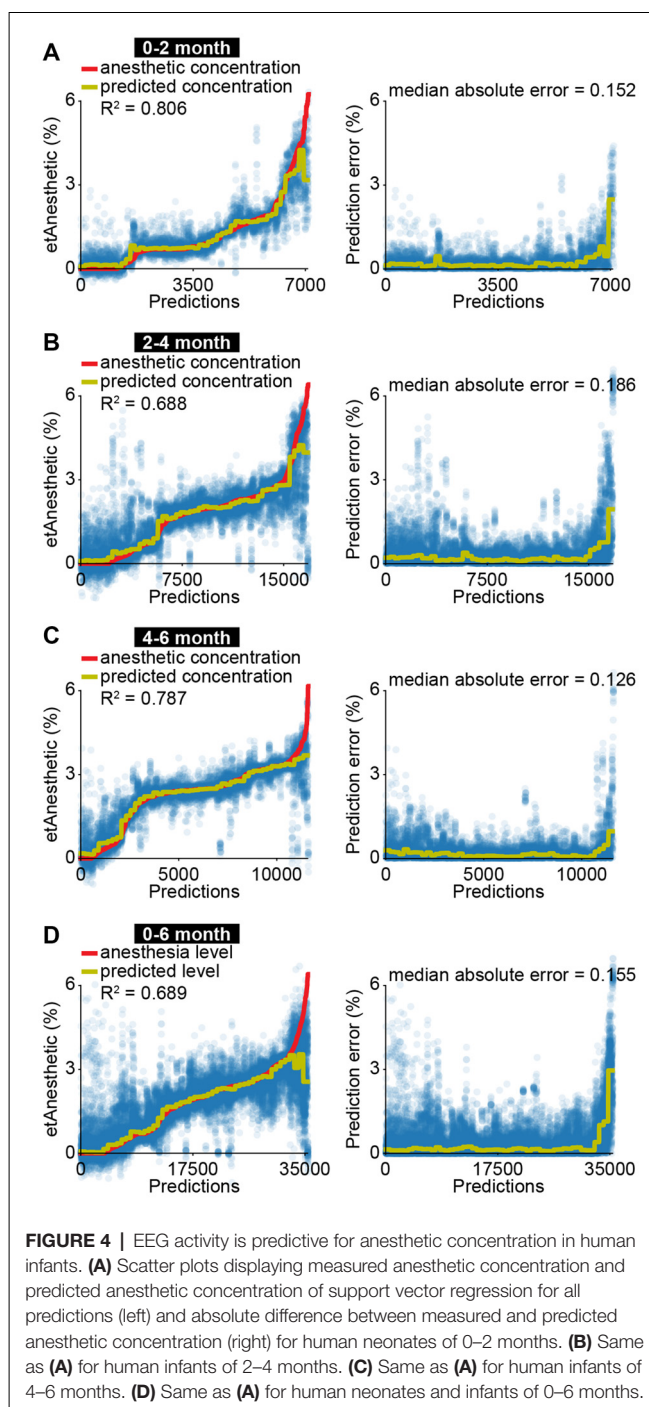
A Model to Predict End-Tidal Volume of Sevoflurane Anesthesia in Human Neonates and Infants

The correlation of EEG activity with etAnesthetic as well as the similar effects of anesthesia in neonatal mice and in humans from birth to 2 months old, suggests that anesthetic depth in babies might be predicted using similar features to those used in neonatal mice. To test this, we used a machine-learning algorithm with a similar architecture as the one we developed for neonatal mice (**Supplementary Figure S3**). The algorithm was modified to account for the developmental switch from broadband suppression to frequency-specific modulation by training three different regressors using 2 and 4 months as cut-offs. All regressors received the same input features (see “Materials and Methods” section and **Supplementary Figure S5**). Features derived from EEG activity were able to predict etAnesthetic with high accuracy for all age groups (0–2 months $R^2 = 0.806$, 2–4 months $R^2 = 0.688$, 4–6 months $R^2 = 0.787$; **Figures 4A–C**). In line with the frequency-specific alterations observed only in the older age groups, frequency-related features were rated more important for prediction of anesthesia depth in infants of 2–4 and 4–6 months than in neonates of 0–2 months (**Supplementary Figures S7A–C**). Predicting anesthesia depth for all ages with a single classifier considering age as an input feature performed with high accuracy (0–6 months $R^2 = 0.689$; **Figure 4D**, **Supplementary Figure S7D**). Training the predictor with only 20% of the data and testing it on the remaining 80% resulted in a reduced, but still solid prediction ($R^2 = 0.512$, median absolute error = 0.209) indicating the robustness of the predictor (**Supplementary Figure S8A**). This result confirms the age-varying effects of anesthesia on the brain and stresses the importance of considering age when developing algorithms aiming to assess anesthetic depth. Predicting anesthesia depth with a reduced number of four EEG channels (F4, P4, F3, P3) or two EEG channels (P4, P3) often used for long-term monitoring yielded similar results (four channels $R^2 = 0.713$, median absolute error = 0.134; two channels $R^2 = 0.671$, median absolute error = 0.161; **Supplementary Figures S8B,C**).

Thus, mouse and human neonates show similar changes in network activity in response to anesthesia. These results highlight how neurophysiological activity could be beneficial for future attempts at predicting anesthetic depth in clinical settings.

DISCUSSION

Monitoring brain function during anesthesia is desirable to avoid intraoperative awareness and side effects resulting from unnecessarily high doses of anesthetics. Since consciousness is an elusive concept and cannot be directly measured, EEG features have been used to guide anesthesia delivery during human surgery. Monitoring methods developed for adults perform poorly in human neonates and infants, particularly during the first months of life (Davidson et al., 2005; Hayashi et al., 2012; Poorun et al., 2016; Koch et al., 2017). Age-specific effects of anesthetics on immature brain activity are considered



the main reason for such poor performance. Implementation of neonate- and infant-specific anesthesia monitors requires elucidation of distinct anesthesia-induced EEG features during early development. We took advantage of a translational approach to address this open question. We first carried out an in-depth investigation of anesthetic effects on brain activity in neonatal mice, and then applied this knowledge to develop features that would correlate with an anesthetic concentration in human neonates.

In contrast to the continuous EEG signal observed in adults, neonatal EEG around birth is characterized by a highly discontinuous and fragmented temporal organization, with bursts of cerebral activity (active periods) alternating with interburst intervals lacking activity (silent periods; Anderson et al., 1985; Connell et al., 1987; Stockard-Pope et al., 1992; Lamblin et al., 1999; Vecchierini et al., 2003, 2007; Stevenson et al., 2017). Neonatal mice show a similar discontinuous organization of cortical activity (Khazipov et al., 2004; Hanganu et al., 2006; Brockmann et al., 2011). In accordance with the similar organization of early activity patterns in age-matched mouse pups and human infants, we found comparable effects of anesthesia on LFP and EEG signals, respectively.

It is well established that in the adult rodent and human brain most anesthetics favor slow oscillations at the expense of faster ones, thereby slowing the EEG rhythm (Alkire et al., 2008; Chauvette et al., 2011; Purdon et al., 2015). This principle is thought to underlie most algorithms that are clinically used to predict anesthesia depth (Davidson et al., 2005). Indeed, such algorithms perform poorly with anesthetics, such as ketamine, that do not share this mechanism of action (Hans et al., 2005). In line with previous studies (Ackman et al., 2014; Kirmse et al., 2015), we report that both urethane and isoflurane anesthesia affect brain activity in a different way in neonatal mice. Instead of favoring slow oscillations at the expense of faster ones, anesthesia in neonatal mice broadly suppresses activity in a frequency-unspecific manner. The dampening of cortical activity for human infants of 0–2 months suggests a development specific effect of anesthesia on immature brain activity that translates between mice and humans.

In rodents, the switch from activity suppression to frequency-specific modulation of neuronal activity by anesthesia has been reported to occur around P12 (Ackman et al., 2014). This coincides with the emergence of slow oscillations during sleep, suggested to depend on the maturation of thalamocortical networks (Steriade et al., 1993; Ackman et al., 2014). Consistent with our previous studies evaluating EEG properties of this data set, we found that theta and alpha oscillatory activity under anesthesia emerges in humans at around 4 months postnatal age (Cornelissen et al., 2015, 2017, 2018a). Developmental changes in the brain explain the changes in EEG dynamics that occur with postnatal age. In humans, gross brain development occurs in a caudal to rostral direction, with myelination of the medulla, pons, and thalamus starting within the first few postnatal weeks, and frontal cortex myelination starting around 3–4 postnatal months (Brody et al., 1987; Kinney et al., 1988). Regional differences in the rate of synaptogenesis, glucose metabolism and myelination across the cortex occur between subcortical and cortical regions, and between different regions of the cortex during the first 12 postnatal months in human infants (Huttenlocher and Dabholkar, 1997; Tau and Peterson, 2010; Dehorter et al., 2012; Catts et al., 2013; Semple et al., 2013; Murata and Colonnese, 2019). A key role in brain development is played by subplate neurons, the first neurons generated in the cerebral cortex, which guide the formation of thalamocortical connections (Kanold and Luhmann, 2010; Kostović and Judas, 2010). The subplate cells form the first functional connections

and relay oscillatory activity in the developing brain (Kanold and Luhmann, 2010). Alpha oscillations in the anesthetized brain are postulated to be produced by thalamocortical circuits, and the gradual emergence of highly powered alpha oscillations at 4-months of age suggests an important developmental milestone has been reached in the processes guided by the subplate neurons. Future studies with a wider age range in mice and humans, including data of human infants studied at preterm, and children in older than 6 months of age, may deepen the understanding of anesthetic effects on brain activity throughout development.

The anesthetics evaluated across species in this study were comparable but not identical in terms of mechanism of action. Moreover, anesthetic management practices used in mice were simplified compared to commonly-used anesthetic practices in the clinic. Multimodal anesthesia requires the use of low-dose anesthetics in combination with analgesic and neuromuscular blocking agents to provide optimal anesthesia and reduce the side effect. These agents act on different drug targets in the nervous system and may have subtle but different effects on brain oscillatory activity (Brown et al., 2018).

In adult human volunteers, the correlation with anesthetic depth and EEG parameters can be performed using verbal reports to establish a threshold for unconsciousness (Purdon et al., 2015). However, in non-verbal populations such as human infants, one must rely on indirect behavioral measures which are more readily performed on emergence rather than induction and incision (Cornelissen et al., 2018b). Future investigations need to include surgical incision and other stimuli into the mouse models to understand with greater granularity the anesthetic titration around the minimal concentrations required to suppress movement, autonomic, and cortical responses to noxious stimuli.

In summary, we report that the suppression of brain activity in mouse and human neonates correlates with anesthetic concentration. The detailed understanding of anesthesia effects on network activity in mice allowed us to identify features and develop a machine-learning algorithm that is able to predict anesthetic concentration from EEG recordings in human neonates. We propose that, after appropriate training, an algorithm based on what we introduce here could learn to associate specific EEG effects with certain anesthetic doses. Eventual mismatches between administered and predicted anesthetic dose would then identify patients that are particularly sensitive/insensitive to an anesthetic, thus helping the anesthetist in administering appropriate levels of anesthetics. By these means, the risk of adverse neurodevelopmental outcome might be mitigated.

ETHICS STATEMENT

All animal experiments were performed in compliance with the German laws and the guidelines of the European Community for the use of animals in research and were approved by the local ethical committee (G132/12, G17/015, N18/015). Human neonates and infants who were scheduled for an elective surgical procedure were recruited from the pre-operative clinic at Boston Children's Hospital from 12/2012 to 08/2018 (under Institutional

Review Board P-3544, with written informed consent obtained from parents/legal guardians).

AUTHOR CONTRIBUTIONS

MC, SB and IH-O designed the experiments. MC, SB, SG, JK, JP, and LC carried out the experiments. MC, SB, SG, JK and JP analyzed the data. MC, SB, LC, CB and IH-O interpreted the data and wrote the article. All authors discussed and commented on the manuscript.

FUNDING

This work was funded by grants from the European Research Council (ERC-2015-CoG 681577 to IH-O), the German Research

Foundation (Ha 4466/10-1, SPP 1665, SFB 936 B5 to IH-O) and the International Anesthesia Research Society (to LC). IH-O is a founding member of FENS Kavli Network of Excellence. This manuscript has been released as a Pre-Print at BioRxiv.

ACKNOWLEDGMENTS

We thank P. Putthoff, A. Marquardt, A. Dahlmann, and K. Titze for excellent technical assistance.

SUPPLEMENTARY MATERIAL

The Supplementary Material for this article can be found online at: <https://www.frontiersin.org/articles/10.3389/fncir.2019.00038/full#supplementary-material>

REFERENCES

- Ackman, J. B., Zeng, H., and Crair, M. C. (2014). Structured dynamics of neural activity across developing neocortex. *BioRxiv* [Preprint]. doi: 10.1101/012237
- Ahlbeck, J., Song, L., Chini, M., Bitzenhofer, S. H., and Hanganu-Opatz, I. L. (2018). Glutamatergic drive along the septo-temporal axis of hippocampus boosts prelimbic oscillations in the neonatal mouse. *Elife* 7:e33158. doi: 10.7554/eLife.33158
- Alkire, M. T., Hudetz, A. G., and Tononi, G. (2008). Consciousness and anesthesia. *Science* 322, 876–880. doi: 10.1126/science.1149213
- Anderson, C. M., Torres, F., and Faoro, A. (1985). The EEG of the early premature. *Electroencephalogr. Clin. Neurophysiol.* 60, 95–105. doi: 10.1016/0013-4694(85)90015-X
- Bettinardi, R. G., Tort-Colet, N., Ruiz-Mejias, M., Sanchez-Vives, M. V., and Deco, G. (2015). Gradual emergence of spontaneous correlated brain activity during fading of general anesthesia in rats: evidences from fMRI and local field potentials. *Neuroimage* 114, 185–198. doi: 10.1016/j.neuroimage.2015.03.037
- Bitzenhofer, S. H., Ahlbeck, J., Wolff, A., Wiegert, J. S., Gee, C. E., Oertner, T. G., et al. (2017). Layer-specific optogenetic activation of pyramidal neurons causes beta-gamma entrainment of neonatal networks. *Nat. Commun.* 8:14563. doi: 10.1038/ncomms14563
- Brockmann, M. D., Pöschel, B., Cichon, N., and Hanganu-Opatz, I. L. (2011). Coupled oscillations mediate directed interactions between prefrontal cortex and hippocampus of the neonatal rat. *Neuron* 71, 332–347. doi: 10.1016/j.neuron.2011.05.041
- Brody, B. A., Kinney, H. C., Kroman, A. S., and Gilles, F. H. (1987). Sequence of central-nervous-system myelination in human infancy: I. An autopsy study of myelination. *J. Neuropath. Exp. Neurol.* 46, 283–301. doi: 10.1097/00005072-198705000-00005
- Brown, E. N., Pavone, K. J., and Naranjo, M. (2018). Multimodal general anesthesia: theory and practice. *Anesth. Analg.* 127, 1246–1258. doi: 10.1213/ANE.0000000000003668
- Catts, V. S., Fung, S. J., Long, L. E., Joshi, D., Vercammen, A., Allen, K. M., et al. (2013). Rethinking schizophrenia in the context of normal neurodevelopment. *Front. Cell. Neurosci.* 7:60. doi: 10.3389/fncel.2013.00060
- Chang, P. S., Walker, S. M., and Fitzgerald, M. (2016). Differential suppression of spontaneous and noxious-evoked somatosensory cortical activity by isoflurane in the neonatal rat. *Anesthesiology* 124, 885–898. doi: 10.1097/ALN.0000000000001017
- Chauvette, S., Crochet, S., Volgushev, M., and Timofeev, I. (2011). Properties of slow oscillation during slow-wave sleep and anesthesia in cats. *J. Neurosci.* 31, 14998–15008. doi: 10.1523/JNEUROSCI.2339-11.2011
- Cichon, N. B., Denker, M., Grün, S., and Hanganu-Opatz, I. L. (2014). Unsupervised classification of neocortical activity patterns in neonatal and pre-juvenile rodents. *Front. Neural Circuits* 8:50. doi: 10.3389/fncir.2014.00050
- Colonnese, M. T., and Khazipov, R. (2010). “Slow activity transients” in infant rat visual cortex: a spreading synchronous oscillation patterned by retinal waves. *J. Neurosci.* 30, 4325–4337. doi: 10.1523/JNEUROSCI.4995-09.2010
- Connell, J. A., Oozer, R., and Dubowitz, V. (1987). Continuous 4-channel EEG monitoring: a guide to interpretation, with normal values, in preterm infants. *Neuropediatrics* 18, 138–145. doi: 10.1055/s-2008-1052466
- Cornelissen, L., Bergin, A. M., Lobo, K., Donado, C., Soul, J. S., and Berde, C. B. (2017). Electroencephalographic discontinuity during sevoflurane anesthesia in infants and children. *Paediatr. Anaesth.* 27, 251–262. doi: 10.1111/pan.13061
- Cornelissen, L., Donado, C., Lee, J. M., Liang, N. E., Mills, I., Tou, A., et al. (2018a). Clinical signs and electroencephalographic patterns of emergence from sevoflurane anaesthesia in children: an observational study. *Eur. J. Anaesthesiol.* 35, 49–59. doi: 10.1097/EJA.0000000000000739
- Cornelissen, L., Kim, S. E., Lee, J. M., Brown, E. N., Purdon, P. L., and Berde, C. B. (2018b). Electroencephalographic markers of brain development during sevoflurane anaesthesia in children up to 3 years old. *Br. J. Anaesth.* 120, 1274–1286. doi: 10.1016/j.bja.2018.01.037
- Cornelissen, L., Kim, S. E., Purdon, P. L., Brown, E. N., and Berde, C. B. (2015). Age-dependent electroencephalogram (EEG) patterns during sevoflurane general anesthesia in infants. *Elife* 4:e06513. doi: 10.7554/eLife.06513
- Davidson, A. J., Huang, G. H., Rebmann, C. S., and Ellery, C. (2005). Performance of entropy and bispectral index as measures of anaesthesia effect in children of different ages. *Br. J. Anaesth.* 95, 674–679. doi: 10.1093/bja/aei247
- Dehorter, N., Vinay, L., Hammond, C., and Ben-Ari, Y. (2012). Timing of developmental sequences in different brain structures: physiological and pathological implications. *Eur. J. Neurosci.* 35, 1846–1856. doi: 10.1111/j.1460-9568.2012.08152.x
- Ferrarelli, F., Massimini, M., Sarasso, S., Casali, A., Riedner, B. A., Angelini, G., et al. (2010). Breakdown in cortical effective connectivity during midazolam-induced loss of consciousness. *Proc. Natl. Acad. Sci. U S A* 107, 2681–2686. doi: 10.1073/pnas.0913008107
- Franks, N. P. (2006). Molecular targets underlying general anaesthesia. *Br. J. Pharmacol.* 147, S72–S81. doi: 10.1038/sj.bjp.0706441
- Gao, R., Peterson, E. J., and Voytek, B. (2017). Inferring synaptic excitation/inhibition balance from field potentials. *Neuroimage* 158, 70–78. doi: 10.1016/j.neuroimage.2017.06.078
- Glass, P. S., Bloom, M., Kears, L., Rosow, C., Sebel, P., and Manberg, P. (1997). Bispectral analysis measures sedation and memory effects of propofol, midazolam, isoflurane and alfentanil in healthy volunteers. *Anesthesiology* 86, 836–847. doi: 10.1097/0000542-199704000-00014
- Gretenkord, S., Kostka, J. K., Hartung, H., Watznauer, K., Fleck, D., Minier-Toribio, A., et al. (2019). Coordinated electrical activity in the olfactory bulb

- gates the oscillatory entrainment of entorhinal networks in neonatal mice. *PLoS Biol.* 17:e2006994. doi: 10.1371/journal.pbio.2006994
- Hagihira, S. (2015). Changes in the electroencephalogram during anaesthesia and their physiological basis. *Br. J. Anaesth.* 115, i27–i31. doi: 10.1093/bja/aev212
- Hajat, Z., Ahmad, N., and Andrzejowski, J. (2017). The role and limitations of EEG-based depth of anaesthesia monitoring in theatres and intensive care. *Anaesthesia* 72, 38–47. doi: 10.1111/anae.13739
- Hanganu, I. L., Ben-Ari, Y., and Khazipov, R. (2006). Retinal waves trigger spindle bursts in the neonatal rat visual cortex. *J. Neurosci.* 26, 6728–6736. doi: 10.1523/JNEUROSCI.0752-06.2006
- Hans, P., Dewandre, P. Y., Brichant, J. F., and Bonhomme, V. (2005). Comparative effects of ketamine on bispectral index and spectral entropy of the electroencephalogram under sevoflurane anaesthesia. *Br. J. Anaesth.* 94, 336–340. doi: 10.1093/bja/aei047
- Hayashi, K., Shigemi, K., and Sawa, T. (2012). Neonatal electroencephalography shows low sensitivity to anesthesia. *Neurosci. Lett.* 517, 87–91. doi: 10.1016/j.neulet.2012.04.028
- Huh, Y., and Cho, J. (2013). Urethane anesthesia depresses activities of thalamocortical neurons and alters its response to nociception in terms of dual firing modes. *Front. Behav. Neurosci.* 7:141. doi: 10.3389/fnbeh.2013.00141
- Huttenlocher, P. R., and Dabholkar, A. S. (1997). Regional differences in synaptogenesis in human cerebral cortex. *J. Comp. Neurol.* 387, 167–178. doi: 10.1002/(sici)1096-9861(19971020)387:2<167::aid-cne1>3.0.co;2-z
- Kalkman, C. J., Peelen, L. M., and Moons, K. G. (2011). Pick up the pieces: depth of anesthesia and long-term mortality. *Anesthesiology* 114, 485–487. doi: 10.1097/ALN.0b013e31820c2ba2
- Kanold, P. O., and Luhmann, H. J. (2010). The subplate and early cortical circuits. *Annu. Rev. Neurosci.* 33, 23–48. doi: 10.1146/annurev-neuro-060909-153244
- Kertai, M. D., Whitlock, E. L., and Avidan, M. S. (2012). Brain monitoring with electroencephalography and the electroencephalogram-derived bispectral index during cardiac surgery. *Anesth. Analg.* 114, 533–546. doi: 10.1213/ANE.0b013e31823ee030
- Khazipov, R., Sirota, A., Leinekugel, X., Holmes, G. L., Ben-Ari, Y., and Buzsáki, G. (2004). Early motor activity drives spindle bursts in the developing somatosensory cortex. *Nature* 432, 758–761. doi: 10.1038/nature03132
- Kinney, H. C., Brody, B. A., Kloman, A. S., and Gilles, F. H. (1988). Sequence of Central Nervous-System Myelination in Human Infancy .2. Patterns of Myelination in Autopsied Infants. *J. Neuropathol. Exp. Neurol.* 47, 217–234. doi: 10.1097/00005072-198805000-00003
- Kirmse, K., Kummer, M., Kovalchuk, Y., Witte, O. W., Garaschuk, O., and Holthoff, K. (2015). GABA depolarizes immature neurons and inhibits network activity in the neonatal neocortex *in vivo*. *Nat. Commun.* 6:7750. doi: 10.1038/ncomms8750
- Koch, S., Stegherr, A. M., Morgeli, R., Kramer, S., Toubekis, E., Lichtner, G., et al. (2017). Electroencephalogram dynamics in children during different levels of anaesthetic depth. *Clin. Neurophysiol.* 128, 2014–2021. doi: 10.1016/j.clinph.2017.07.417
- Kostović, I., and Judas, M. (2010). The development of the subplate and thalamocortical connections in the human foetal brain. *Acta Paediatr.* 99, 1119–1127. doi: 10.1111/j.1651-2227.2010.01811.x
- Kreuzer, M. (2017). EEG based monitoring of general anesthesia: taking the next steps. *Front. Comput. Neurosci.* 11:56. doi: 10.3389/fncom.2017.00056
- Lamblin, M. D., André, M., Challamel, M. J., Curzi-Dascalova, L., d'Allest, A. M., De Giovanni, E., et al. (1999). Electroencephalography of the premature and term newborn. Maturational aspects and glossary. *Neurophysiol. Clin.* 29, 123–219. doi: 10.1016/S0987-7053(99)80051-3
- Lewis, L. D., Weiner, V. S., Mukamel, E. A., Donoghue, J. A., Eskandar, E. N., Madsen, J. R., et al. (2012). Rapid fragmentation of neuronal networks at the onset of propofol-induced unconsciousness. *Proc. Natl. Acad. Sci. U S A* 109, E3377–E3386. doi: 10.1073/pnas.1210907109
- Liang, Z., Wang, Y., Sun, X., Li, D., Voss, L. J., Sleight, J. W., et al. (2015). EEG entropy measures in anesthesia. *Front. Comput. Neurosci.* 9:16. doi: 10.3389/fncom.2015.00016
- Liu, Q., Ma, L., Fan, S. Z., Abbod, M. F., and Shieh, J. S. (2018). Sample entropy analysis for the estimating depth of anaesthesia through human EEG signal at different levels of unconsciousness during surgeries. *PeerJ* 6:e4817. doi: 10.7717/peerj.4817
- Lo, S. S., Sobol, J. B., Mallavaram, N., Carson, M., Chang, C., Grieve, P. G., et al. (2009). Anesthetic-specific electroencephalographic patterns during emergence from sevoflurane and isoflurane in infants and children. *Paediatr. Anaesth.* 19, 1157–1165. doi: 10.1111/j.1460-9592.2009.03128.x
- Migut, M. A., Worring, M., and Veenman, C. J. (2015). Visualizing multi-dimensional decision boundaries in 2D. *Data Min. Knowl. Discov.* 29, 273–295. doi: 10.1007/s10618-013-0342-x
- Milh, M., Kaminska, A., Huon, C., Lapillonne, A., Ben-Ari, Y., and Khazipov, R. (2007). Rapid cortical oscillations and early motor activity in premature human neonate. *Cereb. Cortex* 17, 1582–1594. doi: 10.1093/cercor/bhl069
- Murata, Y., and Colonnese, M. T. (2019). Thalamic inhibitory circuits and network activity development. *Brain Res.* 1706, 13–23. doi: 10.1016/j.brainres.2018.10.024
- Nolte, G., Bai, O., Wheaton, L., Mari, Z., Vorbach, S., and Hallett, M. (2004). Identifying true brain interaction from EEG data using the imaginary part of coherency. *Clin. Neurophysiol.* 115, 2292–2307. doi: 10.1016/j.clinph.2004.04.029
- O'Toole, J. M., Boylan, G. B., Vanhatalo, S., and Stevenson, N. J. (2016). Estimating functional brain maturity in very and extremely preterm neonates using automated analysis of the electroencephalogram. *Clin. Neurophysiol.* 127, 2910–2918. doi: 10.1016/j.clinph.2016.02.024
- Pagliardini, S., Funk, G. D., and Dickson, C. T. (2013). Breathing and brain state: urethane anesthesia as a model for natural sleep. *Respir. Physiol. Neurobiol.* 188, 324–332. doi: 10.1016/j.resp.2013.05.035
- Poorun, R., Hartley, C., Goksan, S., Worley, A., Boyd, S., Cornelissen, L., et al. (2016). Electroencephalography during general anaesthesia differs between term-born and premature-born children. *Clin. Neurophysiol.* 127, 1216–1222. doi: 10.1016/j.clinph.2015.10.041
- Pritchep, L. S., Gugino, L. D., John, E. R., Chabot, R. J., Howard, B., Merkin, H., et al. (2004). The patient state index as an indicator of the level of hypnosis under general anaesthesia. *Br. J. Anaesth.* 92, 393–399. doi: 10.1093/bja/aeh082
- Punjasawadwong, Y., Phongchiewboon, A., and Bunchungmongkol, N. (2014). Bispectral index for improving anaesthetic delivery and postoperative recovery. *Cochrane Database Syst. Rev.* 6:CD003843. doi: 10.1002/14651858.CD003843
- Purdon, P. L., Sampson, A., Pavone, K. J., and Brown, E. N. (2015). Clinical electroencephalography for anesthesiologists: Part I: background and basic signatures. *Anesthesiology* 123, 937–960. doi: 10.1097/ALN.0000000000000841
- Sarasso, S., Boly, M., Napolitani, M., Gosseries, O., Charland-Verville, V., Casarotto, S., et al. (2015). Consciousness and complexity during unresponsiveness induced by propofol, Xenon and Ketamine. *Curr. Biol.* 25, 3099–3105. doi: 10.1016/j.cub.2015.10.014
- Semple, B. D., Blomgren, K., Gimlin, K., Ferriero, D. M., and Noble-Haeusslein, L. J. (2013). Brain development in rodents and humans: identifying benchmarks of maturation and vulnerability to injury across species. *Prog. Neurobiol.* 106–107, 1–16. doi: 10.1016/j.pneurobio.2013.04.001
- Steriade, M., Nuñez, A., and Amzica, F. (1993). Intracellular analysis of relations between the slow (<1 Hz) neocortical oscillation and other sleep rhythms of the electroencephalogram. *J. Neurosci.* 13, 3266–3283. doi: 10.1523/jneurosci.13-08-03266.1993
- Stevenson, N. J., Oberdorfer, L., Koolen, N., O'Toole, J. M., Werther, T., Klebermass-Schrehof, K., et al. (2017). Functional maturation in preterm infants measured by serial recording of cortical activity. *Sci. Rep.* 7:12969. doi: 10.1038/s41598-017-13537-3
- Stockard-Pope, J. E., Werner, S. S., and Bickford, R. G. (1992). *Atlas of Neonatal Electroencephalography*. New York, NY: Raven Press.
- Stolwijk, L. J., Weeke, L. C., de Vries, L. S., van Herwaarden, M. Y. A., van der Zee, D. C., van der Werff, D. B. M., et al. (2017). Effect of general anesthesia on neonatal aEEG-A cohort study of patients with non-cardiac

- congenital anomalies. *PLoS One* 12:e0183581. doi: 10.1371/journal.pone.0183581
- Tau, G. Z., and Peterson, B. S. (2010). Normal development of brain circuits. *Neuropsychopharmacology* 35, 147–168. doi: 10.1038/npp.2009.115
- Vecchierini, M. F., André, M., and d'Allest, A. M. (2007). Normal EEG of premature infants born between 24 and 30 weeks gestational age: terminology, definitions and maturation aspects. *Neurophysiol. Clin.* 37, 311–323. doi: 10.1016/j.neucli.2007.10.008
- Vecchierini, M. F., d'Allest, A. M., and Verpillat, P. (2003). EEG patterns in 10 extreme premature neonates with normal neurological outcome: qualitative and quantitative data. *Brain Dev.* 25, 330–337. doi: 10.1016/s0387-7604(03)00007-x
- Vinck, M., van Wingerden, M., Womelsdorf, T., Fries, P., and Pennartz, C. M. (2010). The pairwise phase consistency: a bias-free measure of rhythmic neuronal synchronization. *Neuroimage* 51, 112–122. doi: 10.1016/j.neuroimage.2010.01.073
- Voss, L., and Sleigh, J. (2007). Monitoring consciousness: the current status of EEG-based depth of anaesthesia monitors. *Best Pract. Res. Clin. Anaesthesiol.* 21, 313–325. doi: 10.1016/j.bpa.2007.04.003

Conflict of Interest Statement: The authors declare that the research was conducted in the absence of any commercial or financial relationships that could be construed as a potential conflict of interest.

Copyright © 2019 Chini, Gretenkord, Kostka, Pöpplau, Cornelissen, Berde, Hanganu-Opatz and Bitzenhofer. This is an open-access article distributed under the terms of the Creative Commons Attribution License (CC BY). The use, distribution or reproduction in other forums is permitted, provided the original author(s) and the copyright owner(s) are credited and that the original publication in this journal is cited, in accordance with accepted academic practice. No use, distribution or reproduction is permitted which does not comply with these terms.



Microglia Regulate Pruning of Specialized Synapses in the Auditory Brainstem

Giedre Milinkeviciute¹, Caden M. Henningfield¹, Michael A. Muniak^{2,3,4}, Sima M. Chokr¹, Kim N. Green¹ and Karina S. Cramer^{1*}

¹ Department of Neurobiology and Behavior, University of California, Irvine, Irvine, CA, United States, ² Vollum Institute, Oregon Health & Science University, Portland, OR, United States, ³ Hearing Research, Garvan Institute of Medical Research, Sydney, NSW, Australia, ⁴ St Vincent's Clinical School, UNSW Sydney, Sydney, NSW, Australia

OPEN ACCESS

Edited by:

Catherine Carr,
University of Maryland, College Park,
United States

Reviewed by:

José M. Juiz,
Universidad de Castilla-La Mancha,
Spain
Diasynou Fioravante,
University of California, Davis,
United States

*Correspondence:

Karina S. Cramer
cramerks@uci.edu

Received: 17 May 2019

Accepted: 30 July 2019

Published: 28 August 2019

Citation:

Milinkeviciute G, Henningfield CM, Muniak MA, Chokr SM, Green KN and Cramer KS (2019) Microglia Regulate Pruning of Specialized Synapses in the Auditory Brainstem. *Front. Neural Circuits* 13:55. doi: 10.3389/fncir.2019.00055

The assembly of uniquely organized sound localization circuits in the brainstem requires precise developmental mechanisms. Glial cells have been shown to shape synaptic connections in the retinogeniculate system during development, but their contributions to specialized auditory synapses have not been identified. Here we investigated the role of microglia in auditory brainstem circuit assembly, focusing on the formation and pruning of the calyx of Held in the medial nucleus of the trapezoid body (MNTB). Microglia were pharmacologically depleted in mice early in development using subcutaneous injections of an inhibitor of colony stimulating factor 1 receptor, which is essential for microglia survival. Brainstems were examined prior to and just after hearing onset, at postnatal days (P) 8 and P13, respectively. We found that at P13 there were significantly more polyinnervated MNTB neurons when microglia were depleted, consistent with a defect in pruning. Expression of glial fibrillary acidic protein (GFAP), a mature astrocyte marker that normally appears in the MNTB late in development, was significantly decreased in microglia-depleted mice at P13, suggesting a delay in astrocyte maturation. Our results demonstrate that monoinnervation of MNTB neurons by the calyx of Held is significantly disrupted or delayed in the absence of microglia. This finding may reflect a direct role for microglia in synaptic pruning. A secondary role for microglia may be in the maturation of astrocytes in MNTB. These findings highlight the significant function of glia in pruning during calyx of Held development.

Keywords: microglia, calyx of Held, MNTB, pruning, auditory brainstem, CSF1R inhibitors, depletion

INTRODUCTION

Binaural cues used for sound localization are initially processed in auditory brainstem circuits that require speed and reliability (Trussell, 1999). Accordingly, these pathways display specialized synapses. A key component is the calyx of Held (1893), the large, encapsulating excitatory axon terminal of globular bushy cells (GBC) in the anteroventral cochlear nucleus (AVCN) that terminates in the contralateral medial nucleus of the trapezoid body (MNTB; Morest, 1968; Smith et al., 1991; Kandler and Friauf, 1993). This synapse possesses several hundred active sites and

a large readily releasable pool of synaptic vesicles that allow for fast, sustained, and precise signaling to MNTB neurons (Borst and Sakmann, 1996; Taschenberger et al., 2002).

Medial nucleus of the trapezoid body neurons also receive other excitatory inputs such as collaterals of spherical bushy cells (Cant and Casseday, 1986), GBCs (Hamann et al., 2003), or descending input from higher auditory structures (Kuwabara et al., 1991) as well as inhibitory inputs (Albrecht et al., 2014). The MNTB is a sign-inverting relay nucleus that sends glycinergic inhibitory projections to several auditory brainstem nuclei, including the lateral superior olive (LSO; Kuwabara and Zook, 1991; Tollin, 2003) and medial superior olive (MSO; Spangler et al., 1985; Kuwabara and Zook, 1992) on the same side. The LSO also receives frequency-matched excitatory input from the ipsilateral AVCN (Sanes, 1990; Glendenning et al., 1992) and uses the balance of inhibitory MNTB and excitatory VCN inputs to compute interaural intensity differences used in sound localization (Figure 1A; Tollin, 2003; Kandler and Gillespie, 2005; Grothe et al., 2010). In the MSO, inhibitory input is needed for computation of interaural time differences, which provide sound localization cues for lower frequencies (Brand et al., 2002; Pecka et al., 2008; Myoga et al., 2014). The MNTB is thus a key relay nucleus for many aspects of auditory processing.

The calyx of Held undergoes major changes during development. In early postnatal development, axonal collaterals form multiple small “protocalyces” on MNTB neurons (Kandler and Friauf, 1993; Hoffpauir et al., 2006). These synapses are then refined and excess synapses are pruned until a single calyx remains on each MNTB neuron (Morest, 1968; Satzler et al., 2002; Hoffpauir et al., 2006; Holcomb et al., 2013). This pruning results in a largely one-to-one innervation pattern from the AVCN to the MNTB (Harrison and Warr, 1962; Friauf and Ostwald, 1988; Bergsman et al., 2004; Wimmer et al., 2004).

Communication between neurons and glia is required for the establishment of functional neural circuits (Reemst et al., 2016; Neniskyte and Gross, 2017). Microglia, the resident immune cells of the brain, are critical for brain wiring (Hammond et al., 2018) and synaptic pruning during development (Paolicelli et al., 2011; Ji et al., 2013). Their gene expression profiles, and likely their functions, vary with brain region (Grabert et al., 2016; De Biase and Bonci, 2018; Masuda et al., 2019). Microglia are most diverse in the developing mouse brain, with more homogenous populations present in the adult brain (Hammond et al., 2019; Li et al., 2019). We tested whether brainstem microglia contribute to the assembly of specialized auditory pathways. In the brainstem, microglia appear in the AVCN by postnatal day 0 (P0) and by P6 they are seen in the MNTB. Microglia peak in number during the second postnatal week, coinciding with the maturation of the calyx of Held. Several studies have shown that microglia influence expression of astrocytic proteins (Elmore et al., 2014; Spangenberg et al., 2016; Jin et al., 2017). Both astrocytes and microglia are found in close proximity to the developing calyx, indicating their possible involvement in its growth and maturation (Holcomb et al., 2013; Dinh et al., 2014).

Here, we treated animals during postnatal development with an inhibitor of colony stimulating factor 1 receptor (CSF1R), a tyrosine kinase receptor essential for microglia survival

(Stanley et al., 1997; Erblich et al., 2011; Elmore et al., 2014). We demonstrated that this treatment effectively eliminated microglia during the postnatal period. We found that microglia depletion was associated with reduced expression of the mature astrocytic marker, glial fibrillary acidic protein (GFAP), suggesting a delay in astrocyte maturation. Significantly, elimination of microglia prevented the pruning of polyinnervated MNTB neurons. These results suggest that microglia are needed for synaptic pruning in the MNTB.

MATERIALS AND METHODS

Animals

We used 42 postnatal day 8 (P8) and 46 P13 wild-type C57BL/6 mice of both sexes. All procedures were approved by the University of California, Irvine Institutional Animal Care and Use Committee.

Treatment

Animals were treated with BLZ945 (MW: 398.48, MedChem Express HY-12768/CS-3971), a small molecule inhibitor of CSF1R (Pyonteck et al., 2013), to eliminate microglia. BLZ945 was dissolved in dimethylsulfoxide (DMSO; D136-1; Thermo Fisher Scientific) by gradually adding it to the vial with BLZ945 and briefly vortexing. 0.01 mL of solution was administered subcutaneously (sc) at a dose of approximately 200 mg/kg at P2. The same volume of drug was administered at P4 and P6 for the P8 endpoint. Additional injections were delivered at P8 and P10 for the animals perfused at P13. DMSO-only injections were used as controls (Figure 1B). At P8 or P13 mice were weighed and perfused transcardially with 0.9% saline followed by 4% paraformaldehyde (PFA) in 0.1 M phosphate buffer, pH 7.3 (PBS). Brainstems were dissected and postfixed in PFA solution. After 2–3 h, brains were equilibrated in a 30% sucrose solution in 0.1 M PBS then sectioned coronally at 18 μ m using a cryostat (CM 1850-3-1; Leica Microsystems). Sections were mounted on chrome-alum coated glass slides in a 1-in-5 series.

Neuronal Tracing

In 11 animals at P8 and 13 animals at P13 we performed neuronal tracing to fill calyces of Held in the MNTB. Mice were perfused transcardially with artificial cerebrospinal fluid (aCSF; 130 mM NaCl, 3 mM KCl, 1.2 mM KH_2PO_4 , 20mM NaHCO_3 , 3 mM HEPES, 10 mM glucose, 2 mM CaCl_2 , 1.3 mM MgSO_4 perfused with 95% O_2 and 5% CO_2). Brains were quickly dissected and placed in a chamber with oxygenated aCSF.

The brain was temporarily transferred to a Petri dish with aCSF and axonal projections from the AVCN to the MNTB were filled using a rhodamine dextran amine (RDA; MW 3000, Invitrogen) solution (6.35% RDA with 0.4% Triton-X100 in PBS). A pulled glass micropipette was filled with RDA and pulses of RDA were delivered close to the midline in the ventral acoustic stria (VAS) using an Electro Square Porator (ECM830; BTX) at a rate of 5 pulses per second (pps) at 55 V for 50 ms. These pulses resulted in sparse labeling of GBC axons and calyces of Held on both sides of the brainstem (Figures 1C,D). In some

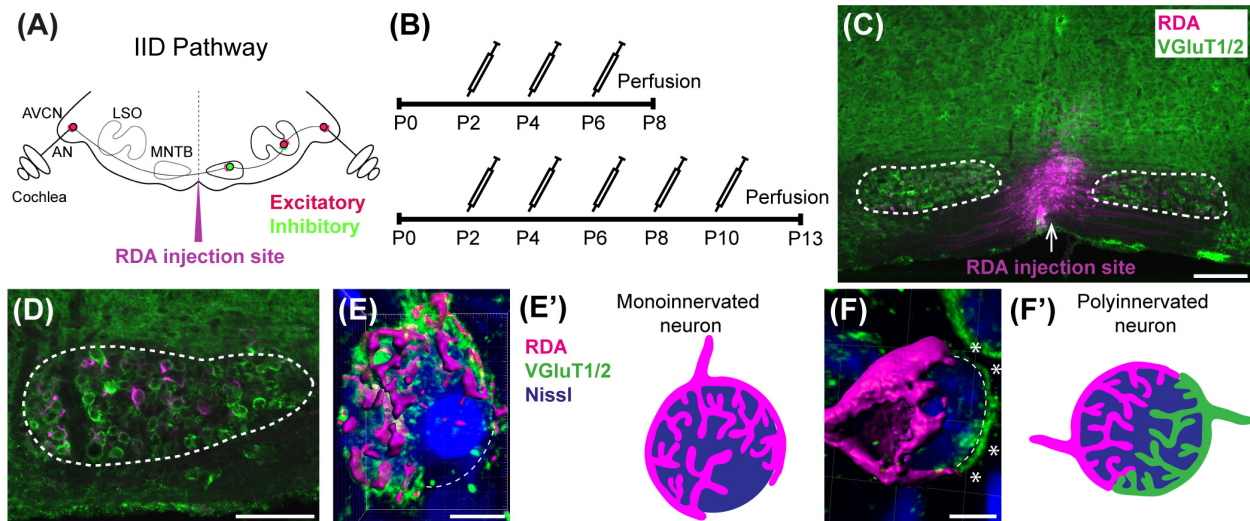


FIGURE 1 | Calyx labeling, reconstruction in 3D, and analysis. **(A)** A schematic of the interaural intensity differences (IID) pathway and RDA injection site in the VAS to sparsely label calyces of Held in the MNTB. GBCs in the AVCN receive direct input from the AN. In turn, GBCs synapse on inhibitory neurons in the contralateral MNTB. MNTB neurons then innervate excitatory neurons in the LSO. LSO neurons also receive tonotopically matched excitatory terminals from SBCs in the ipsilateral AVCN. LSO neurons compute the balance of frequency-matched inhibition and excitation arising from both ears to determine the sound source location in the horizontal plane. **(B)** Timeline of injections. Two age cohorts were included in the study. The P8 mice group received vehicle or BLZ945 injections at P2, P4, and P6, and then were perfused at P8. Animals in the P13 age group were injected every 2 days from P2 until P10, and then perfused at P13. **(C)** A photograph of an RDA injection site (magenta) in the VAS and sparsely labeled calyces in the mouse brainstem. VGluT1/2 labeling is shown in green. **(D)** A higher magnification of the left MNTB with sparsely RDA-labeled calyces of Held. **(E)** Reconstructed calyx area used for size and volume measurements (magenta). MNTB neurons were classified into mono- or polyinnervated based on the presence of PV or VGluT1/2 labeling outside the RDA-labeled calyx. Shown is an example of a mono-innervated neuron. VGluT1/2 labeling is present and is co-localized to the RDA-labeled calyx. Dashed line indicates approximate boundary of the Nissl-stained neuron that is contacted by the RDA-filled calyx of Held. **(E')** Schematic illustration of a mono-innervated MNTB neuron contacted by an RDA-labeled calyx. **(F)** An example of a polyinnervated MNTB neuron. It is contacted by an RDA-filled calyx and an additional VGluT1/2 positive calyceal input (indicated by white asterisks) around the remaining surface of the same neuron (dashed line). **(F')** Schematic illustration of a polyinnervated MNTB neuron. Both the RDA-labeled calyx and one or more additional inputs terminate on the same MNTB neuron. Scale bar in panel **(C)** = 200 μ m; scale bar in panel **(D)** = 100 μ m; scale bar in panel **(E)** = 6 μ m; scale bar in panel **(F)** = 5 μ m. Abbreviations: AN – auditory nerve, AVCN – anterior ventral cochlear nucleus, GBC – globular bushy cell, LSO – lateral superior olive, MNTB – medial nucleus of the trapezoid body, SBC – spherical bushy cell, VAS – ventral acoustic stria. Panel **(A)** has been adapted from Joris and Yin (1998).

cases, sequential labeling was performed with Alexa 488 dextran amine (DA488; 6.35% with 0.4% Triton-X100 in PBS) so that a single brainstem would have AVCN axons sparsely labeled with two different fluorophores. The brain was then placed back into the aCSF chamber for approximately 2 h under continuous oxygenation to allow for dye transport. The tissue was then transferred to 4% PFA solution for another 2 h followed by incubation in 30% sucrose solution in 0.1 M PBS. Brainstems were cryosectioned in the coronal plane at 18 μ m and mounted on an alternating series of four slides. Slides with adequately labeled axons and calyces of Held were immunolabeled for parvalbumin (PV) at P8 and for vesicular glutamate transporters 1 and 2 (VGluT1/2) at P13.

Immunofluorescence

We performed immunofluorescence for a calcium binding protein specific for microglia (IBA1), VGluT1/2, vesicular GABA transporter (VGAT), synaptophysin1 (Syn), PV, and astrocytic markers – S100 calcium-binding protein B (S100 β), aldehyde dehydrogenase 1 family member L1 (ALDH1L1), and GFAP.

Mounted sections were surrounded with a PAP pen hydrophobic barrier and rinsed in 0.1 M PBS for 10 min. For antigen retrieval, tissue was incubated for 5 min in 0.1%

sodium dodecyl sulfate in 0.1 M PBS solution followed by washes in 0.1 M PBS. Sections were then blocked with normal goat blocking solution containing 5% normal goat serum (NGS; Vector Laboratories S-1000) and 0.3% Triton X-100 (Acros 9002-93-1) in 0.1 M PBS for 1 h in a humidity chamber at room temperature followed by overnight incubation in primary antibodies. The tissue was then rinsed in 0.1 M PBS and incubated for 1 h in goat anti-rabbit, anti-guinea pig, or anti-chicken secondary antibody tagged with an Alexa (Invitrogen) fluorophore. Sections were washed in 0.1 M PBS and incubated in red or blue fluorescent Nissl stain (NeuroTrace 530/615 or 435/455, Life Technologies N21482 or N21479) diluted 1:200 in 0.3% Triton X-100 in 0.1 M PBS. After 1 h, tissue was rinsed in 0.1 M PBS and coverslipped with Glycergel mounting medium (Dako C0563).

For PV labeling, tissue was incubated for 3 h in a blocking solution made of 10% bovine serum albumin (Sigma 1002552698), 5% NGS, and 0.1% Triton X-100 in 0.1 M PBS followed by a 48-h incubation with mouse anti-PV primary antibody at 4°C. Sections were then allowed to equilibrate at room temperature for 30 min and rinsed 5 times in 0.1 M PBS. Tissue was placed in the blocking solution for 30 min then incubated in goat anti-mouse secondary antibody tagged

with an Alexa 488 fluorophore. Three hours later, slides were rinsed and incubated for 1 h in fluorescent Nissl stain diluted 1:200 in 0.3% Triton X-100 in 0.1 M PBS, washed 3 times and coverslipped with Glycergel mounting medium. The list of primary and secondary antibodies used in this study and their concentrations are listed in **Table 1**.

Fluorescent Microscopy

We acquired 10× and 20× magnification images of sections throughout the rostro-caudal extent of the MNTB using a Zeiss Axioskop-2 microscope, an Axiocam camera, and Axiovision software. We analyzed the MNTB on both sides of the midline, including only sections with an intact MNTB. For each animal in our analysis, at least three sections were included per primary antibody.

Microglial, Astrocytic, and Synaptic Protein Areal Coverage Analysis

For each specimen, a series of 20× multichannel fluorescent photographs spanning the rostro-caudal extent of the MNTB was assembled as an image stack in FIJI (Schindelin et al., 2012). For each section, the channel corresponding to Nissl-staining was used to outline the boundary of the MNTB, which was stored as a region-of-interest (ROI) polygon in FIJI. All subsequent operations were performed on the image channel corresponding to the immunolabeling of interest (e.g., VGAT). To correct for minor irregularities in overall illumination and/or labeling intensity across a set of sections, a level adjustment was applied such that the mean pixel intensity within each MNTB ROI was equivalent across all sections of an image stack without causing over- or undersaturation. Only global (section-wide) adjustments of pixel values were permitted; local manipulations were not made.

To identify positive immunolabeling, a histogram of pixel intensity was constructed based on all pixels within all MNTB ROIs in the image stack. This histogram was used as the input for automatic image thresholding in FIJI where a threshold value was

computed using the *Default* algorithm and applied to all images in the stack. Label/optical density for each section was evaluated and the areal coverage ratio was quantified as the total number of thresholded pixels within a given MNTB ROI.

Microglia Counts

Each section used for IBA1 areal coverage analysis was examined for microglial cell counts. Microglial cell bodies were identified by a small cell body with processes radiating out of it. Microglia were not counted if only IBA1-positive processes but no somata were present. If a microglial cell body was on the edge of the MNTB ROI (drawn with reference to Nissl staining), it was excluded if <50% of the soma was inside of the ROI. IBA1-positive cells were counted using FIJI's "Cell Counter" plugin. The average number of cells per MNTB slice was calculated by dividing the microglia count by the number of MNTB slices examined.

Confocal Microscopy

Rhodamine dextran amine-labeled and PV- (P8) or VGluT1/2-immunolabeled (P13) tissue was used for confocal microscopy (Leica SP8, 63× oil objective, zoom: 1.5, pinhole: 1) and subsequent analysis. Nissl, RDA, and PV or VGluT1/2 z-stack images of calyces of Held were acquired at a resolution of 1024 × 1024 pixels, with a z-step size of 0.5 μm (Grande et al., 2014; Wang et al., 2018). Gain and offset were set for each fluorescent channel and each slide separately. In a few cases settings were adjusted to account for differences in labeling intensity between sections on the same slide. Image stacks were exported and the surface area and volume of calyces of Held were analyzed using the surface module in Imaris software (v9.2.1; Bitplane). Calyces throughout the MNTB were randomly labeled with RDA and, thus, the entire medio-lateral extent of the MNTB was analyzed. Surfaces of RDA-labeled calyces of Held were reconstructed using the default mode and then manually adjusted to achieve as accurate RDA fill of the calyx of Held as possible (**Figure 1**). Sections were coded and analyzed blind to treatment group. We did not change the intensity of

TABLE 1 | List of antibodies used in the project.

Antigen	Host	RRID	Cat. no.	Source	Dilution
Primary antibodies					
ALDH1L1	Rabbit	N/A	ab177463	Abcam	1:500
IBA1	Rabbit	AB_839504	019-19741	Wako	1:500
GFAP	Chicken	AB_304558	ab4674	Abcam	1:1000
GlyT2	Rabbit	AB_2619997	272 003	Synaptic Systems	1:200
S100β	Rabbit	AB_882426	ab52642	Abcam	1:500
Synaptophysin	Guinea Pig	AB_1210382	101 004	Synaptic Systems	1:500
VGAT	Rabbit	AB_2492282	2100-VGAT	PhosphoSolutions	1:200
VGluT1/2	Rabbit	AB_2285905	135 503	Synaptic Systems	1:200
Secondary antibodies					
Alexa 488	Chicken	AB_2534096	A11039	Thermo Fisher Scientific	1:200
Alexa 488	Guinea Pig	AB_2534117	A11073	Thermo Fisher Scientific	1:500
Alexa 488	Rabbit	AB_2633280	A32731	Thermo Fisher Scientific	1:500
Alexa 647	Rabbit	AB_2535812	A21244	Thermo Fisher Scientific	1:500
Alexa 647	Guinea Pig	AB_2735091	A21450	Thermo Fisher Scientific	1:500

confocal stacks to avoid affecting surface area and volumetric results. Only complete or near complete RDA-filled calyces of Held with visible labeled preterminal axon segments were included in the analysis. However, the preterminal axon itself was cropped out of the images where possible. Additionally, RDA-labeled calyces that were too close to one another to be individually reconstructed were excluded from the analysis. All calyces that matched the criteria were analyzed from at least one slide for each animal used. If the number of labeled calyces from one slide was too small (<3), an additional slide was used, however, care was taken to avoid examining serial sections (Table 2).

Determination of Monoinnervation

At the time of surface rendering, the mono- or polyinnervation status of the postsynaptic neuron was evaluated. Sparse RDA-labeled brainstems were immunolabeled for PV (P8) or VGluT1/2 (P13) and MNTB cells with RDA-labeled input were analyzed. For a monoinnervated MNTB neuron, there would be no PV or VGluT1/2 labeling outside an RDA-labeled calyx (Figures 1E,E'). If additional inputs were present, we would see PV or VGluT1/2 along the surface of the MNTB neuron but outside the RDA-labeled calyx (Figures 1F,F'). MNTB neurons normally transition through a period in which a single dominant input is seen as early as P6 (Holcomb et al., 2013) and thus smaller calyces may be transiently present. However, small areas of spurious labeling with presynaptic markers outside the RDA label would not necessarily correspond to

additional calyces (Cant and Casseday, 1986; Kuwabara et al., 1991; Smith et al., 1998). We set a threshold such that if PV or VGluT1/2 labeling outside the RDA-labeled calyx covered 25% or more of the MNTB cell surface, we considered that MNTB cell to be polyinnervated. This percent coverage was an estimated subjective score made blind to treatment group, and was roughly the size of the smallest calyces we labeled (see section “Results”). We then determined the percentage of analyzed MNTB neurons that were polyinnervated for each group (Table 2).

Neuronal Density

To test for effects of drug treatment on cell number, we determined the cell density in AVCN (n = 4 DMSO; n = 4 BLZ945) and MNTB (n = 9 DMSO; n = 9 BLZ945) at P13. Tissue was prepared as described previously and cells were plotted using blue fluorescent Nissl staining. Fiji’s “Cell Counter” was used to count neurons within the ROI of each AVCN and MNTB (see above). Principle neurons of the MNTB were identified as homogenous cells that were round or slightly oval in shape and similar in size (Hoffpauir et al., 2006; Weatherstone et al., 2017). Only neuronal bodies with a visible nucleus and nucleolus were counted in every fifth section throughout the MNTB on both sides of the midline, including only intact MNTB sections. Neuronal density was calculated by dividing the sum of neuronal counts from each MNTB by the sum of MNTB area in the slices used for analysis.

TABLE 2 | Numbers of calyces of Held analyzed.

Treatment	Age	Animals used	Animal ID	Calyces measured	N neurons scored for innervation	N polyinnervated neurons
DMSO	P8	6	B143	12	15	13
			B144	8	13	11
			B153	13	11	11
			B156	9	15	10
			B160	11	15	15
			B216	8	9	6
BLZ945	P8	5	B141	13	10	9
			B149	10	22	16
			B154	11	14	11
			B217	12	7	4
			B215	19	23	14
DMSO	P13	6	B432	3	4	1
			B438	10	11	1
			B455	10	12	1
			B459	7	6	0
			B460	8	10	0
			B461	8	10	2
BLZ945	P13	7	B429	5	6	5
			B437	9	11	5
			B439	6	10	5
			B454	9	12	2
			B456	11	12	5
			B457	11	15	4
			B458	11	9	3

VGLUT1/2 Co-localization With EGFP-Labeled Microglia

We performed VGLUT1/2 immunofluorescence in $CX3CR1^{+}/EGFP$ reporter mice to investigate a possible internalization of presynaptic proteins in microglia. These mice have enhanced green fluorescent protein (EGFP) inserted into exon 2 of $CX3CR1$, resulting in EGFP-positive microglial cells (Jung et al., 2000). We used 3 heterozygous mice at P8 and 3 at P13. Animals were perfused as described above and the same immunolabeling protocol was used to label for VGLUT1/2. High resolution confocal imaging was used to build z-stacks through the microglial cell (Leica SP8, 63 \times oil objective, zoom: 3.5, pinhole: 0.6, resolution of 2048 \times 2048 pixels, z-step size of 0.5 μ m). Subsequently, z-stacks were deconvolved using Huyens essentials software and examined using Imaris. Due to the nature of on-slide immunolabeling, VGLUT1/2 antibody penetration was not always complete, thus, z-stacks were cropped so that EGFP-positive microglia were in the same focal plane as VGLUT1/2 labeling. A co-localization function in Imaris was used to build the co-localization channel and thresholds of overlap of EGFP and VGLUT1/2 channels were set to 10% and kept the same for all microglial cells analyzed. A total of five microglial cells per animal were imaged from non-consecutive sections, thus, 15 cells per age group in total.

Software Accessibility

Fiji scripts will be made available upon request to Dr. Michael A. Muniak.

Experimental Design and Statistical Analysis

To account for variability among litters, multiple litters were used and each of them was divided into control and experimental animals. Mice for each cohort were allocated randomly. Quantitative results for all cell counts, calyx of Held sizes, neuronal density, and innervation status as well as coverage of positive immunohistochemistry are represented by mean scores \pm standard error of mean (SEM) and were analyzed using Prism (v7; GraphPad Software). Comparisons between different treatment and age groups were made using a two-way ANOVA and Sidak's multiple comparisons test unless stated otherwise. Statistical significance was accepted at $p < 0.05$. Details of statistical analysis are presented in **Table 3**.

RESULTS

Microglia Depletion With BLZ945

Two age groups of mice were selected for the experiment: P8 and P13, corresponding to ages before and after hearing onset, respectively. A total of 38 mice were used for the P8 age cohort, of which 20 were injected with DMSO and 18 with BLZ945. A total of 46 animals were included in the P13 age group, of which 26 were injected with DMSO and 20 with BLZ945. Littermate controls were used in each age cohort.

BLZ945-treated mice were smaller and had some craniofacial changes, such as shorter snouts and smaller teeth, than their control littermates. This effect is akin to the phenotype seen in CSF1R KO mice (Dai et al., 2002). Occasionally, BLZ945 treatment resulted in loss of pigment, in particular, in areas around the ears and neck. Overall, survival rates were near 100% for DMSO and 75% for BLZ945. We examined expression patterns of microglial marker IBA1 in response to vehicle or BLZ945 injections. At P8 we found microglia distributed throughout the extent of the AVCN and MNTB in the control group (**Figures 2A,B**). However, three subcutaneous injections (at P2, P4, and P6) of BLZ945 in developing pups, in most cases, completely depleted microglia in the brainstems of the P8 mice (**Figures 2C,D**). At P13, microglia were more numerous in the MNTB of the vehicle treated mice (**Figures 2E,F**), while the experimental group showed very little if any IBA1-positive labeling (**Figures 2G,H**). Thus, BLZ945 injections successfully depleted microglia in the MNTB and its presynaptic nucleus, the AVCN. We did not observe any apparent cellular debris from microglia, likely because the BLZ945 treatment was initiated before microglia normally populate the MNTB (Dinh et al., 2014). Cellular debris was also not present in adult mice after a few days of treatment with CSF1R inhibitors (Elmore et al., 2014).

We quantified IBA1 labeling in the MNTB using the areal coverage ratio of immunolabeling, as described in section "Materials and Methods." BLZ945 treatment resulted in a significant decrease in microglia coverage in both P8 and P13 pups when compared to their age-matched littermate controls (P8: $p = 0.0036$; P13: $p < 0.0001$). Microglial coverage significantly increased with age in the control group ($p < 0.0001$; **Figure 2J**). Consequently, repeated BLZ945 delivery during the first two postnatal weeks depleted microglia and prevented them from reappearing by 3 days after the last injection (at P10). The same IBA1-labeled tissue was used to calculate the average number of microglial cells per MNTB slice (**Figures 2I,K**). At P8, there were significantly more microglia present in control than in BLZ945-treated mice ($p < 0.0001$). The difference remained significant after hearing onset ($p < 0.0001$). Additionally, microglial count increased with age in the control group ($p < 0.0001$) while there was no change observed between the two BLZ945 injected groups ($p = 0.6644$).

Mice treated with BLZ945 appeared smaller than their age-matched littermates, thus, we compared the weights of animals used for the experiment and also measured their brain weight. While there was no significant difference observed at P8 in animal weight ($p = 0.0574$), microglia depleted animals sacrificed at P13 weighed significantly less than DMSO injected controls ($p < 0.0001$). However, both vehicle and CSF1R inhibitor injected mice were significantly heavier after the onset of hearing than before ($p < 0.0001$ and $p < 0.0001$, respectively; **Figure 2L**). Consequently, both experimental groups gained weight with age but animals without microglia gained significantly less. Interestingly, there was no significant difference between the brain weight of control and BLZ945-injected mice at P8 ($p = 0.2951$) and P13 ($p = 0.5375$). Brain weight of mice in

TABLE 3 | Statistical analysis.

Figures	Sample size (n)	Mean \pm SEM	Treatment effect (DMSO-BLZ945)	Age effect (P8-P13)
Figure 2J	DMSO: P8 = 11, P13 = 11; BLZ945: P8 = 13, P13 = 9	DMSO: P8 0.01 ± 0.001 , P13: 0.04 ± 0.01 ; BLZ945: P8 0 ± 0 , P13 0.001 ± 0.0002	P8: $p = 0.0036$, DF = 40; P13: $p < 0.0001$, DF = 40	DMSO: $p < 0.0001$, DF = 40; BLZ945: $p = 0.9869$, DF = 40
Figure 2K	DMSO: P8 = 11, P13 = 10; BLZ945: P8 = 13; P13 = 9	DMSO: P8 3.41 ± 0.33 , P13: 5.78 ± 0.30 ; BLZ945: P8 0 ± 0 , P13 0.25 ± 0.06	P8: $p < 0.0001$, DF = 39; P13: $p < 0.0001$, DF = 39	DMSO: $p < 0.0001$, DF = 39; BLZ945: $p = 0.6644$, DF = 39
Figure 2L	DMSO: P8 = 11, P13 = 10; BLZ945: P8 = 14; P13 = 9	DMSO: P8 4.28 ± 0.14 , P13: 7.22 ± 0.19 ; BLZ945: P8 3.67 ± 0.21 , P13 5.36 ± 0.26	P8: $p = 0.0574$, DF = 40; P13: $p < 0.0001$, DF = 40	DMSO: $p < 0.0001$, DF = 40; BLZ945: $p < 0.0001$, DF = 40
Figure 2M	DMSO: P8 = 11, P13 = 10; BLZ945: P8 = 14; P13 = 9	DMSO: P8 0.31 ± 0.01 , P13: 0.41 ± 0.01 ; BLZ945: P8 0.30 ± 0.01 , P13 0.40 ± 0.01	P8: $p = 0.2951$, DF = 39; P13: $p = 0.5375$, DF = 39	DMSO: $p < 0.0001$, DF = 39; BLZ945: $p < 0.0001$, DF = 39
Figure 3M	DMSO: P8 = 8, P13 = 10; BLZ945: P8 = 10; P13 = 8	DMSO: P8 0.24 ± 0.02 , P13: 0.26 ± 0.01 ; BLZ945: P8 0.26 ± 0.01 , P13 0.26 ± 0.02	P8: $p = 0.2971$, DF = 38; P13: $p = 0.9982$, DF = 38	DMSO: $p = 0.5207$, DF = 38; BLZ945: $p = 0.8819$, DF = 38
Figure 3N	DMSO: P8 = 11, P13 = 10; BLZ945: P8 = 12; P13 = 9	DMSO: P8 0.23 ± 0.01 , P13: 0.27 ± 0.01 ; BLZ945: P8 0.24 ± 0.01 , P13 0.27 ± 0.01	P8: $p = 0.8814$, DF = 32; P13: $p > 0.9999$, DF = 32	DMSO: $p = 0.0667$, DF = 32; BLZ945: $p = 0.1707$, DF = 32
Figure 3O	DMSO: P8 = 11, P13 = 10; BLZ945: P8 = 12; P13 = 9	DMSO: P8 0.02 ± 0 , P13: 0.04 ± 0 ; BLZ945: P8 0.02 ± 0 , P13 0.02 ± 0	P8: $p = 0.9307$, DF = 38; P13: $p = 0.0042$, DF = 38	DMSO: $p < 0.0001$, DF = 38; BLZ945: $p = 0.5687$, DF = 38
Figure 5M	DMSO: P8 = 11, P13 = 10; BLZ945: P8 = 13; P13 = 9	DMSO: P8 0.18 ± 0.01 , P13: 0.17 ± 0.01 ; BLZ945: P8 0.19 ± 0.01 , P13 0.19 ± 0.01	P8: $p = 0.3952$, DF = 39; P13: $p = 0.3401$, DF = 39	DMSO: $p = 0.7678$, DF = 39; BLZ945: $p = 0.9012$, DF = 39
Figure 5N	DMSO: P8 = 11, P13 = 7; BLZ945: P8 = 12; P13 = 9	DMSO: P8 0.16 ± 0.005 , P13: 0.22 ± 0.02 ; BLZ945: P8 0.15 ± 0.01 , P13 0.20 ± 0.02	P8: $p = 0.8088$, DF = 35; P13: $p = 0.5781$, DF = 35	DMSO: $p = 0.0011$, DF = 35; BLZ945: $p = 0.0018$, DF = 35
Figure 5O	DMSO: P8 = 11, P13 = 10; BLZ945: P8 = 13; P13 = 9	DMSO: P8 0.23 ± 0.005 , P13: 0.27 ± 0.01 ; BLZ945: P8 0.24 ± 0.01 , P13 0.26 ± 0.02	P8: $p = 0.8992$, DF = 39; P13: $p = 0.9016$, DF = 39	DMSO: $p = 0.0328$, DF = 39; BLZ945: $p = 0.1836$, DF = 39
Figure 7A	DMSO: P8 = 6, P13 = 6; BLZ945: P8 = 5; P13 = 7	DMSO: P8 $84.10\% \pm 6.11\%$, P13 $10.40\% \pm 4.19\%$; BLZ945: P8 $71.86\% \pm 5.97\%$, P13 $42.45\% \pm 8.07\%$	P8: $p = 0.3914$, DF = 20; P13: $p = 0.0035$, DF = 20	DMSO: $p < 0.0001$, DF = 20; BLZ945: $p = 0.0101$, DF = 20
Figure 7B	AVCN DMO: P13 = 4; AVCN BLZ945: P13 = 4; MNTB DMSO: P13 = 9; MNTB BLZ945: P13 = 9	AVCN DMSO: P13 0.0015 ± 0.0001 ; AVCN BLZ945: P13 0.0016 ± 0.0001 ; MNTB DMSO: P13 0.0013 ± 0.00004932 ; MNTB BLZ945: P13 0.0014 ± 0.00003985	P13 AVCN: $p = 0.8693$, $t = 0.1717$; DF = 6; P13 MNTB: $p = 0.1052$, $t = 1.717$; DF = 16	N/A
Figure 7C	DMSO: P8 = 6, P13 = 6; BLZ945: P8 = 5; P13 = 7	DMSO: P8 $654.5 \mu\text{m}^2 \pm 70.56$ μm^2 , P13: $947.7 \mu\text{m}^2 \pm 110.6$ μm^2 ; BLZ945: P8 702.6 $\mu\text{m}^2 \pm 58.57 \mu\text{m}^2$, P13 896.6 $\mu\text{m}^2 \pm 32.52 \mu\text{m}^2$	P8: $p = 0.8840$, DF = 20; P13: $p = 0.8480$, DF = 20	DMSO: $p = 0.0191$, DF = 20; BLZ945: $p = 0.1470$, DF = 20
Figure 7D	DMSO: P8 = 6, P13 = 6; BLZ945: P8 = 5; P13 = 7	DMSO: P8 $237 \mu\text{m}^3 \pm 28.64$ μm^3 , P13: $358.9 \mu\text{m}^3 \pm 53.67$ μm^3 ; BLZ945: P8 242.6 $\mu\text{m}^3 \pm 22.19 \mu\text{m}^3$, P13 318.5 $\mu\text{m}^3 \pm 19.9 \mu\text{m}^3$	P8: $p = 0.9924$, DF = 20; P13: $p = 0.6299$, DF = 20	DMSO: $p = 0.0380$, DF = 20; BLZ945: $p = 0.2487$, DF = 20

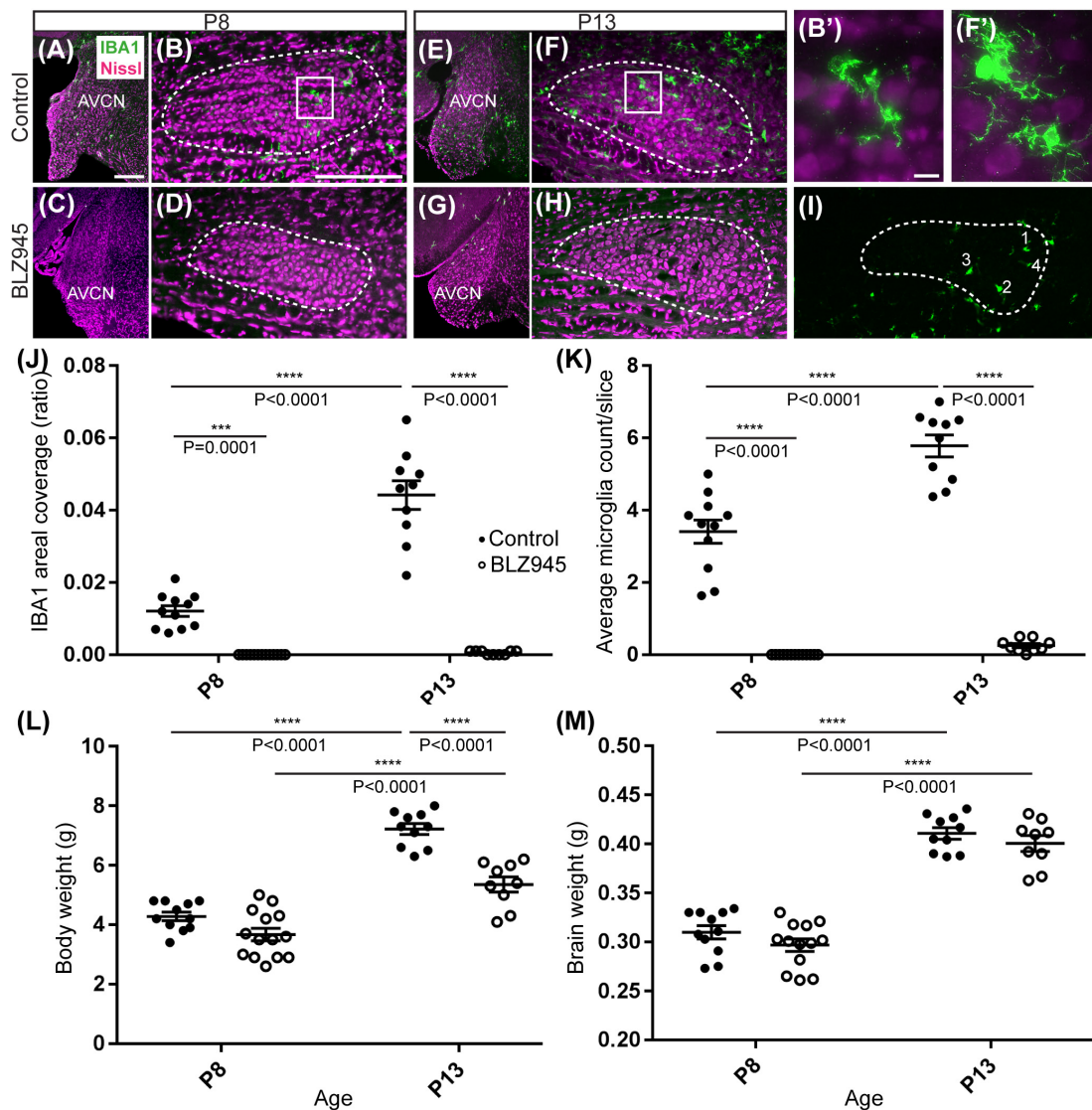


FIGURE 2 | Microglia depletion with BLZ945. **(A)** Microglia (green) are observed within the AVCN and **(B)** MNTB (dashed line) at P8 in control mice. **(B')** Inset from panel **(B)**. A higher magnification of the IBA1-labeled microglia from the MNTB of a control mouse at P8. **(C)** BLZ945 treatment eliminates microglia in the AVCN and **(D)** MNTB at P8. **(E)** At P13 microglia are more abundant than at P8 in control AVCN and **(F)** MNTB. **(F')** Inset from panel **(F)**. A higher magnification of the IBA1-labeled microglia from the MNTB of a control mouse at P13. **(G)** BLZ945 treatment eliminates microglia almost completely in the AVCN and **(H)** MNTB at P13. **(I)** Microglia counts in MNTB. Example of how microglial cell bodies were identified within the MNTB ROI. **(J)** Areal coverage ratio of IBA1 immunolabel. Microglia are significantly reduced at P8 and P13 in BLZ945-injected mice when compared to their age-matched controls. Microglia significantly increase with age in control animals but they remain almost absent in the MNTB of BLZ945-injected mice. **(K)** Microglia numbers per MNTB slice are significantly larger in control than BLZ945-treated mice at P8 and P13. Microglia increase in number in control animals with age but this increase was not observed in the BLZ945 injected group. **(L)** Control and BLZ945 injected animals gain weight with age, but mice without microglia weigh significantly less than their control littermates at P13. **(M)** Brains of control and BLZ945 injected animals significantly increased in weight with age. There was no significant difference between the brain of DMSO- and BLZ945-injected mice at P8 and P13. Scale bar in panel **(A)** = 100 μ m, applies to panels **(A,C,E,G)**. Scale bar in panel **(B)** = 200 μ m, applies to panels **(B,D,F,H,I)**. Scale bar in panel **(B')** = 10 μ m and applies to the panel **(F')**.

both treatment groups significantly increased with age (DMSO: $p < 0.0001$; BLZ945: $p < 0.0001$; **Figure 2M**).

BLZ945 Effect on Astrocytes

Three antibodies for astrocytic markers previously shown to be expressed in the mouse brainstem (Dinh et al., 2014) were used to label astrocytes in the MNTB before and after hearing onset.

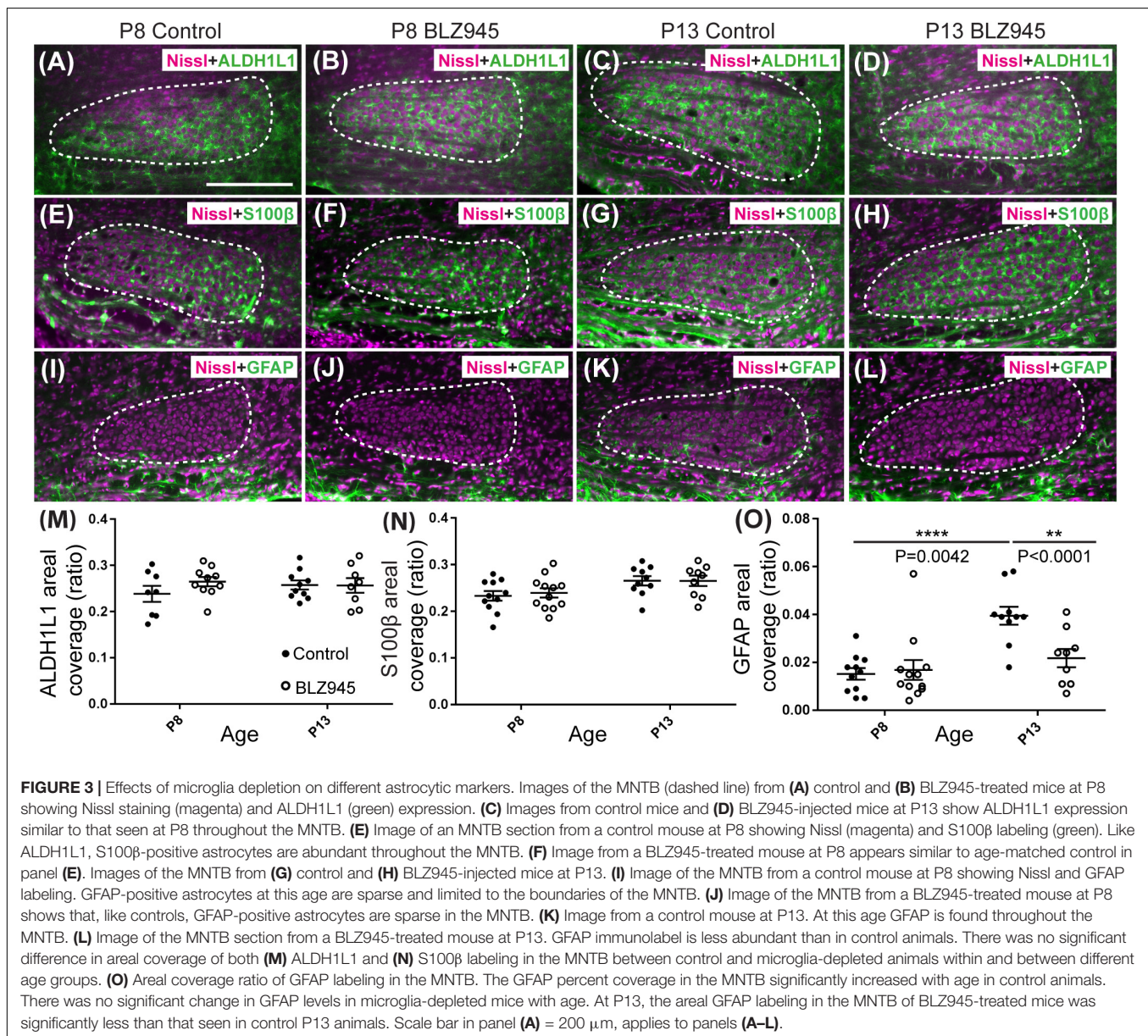
S100 β and ALDH1L1 are early appearing markers in the MNTB, whereas GFAP appears later (Dinh et al., 2014). Tissue from DMSO- and BLZ945-injected mice was analyzed in the same way as that for IBA1 as described in section “Materials and Methods.” Numerous S100 β and ALDH1L1 positive astrocytes were present throughout the MNTB of both control and experimental animals at P8 and P13. ALDH1L1 and S100 β

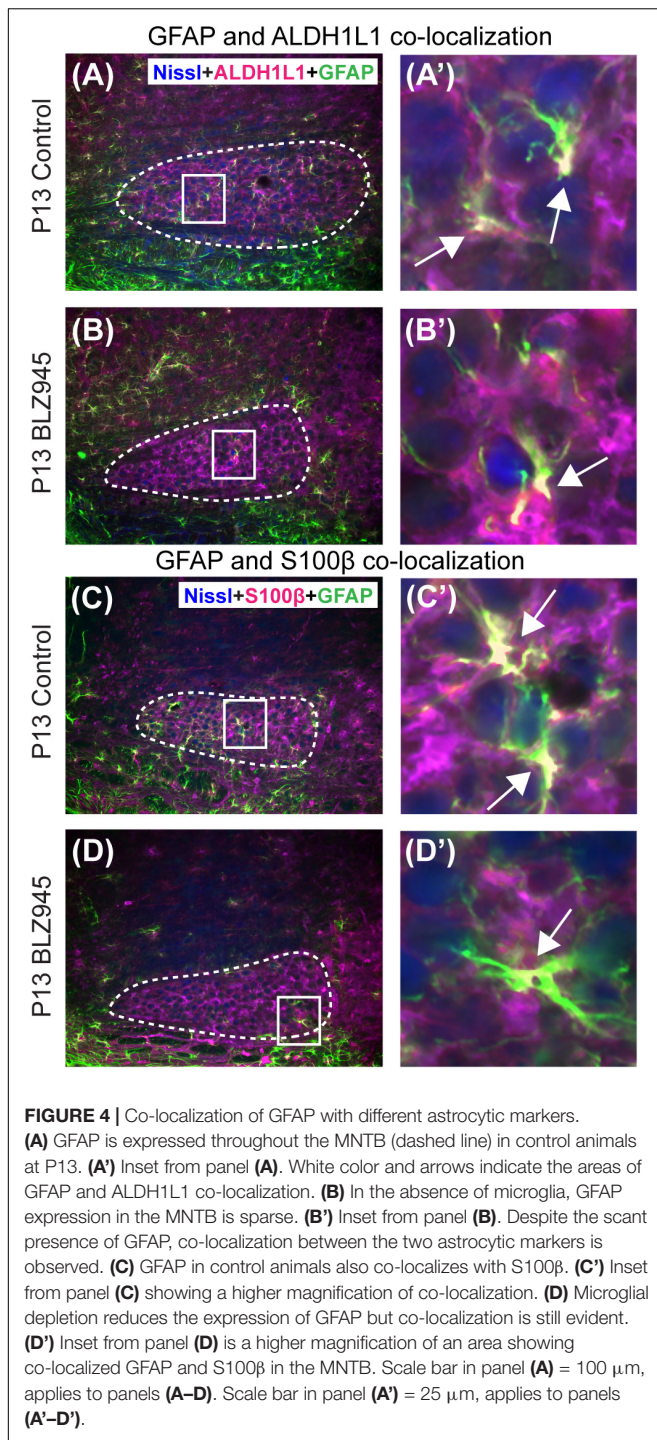
immunolabeling appeared to be very similar with both types of astrocytes surrounding neuronal somata (Figures 3A–H). After quantifying areal coverage of ALDH1L1 and S100 β labeling in the MNTB, no significant difference was observed between the control and treated mice at P8 (ALDH1L1: $p = 0.2971$; S100 β : $p = 0.8814$) or at P13 (ALDH1L1: $p = 0.9982$; S100 β : $p > 0.9999$). Additionally, the amount of these proteins remained very similar before and after hearing onset (ALDH1L1: DMSO $p = 0.5207$; BLZ945 $p = 0.8819$; S100 β : DMSO $p = 0.0667$; BLZ945 $p = 0.1707$; Figures 3M,N).

As previously shown (Dinh et al., 2014), immunolabeling for the mature astrocyte marker GFAP was minimal at P8 (Figures 3I,J). At P13, GFAP immunolabeling could be seen in the MNTB in control mice (Figure 3K) but relatively little was seen in the MNTB of experimental animals

(Figure 3L). Quantification of GFAP areal coverage revealed no difference between the control and BLZ945-treated groups at P8 ($p = 0.9307$). GFAP-positive MNTB area significantly increased with age in control ($p < 0.0001$) but not experimental animals ($p = 0.5687$). At P13, we found significantly smaller GFAP areal coverage in the MNTB of microglia-depleted mice than in control mice ($p = 0.0042$; Figure 3O).

Glial fibrillary acidic protein may be a marker for mature astrocytes (Gomes et al., 1999). We used 5 DMSO and 4 BLZ945-injected mice to label the tissue for GFAP and ALDH1L1 at P13. We examined MNTB area for co-localization between the two astrocytic markers (Figures 4A,B). A high degree of co-localization was observed in both control and microglia depleted animals. The same effect was seen when tissue from 10 DMSO and 9 BLZ945-treated mice was labeled for GFAP





and S100β (Figures 4C,D). Taken together, the results do not show effects of microglia depletion on astrocytes during early development, but rather that removal of microglia may impede the maturation of astrocytes.

BLZ945 Effect on Synaptic Proteins

The MNTB receives the majority of its excitatory input from the AVCN (Billups, 2005) and inhibitory input from the

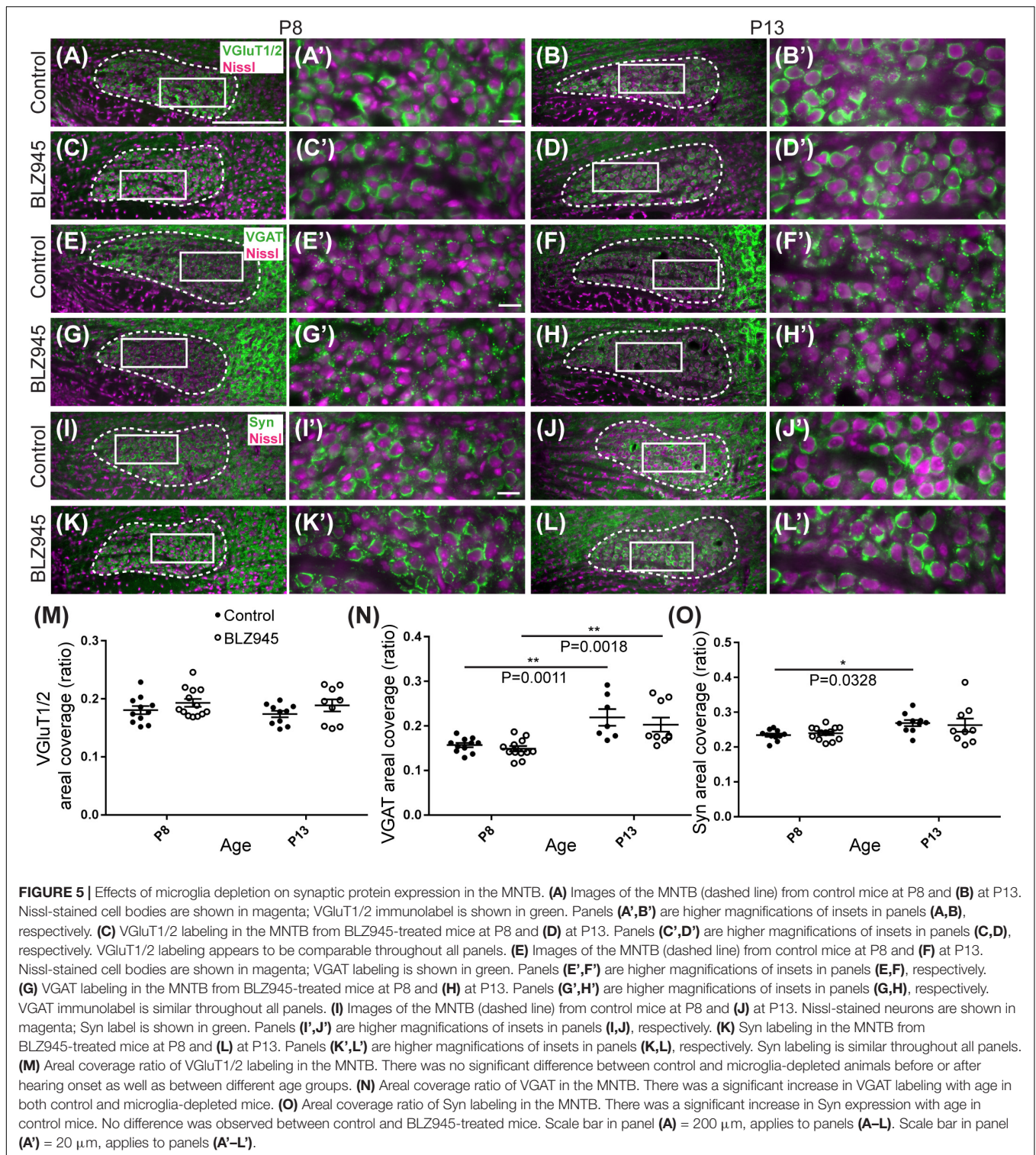
ventral nucleus of the trapezoid body (Albrecht et al., 2014). To evaluate the expression of synaptic inputs in the presence or absence of microglia, we carried out immunofluorescence labeling for VGluT1/2 and VGAT which correspond to excitatory (Freneau et al., 2001; Herzog et al., 2001; Kaneko et al., 2002) and inhibitory (McIntire et al., 1997; Wang et al., 2009) neurotransmitter transporters, respectively. Additionally, we immunolabeled for Syn, a presynaptic protein associated with small synaptic vesicles (Ngsee et al., 1990; Calakos and Scheller, 1994) to represent combined presynaptic inputs (Figure 5).

VGluT1/2 labeling in the MNTB of mature animals produces ring-like structures as calyces of Held nearly completely surround MNTB neurons. We quantified the coverage of VGluT1/2 and found no significant difference when compared to their littermate controls at P8 ($p = 0.3952$) or P13 ($p = 0.3401$). Comparisons between the two age groups did not show any significant change in VGluT1/2 expression either in control ($p = 0.7678$) or in treated animal groups ($p = 0.9012$; Figure 5M). Thus, microglia depletion did not significantly impact the expression of VGluT1/2.

While excitatory input dominates MNTB neurons (Billups, 2005), VGAT expression was observed in the MNTB at P8 and P13. Inhibitory inputs contacted mainly neuronal somata (Figures 5E–H'). VGAT coverage in BLZ945-treated mice did not differ significantly from control mice at P8 ($p = 0.8088$) or at P13 ($p = 0.5781$). However, in both control and treated animal groups, VGAT coverage significantly increased with age ($p = 0.0011$ and $p = 0.0018$, respectively; Figure 5N). Similarly, Syn levels showed no significant difference between control and BLZ945 groups at both P8 ($p = 0.8992$) and P13 ($p = 0.9016$). On the other hand, we found a significant increase in Syn levels in control mice between P8 and P13 ($p = 0.0328$). No age effect was observed in BLZ945-treated animals ($p = 0.1836$; Figure 5L). Taken together, these observations suggest that microglia are not needed for normal levels of synaptic protein expression before or after hearing onset.

Microglia Depletion Impairs Pruning of Excess Calyces

We evaluated the innervation status of MNTB neurons in the absence of microglia using sparse labeling of calyces together with broad labeling of presynaptic proteins (see section “Materials and Methods”). For the P8 endpoint, we used PV immunofluorescence to label calyces of Held. Early in development, calyces of Held are PV positive while MNTB neurons are not (Lohmann and Friauf, 1996; Caicedo et al., 1997; Felmy and Schneggenburger, 2004; Kulesza, 2014), allowing us to distinguish inputs from their target somata. Between P8 and P10, MNTB neurons also start expressing PV, making the boundary between the calyx of Held and the cell body less obvious. Therefore, in the P13 age group, we used VGluT1/2 immunofluorescence, which labeled all excitatory terminals surrounding MNTB neurons including calyces of Held. RDA-labeled calyces combined with PV or VGluT1/2



labeling allowed us to assess whether an MNTB neuron is contacted by multiple excitatory inputs or a single main input. Our RDA labeling method was sparse and extended across the VAS, allowing us to examine RDA-filled endings throughout the medio-lateral extent of the MNTB. A neuron

was classified as monoinnervated if the cell was contacted just by an RDA-filled calyx of Held (**Figures 1E,E'**). A cell was classified as polyinnervated if presynaptic proteins on an MNTB neuron were found outside an RDA-labeled calyx (**Figures 1E,F', 6**). We found that at P8 in both control

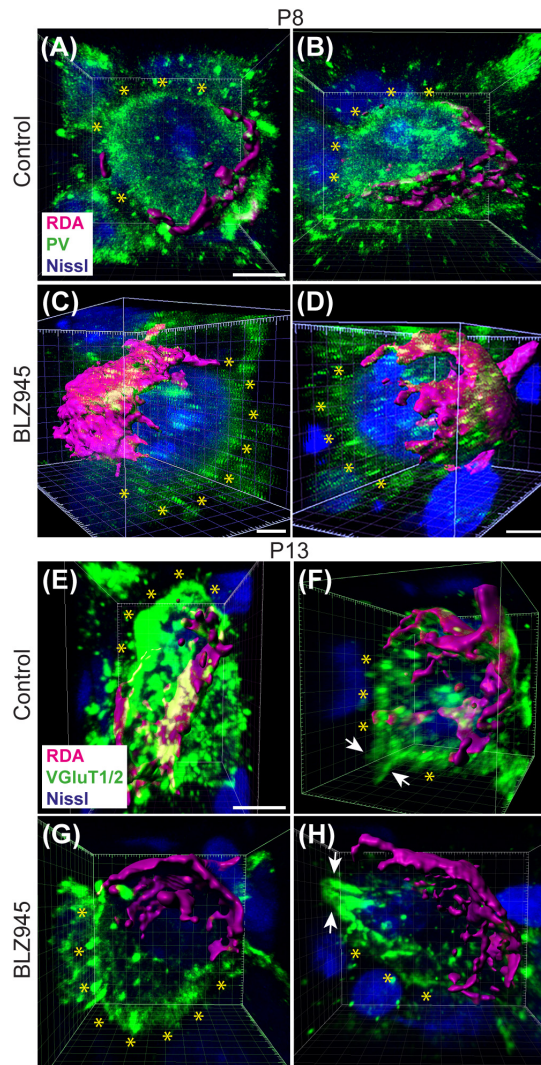


FIGURE 6 | Confocal analysis of polyinnervated neurons in the presence or absence of microglia. **(A,B)** Images showing reconstructed RDA-labeled calyces of Held (magenta) terminating on MNTB principal neurons in control mice at P8. Both are examples of polyinnervated MNTB neurons as evidenced by RDA-labeled calyces and additional PV (green) labeling (asterisks) outside of RDA-labeled calyces. **(C,D)** Examples of polyinnervated neurons in BLZ945-treated mice at P8. **(E,F)** Examples of polyinnervated neurons in control mice at P13. Asterisks indicate VGluT1/2 labeling on neurons in addition to RDA-filled calyces of Held. **(G,H)** Images of polyinnervated neurons in BLZ945-treated mice at P13. Scale bar in panel **(A)** = 3 μm , applies to panels **(A,B)**. Scale bar in panels **(C,D)** = 3 μm . Scale bar in panel **(E)** = 3 μm , applies to panels **(E-H)**.

and BLZ945-injected groups, the majority of neurons in the MNTB were still polyinnervated. Microglial depletion did not affect the number of polyinnervated MNTB neurons at P8 ($p = 0.3914$). As expected, in control animals the percentage of polyinnervated neurons significantly decreased with age ($p < 0.0001$). Polyinnervation also decreased with age for BLZ945-treated mice ($p = 0.0101$). However, microglia-depleted animals contained significantly more polyinnervated neurons

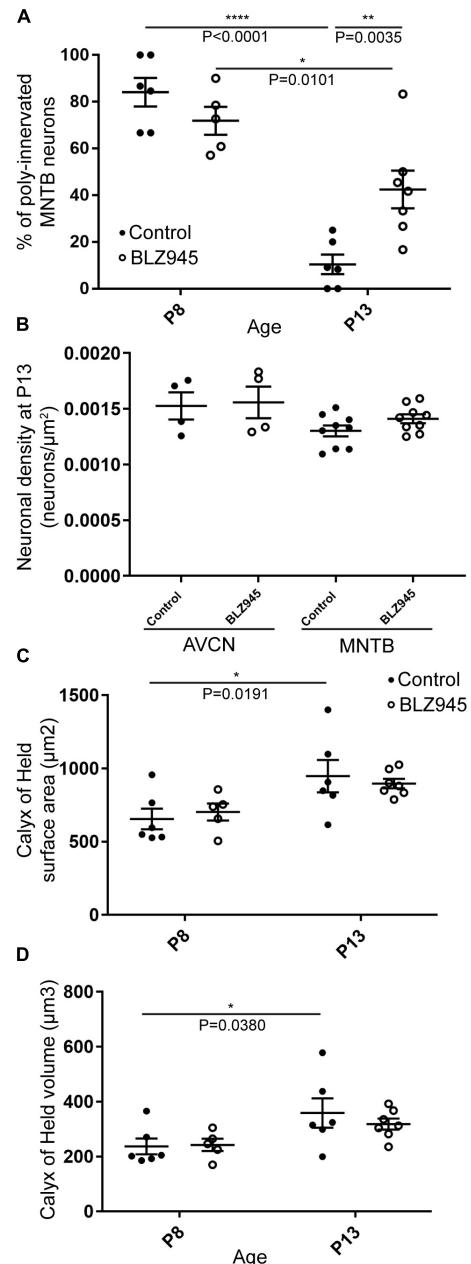


FIGURE 7 | BLZ945 effect on the innervation of MNTB neurons and the size of the calyx of Held. **(A)** Percentage of polyinnervated MNTB neurons was calculated for each group. Before hearing onset, most of neurons in the MNTB were polyinnervated in both control and BLZ945-injected animals. The number of polyinnervated neurons significantly decreased at P13 in both experimental groups, but there were significantly more polyinnervated neurons remaining in microglia-depleted mice. **(B)** Neuronal density in AVCN and MNTB was calculated in control and microglia-depleted animals at P13 and there was no significant difference found between the two cohorts in either of the nuclei analyzed. **(C)** The surface area of calyces of Held was measured after 3D reconstruction of confocal z-stacks. There was no difference in surface area between control and BLZ945-treated mice at P8 or P13. In control animals, calyces grew significantly larger with age. **(D)** The volume of calyces of Held was also measured and was similar in control and treated animals at both ages. The volume of calyces significantly increased with age only in the control group.

than control animals at P13 ($p = 0.0035$; **Figure 7A**). To test whether BLZ945 treatment had an effect on neuronal counts, we evaluated neuronal density in the AVCN and MNTB at P13. We did not find any difference between control and BLZ945-injected animals, indicating no changes in cell number between the treatment groups in the AVCN ($p = 0.8693$; unpaired t -test; **Figure 7B**) as well as MNTB ($p = 0.1052$; unpaired t -test; **Figure 7B**). Thus, the absence of microglia prevented or slowed down the pruning of excitatory inputs from the MNTB neurons resulting in reduced monoinnervation. The observed effect was not due to the increase in neuronal numbers in the AVCN or the decrease in neuronal count in the MNTB.

We did not observe any effect of microglia depletion on the surface area (P8: $p = 0.8840$; P13: $p = 0.8480$; **Figure 7C**) or volume (P8: $p = 0.9924$; P13: $p = 0.6299$; **Figure 7D**) of calyces of Held. Calyces of Held of control animals significantly increased in both surface area ($p = 0.0191$) and volume with age ($p = 0.0380$) while there was no difference observed between calyceal sizes of microglia-depleted animals between P8 and P13 (surface area: $p = 0.1470$; volume: $p = 0.2487$; **Figures 7C,D** and **Table 2**).

Multiple Calyces Are Found on Principal Neurons of MNTB in Untreated and DMSO-Injected Mice

Given the unexpectedly high level of polyinnervation in P8 animals in both treatment groups, we used sequential dye labeling (RDA and DA488) in untreated and control animals to verify the presence of multiple inputs. Dextran tags with two different fluorophores were electroporated in the VAS of untreated ($N = 4$) and DMSO-treated animals ($N = 3$) at P8. In every animal we found examples of polyinnervation (**Figures 8A–F''''**). Both RDA and DA488 labeled calyces were found to converge on the same neuron in the MNTB, often seen with a portion of their preterminal axons. Evaluations were only observational as injections were sparse and differed in size. We used this method to evaluate polyinnervation at P13. Although the percentage of polyinnervated neurons was only $\sim 10\%$ in control animals at P13 (**Figure 7A**), we found examples of polyinnervation in all 3 of the double-labeled brainstems (**Figures 8G–I''''**).

Microglial Association With VGluT1/2 Immunolabel

As microglia depletion was associated with impaired pruning, we next sought to determine whether presynaptic proteins are internalized in microglia during normal development. We collected tissue containing the MNTB from 3 $CX3CR1^{+}/EGFP$ mice at P8 and P13 and immunolabeled for VGluT1/2 (**Figure 9**). In our analysis of five microglial cells from each animal, we found that every cell made extensive contacts with VGluT1/2-positive terminals. In addition, we consistently found small regions of VGluT1/2-labeled particles inside of the somata of EGFP-positive cells.

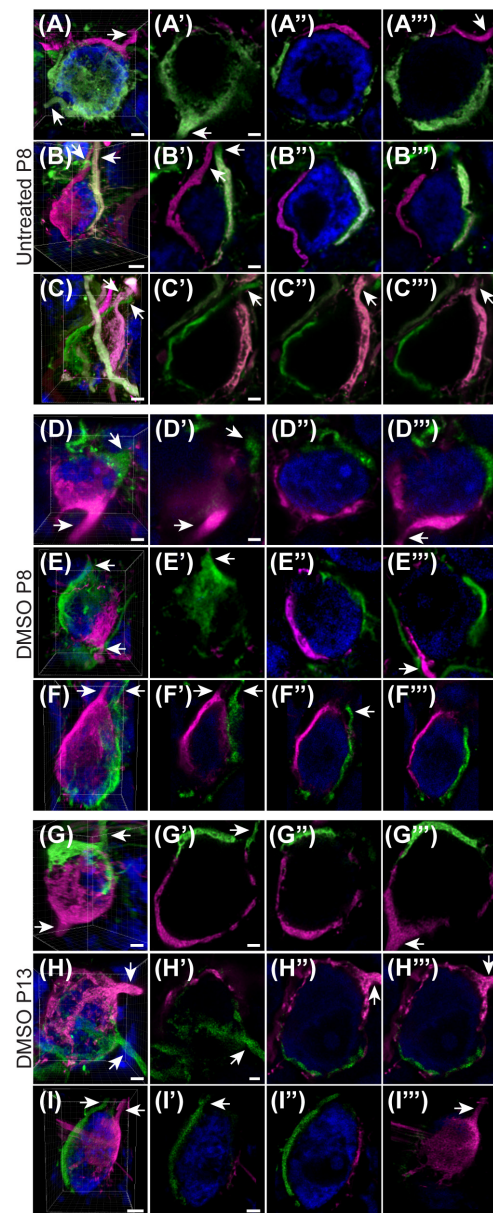


FIGURE 8 | Sequential tracing with RDA and DA488 in the VAS of wild-type and DMSO-injected mice. **(A–C)** Examples of polyinnervated neurons contacted by RDA- and DA488-labeled calyces of Held in wild-type mice at P8. Arrows indicate axons. **(A'–C''')** Individual optical sections through the neurons shown in panels **(A–C)** display polyinnervation on a single MNTB neuron. **(D–F)** 3D reconstructions of two separate calyceal inputs contacting the same neuron in the MNTB of DMSO-treated mice at P8. **(D'–F''')** Optical sections through the neurons shown in panels **(D–F)**. **(G–I)** 3D images of reconstructed RDA- and DA488-filled calyces synapsing on a single MNTB neuron in DMSO-injected mice at P13. **(G'–I''')** Sections through the neurons in panels **(G–I)** revealing multiple calyceal inputs. Scale bars in panels **(A,C,D)** = 3 μm . Scale bars in panels **(A',C')** = 2 μm and apply to panels **(A'–A''',C'–C''')**. Scale bar in panel **(B)** = 4 μm . Scale bar in panel **(B')** = 2 μm and applies to panels **(B'–B''')**. Scale bars in panels **(D,F)** = 3 μm . Scale bar in panel **(D')** = 2 μm and applies to corresponding panels **(D'–F''')**. Scale bars in panels **(G,H)** = 3 μm . Scale bars in panels **(G',H')** = 2 μm and apply to panels **(G'–H''')**. Scale bar in panel **(I)** = 5 μm . Scale bar in panel **(I')** = 3 μm and applies to panels **(I'–I''')**.

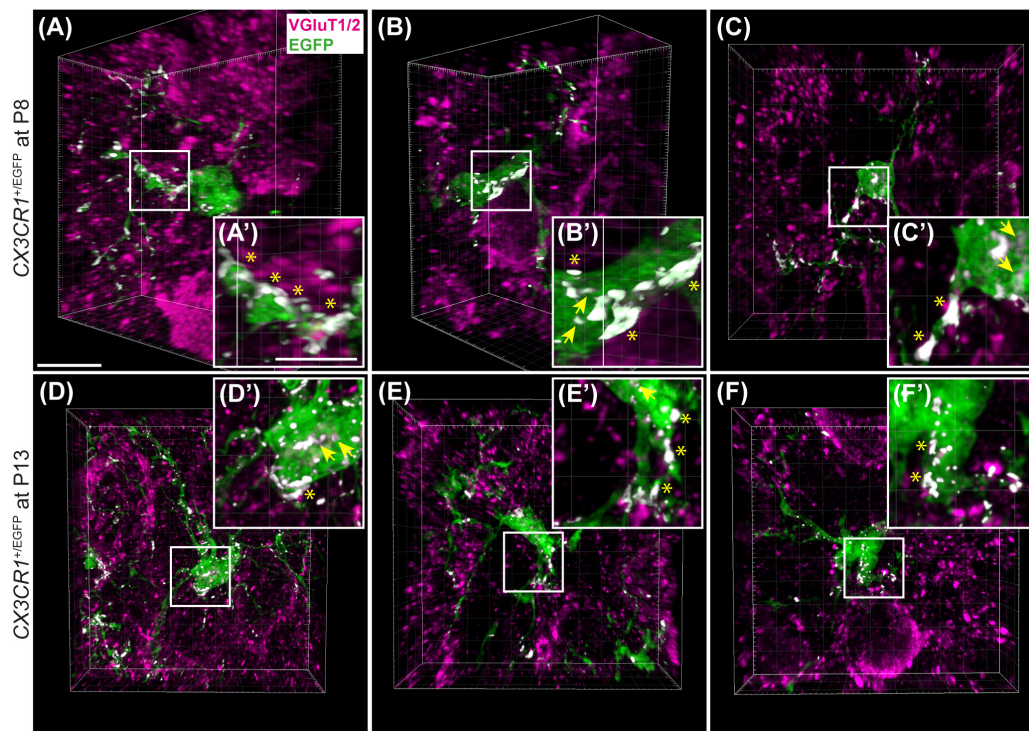


FIGURE 9 | Microglial association with VGLUT1/2-positive puncta. **(A–C)** 3D reconstructions of EGFP-positive microglia (green) and VGLUT1/2 immunolabeling (magenta) in $CX3CR1^{+/EGFP}$ mice at P8. White patches denote EGFP and VGLUT1/2 co-localization areas. **(A'–C')** Higher magnification images from panels **(A–C)**. Asterisks point to overlapping areas at the surface of microglial processes or cell bodies. Arrows denote internalized VGLUT1/2 particles. **(D–F)** 3D confocal z-stack reconstructions of microglial cells and VGLUT1/2 labeling in $CX3CR1^{+/EGFP}$ mice at P13. **(D'–F')** Higher magnification images of areas of co-localization between EGFP and VGLUT1/2 (white). At both ages, association between EGFP and VGLUT1/2 is clearly visible. Co-localization is more frequently observed at the glial surface than as internalized excitatory puncta. Scale bar in panel **(A)** = 200 μ m and applies to panels **(A–F)**. Scale bar in panel **(A')** = 5 μ m and applies to panels **(A'–F')**.

DISCUSSION

We have optimized a procedure for near complete elimination of microglia in early postnatal mice. We used this approach to test the contribution of microglia to the development of specialized neural circuits in the brainstem. We found that microglia depletion reduced the expression levels of the mature astrocyte marker GFAP, but did not affect early appearing astrocytic markers or expression levels of excitatory and inhibitory presynaptic proteins. We showed that while microglia depletion did not alter the neuronal numbers or the size of the calyx of Held, it led to impaired pruning of excess synapses terminating in the MNTB (Figure 10).

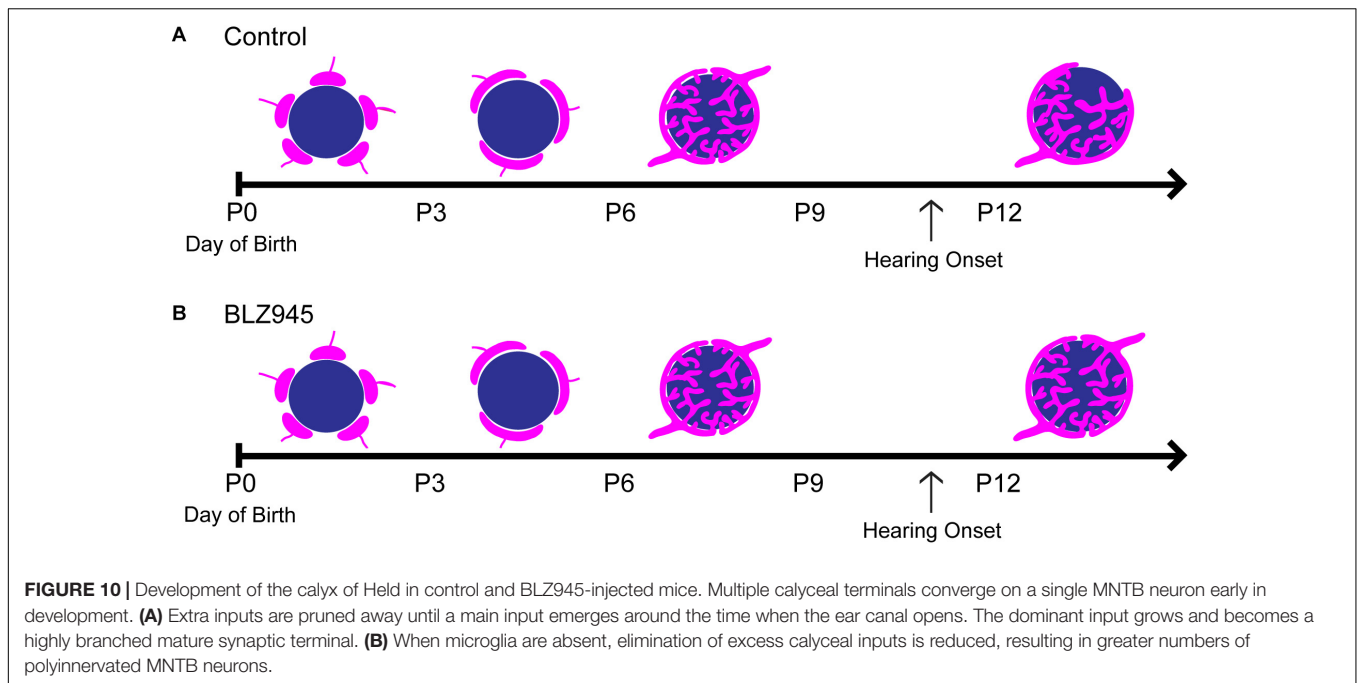
Microglia Function in Calyx of Held Development

The function of microglia in the auditory system has been explored in the context of acoustic trauma (Baizer et al., 2015) and cochlear lesions (Campos Torres et al., 1999; Janz and Illing, 2014) but the role of microglia in developmental pruning at the large and specialized calyx of Held has not been studied. We found that at P8, both control and BLZ945-treated animals contained a rather high percentage of polyinnervated MNTB neurons, and at P13, microglial elimination resulted in

significantly greater numbers of polyinnervated neurons. In the control group, the number of polyinnervated cells in the MNTB significantly decreased with age.

Polyinnervation of MNTB Neurons

Previous studies have described the formation of the calyx from the protocalyx into a cup-shaped structure enveloping ~50% of the postsynaptic neuron (Morest, 1968; Satzler et al., 2002). Rapid growth of calyces during the first postnatal week was determined in the rat using light microscopy (Kandler and Friauf, 1993; Rodriguez-Contreras et al., 2008). In mice, monoinnervation was observed by P4 with the number of polyinnervated neurons decreasing by half in the second postnatal week using electron microscopy and physiological techniques (Hoffpauir et al., 2006). The presence of a single dominant input on the majority of MNTB neurons was shown by P6 and monoinnervation by P9 (Holcomb et al., 2013). In contrast, other studies demonstrated polyinnervation of MNTB neurons after the first postnatal week in rodents using physiological (Bergsman et al., 2004) and anatomical methods (Wimmer et al., 2004), although the incidence was small. Smith et al. (1998) suggested that the variation seen in the excitatory input coverage (in cat, 40–50% of neuronal surface) may be due to some MNTB cells receiving two calyces or non-calyceal excitatory inputs (Smith et al., 1998). We used PV to look for signs of polyinnervation at



P8, as early in development PV is expressed in calyces (Lohmann and Friauf, 1996; Felmy and Schneggenburger, 2004; Kulesza, 2014). Thus, a PV-positive area outside the RDA labeling most likely represents an additional calyx. Moreover, in some cases we observed two calyces along with their preterminal axons converging on a single MNTB neuron. It is also possible that the smallest excitatory inputs observed outside the RDA-labeled calyx are actually non-calyceal collateral inputs from axons forming calyces on the neighboring neurons (Kuwabara et al., 1991; Hamann et al., 2003) or collaterals of axons from SBCs (Cant and Casseday, 1986). However, we occasionally observed small RDA-filled calyces along with their preterminal axons that contacted only about 25% of the neuronal surface, suggesting that small inputs could be actually small calyces rather than excitatory collaterals.

Several factors might account for the discrepancy in levels of polyinnervation using these diverse approaches. Electrophysiological techniques may underestimate the convergence of synaptic inputs due to severing of axons in brain slice preparations or shared stimulation thresholds that are hard to resolve. Additionally, electron microscopy data are challenged by the limited number of cells that can be examined. We used confocal imaging and 3D reconstruction of multiple labeled calyces from multiple animals, thus increasing the number of examples. However, we were restricted by random labeling of calyces throughout the MNTB as well as the number of calyces that fulfilled the selection criteria. It did not appear that DMSO treatment alone impaired the pruning of calyces at P8, as our sequential two-color dye electroporation revealed some examples of polyinnervation in every animal examined, with or without prior DMSO treatment. Our P13 control group showed predominant monoinnervation in the MNTB, in agreement with other studies showing that pruning largely takes place

prior to this age. However, microglial depletion impaired or delayed this developmental process and resulted in significantly more neurons that were still polyinnervated by multiple calyceal synapses. Further studies are needed to determine the physiological effects of increased polyinnervation in MNTB.

Branching of GBC Axons

Some GBC axons can branch and give rise to multiple calyces. The branching site can be distant to (Spirou et al., 1990; Kuwabara et al., 1991; Smith et al., 1991) or near its target (Rodriguez-Contreras et al., 2006). In rodents, branching sites are rarely found outside of the MNTB (Friauf and Ostwald, 1988; Kuwabara et al., 1991; Rodriguez-Contreras et al., 2006). These studies also indicate that multiple calyces formed by the same axon contact different neurons in the MNTB. Our experiments show RDA- and DA488-labeled calyces converging on a single MNTB neuron. We do not know whether we labeled the axon coming from the same GBC and branching before the electroporation site or if the labeled axons belong to two different GBCs in the AVCN. If axon branching occurred close to its target, we would expect to occasionally encounter two RDA- or DA488-labeled calyces contacting the same neuron. However, we observed few such cases, consistent with the interpretation that labeled inputs generally arose from distinct GBCs.

Glial Cell Interactions

Astrocyte-synapse communication plays an important role in synapse development throughout the brain. In rodent cerebral cortex, a significant period of synaptogenesis occurs at postnatal weeks two and three, the time when birth and differentiation of astrocytes is complete (Freeman, 2010; Allen and Eroglu, 2017). Astrocyte-specific transcription factors that drive heterogeneity of astrocytes are still not known (Freeman, 2010). Studies

indicate that the intermediate filament GFAP is a marker for mature astrocytes (Eng et al., 1971; Pixley and de Vellis, 1984; Wofchuk and Rodnight, 1995) as well as for reactive astrocytes, as GFAP immunostaining peaks 1 week after bilateral cochlear ablation in the CN of rats (Fuentes-Santamaria et al., 2013, 2017). In the auditory brainstem, glial cell expansion coincides with neural circuit development (Brandebura et al., 2018) and astrocytic markers appear at distinct times during postnatal development. In the MNTB, ALDH1L1-positive cells are present at P0, while S100 β expression is sparse and GFAP expression is completely absent. S100 β expression is seen throughout the MNTB at P6, while GFAP is observed at P14 (Dinh et al., 2014; Saliu et al., 2014). Thus, it is possible that expression of specific astrocytic markers signifies distinct processes at different developmental stages.

While ALDH1L1 and S100 β expression was not affected by microglia depletion, we showed a decrease in GFAP levels at P13 following BLZ945 injection. Our results differ from some previous microglial depletion studies done in adult mice where a significant increase in GFAP mRNA was found with no change in cell numbers (Elmore et al., 2014; Jin et al., 2017). Our findings also contrast with a study done in 5xfAD Alzheimer's model mice, in which the effect of microglia depletion on GFAP expression depended on the presence of pathology and the brain region examined (Spangenberg et al., 2016). Differences may be attributed to the age of the animals as well as the specific brain region investigated (Grabert et al., 2016; Spangenberg et al., 2016; De Biase and Bonci, 2018). Previous studies demonstrated interactions between microglia and astrocytes (Walton et al., 2006; Antony et al., 2011; Reemst et al., 2016) and an astrocytic role in pruning (Chung et al., 2015; Allen and Eroglu, 2017; Bosworth and Allen, 2017). A study done in rats showed that microglia are necessary for GFAP expression in astrocytes in disease states (Liddel et al., 2017), a characteristic that may be recapitulated during development in the MNTB. The effects of microglia depletion on GFAP expression suggest a role for microglia in astrocyte maturation. This role occurs after synaptic pruning in the MNTB is largely complete.

Microglial Function in Synaptic Pruning

It is well established that microglia have a fundamental role in effective neural wiring of the brain through regulated apoptosis, neurogenesis (Casano and Peri, 2015; Sato, 2015; Vilalta and Brown, 2018), promotion of synaptic formation and maturation (Hoshiko et al., 2012; Miyamoto et al., 2016), and synaptic pruning in normal and pathological conditions (Paolicelli et al., 2011; Schafer and Stevens, 2015; Neniskyte and Gross, 2017). We observed that microglial processes make substantial contacts with VGluT1/2-positive puncta, and we consistently observed small regions of presynaptic proteins internalized in microglial somata. It is thus possible that microglia may be engulfing some presynaptic materials as well as identifying and tagging synapses for potential elimination by other cells. Moreover, microglia-synapse contacts may reflect trophocytosis (partial phagocytosis, or "nibbling") of presynaptic structures (Schafer et al., 2012; Weinhard et al., 2018). This process was demonstrated in a detailed study carried out in the mouse hippocampus. The

authors showed that boutons descended into the microglial cytoplasm, followed by the closure of the membrane and the subsequent trafficking of engulfed presynaptic material or axonal processes. Interestingly, the study demonstrated that the complement signaling pathway, previously shown to be involved in elimination of apoptotic cells (Iram et al., 2016) and synapses (Stevens et al., 2007; Thielens et al., 2017), is not required for trophocytosis of presynaptic elements (Weinhard et al., 2018). Whether this phenomenon generalizes to auditory system development is not clear. Further exploration of these pathways is needed to understand the mechanisms through which glial cells help to shape neural circuitry in the auditory system.

DATA AVAILABILITY

The datasets generated for this study are available on request to the corresponding author.

ETHICS STATEMENT

Animal Subjects: The animal study was reviewed and approved by University of California Irvine Institutional Animal Care and Use Committee.

AUTHOR CONTRIBUTIONS

GM and KC conceived and designed the study, and analyzed and interpreted the data. KG and MM contributed to analytical tools. GM, CH, and SC acquired the data. GM, CH, MM, KG, and KC drafted the manuscript. All authors took full responsibility for the integrity of the data and accuracy of the analysis.

FUNDING

This work was supported by NIH R01 DC010796, NIH R01 NS083801, and NIH R01 AG056768, by a grant from the Australian National Health and Medical Research Council (NHMRC; Grant No. 1080652), Oticon Foundation (Grant No. 15-1814), and by a gift from Alan and Lynne Rydge. The authors wish to acknowledge the support of the Chao Family Comprehensive Cancer Center Optical Biology Core Shared Resource, supported by the National Cancer Institute under award number NIH P30 CA062203. The content is solely the responsibility of the authors and does not necessarily represent the official views of the National Institutes of Health.

ACKNOWLEDGMENTS

We thank Forrest P. Weghorst for helpful comments on the manuscript. We also thank Dr. Adeela Syed at the Optical Biology Core Facility of the Developmental Biology Center at the University of California, Irvine, for her advice and help with confocal imaging and analysis.

REFERENCES

- Albrecht, O., Dondzillo, A., Mayer, F., Thompson, J. A., and Klug, A. (2014). Inhibitory projections from the ventral nucleus of the trapezoid body to the medial nucleus of the trapezoid body in the mouse. *Front. Neural Circuits* 8:83. doi: 10.3389/fncir.2014.00083
- Allen, N. J., and Eroglu, C. (2017). Cell biology of astrocyte-synapse interactions. *Neuron* 96, 697–708. doi: 10.1016/j.neuron.2017.09.056
- Antony, J. M., Paquin, A., Nutt, S. L., Kaplan, D. R., and Miller, F. D. (2011). Endogenous microglia regulate development of embryonic cortical precursor cells. *J. Neurosci. Res.* 89, 286–298. doi: 10.1002/jnr.22533
- Baizer, J. S., Wong, K. M., Manohar, S., Hayes, S. H., Ding, D., Dingman, R., et al. (2015). Effects of acoustic trauma on the auditory system of the rat: the role of microglia. *Neuroscience* 303, 299–311. doi: 10.1016/j.neuroscience.2015.07.004
- Bergsman, J. B., De Camilli, P., and McCormick, D. A. (2004). Multiple large inputs to principal cells in the mouse medial nucleus of the trapezoid body. *J. Neurophysiol.* 92, 545–552. doi: 10.1152/jn.00927.2003
- Billups, B. (2005). Colocalization of vesicular glutamate transporters in the rat superior olivary complex. *Neurosci. Lett.* 382, 66–70. doi: 10.1016/j.neulet.2005.02.071
- Borst, J. G., and Sakmann, B. (1996). Calcium influx and transmitter release in a fast CNS synapse. *Nature* 383, 431–434. doi: 10.1038/383431a0
- Bosworth, A. P., and Allen, N. J. (2017). The diverse actions of astrocytes during synaptic development. *Curr. Opin. Neurobiol.* 47, 38–43. doi: 10.1016/j.conb.2017.08.017
- Brand, A., Behrend, O., Marquardt, T., McAlpine, D., and Grothe, B. (2002). Precise inhibition is essential for microsecond interaural time difference coding. *Nature* 417, 543–547. doi: 10.1038/417543a
- Brandebura, A. N., Morehead, M., Heller, D. T., Holcomb, P., Kolson, D. R., Jones, G., et al. (2018). Glial cell expansion coincides with neural circuit formation in the developing auditory brainstem. *Dev. Neurobiol.* 78, 1097–1116. doi: 10.1002/dneu.22633
- Caicedo, A., d'Aldin, C., Eybalin, M., and Puel, J. L. (1997). Temporary sensory deprivation changes calcium-binding proteins levels in the auditory brainstem. *J. Comp. Neurol.* 378, 1–15. doi: 10.1002/(sici)1096-9861(19970203)378:1<1::aid-cne1>3.0.co;2-8
- Calakos, N., and Scheller, R. H. (1994). Vesicle-associated membrane protein and synaptophysin are associated on the synaptic vesicle. *J. Biol. Chem.* 269, 24534–24537.
- Campos Torres, A., Vidal, P. P., and de Waele, C. (1999). Evidence for a microglial reaction within the vestibular and cochlear nuclei following inner ear lesion in the rat. *Neuroscience* 92, 1475–1490. doi: 10.1016/s0306-4522(99)00078-0
- Cant, N. B., and Casseday, J. H. (1986). Projections from the anteroventral cochlear nucleus to the lateral and medial superior olivary nuclei. *J. Comp. Neurol.* 247, 457–476. doi: 10.1002/cne.902470406
- Casano, A. M., and Peri, F. (2015). Microglia: multitasking specialists of the brain. *Dev. Cell* 32, 469–477. doi: 10.1016/j.devcel.2015.01.018
- Chung, W. S., Allen, N. J., and Eroglu, C. (2015). Astrocytes control synapse formation, function, and elimination. *Cold Spring Harb. Perspect. Biol.* 7:a020370. doi: 10.1101/cshperspect.a020370
- Dai, X. M., Ryan, G. R., Hapel, A. J., Dominguez, M. G., Russell, R. G., Kapp, S., et al. (2002). Targeted disruption of the mouse colony-stimulating factor 1 receptor gene results in osteopetrosis, mononuclear phagocyte deficiency, increased primitive progenitor cell frequencies, and reproductive defects. *Blood* 99, 111–120. doi: 10.1182/blood.v99.1.111
- De Biase, L. M., and Bonci, A. (2018). Region-specific phenotypes of microglia: the role of local regulatory cues. *Neuroscientist* doi: 10.1177/1073858418800996 [Epub ahead of print].
- Dinh, M. L., Koppel, S. J., Korn, M. J., and Cramer, K. S. (2014). Distribution of glial cells in the auditory brainstem: normal development and effects of unilateral lesion. *Neuroscience* 278, 237–252. doi: 10.1016/j.neuroscience.2014.08.016
- Elmore, M. R., Najafi, A. R., Koike, M. A., Dagher, N. N., Spangenberg, E. E., Rice, R. A., et al. (2014). Colony-stimulating factor 1 receptor signaling is necessary for microglia viability, unmasking a microglia progenitor cell in the adult brain. *Neuron* 82, 380–397. doi: 10.1016/j.neuron.2014.02.040
- Eng, L. F., Vanderhaeghen, J. J., Bignami, A., and Gerstl, B. (1971). An acidic protein isolated from fibrous astrocytes. *Brain Res.* 28, 351–354. doi: 10.1016/0006-8993(71)90668-8
- Erblich, B., Zhu, L., Etgen, A. M., Dobrenis, K., and Pollard, J. W. (2011). Absence of colony stimulation factor-1 receptor results in loss of microglia, disrupted brain development and olfactory deficits. *PLoS One* 6:e26317. doi: 10.1371/journal.pone.0026317
- Felmy, F., and Schneggenburger, R. (2004). Developmental expression of the Ca²⁺-binding proteins calretinin and parvalbumin at the calyx of Held of rats and mice. *Eur. J. Neurosci.* 20, 1473–1482. doi: 10.1111/j.1460-9568.2004.03604.x
- Freeman, M. R. (2010). Specification and morphogenesis of astrocytes. *Science* 330, 774–778. doi: 10.1126/science.1190928
- Fremeau, R. T. Jr., Troyer, M. D., Pahner, I., Nygaard, G. O., Tran, C. H., Reimer, R. J., et al. (2001). The expression of vesicular glutamate transporters defines two classes of excitatory synapse. *Neuron* 31, 247–260. doi: 10.1016/s0896-6273(01)00344-0
- Friauf, E., and Ostwald, J. (1988). Divergent projections of physiologically characterized rat ventral cochlear nucleus neurons as shown by intra-axonal injection of horseradish peroxidase. *Exp. Brain Res.* 73, 263–284.
- Fuentes-Santamaria, V., Alvarado, J. C., Gabaldon-Ull, M. C., and Manuel Juiz, J. (2013). Upregulation of insulin-like growth factor and interleukin 1beta occurs in neurons but not in glial cells in the cochlear nucleus following cochlear ablation. *J. Comp. Neurol.* 521, 3478–3499. doi: 10.1002/cne.23362
- Fuentes-Santamaria, V., Alvarado, J. C., Melgar-Rojas, P., Gabaldon-Ull, M. C., Miller, J. M., and Juiz, J. M. (2017). The role of glia in the peripheral and central auditory system following noise overexposure: contribution of TNF-alpha and IL-1beta to the pathogenesis of hearing loss. *Front. Neuroanat.* 11:9. doi: 10.3389/fnana.2017.00009
- Glendenning, K. K., Baker, B. N., Hutson, K. A., and Masterton, R. B. (1992). Acoustic chiasm V: inhibition and excitation in the ipsilateral and contralateral projections of LSO. *J. Comp. Neurol.* 319, 100–122. doi: 10.1002/cne.903190110
- Gomes, F. C., Paulin, D., and Moura Neto, V. (1999). Glial fibrillary acidic protein (GFAP): modulation by growth factors and its implication in astrocyte differentiation. *Braz. J. Med. Biol. Res.* 32, 619–631. doi: 10.1590/s0100-879x1999000500016
- Grabert, K., Michael, T., Karavolos, M. H., Clohisey, S., Baillie, J. K., Stevens, M. P., et al. (2016). Microglial brain region-dependent diversity and selective regional sensitivities to aging. *Nat. Neurosci.* 19, 504–516. doi: 10.1038/nn.4222
- Grande, G., Negandhi, J., Harrison, R. V., and Wang, L. Y. (2014). Remodelling at the calyx of Held-MNTB synapse in mice developing with unilateral conductive hearing loss. *J. Physiol.* 592, 1581–1600. doi: 10.1113/jphysiol.2013.268839
- Grothe, B., Pecka, M., and McAlpine, D. (2010). Mechanisms of sound localization in mammals. *Physiol. Rev.* 90, 983–1012. doi: 10.1152/physrev.00026.2009
- Hamann, M., Billups, B., and Forsythe, I. D. (2003). Non-calyceal excitatory inputs mediate low fidelity synaptic transmission in rat auditory brainstem slices. *Eur. J. Neurosci.* 18, 2899–2902. doi: 10.1111/j.1460-9568.2003.03017.x
- Hammond, T. R., Dufort, C., Dissing-Olesen, L., Giera, S., Young, A., Wysoker, A., et al. (2019). Single-cell RNA sequencing of microglia throughout the mouse lifespan and in the injured brain reveals complex cell-state changes. *Immunity* 50:e256. doi: 10.1016/j.immuni.2018.11.004
- Hammond, T. R., Robertson, D., and Stevens, B. (2018). Microglia and the brain: complementary partners in development and disease. *Annu. Rev. Cell Dev. Biol.* 34, 523–544. doi: 10.1146/annurev-cellbio-100616-060509
- Harrison, J. M., and Warr, W. B. (1962). A study of the cochlear nuclei and ascending auditory pathways of the medulla. *J. Comp. Neurol.* 119, 341–379. doi: 10.1002/cne.901190306
- Held, H. (1893). Die centrale gehorleitung. *Arch. Anat. Physiol. Anat. Abt.* 17, 201–248.
- Herzog, E., Bellenchi, G. C., Gras, C., Bernard, V., Ravassard, P., Bedet, C., et al. (2001). The existence of a second vesicular glutamate transporter specifies subpopulations of glutamatergic neurons. *J. Neurosci.* 21:RC181.
- Hoffpau, B. K., Grimes, J. L., Mathers, P. H., and Spiro, G. A. (2006). Synaptogenesis of the calyx of Held: rapid onset of function and one-to-one morphological innervation. *J. Neurosci.* 26, 5511–5523. doi: 10.1523/jneurosci.5525-05.2006
- Holcomb, P. S., Hoffpau, B. K., Hoyson, M. C., Jackson, D. R., Deerinck, T. J., Marrs, G. S., et al. (2013). Synaptic inputs compete during rapid formation of the calyx of Held: a new model system for neural development. *J. Neurosci.* 33, 12954–12969. doi: 10.1523/JNEUROSCI.1087-13.2013
- Hoshiko, M., Arnoux, I., Avignone, E., Yamamoto, N., and Audinat, E. (2012). Deficiency of the microglial receptor CX3CR1 impairs postnatal functional

- development of thalamocortical synapses in the barrel cortex. *J. Neurosci.* 32, 15106–15111. doi: 10.1523/JNEUROSCI.1167-12.2012
- Iram, T., Ramirez-Ortiz, Z., Byrne, M. H., Coleman, U. A., Kingery, N. D., Means, T. K., et al. (2016). Megf10 Is a receptor for C1Q that mediates clearance of apoptotic cells by astrocytes. *J. Neurosci.* 36, 5185–5192. doi: 10.1523/JNEUROSCI.3850-15.2016
- Janz, P., and Illing, R. B. (2014). A role for microglial cells in reshaping neuronal circuitry of the adult rat auditory brainstem after its sensory deafferentation. *J. Neurosci. Res.* 92, 432–445. doi: 10.1002/jnr.23334
- Ji, K., Akgul, G., Wollmuth, L. P., and Tsirka, S. E. (2013). Microglia actively regulate the number of functional synapses. *PLoS One* 8:e56293. doi: 10.1371/journal.pone.0056293
- Jin, W. N., Shi, S. X., Li, Z., Li, M., Wood, K., Gonzales, R. J., et al. (2017). Depletion of microglia exacerbates postischemic inflammation and brain injury. *J. Cereb. Blood Flow Metab.* 37, 2224–2236. doi: 10.1177/0271678x17694185
- Joris, P. X., and Yin, T. C. (1998). Envelope coding in the lateral superior olive. III. Comparison with afferent pathways. *J. Neurophysiol.* 79, 253–269. doi: 10.1152/jn.1998.79.1.253
- Jung, S., Aliberti, J., Graemmel, P., Sunshine, M. J., Kreutzberg, G. W., Sher, A., et al. (2000). Analysis of fractalkine receptor CX(3)CR1 function by targeted deletion and green fluorescent protein reporter gene insertion. *Mol. Cell. Biol.* 20, 4106–4114. doi: 10.1128/mcb.20.11.4106-4114.2000
- Kandler, K., and Friauf, E. (1993). Pre- and postnatal development of efferent connections of the cochlear nucleus in the rat. *J. Comp. Neurol.* 328, 161–184. doi: 10.1002/cne.903280202
- Kandler, K., and Gillespie, D. C. (2005). Developmental refinement of inhibitory sound-localization circuits. *Trends Neurosci.* 28, 290–296. doi: 10.1016/j.tins.2005.04.007
- Kaneko, T., Fujiyama, F., and Hioki, H. (2002). Immunohistochemical localization of candidates for vesicular glutamate transporters in the rat brain. *J. Comp. Neurol.* 444, 39–62. doi: 10.1002/cne.10129
- Kulesza, R. J. Jr. (2014). Characterization of human auditory brainstem circuits by calcium-binding protein immunohistochemistry. *Neuroscience* 258, 318–331. doi: 10.1016/j.neuroscience.2013.11.035
- Kuwabara, N., DiCaprio, R. A., and Zook, J. M. (1991). Afferents to the medial nucleus of the trapezoid body and their collateral projections. *J. Comp. Neurol.* 314, 684–706. doi: 10.1002/cne.903140405
- Kuwabara, N., and Zook, J. M. (1991). Classification of the principal cells of the medial nucleus of the trapezoid body. *J. Comp. Neurol.* 314, 707–720. doi: 10.1002/cne.903140406
- Kuwabara, N., and Zook, J. M. (1992). Projections to the medial superior olive from the medial and lateral nuclei of the trapezoid body in rodents and bats. *J. Comp. Neurol.* 324, 522–538. doi: 10.1002/cne.903240406
- Li, Q., Cheng, Z., Zhou, L., Darmanis, S., Neff, N. F., Okamoto, J., et al. (2019). Developmental heterogeneity of microglia and brain myeloid cells revealed by deep single-cell RNA sequencing. *Neuron* 101:e210. doi: 10.1016/j.neuron.2018.12.006
- Liddelow, S. A., Guttenplan, K. A., Clarke, L. E., Bennett, F. C., Bohlen, C. J., Schirmer, L., et al. (2017). Neurotoxic reactive astrocytes are induced by activated microglia. *Nature* 541, 481–487. doi: 10.1038/nature21029
- Lohmann, C., and Friauf, E. (1996). Distribution of the calcium-binding proteins parvalbumin and calretinin in the auditory brainstem of adult and developing rats. *J. Comp. Neurol.* 367, 90–109. doi: 10.1002/(sici)1096-9861(19960325)367:1<90::aid-cne7>3.0.co;2-e
- Masuda, T., Sankowski, R., Staszewski, O., Bottcher, C., Amann, L., Sagar Scheiwe, C., et al. (2019). Spatial and temporal heterogeneity of mouse and human microglia at single-cell resolution. *Nature* 566, 388–392. doi: 10.1038/s41586-019-0924-x
- McIntire, S. L., Reimer, R. J., Schuske, K., Edwards, R. H., and Jorgensen, E. M. (1997). Identification and characterization of the vesicular GABA transporter. *Nature* 389, 870–876. doi: 10.1038/39908
- Miyamoto, A., Wake, H., Ishikawa, A. W., Eto, K., Shibata, K., Murakoshi, H., et al. (2016). Microglia contact induces synapse formation in developing somatosensory cortex. *Nat. Commun.* 7:12540. doi: 10.1038/ncomms12540
- Morest, D. K. (1968). The growth of synaptic endings in the mammalian brain: a study of the calyces of the trapezoid body. *Z. Anat. Entwicklungsgesch.* 127, 201–220. doi: 10.1007/bf00526129
- Myoga, M. H., Lehnert, S., Leibold, C., Felmy, F., and Grothe, B. (2014). Glycinergic inhibition tunes coincidence detection in the auditory brainstem. *Nat. Commun.* 5:3790. doi: 10.1038/ncomms4790
- Neniskyte, U., and Gross, C. T. (2017). Errant gardeners: glial-cell-dependent synaptic pruning and neurodevelopmental disorders. *Nat. Rev. Neurosci.* 18, 658–670. doi: 10.1038/nrn.2017.110
- Ngsee, J. K., Trimble, W. S., Elferink, L. A., Wendland, B., Miller, K., Calakos, N., et al. (1990). Molecular analysis of proteins associated with the synaptic vesicle membrane. *Cold Spring Harb. Symp. Quant. Biol.* 55, 111–118. doi: 10.1101/sqb.1990.055.01.014
- Paolicelli, R. C., Bolasco, G., Pagani, F., Maggi, L., Scianni, M., Panzanelli, P., et al. (2011). Synaptic pruning by microglia is necessary for normal brain development. *Science* 333, 1456–1458. doi: 10.1126/science.1202529
- Pecka, M., Brand, A., Behrend, O., and Grothe, B. (2008). Interaural time difference processing in the mammalian medial superior olive: the role of glycinergic inhibition. *J. Neurosci.* 28, 6914–6925. doi: 10.1523/jneurosci.1660-08.2008
- Pixley, S. K., and de Vellis, J. (1984). Transition between immature radial glia and mature astrocytes studied with a monoclonal antibody to vimentin. *Brain Res.* 317, 201–209. doi: 10.1016/0165-3806(84)90097-x
- Pyonteck, S. M., Akkari, L., Schuhmacher, A. J., Bowman, R. L., Sevenich, L., Quail, D. F., et al. (2013). CSF-1R inhibition alters macrophage polarization and blocks glioma progression. *Nat. Med.* 19, 1264–1272. doi: 10.1038/nm.3337
- Reemst, K., Noctor, S. C., Lucassen, P. J., and Hol, E. M. (2016). The indispensable roles of microglia and astrocytes during brain development. *Front. Human Neurosci.* 10:566. doi: 10.3389/fnhum.2016.00566
- Rodriguez-Contreras, A., de Lange, R. P., Lucassen, P. J., and Borst, J. G. (2006). Branching of calyceal afferents during postnatal development in the rat auditory brainstem. *J. Comp. Neurol.* 496, 214–228. doi: 10.1002/cne.20918
- Rodriguez-Contreras, A., van Hoeve, J. S., Habets, R. L., Locher, H., and Borst, J. G. (2008). Dynamic development of the calyx of Held synapse. *Proc. Natl. Acad. Sci. U.S.A.* 105, 5603–5608. doi: 10.1073/pnas.0801395105
- Saliu, A., Adise, S., Xian, S., Kudelska, K., and Rodriguez-Contreras, A. (2014). Natural and lesion-induced decrease in cell proliferation in the medial nucleus of the trapezoid body during hearing development. *J. Comp. Neurol.* 522, 971–985. doi: 10.1002/cne.23473
- Sanes, D. H. (1990). An in vitro analysis of sound localization mechanisms in the gerbil lateral superior olive. *J. Neurosci.* 10, 3494–3506. doi: 10.1523/jneurosci.10-11-03494.1990
- Sato, K. (2015). Effects of microglia on neurogenesis. *Glia* 63, 1394–1405. doi: 10.1002/glia.22858
- Satzler, K., Sohl, L. F., Bollmann, J. H., Borst, J. G., Frotscher, M., Sakmann, B., et al. (2002). Three-dimensional reconstruction of a calyx of Held and its postsynaptic principal neuron in the medial nucleus of the trapezoid body. *J. Neurosci.* 22, 10567–10579. doi: 10.1523/jneurosci.22-24-10567.2002
- Schafer, D. P., Lehrman, E. K., Kautzman, A. G., Koyama, R., Mardinly, A. R., Yamasaki, R., et al. (2012). Microglia sculpt postnatal neural circuits in an activity and complement-dependent manner. *Neuron* 74, 691–705. doi: 10.1016/j.neuron.2012.03.026
- Schafer, D. P., and Stevens, B. (2015). Microglia function in central nervous system development and plasticity. *Cold Spring Harb. Perspect. Biol.* 7:a020545. doi: 10.1101/cshperspect.a020545
- Schindelin, J., Arganda-Carreras, I., Frise, E., Kaynig, V., Longair, M., Pietzsch, T., et al. (2012). Fiji: an open-source platform for biological-image analysis. *Nat. Methods* 9, 676–682. doi: 10.1038/nmeth.2019
- Smith, P. H., Joris, P. X., Carney, L. H., and Yin, T. C. (1991). Projections of physiologically characterized globular bushy cell axons from the cochlear nucleus of the cat. *J. Comp. Neurol.* 304, 387–407. doi: 10.1002/cne.903040305
- Smith, P. H., Joris, P. X., and Yin, T. C. (1998). Anatomy and physiology of principal cells of the medial nucleus of the trapezoid body (MNTB) of the cat. *J. Neurophysiol.* 79, 3127–3142. doi: 10.1152/jn.1998.79.6.3127
- Spangenberg, E. E., Lee, R. J., Najafi, A. R., Rice, R. A., Elmore, M. R., Blurton-Jones, M., et al. (2016). Eliminating microglia in Alzheimer's mice prevents neuronal loss without modulating amyloid-beta pathology. *Brain* 139, 1265–1281. doi: 10.1093/brain/aww016
- Spangler, K. M., Warr, W. B., and Henkel, C. K. (1985). The projections of principal cells of the medial nucleus of the trapezoid body in the cat. *J. Comp. Neurol.* 238, 249–262. doi: 10.1002/cne.902380302

- Spirou, G. A., Brownell, W. E., and Zidanic, M. (1990). Recordings from cat trapezoid body and HRP labeling of globular bushy cell axons. *J. Neurophysiol.* 63, 1169–1190. doi: 10.1152/jn.1990.63.5.1169
- Stanley, E. R., Berg, K. L., Einstein, D. B., Lee, P. S., Pixley, F. J., Wang, Y., et al. (1997). Biology and action of colony-stimulating factor-1. *Mol. Reprod. Dev.* 46, 4–10.
- Stevens, B., Allen, N. J., Vazquez, L. E., Howell, G. R., Christopherson, K. S., Nouri, N., et al. (2007). The classical complement cascade mediates CNS synapse elimination. *Cell* 131, 1164–1178. doi: 10.1016/j.cell.2007.10.036
- Taschenberger, H., Leao, R. M., Rowland, K. C., Spirou, G. A., and von Gersdorff, H. (2002). Optimizing synaptic architecture and efficiency for high-frequency transmission. *Neuron* 36, 1127–1143. doi: 10.1016/s0896-6273(02)01137-6
- Thielens, N. M., Tedesco, F., Bohlson, S. S., Gaboriaud, C., and Tenner, A. J. (2017). C1q: a fresh look upon an old molecule. *Mol. Immunol.* 89, 73–83. doi: 10.1016/j.molimm.2017.05.025
- Tollin, D. J. (2003). The lateral superior olive: a functional role in sound source localization. *Neuroscientist* 9, 127–143. doi: 10.1177/1073858403252228
- Trussell, L. O. (1999). Synaptic mechanisms for coding timing in auditory neurons. *Annu. Rev. Physiol.* 61, 477–496. doi: 10.1146/annurev.physiol.61.1.477
- Vilalta, A., and Brown, G. C. (2018). Neurophagy, the phagocytosis of live neurons and synapses by glia, contributes to brain development and disease. *FEBS J.* 285, 3566–3575. doi: 10.1111/febs.14323
- Walton, N. M., Sutter, B. M., Laywell, E. D., Levkoff, L. H., Kearns, S. M., Marshall, G. P. II, et al. (2006). Microglia instruct subventricular zone neurogenesis. *Glia* 54, 815–825. doi: 10.1002/glia.20419
- Wang, T., van Woerden, G. M., Elgersma, Y., and Borst, J. G. G. (2018). Enhanced transmission at the calyx of held synapse in a mouse model for angelman syndrome. *Front. Cell. Neurosci.* 11:418. doi: 10.3389/fncel.2017.00418
- Wang, Y., Kakizaki, T., Sakagami, H., Saito, K., Ebihara, S., Kato, M., et al. (2009). Fluorescent labeling of both GABAergic and glycinergic neurons in vesicular GABA transporter (VGAT)-venus transgenic mouse. *Neuroscience* 164, 1031–1043. doi: 10.1016/j.neuroscience.2009.09.010
- Weatherstone, J. H., Kopp-Scheinflug, C., Pilati, N., Wang, Y., Forsythe, I. D., Rubel, E. W., et al. (2017). Maintenance of neuronal size gradient in MNTB requires sound-evoked activity. *J. Neurophysiol.* 117, 756–766. doi: 10.1152/jn.00528.2016
- Weinhard, L., di Bartolomei, G., Bolasco, G., Machado, P., Schieber, N. L., Neniskyte, U., et al. (2018). Microglia remodel synapses by presynaptic trogocytosis and spine head filopodia induction. *Nat. Commun.* 9:1228. doi: 10.1038/s41467-018-03566-5
- Wimmer, V. C., Nevian, T., and Kuner, T. (2004). Targeted in vivo expression of proteins in the calyx of Held. *Pflugers Arch.* 449, 319–333.
- Wofchuk, S. T., and Rodnight, R. (1995). Age-dependent changes in the regulation by external calcium ions of the phosphorylation of glial fibrillary acidic protein in slices of rat hippocampus. *Brain Res. Dev. Brain Res.* 85, 181–186. doi: 10.1016/0165-3806(94)00208-h

Conflict of Interest Statement: The authors declare that the research was conducted in the absence of any commercial or financial relationships that could be construed as a potential conflict of interest.

Copyright © 2019 Milinkeviciute, Henningfield, Muniak, Chokr, Green and Cramer. This is an open-access article distributed under the terms of the Creative Commons Attribution License (CC BY). The use, distribution or reproduction in other forums is permitted, provided the original author(s) and the copyright owner(s) are credited and that the original publication in this journal is cited, in accordance with accepted academic practice. No use, distribution or reproduction is permitted which does not comply with these terms.



Spontaneous Activity Patterns Are Altered in the Developing Visual Cortex of the *Fmr1* Knockout Mouse

Juliette E. Cheyne¹, Nawal Zabouri¹, David Baddeley² and Christian Lohmann^{1,3*}

¹ Department of Synapse and Network Development, Netherlands Institute for Neuroscience, Amsterdam, Netherlands,

² Auckland Bioengineering Institute, University of Auckland, Auckland, New Zealand, ³ Department of Functional Genomics, Center for Neurogenomics and Cognitive Research, VU University Amsterdam, Amsterdam, Netherlands

OPEN ACCESS

Edited by:

Qian-Quan Sun,
University of Wyoming, United States

Reviewed by:

Xinyu Zhao,
University of Wisconsin–Madison,
United States
Khaleel A. Razak,
University of California, Riverside,
United States
Carlos Portera-Cailliau,
University of California, Los Angeles,
United States

*Correspondence:

Christian Lohmann
c.lohmann@nin.knaw.nl

Received: 14 May 2019

Accepted: 19 August 2019

Published: 26 September 2019

Citation:

Cheyne JE, Zabouri N,
Baddeley D and Lohmann C (2019)
Spontaneous Activity Patterns Are
Altered in the Developing Visual
Cortex of the *Fmr1* Knockout Mouse.
Front. Neural Circuits 13:57.
doi: 10.3389/fncir.2019.00057

Fragile X syndrome (FXS) is the most prevalent inherited cause of autism and is accompanied by behavioral and sensory deficits. Errors in the wiring of the brain during early development likely contribute to these deficits, but the underlying mechanisms are unclear. Spontaneous activity patterns, which are required for fine-tuning neuronal networks before the senses become active, are perturbed in rodent models of FXS. Here, we investigated spontaneous network activity patterns in the developing visual cortex of the *Fmr1* knockout mouse using *in vivo* calcium imaging during the second postnatal week, before eye opening. We found that while the frequency, mean amplitude and duration of spontaneous network events were unchanged in the knockout mouse, pair-wise correlations between neurons were increased compared to wild type littermate controls. Further analysis revealed that interneuronal correlations were not generally increased, rather that low-synchronization events occurred relatively less frequently than high-synchronization events. Low-, but not high-, synchronization events have been associated with retinal inputs previously. Since we found that spontaneous retinal waves were normal in the knockout, our results suggest that peripherally driven activity is underrepresented in the *Fmr1* KO visual cortex. Therefore, we propose that central gating of retinal inputs may be affected in FXS and that peripherally and centrally driven activity patterns are already unbalanced before eye opening in this disorder.

Keywords: fragile X mental retardation, *in vivo* calcium imaging, sensory integration, 2-photon microscopy, transgenic mouse

INTRODUCTION

Autism spectrum disorders (ASD) are a group of neurodevelopmental disorders that have been characterized traditionally by core features such as weak social communication, restricted interests, and repetitive behaviors. More recently, it has become clear that these disorders are also associated with compromised sensory processing, including vision (Kogan et al., 2004; Knoth et al., 2014; Dickinson et al., 2016; Ethridge et al., 2017; Yamasaki et al., 2017). Changes in sensory perception may underlie the complex behavioral traits described previously (Baum et al., 2015; Yamasaki et al., 2017; Rais et al., 2018). Studies in animal models of ASD found alterations in sensory perception and plasticity as well (Dolen et al., 2007; Berzhanskaya et al., 2016; Orefice et al., 2016; He et al., 2017; Goel et al., 2018; Wen et al., 2019). Miswiring of central sensory pathways may underlie these

symptoms (Yamasaki et al., 2017; Goswami et al., 2019); however, the developmental mechanisms that cause miswiring of sensory pathways in ASD and neurodevelopmental disorders in general are unknown (Di Martino et al., 2014; Park et al., 2016).

The wiring of neuronal networks is driven by molecular cues early on and later refined by activity-dependent mechanisms (Sanes and Yamagata, 2009; Kirkby et al., 2013). Before the onset of sensation, spontaneous activity is required for fine-tuning synaptic connections for sensory processing; thereafter, experience further adapts sensory networks to the prevalent conditions in the environment (Villiers-Sidani et al., 2007; Caras and Sanes, 2015; Soutar et al., 2016). Perturbed mechanisms at all these developmental stages may contribute to neurodevelopmental syndromes (Meredith, 2015; Sanders, 2015).

Fragile X syndrome (FXS) is the most common genetic cause of autism and has been investigated extensively in patients and animal models (Hagerman et al., 2017), in particular the *Fmr1* knockout mouse (The Dutch-Belgian Fragile X Consortium, 1994; Mientjes et al., 2006). These studies confirmed sensory phenotypes in both humans and mice (Kogan et al., 2004; Dolen et al., 2007; Knoth et al., 2014; Zhang et al., 2014) and these phenotypes are most likely caused by compromised synaptic connectivity (Bureau et al., 2008; Gibson et al., 2008; La Fata et al., 2014). Importantly, spontaneous activity patterns are perturbed during development, suggesting that errors in early activity-dependent synaptic refinement may impair synaptic connections in the FXS brain. For example, spontaneous network events in the somatosensory cortex of the *Fmr1* KO mouse show increased correlations (Goncalves et al., 2013), which may render these activity patterns less suitable for refining developing networks (Leighton and Lohmann, 2016).

Here, we investigated spontaneous activity patterns in the developing primary visual cortex of the *Fmr1* KO mouse (Mientjes et al., 2006) before eye opening. We find increased inter-neuronal correlations in the developing visual cortex, similar to previous findings in the somatosensory cortex (Goncalves et al., 2013). Further analysis suggested, however, that there is not a general increase in correlations, but rather a relative decrease of low- vs. high-synchronicity network events. Low-synchronicity events (L-events) have previously been associated with inputs from the retina (Siegel et al., 2012). Thus, our results suggest that retinally driven activity is underrepresented in cortical *Fmr1* KO activity patterns. Since we show here that retinal waves are normal in the knockout, we propose that central gating in the ascending visual pathway may be affected in FXS, even before the onset of vision.

MATERIALS AND METHODS

Animals

All experimental procedures were approved by the Institutional Animal Care and Use Committee of the Royal Netherlands Academy of Arts and Sciences. The *Fmr1* KO mouse line used here was previously backcrossed to C57Bl/6J mice at least seven generations (Mientjes et al., 2006; de Vrij et al., 2008). The mice used in this study were bred from heterozygote *Fmr1*

(*Fmr1*^{+/-}) mothers and wild type fathers (WT, C57Bl/6J). Only male KO mice (*Fmr1*^{y/-}) were used in experiments, with littermate (wild type, *Fmr1*^{y/+}) males as controls. Experiments and initial analysis were performed blind to the genotype. There were no significant differences in weight (control: 6.79 ± 0.32 g, *n* = 20; FX: 6.51 ± 0.27 g, *n* = 18; *p* > 0.05) or age (control: 10.20 ± 0.29 days, *n* = 20, FX: 10.39 ± 0.26 days, *n* = 18, *p* > 0.05) between KO mice and WT mice for the cortical experiments. In the retinal experiments the weight (control: 5.58 ± 0.31 g, *n* = 15, FX: 5.34 ± 0.22 g, *n* = 17, *p* > 0.05) and age (control: 9.60 ± 0.31 days, *n* = 15, FX: 9.94 ± 0.20 days, *n* = 17, *p* > 0.05) also did not differ between KO mice and WT mice. All of the mice had closed eyes at the time of the experiment which fits with previous research showing that C57Bl/6J mice open their eyes at P12–P14 (Rocheffort et al., 2009).

Genotyping

Mouse genotypes were determined *post hoc* by polymerase chain reaction (PCR) using the following primers: for KO mice (GCCTCACATCCTAGCCCTCTAC and CCCACTGGGAGAGGATTATTTGGG) and for WT mice (GCCTCACATCC TAGCCCTCTAC and CCCACAAAGTTGATTCCCCAGA). Tail samples were digested overnight with proteinase K (0.2 µg/µL) in 500 µL tail lysis buffer (in mM: 100 Tris-HCl, 5 EDTA, 200 NaCl, and 0.2% SDS) at 56°C. Proteins were pelleted by centrifugation (14,000 rpm for 3 min); DNA was isolated and precipitated with 500 µL of isopropanol. Following centrifugation (14,000 rpm for 1 min) the DNA pellet was dried and subsequently resuspended in 50 µL Tris-EDTA buffer. The PCR mix was prepared by adding: 2.6 µL of 10× buffer, 0.25 µL dNTPs (20 mM), 0.5 µL primer mix (10 µM), 0.15 µL Taq polymerase, and milliQ water up to a total of 25 µL for each sample. 1 µL of mouse DNA was added and the mixture was kept at 95°C for 5 min followed by 40 cycles (10 s at 95°C, 20 s at 60°C, and 45 s at 72°C) and 72°C for 10 min to finish.

Visual Cortex Imaging

In vivo imaging experiments were performed as described previously (Siegel et al., 2012). Briefly, P8–14 mice were anesthetized with isoflurane (2% in 1.7 L/min O₂), attached to a head bar with super glue and stabilized with dental cement (Heraeus Kulzer). Isoflurane was then reduced to 0.7% for the remainder of the experiment during which temperature was maintained at 36–37°C and heart beat was continuously monitored (control: 329.15 ± 16.17 bpm, *n* = 20, FX: 323.89 ± 17.94 bpm, *n* = 18, *p* > 0.05). At this level of isoflurane, animals remained anesthetized as they showed limited movement and a lack of reflexes. However, their breathing was rapid and shallow, and heart rates were high indicating that they were lightly anesthetized, as they lacked low gasping respiration and low heart rates typical in deeply anesthetized mice of this age. A craniotomy was made above the visual cortex without perforating the dura. The exposed cortical surface was kept moist with cortex buffer (in mM: 125 NaCl, 5 KCl, 10 glucose, 10 HEPES, 2 MgSO₄ and 2 CaCl₂, pH 7.4). A large population of layer 2/3 neurons was then labeled by bolus loading with

the calcium-sensitive dye Oregon Green BAPTA-1 AM (OGB1-AM, Life Technologies, O-6807) or Cal-590 AM (AAT Bioquest, 20510) diluted in 4 μ L pluronic F-127 (20% solution in DMSO, Life Technologies, P-3000MP), and 36 μ L dye buffer (in mM: 150 NaCl, 2.5 KCl, and 10 HEPES, pH 7.4). Dye was injected into layer 2/3 through a glass pipette (3–7 M Ω) using a picospritzer (12 min, 10–12 psi, Toohey). After 1 h the craniotomy was covered with 1.5% agarose for extra stability and imaging was performed to monitor spontaneous network activity in the same set of neurons (Mean cell number: Control: 91.80 ± 10.03 , $n = 20$, FX: 80.17 ± 6.84 , $n = 18$, $p > 0.05$) for approximately 40 min (Mean imaging time: Control: 38.31 ± 2.69 min, $n = 20$, FX: 43.42 ± 2.78 min, $n = 18$. Total duration recorded: Control: 766 min, FX: 781 min). Consecutive xyt-stacks (256 \times 256, 600 nm pixel size, 5 Hz) were obtained through a 40 \times water-immersion objective (0.8 NA, Olympus) with a two-photon microscope (Movable Objective Microscope, Sutter Instrument or A1R-MP, Nikon) and a mode-locked Ti:Sapphire laser (at $\lambda = 810$ nm; Spectra Physics or Coherent) controlled by custom made Labview (National Instruments) software or ScanImage (Pologruto et al., 2003). 5-min recordings were obtained with only short breaks for re-focusing when necessary.

Visual Cortex Image Analysis

Recordings of spontaneous network activity in the cortex were analyzed with ImageJ (NIH) and custom-written Matlab scripts (MathWorks). To remove movement artifacts and align all recordings we performed image alignment based on the enhanced correlation coefficient algorithm (Evangelidis and Psarakis, 2008). $\Delta F/F_0$ stacks were generated by subtracting and dividing each frame by the baseline fluorescence (F_0). Regions of interest (ROIs) were placed on cells that showed clear activity and were visible in all recordings. Glial cells in the field of view showed elevated basal intensity and were not active. All included ROIs were neuronal. $\Delta F/F_0$ traces were obtained by calculating the mean intensity within the ROI for each frame. Increases in fluorescence intensity, which reflect increases in the intracellular calcium concentration due to action potential firing, were then detected semi-automatically for all ROIs and the maximum amplitudes and timings were determined. The detection threshold was adjusted for each experiment (at least 2 \times the noise) but remained the same within an experiment. A network event was defined as activity across multiple neurons during consecutive frames (<15 frames separation). The participation rate for each event was determined by summing the number of active cells and dividing by the total number of ROIs. Events with less than 20% participation were not analyzed further. Previously we found that two types of activity occur in the visual cortex at this developmental age: L-events are low participation (20–80%) and low amplitude events that are generated in the retina and transmitted to the cortex, while H-events are high participation (>80%) and high amplitude events that are generated within the cortex (Siegel et al., 2012). Here we also divided the data into H-events and L-events based on participation (above or below 80%). We found that varying the cut-off between 70 and 90% did not affect the results presented in this study (not shown).

To analyze synchrony, we calculated Pearson's correlations for each neuron pair in each experiment. Correlations were calculated on binarized activity traces of each neuron where each neuron was given a value of 0 for each inactive frame and a value of 1 for each frame of each burst it was active in. Burst duration was determined as the difference between the peak frame of the first and last cell to become active. To compare the correlation means we averaged across all pairs within 200 μ m for each animal. The distance between the two cells was calculated as a straight line connecting the center of each ROI. We excluded animals that had fewer than 10 events in the recorded time (6 mice were excluded, 4 WT and 2 KO).

Retinal Imaging

Postnatal day 8–11 (P8–11) mice were anesthetized by inhalation of isoflurane (2% in 1.7 L/min O₂) and killed by decapitation. The eyes were removed and placed into ice cold modified Hank's balanced salt solution (HBSS, Life Technologies, in mM: 3.26 CaCl₂, 0.493 MgCl₂, 0.406 MgSO₄, 5.33 KCl, 0.441 KH₂PO₄, 4.17 NaHCO₃, 138 NaCl, 0.336 Na₂HPO₄, and 5.56 D-glucose) and dissected to isolate the retinas. Ganglion cells were labeled by injection of OGB1-AM (prepared as for visual cortex imaging) just below the inner limiting membrane with a glass pipette (1.5–5 M Ω , 3 min, 15 psi). After 1 h cells retinas were placed in a heated chamber (35°C) and imaged to monitor spontaneous network activity for \sim 45 min (Mean imaging time: Control: 47.33 ± 1.18 min, $n = 15$, FX: 41.76 ± 1.05 min, $n = 17$. Total duration recorded: Control: 710 min, FX: 710 min). Consecutive xyt-stacks (500 \times 500 pixels, 1.6 μ m pixel size, 10 Hz) were obtained through a 20 \times water-immersion objective (0.5 NA, Olympus) with a CCD camera (iXon+; Andor Technology) and LED-based excitation illumination (pE-2; CoolLed) controlled by custom-built software (Labview, National Instruments).

Retinal Image Analysis

Recordings of spontaneous network activity in the retina were analyzed in a similar way to the cortical recordings. However, due to the large field of view and resulting small size of neuronal somas we did not analyze retinal activity in individual neurons. Instead, we downsized the images into 10 \times 10 pixel bins and analyzed activity in the resulting 100 pixels. $\Delta F/F_0$ stacks were generated as described above and the $\Delta F/F_0$ traces were obtained for each pixel. Activity was then detected as for the cortical experiments except the same threshold was used for all experiments.

Retinal wave front velocities were quantified using custom python code implemented as part of the python-microscopy project¹. Full resolution $\Delta F/F_0$ stacks were smoothed with a Gaussian (radius of 10 pixels) to reduce noise. The positions of wave front peaks in each frame were estimated as the zero-crossings of the time derivative of intensity as follows: (1) A low threshold was used to establish a mask of areas where calcium was elevated and to eliminate the inactive areas whose intensity was roughly constant over time, (2) in pixels above this threshold, an approximate temporal derivative of the intensity ($\Delta_t I$) was

¹www.python-microscopy.org

calculated by taking the difference between consecutive frames, (3) zero-crossings were detected by finding all pixels where $|\Delta I|$ was less than a threshold (chosen to give a gap-free wave front ~ 4 –5 pixels wide) and skeletonizing the resulting masks. The direction of propagation of these wave fronts was estimated using a regularized version of optical flow algorithm described previously (Fleet and Weiss, 2006) applied to the filtered intensity data. Velocities were then estimated at each point on the wave front by looking along the optical flow direction, extracting the closest position of the wave front along this vector in each of the 5 frames before and after the current frame, and performing a linear least-squares fit to these positions as a function of time.

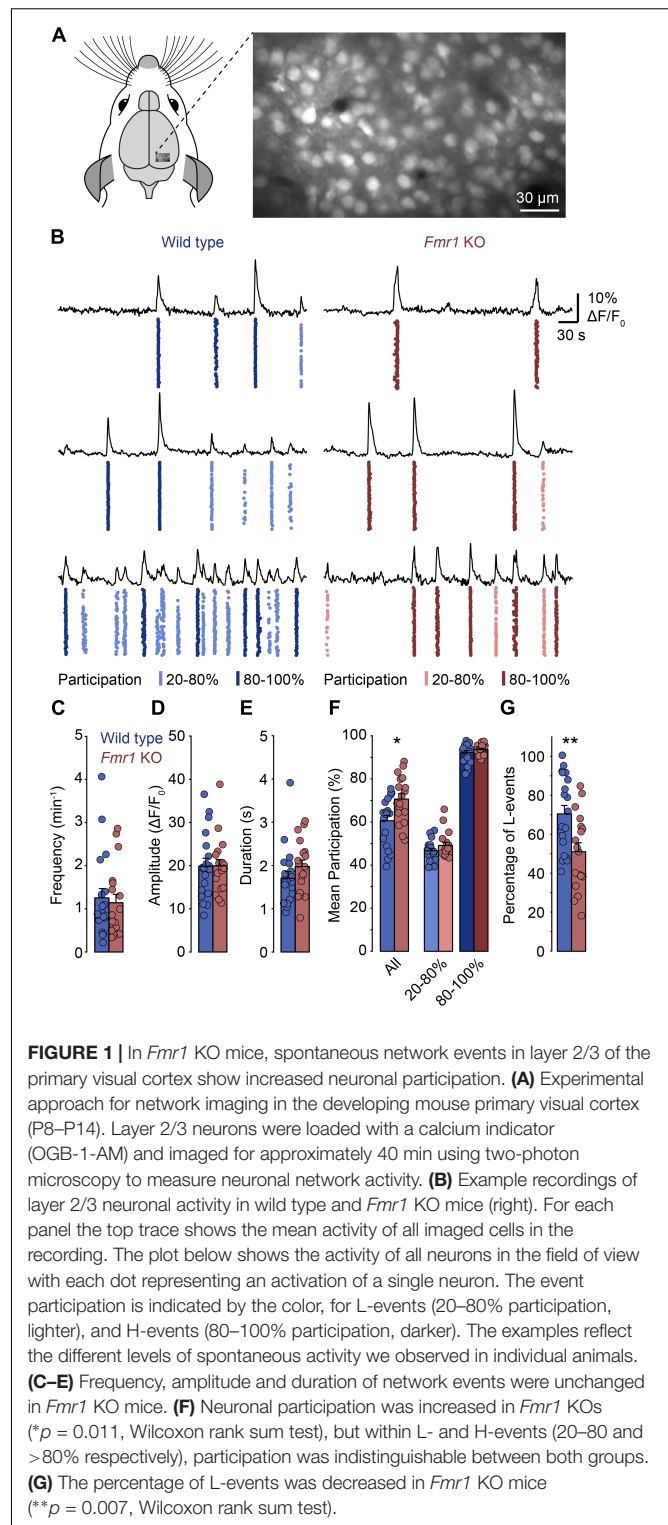
Statistics

To test for statistical differences between groups we used the Wilcoxon rank sum test. Data are presented as means \pm SEM with n as the number of animals.

RESULTS

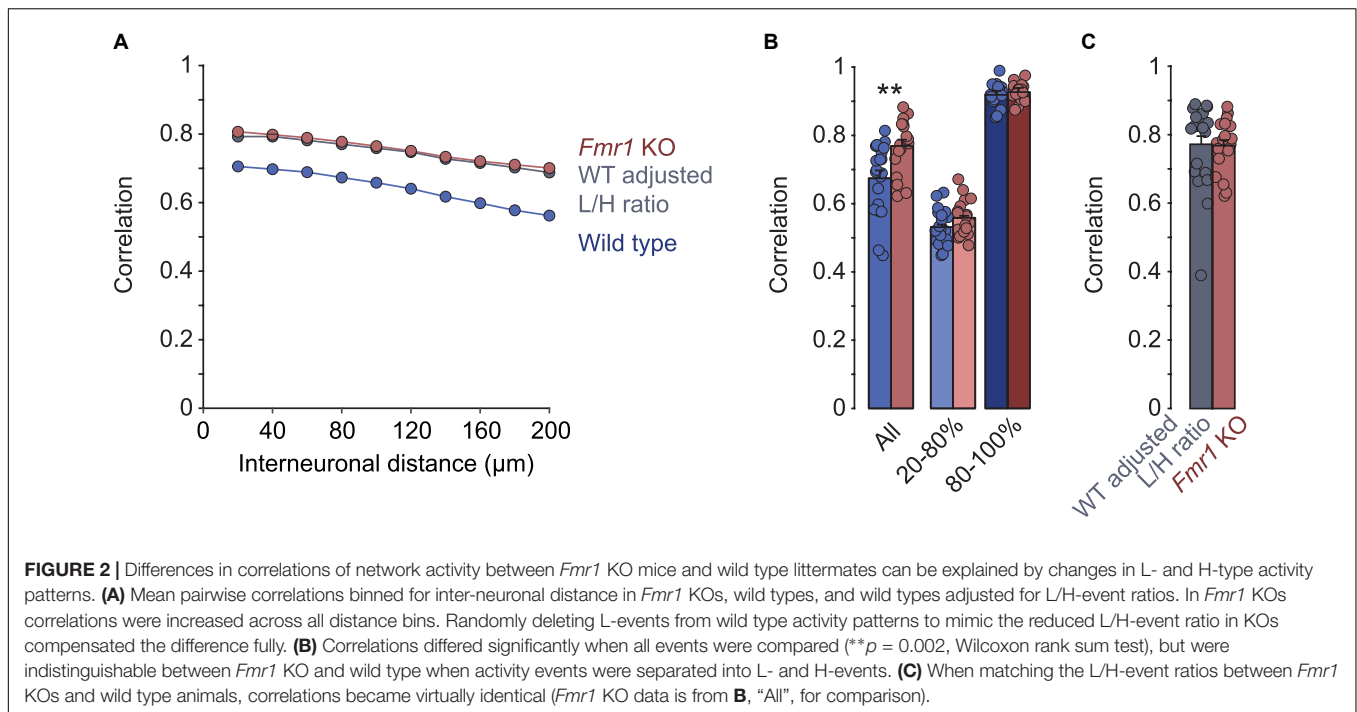
To determine whether spontaneous network activity patterns are altered in the developing visual cortex of FXS mice we performed *in vivo* calcium imaging in the primary visual cortex of lightly anesthetized *Fmr1* knockout mice (*Fmr1*^{-/-}) and wild type littermate controls (*Fmr1*^{+/+}) at postnatal day (P) 8–14 (Figure 1). Previously, we found that low levels of anesthesia (0.7 – 1% isoflurane) reduce the frequency of spontaneous network events, but do not change their basic properties (Siegel et al., 2012). We labeled layer 2/3 neurons with a fluorescent calcium indicator (Oregon Green BAPTA-1 or Cal-590) by bolus injection (Figure 1A) and recorded neuronal activity using two-photon imaging. Increases in somatic calcium, which reflect action potential firing, were monitored continuously in large populations of neurons for approximately 40 min (Figure 1B).

In both wild type and *Fmr1* KO mice, we observed repetitive events of synchronized network activity as described previously (Figure 1B; Hanganu et al., 2006; Golshani et al., 2009; Rochefort et al., 2009; Colonnese et al., 2010; Siegel et al., 2012). In most animals, there was no or little activity in between these network events, as is typically observed during this developmental stage. We found that the frequency, the mean amplitude and the duration of network events were indistinguishable between *Fmr1* KOs and controls (Figures 1C–E). In contrast, the mean participation was significantly higher in *Fmr1* KOs than in wild type animals (Figure 1F). Previously, we had identified two activity patterns in the developing visual cortex before eye-opening: L-events with low participation rates that are dependent on retinal wave activity and H-events where almost all neurons participate, which are independent of retinal inputs (Siegel et al., 2012). When we separated network events in the present data sets and compared participation rates within L-events (20–80% participation) and H-events (80–100% participation), we found that within these groups there was no change in participation (Figure 1F). This suggested that in *Fmr1* KO mice overall participation was not generally increased, but that the relative contribution of L- and H-events differed in the knockout mouse.



Indeed, we found that the proportion of L-events was decreased in the *Fmr1* KO mouse (Figure 1G).

A previous study found that in the somatosensory cortex of *Fmr1* KO mice, neuronal activity was more correlated than in wild type controls (Goncalves et al., 2013). To compare these



results with the primary visual cortex, we analyzed pair-wise correlations of the calcium traces of layer 2/3 neurons in our recordings. Like in the somatosensory cortex, we observed a decrease in correlations with increasing distance between them, in both *Fmr1* KO ($R^2 = 0.99$, $p < 0.001$) and control ($R^2 = 0.98$, $p < 0.001$) mice (**Figure 2A**). In addition, correlations were higher in the *Fmr1* KO mouse compared to controls across all distance bins (**Figures 2A,B**). We did not observe significant age related changes of these correlations or their differences between genotypes (**Supplementary Figure 1**). Surprisingly, we found that correlation coefficients when determined for L- and H-events separately were virtually identical in *Fmr1* KO and control mice (**Figure 2B**). Again, this observation suggested that we did not observe a global increase in correlations, but rather a shift toward a higher fraction of high-correlation network events (H-events). To test the plausibility of this idea we randomly deleted L-events from the control dataset to match the percentage of L-events of *Fmr1* KO and control recordings (WT adjusted L/H ratio). This adjustment increased the overall correlations to the same level as those seen in *Fmr1* KO mice (**Figures 2A,C**), confirming that a shift in L-/H-event ratio could explain the increased correlations in the *Fmr1* KO visual cortex.

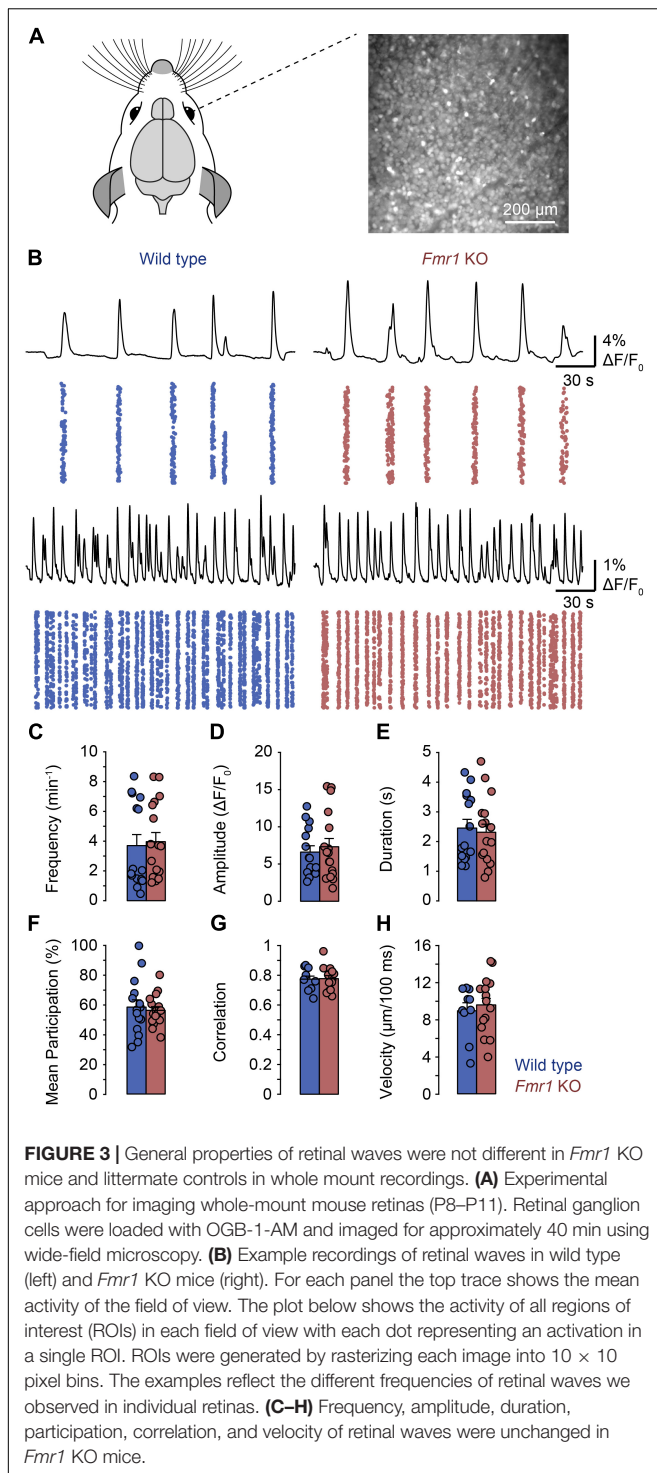
Since we previously found that L-, but not H-events are dependent on retinal wave activity, the present observations suggested that the representation of inputs from the sensory periphery is reduced in comparison to intrinsically generated activity patterns. Therefore, we asked whether retinal waves were affected in the *Fmr1* KO mouse. We performed calcium imaging in retinal whole mounts from P8–P11 *Fmr1* KO and control mice (**Figure 3A**). We observed retinal waves in both preparations (**Figure 3B**) and found no differences in frequency, amplitude, duration, participation or correlation

between them (**Figures 3C–G**). In addition, we analyzed the velocity of retinal waves but found no difference between *Fmr1* KO and control mice (**Figure 3H**). Thus, peripheral activity is underrepresented in the *Fmr1* KO visual cortex, despite normal retinal waves, suggesting differences in central processing of peripheral activity in FXS.

DISCUSSION

Neurodevelopmental disorders are associated with aberrant spontaneous activity patterns during early stages of brain development. Here, we show that in the visual cortex of the *Fmr1* KO mouse, neuronal correlations are increased compared to wild type littermates. The distribution of correlations suggest that this is not a consequence of generally increased correlations, but rather a redistribution of the contribution of two distinct, previously described activity patterns. Specifically, we see a relative decrease in those activity patterns that are dependent on retinal inputs even though retinal waves are unchanged in this FXS mouse model.

Like in the somatosensory cortex (Goncalves et al., 2013), we observe here an increase in the mean correlation coefficient when we compare activity patterns between pairs of neurons in *Fmr1* KO mice and wild type littermates. This increase is quantitatively and qualitatively very similar to the increase in the somatosensory cortex, as it affects pairs of neurons of all distances and translates to a change of approximately 10–20%. While in the somatosensory cortex differences become most pronounced by P14, we see differences in the visual cortex already at P8–P14. These differences are apparent in lightly anesthetized animals, whereas a significant difference between KO and wild



type has been described in the somatosensory cortex only in awake animals (Goncalves et al., 2013). Despite the differences in detail between the primary visual and somatosensory cortices, these studies show that cortical activity patterns in *Fmr1* KO mice are associated with increased neuronal correlations. Similar findings have been observed at P0–P7 (La Fata et al., 2014).

Surprisingly, we find that increases in correlations do not distribute evenly across all types of events. When splitting events into high and low participation activity as described previously (Siegel et al., 2012) participation rates and correlations are unchanged in either group. We conclude therefore, that correlations are not generally increased, but rather that a change in contribution of these two types of activity patterns causes the increased mean correlations in the *Fmr1* KO visual cortex. This conclusion is supported by (1) the overall reduction in the L-/H-event ratio and (2) the fact that matching the L/H-event ratio between *Fmr1* KO and control activity fully equalizes the correlations between both conditions. Since L-events, but not H-events, have been associated with retinal inputs (Siegel et al., 2012), these observations suggest that peripheral activity is underrepresented in the *Fmr1* KO visual cortex before eye opening. Peripheral and central inputs may have complementary functions in cortical wiring (Siegel et al., 2012; Leighton and Lohmann, 2016), consequently, changes in their relative frequencies are likely to perturb synapse development.

Deficits in photoreceptor function have been described in the *Fmr1* KO mouse (Rossignol et al., 2014) therefore, we tested whether changes in early retinal activity could explain this difference. However, retinal waves are not affected in the *Fmr1* KO mouse, since their frequency, amplitude, and correlation are indistinguishable between KOs and controls.

What could explain the reduced representation of retinal inputs in the *Fmr1* KO visual cortex? A good candidate might be alterations in inhibitory neuron function. Early differences in inhibitory function have been implicated in neurodevelopmental disorders in general and FXS in particular (Marin, 2012; Le Magueresse and Monyer, 2013; Cellot and Cherubini, 2014; Tyzio et al., 2014; Goel et al., 2018). Furthermore, different types of interneurons are at pivotal positions within cortical networks to gate specifically bottom-up or horizontal activity. While PV neurons selectively target bottom-up connections, other interneurons, like the somatostatin expressing interneuron type, regulate horizontal activity spread (Tremblay et al., 2016; van Versendaal and Levelt, 2016; Wood et al., 2017). In addition, during development, cortical interneurons control spontaneous and early sensory evoked activity in a cell-type specific manner (Marques-Smith et al., 2016; Tuncdemir et al., 2016; Che et al., 2018). Therefore, selective alterations e.g., in PV neuron function could specifically decrease the effectiveness of ascending sensory pathways and thereby dampen cortical inputs from the periphery (Khazipov et al., 2013; Goel et al., 2018). Alternatively or in addition, differences in the excitability or synaptic function of excitatory connections at the level of the cortex or the lateral geniculate nucleus (Murata and Colonnese, 2016) might be involved as well. For example, a delay in the maturation of thalamo-cortical synapses has been described in the somatosensory cortex of *Fmr1* KO mice (Harlow et al., 2010). A similar delay of synapse development in the ascending visual pathways could explain the reduced transmission of retinal activity into the cortex during the second postnatal week, too.

Imbalanced contribution of external vs. internal activity streams have been observed in neurodevelopmental disorders (Courchesne and Pierce, 2005; Geschwind and Levitt, 2007).

Thus, the findings described here, suggest that network imbalances already manifest early in development, before the onset of sensation. If this can be generalized beyond FXS, diagnosis of neurodevelopmental disorders may be possible earlier than previously thought and thus facilitate earlier and more promising treatments in the future.

DATA AVAILABILITY

The datasets generated for this study are available on request to the corresponding author.

ETHICS STATEMENT

The animal study was reviewed and approved by the Animal Care and Use Committee of the Royal Netherlands Academy of Arts and Sciences.

AUTHOR CONTRIBUTIONS

JC and CL conceived and designed the study, and wrote the manuscript. JC and NZ collected the data. JC and DB contributed to the data and analysis of the tools. JC performed the analysis,

and contributed to all except the retinal velocity analysis, which was written by DB.

FUNDING

This work was supported by grants of Netherlands Organization for Scientific Research (NWO, ALW Open Program Grants Nos. 822.02.006 and ALWOP.216; ALW Vici Grant No. 865.12.001), ZonMW (Top Grants Nos. 91210009 and 9126021), the “Stichting Vrienden van het Herseninstituut” (CL) and by a fellowship of the fond de recherche santé, Québec to NZ.

ACKNOWLEDGMENTS

We thank Christiaan Levelt, Paloma Maldonado, and Victoria Busch for their comments on the manuscript. We also thank Johan Winnubst for help with image processing software.

SUPPLEMENTARY MATERIAL

The Supplementary Material for this article can be found online at: <https://www.frontiersin.org/articles/10.3389/fncir.2019.00057/full#supplementary-material>

REFERENCES

- Baum, S. H., Stevenson, R. A., and Wallace, M. T. (2015). Behavioral, perceptual, and neural alterations in sensory and multisensory function in autism spectrum disorder. *Prog. Neurobiol.* 134, 140–160. doi: 10.1016/j.pneurobio.2015.09.007
- Berzhanskaya, J., Phillips, M. A., Gorin, A., Lai, C., Shen, J., and Colonnese, M. T. (2016). Disrupted cortical state regulation in a rat model of fragile x syndrome. *Cereb. Cortex* 27:bhv331. doi: 10.1093/cercor/bhv331
- Bureau, I., Shepherd, G. M. G., and Svoboda, K. (2008). Circuit and plasticity defects in the developing somatosensory cortex of *fmr1* knock-out mice. *J. Neurosci.* 28, 5178–5188. doi: 10.1523/JNEUROSCI.1076-08.2008
- Caras, M. L., and Sanes, D. H. (2015). Sustained perceptual deficits from transient sensory deprivation. *J. Neurosci. Off. J. Soc. Neurosci.* 35, 10831–10842. doi: 10.1523/JNEUROSCI.0837-15.2015
- Cellot, G., and Cherubini, E. (2014). GABAergic signaling as therapeutic target for autism spectrum disorders. *Front. Pediatr.* 2:70. doi: 10.3389/fped.2014.00070
- Che, A., Babij, R., Iannone, A. F., Fetcho, R. N., Ferrer, M., Liston, C., et al. (2018). Layer I interneurons sharpen sensory maps during neonatal development. *Neuron* 99, 98–116. doi: 10.1016/j.neuron.2018.06.002
- Colonnese, M. T., Kaminska, A., Minlebaev, M., Milh, M., Bloem, B., Lescure, S., et al. (2010). A conserved switch in sensory processing prepares developing neocortex for vision. *Neuron* 67, 480–498. doi: 10.1016/j.neuron.2010.07.015
- Courchesne, E., and Pierce, K. (2005). Why the frontal cortex in autism might be talking only to itself: local over-connectivity but long-distance disconnection. *Curr. Opin. Neurobiol.* 15, 225–230. doi: 10.1016/j.conb.2005.03.001
- de Vrij, F. M., Levenga, J., van der Linde, H. C., Koekkoek, S. K., De Zeeuw, C. I., Nelson, D. L., et al. (2008). Rescue of behavioral phenotype and neuronal protrusion morphology in *Fmr1* KO mice. *Neurobiol. Dis.* 31, 127–132. doi: 10.1016/j.nbd.2008.04.002
- Di Martino, A., Fair, D. A., Kelly, C., Satterthwaite, T. D., Castellanos, F. X., Thomason, M. E., et al. (2014). Unraveling the miswired connectome: a developmental perspective. *Neuron* 83, 1335–1353. doi: 10.1016/j.neuron.2014.08.050
- Dickinson, A., Bruyns-Haylett, M., Smith, R., Jones, M., and Milne, E. (2016). Superior orientation discrimination and increased peak gamma frequency in autism spectrum conditions. *J. Abnorm. Psychol.* 125, 412–422. doi: 10.1037/abn0000148
- Dolen, G., Osterweil, E., Rao, B. S., Smith, G. B., Auerbach, B. D., Chattarji, S., et al. (2007). Correction of fragile X syndrome in mice. *Neuron* 56, 955–962. doi: 10.1016/j.neuron.2007.12.001
- Ethridge, L. E., White, S. P., Mosconi, M. W., Wang, J., Pedapati, E. V., Erickson, C. A., et al. (2017). Neural synchronization deficits linked to cortical hyperexcitability and auditory hypersensitivity in fragile X syndrome. *Mol. Autism* 8:22. doi: 10.1186/s13229-017-0140-1
- Evangelidis, G. D., and Psarakis, E. Z. (2008). Parametric Image alignment using enhanced correlation coefficient maximization. *IEEE Trans. Pattern Anal. Mach. Intell.* 30, 1858–1865. doi: 10.1109/TPAMI.2008.113
- Fleet, D., and Weiss, Y. (2006). *Optical Flow Estimation. In: Handbook of Mathematical Models in Computer Vision.* Boston, MA: Springer.
- Geschwind, D. H., and Levitt, P. (2007). Autism spectrum disorders: developmental disconnection syndromes. *Curr. Opin. Neurobiol.* 17, 103–111. doi: 10.1016/j.conb.2007.01.009
- Gibson, J. R., Bartley, A. F., Hays, S. A., and Huber, K. M. (2008). Imbalance of neocortical excitation and inhibition and altered UP states reflect network hyperexcitability in the mouse model of fragile X syndrome. *J. Neuro. Physiol.* 100, 2615–2626. doi: 10.1152/jn.90752.2008
- Goel, A., Cantu, D. A., Guilfoyle, J., Chaudhari, G. R., Newadkar, A., Todisco, B., et al. (2018). Impaired perceptual learning in a mouse model of Fragile X syndrome is mediated by parvalbumin neuron dysfunction and is reversible. *Nat. Neurosci.* 21, 1404–1411. doi: 10.1038/s41593-018-0231-0
- Golshani, P., Goncalves, J. T., Khoshkhoo, S., Mostany, R., Smirnakis, S., and Portera-Cailliau, C. (2009). Internally mediated developmental desynchronization of neocortical network activity. *J. Neurosci.* 29, 10890–10899. doi: 10.1523/JNEUROSCI.2012-09.2009
- Goncalves, J. T., Anstey, J. E., Golshani, P., and Portera-Cailliau, C. (2013). Circuit level defects in the developing neocortex of Fragile X mice. *Nat. Neurosci.* 16, 903–909. doi: 10.1038/nn.3415
- Goswami, S., Cavalier, S., Sridhar, V., Huber, K. M., and Gibson, J. R. (2019). Local cortical circuit correlates of altered EEG in the mouse model of Fragile X syndrome. *Neurobiol. Dis.* 124, 563–572. doi: 10.1016/j.nbd.2019.01.002

- Hagerman, R. J., Berry-Kravis, E., Hazlett, H. C., Bailey, D. B., Moine, H., Kooy, R. F., et al. (2017). Fragile X syndrome. *Nat. Rev. Dis. Primer.* 3:17065.
- Hanganu, I. L., Ben Ari, Y., and Khazipov, R. (2006). Retinal waves trigger spindle bursts in the neonatal rat visual cortex. *J. Neurosci.* 26, 6728–6736. doi: 10.1523/jneurosci.0752-06.2006
- Harlow, E. G., Till, S. M., Russell, T. A., Wijetunge, L. S., Kind, P., and Contractor, A. (2010). Critical period plasticity is disrupted in the barrel cortex of *fmr1* knockout mice. *Neuron* 65, 385–398. doi: 10.1016/j.neuron.2010.01.024
- He, C. X., Cantu, D. A., Mantri, S. S., Zeiger, W. A., Goel, A., and Portera-Cailliau, C. (2017). Tactile defensiveness and impaired adaptation of neuronal activity in the *fmr1* knock-out mouse model of autism. *J. Neurosci.* 37, 6475–6487. doi: 10.1523/JNEUROSCI.0651-17.2017
- Khazipov, R., Minlebaev, M., and Valeeva, G. (2013). Early gamma oscillations. *Neuroscience* 250, 240–252. doi: 10.1016/j.neuroscience.2013.07.019
- Kirkby, L. A., Sack, G. S., Firl, A., and Feller, M. B. (2013). A Role for correlated spontaneous activity in the assembly of neural circuits. *Neuron* 80, 1129–1144. doi: 10.1016/j.neuron.2013.10.030
- Knoth, I. S., Vannasing, P., Major, P., Michaud, J. L., and Lippé, S. (2014). Alterations of visual and auditory evoked potentials in fragile X syndrome. *Int. J. Dev. Neurosci.* 36, 90–97. doi: 10.1016/j.ijdevneu.2014.05.003
- Kogan, C. S., Boutet, I., Cornish, K., Zangenehpour, S., Mullen, K. T., Holden, J. J., et al. (2004). Differential impact of the FMR1 gene on visual processing in fragile X syndrome. *Brain* 127, 591–601. doi: 10.1093/brain/awh069
- La Fata, G., Gärtner, A., Domínguez-Iturza, N., Dresselaers, T., Dawitz, J., Poorthuis, R. B., et al. (2014). FMRP regulates multipolar to bipolar transition affecting neuronal migration and cortical circuitry. *Nat. Neurosci.* 17, 1693–1700. doi: 10.1038/nn.3870
- Le Mageresse, C., and Monyer, H. (2013). GABAergic interneurons shape the functional maturation of the cortex. *Neuron* 77, 388–405. doi: 10.1016/j.neuron.2013.01.011
- Leighton, A. H., and Lohmann, C. (2016). The wiring of developing sensory circuits-from patterned spontaneous activity to synaptic plasticity mechanisms. *Front. Neural. Circuits* 10:71.
- Marin, O. (2012). Interneuron dysfunction in psychiatric disorders. *Nat. Rev. Neurosci.* 13, 107–120. doi: 10.1038/nrn3155
- Marques-Smith, A., Lyngholm, D., Kaufmann, A.-K., Stacey, J. A., Hoerder-Suabedissen, A., Becker, E. B. E., et al. (2016). A transient transaminergic gabaergic interneuron circuit connects thalamocortical recipient layers in neonatal somatosensory cortex. *Neuron* 89, 536–549. doi: 10.1016/j.neuron.2016.01.015
- Meredith, R. M. (2015). Sensitive and critical periods during neurotypical and aberrant neurodevelopment: a framework for neurodevelopmental disorders. *Neurosci. Biobehav. Rev.* 50C, 180–188. doi: 10.1016/j.neubiorev.2014.12.001
- Mientjes, E. J., Nieuwenhuizen, I., Kirkpatrick, L., Zu, T., Hoogeveen-Westerveld, M., Severijnen, L., et al. (2006). The generation of a conditional *Fmr1* knock out mouse model to study *Fmrp* function in vivo. *Neurobiol. Dis.* 21, 549–555. doi: 10.1016/j.nbd.2005.08.019
- Murata, Y., and Colonnese, M. T. (2016). An excitatory cortical feedback loop gates retinal wave transmission in rodent thalamus Nelson SB, ed. *eLife* 5:e18816.
- Orefice, L. L., Zimmerman, A. L., Chirila, A. M., Sloboda, S. J., Head, J. P., and Ginty, D. D. (2016). Peripheral mechanosensory neuron dysfunction underlies tactile and behavioral deficits in mouse models of ASDs. *Cell* 166, 299–313. doi: 10.1016/j.cell.2016.05.033
- Park, H. R., Lee, J. M., Moon, H. E., Lee, D. S., Kim, B.-N., Kim, J., et al. (2016). A short review on the current understanding of autism spectrum disorders. *Exp. Neurobiol.* 25, 1–13. doi: 10.5607/en.2016.25.1.1
- Pologruto, T. A., Sabatini, B. L., and Svoboda, K. (2003). ScanImage: flexible software for operating laser scanning microscopes. *Biomed Eng. Online* 2:13.
- Rais, M., Binder, D. K., Razak, K. A., and Ethell, I. M. (2018). Sensory processing phenotypes in fragile X syndrome. *ASN Neuro.* 10:1759091418801092. doi: 10.1177/1759091418801092
- Rocheffort, N. L., Garaschuk, O., Milos, R. I., Narushima, M., Marandi, N., Pichler, B., et al. (2009). Sparsification of neuronal activity in the visual cortex at eye-opening. *Proc. Natl. Acad. Sci. U.S.A.* 106, 15049–15054. doi: 10.1073/pnas.0907660106
- Rossignol, R., Ranchon-Cole, I., Pâris, A., Herzine, A., Perche, A., Laurenceau, D., et al. (2014). Visual sensorial impairments in neurodevelopmental disorders: evidence for a retinal phenotype in fragile X syndrome. *PLoS One* 9:e105996. doi: 10.1371/journal.pone.0105996
- Sanders, S. J. (2015). First glimpses of the neurobiology of autism spectrum disorder. *Curr. Opin. Genet. Dev.* 33, 80–92. doi: 10.1016/j.gde.2015.10.002
- Sanes, J. R., and Yamagata, M. (2009). Many paths to synaptic specificity. *Annu. Cell Dev. Biol.* 25, 161–195. doi: 10.1146/annurev.cellbio.24.110707.175402
- Siegel, F., Heimel, J. A., Peters, J., and Lohmann, C. (2012). Peripheral and central inputs shape network dynamics in the developing visual cortex in vivo. *Curr. Biol.* 22, 253–258. doi: 10.1016/j.cub.2011.12.026
- Soutar, C. N., Rosen, L. G., Rodier, S. G., and Dringenberg, H. C. (2016). Effects of patterned sound deprivation on short- and long-term plasticity in the rat thalamocortical auditory system in vivo. *Neural Plast.* 2016:3407135. doi: 10.1155/2016/3407135
- The Dutch-Belgian Fragile X Consortium (1994). *Fmr1* knockout mice: a model to study fragile X mental retardation. *Cell* 78, 23–33.
- Tremblay, R., Lee, S., and Rudy, B. (2016). GABAergic interneurons in the neocortex: from cellular properties to circuits. *Neuron* 91, 260–292. doi: 10.1016/j.neuron.2016.06.033
- Tuncdemir, S. N., Wamsley, B., Stam, F. J., Osakada, F., Goulding, M., Callaway, E. M., et al. (2016). Early somatostatin interneuron connectivity mediates the maturation of deep layer cortical circuits. *Neuron* 89, 521–535. doi: 10.1016/j.neuron.2015.11.020
- Tyzio, R., Nardou, R., Ferrari, D. C., Tsintsadze, T., Shahrokhi, A., Eftekhari, S., et al. (2014). Oxytocin-mediated GABA inhibition during delivery attenuates autism pathogenesis in rodent offspring. *Science* 343, 675–679. doi: 10.1126/science.1247190
- van Versendaal, D., and Levelt, C. N. (2016). Inhibitory interneurons in visual cortical plasticity. *Cell Mol. Life Sci. CMLS* 73, 3677–3691. doi: 10.1007/s00018-016-2264-4
- Villiers-Sidani, E., de Chang, E. F., Bao, S., and Merzenich, M. M. (2007). Critical period window for spectral tuning defined in the primary auditory cortex (a1) in the rat. *J. Neurosci.* 27, 180–189. doi: 10.1523/jneurosci.3227-06.2007
- Wen, T. H., Lovelace, J. W., Ethell, I. M., Binder, D. K., and Razak, K. A. (2019). Developmental changes in EEG phenotypes in a mouse model of fragile X syndrome. *Neuroscience* 398, 126–143. doi: 10.1016/j.neuroscience.2018.11.047
- Wood, K. C., Blackwell, J. M., and Geffen, M. N. (2017). Cortical inhibitory interneurons control sensory processing. *Curr. Opin. Neurobiol.* 46, 200–207. doi: 10.1016/j.conb.2017.08.018
- Yamasaki, T., Maekawa, T., Fujita, T., and Tobimatsu, S. (2017). Connectopathy in autism spectrum disorders: a review of evidence from visual evoked potentials and diffusion magnetic resonance imaging. *Front. Neurosci.* 11:627. doi: 10.3389/fnins.2017.00627
- Zhang, Y., Bonnan, A., Bony, G., Ferezou, I., Pietropaolo, S., Ginger, M., et al. (2014). Dendritic channelopathies contribute to neocortical and sensory hyperexcitability in *Fmr1*-/- mice. *Nat. Neurosci.* 17, 1701–1709. doi: 10.1038/nn.3864

Conflict of Interest Statement: The authors declare that the research was conducted in the absence of any commercial or financial relationships that could be construed as a potential conflict of interest.

Copyright © 2019 Cheyne, Zabouri, Baddeley and Lohmann. This is an open-access article distributed under the terms of the Creative Commons Attribution License (CC BY). The use, distribution or reproduction in other forums is permitted, provided the original author(s) and the copyright owner(s) are credited and that the original publication in this journal is cited, in accordance with accepted academic practice. No use, distribution or reproduction is permitted which does not comply with these terms.



Multiplex Neural Circuit Tracing With G-Deleted Rabies Viral Vectors

Toshiaki Suzuki¹, Nao Morimoto^{1,2}, Akinori Akaike¹ and Fumitaka Osakada^{1,2,3,4*}

¹Laboratory of Cellular Pharmacology, Graduate School of Pharmaceutical Sciences, Nagoya University, Nagoya, Japan,

²Laboratory of Neural Information Processing, Institute for Advanced Research, Nagoya University, Nagoya, Japan, ³Institute of Nano-Life-Systems, Institutes of Innovation for Future Society, Nagoya University, Nagoya, Japan, ⁴PRESTO/CREST, Japan Science and Technology Agency, Saitama, Japan

OPEN ACCESS

Edited by:

Yoshiyuki Kubota,
National Institute for Physiological
Sciences (NIPS), Japan

Reviewed by:

Yumiko Yoshimura,
National Institute for Physiological
Sciences (NIPS), Japan
Masahiko Takada,
Kyoto University, Japan

*Correspondence:

Fumitaka Osakada
fosakada@ps.nagoya-u.ac.jp

Received: 08 September 2019

Accepted: 14 November 2019

Published: 10 January 2020

Citation:

Suzuki T, Morimoto N, Akaike A and
Osakada F (2020) Multiplex Neural
Circuit Tracing With G-Deleted
Rabies Viral Vectors.
Front. Neural Circuits 13:77.
doi: 10.3389/fncir.2019.00077

Neural circuits interconnect to organize large-scale networks that generate perception, cognition, memory, and behavior. Information in the nervous system is processed both through parallel, independent circuits and through intermixing circuits. Analyzing the interaction between circuits is particularly indispensable for elucidating how the brain functions. Monosynaptic circuit tracing with glycoprotein (G) gene-deleted rabies viral vectors (RVΔG) comprises a powerful approach for studying the structure and function of neural circuits. Pseudotyping of RVΔG with the foreign envelope EnvA permits expression of transgenes such as fluorescent proteins, genetically-encoded sensors, or optogenetic tools in cells expressing TVA, a cognate receptor for EnvA. Trans-complementation with rabies virus glycoproteins (RV-G) enables trans-synaptic labeling of input neurons directly connected to the starter neurons expressing both TVA and RV-G. However, it remains challenging to simultaneously map neuronal connections from multiple cell populations and their interactions between intermixing circuits solely with the EnvA/TVA-mediated RV tracing system in a single animal. To overcome this limitation, here, we multiplexed RVΔG circuit tracing by optimizing distinct viral envelopes (oEnvX) and their corresponding receptors (oTVX). Based on the EnvB/TVB and EnvE/DR46-TVH systems derived from the avian sarcoma leukosis virus (ASLV), we developed optimized TVB receptors with lower or higher affinity (oTVB-L or oTVB-H) and the chimeric envelope oEnvB, as well as an optimized TVE receptor with higher affinity (oTVE-H) and its chimeric envelope oEnvE. We demonstrated independence of RVΔG infection between the oEnvA/oTVA, oEnvB/oTVB, and oEnvE/oTVE systems and *in vivo* proof-of-concept for multiplex circuit tracing from two distinct classes of layer 5 neurons targeting either other cortical or subcortical areas. We also successfully labeled common input of the lateral geniculate nucleus to both cortico-cortical layer 5 neurons and inhibitory neurons of the mouse V1 with multiplex RVΔG tracing. These oEnvA/oTVA, oEnvB/oTVB, and oEnvE/oTVE systems allow for differential labeling of distinct circuits to uncover the mechanisms underlying parallel processing through independent circuits and integrated processing through interaction between circuits in the brain.

Keywords: rabies virus, transsynaptic targeting, neural circuit, multiplex, anatomy

INTRODUCTION

The function of the nervous system arises from complex interactions between networks of neurons composed of multiple cell types. Each cell type has its own molecular, morphological, neurophysiological, and anatomical properties and organizes unique neural circuits. The wiring patterns of individual cell types underlie how neural circuits process and represent information. Detailed information on the cell types and their connectivity, in addition to the spatiotemporal patterns of activity in neural circuits, is essential for understanding how the brain functions. Parallel information processing through independent circuits is a commonly-used strategy in the brain (Nassi and Callaway, 2009), but processed information is combined by integration of neural circuits. Interaction between circuits underlies diverse and complex computations that generate perception, cognition, memory, and behavior. Thus, the combination of parallel processing through independent circuits and integrated processing through interaction between circuits is the fundamental principle of neural circuits and computations in the brain. Despite the advances in methods for linking cell types to neural circuits (Arenkiel and Ehlers, 2009; Luo et al., 2018), a major impediment in elucidating how information processing is integrated in the nervous system is lack of means for the dissection of the complex interactions between neural circuits.

The development of viral vectors has transformed the field of neuroanatomy. In particular, G-deleted rabies viral vectors (RVΔG) have been used to reveal neuronal connectivity in the mammalian nervous system (Wickersham et al., 2007; Marshel et al., 2010; Wall et al., 2010; Osakada et al., 2011; Rancz et al., 2011; Watabe-Uchida et al., 2012; Miyamichi et al., 2013; Osakada and Callaway, 2013; Zhu et al., 2014; Bourane et al., 2015; Wertz et al., 2015; Vaziri and Connor, 2016; François et al., 2017; Sun et al., 2017; Kaelberer et al., 2018). Rabies viruses infect neurons through axon terminals and spread across the synapses between neurons in a retrograde direction (Ugolini, 1995, 2010). To take advantage of their trans-synaptic spread property, cell-type-specific infection of rabies viral vectors is required for mapping the neuronal connectivity of target cell types in the brain. Rabies viruses are enveloped viruses with the rabies virus glycoprotein (RV-G) gene as a native envelope. As the glycoprotein gene is deleted from the viral genome, the envelope of G-deleted rabies viruses can be replaced with a foreign one to change their tropism, so-called pseudotyping (Mebatsion et al., 1996; Etessami et al., 2000; Wickersham et al., 2007). Pseudotyping of RVΔG with a foreign glycoprotein allows viral targeting to specific cell populations that express its receptor. The EnvA/TVA is an avian sarcoma leukosis virus (ASLV) infection system that is not recognized by mammalian cells (Bates et al., 1993; Young et al., 1993; Wickersham et al., 2007). The basic approach for targeting specific cell types is that the initial RV infection is targeted to cells of interest by selectively expressing TVA, a specific receptor for EnvA, in those cells *via* viral vectors, transgenic mice, or *in vivo* electroporation (Wickersham et al., 2007; Marshel et al., 2010; Wall et al., 2010,

2016; Rancz et al., 2011; Watabe-Uchida et al., 2012; Miyamichi et al., 2013; Osakada and Callaway, 2013; Zampieri et al., 2014; Zhu et al., 2014; Kim et al., 2015; Wertz et al., 2015; Faget et al., 2016; Beier et al., 2017; Kaelberer et al., 2018). Co-expression of TVA and rabies glycoprotein RV-G in target neurons referred to as “starter cells,” allows RVΔG to retrogradely spread to presynaptic neurons directly connected to the starter cells.

This RVΔG monosynaptic tracing represents a powerful approach in mice, zebrafish, cats, and non-human primates (Liu et al., 2013; Dohaku et al., 2019). However, several challenges regarding the development of rabies viral vectors still remain. Especially, analyzing the relationships between neural circuits currently presents a substantial bottleneck to revealing the segregation and integration of complex neural circuits. The EnvA/TVA system for rabies viral tracing allows labeling of only single cell types and their presynaptic neurons. Thus, it has been impossible to reveal the structure, function, and interaction of complicated intermixing circuits organized by multiple cell types (Glickfeld et al., 2013; Yamashita et al., 2013; Lur et al., 2016; Kim et al., 2018). In addition, development of multi-colored, genetically-encoded fluorescent proteins, biosensors, and actuators have allowed us to simultaneously observe different populations in real-time (Chen et al., 2013; Marvin et al., 2013, 2019; Dana et al., 2016; Jing et al., 2018; Luo et al., 2018; Patriarchi et al., 2018; Sun et al., 2018; Abdelfattah et al., 2019; Inoue et al., 2019). By incorporating these tools into the RVΔG tracing system, it is possible to directly link circuits and function (Osakada et al., 2011; Wertz et al., 2015; Tian et al., 2016). Visualizing distinct neural populations with their corresponding fluorescent reporters in real-time is a powerful approach for physiological and behavioral studies. To distinguish starter neurons and presynaptic neurons, it is also required to label starter cells with a reporter that differs in color and is included in the expression cassette of TVA and RV-G. In the present study, we aimed to develop new infection systems of RVΔG to reveal circuit structure, function, and interaction of multiple cell types in the brain.

Here, we first introduced new infection systems using EnvB, EnvC, and EnvE that can be used for pseudotyping RVΔG to restrict viral infection to a specific population in the mouse brain. To eliminate pseudo-negative populations as well as cross-infectivity, we further optimized receptors of EnvB, EnvC, and EnvE to simultaneously dissect multiple circuits. We named these optimized infection systems “oEnvX/oTVX systems” (optimized EnvX/TVX). In conjunction with different colors of reporter fluorescence such as GFP, RFP, BFP, and iRFP, and functional fluorescent probes including genetically encoded sensors for Ca²⁺, voltage, and neurotransmitters (Chen et al., 2013; Marvin et al., 2013, 2019; Dana et al., 2016; Jing et al., 2018; Patriarchi et al., 2018; Sun et al., 2018; Abdelfattah et al., 2019; Inoue et al., 2019), the multiplexable virus infection systems will allow for *in vivo* interrogation of complex overlapping neural circuits in a single animal. The present study expands the utility of the RVΔG tracing system to simultaneously label and characterize multiple circuits in single animals. The multiplex RVΔG tracing system promises to advance our understanding of the circuit-level

mechanisms underlying information processing in the central nervous system.

MATERIALS AND METHODS

Plasmid Construction

All plasmid construction using polymerase chain reaction (PCR) was performed with PrimeSTAR Max DNA Polymerase (TaKaRa, Tokyo, Japan) on a PCR thermal cycler (Dice Touch, TaKaRa). Plasmids and PCR products were digested with appropriate restriction enzymes (New England BioLabs, Ipswich, MA, USA) at optimal conditions. Plasmid and PCR fragments were assembled with either NEBuilder HiFi DNA Assembly Master Mix (New England BioLabs, Ipswich, MA, USA) or DNA Ligation Kit Mighty Mix (TaKaRa). Chemically-competent Stbl3 *E. coli* (Thermo Fisher Scientific, Waltham, MA, USA) was transformed with AAV plasmids, and chemically-competent XL10-Gold *E. coli* (Agilent Technology, Santa Clara, CA, USA) was used for the other plasmids. The *E. coli* was grown in LB medium (Kanto chemical, Tokyo, Japan) on an LB plate containing ampicillin (100 µg/ml). Plasmids were inspected by diagnostic digestions with appropriate restriction enzymes and sequenced before virus production.

Cell Culture

HEK293t cells were obtained from RIKEN Cell Bank (Saitama, Japan). HEK-TVA, HEK-TVB, BHK-T7, BHK-EnvA, BHK-EnvB, and B7GG cells were gifted by Dr. Callaway (Salk Institute for Biological Studies, La Jolla, CA, USA; Wickersham et al., 2007; Choi et al., 2010; Osakada et al., 2011; Osakada and Callaway, 2013). These cells were maintained in DMEM (Wako, Osaka, Japan), supplemented with 10% fetal bovine serum (FBS; Sigma, St. Louis, MI, USA), 100 U/ml penicillin G, and 100 µg/ml streptomycin (Wako). Cells were cultured in a humidified atmosphere of 5% CO₂ and 95% air at 37°C.

Generation of Cell Lines

HEK-DR46TVB and B7-oEnvE cells were established by the piggyBac system (Ding et al., 2005). pPB-CAG-DR46TVB-IRES-BSD or pPB-CAG-oEnvE-IRES-BSD with pCAG-PBase were co-transfected in HEK293t cells or BHK-T7 cells using Opti-MEM (Thermo Fisher Scientific, Waltham, MA, USA) and Polyethylenimine “Max” (Polyscience Inc., Warrington, PA, USA). Transfected cells were selected in the presence of blasticidin at a concentration of 100 µg/ml (InvivoGen, San Diego, CA, USA). HEK-DR46TVB and B7-oEnvE cells were maintained in DMEM (Wako), supplemented with 10% FBS (Sigma, St. Louis, MI, USA) in a humidified atmosphere of 5% CO₂ and 95% air at 37°C.

RVΔG Production

RVΔG was produced as described previously (Osakada et al., 2011; Osakada and Callaway, 2013). Briefly, RVΔG-GFP, RVΔG-DsRedexpress, and RVΔG-tagBFP were recovered in B7GG cells by transfection with pcDNA-B19G, pcDNA-B19N, pcDNA-B19P, pcDNA-B19L, and corresponding

genomic plasmid (pSADΔG-GFP, pSAD-ΔG-DsRedexpress, or pSAD-ΔG-tagBFP) by Lipofectamine 2000 (Thermo Fisher Scientific, Waltham, MA, USA). The B7GG cells during virus production were cultured in DMEM and supplemented with 10% FBS (Sigma, St. Louis, MI, USA) in a humidified atmosphere of 3% CO₂ at 35°C. BHK-oEnvA, BHK-oEnvB, or B7-oEnvE cells were infected with recovered viruses for pseudotyping RVΔG with oEnvA, oEnvB, or oEnvE (see also **Figure 1B**). The virus-containing medium was concentrated by two rounds of ultra-centrifugation (Beckman Coulter, Brea, CA, USA). The infectious titers were determined on HEK-TVA, HEK-TVB, and HEK-DR46TVB cells. HEK293t cells were used to inspect for contamination with unpseudotyped rabies viruses. Virus aliquots were stored at −80°C until use. The titers of the rabies viral vectors used in the present study were 7.0×10^5 – 2.9×10^9 infectious units/ml.

AAV Production

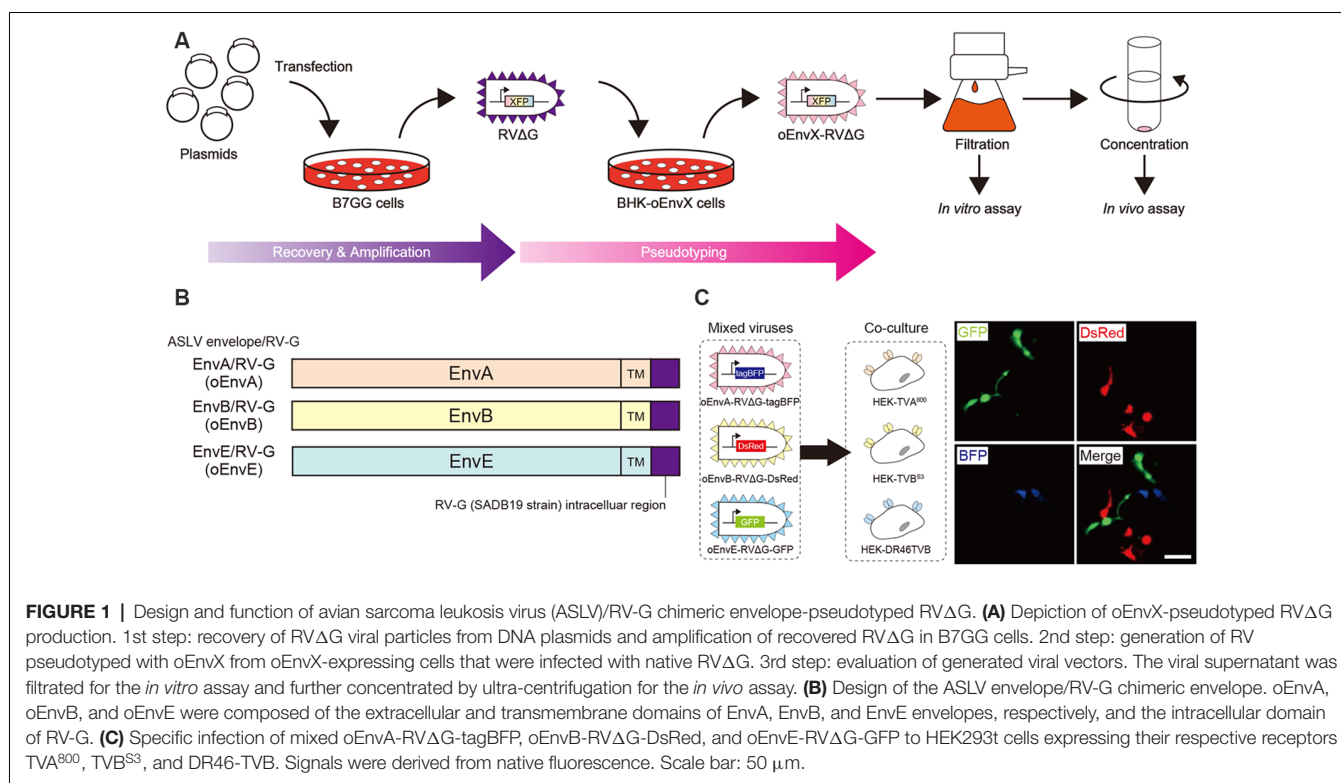
AAVs were generated in HEK293t cells with triple-transfection methods with some modifications (Xiao et al., 1998). Briefly, AAV2/2, AAV2/9, and AAV2retro were generated by transfection of HEK293t cells with pHelper (Cell BioLabs, San Diego, CA, USA), the rep/cap vector (pXR2 for AAV2/2, pAAV2.9 for AAV2/9, or rAAV2-retro helper for AAV2retro) and pAAV genomic vector. Three days post-transfection, virus-producing cells were collected and lysed by freeze and thaw for purification. After centrifugation, the supernatant was loaded on gradients (15%, 25%, 40%, and 58%) of iodexanol OptiPrep (Alere Technologies AS, Stirling, Scotland). After centrifugation at 16000 g at 15°C for 3 h, 100–150 µl upper from 58% iodexanol layer was collected. Virus aliquots were stored at −80°C until use. The titers of AAV used in the present study were 5.0×10^2 infectious units/ml (HEK293t cells) or 1.0×10^{11} – 1.8×10^{14} viral genome/ml quantitative PCR (qPCR; Aurnhammer et al., 2012).

Animals

Animals were treated in accordance with the Guidelines of Animal Experiments of Nagoya University. All animal experiments in this study were approved by the Animal Care and Use Committee of Nagoya University. All efforts to reduce the number of animals used and minimize the suffering and pain of animals were made. C57BL/6J mice were purchased from Nihon SLC (Shizuoka, Japan). Tlx3-Cre mice (PL56) were obtained from the Jackson Laboratory (Bar Harbor, ME, USA). Genotyping for Tlx3-Cre mice was performed according to the protocol of Mutant Mouse Resource and Research Center: UC Davis. These animals were maintained in a temperature-controlled room (24 ± 1°C) under a 12 h light/dark cycle with *ad libitum* access to food and water.

Viral Injection

Viral injections were conducted according to the procedures described previously (Osakada et al., 2011) with slight modifications. Briefly, 8-week-old male mice were anesthetized with mixed anesthetic agents (1 ml/kg, i.p.) composed of



75 μg/ml medetomidine hydrochloride (Domitol; Meiji Seika Pharma Company Limited, Tokyo, Japan), 400 μg/ml midazolam (Dormicum; Astellas Pharma Inc., Tokyo, Japan), and 500 μg/ml butorphanol (Vetorphale; Meiji Seika Pharma Company Limited). Anesthetized mice were mounted on a stereotaxic apparatus (David Kopf Instruments, Tujunga, CA, USA). The skull was exposed *via* a small incision, and a small hole was drilled for injection. The virus was loaded into glass pipettes (tip diameter, ≈30 μm; bevel, 45°), pulled on a micropipette puller (P-1000, Sutter Instrument, Novato, CA, USA) and grinded on a microgrinder (EG-401, Narishige, Tokyo, Japan). Before injection of the virus, the pipette was retained in the brain for 5 min after penetration. Three hundred to five hundred nanoliter of virus was injected into the following locations at a rate of 100 nl/min: the V1 (following coordinates: 3.0–3.4 mm rostral, 2.4 mm lateral relative to the bregma and 0.4–0.5 mm ventral to the pia), V2L (3.7 mm rostral, 3.5 mm lateral relative to the bregma and 0.4–0.5 mm ventral to the pia), and SC (3.2 mm rostral, 0.3–0.4 mm lateral relative to the bregma and 2.0 mm ventral to the pia) using a picospritzer (General Valve Corp. Fairfield, NJ, USA). After completion of the injection, the pipette was retained in the brain for another 5 min. No mouse that received viral injection in the brain showed abnormal behavior.

Histological Analysis

Animals were deeply anesthetized by pentobarbital (Somnopenyl, Kyoritsu Seiyaku Company Limited, Tokyo, Japan) and transcardially perfused with 4% paraformaldehyde in phosphate-buffered saline (PBS). The brains were post-fixed with

4% paraformaldehyde in PBS and cryopreserved overnight in 2% paraformaldehyde/15% sucrose in PBS and then maintained in 30% sucrose in PBS. The brains were sectioned on a freezing microtome (REM-710, Yamato, Saitama, Japan) at 50 μm thickness. For enhancement of native signals, some brain sections were processed for immunostaining as described previously (Osakada et al., 2008, 2011). The primary antibodies and their working dilutions were as follows: rabbit anti-GFP polyclonal (1:2,000, Abcam, UK) and rabbit anti-DsRed polyclonal (1:1,000, Clontech-Takara, Japan). Labeled cells were visualized with the following fluorescent secondary antibodies: anti-mouse IgG and anti-rabbit IgG conjugated with Alexa Flour 488 or Alexa Flour 594 (1:1,000, Jackson ImmunoResearch, West Grove, PA, USA). The sections were mounted on slide glasses with anti-fade solution (Nakalai, Kyoto, Japan). Labeled cells were imaged with a confocal laser-scanning microscope with GaAsP detectors (LSM800, Zeiss, Jena, Germany) using a 10× (NA 0.45, Zeiss, Jena, Germany), 20× (NA 0.75, Zeiss, Jena, Germany), or 40× objective lens (NA 1.2, Zeiss, Jena, Germany).

Statistical Analysis

Data are expressed as means ± SEM. All sets of experiments were performed at least three times. The statistical significance of the difference between groups was determined by one-way ANOVA, followed by Tukey's or Dunnett's test using R (R Foundation, Vienna, Austria¹). Probability values lower than 5% were considered statistically significant.

¹<https://www.r-project.org/>

RESULTS

Development of a Chimeric ASLV/RV-G Envelope-Pseudotyped RVΔG

Glycoproteins of enveloped viruses such as rabies viruses recognize and bind to their cell receptors, leading to viral entry. Rabies viruses infect neurons through axon terminals (Ugolini, 1995, 2010). Through replication and transcription in the infected cells, rabies viruses spread across the synapses located between the neurons in the nervous system. Deleting native envelope glycoprotein genes from the rabies genome and pseudotyping the RVΔG with a foreign glycoprotein, such as the EnvA derived from ASLV, allows targeting of viral vectors to specific cell populations that express the receptors of foreign glycoproteins such as TVA (Mebatsion et al., 1996; Etesami et al., 2000; Wickersham et al., 2007; Osakada and Callaway, 2013; **Figure 1A**). Notably, ASLV uses various other viral envelopes such as EnvB, C, D, E, and J, in addition to EnvA (Barnard and Young, 2003; Barnard et al., 2006). The cloning of ASLV envelopes and their receptors has revealed their specificity (Barnard et al., 2006; Chai and Bates, 2006): TVB^{S1} for EnvB and EnvE, TVB^{S3} for EnvB, TVC for EnvC, and TVJ for EnvJ (Smith et al., 1998; Adkins et al., 2000; Elleder et al., 2005; Chai and Bates, 2006). By using these systems, lentiviral vectors pseudotyped with EnvB, EnvC, and EnvE have been reported to infect cells expressing their corresponding receptors (Matsuyama et al., 2015).

To take advantage of this system to target rabies viral vectors to a particular cell population, RVΔG needs to be pseudotyped with the foreign ASLV envelopes. However, ASLV native envelope proteins are optimized to ASLV but not to rabies viruses. Thus, engineering envelope proteins is required for packaging the rabies viral core with the foreign envelopes. First, we designed chimeric glycoproteins because the native EnvXs envelopes are not compatible with rabies viral cores. Previous reports have used the EnvA/RV-G chimeric protein consisting of an extracellular domain of EnvA and an intracellular domain of rabies viral glycoproteins for RVΔG pseudotyping (Wickersham et al., 2007; Osakada and Callaway, 2013). According to the EnvA/RV-G design, we replaced the intracellular domain of EnvB, EnvC, or EnvE with that of the rabies viral glycoprotein RV-G to generate EnvB/RV-G, EnvC/RV-G, or EnvE/RV-G, respectively. To differentiate the chimeric glycoproteins (EnvX/RV-G) for RVΔG from the native glycoproteins (EnvX) for ASLV, we termed the optimized chimeric glycoproteins EnvX/RV-G “oEnvX” (i.e., EnvA/RV-G for oEnvA, EnvB/RV-G for oEnvB, EnvC/RV-G for oEnvC, and EnvE/RV-G for oEnvE; **Figure 1B**). EnvD was excluded from this procedure because the EnvD-packaged virus may infect mammalian cells that lack foreign receptors (Bova et al., 1988). EnvJ was also omitted because TVJ, an EnvJ receptor, is a sodium-proton exchanger that may potentially affect neuronal activity (Chai and Bates, 2006; Matsuyama et al., 2015).

Using these chimeric envelopes, we next produced pseudotyped RVΔG with oEnvB, oEnvC, or oEnvE, by transiently expressing them in BHK cells by plasmid transfection.

First, we determined whether these pseudotyped RVΔG can infect the mammalian HEK293t cells without introducing the ASLV receptors. No infection with oEnvB- or oEnvE-pseudotyped RVΔG was observed in HEK293t cells (**Table 1**). However, we found a degree of infection with oEnvC-pseudotyped RVΔG in HEK293t cells (data not shown), suggesting non-specific infection in mammalian cells.

Thus, we excluded the oEnvC/TVC system from the following studies. To test for the specificity of the pseudotyped RVΔG, we determined whether a mixture of oEnvA-, oEnvB-, and oEnvE-pseudotyped RVΔGs could cause cross-infection to a coculture of TVA⁸⁰⁰-, TVB^{S3}-, and DR46-TVB-expressing cells. To distinguish viral infection in three independent cell groups in a mixed population, we prepared pseudotyped RVΔG with distinct envelopes that encode different fluorescent proteins: oEnvA-RVΔG-tagBFP (blue), oEnvB-RVΔG-DsRed (red), and oEnvE-RVΔG-GFP (green; **Figure 1C**). We applied the mixture of the viruses to the mixed culture of those TVX-expressing cells. Three days after viral infection, the infected cells expressed only one fluorescent protein. No cells expressed multiple colored fluorescent proteins. Therefore, we conclude that oEnvA-, oEnvB-, and oEnvE-RVΔG specifically infect cells expressing TVA⁸⁰⁰, TVB^{S3}, and DR46-TVB, respectively. These results imply that oEnvA/TVA, oEnvB/TVB, and oEnvE/DR46-TVB can be applied to multiplexing RVΔG infection.

To apply the multiplex infection system *in vivo*, we need to obtain the pseudotyped RVΔG at high titers. We next attempted to establish an efficient virus-production system. Since cell lines expressing EnvA/RV-G or EnvB/RV-G generated high titers of the pseudotyped RVΔG (Wickersham et al., 2007; Choi et al., 2010; Osakada et al., 2011), we also generated an oEnvE-expressing cell line. Generally, the efficiency of RVΔG pseudotyping depends on the expression level of the envelope of the host cell. Therefore, to establish a cell line expressing an envelope protein at a higher expression level, we used the piggyBac transposon system that enables integrating multiple copies of exogenous genes into the chromosomal DNA of the host cells (Ding et al., 2005). We successfully generated BHK-T7 cells stably expressing oEnvE and named them B7-oEnvE cells. Using these oEnvX-cell lines, we successfully produced pseudotyped RVΔG at a high titer: oEnvA-RVΔG at 5.3×10^7 , oEnvB-RVΔG at 4.2×10^6 , and oEnvE-RVΔG at 7.0×10^5 (**Table 1**). These results suggest that the stable cell lines expressing chimeric envelopes can efficiently generate high titers of pseudotyped RVΔG that can be used for *in vivo* experiments.

Generation of the Optimized oEnvA/oTVA System

For multiplex RVΔG tracing, we need to reliably visualize starter neurons expressing TVX receptors. For this purpose, we also envisioned to functionally characterize the connectionally defined neurons by combining RVΔG trans-synaptic tracing with *in vivo* functional imaging. To reveal the relationship between neuronal connectivity and function, we used fluorescent indicators for calcium, voltage, or neurotransmitters together with the RVΔG system for *in vivo* functional imaging. The hurdle

TABLE 1 | No cross-infectivity of oEnvA-RVΔG, oEnvB-RVΔG, and oEnvE-RVΔG.

Virus Name	Infectious Units (/ml)			
	HEK-TVA ⁸⁰⁰	HEK-TVB ^{S3}	HEK-DR46-TVB	HEK293t
oEnvA-RVΔG-DsRed	5.3×10^7	n.d.	n.d.	n.d.
oEnvB-RVΔG-GFP	n.d.	4.2×10^6	n.d.	n.d.
oEnvE-RVΔG-DsRed	n.d.	n.d.	7.0×10^5	n.d.

HEK cells expressing either TVA, TVB, or DR46TVB were respectively infected with oEnvA-RVΔG, oEnvB-RVΔG, or oEnvE-RVΔG. No infections with oEnvA-RVΔG, oEnvB-RVΔG, and oEnvE-RVΔG were observed in HEK293t cells. Data represent the infectious units. n.d.: not detected.

of such an experiment is that co-labeling of the connectionally defined neurons with fluorescent reporters (green or red) and indicators is not useful, as many fluorescent indicators such as GCaMP, XCaMPs, jRGECO, iGluRSnFr, and dLight1 are of the same color (Chen et al., 2013; Marvin et al., 2013, 2019; Dana et al., 2016; Jing et al., 2018; Patriarchi et al., 2018; Sun et al., 2018; Inoue et al., 2019). Thus, infrared fluorescent reporters that do not interfere with green and red fluorescence are required for co-labeling of the connectionally defined neurons (Shcherbakova and Verkhusa, 2013). Therefore, to simultaneously visualize multiple circuits with different colors, we generated an infrared-tagged TVA receptor for starter neuron labeling.

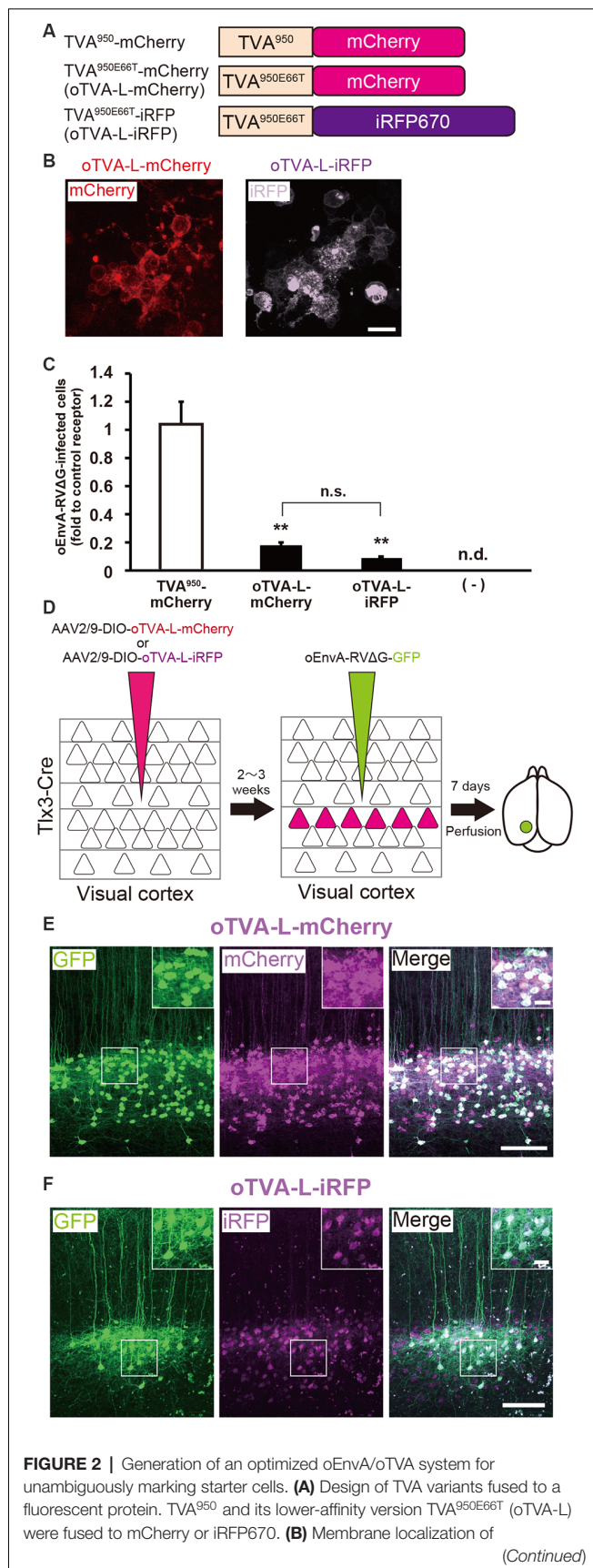
TVA has variants with different affinities. Among them, the original type TVA⁸⁰⁰ displays the highest affinity to EnvA; however, TVA⁸⁰⁰ is a glycosylphosphatidylinositol-anchored receptor without a transmembrane region (Bates et al., 1993; Gray et al., 2011). Thus, its N-terminal cannot be fused to a fluorescent protein for its visualization. Conversely, TVA⁹⁵⁰ is a single transmembrane receptor and can be fused to a fluorescent protein for the visualization of TVA-expressing starter cells: TVA⁹⁵⁰-EYFP (Faget et al., 2016), TVA⁹⁵⁰-mCherry (Watabe-Uchida et al., 2012), and low-affinity mutant TVA^{950E66T}-mCherry (Miyamichi et al., 2013). The high sensitivity of TVA⁹⁵⁰-mCherry causes oEnvA-RVΔG-GFP infection to cells expressing TVA⁹⁵⁰-mCherry at a level where mCherry signals are not detected. Using TVA⁹⁵⁰-mCherry for rabies trans-complementation experiments, the starter cells appear mCherry-negative and GFP-positive with subsequent pseudo-negative results. To overcome this issue, we utilized TVA^{950E66T}, a mutant TVA at E66T, with a lower affinity to oEnvA-RVΔG viruses (Rong et al., 1998; Miyamichi et al., 2013). Accordingly, the cells expressing TVA^{950E66T}-mCherry at higher levels can be infected with oEnvA-RVΔG viruses allowing elimination of pseudo-negative cell populations because starter cells expressing high levels of mCherry can be unambiguously observed. Cells expressing lower levels of TVA^{950E66T} with undetectable mCherry cannot be infected with oEnvA-RVΔG viruses. The strength of TVA^{950E66T}-mCherry is the clear and reliable visualization of starter neurons during rabies tracing experiments because a high TVA^{950E66T}-mCherry expression is required for oEnvA-RVΔG infection.

To develop a new TVA that could be used together with green and red fluorescence, we generated TVA^{950E66T} fused with iRFP670 (termed “oTVA-L-iRFP”) as a reporter, the brightest infrared fluorescent protein at present (Shcherbakova and Verkhusa, 2013; Shcherbakova et al., 2018; **Figure 2A**).

First, to examine the subcellular localization of oTVA-L-iRFP, the encoding plasmid was transfected into HEK293t cells (**Figure 2B**). Confocal microscopy revealed that the iRFP670 signals derived from oTVA-L were localized on the cell membrane, consistent with TVA^{950E66T}-mCherry membrane localization. We next investigated whether oEnvA-RVΔG could infect the oTVA-L-iRFP-expressing cells (**Figure 2C**). oEnvA-RVΔG-GFP was applied to the oTVA-L-iRFP-transfected HEK293t cells. Most iRFP⁺ cells were also GFP-positive. While the TVA⁹⁵⁰-expressing cells were efficiently infected with oEnvA-RVΔG, infection of oTVA-L-iRFP-expressing cells was comparable to that of oTVA-L-mCherry-expressing cells. These results indicate that oTVA-L-iRFP can be used as a receptor for oEnvA-RVΔG *in vitro*, similar to oTVA-L-mCherry.

We next evaluated the *in vivo* function of oTVA-L-mCherry and oTVA-L-iRFP to determine whether they could be used for rabies tracing experiments in the mouse brain. To introduce oTVA-L to a specific population in the brain, we used *Trlx3-Cre* mice, in which layer 5 cortical neurons specifically express Cre recombinase (Kim et al., 2015; **Figure 2D**). AAV2/9-CAG-DIO-oTVA-mCherry or AAV2/9-CAG-DIO-oTVA-L-iRFP that expresses oTVA-L-mCherry or oTVA-L-iRFP in a Cre-dependent manner, respectively was used as control. We injected AAV2/9-CAG-DIO-oTVA-L-mCherry or AAV2/9-CAG-DIO-oTVA-L-iRFP into the primary visual cortex (V1) of *Trlx3-Cre* mice and then oEnvA-RVΔG-GFP in the AAV-injection location (**Figure 2D**). Seven days after oEnvA-RVΔG injection, we fixed and sectioned the brain of the virus-injected mice. The signal of mCherry was specifically observed in layer 5 neurons around the V1 injection site (**Figure 2E**), indicating that oTVA-L was expressed in layer 5 neurons in a Cre-dependent manner. Part of the mCherry⁺ cells expressed GFP in layer 5. All GFP⁺ cells were also mCherry-positive in layer 5, and none of the GFP⁺ cells were distributed in the other V1 layers (total 444 mCherry-expressing neurons/444 GFP-expressing neurons from three mice). These results indicate that oEnvA-RVΔG-GFP specifically infected the oTVA-L-mCherry-expressing neurons in layer 5 of the mouse cortex.

Similar results were obtained for oTVA-L-iRFP (**Figure 2F**). iRFP-positive cells were localized in layer 5 of the V1. Part of the iRFP⁺ cells expressed GFP in layer 5. All GFP⁺ cells were positive for iRFP670 in layer 5 (total 261 iRFP-expressing neurons/261 GFP-expressing neurons from three mice). These results indicate that oEnvA-RVΔG-GFP specifically infected the oTVA-L-iRFP-expressing neurons *in vivo*. No infection with



Generation of the Optimized oEnvB/oTVB System

EnvA/TVA allows viral targeting to a particular cell population. To target two distinct populations with two different viruses, we next designed an additional infection system based on the EnvB/TVB system. oEnvB-pseudotyped rabies viral vectors have the potential to infect *via* TVB *in vivo* (Choi et al., 2010). We first attempted to develop TVB, a receptor for oEnvB-enveloped viruses. As the original TVB has several use issues, we optimized the TVB receptors for the rabies tracing experiments focusing on envelope affinity and fluorescence reporter detectivity to utilize the EnvB/TVB system for restricted viral transduction in a specific neuronal population.

TVB reportedly has the following variants with different affinities for various ASLVs: TVB^{S1}, TVB^{r2}, TVB^{S3}, and TVB^T (Brojatsch et al., 1996; Adkins et al., 1997, 2000; Smith et al., 1998). Among the several subtypes, we selected TVB^{S3} because it does not recognize and bind to EnvE, whereas the other TVB variants bind to both EnvB and EnvE (Adkins et al., 2000; Klucking and Young, 2004; Reinisová et al., 2008; Matsuyama et al., 2015). However, TVB is a homolog of the mammalian TNF-related apoptosis-inducing ligand death receptor 4/5; when ASLV-B and ASLV-E infected cells *via* TVB, TVB induced

TABLE 2 | Specificity of oTVA-L, oTVB-L, and oTVE-H.

Chimeric Envelope	Number of Infected Cells			
	oTVA-L (TVA ^{950E66T})	oTVB-H (TVB ^{S3} -TVA)	oTVE-H (DR46-TVb-TVA)	(-)
oEnvA-RVΔG	119 ± 8.5	n.d.	n.d.	n.d.
oEnvB-RVΔG	n.d.	112 ± 11	n.d.	n.d.
oEnvE-RVΔG	n.d.	n.d.	>200	n.d.

HEK cells expressing either oTVA-L, oTVB-L, and oTVE-H were specifically infected with oEnvA-RVΔG, oEnvB-RVΔG, or oEnvE-RVΔG. oTVA-L, oTVB-L, and oTVE-H were specific to oEnvA-RVΔG, oEnvB-RVΔG, and oEnvE-RVΔG, respectively. No infections with oEnvA-RVΔG, oEnvB-RVΔG, and oEnvE-RVΔG were observed in HEK293t cells. Data represent the infectious units. n.d.: not detected.

apoptosis (Brojatsch et al., 1996, 2000; Smith et al., 1998; Klucking et al., 2005). The death domain of TVB has been reported to be responsible for inducing apoptosis (Adkins et al., 2000). To maintain the infected neurons healthy during the viral tracing experiments, we deleted the death domain from the full-length of the TVB receptor. Additionally, to visualize the TVB-expressing cells, we replaced the TVB^{S3} death domain with tagBFP, the brightest fluorescent blue protein (Figure 3A). The tagBFP signal was weakly observed at the cell membrane and strongly at the cytoplasm of HEK293t cells transfected with a TVB^{S3}-tagBFP plasmid (Figure 3B). Cytoplasm aggregation could cause cell cytotoxicity (Eisele et al., 2015; Boland et al., 2018). Thus, to reduce TVB^{S3}-tagBFP aggregation, we designed a new TVB receptor. First, we attempted to insert a GGG peptide linker as a fusion protein, such as TVA⁹⁵⁰-mCherry, into the TVB^{S3}-tagBFP segment. However, no change was shown (data not shown). As TVA⁹⁵⁰ was distributed on the membrane (Figure 2B), we replaced the TVB cytoplasmic tail with TVA⁹⁵⁰ to generate a TVB^{S3}-TVA chimera receptor (Figure 3A, Supplementary Figure S2). The TVB^{S3}-TVA chimera receptor was fused to tagBFP and expressed in the cell membrane without aggregating inside the cell (Figure 3B). To determine whether the cells expressing these TVB variants could be infected with oEnvB-RVΔG, we transfected HEK293t cells with TVB^{S3}-TVA-tagBFP and then we applied oEnvB-RVΔG-DsRed to the transfected cells (Figure 3C). Three days after the viral infection, TVB^{S3}-TVA-tagBFP-expressing cells were positive for DsRed. TVB^{S3}-TVA-tagBFP had higher infection efficiency by oEnvB-RVΔG compared to TVB^{S3}-tagBFP. We termed the TVB^{S3}-TVA receptor “oTVB-H” (optimized TVB with the highest affinity). We further assessed the cross-infectivity of oTVB-H to oEnvX-pseudotyped RVΔG. Each oEnvX-pseudotyped RVΔG was applied to oTVB-H-expressing HEK293t cells (Table 2). The oEnvB-RVΔG infected the oTVB-H-expressing cells whereas oEnvA-RVΔG and oEnvE-RVΔG did not. Taken together, these results indicate that oTVB-H is a high-affinity receptor with a specificity to oEnvB-RVΔG.

We next investigated whether oTVB-H can be used for viral targeting of a specific population in the brain. To restrict the viral infection to a particular cell population, we again used Tlx3-Cre mice, a layer 5-specific Cre-line; we injected Cre-dependent AAV expressing oTVB-H-tagBFP (AAV2/9-CAG-DIO-oTVB-H-tagBFP) to the V1 of Tlx3-Cre mice (Figure 3D). oEnvB-RVΔG-DsRed was injected at the same location in the V1 2–3 weeks after the AAV injection. The DsRed signal was observed in layer 5 neurons in Tlx3-Cre mice, but not in the

neurons or glia of other layers; however, the DsRed⁺ cells in layer 5 were tagBFP-negative (Figure 3E). Tlx3-Cre mice that received injections of oEnvB-RVΔG-DsRed but not of AAV2/9-CAG-DIO-oTVB-H-tagBFP were used as controls, and as expected, no DsRed⁺ cells were observed in the absence of oTVB-H. Our results suggest that the oEnvB-RVΔG-DsRed-infected layer 5 neurons express oTVB-H in a Cre-dependent manner, probably because oTVB-H is markedly sensitive to oEnvB-RVΔG infection; even when the BFP reporter signal cannot be detected due to the low expression level of oTVB-H-BFP, oEnvB-RVΔG can still infect these cells.

To overcome this issue, we attempted to clearly visualize the starter cells with fluorescent reporters by developing a low-affinity type TVB receptor, as shown in the cases of TVA⁹⁵⁰ and TVA^{950E66T} (Watabe-Uchida et al., 2012; Miyamichi et al., 2013; Figure 2). To obtain an ideal receptor, we compared it with other TVB subtypes (Figure 3F). TVB has four subtypes (TVB^{S1}, TVB^{r2}, TVB^{S3}, and TVB^T) that can recognize and bind to ASLV-B (Brojatsch et al., 1996; Reinisová et al., 2008). The extracellular domain of TVB is composed of three cysteine-rich domains (CRDs; Hymowitz et al., 1999; Adkins et al., 2000; Reinisová et al., 2008). In general, CRD1 is essential for ASLV-B recognition, but CRD2 and CRD3 are not necessary for ASLV-B interaction. Importantly, when these CRD2 and CRD3 domains were mutated or deleted in TVB, ASLV-B infection efficiency tended to decrease (Adkins et al., 2001; Klucking and Young, 2004). Thus, we hypothesized that we can design TVB receptors with lower affinity and higher specificity to EnvB by mutations or deletions of CRD2 and CRD3 from the TVB extracellular domain. Consequently, we designed four TVB mutants that contained a TVA intracellular domain: TVB^{S1}-TVA-tagBFP, TVB^{r2}-TVA-tagBFP, TVB^{S3ΔCRD2}-TVA-tagBFP, and TVB^{S3ΔCRD3}-TVA-tagBFP (Figure 3F). Compared to TVB^{S3}, TVB^{S1} has only one mutation (S62C) at CRD2, and TVB^{r2} has two mutations at CRD2 (S62C) and CRD3 (C125S; Reinisová et al., 2008). Previous reports have revealed that TVB^{S1} whose CRD2 or CRD3 was deleted showed reduced ASLV-E and stable or slightly reduced ASLV-B infectivity (Adkins et al., 2001; Klucking and Young, 2004). Thus, we expected that chimeric TVB^{r2} or TVB^{S3} without CRD2 or CRD3 would have a lower affinity and higher specificity to EnvB. Accordingly, we generated a CRD2-deleted mutant TVB^{S3ΔCRD2} and a CRD3-deleted mutant TVB^{S3ΔCRD3} (Supplementary Figure S2). To evaluate the *in vitro* localization and function of these TVB mutant receptors, we transfected HEK293t cells with plasmids coding for those mutant receptors and then applied oEnvB-RVΔG-DsRed or oEnvE-RVΔG-GFP to those cells (Figures 3G,H)

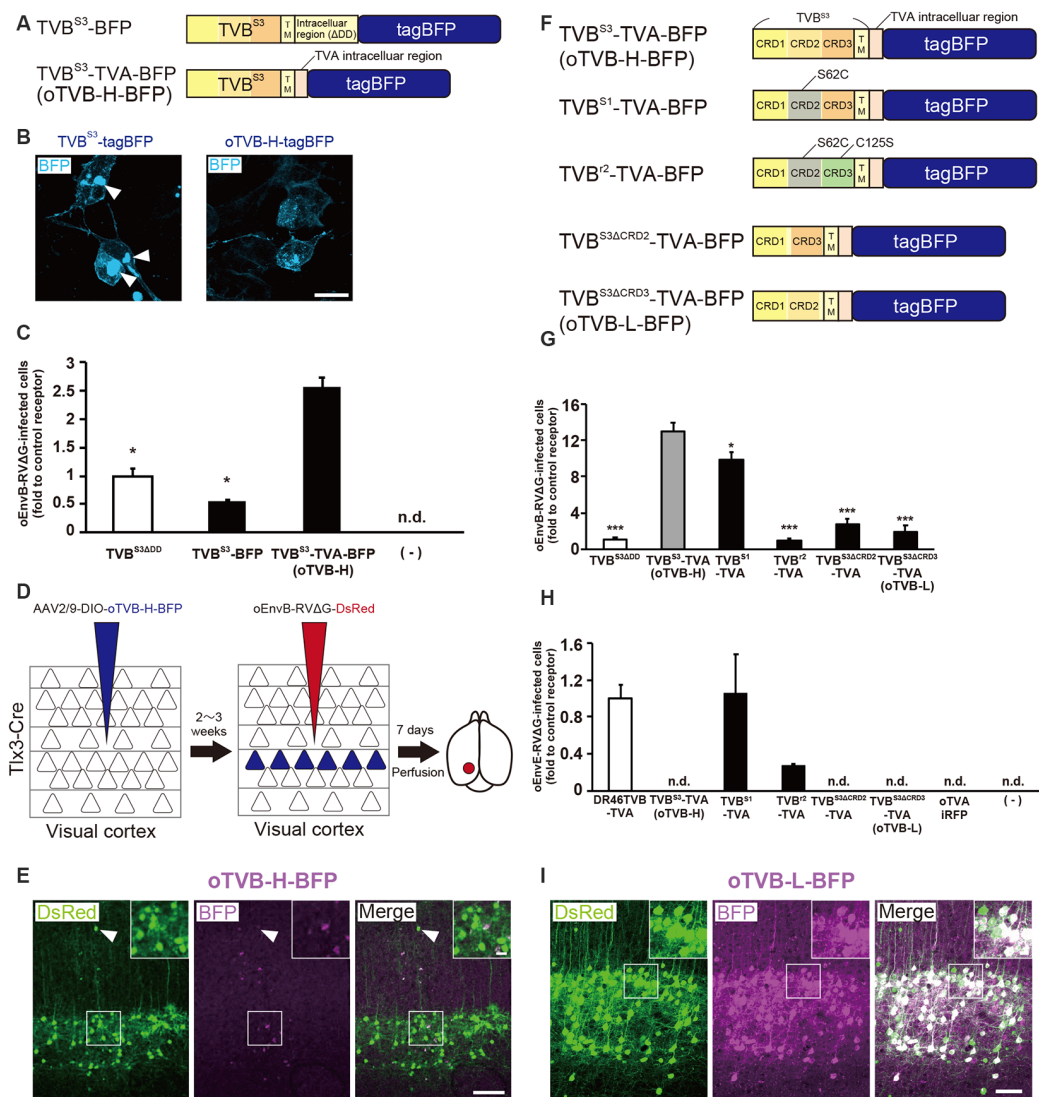


FIGURE 3 | Generation of an optimized oEnvB/oTVB system for viral targeting. **(A)** Design of TVB variants fused to a blue fluorescent protein. TVB^{S3ΔDD}-BFP was deficient in the death domain from TVB^{S3} and fused to tagBFP. TVB^{S3ΔDD}-TVA-BFP (oTVB-H) has a TVA⁹⁵⁰ intracellular region instead of the TVB^{S3} intracellular region and fused-tagBFP. **(B)** Subcellular localization of TVB^{S3}-BFP (left) and oTVB-H-BFP (right) in transfected-HEK293T cells. Abnormal localization of TVB^{S3}-BFP in the cell membrane and cytoplasmic region. Arrowhead: aggregation of oTVB-H-BFP. Membrane localization of oTVB-H-BFP. Scale bar: 20 μm. **(C)** Infectious efficiency of oEnvB-RVΔG to cells expressing TVB^{S3ΔDD}, TVB^{S3}-BFP, or oTVB-H-BFP. Each column represents the mean ± SEM (*n* = 3). **P* < 0.05 vs. oTVB-H (Tukey's multiple tests). n.d.; not detected. **(D)** *In vivo* evaluation of oTVB-H function in the mouse brain. AAV2/9-DIO-oTVB-H-BFP was injected to the V1 of Tlx3-Cre mice to introduce oTVB-H in layer 5 neurons. oEnvB-RVΔG-DsRed was injected at the location of the AAV injection. **(E)** Evaluation of *in vivo* function of TVB^{S3}-TVA-BFP (oTVB-H) in Tlx3-Cre mice. oEnvB-RVΔG-DsRed infected layer 5 neurons without visible oTVB-H-tagBFP signals, suggesting that oTVB-H was sufficiently sensitive for oEnvB-RVΔG-DsRed to infect cells expressing oTVB-H at a low expression level. The arrowhead indicates non-specific infection to neurons in layer 2/3. Signals were derived from native fluorescence. Scale bar: 100 μm. The inset shows high magnifications of areas indicated by the white square. Scale bar: 20 μm. **(F)** Generation of TVB mutants fused with a blue fluorescent protein. TVB^{S1} has one mutation (S62C). TVB² has two mutations (S62C and C125S). TVB^{S3ΔCRD2} is devoid of CRD2 from TVB^{S3}. TVB^{S3ΔCRD3} is devoid of CRD3 from TVB^{S3}. **(G,H)** Infection efficiency of **(G)** oEnvB-RVΔG and **(H)** oEnvB-RVΔG to cells expressing one of the tagBFP-fused TVB mutants. Each column represents the mean ± SEM (*n* = 3). **P* < 0.05, ****P* < 0.001 vs. TVB^{S3}-TVA-BFP (oTVB-H) (Dunnett's multiple test). **(I)** Evaluation of *in vivo* function of TVB^{S3ΔCRD3}-TVA-BFP (oTVB-L). oEnvB-RVΔG-DsRed infected oTVB-L-BFP-expressing neurons of layer 5-specific Tlx3-Cre mice. Signals were derived from native fluorescence. Scale bar: 100 μm. The inset shows high magnifications of areas indicated by the white square. Scale bar: 20 μm.

because several lines of evidence have indicated that TVB^{S1} and TVB^T have affinities to ASLV-B and ASLV-E (Brojtsch et al., 2000; Klucking and Young, 2004; Matsuyama et al., 2015). We counted the number of infected cells 3 days after the infection.

The cells expressing each TVB mutant receptor were infected with oEnvB-RVΔG-DsRed at a different efficiency (Figure 3G). The oTVB-H-expressing cells were the most efficiently infected with oEnvB-RVΔG-DsRed but did not show infectivity with

oEnvE-RVΔG-GFP (**Figures 3G,H**). TVB⁷²-TVA showed the lowest affinity to oEnvB-RVΔG and limited affinity to oEnvE-RVΔG. Notably, HEK293t cells expressing DR46TVB-TVA, TVB^{S1}-TVA, and TVB⁷²-TVA were infected with oEnvE-RVΔG, but no infection with oEnvE-RVΔG was observed in HEK293t cells expressing TVB^{S3ΔCRD2}-TVA, TVB^{S3ΔCRD3}-TVA, or oTVA-iRFP (**Figure 3H**). TVB^{S3ΔCRD2}-TVA-tagBFP and TVB^{S3ΔCRD3}-TVA-tagBFP had the lowest affinity and highest specificity to oEnvB-RVΔG but not to oEnvE-RVΔG. These results suggest that TVB^{S3ΔCRD3}-TVA can be used as a specific TVB receptor with the lowest affinity to oEnvB-RVΔG. Hereafter, we refer to TVB^{S3ΔCRD3}-TVA as “oTVB-L” (optimized TVB with the lowest affinity).

Then, we tested whether oTVB-L-tagBFP can be used for *in vivo* viral targeting to specific cell types and unambiguous visualization of the infected cells. We injected Cre-dependent AAV expressing oTVB-L-tagBFP (AAV2/9-CAG-DIO-oTVB-L-tagBFP) into the V1 of Tlx3-Cre mice to restrict oTVB-L-tagBFP expression to layer 5 neurons (**Figure 3I**). Three weeks after injection, the tagBFP signal was distributed in layer 5 neurons of the V1. We subsequently examined whether oEnvB-RVΔG could infect oTVB-L-expressing neurons *in vivo* and whether the oTVB-L-expressing cells could be visible and unambiguously identified as starter neurons for rabies tracing experiments. We injected AAV2/9-CAG-DIO-oTVB-L-tagBFP into the V1 of Tlx3-Cre mice, and then oEnvB-RVΔG-DsRed into the same location. BFP signals were observed in layer 5 neurons of the mouse V1. A total of $84.8 \pm 4.2\%$ of DsRed⁺ cells co-expressed tagBFP (total 325/347 neurons from four mice; **Figure 3I**). Conversely, no infection with oEnvB-RVΔG-DsRed was observed in the absence of oTVB-L in mice that were not subjected to injection of oTVB-L-tagBFP-expressing AAV (**Supplementary Figure S1B**). These results indicate that oEnvB-RVΔG infected the oTVB-L-expressing neurons and that oTVB-L-tagBFP reliably visualized the oEnvB-RVΔG-infected neurons. Moreover, oTVB-H is too sensitive for use in *in vivo* viral targeting because of its low expression level that can lead to viral infection, thereby generating pseudo-negative populations even when its intrinsic reporter signal is invisible (**Figure 3F**). Taken together, we conclude that oTVB-L is suitable for oEnvB-RVΔG-targeting to particular populations *in vivo*.

Generation of the Optimized oEnvE/oTVE System

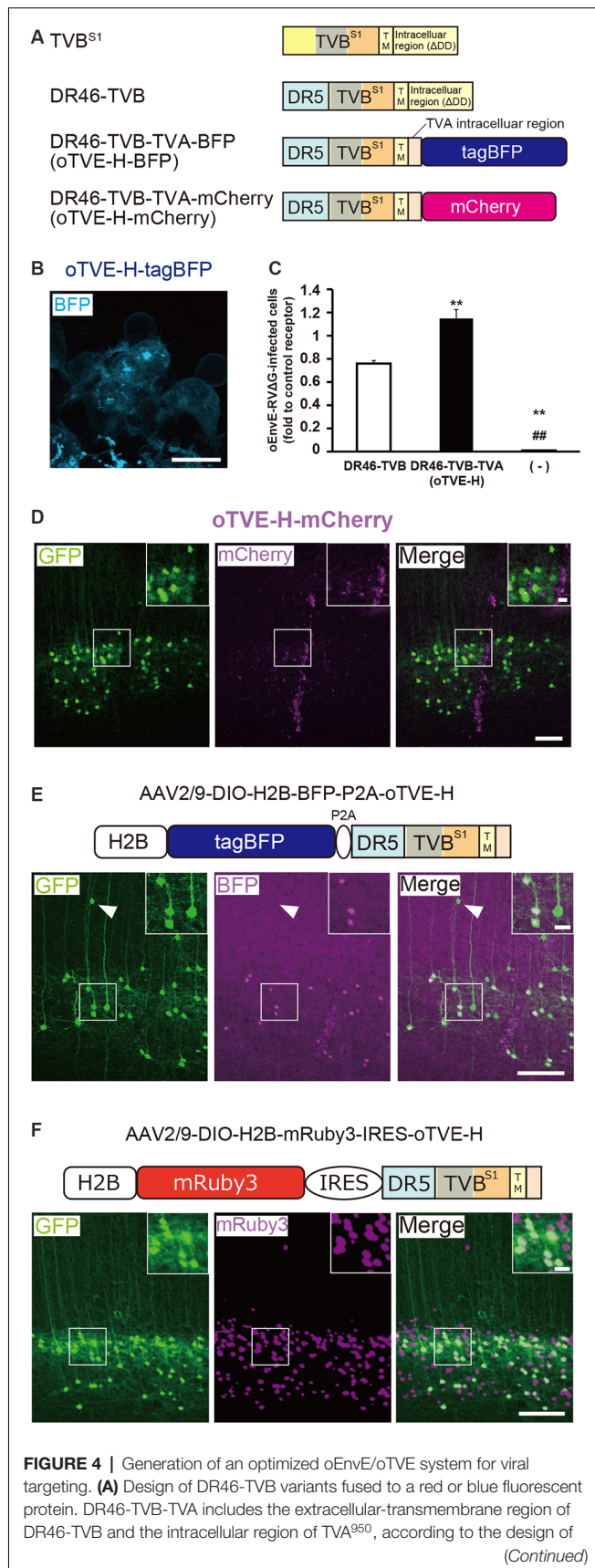
We next aimed to develop optimized DR46-TVB receptors that would allow specific targeting of EnvE viruses in the mammalian brain (Klucking and Young, 2004; Matsuyama et al., 2015). Intriguingly, DR46-TVB has been developed as an EnvE-specific receptor by replacing the TVB^{S1} CRD1 region with a corresponding region of death receptor 5 (Klucking and Young, 2004). Thus, we further optimized DR46-TVB as a tumor virus subgroup E (TVE)-specific viral receptor suitable for the rabies tracing experiments (**Figure 4A**). Interestingly, DR46-TVB shares the same transmembrane and cytoplasmic domains with the original TVB. As TVB did not show clear membrane localization in the mammalian cells, we endowed the clear membrane localization and the

fluorescent-protein-tagging of DR46-TVB to efficiently and unambiguously visualize the starter neurons. For that purpose, we followed the same strategy as that used for oTVB. We swapped the intracellular domain of DR46-TVB with the intracellular domain of TVA to generate DR46-TVB-TVA and then we fused the C-terminus of the DR46-TVB-TVA to tagBFP or to mCherry to use it along with TVA^{950E66T}-iRFP670 (**Figure 4A**, **Supplementary Figure S2**). We termed DR46-TVB-TVA “oTVE-H” (optimized DR46-TVB with a high affinity for oEnvE-pseudotyped viruses). Both oTVE-H-tagBFP and oTVE-H-mCherry were localized on the cell membrane of the transfected HEK293t cells (**Figure 4B**).

Next, we determined whether the cells expressing oTVE-H can be infected with oEnvE-RVΔG *in vitro* (**Figure 4C**). We transfected HEK293t cells with the oTVE-H-coding plasmid and subsequently applied oEnvE-RVΔG. oEnvE-RVΔG significantly infected the oTVE-H-expressing HEK293t cells. The infection efficiency of oTVE-H was higher than that of DR46-TVB. The higher infection efficiency of oTVE-H can be attributed to its higher membrane localization compared with that of DR46-TVB. We further investigated the specificity and cross-infectivity of oTVE-H to oEnvX-RVΔG *in vitro* (**Table 2**). We applied oEnvX-RVΔG to oTVE-H-expressing HEK cells and we found that oEnvE-RVΔG infected them, whereas oEnvA-RVΔG and oEnvB-RVΔG did not. Consequently, these results suggest that oTVE-H can be used as a specific receptor for oEnvE-RVΔG targeting.

To evaluate whether oTVE-H allows viral targeting to a specific population *in vivo*, we injected Cre-dependent AAV expressing oTVE-H-mCherry (AAV2/9-CAG-DIO-oTVE-H-mCherry) in the V1 of layer 5-specific Tlx3-Cre mice, as previously performed with oTVA-L and oTVB, and then injected oEnvE-RVΔG-GFP into the same location (**Figure 4D**). We observed some GFP-expressing neurons in layer 5 around the injection site, but not any mCherry-expressing neurons. No infection with oEnvE-RVΔG-GFP was observed in mice lacking oTVE-H expression (**Supplementary Figure S1C**). It is plausible that although a small amount of oTVE-H-mCherry was expressed in layer 5 neurons at the level of an invisible fluorescent reporter signal, its affinity to oEnvE-RVΔG was too high; thus, oTVE-H recognized oEnvE-RVΔG and led to viral infection.

As previously performed with oTVA-L or oTVB-L for unambiguous labeling of target cells *in vivo* (**Figures 2, 3**), we sought to reduce oTVE-H affinity. Previous reports have indicated that the CRD2 region of TVB^{S1} is important for ASLV-E infection, and the recognition site is composed of three residues in CRD2 (Klucking and Young, 2004). Thus, according to the TVB^{S1} mutation (Klucking and Young, 2004), we generated CRD region-deleted oTVE-H (DR46-TVB^{ΔCRD2}-TVA and DR46-TVB^{ΔCRD3}-TVA) and single mutated oTVE-H receptors (DR46-TVB^{Y102A}-TVA, DR46-TVB^{N107A}-TVA, and DR46-TVB^{N108A}-TVA) fused to tagBFP (**Supplementary Figure S3**). The tagBFP signals of every receptor mutant were observed on the membrane of the transfected-HEK293t cells but none of them recognized oEnvE-RVΔG (data not shown).

**FIGURE 4 |** Continued

oTVb (see **Figures 3A,B**). **(B)** Membrane localization of DR46-TVb-TVA (oTVE-H)-BFP in HEK293T cells. The TagBFP signal was observed in the cell membrane. Signals were derived from native fluorescence. Scale bar: 20 μ m. **(C)** Infection efficiency of oEnvE-RVΔG to cells expressing DR46-TVb or oTVE-H. Each column represents the mean \pm SEM ($n = 3$). ** $P < 0.01$ vs. DR46-TVb, ## $P < 0.01$ vs. oTVE-H (Tukey's multiple tests). **(D)** Evaluation of *in vivo* function of oTVE-H-mCherry in Tlx3-Cre mice. Typical images of oEnvE-RVΔG-GFP-infected layer 5 neurons although the layer 5 neurons do not have visible expression of oTVE-H-mCherry. These data suggest that oTVE-H was sufficiently sensitive for oEnvE-RVΔG-GFP to infect layer 5 neurons expressing oTVE-H at a low expression level. Scale bar: 100 μ m. The inset shows high magnifications of areas indicated by the white square. Signals were derived from native fluorescence. Scale bar: 20 μ m. **(E)** The 2A-mediated oTVE-H expression system. oTVE-H was introduced by the H2B-tagBFP-P2A-oTVE-H cassette. oEnvE-RVΔG-GFP infected neurons expressing both nuclear H2B-tagBFP and oTVE-H in Tlx3-Cre mice. The arrowhead indicates non-specific infection to neurons in layers 2/3. Signals were derived from native fluorescence. Scale bar: 100 μ m. The inset shows high magnifications of areas indicated by the white square. Scale bar: 20 μ m. **(F)** The IRES-mediated the oTVE expression system for reliable detection of oTVE-H-expressing cells. oTVE-H was expressed downstream of the IRES sequence. oEnvE-RVΔG-GFP infected neurons expressing visible H2B-mRuby3 as well as oTVE-H in Tlx3-Cre mice. oEnvE-RVΔG-GFP-infected neurons expressed nuclear mRuby3. Signals were derived from native fluorescence. Scale bar: 100 μ m. The inset shows high magnifications of areas indicated by the white square. Scale bar: 20 μ m.

Clear labeling of starter neurons is essential to determine the post-synaptic neurons in rabies tracing experiments, although the cells expressing oTVE-H-mCherry can be infected with oEnvE-RVΔG even when its expression is too low to be detected. It is conceivable that oTVE-H is inefficiently expressed in the mouse brain and its fused-reporter signal is barely detected. Thus, to reliably visualize target cells expressing oTVE-H, we first used a 2A-mediated bicistronic expression system (Szymczak et al., 2004; Chng et al., 2015) with a fluorescence reporter but without immunostaining (**Figure 4E**). We designed a bicistronic viral vector that expressed the two nuclear-localized transgenes tagBFP and oTVE-H (AAV2/9-CAG-DIO-H2B-tagBFP-p2A-oTVE-H). Then, we injected this AAV into the V1 of Tlx3-Cre mice and 2–3 weeks later oEnvE-RVΔG-GFP was injected into the same site. Seven days after RV injection, we counted the number of GFP/tagBFP-double-positive neurons in the V1. The results showed that $84.4 \pm 4.4\%$ of the GFP⁺ neurons also expressed H2B-tagBFP (total 547/659 neurons from three mice). GFP-positive and H2B-tagBFP-negative neurons were observed outside layer 5 of the cortex. This is because leak expression of oTVE-H derived from AAV-DIO vectors induced oEnvE-RVΔG-GFP infection. These results suggest that the 2A-system permits labeling and detection of the starter neurons with a fluorescence reporter and that only a small amount of oTVE-H is needed for the infection of oEnvE-RVΔG even at a barely visible expression level of its reporter fluorescence.

To reliably label and detect oTVE-H-expression cells for circuit mapping, we hypothesized that if oTVE-H expression could be reduced and its reporter fluorescence could be increased, we would be able to unambiguously detect oEnvE-RVΔG-infected neurons without immunostaining. Thus, we used another bicistronic system, the internal ribosome entry

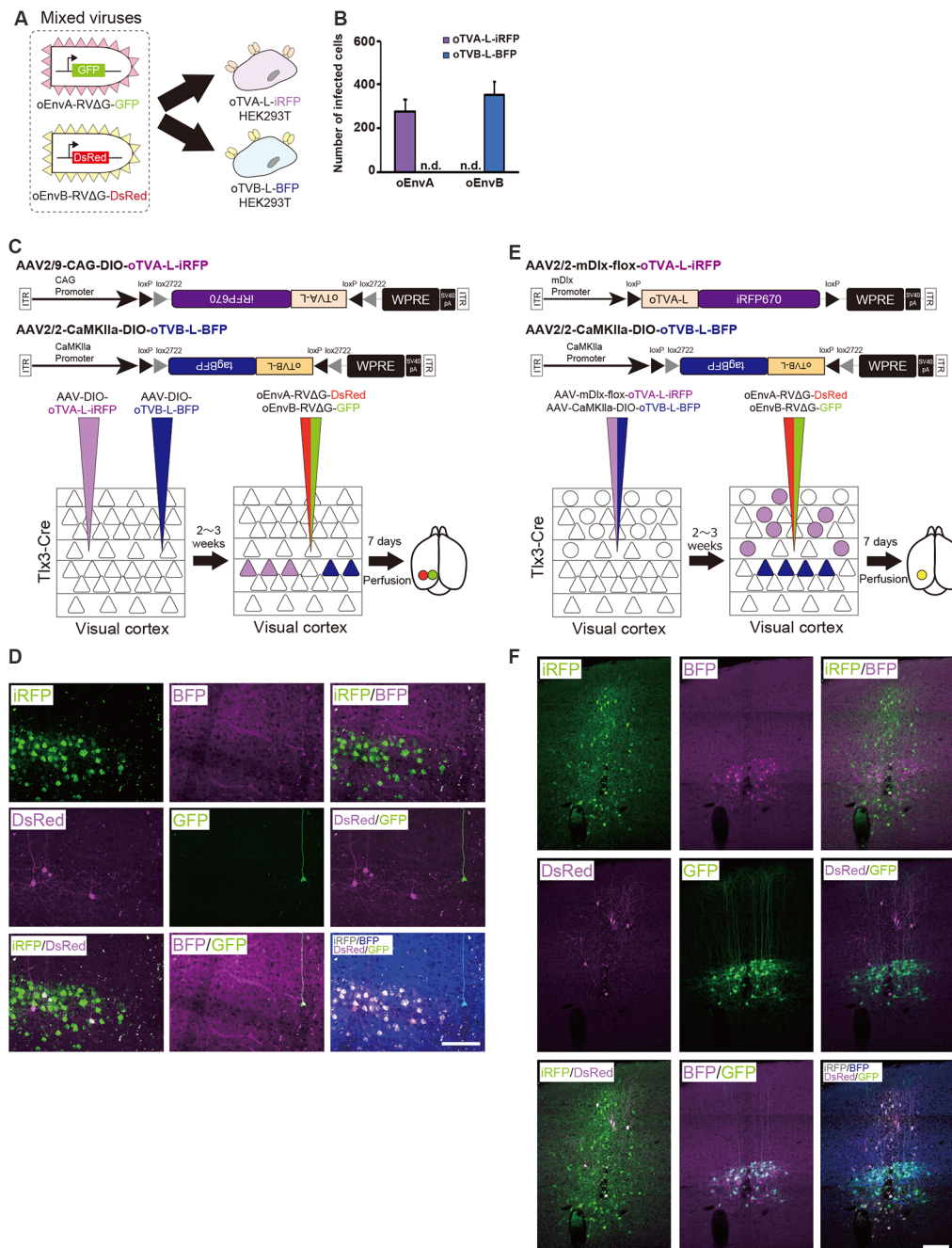


FIGURE 5 | Independence of the oEnvA/oTVA and oEnvB/oTVB systems. **(A)** *In vitro* evaluation of specificity of oEnvA-RVΔG-GFP and oEnvB-RVΔG-DsRed to cells expressing either oTVA-L-iRFP or oTVB-L-BFP. oEnvA-RV and oEnvB-RV mixed viruses applied to HEK293t cells expressing oTVA-L-iRFP or oTVB-L-BFP transiently. **(B)** No cross-infectivity of oEnvA-RVΔG-GFP and oEnvB-RVΔG-DsRed to cells expressing either oTVA-L-iRFP or oTVB-L-BFP. Evaluation of *in vitro* infectious specificity. Each column represents the mean \pm SEM ($n = 3$). n.d.: not detected. **(C)** *In vivo* infectious specificity of oTVA-L-iRFP and oTVB-L-BFP that are expressed in two different locations of the brain. AAV-CAG-DIO-oTVA-L-iRFP and AAV-CaMKIIa-DIO-oTVB-L-BFP were injected in two different locations of Tlx3-Cre mice, 800 μ m apart. A mixture of oEnvA-RVΔG-DsRed and oEnvB-RVΔG-GFP was injected between the two injection sites of AAV. **(D)** Non-co-infection with oEnvA-RVΔG and oEnvB-RVΔG. Signals were derived from native fluorescence. Scale bar: 100 μ m. **(E)** *In vivo* infection specificity of oTVA-L-iRFP and oTVB-L-BFP that are expressed in two different cell types. oTVA-L-iRFP and oTVB-L-BFP are exclusively expressed by a distinct promoter and a transgenic Cre line. Inhibitory neurons were targeted by the inhibitory neuron-specific mDlx promoter and layer 5 neurons recombined the AAV genome to excise the flox cassette and eliminate gene expressions. Excitatory neurons in layer 5 of the cortex were targeted by a combination of the excitatory neuron-specific CaMKIIa promoter and the layer 5-specific Tlx3-Cre line. AAV-mDlx-oTVA-L-iRFP and AAV-CaMKIIa-DIO-oTVB-L-BFP were co-injected into the V1 of Tlx3-Cre mice. oEnvA-RVΔG-DsRed and oEnvB-RVΔG-GFP were co-injected into the location of the AAV injection. **(F)** No cross-infectivity between oEnvA-RVΔG and oEnvB-RVΔG. Signals were derived from native fluorescence. Scale bar: 100 μ m.

site (IRES) system, which can adjust oTVE-H expression to a lower level (**Figure 4F**). We generated AAV vectors that allow for lower expression of oTVE-H (AAV2/9-CAG-DIO-H2B-mRuby3-IRES-oTVE-H). This system enables bicistronic expression but the expression level of the second gene (oTVE-H) after the IRES sequence is lower than that of the first gene (H2B-mRuby3; Mizuguchi et al., 2000; Mardinly et al., 2018). We injected AAV2/9-CAG-DIO-H2B-mRuby3-IRES-oTVE-H into the V1 and then applied oEnvE-RVΔG-GFP into the same injection site (**Figure 4F**); $99.0 \pm 0.4\%$ of GFP⁺ cells also expressed H2B-mRuby3 (total 590/595 neurons from three mice). Compared to the 2A system that enables the bicistronic expression of two genes at the same expression level (Chng et al., 2015), the IRES-mediated oTVE expression system facilitates the unambiguous detection of oEnvE-RVΔG-infected neurons without the need of immunostaining signal enhancement (**Figures 4E,F**).

Next, we examined whether the oEnvE/oTVE system can be used for circuit tracing. We injected AAV expressing both oTVE and oG in a Cre-dependent manner into the mouse V1 of Tlx3-Cre mice. Three weeks after the AAV injection, oEnvE-RVΔG-GFP was injected into the same injection site. Ten days after the rabies injection, we found GFP⁺ presynaptic cells in the V1 and dorsal lateral geniculate nucleus (dLGN; **Supplementary Figure S4**), which is consistent with the previous report (Kim et al., 2015). These results suggest that the oEnvE/oTVE system could be used for trans-synaptic circuit tracing.

In the present study, we developed the chimeric envelope protein, oEnvE, and its cognate high-affinity receptor, oTVE. AAV vectors carrying the IRES-mediated bicistronic system could introduce oTVE-H in starter cells for oEnvE-RVΔG targeting. The oEnvE/oTVE system can be used for circuit mapping for particular cell populations in the mammalian nervous system.

Independence Between the oEnvA/oTVA and oEnvB/oTVB Systems *in vivo*

To differentially dissect and visualize two independent cell populations with fluorescent proteins, we next applied both the oEnvA/oTVA and oEnvB/oTVB systems to the mouse brain. To trace circuits with RVΔG, we needed to reliably label starter cells and introduce two genes RV-G and oTVX in the starter cells. For that purpose, we used a 2A element to express both genes from the AAV genome. To label two different populations, we selected oTVA-L and oTVB-L, as both are low-affinity receptors to the corresponding envelopes (**Figures 2E,F, 3I**). Initially, to assess the specificity and cross-infectivity of oTVA-L-iRFP and oTVB-L-tagBFP, we performed an *in vitro* assay by preparing the oTVA-L-iRFP- and oTVB-L-tagBFP-expressing HEK293t cells individually and then applied a mixture of oEnvA-RVΔG-GFP and oEnvB-RVΔG-DsRed into each culture (**Figure 5A**). Three days after the viral infection, 100% of the GFP⁺ cells expressed iRFP670 and 0% of the GFP⁺ cells expressed BFP (**Figure 5B**). Similarly, 100% of the DsRed⁺ cells expressed BFP and 0% of the DsRed⁺ cells expressed iRFP670. These results indicate that

oTVA-L and oTVB-L, respectively recognized oEnvA-RVΔG and oEnvB-RVΔG without cross-reaction.

Next, we investigated the *in vivo* specificity and cross-infectivity of oEnvA-RVΔG and oEnvB-RVΔG. We introduced oTVA-L and oTVB-L separately in two different locations of the mouse brain (**Figure 5C**). We injected oTVA-L-iRFP-expressing AAV and oTVB-L-tagBFP-expressing AAV at the medial and lateral V1 (0.8 mm apart) of Tlx3-Cre mice, respectively, and subsequently injected a mixture of oEnvA-RVΔG-DsRed and oEnvB-RVΔG-GFP between the AAV-injection sites. Seven days after the RV injection, we sacrificed the mice and observed the injection sites of the sectioned brain. Indeed, iRFP⁺ and tagBFP⁺ cells were exclusively distributed in the V1 (from three mice). No co-infection was observed between the oTVA-L-iRFP- and oTVB-L-tagBFP-expressing AAV (**Figure 5D**). All oEnvA-RVΔG-derived DsRed⁺ neurons also expressed iRFP670. Moreover, most oEnvB-RVΔG-derived GFP⁺ neurons also expressed BFP; the rest of the GFP⁺ neurons there was no BFP signal observed, but all GFP⁺ neurons were observed in the medial V1 injection site of the oTVB-L-tagBFP-expressing virus (**Supplementary Table S1**). Thus, the receptors did not recognize the non-corresponding envelopes.

To further demonstrate the specificity and independence of the oEnvA/oTVA and oEnvB/oTVB systems, we constructed two helper viruses: the first one carried an inhibitory-neuron-specific mDlx promoter (Dimidschstein et al., 2016) that allowed the inhibitory neurons to express oTVA-L-iRFP, and the other expressed oTVB-L-tagBFP in Tlx3-Cre mice, a layer 5 excitatory neuron-specific line, in a Cre-dependent manner (**Figure 5E**). We injected the mixture of these two AAVs to the V1 of Tlx3-Cre mice and then the mixture of oEnvA-RVΔG-DsRed and oEnvB-RVΔG-GFP to the location of the AAV injection. Most DsRed-expressing neurons were iRFP-positive while majority of GFP-expressing neurons were tagBFP-positive (**Figure 5F, Supplementary Table S1**). No GFP/DsRed-double-positive cells were observed in the injected mice. These results indicate that the oEnvA/oTVA-L and oEnvB/oTVB-L systems targeted inhibitory and layer 5 excitatory neurons in the mouse cortex, respectively, in a mutually exclusive manner.

In conclusion, we demonstrated that the oEnvA/oTVA-L and oEnvB/oTVB-L systems can be used in simultaneous *in vivo* targeting of RVΔG in single animals. Using the oEnvA/oTVA-L and oEnvB/oTVB-L systems for RVΔG enables differentially dissecting and visualizing two independent cell populations with fluorescent proteins.

Simultaneous Trans-synaptic Tracing Using the oEnvA/oTVA and oEnvB/oTVB Systems

To perform a simple proof-of-concept experiment for simultaneous multiplex circuit tracing, we aimed to dissect multiple neural circuits using the oEnvA/oTVA and oEnvB/oTVB systems that we developed for the purposes of the present study. V1 neurons are heterogeneous; excitatory neurons even on the same layer have different connection patterns, and inhibitory neurons have different biochemical markers,

morphological features, electrophysiological properties, and connection patterns. Layer 5 neurons in the V1 comprise at least two different cell types depending on their projection targets (Brown and Hestrin, 2009; Lur et al., 2016). The first one projects to the cortical areas, such as the higher visual areas, and the other to subcortical areas, such as the superior colliculus (SC; Brown and Hestrin, 2009; Lur et al., 2016). These two types of layer 5 neurons that project to different target regions are locally intermingled.

To distinguish these two different layer-5 cell types and their corresponding presynaptic networks, we introduced the oEnvA/oTVA and oEnvB/oTVB systems to each population (Figure 6A). The AAV2retro capsid allows AAV to retrogradely infect projection neurons through axon terminals (Teruo et al., 2016). We first planned to develop an AAV2retro-CAG-oTVA-L-iRFP-P2A-oG (ITR-ITR: >4.9 kbps) that would simultaneously express both oTVA-L-iRFP and the optimized rabies glycoprotein oG. However, the AAV genome is limited (<4.7 kbps; Dong et al., 1996; Allocca et al., 2008), so we could not obtain sufficient AAV to be usable *in vivo*. Then, to maximize space for transgenes within the AAV packaging capacity without compromising transgene expression, we used a shorter universal promoter and a shorter polyA sequence to accommodate TVX, oG, and a fluorescent reporter such as, pAAV-CBh-oTVA-L-iRFP-P2A-oG-WPRE3-SV40 late polyA (ITR-ITR: approximately 4.3 kbps; Choi et al., 2014).

We administered two injections of retrograde AAVs to Tlx3-Cre mice. First, Cre- and projection-dependent, retrograde AAV expressing oTVA-L-iRFP and oG (AAV2retro-CBh-DIO-oTVA-L-iRFP-P2A-oG-WPRE3-SV40 late polyA) were injected into the lateral higher visual area (V2L: the putative area LM) to introduce both TVA and oG to V2L-projecting layer 5 neurons (Kim et al., 2016; Figures 6A,B). Second, projection-dependent, retrograde AAV expressing oTVB-L-tagBFP and oG (AAV2retro-CBh-oTVB-L-BFP-P2A-oG-WPRE3-SV40 late polyA) was injected in the SC to introduce both oTVB and oG to SC-projecting neurons (Lur et al., 2016; Figures 6A,B). iRFP⁺ cells were observed in layer 5 of the mouse V1, suggesting that V2L-projecting layer 5 neurons of V1 were labeled in a Cre-dependent and retrograde manner (Figure 6C). BFP⁺ neurons were also observed in layer 5, suggesting that the SC-projecting V1 neurons were retrogradely labeled. Using the conditional AAVs in Tlx3-Cre mice, we succeeded in specific labeling of layer 5 neurons projecting to either the V2L or SC area with oTVA-L or oTVB-L, respectively.

To identify their presynaptic inputs, we next injected oEnvA-RVΔG-DsRed and oEnvB-RVΔG-GFP into the V1 of the AAV-injected Tlx3-Cre mice 2–3 weeks after the AAV injections. Ten days after the rabies viral injection, we sacrificed the animals for histological analysis. Most DsRed⁺ cells in upper layer 5 were positive for iRFP670, indicating that oEnvA-RVΔG-DsRed infected oTVA-L-iRFP⁺ cells in upper layer 5 of the V1 and that the DsRed/iRFP-double-positive cells were starter cells for trans-synaptic tracing of RVΔG-DsRed. RVΔG-DsRed spread to the presynaptic cells following trans-complementation with oG (Figures 6B–I). DsRed-positive and

iRFP670-negative cells were mainly observed in layer 2/3 and 4 of the V1 (Figure 6C), V2L (Figures 6D,E), and dLGN (Figures 6F,H). Likewise, most GFP⁺ cells in lower layer 5 were also tagBFP-positive, indicating that oEnvB-RVΔG-GFP infected the oTVB-L-tagBFP⁺ cells in lower layer 5 of the V1, while the GFP/BFP-double-positive cells were the starter cells for trans-synaptic tracing of RVΔG-GFP. The GFP⁺ cells were more widely spread in V1, the higher visual areas V2ML and V2MM (Figure 6E), association cortical areas (medial parietal association; Figure 6G), and various thalamic areas including the dLGN, LP (Figures 6F,H), and anterior thalamic nuclei (Figure 6I). Additionally, GFP⁺ and DsRed⁺ neurons were not observed in any of the brain regions. These results suggest that V2L-projecting V1 neurons on layer 5 received inputs from V1 local circuits, feedback from higher visual areas, and visual-related thalamic areas, whereas SC-projecting V1 neurons received inputs from V1 local circuits, feedback from higher visual and association cortical areas, and visual and non-visual thalamic nuclei.

Therefore, we conclude that the multiplexed neural circuit tracing with RVΔG enabled the simultaneous dissection of multiple neural circuits in the brain.

Labeling of Common Input to Different Cell Populations With Multiplex Circuit Tracing

In the next set of experiments, we examined whether common input to two distinct cell populations can be detected by multiplex circuit tracing *in vivo*, which can be detected as co-infected cells with two viral vectors in multiplex circuit tracing. Many lines of evidence have shown that dLGN neurons send projections to neurons in layers 4, 5, and 6 of the V1 (Blasdel and Lund, 1983; Antonini et al., 1999; Constantinople and Bruno, 2013; Kim et al., 2015). A recent study revealed that parvalbumin (PV)-expressing inhibitory neurons in the V1 receives input from dLGN neurons (Kim et al., 2016).

Based on these reports, we performed multiplex RV tracing from the inhibitory neurons and layer 5 neurons of the V1 in single animals to determine whether inhibitory neurons and layer 5 excitatory neurons of the V1 share common input (Figure 7A). Cortico-cortical layer 5 neurons of the V1 were labeled with Cre-dependent AAV expressing oTVB under the excitatory-neuron-specific CaMKIIa promoter in layer 5-specific Tlx3-Cre mice. Inhibitory neurons of the V1 were labeled with AAV expressing oTVA under the inhibitory-neuron-specific mDlx promoter using the flox cassette that is excised by recombination in the Cre-expressing cells to eliminate oTVA expression in layer 5 excitatory neurons of Tlx3-Cre mice. Using this viral system, oTVA and oTVB can be exclusively introduced to layer 5 excitatory neurons and inhibitory neurons, respectively. Additionally, to complement RVΔG *in trans*, we co-injected AAV expressing the rabies glycoprotein oG under the strong ubiquitous CAG promoter, as the level of gene expressions driven by the CaMKIIa and mDlx promoters differs. Three weeks after the AAV injection, oEnvA-RVΔG-DsRed and oEnvB-RVΔG-GFP were co-injected in the same location of the V1 injection of AAVs. We observed oTVA-L-iRFP-positive cells in inhibitory

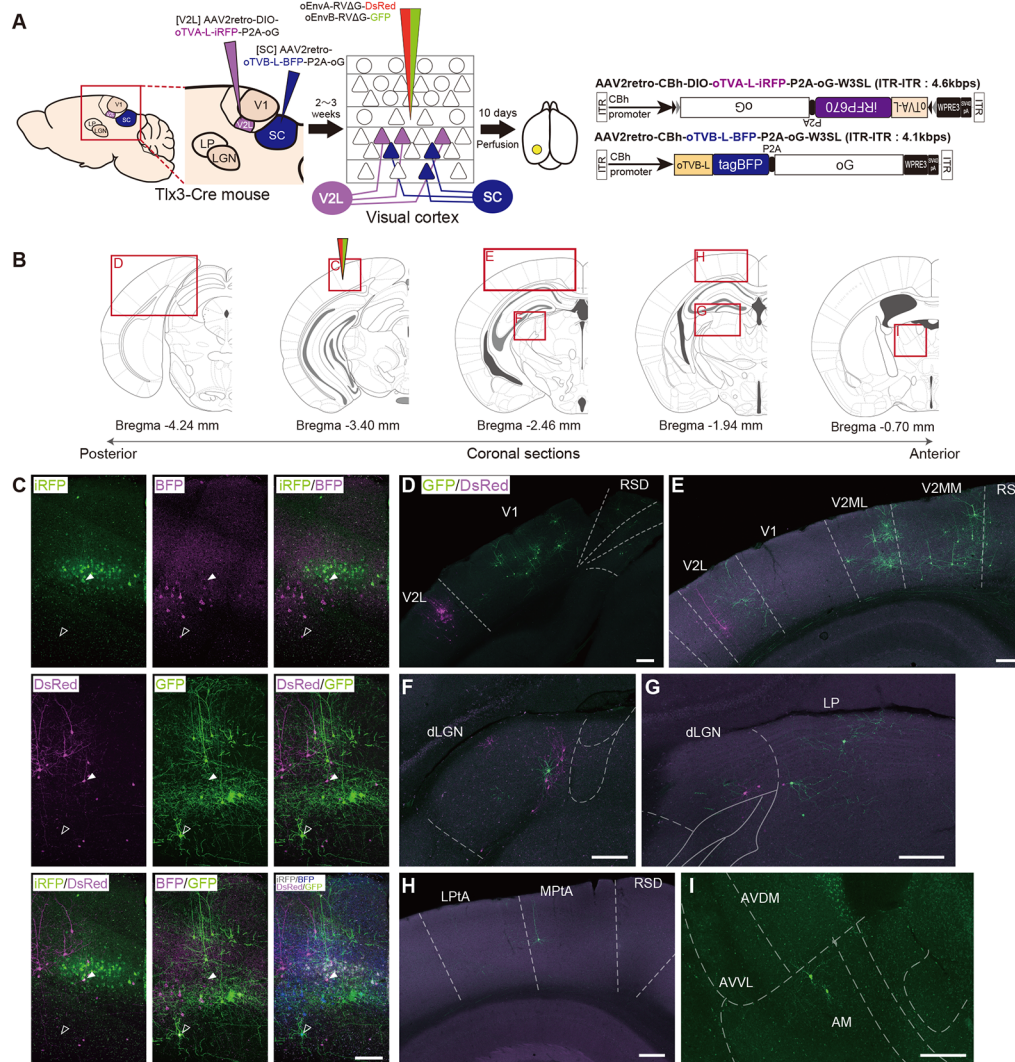


FIGURE 6 | Multiplex circuit tracing with the oEnvA/oTVA and oEnvB/oTVB systems. **(A)** Multiplex monosynaptic tracing of two distinct classes of layer 5 neurons targeting either other cortical or subcortical areas. Retrograde AAVs were injected into two different locations of layer 5-specific Tlx3-Cre mice: AAV2retro-CBh-DIO-oTVA-L-iRFP-P2A-oG and AAV2retro-CBh-DIO-oTVB-L-BFP-P2A-oG in the lateral area of the higher visual cortex (V2L) and superior colliculus (SC), respectively. V2L-projecting V1 neurons in layer 5 expressed both oTVA-L-iRFP and oG while SC-projecting V1 neurons expressed both oTVB-L-BFP and oG. After the AAV injections, oEnvA-RVΔG-DsRed and oEnvB-RVΔG-GFP were co-injected into the V1. **(B)** Coronal brain sections illustrating anatomical regions shown in **(C-I)**; adapted from *The Mouse Brain in Stereotaxic Coordinates*, 3rd edition, Paxinos and Franklin, 2008; **(G)**. **(C)** Viral targeting to two distinct classes of layer 5 neurons depending on projection targets. oTVA-L-iRFP-expressing starter neurons were specifically infected with oEnvA-RVΔG-DsRed, whereas oTVB-L-BFP-expressing starter neurons were infected with oEnvB-RVΔG-GFP. DsRed and GFP signals were enhanced by immunostaining. Closed arrowheads indicate oTVA-L-iRFP⁺/oEnvA-RVΔG-DsRed⁺ starter neurons. Opened arrowheads indicate oTVB-L-BFP⁺/oEnvB-RVΔG-GFP⁺ starter neurons. Scale bar: 100 μm. **(D-I)** Distributions of presynaptic neurons connected to two distinct classes of layer 5 neurons. Neurons trans-synaptically infected with RVΔG-DsRed and RVΔG-GFP were distributed in the V1, V2L, and RSD **(D)**, V1, V2L, V2ML, V2MM, and RSD **(E)**, dLGN **(F)**, dLGN and LP **(G)**, LPTA, MPTA, and RSD **(H)**, AM, AVDM, and AVL **(I)**. DsRed and GFP signals were enhanced by immunostaining. Scale bar: 200 μm. Abbreviations: AM, anteromedial thalamic nucleus; AVDM, anteroventral thalamic nucleus, dorsomedial part; AVL, anteroventral thalamic nucleus, ventrolateral part; RSD, retrosplenial dysgranular cortex; dLGN, dorsal lateral geniculate nucleus; LP, lateral parietal association cortex; LPTA, medial parietal association cortex; MPTA, lateral posterior thalamic nucleus; V2L, secondary visual cortex, lateral area; V2ML, secondary visual cortex, mediolateral area; V2MM, secondary visual cortex, mediomedial area.

neurons across layers and oTVB-L-BFP-positive cells (cell membrane-localized BFP) in layer 5 of the V1. We also found GFP⁺ and DsRed⁺ cells, indicating that common input was detected as co-infection with both oEnvA-RVΔG-DsRed and oEnvB-RVΔG-GFP. Interestingly, GFP⁺/DsRed⁺ neurons were distributed in the V1 (**Figure 7B**) and dLGN

(**Figures 7C-E**). These results indicate that inhibitory neurons and layer 5 excitatory neurons of the V1 share common input from V1 local circuits and from dLGN neurons.

We found that dLGN neurons provide divergent input to both layer 5 excitatory and inhibitory neurons of the V1 in the mouse visual system. The common input to both layer

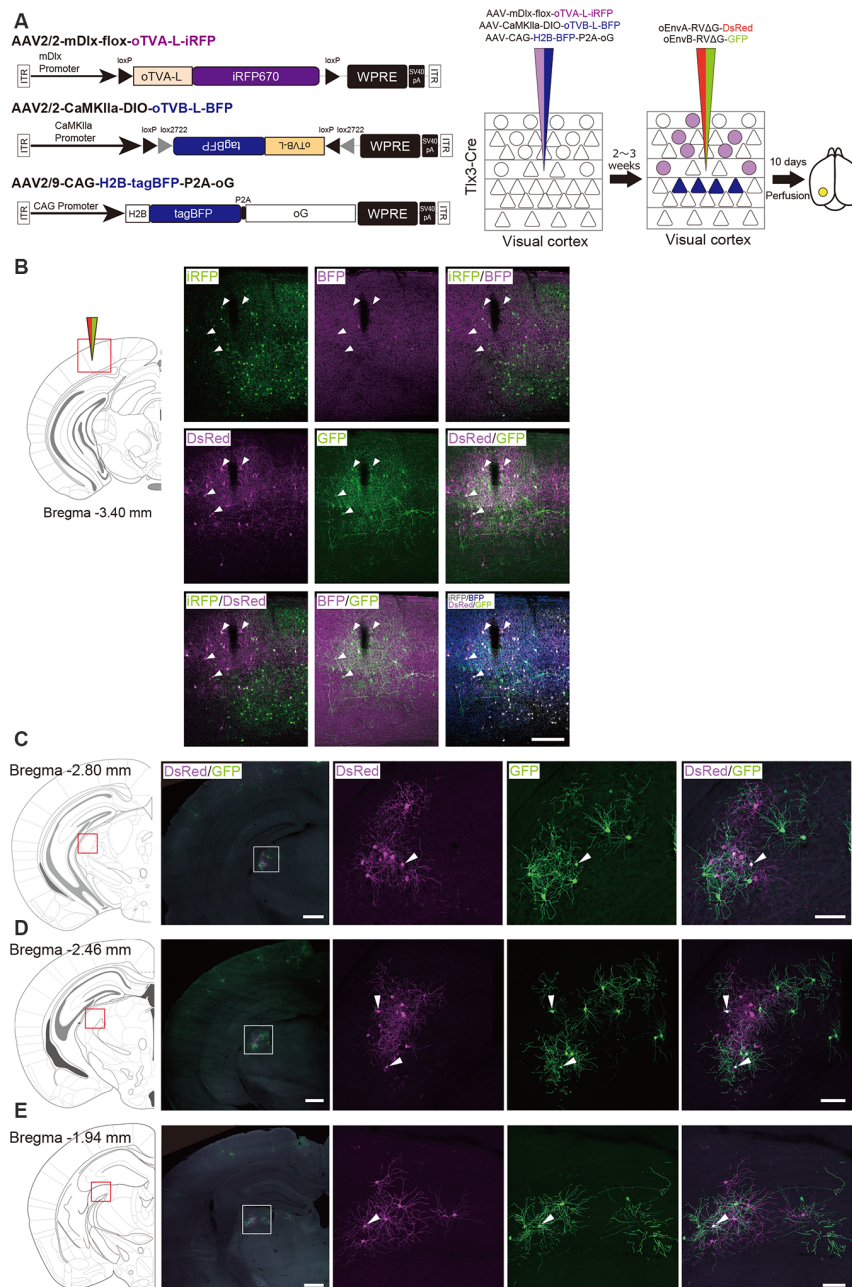


FIGURE 7 | Labeling of common input with multiplex circuit tracing. **(A)** Multiplex monosynaptic tracing of two distinct classes of layer 5 excitatory or inhibitory neurons. Mixed AAVs were injected into the V1 of layer 5-specific Tlx3-Cre mice: AAV2/2-mDlx-flox-oTVA-L-iRFP, AAV2/2-CaMKIIa-DIO-oTVB-L-BFP, and AAV2/9-CAG-H2B-tagBFP-P2A-oG. After the AAV injection, oEnvA-RVΔG-DsRed and oEnvB-RVΔG-GFP were co-injected into the same location of the V1. **(B)** Viral targeting to two distinct classes of V1 neurons depending on cell types. oTVA-L-iRFP-expressing inhibitory neurons were specifically infected with oEnvA-RVΔG-DsRed, whereas oTVB-L-BFP-expressing excitatory neurons in layer 5 were infected with oEnvB-RVΔG-GFP. The rabies glycoprotein oG was expressed in cells positive for nuclear tagBFP. Closed arrowheads indicate presynaptic neurons co-infected with both oEnvA-RVΔG-DsRed and oEnvB-RVΔG-GFP. DsRed and GFP signals were enhanced by immunostaining. Scale bar: 200 μ m. **(C–E)** Low and high magnification images of dLGN neurons monosynaptically connected to two distinct classes of V1 neurons. DsRed and GFP signals were enhanced by immunostaining. Closed arrowheads indicate presynaptic neurons co-infected with both oEnvA-RVΔG-DsRed and oEnvB-RVΔG-GFP. Scale bar of overview: 500 μ m. Scale bar of dLGN view: 100 μ m. Coronal brain sections illustrating anatomical regions shown in **(B–E)**; adapted from The Mouse Brain in Stereotaxic Coordinates, 3rd edition, Paxinos and Franklin, 2008).

5 excitatory and inhibitory neurons could provide a sub-network structure crucial for shaping the receptive field properties of V1 neurons. Taking together, we conclude that multiplex neural

circuit tracing with RVΔG allows detecting common input to different cell populations and analyzing complex computations between circuits.

DISCUSSION

Multiplex Neural Circuit Tracing With G-Deleted Rabies Viral Vectors

The brain is a complex and dynamic structure composed of heterogeneous neuronal populations that are organized in distinct neural circuits to generate perception and behavior (Harris and Mrsic-Flogel, 2013; Tasic et al., 2016, 2018). Information is processed not only through paralleled, independent circuits but also by integration between circuits in the nervous system including the retina and brain (Nassi and Callaway, 2009). Much progress has been made toward elucidating cell-type-specific connectivity at the whole-brain level. However, information integration in the brain remains elusive. Thus, dissection of the interaction between intermixing circuits will provide better opportunities to reveal the neural circuits and computations underlying integration of information processing. Here, we multiplexed the infection systems of RVΔG and demonstrated their implementation in the mouse brain. We introduced oEnvA/oTVA, oEnvB/oTVB, and oEnvE/oTVE systems to simultaneously target distinct cell populations with RVΔG. Our work provided proof-of-concept for multiplex circuit tracing with RVΔG in a single animal.

Our *in vivo* proof-of-concept experiment showed the simultaneous labeling of the two distinct classes of layer 5 neurons targeting either other cortical or subcortical areas. Using both the oEnvA/oTVA and oEnvB/oTVB systems, we differentially labeled two distinct populations with different colors in single animals. Their presynaptic inputs were also labeled with trans-synaptic spread of different-colored RVΔG. We found that SC-projecting layer 5 neurons of the V1 received input from local circuits and motor-related areas, while LM-projecting layer 5 neurons of the V1 received input from local circuits and visual-related areas including higher visual areas. We did not find any connections between SC-projecting layer 5 neurons and LM-projecting layer 5 neurons in V1 as co-infection. This result is consistent with the recent study by Maruoka et al. (2017). Maruoka et al. (2017) revealed lattice organization composed of cell type-specific microcolumns in layer 5; subcortical projection neurons formed radial clusters called microcolumns, while cortical projection neurons were also organized into microcolumns that were aligned radially in an orientation parallel to the microcolumns composed of subcortical projection neurons. Maruoka et al. (2017) also demonstrated that subcortical projection neurons were rarely connected with cortical projection neurons whereas subcortical projection neurons had reciprocal connections with each other and cortical projection neurons were also interconnected. In addition, we did not observe any co-infected cells with two rabies viral vectors outside V1, suggesting that the presynaptic network organization of layer 5 neurons differs depending on the output target; layer 5 neurons in V1 pool distinct information depending on their projection target. However, it is difficult to conclude that there is no common input between SC-projecting and LM-projecting layer 5 neurons in the V1 in this set of experiments. Although the SC-projecting layer 5 starter neurons

were distributed in the vicinity of the LM-projecting starter neurons in the V1, the retinotopic location of SC-projecting layer 5 starter cells can be mismatched with that of LM-projecting layer 5 starter cells. It is possible that the cells responsible for the same location of the visual space can interact with each other and their presynaptic networks may overlap, whereas the cells responsible for different locations of the visual space may not share common input.

In another set of experiments, the multiplex circuit tracing labeled the common input to different cell populations; we found that dLGN neurons were directly connected to both cortico-cortical layer 5 neurons and inhibitory neurons of the mouse V1. It is known that the most canonical thalamocortical connection is between dLGN neurons and layer 4 neurons of the V1. However, Kim et al. (2016) demonstrated using rabies tracing that PV-expressing inhibitory neurons in the V1 receive input from dLGN neurons. Additionally, they revealed that layer 5 excitatory neurons in the V1 also receive input from dLGN neurons (Kim et al., 2015). Several lines of evidence have indicated that dLGN neurons provide collateral connections to layer 5 and 6 neurons of the V1, in addition to layer 4 neurons (Blasdel and Lund, 1983; Antonini et al., 1999). To our knowledge, no study has revealed that layer 5 and inhibitory neurons of the V1 share common excitatory input from dLGN neurons. This divergent thalamocortical input could play unique roles in shaping the receptive field properties of V1 neurons. Further physiological studies are warranted to determine how the common input participates in circuit computation and visual information processing in the V1.

Viral Receptors With Higher or Lower Affinity

TVA fused to a fluorescent protein has been used to visualize TVA-expressing starter cells: TVA⁹⁵⁰-EYFP (Faget et al., 2016), TVA⁹⁵⁰-mCherry (Watabe-Uchida et al., 2012), and the low-affinity mutant TVA^{950E66T}-mCherry (Miyamichi et al., 2013). TVA⁹⁵⁰-EYFP and TVA⁹⁵⁰-mCherry are highly sensitive to viral infection despite low expression of TVA⁹⁵⁰ caused by leak expression even though their fluorescent reporters (EYFP and mCherry) fused to TVA⁹⁵⁰ were invisible. For example, in transgenic mice expressing Cre in a specific cell population, Cre-negative cells can express a small amount of TVA⁹⁵⁰ due to leak expression, which leads to non-specific infection with EnvA-RVΔG. However, when using TVA^{950E66T}-mCherry for rabies viral targeting in Cre-expressing transgenic mice, oEnvA-RVΔG cannot infect the cells expressing a small amount of TVA^{950E66T}-mCherry, which are invisible under a fluorescent microscope because of the low affinity of TVA^{950E66T} to oEnvA (Rong et al., 1998; Miyamichi et al., 2013). The strength of this TVA^{950E66T}-mCherry constitutes clear and reliable visualization of starter neurons in rabies tracing experiments because high expression of TVA^{950E66T}-mCherry is required for oEnvA-RVΔG infection. Thus, a lower-affinity version of TVA (oTVA-L) is ideal for rabies viral tracing.

oEnvA-RVΔG, oEnvB-RVΔG, and oEnvE-RVΔG showed specific infectivity to cells expressing their corresponding receptors, TVA⁸⁰⁰, TVB^{S3}, and DR46-TVb (Figure 1C and

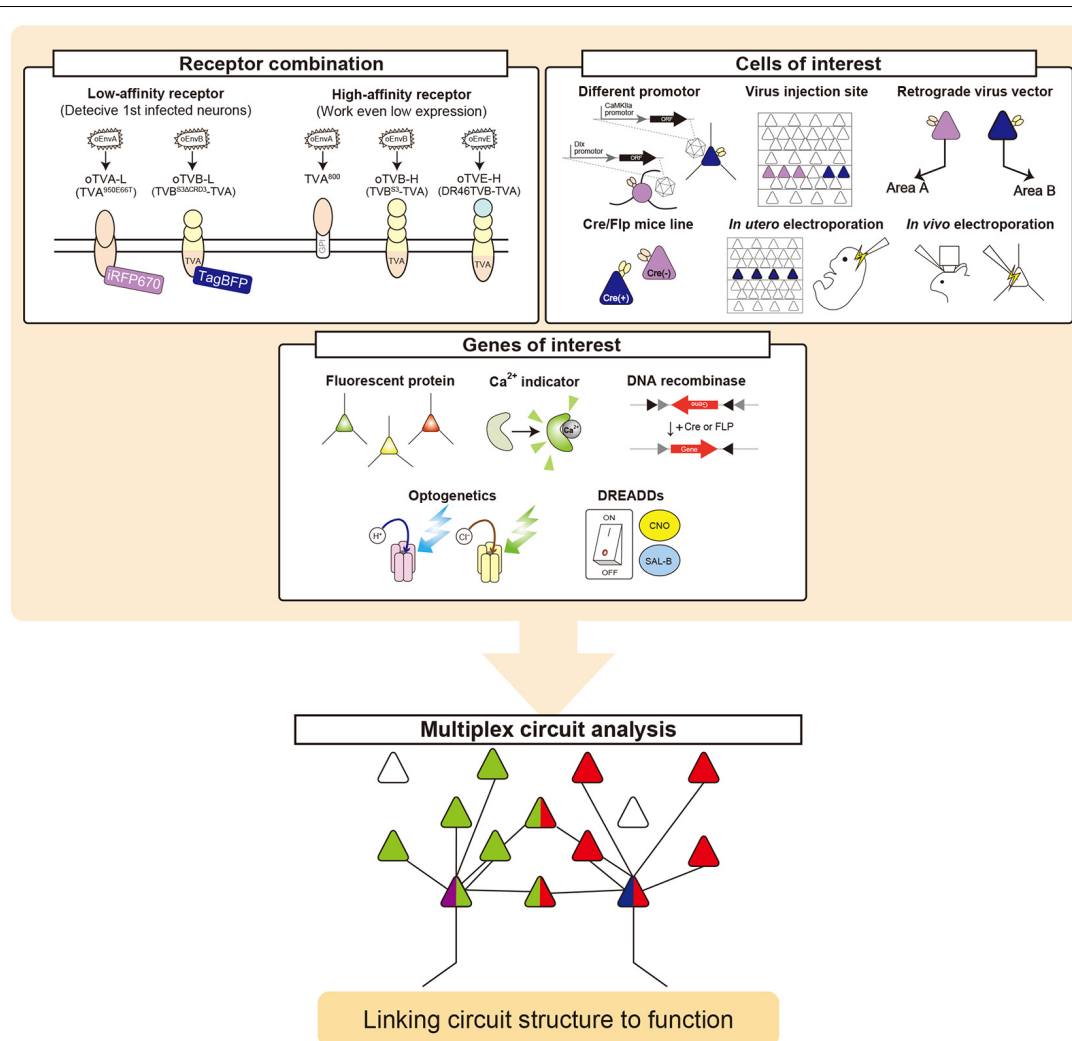


FIGURE 8 | Multiplex circuit analysis with rabies viral vectors. Simultaneous RV trans-synaptic tracing can be achieved by designing three steps. (1) Select viral envelopes and their receptors. oEnvX/oTVX systems developed in the present study can be used for rabies viral targeting. (2) Select cells of interest. Cell-type-specific promoters, connection-mediated gene transfer, electroporation, and transgenic animals are available to target particular populations. (3) Select genes of interest. Fluorescent proteins, imaging probes, optogenetic/chemogenetic tools, and recombinases can be expressed from the rabies viral vectors.

Table 1). Based on this specificity, we developed both higher-affinity and lower-affinity receptors, termed oTVB-H, oTVB-L, and oTVE-H. oTVB-H and oTVB-L are the respective higher and lower-affinity versions of TVB. oTVE-H is a receptor with higher affinity to oEnvE-RVΔG. Here, we propose to use optimal viral receptors depending on the purpose and design of experiments.





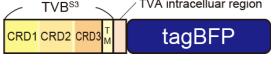
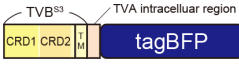
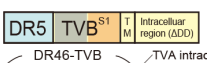
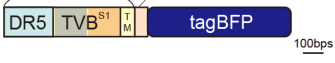
For cell-type-specific circuit tracing, using transgenic mouse lines expressing Cre, Flp, or tTA in a specific population is the most reliable and straightforward approach to define starter cells in mice. For that purpose, viral receptors with lower affinity, such as oTVA-L and oTVB-L, are recommended because leak expressions of viral receptors can be ignored. Typically, we used AAV vectors for introducing oTVA-L and oTVB-L and fluorescent reporters. In this study, we also developed high-affinity receptors, oTVB-H and oTVE-H. Higher-affinity versions are also applicable for

AAV-mediated circuit tracing along with the IRES system for introducing both receptors and fluorescent reporters as shown in **Figure 4E**. Notably, as TVA⁸⁰⁰, high-affinity type TVA (Marshall et al., 2010; Gray et al., 2011; Rancz et al., 2011; Wertz et al., 2015), was used for labeling the single cell network *in vivo*; both oTVB-H and oTVE-H are suitable for single-cell electroporation followed by single-cell-initiated RVΔG tracing.

Application of Multiplex Circuit Tracing

Using the multiplex RVΔG tracing system that we developed in this study, various questions can be addressed regarding the circuit-level mechanisms of information processing. To utilize multiplex circuit tracing, we need to consider two parameters (**Figure 8**): (1) how to introduce the viral receptors (**Table 3**); and (2) which genes to express. (1) Using

TABLE 3 | oEnvX-RVΔG receptors which are available.

Chimeric Envelope	Receptor Name	Fused Reporter	Structure	Detectivity of Starter Neurons	Sensibility	References
oEnvA	TVA ⁸⁰⁰	—		—	+++	Marshall et al. (2010)
	TVA ⁹⁵⁰	mCherry EYFP		Δ	++	Watabe-Uchida et al. (2012) and Faget et al. (2016)
	TVA ^{950E66T} (oTVA-L)	mCherry EYFP		⊙	+	Miyamichi et al. (2013) This study
oEnvB	TVB ^{S3}	—		—	+	Brojatsch et al. (1996)
	TVB ^{S3} -TVA (oTVB-H)	tagBFP		Δ	+++	This study
	TVB ^{S3ΔCRD3} -TVA (oTVB-L)	tagBFP		○	++	This study
oEnvE	DR46-TVb	—		—	++	Klucking and Young (2004)
	DR46-TVb-TVA (oTVE-H)	mCherry tagBFP		Δ (with IRES : ⊙)	+++	This study

In the detectivity of starter neurons, each symbol indicates the following: ⊙: the fluorescence reporter detects starter neurons almost perfectly at >90%. ○: the fluorescence reporter detects starter neurons at >80% and produces some pseudo-negative cells. Δ: the fluorescence reporter cannot easily detect starter neurons and produces many pseudo-negative cells.

transgenic mouse lines marking specific cell populations is the most straightforward and easiest method to introduce both viral receptors and RV-G. Tissue-specific promoters (e.g., human synapsin promoter; pan-neurons), brain-region-specific promoters (e.g., Ple67/FEV promoter; Raphe nuclei neurons, Ple155/PCP2 promoter; cerebellum Purkinje cells; de Leeuw et al., 2016), cell-type-specific promoters (e.g., CaMKIIa promoter; excitatory neurons, Dlx promoter; inhibitory neurons; Yaguchi et al., 2013; Dimidschstein et al., 2016), or activity-dependent promoters (e.g., E-SARE promoter; Kawashima et al., 2009, 2013) are also powerful when used within viral vectors. In conjunction with the transgenic Cre/Flp mouse lines or Cre/Flp-expressing viral vectors, Cre/Flp-dependent viral vectors carry the Flex or DIO/DO cassette that restricts expression by recombination (Gradinaru et al., 2010; Saunders et al., 2012; Fenno et al., 2014). tTA/rtTA-expressing transgenic mouse lines can be interfaced with AAV or HIV vectors carrying the tetO promoter. When retrograde infective vectors (e.g., AAV2retro, RV-G-pseudotyped lentivirus, Canine adenovirus type 2) are used, local area neurons can be separated by their projection area. An intersectional strategy using a combination of recombinases and activators can increase the specificity of target cells. (2) RVΔG can be used for both anatomical and physiological studies (Osakada et al., 2011; Wertz et al., 2015; Tian et al., 2016). RVΔG can accommodate a larger size of transgenes in their viral genome than can AAVs. Further, multiple genes can be expressed without using IRES or 2A elements (Osakada et al., 2011; Osakada and Callaway,

2013). Genetically-encoded sensors for calcium, voltage, and neurotransmitters are powerful to characterize connectionally-defined circuits (Chen et al., 2013; Marvin et al., 2013, 2019; Dana et al., 2016; Jing et al., 2018; Patriarchi et al., 2018; Sun et al., 2018; Abdelfattah et al., 2019; Inoue et al., 2019). Chemogenetic manipulation using rabies-mediated DREADD expressions (e.g., hm3dq, hm4di, PSAM, and KORD) can relate neuronal connectivity and activity to behavior (Armbruster et al., 2007; Alexander et al., 2009; Magnus et al., 2011; Vardy et al., 2015). Combining optogenetic tools (e.g., Channelrhodopsin2, ChRmine), the manipulation of connected populations will be feasible with implantation of optic fibers in the brain (Osakada et al., 2011; Tian et al., 2016) and even with two-photon excitation with single-cell resolution (Mardinly et al., 2018; Carrillo-Reid et al., 2019; Marshall et al., 2019).

Limitations and Future Challenges

Optical techniques have become indispensable for neuroscientific research in recent decades (Yang and Yuste, 2017). Genetically-encoded indicators of calcium, voltage, neurotransmitters, and metabolism as well as optogenetic and chemogenetic actuators allow multi-modal interrogation of neural circuit function (Luo et al., 2018). These multi-colored, genetically-encoded biosensors and actuators will fit our multiplex rabies viral tracing. However, the number of colors we can use is limited due to the limitation of genetically-encoded fluorescent proteins. Accordingly, the number of circuits we can simultaneously analyze is also currently limited.

To overcome these limitations, chemical tags could be a viable alternative to fluorescent proteins. Genetically-encoded chemical tags, such as Halo-tag, SNAP-tag, CLIP-tag, and TMP-tag, were labeled with synthetic fluorophores (Gautier et al., 2008; Los et al., 2008; Chen et al., 2012; Kohl et al., 2014). Interfacing chemical tagging with rabies tracing is also powerful for multiplexed circuit analyses because more choices of fluorescence spectrum and photochemical properties are available with chemical tags than with fluorescent proteins. Synthetic fluorophores cover the spectrum from the UV to near-IR range, expanding the possible spectrum range and the repertoire of fluorescence labels. Thus, chemical tagging will enable advances in multiplexed capacity and the applications of neural circuit tracing.

Rabies viral vectors are powerful tools for labeling synaptically-connected neurons throughout the brain. Despite the strength in anatomical studies, application of RVΔG tracing in physiological and behavioral studies remains limited because of its toxicity (Osakada et al., 2011; Wertz et al., 2015; Tian et al., 2016), although the toxicity of RVΔG viral vectors is much lower than that of other replication-competent viruses such as HSV. The viral toxicity derives from the trans-synaptic spread feature of replication-competent rabies vectors. It is notable that viral toxicity and trans-synaptic spread are in tradeoff. Several approaches have been developed to reduce the toxicity of RVΔG vectors. Large protein (L) deleted rabies viral vectors expressing Cre recombinase minimized the toxicity in transgenic mice expressing a reporter in a Cre-dependent manner (Chatterjee et al., 2018). This is because L-deleted RVΔG vectors are deficient in the replication of the RV genome. However, L-deleted RVΔG vectors do not replicate in infected neurons, thereby failing in viral spread to their presynaptic neurons due to lack of replication ability. Although trans-complementation of L and G allows replication of L-deleted RVΔG vectors and viral spread from starter cells, L-deleted RVΔG vectors will kill the L-expressing starter cells. Self-inactivating RVΔG also controlled its viral replication using PEST and TEV signals to extend the survival periods of infected neurons (Ciabatti et al., 2017). However, numerous researchers failed to reproduce the original report by Ciabatti et al. (2017), probably because rabies viruses obtain new mutations in the viral genome (Matsuyama et al., 2019). Further improvements of rabies viral vectors that have lower toxicity but maintain trans-synaptic spread ability are required for neural circuit research.

Revealing parallel processing through independent circuits and integrated processing through interaction between circuits is pivotal in understanding how the brain functions. The multiplex RV tracing that we developed in the present study will facilitate the in-depth understanding of the principles of neural circuits and computations in the brain.

DATA AVAILABILITY STATEMENT

All datasets generated for this study are included in the article/**Supplementary Material**.

ETHICS STATEMENT

The animal study was reviewed and approved by the Animal Care and Use Committee in Nagoya University.

AUTHOR CONTRIBUTIONS

TS performed experiments. TS, NM, and FO analyzed the data. TS, NM, AA, and FO wrote the manuscript. FO designed the study and supervised this study.

FUNDING

This work was supported by Grants-in-Aid from the Japan Society for the Promotion of Science (FO), Brain/MINDS from the Japan Agency for Medical Research and Development (FO), PRESTO and CREST from the Japan Science and Technology Agency (FO), the Brain Sciences Project of the Center for Novel Science Initiatives from the National Institutes of Natural Sciences (FO), the Kanae Foundation for the Promotion of Medical Science (FO), the Naito Foundation (FO), the Uehara Memorial Foundation (FO), the Takeda Science Foundation (FO), Japan Foundation of Applied Enzymology (FO), and Rikaken Foundation (TS).

ACKNOWLEDGMENTS

We thank members of the Osakada laboratory for stimulating discussions. Dr. Edward M. Callaway (Salk Institute for Biological Studies) for the HEK-TVA, HEK-TVB, BHK-EnvA, BHK-EnvB, B7GG cells. Dr. Shinji Masui (Kyoto University) for the transposon system. Dr. Yasushi Miyashita (University of Tokyo) for the EnvX and TVX systems. Dr. Yusuke Miyanari (National Institute for Basic Biology) for the iRFP670 plasmid.

SUPPLEMENTARY MATERIAL

The Supplementary Material for this article can be found online at: <https://www.frontiersin.org/articles/10.3389/fncir.2019.00077/full#supplementary-material>.

FIGURE S1 | Control injection of oEnvX-RVΔG in the absence of oTVX. No cells were infected with oEnvA-RVΔG-DsRed (**A**), oEnvB-RVΔG-DsRed (**B**), or oEnvE-RVΔG-GFP (**C**) without injection of AAV expressing corresponding receptor oTVX. These results indicate no sign of contamination by unspodotyped RVΔG in oEnvA-RVΔG-DsRed (**A**), oEnvB-RVΔG-DsRed (**B**), and oEnvE-RVΔG-GFP (**C**). Arrowheads indicate viral injection sites. Scale bar: 100 μm.

FIGURE S2 | Protein sequence alignment for TVB^{S3}, oTVB-H, and oTVB-L. Colored regions indicate functional domains: CRD1, CRD2, CRD3, and a transmembrane region. Gray boxes indicate absent or different amino acid.

FIGURE S3 | Protein sequence alignment for DR46-TVH and oTVE-H. Colored regions indicate the functional domains: death receptor 5, CRD2, CRD3, and a transmembrane region. Gray boxes indicate different or absent amino acid. Red characters indicate an essential amino acid for EnvE recognition.

FIGURE S4 | Trans-synaptic tracing using the oEnvE/oTVE system. (**A**) Monosynaptic tracing of layer 5 excitatory neurons in V1. Mixed AAVs were injected into the V1 of layer 5-specific Tlx3-Cre mice: AAV2/9-CAG-DIO-H2B-mRuby3-IRES-oTVE-H and AAV2/9-CAG-DIO-oG. After the AAV

injection, oEnvE-RVΔG-GFP were co-injected into the same location of the V1. **(B–C)** Typical images of the monosynaptically restricted tracing to the layer 5 neurons of V1. H2B-mRuby3-expressing neurons (nuclear-localized mRuby3) of the mouse V1 were specifically infected with oEnvE-RVΔG-GFP. GFP signals were enhanced by immunostaining. **(B)** Starter neurons and their presynaptic neurons in the V1. Closed arrowheads indicate

H2B-mRuby3⁺/oEnvE-RVΔG-GFP⁺ starter neurons. Scale bar: 100 μm.

(C) Presynaptic neurons in the dLGN. Scale bar: 50 μm.

TABLE S1 | Percentages of co-infected cells. Percentage of oEnvE-RVΔG-expressing cells in oTVX-expressing cells in **Figures 5C–F** were shown. Data were obtained from three mice.

REFERENCES

- Abdelfattah, A. S., Kawashima, T., Singh, A., Novak, O., Liu, H., Shuai, Y., et al. (2019). Bright and photostable chemigenetic indicators for extended *in vivo* voltage imaging. *Science* 365, 699–704. doi: 10.1126/science.aav6416
- Adkins, H. B., Blacklow, S. C., and Young, J. A. T. (2001). Two functionally distinct forms of a retroviral receptor explain the nonreciprocal receptor interference among subgroups B, D, and E avian leukosis viruses. *J. Virol.* 75, 3520–3526. doi: 10.1128/JVI.75.8.3520-3526.2001
- Adkins, H. B., Brojatsch, J., Naughton, J., Rolls, M. M., Pesola, J. M., and Young, J. A. T. (1997). Identification of a cellular receptor for subgroup E avian leukosis virus. *Proc. Natl. Acad. Sci. U S A* 94, 11617–11622. doi: 10.1073/pnas.94.21.11617
- Adkins, H. B., Brojatsch, J., and Young, J. A. T. (2000). Identification and characterization of a shared TNFR-related receptor for subgroup B, D, and E avian leukosis viruses reveal cysteine residues required specifically for subgroup E viral entry. *J. Virol.* 74, 3572–3578. doi: 10.1128/jvi.74.8.3572-3578.2000
- Alexander, G. M., Rogan, S. C., Abbas, A. I., Armbruster, B. N., Pei, Y., Allen, J. A., et al. (2009). Remote control of neuronal activity in transgenic mice expressing evolved G protein-coupled receptors. *Neuron* 63, 27–39. doi: 10.1016/j.neuron.2009.06.014
- Allocca, M., Doria, M., Petrillo, M., Colella, P., Garcia-Hoyos, M., Gibbs, D., et al. (2008). Serotype-dependent packaging of large genes in adeno-associated viral vectors results in effective gene delivery in mice. *J. Clin. Invest.* 118, 1955–1964. doi: 10.1172/JCI34316
- Antonini, A., Fagioli, M., and Stryker, M. P. (1999). Anatomical correlates of functional plasticity in mouse visual cortex. *J. Neurosci.* 19, 4388–4406. doi: 10.1523/jneurosci.19-11.04388.1999
- Arenkiel, B. R., and Ehlers, M. D. (2009). Molecular genetics and imaging technologies for circuit-based neuroanatomy. *Nature* 461, 900–907. doi: 10.1038/nature08536
- Armbruster, B. N., Li, X., Pausch, M. H., Herlitze, S., and Roth, B. L. (2007). Evolving the lock to fit the key to create a family of G protein-coupled receptors potentially activated by an inert ligand. *Proc. Natl. Acad. Sci. U S A* 104, 5163–5168. doi: 10.1073/pnas.0700293104
- Aurnhammer, C., Haase, M., Muether, N., Hausl, M., Rauschhuber, C., Huber, I., et al. (2012). Universal real-time PCR for the detection and quantification of adeno-associated virus serotype 2-derived inverted terminal repeat sequences. *Hum. Gene Ther. Methods* 23, 18–28. doi: 10.1089/hgtb.2011.034
- Barnard, R. J. O., and Young, J. A. T. (2003). Alpharetrovirus envelope-receptor interactions. *Curr. Top. Microbiol. Immunol.* 281, 107–136. doi: 10.1007/978-3-642-19012-4_3
- Barnard, R. J. O., Ellender, D., and Young, J. A. T. (2006). Avian sarcoma and leukosis virus-receptor interactions: from classical genetics to novel insights into virus-cell membrane fusion. *Virology* 344, 25–29. doi: 10.1016/j.virol.2005.09.021
- Bates, P., Young, J. A. T., and Varmus, H. E. (1993). A receptor for subgroup A Rous sarcoma virus is related to the low density lipoprotein receptor. *Cell* 74, 1043–1051. doi: 10.1016/0092-8674(93)90726-7
- Beier, K. T., Kim, C. K., Hoerbelt, P., Hung, L. W., Heifets, B. D., Deloach, K. E., et al. (2017). Rabies screen reveals GPe control of cocaine-triggered plasticity. *Nature* 549, 345–350. doi: 10.1038/nature23888
- Blasdel, G. G., and Lund, J. S. (1983). Termination of afferent axons in macaque striate cortex. *J. Neurosci.* 3, 1389–1413. doi: 10.1523/JNEUROSCI.03-07.01389.1983
- Boland, B., Yu, W. H., Corti, O., Mollereau, B., Henriques, A., Bezard, E., et al. (2018). Promoting the clearance of neurotoxic proteins in neurodegenerative disorders of ageing. *Nat. Rev. Drug Discov.* 17, 660–688. doi: 10.1038/nrd.2018.109
- Bourane, S., Duan, B., Koch, S. C., Dalet, A., Britz, O., Garcia-Campmany, L., et al. (2015). Gate control of mechanical itch by a subpopulation of spinal cord interneurons. *Science* 350, 550–554. doi: 10.1126/science.aac8653
- Bova, C. A., Olsen, J. C., and Swanson, R. (1988). The avian retrovirus env gene family: molecular analysis of host range and antigenic variants. *J. Virol.* 62, 75–83.
- Brojatsch, J., Naughton, J., Adkins, H. B., and Young, J. A. T. (2000). TVB receptors for cytopathic and noncytopathic subgroups of avian leukosis viruses are functional death receptors. *J. Virol.* 74, 11490–11494. doi: 10.1128/jvi.74.24.11490-11494.2000
- Brojatsch, J., Naughton, J., Rolls, M. M., Ziegler, K., and Young, J. A. T. (1996). CAR1, a TNFR-related protein, is a cellular receptor for cytopathic avian leukosis-sarcoma viruses and mediates apoptosis. *Cell* 87, 845–855. doi: 10.1016/s0092-8674(00)81992-3
- Brown, S. P., and Hestrin, S. (2009). Intracortical circuits of pyramidal neurons reflect their long-range axonal targets. *Nature* 457, 1133–1136. doi: 10.1038/nature07658
- Carrillo-Reid, L., Han, S., Yang, W., Akrouh, A., and Yuste, R. (2019). Controlling visually guided behavior by holographic recalling of cortical ensembles. *Cell* 178, 447.e5–457.e5. doi: 10.1016/j.cell.2019.05.045
- Chai, N., and Bates, P. (2006). Na⁺/H⁺ exchanger type 1 is a receptor for pathogenic subgroup J avian leukosis virus. *Proc. Natl. Acad. Sci. U S A* 103, 5531–5536. doi: 10.1073/pnas.0509785103
- Chatterjee, S., Sullivan, H. A., MacLennan, B. J., Xu, R., Hou, Y., Lavin, T. K., et al. (2018). Nontoxic, double-deletion-mutant rabies viral vectors for retrograde targeting of projection neurons. *Nat. Neurosci.* 21, 638–646. doi: 10.1038/s41593-018-0091-7
- Chen, T. W., Wardill, T. J., Sun, Y., Pulver, S. R., Renninger, S. L., Baohan, A., et al. (2013). Ultrasensitive fluorescent proteins for imaging neuronal activity. *Nature* 499, 295–300. doi: 10.1038/nature12354
- Chen, Z., Jing, C., Gallagher, S. S., Sheetz, M. P., and Cornish, V. W. (2012). Second-generation covalent TMP-tag for live cell imaging. *J. Am. Chem. Soc.* 134, 13692–13699. doi: 10.1021/ja303374p
- Chng, J., Wang, T., Nian, R., Lau, A., Hoi, K. M., Ho, S. C. L., et al. (2015). Cleavage efficient 2A peptides for high level monoclonal antibody expression in CHO cells. *MAbs* 7, 403–412. doi: 10.1080/19420862.2015.1008351
- Choi, J. H., Yu, N. K., Baek, G. C., Bakes, J., Seo, D., Nam, H. J., et al. (2014). Optimization of AAV expression cassettes to improve packaging capacity and transgene expression in neurons. *Mol. Brain* 7:17. doi: 10.1186/1756-6606-7-17
- Choi, J., Young, J. A. T., and Callaway, E. M. (2010). Selective viral vector transduction of ErbB4 expressing cortical interneurons *in vivo* with a viral receptor-ligand bridge protein. *Proc. Natl. Acad. Sci. U S A* 107, 16703–16708. doi: 10.1073/pnas.1006233107
- Ciabatti, E., González-Rueda, A., Mariotti, L., Morgese, F., and Tripodi, M. (2017). Life-long genetic and functional access to neural circuits using self-inactivating rabies virus. *Cell* 170, 382.e14–392.e14. doi: 10.1016/j.cell.2017.06.014
- Constantinople, C. M., and Bruno, R. M. (2013). Deep cortical layers are activated directly by thalamus. *Science* 340, 1591–1594. doi: 10.1126/science.1236425
- Dana, H., Mohar, B., Sun, Y., Narayan, S., Gordus, A., Hasseman, J. P., et al. (2016). Sensitive red protein calcium indicators for imaging neural activity. *Elife* 5:e12727. doi: 10.7554/eLife.12727
- de Leeuw, C. N., Korecki, A. J., Berry, G. E., Hickmott, J. W., Lam, S. L., Lengyel, T. C., et al. (2016). rAAV-compatible MiniPromoters for restricted expression in the brain and eye. *Mol. Brain* 9:52. doi: 10.1186/s13041-016-0232-4
- Dimidschstein, J., Chen, Q., Tremblay, R., Rogers, S. L., Saldi, G. A., Guo, L., et al. (2016). A viral strategy for targeting and manipulating interneurons across vertebrate species. *Nat. Neurosci.* 19, 1743–1749. doi: 10.1038/nn.4430
- Ding, S., Wu, X., Li, G., Han, M., Zhuang, Y., and Xu, T. (2005). Efficient transposition of the piggyBac (PB) transposon in mammalian cells and mice. *Cell* 122, 473–483. doi: 10.1016/j.cell.2005.07.013

- Dohaku, R., Yamaguchi, M., Yamamoto, N., Shimizu, T., Osakada, F., and Hibi, M. (2019). Tracing of afferent connections in the zebrafish cerebellum using recombinant rabies virus. *Front. Neural Circuits* 13:30. doi: 10.3389/fncir.2019.00030
- Dong, J. Y., Fan, P. D., and Frizzell, R. A. (1996). Quantitative analysis of the packaging capacity of recombinant adeno-associated virus. *Hum. Gene Ther.* 7, 2101–2112. doi: 10.1089/hum.1996.7.17-2101
- Eisele, Y. S., Monteiro, C., Fearn, C., Encalada, S. E., Wiseman, R. L., Powers, E. T., et al. (2015). Targeting protein aggregation for the treatment of degenerative diseases. *Nat. Rev. Drug Discov.* 14, 759–780. doi: 10.1038/nrd4593
- Elleder, D., Stepanets, V., Melder, D. C., Šenigl, F., Geryk, J., Pajer, P., et al. (2005). The receptor for the subgroup C avian sarcoma and leukosis viruses, Tvc, is related to mammalian butyrophilins, members of the immunoglobulin superfamily. *J. Virol.* 79, 10408–10419. doi: 10.1128/jvi.79.16.10408-10419.2005
- Etessami, R., Conzelmann, K. K., Fadaei-Ghotbi, B., Natelson, B., Tsiang, H., and Ceccaldi, P. E. (2000). Spread and pathogenic characteristics of a G-deficient rabies virus recombinant: an *in vitro* and *in vivo* study. *J. Gen. Virol.* 81, 2147–2153. doi: 10.1099/0022-1317-81-9-2147
- Faget, L., Osakada, F., Duan, J., Ressler, R., Johnson, A. B., Proudfoot, J. A., et al. (2016). Afferent inputs to neurotransmitter-defined cell types in the ventral tegmental area. *Cell Rep.* 15, 2796–2808. doi: 10.1016/j.celrep.2016.05.057
- Fenno, L. E., Mattis, J., Ramakrishnan, C., Hyun, M., Lee, S. Y., He, M., et al. (2014). Targeting cells with single vectors using multiple-feature Boolean logic. *Nat. Methods* 11, 763–772. doi: 10.1038/nmeth.2996
- François, A., Low, S. A., Sypek, E. I., Christensen, A. J., Sotoudeh, C., Beier, K. T., et al. (2017). A brainstem-spinal cord inhibitory circuit for mechanical pain modulation by GABA and enkephalins. *Neuron* 93, 822.e6–839.e6. doi: 10.1016/j.neuron.2017.01.008
- Gautier, A., Juillerat, A., Heinis, C., Corrêa, I. R., Kindermann, M., Beauvais, F., et al. (2008). An engineered protein tag for multiprotein labeling in living cells. *Chem. Biol.* 15, 128–136. doi: 10.1016/j.chembiol.2008.01.007
- Glickfeld, L. L., Andermann, M. L., Bonin, V., and Reid, R. C. (2013). Cortico-cortical projections in mouse visual cortex are functionally target specific. *Nat. Neurosci.* 16, 219–226. doi: 10.1038/nn.3300
- Gradinaru, V., Zhang, F., Ramakrishnan, C., Mattis, J., Prakash, R., Diester, I., et al. (2010). Molecular and cellular approaches for diversifying and extending optogenetics. *Cell* 141, 154–165. doi: 10.1016/j.cell.2010.02.037
- Gray, E. R., Illingworth, C. J. R., Coffin, J. M., and Stoye, J. P. (2011). Binding of more than one Tva800 molecule is required for ASLV-A entry. *Retrovirology* 8:96. doi: 10.1186/1742-4690-8-96
- Harris, K. D., and Mrsic-Flogel, T. D. (2013). Cortical connectivity and sensory coding. *Nature* 503, 51–58. doi: 10.1038/nature12654
- Hymowitz, S. G., Christinger, H. W., Fuh, G., Ultsch, M., O'Connell, M., Kelley, R. F., et al. (1999). Triggering cell death: the crystal structure of Apo2L/TRAIL in a complex with death receptor 5. *Mol. Cell* 4, 563–571. doi: 10.1016/s1097-2765(00)80207-5
- Inoue, M., Takeuchi, A., Manita, S., Horigane, S., Sakamoto, M., Kawakami, R., et al. (2019). Rational engineering of XCaMPs, a multicolor GECI suite for *in vivo* imaging of complex brain circuit dynamics. *Cell* 177, 1346.e24–1360.e24. doi: 10.1016/j.cell.2019.04.007
- Jing, M., Zhang, P., Wang, G., Feng, J., Mesik, L., Zeng, J., et al. (2018). A genetically encoded fluorescent acetylcholine indicator for *in vitro* and *in vivo* studies. *Nat. Biotechnol.* 36, 726–737. doi: 10.1038/nbt.4184
- Kaelberer, M. M., Buchanan, K. L., Klein, M. E., Barth, B. B., Montoya, M. M., Shen, X., et al. (2018). A gut-brain neural circuit for nutrient sensory transduction. *Science* 361:eaat5236. doi: 10.1126/science.aat5236
- Kawashima, T., Kitamura, K., Suzuki, K., Nonaka, M., Kamijo, S., Takemoto-Kimura, S., et al. (2013). Functional labeling of neurons and their projections using the synthetic activity-dependent promoter E-SARE. *Nat. Methods* 10, 889–895. doi: 10.1038/nmeth.2559
- Kawashima, T., Okuno, H., Nonaka, M., Adachi-Morishima, A., Kyo, N., Okamura, M., et al. (2009). Synaptic activity-responsive element in the Arc/Arg3.1 promoter essential for synapse-to-nucleus signaling in activated neurons. *Proc. Natl. Acad. Sci. U S A* 106, 316–321. doi: 10.1073/pnas.0806518106
- Kim, E. J., Jacobs, M. W., Ito-Cole, T., and Callaway, E. M. (2016). Improved monosynaptic neural circuit tracing using engineered rabies virus glycoproteins. *Cell Rep.* 15, 692–699. doi: 10.1016/j.celrep.2016.03.067
- Kim, E. J., Juavinett, A. L., Kyubwa, E. M., Jacobs, M. W., and Callaway, E. M. (2015). Three types of cortical layer 5 neurons that differ in brain-wide connectivity and function. *Neuron* 88, 1253–1267. doi: 10.1016/j.neuron.2015.11.002
- Kim, M.-H., Znamenskiy, P., Iacaruso, M. F., and Mrsic-Flogel, T. D. (2018). Segregated subnetworks of intracortical projection neurons in primary visual cortex. *Neuron* 100, 1313.e6–1321.e6. doi: 10.1016/j.neuron.2018.10.023
- Klucking, S., Collins, A. S., and Young, J. A. T. (2005). Avian sarcoma and leukosis virus cytopathic effect in the absence of TVB death domain signaling. *J. Virol.* 79, 8243–8248. doi: 10.1128/jvi.79.13.8243-8248.2005
- Klucking, S., and Young, J. A. T. (2004). Amino acid residues Tyr-67, Asn-72, and Asp-73 of the TVB receptor are important for subgroup e avian sarcoma and leukosis virus interaction. *Virology* 318, 371–380. doi: 10.1016/j.virol.2003.09.024
- Kohl, J., Ng, J., Cachero, S., Ciabatti, E., Dolan, M.-J., Sutcliffe, B., et al. (2014). Ultrafast tissue staining with chemical tags. *Proc. Natl. Acad. Sci. U S A* 111, E3805–E3814. doi: 10.1073/pnas.1411087111
- Liu, Y. J., Ehrenguber, M. U., Negwer, M., Shao, H. J., Cetin, A. H., and Lyon, D. C. (2013). Tracing inputs to inhibitory or excitatory neurons of mouse and cat visual cortex with a targeted rabies virus. *Curr. Biol.* 23, 1746–1755. doi: 10.1016/j.cub.2013.07.033
- Los, G. V., Encell, L. P., McDougall, M. G., Hartzell, D. D., Karassina, N., Zimprich, C., et al. (2008). HaloTag: a novel protein labeling technology for cell imaging and protein analysis. *ACS Chem. Biol.* 3, 373–382. doi: 10.1021/cb800025k
- Luo, L., Callaway, E. M., and Svoboda, K. (2018). Genetic dissection of neural circuits: a decade of progress. *Neuron* 98, 256–281. doi: 10.1016/j.neuron.2018.03.040
- Lur, G., Vinck, M. A., Tang, L., Cardin, J. A., and Higley, M. J. (2016). Projection-specific visual feature encoding by layer 5 cortical subnetworks. *Cell Rep.* 14, 2538–2545. doi: 10.1016/j.celrep.2016.02.050
- Magnus, C. J., Lee, P. H., Atasoy, D., Su, H. H., Looger, L. L., and Sternson, S. M. (2011). Chemical and genetic engineering of selective ion channel–ligand interactions. *Science* 333, 1292–1296. doi: 10.1126/science.1206606
- Mardinly, A. R., Oldenburg, I. A., Pégard, N. C., Sridharan, S., Lyall, E. H., Chesnov, K., et al. (2018). Precise multimodal optical control of neural ensemble activity. *Nat. Neurosci.* 21, 881–893. doi: 10.1038/s41593-018-0139-8
- Marshall, J. H., Kim, Y. S., Machado, T. A., Quirin, S., Benson, B., Kadmon, J., et al. (2019). Cortical layer-specific critical dynamics triggering perception. *Science* 520:eaaw5202. doi: 10.1126/science.aaw5202
- Marshall, J. H., Mori, T., Nielsen, K. J., and Callaway, E. M. (2010). Targeting single neuronal networks for gene expression and cell labeling *in vivo*. *Neuron* 67, 562–574. doi: 10.1016/j.neuron.2010.08.001
- Maruoka, H., Nakagawa, N., Tsuruno, S., Sakai, S., Yoneda, T., and Hosoya, T. (2017). Lattice system of functionally distinct cell types in the neocortex. *Science* 358, 610–615. doi: 10.1126/science.aam6125
- Marvin, J. S., Borghuis, B. G., Tian, L., Cichon, J., Harnett, M. T., Akerboom, J., et al. (2013). An optimized fluorescent probe for visualizing glutamate neurotransmission. *Nat. Methods* 10, 162–170. doi: 10.1038/nmeth.2333
- Marvin, J. S., Shimoda, Y., Magloire, V., Leite, M., Kawashima, T., Jensen, T. P., et al. (2019). A genetically encoded fluorescent sensor for *in vivo* imaging of GABA. *Nat. Methods* 16, 763–770. doi: 10.1038/s41592-019-0471-2
- Matsuyama, M., Jin, L., Lavin, T. K., Sullivan, H. A., Hou, Y., Lea, N. E., et al. (2019). “Self-inactivating” rabies viruses are just first-generation, ΔG rabies viruses. *bioRxiv* [Preprint] 550640. doi: 10.1101/550640
- Matsuyama, M., Ohashi, Y., Tsubota, T., Yaguchi, M., Kato, S., Kobayashi, K., et al. (2015). Avian sarcoma leukosis virus receptor-envelope system for simultaneous dissection of multiple neural circuits in mammalian brain. *Proc. Natl. Acad. Sci. U S A* 112, E2947–E2956. doi: 10.1073/pnas.1423963112
- Mebatsion, T., Konig, M., and Conzelmann, K. K. (1996). Budding of rabies virus particles in the absence of the spike glycoprotein. *Cell* 84, 941–951. doi: 10.1016/s0092-8674(00)81072-7
- Miyamichi, K., Shlomai-Fuchs, Y., Shu, M., Weissbourd, B. C., Luo, L., and Mizrahi, A. (2013). Dissecting local circuits: parvalbumin interneurons underlie broad feedback control of olfactory bulb output. *Neuron* 80, 1232–1245. doi: 10.1016/j.neuron.2013.08.027

- Mizuguchi, H., Xu, Z., Ishii-Watabe, A., Uchida, E., and Hayakawa, T. (2000). IRES-dependent second gene expression is significantly lower than cap-dependent first gene expression in a bicistronic vector. *Mol. Ther.* 1, 376–382. doi: 10.1006/mthe.2000.0050
- Nassi, J. J., and Callaway, E. M. (2009). Parallel processing strategies of the primate visual system. *Nat. Rev. Neurosci.* 10, 360–372. doi: 10.1038/nrn2619
- Osakada, F., and Callaway, E. M. (2013). Design and generation of recombinant rabies virus vectors. *Nat. Protoc.* 8, 1583–1601. doi: 10.1038/nprot.2013.094
- Osakada, F., Ikeda, H., Mandai, M., Wataya, T., Watanabe, K., Yoshimura, N., et al. (2008). Toward the generation of rod and cone photoreceptors from mouse, monkey and human embryonic stem cells. *Nat. Biotechnol.* 26, 215–224. doi: 10.1038/nbt1384
- Osakada, F., Mori, T., Cetin, A. H., Marshel, J. H., Virgen, B., and Callaway, E. M. (2011). New rabies virus variants for monitoring and manipulating activity and gene expression in defined neural circuits. *Neuron* 71, 617–631. doi: 10.1016/j.neuron.2011.07.005
- Patriarchi, T., Cho, J. R., Merten, K., Howe, M. W., Marley, A., Xiong, W. H., et al. (2018). Ultrafast neuronal imaging of dopamine dynamics with designed genetically encoded sensors. *Science* 360:eaat4422. doi: 10.1126/science.aat4422
- Paxinos, G., and Franklin, K. J. (2008). *The Mouse Brain in Stereotaxic Coordinates*, 3rd edn. (Cambridge, MA: Academic Press).
- Rancz, E. A., Franks, K. M., Schwarz, M. K., Pichler, B., Schaefer, A. T., and Margrie, T. W. (2011). Transfection *via* whole-cell recording *in vivo*: bridging single-cell physiology, genetics and connectomics. *Nat. Neurosci.* 14, 527–532. doi: 10.1038/nn.2765
- Reinisová, M., Senigl, F., Yin, X., Plachy, J., Geryk, J., Elleder, D., et al. (2008). A single-amino-acid substitution in the TvbS1 receptor results in decreased susceptibility to infection by avian sarcoma and leukosis virus subgroups B and D and resistance to infection by subgroup E *in vitro* and *in vivo*. *J. Virol.* 82, 2097–2105. doi: 10.1128/jvi.02206-07
- Rong, L., Gendron, K., Strohl, B., Shenoy, R., Wool-Lewis, R. J., and Bates, P. (1998). Characterization of determinants for envelope binding and infection in tva, the subgroup A avian sarcoma and leukosis virus receptor. *J. Virol.* 72, 4552–4559.
- Saunders, A., Johnson, C. A., and Sabatini, B. L. (2012). Novel recombinant adeno-associated viruses for Cre activated and inactivated transgene expression in neurons. *Front. Neural Circuits* 6:47. doi: 10.3389/fncir.2012.00047
- Shcherbakova, D. M., Stepanenko, O. V., Turoverov, K. K., and Verkhusha, V. V. (2018). Near-infrared fluorescent proteins: multiplexing and optogenetics across scales. *Trends Biotechnol.* 36, 1230–1243. doi: 10.1016/j.tibtech.2018.06.011
- Shcherbakova, D. M., and Verkhusha, V. V. (2013). Near-infrared fluorescent proteins for multicolor *in vivo* imaging. *Nat. Methods* 10, 751–754. doi: 10.1038/nmeth.2521
- Smith, E. J., Brojatsch, J., Naughton, J., and Young, J. A. T. (1998). The CAR1 gene encoding a cellular receptor specific for subgroup B and D avian leukosis viruses maps to the chicken tvb locus. *J. Virol.* 72, 3501–3503.
- Sun, S., Xu, Q., Guo, C., Guan, Y., Liu, Q., and Dong, X. (2017). Leaky gate model: intensity-dependent coding of pain and itch in the spinal cord. *Neuron* 93, 840.e5–853.e5. doi: 10.1016/j.neuron.2017.01.012
- Sun, F., Zeng, J., Jing, M., Zhou, J., Feng, J., Owen, S. F., et al. (2018). A genetically encoded fluorescent sensor enables rapid and specific detection of dopamine in flies, fish, and mice. *Cell* 174, 481.e19–496.e19. doi: 10.1016/j.cell.2018.06.042
- Szymczak, A. L., Workman, C. J., Wang, Y., Vignali, K. M., Dilioglou, S., Vanin, E. F., et al. (2004). Correction of multi-gene deficiency *in vivo* using a single ‘self-cleaving’ 2A peptide-based retroviral vector. *Nat. Biotechnol.* 22, 589–594. doi: 10.1038/nbt0604-760b
- Tasic, B., Menon, V., Nguyen, T. N., Kim, T. K., Jarsky, T., Yao, Z., et al. (2016). Adult mouse cortical cell taxonomy revealed by single cell transcriptomics. *Nat. Neurosci.* 19, 335–346. doi: 10.1038/nn.4216
- Tasic, B., Yao, Z., Graybiel, L. T., Smith, K. A., Nguyen, T. N., Bertagnolli, D., et al. (2018). Shared and distinct transcriptomic cell types across neocortical areas. *Nature* 563, 72–78. doi: 10.1038/s41586-018-0654-5
- Tervo, D. G. R., Hwang, B. Y., Viswanathan, S., Gaj, T., Lavzin, M., Ritola, K. D., et al. (2016). A designer AAV variant permits efficient retrograde access to projection neurons. *Neuron* 92, 372–382. doi: 10.1016/j.neuron.2016.09.021
- Tian, J., Huang, R., Cohen, J. Y., Osakada, F., Kobak, D., Machens, C. K., et al. (2016). Distributed and mixed information in monosynaptic inputs to dopamine neurons. *Neuron* 91, 1374–1389. doi: 10.1016/j.neuron.2016.08.018
- Ugolini, G. (1995). Specificity of rabies virus as a transneuronal tracer of motor networks: transfer from hypoglossal motoneurons to connected second-order and higher order central nervous system cell groups. *J. Comp. Neurol.* 356, 457–480. doi: 10.1002/cne.903560312
- Ugolini, G. (2010). Advances in viral transneuronal tracing. *J. Neurosci. Methods* 194, 2–20. doi: 10.1016/j.jneumeth.2009.12.001
- Vardy, E., Robinson, J. E., Li, C., Olsen, R. H. J., DiBerto, J. F., Giguere, P. M., et al. (2015). A new DREADD facilitates the multiplexed chemogenetic interrogation of behavior. *Neuron* 86, 936–946. doi: 10.1016/j.neuron.2015.03.065
- Vaziri, S., and Connor, C. E. (2016). Representation of gravity-aligned scene structure in ventral pathway visual cortex. *Curr. Biol.* 26, 766–774. doi: 10.1016/j.cub.2016.01.022
- Wall, N. R., De La Parra, M., Sorokin, J. M., Taniguchi, H., Huang, Z. J., and Callaway, E. M. (2016). Brain-wide maps of synaptic input to cortical interneurons. *J. Neurosci.* 36, 4000–4009. doi: 10.1523/JNEUROSCI.3967-15.2016
- Wall, N. R., Wickersham, I. R., Cetin, A., De La Parra, M., and Callaway, E. M. (2010). Monosynaptic circuit tracing *in vivo* through Cre-dependent targeting and complementation of modified rabies virus. *Proc. Natl. Acad. Sci. U S A* 107, 21848–21853. doi: 10.1073/pnas.1011756107
- Watabe-Uchida, M., Zhu, L., Ogawa, S. K., Vamanrao, A., and Uchida, N. (2012). Whole-brain mapping of direct inputs to midbrain dopamine neurons. *Neuron* 74, 858–873. doi: 10.1016/j.neuron.2012.03.017
- Wertz, A., Trenholm, S., Yonehara, K., Hillier, D., Raics, Z., Leinweber, M., et al. (2015). Single-cell-initiated monosynaptic tracing reveals layer-specific cortical network modules. *Science* 349, 70–74. doi: 10.1126/science.aab1687
- Wickersham, I. R., Lyon, D. C., Barnard, R. J. O., Mori, T., Finke, S., Conzelmann, K. K., et al. (2007). Monosynaptic restriction of transsynaptic tracing from single, genetically targeted neurons. *Neuron* 53, 639–647. doi: 10.1016/j.neuron.2007.01.033
- Xiao, X., Li, J., and Samulski, R. J. (1998). Production of high-titer recombinant adeno-associated virus vectors in the absence of helper adenovirus. *J. Virol.* 72, 2224–2232.
- Yaguchi, M., Ohashi, Y., Tsubota, T., Sato, A., Koyano, K. W., Wang, N., et al. (2013). Characterization of the properties of seven promoters in the motor cortex of rats and monkeys after lentiviral vector-mediated gene transfer. *Hum. Gene Ther. Methods* 24, 333–344. doi: 10.1089/hgtb.2012.238
- Yamashita, T., Pala, A., Pedrido, L., Kremer, Y., Welker, E., and Petersen, C. C. H. (2013). Membrane potential dynamics of neocortical projection neurons driving target-specific signals. *Neuron* 80, 1477–1490. doi: 10.1016/j.neuron.2013.10.059
- Yang, W., and Yuste, R. (2017). *in vivo* imaging of neural activity. *Nat. Methods* 14, 349–359. doi: 10.1038/nmeth.4230
- Young, J. A. T., Bates, P., and Varmus, H. E. (1993). Isolation of a chicken gene that confers susceptibility to infection by subgroup A avian leukosis and sarcoma viruses. *J. Virol.* 67, 1811–1816.
- Zampieri, N., Jessell, T. M., and Murray, A. J. (2014). Mapping sensory circuits by anterograde transsynaptic transfer of recombinant rabies virus. *Neuron* 81, 766–778. doi: 10.1016/j.neuron.2013.12.033
- Zhu, Y., Xu, J., Hauswirth, W. W., and DeVries, S. H. (2014). Genetically targeted binary labeling of retinal neurons. *J. Neurosci.* 34, 7845–7861. doi: 10.1523/JNEUROSCI.2960-13.2014

Conflict of Interest: The authors declare that the research was conducted in the absence of any commercial or financial relationships that could be construed as a potential conflict of interest.

Copyright © 2020 Suzuki, Morimoto, Akaike and Osakada. This is an open-access article distributed under the terms of the Creative Commons Attribution License (CC BY). The use, distribution or reproduction in other forums is permitted, provided the original author(s) and the copyright owner(s) are credited and that the original publication in this journal is cited, in accordance with accepted academic practice. No use, distribution or reproduction is permitted which does not comply with these terms.



Structural Neural Connectivity Analysis in Zebrafish With Restricted Anterograde Transneuronal Viral Labeling and Quantitative Brain Mapping

Manxiu Ma^{1,2†}, Stanislav Kler^{1,2†} and Y. Albert Pan^{1,2,3,4*}

¹ Center for Neurobiology Research, Fralin Biomedical Research Institute at VTC, Virginia Tech, Roanoke, VA, United States,

² Department of Neuroscience and Regenerative Medicine, Medical College of Georgia, Augusta University, Augusta, GA, United States, ³ Department of Biomedical Sciences and Pathobiology, Virginia-Maryland College of Veterinary Medicine,

Virginia Tech, Blacksburg, VA, United States, ⁴ Department of Psychiatry and Behavioral Medicine, Virginia Tech Carilion School of Medicine, Roanoke, VA, United States

OPEN ACCESS

Edited by:

Qian-Quan Sun,
University of Wyoming, United States

Reviewed by:

Wolfgang Driever,
University of Freiburg, Germany
Kara Geo Pratt,
University of Wyoming, United States
Masahiko Hibi,
Nagoya University, Japan

*Correspondence:

Y. Albert Pan
yapan@vtc.vt.edu

[†]These authors have contributed
equally to this work

Received: 09 September 2019

Accepted: 30 December 2019

Published: 23 January 2020

Citation:

Ma M, Kler S and Pan YA (2020)
Structural Neural Connectivity Analysis
in Zebrafish With Restricted
Anterograde Transneuronal Viral
Labeling and Quantitative Brain
Mapping. *Front. Neural Circuits* 13:85.
doi: 10.3389/fncir.2019.00085

The unique combination of small size, translucency, and powerful genetic tools makes larval zebrafish a uniquely useful vertebrate system to investigate normal and pathological brain structure and function. While functional connectivity can now be assessed by optical imaging (via fluorescent calcium or voltage reporters) at the whole-brain scale, it remains challenging to systematically determine structural connections and identify connectivity changes during development or disease. To address this, we developed Tracer with Restricted Anterograde Spread (TRAS), a novel vesicular stomatitis virus (VSV)-based neural circuit labeling approach. TRAS makes use of replication-incompetent VSV (VSVΔG) and a helper virus (lentivirus) to enable anterograde transneuronal spread between efferent axons and their direct postsynaptic targets but restricts further spread to downstream areas. We integrated TRAS with the Z-Brain zebrafish 3D atlas for quantitative connectivity analysis and identified targets of the retinal and habenular efferent projections, in patterns consistent with previous reports. We compared retinofugal connectivity patterns between wild-type and *down syndrome cell adhesion molecule-like 1 (dscaml1)* mutant zebrafish and revealed differences in topographical distribution. These results demonstrate the utility of TRAS for quantitative structural connectivity analysis that would be valuable for detecting novel efferent targets and mapping connectivity changes underlying neurological or behavioral deficits.

Keywords: transsynaptic, zebrafish, VSV, brain mapping, viral tracing

INTRODUCTION

The function of the brain is closely linked to its structure, i.e., how its billions of constituent cells are wired and connected by trillions of synapses. Understanding how these connections are formed and maintained is key to gaining mechanistic insight toward brain function and identifying the causes and treatments for neuropsychiatric disorders (Belmonte et al., 2004; Lynall et al., 2010; Fornito et al., 2015). Techniques for mapping the structure and function of the brain have progressed

rapidly in past decades, from anatomical structural analysis to functional computation, and from human participants to animal models (Kasthuri et al., 2015; Glasser et al., 2016). However, the large number of neurons and vast spatial scale of neuronal structures (from meters to nanometers) of the mammalian brain makes mapping neuronal networks at the cellular level and correlating them with development and disease a daunting task (Swanson and Lichtman, 2016).

Zebrafish (*Danio rerio*), a small tropical fish, has emerged as an accessible model for studying behavior, neuronal networks, and cellular connectivity (Orger and de Polavieja, 2017). Zebrafish has analogous neuroanatomy and neurochemistry to mammals and can perform complex sensory, motor, and cognitive functions during larval stages (5–10 days post fertilization, dpf). Importantly, at this stage, there are only roughly 100,000 neurons in the brain, 80% of which can be imaged and physiologically recorded in live, behaving animals (Ahrens et al., 2013; Chen et al., 2018; Abdelfattah et al., 2019). As a result, zebrafish whole-brain functional imaging studies have been able to generate cellular resolution neuronal activity maps under different behavioral contexts and linking activity maps to pathological states associated with autism spectrum disorder, schizophrenia, and epilepsy (Sakai et al., 2018; Thyme et al., 2019). The ability to fully interpret patterns of functional connectivity and determine causality for disorders, however, is limited by the lack of detailed structural information on neuronal wiring in zebrafish, which still lags behind other commonly used model organisms like mice, *Drosophila*, and *C. elegans*. Efforts are ongoing to map the full complement of neuronal connections (i.e., connectome) with electron microscopy in the larval and adult zebrafish, but the time and labor-intensive nature of synapse-level reconstruction has thus far restricted investigations to connections within smaller brain regions (Wanner et al., 2016; Hildebrand et al., 2017; Vishwanathan et al., 2017; Svava et al., 2018).

To address this, we sought to develop a virus and light imaging-based structural mapping technique that would allow for quantitative brain-wide mapping of neuronal connectivity in larval zebrafish. Previously, we found that recombinant vesicular stomatitis virus (VSV) can function as an anterograde transsynaptic tracer in a wide range of organisms (Mundell et al., 2015). VSV is a negative-strand RNA virus in the *Rhabdoviridae* family, which also includes the rabies virus (RABV). In contrast to RABV, which spreads retrogradely (from dendrite to presynaptic afferent axons), VSV spreads anterogradely (from efferent axons to their postsynaptic targets) when enveloped by its endogenous glycoprotein (VSV-G) (Beier et al., 2011b; Mundell et al., 2015). VSV injection into the retina of mice, chicken, and larval zebrafish led to highly efficient labeling of the optic nerve and targets of the visual pathway, including both direct retinorecipient connections and third-order neurons in areas further downstream.

These findings open the door for utilizing VSV for zebrafish structural circuit mapping. Substantial limitations, however, still remain. First, the spread of VSV is unrestricted, making it difficult to disambiguate direct (monosynaptic) and indirect (polysynaptic) connections. Second, replication-competent VSV and VSV-G expression are cytotoxic and lead to rapid

deterioration of health in larval zebrafish (Hoffmann et al., 2010; Mundell et al., 2015). Finally, there is no established method for quantifying and annotating viral labeling in zebrafish, which is necessary to correlate anatomical tracing with functional imaging.

In this study, we developed a novel approach utilizing replication-incompetent VSV (VSV Δ G) to achieve restricted anterograde transneuronal spread in zebrafish. We also developed an imaging and processing pipeline to register 3D image stacks to the widely used and extensively annotated Z-Brain digital atlas (Randlett et al., 2015). This method, termed TRAS (Tracer with Restricted Anterograde Spread), allows for a quantitative description of efferent connectivity based on neurotransmitter types and specific locations. We applied TRAS to investigate the axon projection patterns of retinorecipient cells and identified potential connectivity changes in zebrafish carrying a mutation in *down syndrome cell adhesion molecule-like 1* (*dscaml1*), a causal gene for autism spectrum disorder and human cortical abnormalities (Fuerst et al., 2009; Iossifov et al., 2014; Karaca et al., 2015; Galicia et al., 2018; Ma et al., 2020).

MATERIALS AND METHODS

Zebrafish Husbandry

Zebrafish (all ages) were raised under a 14/10 light/dark cycle at 28.5°C. Embryos and larvae were raised in water containing 0.1% Methylene Blue hydrate (Sigma-Aldrich). With the exception of *nacre* mutants, embryos were transferred to E3 buffer containing 0.003% 1-phenyl-2-thiourea (PTU; Sigma-Aldrich) to prevent pigment formation at 24 h post-fertilization. Developmental stages are as described by Kimmel et al. (1995). Sex was not considered as a relevant variable for this study, as laboratory zebrafish remain sexually undifferentiated until 2 weeks of age, beyond the stages being used (0–9 dpf) (Maack and Segner, 2003; Wilson et al., 2014). All experimental procedures are performed in accordance with Institutional Animal Care and Use Committee guidelines at Augusta University and Virginia Tech.

Transgenic and Mutant Zebrafish Lines

The *dscaml1*^{vt1} mutant line was generated by TALEN-targeted mutagenesis, which resulted in a seven base pair deletion and subsequent early translational termination (Ma et al., 2020). The *Tg(elavl3:H2B-GCaMP6f)* line was generously provided by E. Aksay at Weill Cornell Medicine, with permission from M. Ahrens at HHMI Janelia Research Campus (Kawashima et al., 2016). The *vglut2a:GFP* line [*Tg(slc17a6b:EGFP)*] was generously provided by J. Fetcho at Cornell University with permission from S. Higashijima at the National Institute for Basic Biology (Bae et al., 2009).

Preparation of VSV Δ G

VSV was prepared using methods detailed by Beier et al. (2016). 293T cells (ATCC, #CRL-3216) were transfected at 80% confluency on 75 cm² flasks with 7 μ g of *pCI-VSVG* plasmid (Addgene, #1733) and incubated overnight at 37°C. Afterward, cells were infected with VSV Δ G-RFP (VSV Δ G for short) (Beier et al., 2011b) at a multiplicity of infection (m.o.i.) of 0.1.

Viral supernatants were collected for the subsequent 3 days at 24-h intervals and combined. Cell debris was precipitated by centrifugation at 1,000 g for 20 min. To concentrate VSVΔG, viral supernatant was ultracentrifuged for 3 h at 80,000 g with an SW32Ti rotor, and the pellet was resuspended in 100 μl of culture medium. Viral stocks were titered by serial dilution on 90% confluent 293T cells. The number of fluorescent foci was calculated at 2 days post infection (dpi) by identifying RFP-positive cells. Typical viral titer was higher than 1×10^9 focus forming units/ml (ffu/ml).

For *in vitro* trans-complementation of VSVΔG with lentivirus, BHK-21 cells (ATCC, #CCL-10) were seeded into 96-well plates and incubated overnight to reach 20,000 cells per well. Cells were co-infected with VSVΔG (m.o.i. = 0.005) and VSV-G pseudotyped lentivirus (m.o.i. = 0–10,000) (lentivirus-SIN-CMV-eGFP or lentivirus-SIN-Ubi-iCre-mCherry; GT3 Core Facility of the Salk Institute). The typical viral titer for lentivirus stock was 10^{11} – 10^{12} ffu/ml. At 2 h post-infection, cells were washed twice with PBS and incubated with fresh medium supplemented with 2% serum. At 2 dpi, the spread of VSV was visualized by fluorescent microscopy. The media in each well were collected and titered to evaluate viral yield.

Virus Injection

Viral injections were performed as previously described (Mundell et al., 2015; Beier et al., 2016). Briefly, glass capillaries (TW100F-4; World Precision Instruments) were pulled into injection needles with a pipette puller (P-97; Sutter Instruments). The tips of injection needles were trimmed to create a ~ 10 μm opening. Virus injection solution was made by diluting VSVΔG and lentivirus stock with tissue culture medium (DMEM; Fisher Scientific), with Fast Green dye (BP123-10; Fisher Scientific) as the injection marker. Two microliter of injection solution was loaded into the injection needle with a Microloader pipette tip (930001007; Eppendorf), and mounted into a microelectrode holder connected to a pneumatic PicoPump (PV820; World Precision Instruments). Injection volume was determined by calibrating the volume of the injected droplet on a stage micrometer (50-753-2911; Fisher Scientific). The hold pressure of the PicoPump was adjusted so that there was a slight outflow of virus solution when the needle tip was immersed in media.

For retina injection, 2.5 or 3 dpf larvae were anesthetized in Tricaine (0.013% w/v, AC118000500; Fisher Scientific) mounted laterally inside the center chamber of a glass-bottom dish (P50G-1.5-14-F; MatTek) with 1.5% low melting-point agarose (BP1360; Fisher Scientific). After the agarose has solidified, the dish is filled with Tricaine solution (0.013%) to maintain anesthesia. Under a stereo dissecting microscope (SMZ18; Nikon), the needle tip was moved with a micromanipulator (MN-151; Narishige) to approach the fish from the rear and penetrated the temporal retina, with the needle tip being in the neural retina. 0.25–0.5 nl of virus solution (concentrations as described in the Results section) were injected inside the retina. After injection, larvae were recovered from the agarose and returned to a 28°C incubator.

For TRAS labeling, we adjusted viral titer with the aim of achieving cellular labeling in areas innervated by the optic nerve and not in areas two synapses away (e.g., ipsilateral

midbrain, hindbrain, cerebellum, habenula, telencephalon). VSVΔG injected without lentivirus at 10^6 – 10^9 ffu/ml resulted in robust retinal infection at the injection site. When lentivirus (2×10^9 – 10^{11} ffu/ml) was injected along with VSVΔG (10^6 – 10^8), transneuronal spread was observed. For quantitative analysis of retinorecipient cells, we used VSVΔG at 3×10^7 ffu/ml and lentivirus at 3×10^{10} ffu/ml. At these concentrations, we did not see any evidence for multisynaptic spread. It is worth noting that we did find sparse labeling of putative third-order neurons in one experiment that had extensive infection (potentially due to aliquot-specific variations in viral titer) with VSVΔG at 3×10^7 ffu/ml and lentivirus at 3×10^{10} – 10^{11} (1–2 cells in 50% of injected fish, $n = 10$, **Supplementary Figure S1**). We only analyzed the experiments that had no third-order neuron labeling in this study.

For habenula injection, 3 dpf larvae were mounted with the dorsal side up. The agarose and skin above the left habenula were carefully removed with a sharpened tungsten needle (10130-05; Fine Science Tools). The injection needle tip was inserted into the left habenula and remained there for 5 s, allowing the slow outflow of virus solution (VSVΔG at 3×10^8 ffu/ml, lentivirus at 1×10^{11} ffu/ml) to immerse the surrounding tissue. At 1 dpi, larvae with habenula-specific RFP expression were screened and later fixed at 3 dpi for immunohistochemistry and confocal imaging.

Immunohistochemistry

Whole-mount immunohistochemistry was performed as described by Randlett et al. (2015). Zebrafish larvae were fixed overnight with 4% PFA and 0.25% Triton X-100 (Fisher Scientific) in 1X PBS (diluted from 10%PFA; Polysciences), then washed with 1X PBS and 0.25% Triton X-100. H2B-GCaM6f was stained with FluoTag-X4 anti-GFP (N0304-At488; NanoTag); GABA was stained with Rabbit anti-GABA (A2052; Sigma-Aldrich); ERK1/2 was stained with mouse anti-ERK1/2 (4696S; Cell Signaling Technology). The sRIMS solution, which is D-Sorbitol (Sigma-Aldrich) dissolved in PBS with 0.1% Tween-20 (Fisher Scientific) and 0.01% Sodium Azide, was used for optical clearing (Yang et al., 2014). Samples are immersed for 15 min (or until sunken to the bottom of the Eppendorf tube) through a gradient series (8.75–70%) of D-Sorbitol.

Image Acquisition

Epifluorescence images of cultured cells were acquired under a Nikon Eclipse Ts2 inverted fluorescent microscope. Images of zebrafish were acquired using a Nikon A1 laser scanning confocal system with a CFI75 Apochromat LWD 25x water-immersion objective. For TRAS quantification, image stacks were acquired at a standard resolution of $0.49 \times 0.49 \times 2.0$ μm³ per voxel. For efferent tract-tracing, a standard resolution stack and a high-resolution stack ($0.38 \times 0.38 \times 0.5$ μm³ per voxel) were acquired for each fish.

Efferent Tract Tracing

Standard resolution image stacks were morphed to the Z-Brain *elavl3:H2B-RFP* template using CMTK (Randlett et al., 2015). High-resolution stacks were then morphed to its

corresponding low-resolution stacks to register to Z-Brain coordinates. Morphed high-resolution stacks were imported into the neuTube software for tracing, in accordance with the neuTube online manual (<https://www.neutracing.com/manual/>) (Feng et al., 2015). The SWC files were saved and imported into Fiji plugin “Simple Neurite Tracer” then saved as an overlay.

TRAS Quantitation With Z-Brain

Image stacks from 24 wild-type and 26 *dscaml1*^{-/-} larvae were morphed to the Z-Brain *elavl3:H2B-RFP* template using CMTK, using the GCaMP6f channel as reference (Randlett et al., 2015). For retinal ganglion cell arborization field (AF) fluorescent intensity analysis, the *ZBrainAnalysisOfMAPmaps.m* MATLAB script from Z-Brain was used to process each morphed stack individually (VSVΔG channel, no smoothing). From the output files, the total signal intensities from all Z-Brain annotated AFs (AF1-AF9 and the tectum neuropil) from each stack were then compiled and analyzed in the Prism statistical software (GraphPad).

For retinorecipient cell number and distribution analysis, the Fiji software’s ROI manager (Analyze > Tools > ROI manager; extra-large size dot) was used on the morphed VSVΔG channel to mark all VSVΔG+ cells. The marked positions (ROIs) were saved into a zip file and overlaid onto the GCaMP6f channel. The ROIs that were GCaMP6f-negative were removed so that the remaining ROIs represented TRAS-labeled neurons (neuronal ROIs). Next, the neuronal ROIs were overlaid onto the GABA channel to create two subsets: the GABA+ ROIs (inhibitory neurons) and GABA- ROIs (excitatory neurons, created by subtracting the neuronal ROI with the GABA+ ROIs). Lastly, these two ROIs were overlaid onto a Z-brain reference-sized (X:Y:Z = 1,121 × 496 × 276 μm³ at 0.8 × 0.8 × 2 μm³ per voxel) blank stack, with inhibitory neuron ROIs pseudo-colored magenta and excitatory neuron ROIs pseudo-colored green. Then, we created .tif files with the overlaid ROIs.

To quantitate the anatomical distribution of retinorecipient cells, we used a modified Z-Brain workflow. Instead of using the *MakeTheMAPmap.m* MATLAB script, we used a custom Fiji macro script to create the output image file, which were then processed using a modified *ZBrainAnalysisOfMAPmaps.m* MATLAB script that quantifies sum pixel intensity values for neuronal ROIs within each region mask. The output intensity values were converted to cell counts, based on an estimate of the pixel values generated from a single-cell ROI (~18,265). For heatmap display and cohort-wise comparison of individual regions, the intensity signals for each fish were normalized by the sum signal from “Diencephalon” and “Mesencephalon.” The numbers were then imported into MATLAB to make a scaled color map using the *imagesc* function.

Analysis of Topographical Distribution

To analyze the topographical distribution of wild-type and *dscaml1*^{-/-} retinorecipient cells (Figure 5), the ROI files from all fish within a cohort were combined into a single zip file and overlaid into a Z-Brain compatible blank stack, as described previously for single fish ROI image files. The x-y-z coordinates of each ROI dot were used in the *scatter3* function in MATLAB

to create 3-D scatter plots. The same coordinates were imported into GraphPad for analysis of distribution properties. The cumulative frequency statistics were done using the K-S test provided within the Prism software (GraphPad).

RESULTS

Trans-complementation of VSVΔG by VSV-G Coated Lentivirus

For both VSV and RABV, the envelope glycoprotein (G) gene is essential for binding, internalization, membrane fusion, and release of the viral genome into the host cell (Albertini et al., 2012; Kim et al., 2017). A recombinant virus with genomic deletion of the G gene (ΔG) can infect and replicate inside the cell but is unable to spread, unless the host cell complements the virus by providing G *in trans* (Wickersham et al., 2007; Beier et al., 2011b). Trans-complementation can, therefore, be utilized to restrict viral spread to direct synaptic partners. For instance, expressing the RABV glycoprotein (RABV-G) in neurons at the injection site (starter cells) allowed VSVΔG or RABVΔG to spread from the starter cells to their input neurons. Once inside the input neurons, the virus can no longer spread (Wickersham et al., 2007; Beier et al., 2013).

Given VSV’s ability to spread anterogradely across synapses, we asked whether trans-complementing VSVΔG virus with VSV glycoprotein (VSV-G) could enable restricted anterograde spread (Mundell et al., 2015). Our efforts to express VSV-G *in vivo* through transgenesis were unsuccessful, possibly due to the pathogenic effects of VSV-G when persistently expressed (Yee et al., 1994). As an alternative, we tested whether VSV-G protein could be transduced to cells directly. We took advantage of the fact that most commercially available lentiviruses are coated with VSV-G and examined whether concomitant VSVΔG/lentivirus infection could provide sufficient VSV-G to trans-complement VSVΔG *in vitro*. 293T cells were co-infected with VSV-G enveloped, RFP-expressing VSVΔG at low density (m.o.i. = 0.005) and lentivirus at a range of densities (m.o.i. = 0–1,000). At 2 days post-infection (dpi), we visualized the spread of VSVΔG by fluorescent microscopy and determined the yield of newly synthesized VSVΔG in the media. Indeed, lentivirus complemented VSVΔG in a dose-dependent manner, indicating that VSV-G on the envelope of lentivirus could be taken up by VSVΔG to form functional virions (Figures 1A–C).

Lentivirus-mediated trans-complementation was also effective *in vivo*, enabling transneuronal spread. By itself, VSVΔG injection into the eye (0.5 nl at 10⁸ ffu/ml) resulted in retina infection and RFP labeling of the optic nerve, but no cellular labeling in the brain (Figures 1D,E). This suggested that VSVΔG was not released from axon terminals to initiate a new cycle of infection in the brain. When low (5 × 10⁹ ffu) or high titer lentivirus (2 × 10¹⁰ ffu) was co-injected with VSVΔG (10⁸ ffu/ml), we observed cellular labeling in the brain in both conditions, with more spread in injections with high titer lentivirus (Figures 1F,G). This agrees with our *in vitro* results

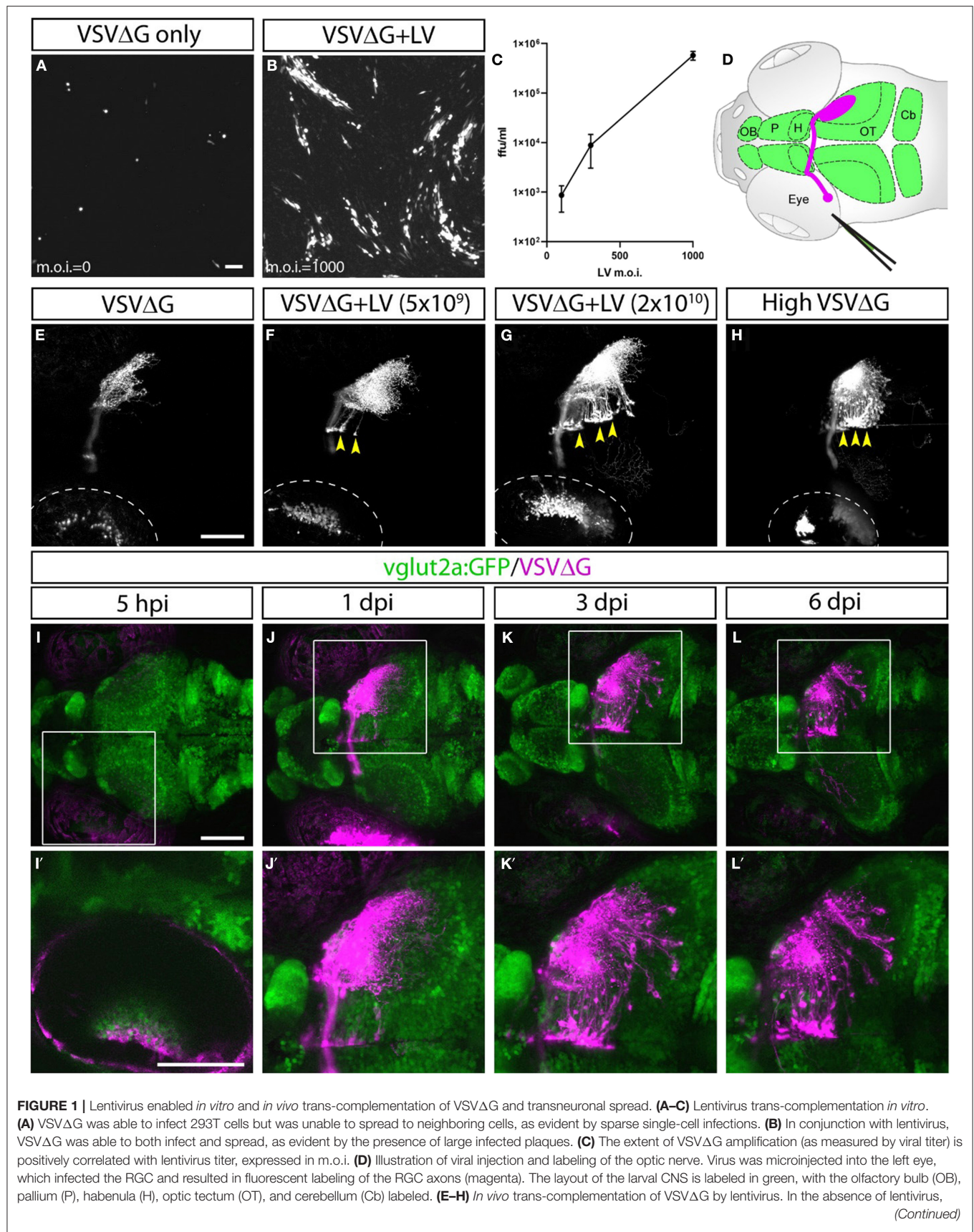


FIGURE 1 | VSVΔG infected RGCs and fluorescently labeled the optic nerve, but no spread in the CNS was observed (**E**). (**F,G**) When lentivirus and VSVΔG were coinjected, cellular labeling was observed in the CNS (yellow arrowheads), indicating transneuronal spread. (**H**) Similar patterns of spread was also seen at very high VSVΔG titer (2×10^9 vs. 10^8 ffu/ml for **E–G**), suggesting that VSVΔG was able to self-complement. (**I–L**) Time course of VSVΔG infection and spread with lentivirus trans-complementation, with RFP expression from VSVΔG (magenta) and GFP expression from the *vglut2a:GFP* transgene (green). Box regions are shown at higher magnifications below (**I'–L'**). Scale bars are 100 μm. Images in the same row are shown at the same scale.

and indicates that high titer lentivirus can trans-complement VSVΔG, allowing viral spread from axon terminals.

The ability of lentivirus to trans-complement was not dependent on what the lentivirus genome encodes. Two types of VSV-G coated lentivirus were tested (lentivirus-SIN-CMV-eGFP and lentivirus-SIN-Ubi-iCre-mCherry). Both were able to mediate trans-complementation, and neither were able to drive transgene expression (eGFP and iCre-mCherry, respectively) on their own in fish at 6 dpi. Lastly, we asked whether VSVΔG could self-complement at higher titer since VSVΔG itself was also enveloped in VSV-G. Indeed, high titer VSVΔG (2×10^9 ffu/ml) could spread from the retinal ganglion cell (RGC) to retinorecipient cells in the brain (**Figure 1H**). Together, these results show that VSV-G from different viral particles could be recycled to form infectious VSV particles. The use of lentivirus provides the additional flexibility to adjust VSVΔG and lentivirus titers to optimize for the extent of starter cell infection and transneuronal spread for sparse or dense labeling (e.g., **Figures 1E,G**).

Restricted Anterograde Spread of VSVΔG in the Zebrafish Visual Pathway

Since lentivirus was supplied at the injected site, only neurons at the injection site (starter cells) should be able to mediate spread. The spread from the starter cells should be limited to direct postsynaptic targets, i.e., anterograde monosynaptic spread. To test this, we examined whether the spatial and temporal patterns of VSVΔG spread were consistent with monosynaptic spread from RGCs to retinorecipient neurons in the brain.

VSVΔG and lentivirus were coinjected into the left temporal retina of anesthetized 3 dpf zebrafish larvae, followed by live confocal imaging at different time points ($n = 9$ animals). Initial RFP expression from VSVΔG was present in the injected (left) eye as early as 5-h post infection (hpi) (**Figures 1I–I'**). Cellular labeling in the contralateral (right) brain was observed at 1 dpi, and more cells were labeled at 3 dpi (**Figures 1J–K'**). At 6 dpi, there was no further spread to other brain regions, compared to 3 dpi (**Figures 1L–L'**). This pattern of labeling is distinct from non-G-deleted (i.e., replication competent) VSV, which rapidly progressed from axonal labeling to cell body labeling in downstream areas like the cerebellum and habenula at 3 dpi (Mundell et al., 2015). These results suggest that lentivirus trans-complementation primarily mediated anterograde monosynaptic spread. We call this new technique Tracer with Restricted Anterograde Spread, or TRAS (pronounced like *trace*).

Efferent Projections of Retinorecipient Cells Were Revealed by TRAS

Retinorecipient cells extend axons to different parts of the brain to mediate visually guided cognitive, sensory, motor, and

homeostatic functions. Previous studies have utilized transgenic reporter lines to characterize efferent projections of subsets of retinorecipient cells, but there has not been a method that could unbiasedly label retinorecipient cells in different brain regions and reveal their efferent projections (Zhang et al., 2017; Helmbrecht et al., 2018; Kramer et al., 2019).

With TRAS, we observed several prominent efferent tracts from retinorecipient neurons, innervating the telencephalon (6 of 9 animals), habenula (2 of 9), tegmentum (8 of 9), contralateral optic tectum (8 of 9), cerebellum (7 of 9), and along the ventral hindbrain (7 of 9) (**Figure 2**, image stack for **Figure 2A** is shown in **Supplementary Video 1**). The less frequently observed efferent projections (i.e., habenula) likely originate from a smaller retinorecipient cell population that was less frequently labeled by the stochastic spread of virus from RGC axon terminals. Overall, these projection patterns are reminiscent of the efferent projections of putative tectal/pretectal retinorecipient neurons identified by sparse transgenic labeling or single-cell photoconversion, further supporting the idea that TRAS primarily labels retinorecipient cells (Sato et al., 2007; Helmbrecht et al., 2018; Kramer et al., 2019). The projection into the telencephalon by retinorecipient neurons, to our best knowledge, has not been reported previously. These axon projections extend rostrally to enter the subpallium and then course dorsally to the caudal pallium. Some axons crossed near the anterior commissure. These pallium-projecting neurons may serve similar roles as the mammalian lateral geniculate neurons to relay sensory information to higher visual areas (Mueller, 2012). These results show that TRAS could be used to identify not only postsynaptic cells but also downstream areas innervated by these cells.

3D Mapping and Cell-Type Characterization

To quantify connectivity patterns, we registered TRAS-labeled image stacks to the Z-Brain zebrafish brain atlas (Randlett et al., 2015). Transgenic fish expressing neuronal-localized nuclear GCaMP6f (*elavl3:H2B-GCaMP6f*) were injected at 2.5 dpf, into the temporal region of the left eye (representing the frontal visual field). Under these conditions, viral infection in the retina is predominantly in the temporal quadrant of the eye (examples of starter cell infection in animals with non-pigmented retina are shown in **Supplementary Figure S2A**). Infected larvae were fixed at 3 dpi and stained with anti-GFP (to amplify the GCaMP6f signal) and anti-GABA. Stained samples were then cleared in sRIMS, a sorbitol-based mounting media that was crucial to resolving single cells and axon tracts in the ventral brain (Yang et al., 2014) (**Figures 3A,B**, **Supplementary Figures S2B,C**). By extracting the Z-Brain *elavl3:H2B-RFP* stack from ZBrainViewer as the reference, image stacks were morphed and aligned

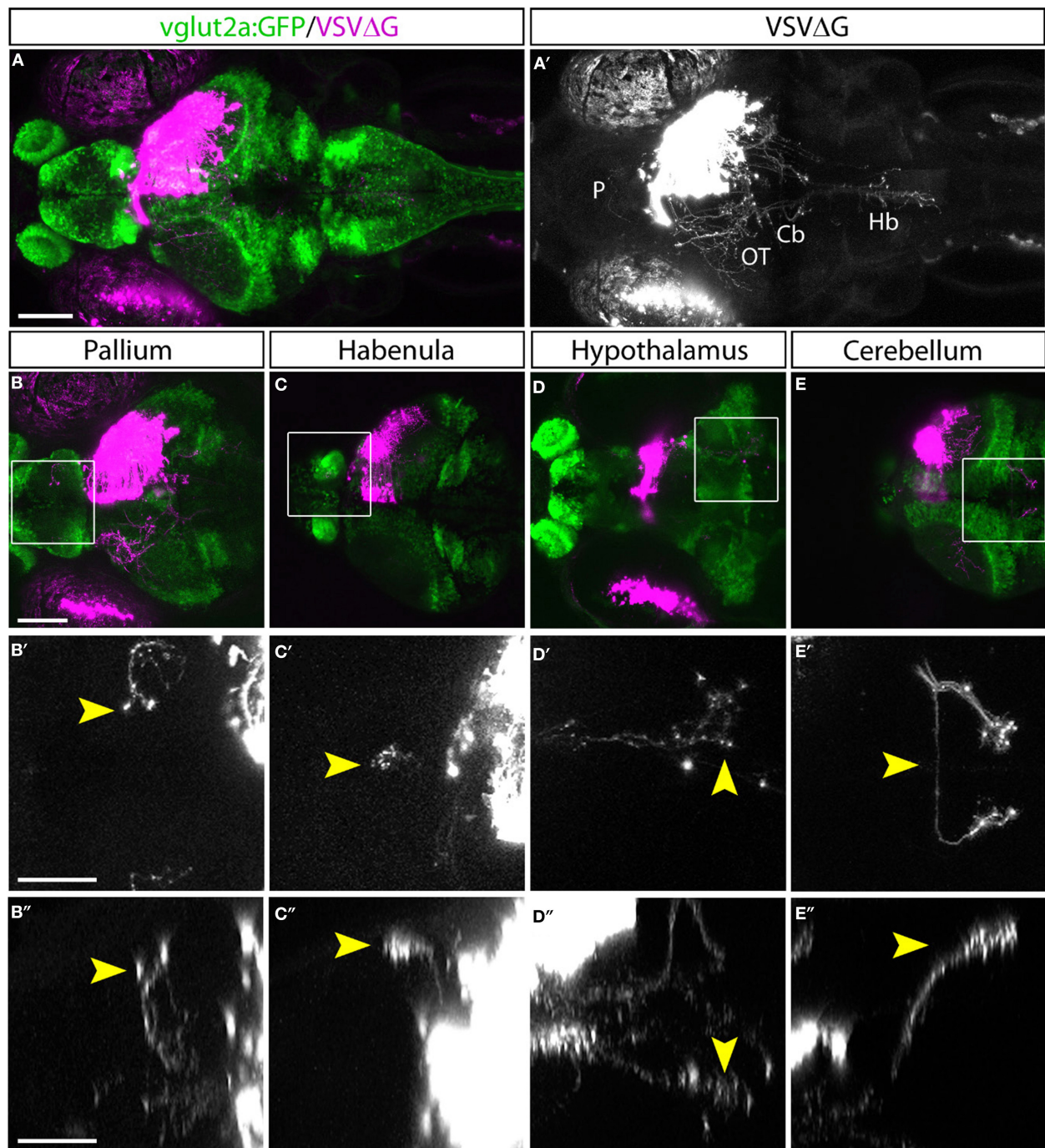
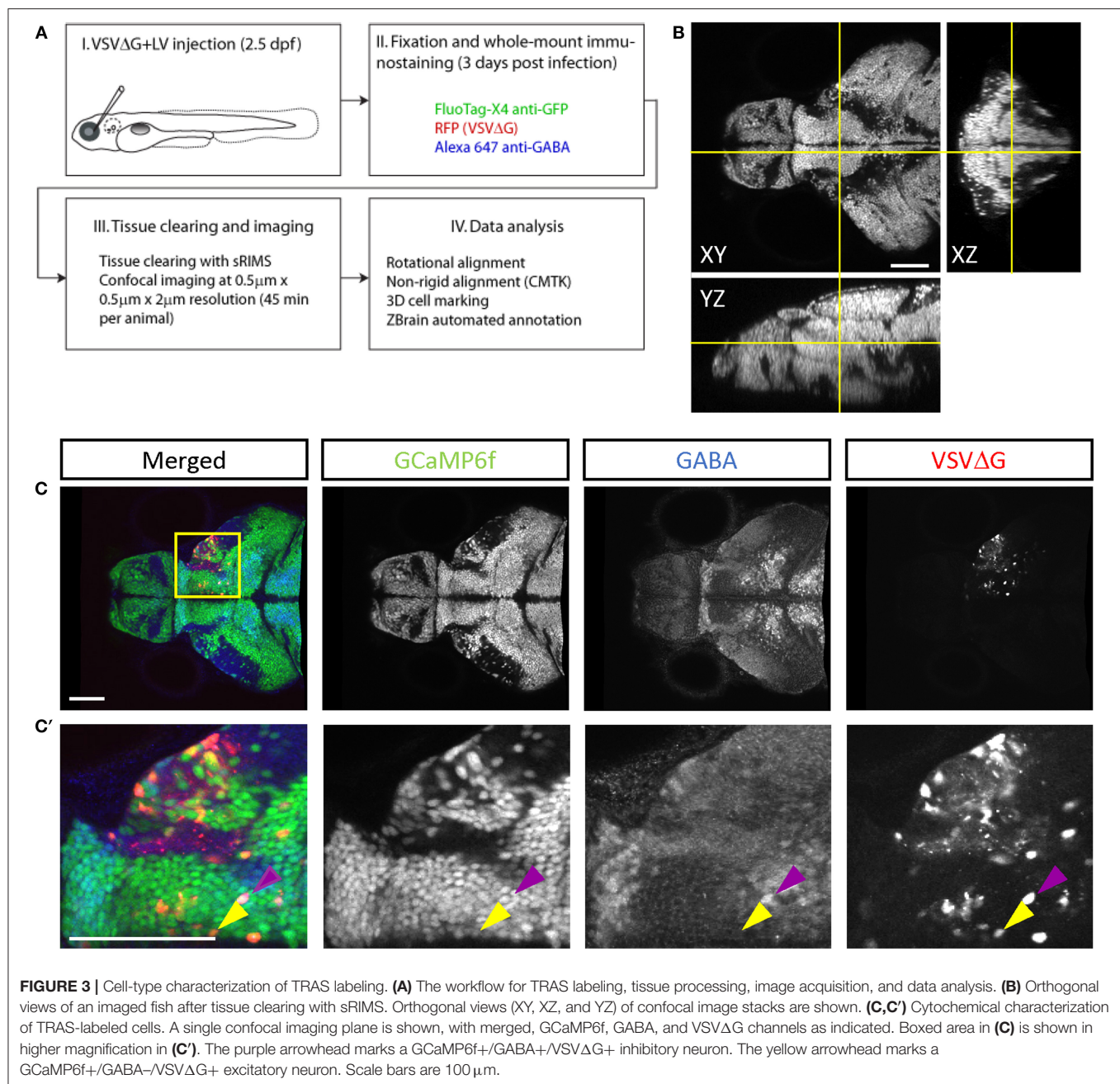


FIGURE 2 | Efferent projections of retinorecipient cells. **(A,A')** Confocal maximal intensity projection (dorsal view) of TRAS-labeled larva, with RFP expression from VSVΔG in magenta **(A)** or white **(A')**. Axon projections can be seen in the pallium (P), optic tectum (OT), cerebellum (Cb), and hindbrain (Hb). **(B-E)** Maximal intensity projection confocal substacks that contained the pallium **(B-B')**, habenula **(C-C')**, hypothalamus **(D-D')**, and cerebellum **(E-E')**. RFP expression from VSVΔG (magenta) and GFP expression from the *vglut2a:GFP* transgene (green) are shown in **B-E**, while boxed region is shown at higher magnification in **B'-E'** (dorsal view) and **B''-E''** (lateral view), with only the RFP channel (white). Yellow arrowheads point to the same efferent projections in the dorsal and lateral views. Scale bars are 100 μm in **(A,B)** and 50 μm in **(B',B'')**. Images in the same row are shown at the same scale.

with the Computational Morphometry Toolkit (CMTK) (Rohlfing and Maurer, 2003; Jefferis et al., 2007; Randlett et al., 2015).

To distinguish different cell types, both transgenic and immunohistochemical markers were used. Nuclear GCaMP6f (expressed only in neurons) was used to distinguish between



neuronal (GCaMP6f+) and GCaMP6f non-expressing (GCaMP6f-, non-neuronal cells and GCaMP6f-negative neurons) cells (**Supplementary Figure S3**). Anti-GABA staining was used to distinguish between non-GABAergic and GABAergic (inhibitory) neurons (Cui et al., 2005) (**Figures 3C–C'**). Since glycinergic neurons are not present in the retinorecipient areas, non-GABAergic retinorecipient neurons are mostly excitatory, with potential inclusion of some GABAergic neurons without soma-localized GABA. After image morphing with CMTK, all TRAS labeled cells were converted into Z-Brain coordinates and categorized into three types: excitatory neurons (GCaMP6f+, GABA-) inhibitory neurons (GCaMP6f+, GABA+), and

GCaMP6f- cells. In total, 24 wild-type and 26 *dscaml1*^{-/-} fish (Ma et al., 2020) (see next section) were analyzed (**Figures 4A,B, Supplementary Video 2**). The overall ratio of excitatory vs. inhibitory cells was similar between wild-type and *dscaml1*^{-/-} cohorts ($p = 0.515$, Chi-square = 0.424). The annotated stack will be made available in the Z-Brain on-line viewer (<http://engertlab.fas.harvard.edu/Z-Brain/>) (Randlett et al., 2015).

The extent of starter cell (RGC) infection and subsequent spread was not significantly different between wild-type and *dscaml1*^{-/-} cohorts. To estimate the number of starter cells, we quantified the RFP fluorescence signal in the RGC arborization fields (AF1-10) (Burrill and Easter, 1994; Robles

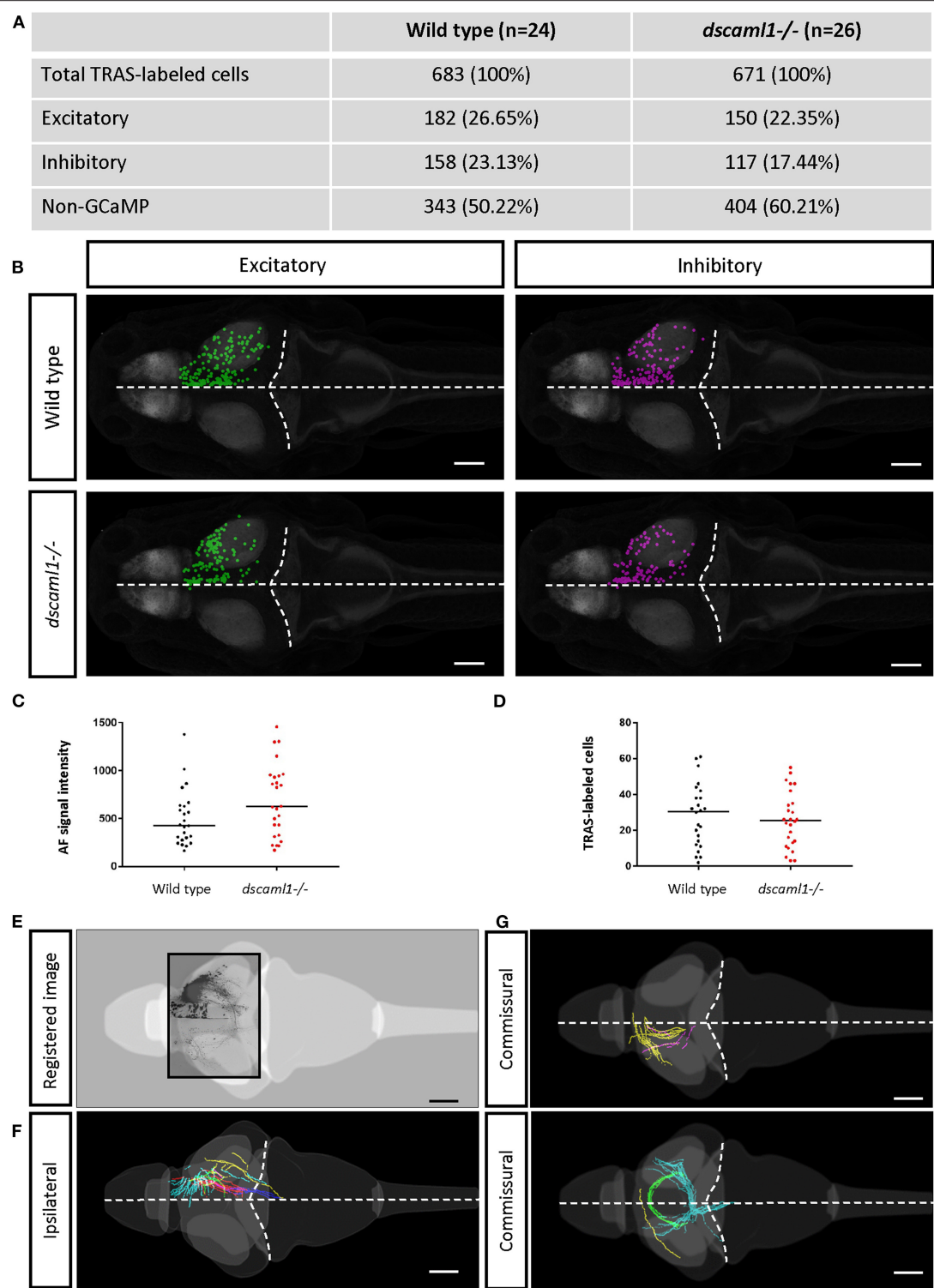
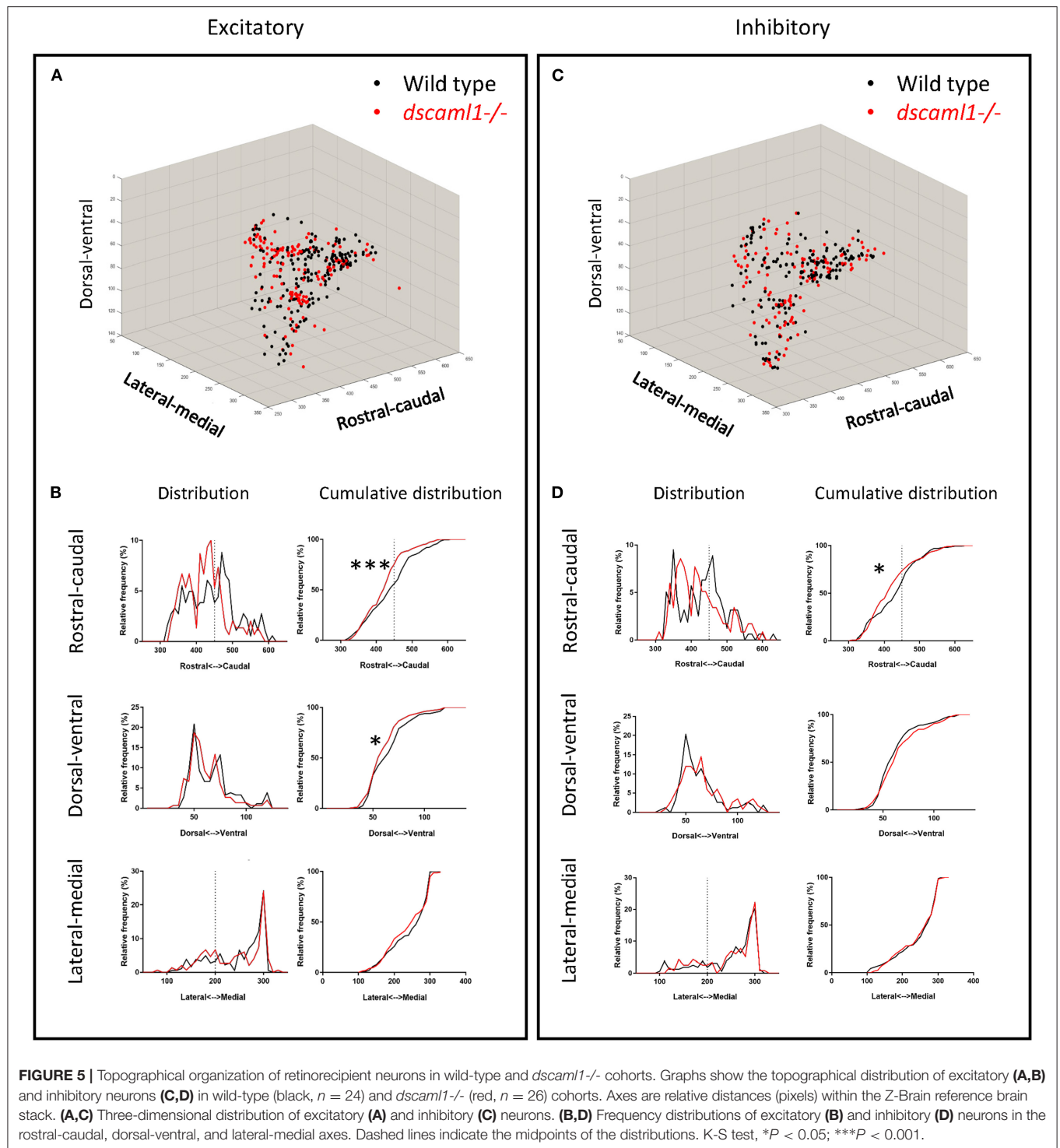


FIGURE 4 | Annotation of TRAS-labeled neurons and efferent axons in the Z-Brain standard brain reference. **(A)** Overview of all annotated TRAS-labeled retinorecipient cells within the wild-type and *dscaml1*^{-/-} cohorts. **(B)** Spatial layout of TRAS-labeled neurons (dorsal view, rostral to the left) overlaid onto the Z-brain reference brain scale, for wild-type (top row) and *dscaml1*^{-/-} (bottom row) cohorts. Green dots mark excitatory neurons, and magenta dots mark inhibitory neurons. **(C)** RGC arborization field (AFs) fluorescent intensity (a proxy for starter cell number) was similar between cohorts. **(D)** The total number of TRAS-labeled cells per fish was not significantly different between cohorts. **(E–G)** Efferent tract tracing from wild-type larvae (*n* = 10). Maximum Z-projection is shown for confocal image **(E)**, traced ipsilateral tracts **(F)**, and commissural tracts **(G)**. Axons with similar trajectories are displayed in the same color. In **(B,E–G)**, the horizontal dashed lines indicate the midline and the curved dashed lines indicate the optic tectum/hindbrain boundary. Scale bars are 100 μ m.



et al., 2014), which are mostly derived from RGC axon terminals. There was no significant difference in arborization field fluorescence between cohorts, suggesting that the extent of starter cell infection was similar (Mann-Whitney U , $p = 0.0932$) (Figure 4C). The total number of TRAS-labeled retinorecipient cells were also not significantly different, suggesting similar

efficiencies in viral spreading between cohorts (Mann-Whitney U , $p = 0.6335$) (Figure 4D).

We verified that Z-Brain registered stacks could also be used as templates for tracing the efferent projections of retinorecipient cells (Figures 4E–G). We acquired high-resolution and low-resolution image stacks for the same fish

and used the high-resolution image stacks for tracing and low-resolution image stacks as the template to register to Z-Brain. We observed ipsilateral and commissural axon tracts, with morphologies that are similar to the tectal efferent tracts described in previous studies (Sato et al., 2007; Helmbrecht et al., 2018).

Comparative Analysis of Retinofugal Connectivity

In addition to normal patterns of retinofugal connectivity, TRAS and Z-Brain can be used to investigate retinofugal connectivity patterns in mutants with visual deficits. We focused on *Down Syndrome Cell Adhesion Molecule Like-1* (*DSCAML1*), a gene mutated in patients with autism spectrum disorder, cortical abnormalities, and developmental disorders (Iossifov et al., 2014; Karaca et al., 2015; Deciphering Developmental Disorders Study, 2017). In zebrafish, *dscaml1* is broadly expressed in visual areas and required for visual and visuomotor behaviors, suggesting an underlying visual circuit deficit (Ma et al., 2020). Therefore, we compared the retinofugal connectivity patterns between 5.5 dpf wild-type fish and their *dscaml1* mutant (*dscaml1*^{-/-}) siblings.

We asked whether the loss of *dscaml1* affected the topographical distribution of retinorecipient neurons (340 and 267 in wild type and *dscaml1*^{-/-}, respectively) (Figure 5). As the initial site of viral infection was in the temporal retina, these retinorecipient neurons likely respond to frontal visual stimuli. The overall distribution was similar between cohorts along the three cardinal axes, but the proportion of retinorecipient cells was significantly shifted in the rostral-caudal and lateral-medial axes. Along the rostral-caudal axis, both excitatory and inhibitory retinorecipient neurons from the *dscaml1*^{-/-} cohort were more rostrally distributed, compared to wild type ($p < 0.001$ and $p < 0.05$ for excitatory and inhibitory neurons, respectively, K-S test). Along the dorsal-ventral axis, the effect of *dscaml1* deficiency was milder. *dscaml1*^{-/-} retinorecipient cells were more dorsally distributed, compared to wild type, but only for excitatory neurons ($p < 0.05$, K-S test). There were no differences in lateral-medial distribution. These results suggest that loss of *dscaml1* may affect the topographic mapping of visual inputs, particularly along the rostral-caudal axes.

Next, we focused on the distribution of retinorecipient cells within specific annotated brain regions. We adapted the Z-Brain quantification tools to measure the sum pixel intensity derived from TRAS-labeled cells for each region (see methods). Among regions defined by anatomy (i.e., not defined by transgene expression), 16 were found to contain, on average, at least 1 retinorecipient cell per animal in the wild-type cohort (Figures 6A,C, Supplementary Figure S4). Two major brain divisions, the mesencephalon and diencephalon, encompassed all of the retinorecipient cells. Within these divisions, the retinorecipient cells are located within subregions corresponding to known to receive retinofugal input, including the preoptic area, hypothalamus, thalamus, eminentia thalami, pretectum, and optic tectum (tectum neuropil, tectum stratum periventriculare, and medial tectal band) (Burrill and Easter, 1994; Zhang et al., 2017; Helmbrecht et al., 2018; Kramer

et al., 2019). We saw no cellular labeling in the olfactory bulb (which innervates the retina), indicating that lentivirus complementation did not facilitate retrograde spread (Li and Dowling, 2000; Mundell et al., 2015). We also identified several retinorecipient areas that, to the best of our knowledge, had not previously been identified (torus semicircularis, tegmentum, posterior tuberculum). Some of these regions also receive retinorecipient efferent projections (tegmentum, poster tuberculum), as mentioned earlier.

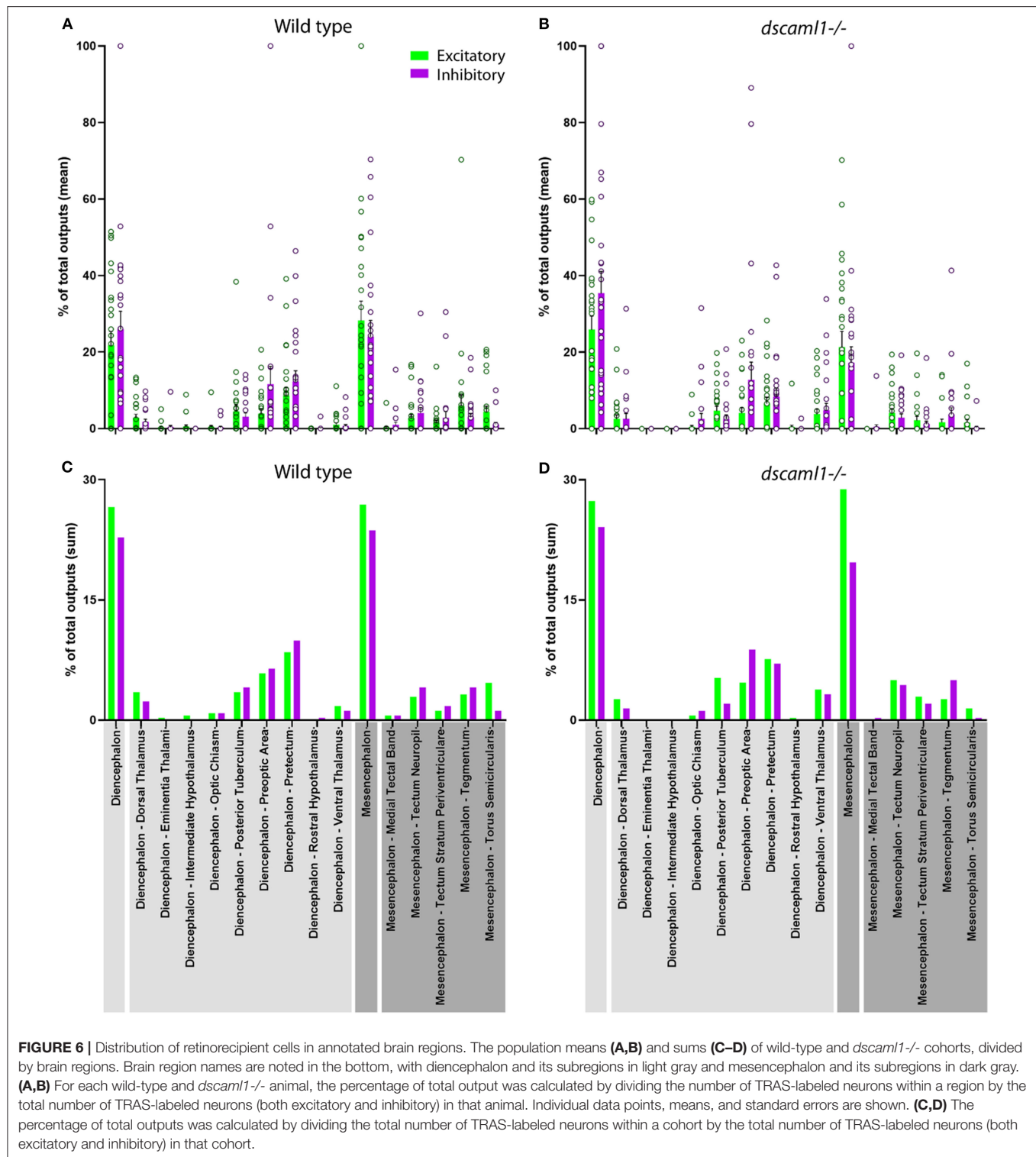
In general, the same areas were innervated in both wild-type and *dscaml1*^{-/-} cohorts, except for two smaller areas that were not innervated in the *dscaml1*^{-/-} cohort (eminentia thalami and intermediate hypothalamus) (Figures 6A,C vs. Figures 6B,D). This result indicates that major retinorecipient areas are innervated by the optic nerve in the *dscaml1*^{-/-} animals.

TRAS Mapping of Habenular-Recipient Neurons

Finally, to test whether TRAS can be applied more generally to other CNS neuronal populations besides RGCs, we examined efferent targeting from the left habenula (Bianco and Wilson, 2009; Amo et al., 2010; Lee et al., 2010; Dreosti et al., 2014; Duboue et al., 2017; Zhang et al., 2017). The bilaterally asymmetrical habenula receives many different sensory cues and is involved in processing social cues, fear learning, and avoidance. The left habenula is known to project to the interpeduncular nucleus (IPN) and superior raphe, providing a suitable pathway to test TRAS mapping in the CNS (Bianco and Wilson, 2009; Amo et al., 2010). VSVΔG and lentivirus were injected into the left habenula of 3 dpf wild-type animals. At 3 dpi, animals for processed for anti-ERK1/2 immunostaining, confocal imaging, and image registration (see methods). Registered image stacks from five animals with selective left habenula labeling were combined (Figures 7A–C'). We observed consistent labeling of the habenular axon tract and the characteristic annular axon terminals in the IPN. Cell bodies near IPN axon terminals were manually marked (Figures 7D–E'). Consistent with previous findings, habenular target cells we labeled within the IPN and raphe nucleus (Amo et al., 2010). We did not observe efferent axons emanating from the habenular-recipient cells (Chou et al., 2016), which suggests that habenular-recipient projection neurons may be relatively rare at this stage. Overall, TRAS labeling in the retina and the habenula demonstrates the general applicability of TRAS for mapping the targets of efferent axons.

DISCUSSION

In this study, we developed TRAS, a new method for monosynaptic anterograde labeling in larval zebrafish. This method was applied to the retinofugal pathway and also validated in the habenula efferent pathway. We showed that TRAS could be combined with the Z-Brain image registration and quantitation pipeline to identify changes in retinofugal connectivity patterns caused by the loss of *dscaml1*. These results demonstrate the broad utility of TRAS for neural circuit studies in zebrafish.



Trans-complementation of VSVΔG by Lentivirus

The structure and function of VSV-G have been extensively studied in the context of viral entry, membrane fusion, toxicity, and subcellular transport (Dotti and Simons, 1990; Thomas

et al., 1993; Ang et al., 2004; Hoffmann et al., 2010; Albertini et al., 2012; Fossati et al., 2014; Kim et al., 2017). VSV-G also determines the infectivity of VSV-G coated viruses (VSV, RABV, lentivirus, retrovirus), which is crucial for their research and clinical applications (Wickersham et al., 2013; Amirache

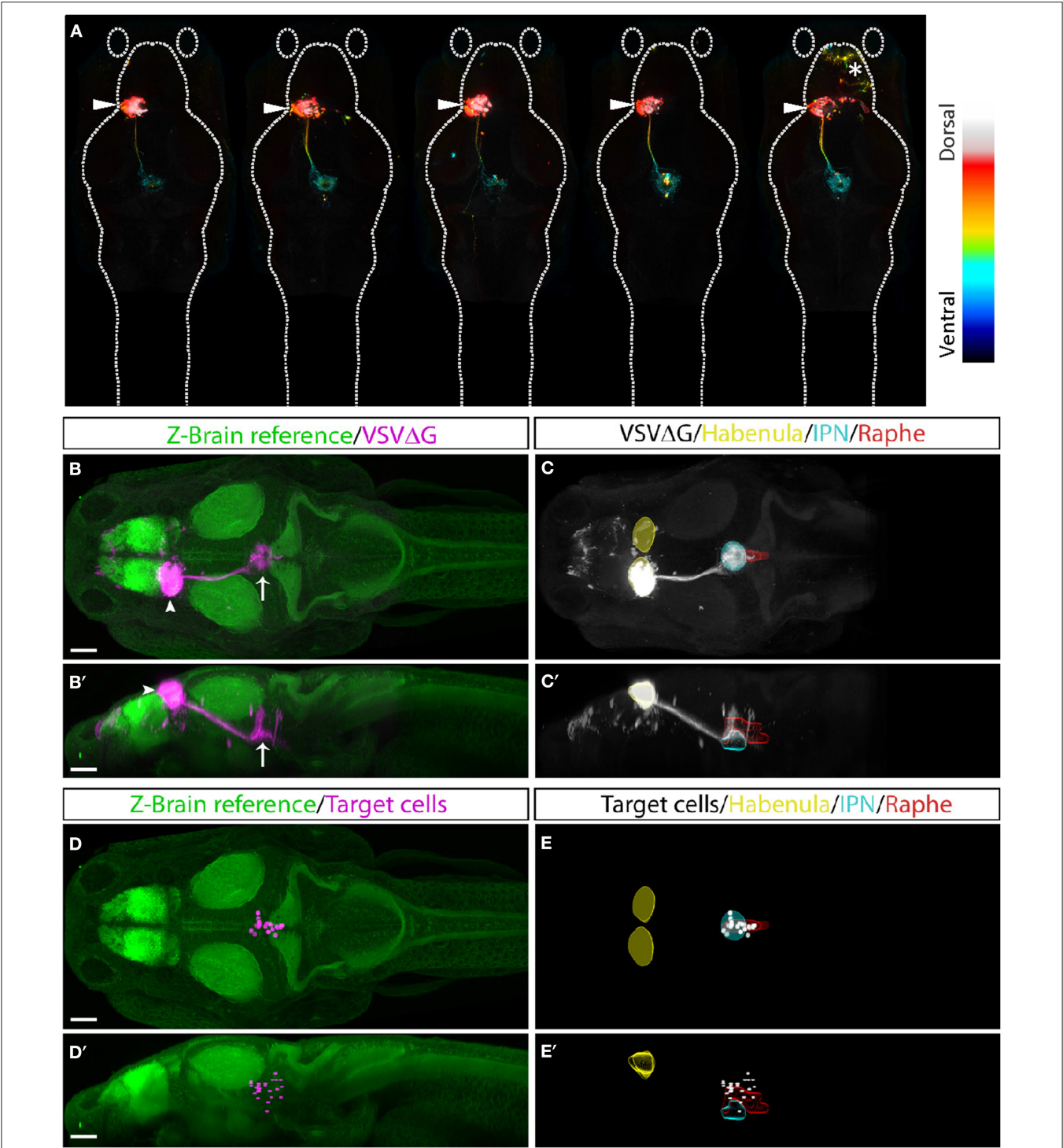


FIGURE 7 | TRAS labeling of habenular target cells. **(A)** Five fish with TRAS tracing from the left habenula (arrowhead), viewed dorsally. The z-dimension is color-coded, as indicated in the lookup table on the right. In one fish (far right), we observed infection in the telencephalon (asterisk). Given the absence of habenula to telencephalon efferents, these cells were likely infected by virus diffusion after injection. **(B–C’)** Combined maximal projection of registered image stacks from the animals shown in **(A)**. The left habenula (arrowhead) projects into the IPN (arrow). RFP expression from VSVΔG infection is shown in magenta **(B,B’)** or white **(C,C’)**. For anatomical reference, images are overlaid on top of the Z-Brain ERK1/2 reference stack (green, **B,B’**), or region outlines for the habenula (yellow), IPN (cyan), and raphe nucleus (red) **(C,C’)**. Dorsal **(B,C)** and lateral **(B’,C’)** views are shown. **(D–E’)** Manually marked habenular target cells (magenta in **D,D’**, white in **E,E’**) are overlaid on top of anatomical references, as described for **(A,B)**. Dorsal **(D,E)** and lateral **(D’,E’)** views are shown. Scale bars are 100 μm. All images are shown at the same scale.

et al., 2014; Mundell et al., 2015; Kobayashi et al., 2016). Our findings revealed a new aspect of VSV-G function, where VSV-G protein from a different viral species can be recycled to generate infectious VSV.

The spread of VSV Δ G from the retina to CNS neurons indicates that VSV-G on the lentivirus surface remained functional after lentivirus infection, and a portion of it was transported anterogradely from the cell body to the axon terminal. At the axon terminal, lentivirus-derived VSV-G was able to re-encapsulate the VSV nucleocapsid and mediate subsequent infection. Although it is possible to achieve transneuronal labeling with high titer of VSV Δ G, TRAS's two-virus system provides the flexibility of adjusting the titer of VSV Δ G based on the demand of the experiment (e.g., sparse vs. dense labeling), while maintaining robust transneuronal spread.

Additionally, the strategy of using lentivirus as a tool for glycoprotein complementation could potentially be applied more broadly. For example, current strategies for RABV monosynaptic tracing utilizes AAV to express RABV glycoprotein, which usually takes several weeks for sufficient glycoprotein expression (Miyamichi et al., 2011). It will be interesting to test whether rabies glycoprotein-coated lentivirus could be a more rapid method to provide glycoprotein for retrograde tracing.

Applying TRAS for Zebrafish Neural Connectivity Analysis

Advances in viral engineering have led to new neural circuit tracing strategies utilizing replication-incompetent viruses (e.g., RABV, AAV, HSV) that are safer to use, less toxic to host cells, and have restricted (mostly monosynaptic) spread (Wickersham et al., 2007; Zingg et al., 2017; Chatterjee et al., 2018; Beier, 2019). Unfortunately, many of the transsynaptic viruses used in mammalian systems either do not infect zebrafish (e.g., AAV) or have low efficiency for transsynaptic spread (e.g., RABV) (Zhu et al., 2009; Dohaku et al., 2019). VSV, in contrast, can infect larval zebrafish and spreads robustly both anterogradely and retrogradely. However, replication-competent VSV has high cytotoxicity and can spread across multiple synapses, making it difficult to distinguish between direct vs. indirect connections (Mundell et al., 2015).

To address these limitations and provide a tool for neural circuit mapping for larval zebrafish, we developed TRAS. TRAS utilizes recombinant VSV with genomic deletion of the glycoprotein gene (VSV Δ G). VSV Δ G can infect cells at the injection site but cannot spread. Although wild-type VSV does not cause serious illness to humans, the use of VSV Δ G further reduces the risk of exposure (Spickler, 2016). The lack of VSV-G expression from the viral genome also helps reduce toxicity to the host cell, as long-term VSV-G expression is known to be cytotoxic (Yee et al., 1994). To complement VSV Δ G, we directly provided VSV-G protein, utilizing lentivirus as the transducing reagent. Compared to transgenic or virus-induced expression, this approach is rapid and transient, therefore minimizing the cellular exposure to VSV-G. Both VSV Δ G and VSV-G coated lentivirus are available from a commercial source, making TRAS an easy method to adopt in a typical neuroscience laboratory.

To expand the utility of TRAS, we developed procedures to register brain images to the Z-Brain anatomical template (Randlett et al., 2015). The combination of neural circuit tracing within a standard 3D-brain atlas is the current state of the art approach for understanding neural network connections, both in zebrafish and mammalian models (Watabe-Uchida et al., 2012; Oh et al., 2014; Helmbrecht et al., 2018; Kramer et al., 2019; Kunst et al., 2019). This approach provides a more objective way to map cells and pathways onto specific brain regions across different experimental animals and promotes cross-referencing between research findings.

We demonstrated that TRAS and Z-Brain could be used for neural circuit mapping in efferent pathways originating from the retina and the left habenula. These are two of the better-studied pathways in larval zebrafish, which allowed us to assess the specificity of TRAS for anterograde labeling of direct postsynaptic targets. By applying TRAS to the habenula, we showed that TRAS could be used to map connections between regions within the central nervous system. It is interesting that we did not observe any efferent axons emanating from the habenular-recipient cells, given the known IPN output pathways described in the adult zebrafish (Chou et al., 2016). Further studies are needed to determine whether any habenular-recipient cells are projection neurons. Overall, TRAS identified all of the target regions described in previous studies, which gives confidence to the future application of TRAS to map unknown neural connections in zebrafish. Furthermore, given that VSV is also an anterograde tracer in mice and chicken, it will be interesting to test whether TRAS can be applied to these experimental systems for neural circuit mapping (Mundell et al., 2015).

Limitations and the Future Development of TRAS

While TRAS offers many advantages as a neural circuit mapping tool, it has similar limitations as other viral tracing techniques (Beier, 2019). In each injected animal, only a subset of the targeted starter cell population is infected, and only a subset of all connections from those starter cells are labeled by trans-neuronal spread. Therefore, the absence of TRAS labeling in a particular region in one animal does not equate an absence of connection in that animal. At the population level, patterns of spread may be affected by synaptic activity, physical distance, the age of the animal, selective biases of viral infection, and viral titer (Callaway and Luo, 2015). Here, we will discuss the limitations specific to TRAS and areas for further technological development.

Specificity of Initial Infection

Since VSV-G binds to a receptor that is widely expressed (LDL receptor) (Finkelshtein et al., 2013), VSV-G coated viruses can infect most cell types. Therefore, the specificity of TRAS depends on precise injection into the brain region of interest. For brain regions smaller than the habenula, a compound microscope with DIC optics would be necessary. To restrict infection to a particular cell type, it may be possible to make use of ASLV-A pseudotyped VSV Δ G that can selectively target neurons expressing an exogenous receptor, TVA (Beier et al., 2011b;

Dohaku et al., 2019). However, potential interactions between virions with different envelope glycoproteins may interfere with the specificity of VSV Δ G infection (Beier et al., 2011a).

Labeling of Direct vs. Indirect Synaptic Targets

Our analysis of retinorecipient cells indicates that TRAS spread anterogradely from the afferent axons to their direct targets. This is based on the fact that lentivirus is only present near the starter cells and that third-order neurons in downstream areas were rarely labeled. The pattern of TRAS labeling is notably more restricted compared to polysynaptic VSV, which labels third-order neurons within 3 days after initial infection (Mundell et al., 2015). However, we cannot rule out that some of the TRAS-labeled cells in primary retinorecipient areas may be indirectly connected to RGCs. Multiple approaches (e.g., electron microscopy, electrophysiology) will be needed to confirm findings from viral tracing.

Physiological Effects of Infection

While the lack of genomic VSV-G expression from VSV Δ G reduces toxicity, other genes expressed from the viral genome can still change the metabolism of the host cell. For instance, the VSV M protein is capable of altering host cell transcription and translation (Ahmed and Lyles, 1998; Connor and Lyles, 2005). Chronic VSV Δ G infection would likely affect the survival of infected neurons and impair its neurophysiological functions. Several approaches for reducing the toxicity of RABV have been reported recently to reduce the function or expression of viral proteins, such as destabilizing the RABV nucleoprotein or deleting the RABV L gene (Ciabatti et al., 2017; Chatterjee et al., 2018). Similar manipulations may also reduce the toxicity of VSV.

Cell-Type Characterization

We have used the *elavl3:H2B-GCaMP6f* transgene and GABA immunoreactivity as markers for post-mitotic neurons and inhibitory neurons, respectively. These markers are widely used in the zebrafish field (Mueller et al., 2006; Mueller and Wullmann, 2015), but it is likely that not all neurons express *elavl3*, and not all GABAergic neurons have GABA immunoreactivity in the soma. Further characterization of the *elavl3* and GABA-immunoreactive populations using alternative excitatory and inhibitory neuron markers (e.g., *vglut2*, *gad1b*) is needed to provide clarity on this issue (Satou et al., 2013).

Optimization of Viral Titer

The efficiency of TRAS depends on the titer of VSV Δ G and lentivirus as well as other factors specific to each experiment, including the condition and duration of virus storage, the tropism of virus to specific cell types, and the age/genetic background of the host. The viral titers for each type of application will need to be adjusted so that VSV Δ G by itself only labels the starter cells, and the addition of lentivirus enables robust monosynaptic spread (Figures 1E–G) (see methods). Low viral titer may result in the absence of labeling in more sparsely connected areas, whereas high viral titer increases the chance of VSV Δ G self-complementation at the axon terminal and multisynaptic spread.

Labeling of Retinorecipient Cells

With TRAS labeling, retinorecipient cells were strongly fluorescent, allowing us to observe and trace the retinorecipient cell efferent tracts. However, the dendritic morphologies of the retinorecipient cells were harder to discern, as the RGC afferents in the vicinity are labeled by the same fluorophore. This also made it difficult to trace the retinorecipient efferent axons back to their cellular origins. For mapping studies where the local projections or morphologies of the recipient cells are important, it will be beneficial to express a distinct fluorophore in the starter cells (e.g., from a transgene).

Mapping With Z-Brain

Z-Brain analysis depends on morphing and registration of image stacks to a reference template, followed by manual identification of labeled neurons. This approach is suitable to test the effects of single genes or pathological states, but likely too laborious as a screening tool to identify candidate genes or screen drugs. Selective fluorescent labeling of neuronal cell bodies (without labeling neurites) and automation of cell detection would be a crucial next step to improve the utility of TRAS.

Connectivity Patterns Associated With *dscaml1* Deficiency

The ability to quantitate efferent connections prompted us to investigate whether TRAS can be used to identify connectivity deficits caused by *dscaml1* deficiency. As mentioned previously, human DSCAML1 mutations are believed to be causative for neurodevelopmental disorders. Additionally, our recent work has found that loss of *dscaml1* significantly impaired visuomotor function associated with light perception and eye movements, suggesting a possible underlying deficit along the visual pathway (Ma et al., 2020).

Using TRAS and Z-Brain quantification, we found that *dscaml1* deficiency might have a role in refining the retinofugal topography and cell-type specificity. On a broader scale, we saw similar patterns of topographic and region-specific projections between wild-type and *dscaml1*^{-/-} cohorts (Figures 5, 6). This indicated that RGC axonal targeting was mostly intact in the *dscaml1* mutants. Interestingly, there was a significant rostral shift in the position in both excitatory and inhibitory retinorecipient cells. Given that RGC axon terminals and retinorecipient cells are both topographically organized, this shift in positioning may result in diminished spatial perception (Stuermer, 1988; Muto et al., 2013; Robles et al., 2014). Further physiological studies will be needed to formally test whether *dscaml1* affects spatial perception in the visual pathway.

CONCLUSIONS

Here, we present the development of TRAS, a new technique that is suitable for mapping neural connectivity in zebrafish. TRAS makes use of a novel lentivirus trans-complementation approach to enable restricted anterograde transneuronal spread by recombinant VSV. We have validated this method in two efferent pathways and identified potential connectivity pattern changes caused by a genetic deficiency in *dscaml1*, a neuronal cell adhesion molecule associated with human neurodevelopmental

disorders. The ability of TRAS to map structural connectivity would enable the discovery of new neural connections and complement existing brain mapping efforts.

DATA AVAILABILITY STATEMENT

The image stacks and other data supporting the findings of this study are available from the corresponding author upon reasonable request. Custom Fiji and MATLAB scripts used of this study are available from the corresponding author upon reasonable request.

ETHICS STATEMENT

The animal study was reviewed and approved by the Institutional Animal Care and Use Committees at Augusta University and Virginia Tech.

AUTHOR CONTRIBUTIONS

MM, SK, and YP conceived the study, performed the experiments, and analyzed the data. SK prepared and characterized recombinant viruses. MM and YP wrote the manuscript, with contributions from SK.

FUNDING

This work was supported by funding from the National Eye Institute of the National Institutes of Health (R01 EY024844 to YP), Center for Innovative Technology (ER14S-001-LS to YP), Augusta University, and Virginia Tech.

ACKNOWLEDGMENTS

We thank the animal care staff at Augusta University and Virginia Tech for animal husbandry, Owen Randlett for help with Z-Brain analysis, Didem Gotz Ayturk, Xiang Ma, and Constance Cepko for reagents and technical expertise for virus

preparation, and members of the Pan lab for helpful suggestions on the manuscript.

SUPPLEMENTARY MATERIAL

The Supplementary Material for this article can be found online at: <https://www.frontiersin.org/articles/10.3389/fncir.2019.00085/full#supplementary-material>

Supplementary Figure S1 | Examples of third-order neuron labeling. Red arrowheads indicate third-order neurons labeled in the hindbrain by TRAS. Yellow dash line marks the border of mesencephalon and cerebellum. Scale bar: 50 μ m.

Supplementary Figure S2 | Retina injection and tissue clearing. **(A)** Examples of RFP expression in the retina of unpigmented (PTU-treated) animals 3 days after virus injection into the temporal retina. Images are lateral views, with rostral side to the left and dorsal side to the top. Yellow dashed lines outline the eye (outer oval) and lens (inner oval). **(B,C)** Tissue clearing with sRIMS solution. Whole-mount ERK1/2 immunolabeling without **(B)** or with sRIMS clearing **(C)**. Orthogonal views (XY, XZ, and YZ) of confocal image stacks are shown, centered just bellowed the cerebellum (intersect of yellow lines). Ventral structures are not visible without sRIMS clearing. Scale bars are 100 μ m.

Supplementary Figure S3 | TRAS labeling of GCaMP6f positive and negative cells. A single confocal imaging plane is shown, with merged, GCaMP6f, GABA, and VSV Δ G channels as indicated. Boxed area in **(A)** is shown in higher magnification in **(A')**. The purple arrowheads mark two GCaMP6f+/GABA+/VSV Δ G+ inhibitory neurons. The orange arrowhead marks a GCaMP6f-/GABA-/VSV Δ G+ cell. Scale bars are 100 μ m.

Supplementary Figure S4 | Signals detected via Z-brain in wild-type and *dscaml1*^{-/-} fish. **(A,B)** Heat map of normalized signals in major anatomical regions from Z-brain showing normalized signals detected within each sample used for analysis, wild-type ($n = 24$) and *dscaml1*^{-/-} ($n = 26$), and their corresponding neuron types **(A)** is excitatory while **(B)** is inhibitory. All signals were descended aligning to Diencephalon.

Supplementary Video 1 | Image stack of TRAS-labeled zebrafish larva, 3 days after the initial infection. VSV Δ G labeling is shown in magenta and *vglut2a:GFP* labeling in green.

Supplementary Video 2 | Excitatory (green) and inhibitory (magenta) retinorecipient cells in wild type **(Left)** and *dscaml1*^{-/-} **(Right)** cohorts. ERK1/2 immunolabeling (white) from Randlett et al. (2015) is overlaid to serve as an anatomical reference.

REFERENCES

- Abdelfattah, A. S., Kawashima, T., Singh, A., Novak, O., Liu, H., Shuai, Y., et al. (2019). Bright and photostable chemigenetic indicators for extended *in vivo* voltage imaging. *Science* 365, 699–704. doi: 10.1126/science.aav6416
- Ahmed, M., and Lyles, D. S. (1998). Effect of vesicular stomatitis virus matrix protein on transcription directed by host RNA polymerases I, II, and III. *J. Virol.* 72, 8413–8419. doi: 10.1128/JVI.72.10.8413-8419.1998
- Ahrens, M. B., Orger, M. B., Robson, D. N., Li, J. M., and Keller, P. J. (2013). Whole-brain functional imaging at cellular resolution using light-sheet microscopy. *Nat. Methods* 10, 413–420. doi: 10.1038/nmeth.2434
- Albertini, A. A., Baquero, E., Ferlin, A., and Gaudin, Y. (2012). Molecular and cellular aspects of rhabdovirus entry. *Viruses* 4, 117–139. doi: 10.3390/v4010117
- Amirache, F., Lévy, C., Costa, C., Mangeot, P.-E., Torbett, B. E., Wang, C. X., et al. (2014). Mystery solved: VSV-G-LVs do not allow efficient gene transfer into unstimulated T cells, B cells, and HSCs because they lack the LDL receptor. *Blood* 123:1422. doi: 10.1182/blood-2013-11-540641
- Amo, R., Aizawa, H., Takahoko, M., Kobayashi, M., Takahashi, R., Aoki, T., et al. (2010). Identification of the zebrafish ventral habenula as a homolog of the mammalian lateral habenula. *J. Neurosci.* 30, 1566–1574. doi: 10.1523/JNEUROSCI.3690-09.2010
- Ang, A. L., Taguchi, T., Francis, S., Folsch, H., Murrells, L. J., Pypaert, M., et al. (2004). Recycling endosomes can serve as intermediates during transport from the Golgi to the plasma membrane of MDCK cells. *J. Cell Biol.* 167, 531–543. doi: 10.1083/jcb.200408165
- Bae, Y. K., Kani, S., Shimizu, T., Tanabe, K., Nojima, H., Kimura, Y., et al. (2009). Anatomy of zebrafish cerebellum and screen for mutations affecting its development. *Dev. Biol.* 330, 406–426. doi: 10.1016/j.ydbio.2009.04.013
- Beier, K. T. (2019). Hitchhiking on the neuronal highway: mechanisms of transsynaptic specificity. *J. Chem. Neuroanat.* 99, 9–17. doi: 10.1016/j.jchemneu.2019.05.001
- Beier, K. T., Mundell, N. A., Pan, Y. A., and Cepko, C. L. (2016). Anterograde or retrograde transsynaptic circuit tracing in vertebrates with vesicular stomatitis virus vectors. *Curr. Protoc. Neurosci.* 74, 1.26.21–1.26.27. doi: 10.1002/0471142301.ns0126s74
- Beier, K. T., Samson, M. E. S., Matsuda, T., and Cepko, C. L. (2011a). Conditional expression of the TVA receptor allows clonal analysis of descendants from Cre-expressing progenitor cells. *Dev. Biol.* 353, 309–320. doi: 10.1016/j.ydbio.2011.03.004

- Beier, K. T., Saunders, A., Oldenburg, I. A., Miyamichi, K., Akhtar, N., Luo, L., et al. (2011b). Anterograde or retrograde transsynaptic labeling of CNS neurons with vesicular stomatitis virus vectors. *Proc. Natl. Acad. Sci. U.S.A.* 108, 15414–15419. doi: 10.1073/pnas.1110854108
- Beier, K. T., Saunders, A. B., Oldenburg, I. A., Sabatini, B. L., and Cepko, C. L. (2013). Vesicular stomatitis virus with the rabies virus glycoprotein directs retrograde transsynaptic transport among neurons *in vivo*. *Front. Neural Circuits* 7:11. doi: 10.3389/fncir.2013.00011
- Belmonte, M. K., Allen, G., Beckel-Mitchener, A., Boulanger, L. M., Carper, R. A., and Webb, S. J. (2004). Autism and abnormal development of brain connectivity. *J. Neurosci.* 24, 9228–9231. doi: 10.1523/JNEUROSCI.3340-04.2004
- Bianco, I. H., and Wilson, S. W. (2009). The habenular nuclei: a conserved asymmetric relay station in the vertebrate brain. *Philos. Trans. R. Soc. London Ser. B Biol. Sci.* 364, 1005–1020. doi: 10.1098/rstb.2008.0213
- Burrill, J. D., and Easter, S. S. Jr. (1994). Development of the retinofugal projections in the embryonic and larval zebrafish (*Brachydanio rerio*). *J. Comp. Neurol.* 346, 583–600. doi: 10.1002/cne.903460410
- Callaway, E. M., and Luo, L. (2015). Monosynaptic circuit tracing with glycoprotein-deleted rabies viruses. *J. Neurosci.* 35:8979. doi: 10.1523/JNEUROSCI.0409-15.2015
- Chatterjee, S., Sullivan, H. A., MacLennan, B. J., Xu, R., Hou, Y., Lavin, T. K., et al. (2018). Nontoxic, double-deletion-mutant rabies viral vectors for retrograde targeting of projection neurons. *Nat. Neurosci.* 21, 638–646. doi: 10.1038/s41593-018-0091-7
- Chen, X., Mu, Y., Hu, Y., Kuan, A. T., Nikitchenko, M., Randlett, O., et al. (2018). Brain-wide organization of neuronal activity and convergent sensorimotor transformations in larval zebrafish. *Neuron* 100, 876–890.e875. doi: 10.1016/j.neuron.2018.09.042
- Chou, M.-Y., Amo, R., Kinoshita, M., Chong, B.-W., Shimazaki, H., Agetsuma, M., et al. (2016). Social conflict resolution regulated by two dorsal habenular subregions in zebrafish. *Science* 352, 87–90. doi: 10.1126/science.aac9508
- Ciabatti, E., Gonzalez-Rueda, A., Mariotti, L., Morgese, F., and Tripodi, M. (2017). Life-long genetic and functional access to neural circuits using self-inactivating rabies virus. *Cell* 170, 382–392.e314. doi: 10.1016/j.cell.2017.06.014
- Connor, J. H., and Lyles, D. S. (2005). Inhibition of host and viral translation during vesicular stomatitis virus infection. eIF2 is responsible for the inhibition of viral but not host translation. *J. Biol. Chem.* 280, 13512–13519. doi: 10.1074/jbc.M501156200
- Cui, W. W., Low, S. E., Hirata, H., Saint-Amant, L., Geisler, R., Hume, R. I., et al. (2005). The Zebrafish *shocked* gene encodes a glycine transporter and is essential for the function of early neural circuits in the CNS. *J. Neurosci.* 25, 6610–6620. doi: 10.1523/JNEUROSCI.5009-04.2005
- Deciphering Developmental Disorders Study (2017). Prevalence and architecture of *de novo* mutations in developmental disorders. *Nature* 542, 433–438. doi: 10.1038/nature21062
- Dohaku, R., Yamaguchi, M., Yamamoto, N., Shimizu, T., Osakada, F., and Hibi, M. (2019). Tracing of afferent connections in the zebrafish cerebellum using recombinant rabies virus. *Front. Neural Circuits* 13:30. doi: 10.3389/fncir.2019.00030
- Dotti, C. G., and Simons, K. (1990). Polarized sorting of viral glycoproteins to the axon and dendrites of hippocampal neurons in culture. *Cell* 62, 63–72. doi: 10.1016/0092-8674(90)90240-F
- Dreosti, E., Vendrell Llopis, N., Carl, M., Yaksi, E., and Wilson, S. W. (2014). Left-right asymmetry is required for the habenulae to respond to both visual and olfactory stimuli. *Curr. Biol.* 24, 440–445. doi: 10.1016/j.cub.2014.01.016
- Duboue, E. R., Hong, E., Eldred, K. C., and Halpern, M. E. (2017). Left habenular activity attenuates fear responses in larval zebrafish. *Curr. Biol.* 27, 2154–2162.e2153. doi: 10.1016/j.cub.2017.06.017
- Feng, L., Zhao, T., and Kim, J. (2015). neuTube 1.0: a new design for efficient neuron reconstruction software based on the SWC format. *eNeuro* 2:ENEURO.0049-14.2014. doi: 10.1523/ENEURO.0049-14.2014
- Finkelstein, D., Werman, A., Novick, D., Barak, S., and Rubinstein, M. (2013). LDL receptor and its family members serve as the cellular receptors for vesicular stomatitis virus. *Proc. Natl. Acad. Sci. U.S.A.* 110, 7306–7311. doi: 10.1073/pnas.1214441110
- Fornito, A., Zalesky, A., and Breakspear, M. (2015). The connectomics of brain disorders. *Nat. Rev. Neurosci.* 16:159. doi: 10.1038/nrn3901
- Fossati, M., Colombo, S. F., and Borgese, N. (2014). A positive signal prevents secretory membrane cargo from recycling between the Golgi and the ER. *EMBO J.* 33, 2080–2097. doi: 10.15252/embj.201488367
- Fuerst, P. G., Bruce, F., Tian, M., Wei, W., Elstrott, J., Feller, M. B., et al. (2009). DSCAM and DSCAML1 function in self-avoidance in multiple cell types in the developing mouse retina. *Neuron* 64, 484–497. doi: 10.1016/j.neuron.2009.09.027
- Galicia, C. A., Sukeena, J. M., Stenkamp, D. L., and Fuerst, P. G. (2018). Expression patterns of dscam and sdk gene paralogs in developing zebrafish retina. *Mol. Vis.* 24, 443–458.
- Glasser, M. F., Coalson, T. S., Robinson, E. C., Hacker, C. D., Harwell, J., Yacoub, E., et al. (2016). A multi-modal parcellation of human cerebral cortex. *Nature* 536:171. doi: 10.1038/nature18933
- Helmbrecht, T. O., Dal Maschio, M., Donovan, J. C., Koutsouli, S., and Baier, H. (2018). Topography of a visuomotor transformation. *Neuron* 100, 1429–1445.e4. doi: 10.1016/j.neuron.2018.10.021
- Hildebrand, D. G. C., Cicconet, M., Torres, R. M., Choi, W., Quan, T. M., Moon, J., et al. (2017). Whole-brain serial-section electron microscopy in larval zebrafish. *Nature* 545, 345–349. doi: 10.1038/nature22356
- Hoffmann, M., Wu, Y. J., Gerber, M., Berger-Rentsch, M., Heimrich, B., Schwemmle, M., et al. (2010). Fusion-active glycoprotein G mediates the cytotoxicity of vesicular stomatitis virus M mutants lacking host shut-off activity. *J. Gen. Virol.* 91, 2782–2793. doi: 10.1099/vir.0.023978-0
- Iossifov, I., O’Roak, B. J., Sanders, S. J., Ronemus, M., Krumm, N., Levy, D., et al. (2014). The contribution of *de novo* coding mutations to autism spectrum disorder. *Nature* 515, 216–221. doi: 10.1038/nature13908
- Jefferis, G. S., Potter, C. J., Chan, A. M., Marin, E. C., Rohlfing, T., Maurer, C. R. Jr., et al. (2007). Comprehensive maps of *Drosophila* higher olfactory centers: spatially segregated fruit and pheromone representation. *Cell* 128, 1187–1203. doi: 10.1016/j.cell.2007.01.040
- Karaca, E., Harel, T., Pehlivan, D., Jhangiani, S. N., Gambin, T., Coban Akdemir, Z., et al. (2015). Genes that affect brain structure and function identified by rare variant analyses of mendelian neurologic disease. *Neuron* 88, 499–513. doi: 10.1016/j.neuron.2015.09.048
- Kasthuri, N., Hayworth, K. J., Berger, D. R., Schalek, R. L., Conchello, J. A., Knowles-Barley, S., et al. (2015). Saturated reconstruction of a volume of neocortex. *Cell* 162, 648–661. doi: 10.1016/j.cell.2015.06.054
- Kawashima, T., Zwart, M. F., Yang, C. T., Mensh, B. D., and Ahrens, M. B. (2016). The serotonergic system tracks the outcomes of actions to mediate short-term motor learning. *Cell* 167, 933–946.e920. doi: 10.1016/j.cell.2016.09.055
- Kim, I. S., Jenni, S., Stanifer, M. L., Roth, E., Whelan, S. P., van Oijen, A. M., et al. (2017). Mechanism of membrane fusion induced by vesicular stomatitis virus G protein. *Proc. Natl. Acad. Sci. U.S.A.* 114, E28–E36. doi: 10.1073/pnas.1618883114
- Kimmel, C. B., Ballard, W. W., Kimmel, S. R., Ullmann, B., and Schilling, T. F. (1995). Stages of embryonic development of the zebrafish. *Dev. Dyn.* 203, 253–310. doi: 10.1002/aja.1002030302
- Kobayashi, K., Kato, S., Inoue, K., Takada, M., and Kobayashi, K. (2016). Altering entry site preference of lentiviral vectors into neuronal cells by pseudotyping with envelope glycoproteins. *Methods Mol. Biol.* 1382, 175–186. doi: 10.1007/978-1-4939-3271-9_12
- Kramer, A., Wu, Y., Baier, H., and Kubo, F. (2019). Neuronal architecture of a visual center that processes optic flow. *Neuron* 103, 118–132.e7. doi: 10.1016/j.neuron.2019.04.018
- Kunst, M., Laurell, E., Mokayes, N., Kramer, A., Kubo, F., Fernandes, A. M., et al. (2019). A cellular-resolution atlas of the larval zebrafish brain. *Neuron* 103, 21–38.e5. doi: 10.2139/ssrn.3257346
- Lee, A., Mathuru, A. S., Teh, C., Kibat, C., Korzh, V., Penney, T. B., et al. (2010). The habenula prevents helpless behavior in larval zebrafish. *Curr. Biol.* 20, 2211–2216. doi: 10.1016/j.cub.2010.11.025
- Li, L., and Dowling, J. E. (2000). Disruption of the olfactoryretinal centrifugal pathway may relate to the visual system defect in night blindness b mutant zebrafish. *J. Neurosci.* 20, 1883–1892. doi: 10.1523/JNEUROSCI.20-05-01883.2000
- Lynall, M.-E., Bassett, D. S., Kerwin, R., McKenna, P. J., Kitzbichler, M., Muller, U., et al. (2010). Functional connectivity and brain networks in schizophrenia. *J. Neurosci.* 30, 9477–9487. doi: 10.1523/JNEUROSCI.0333-10.2010

- Ma, M., Ramirez, A. D., Wang, T., Roberts, R. L., Harmon, K. E., Schoppik, D., et al. (2020). Zebrafish *dscaml1* deficiency impairs retinal patterning and oculomotor function. *J. Neurosci.* 40, 143–158. doi: 10.1523/JNEUROSCI.1783-19.2019
- Maack, G., and Segner, H. (2003). Morphological development of the gonads in zebrafish. *J. Fish Biol.* 62, 895–906. doi: 10.1046/j.1095-8649.2003.00074.x
- Miyamichi, K., Amat, F., Moussavi, F., Wang, C., Wickersham, I., Wall, N. R., et al. (2011). Cortical representations of olfactory input by trans-synaptic tracing. *Nature* 472, 191–196. doi: 10.1038/nature09714
- Mueller, T. (2012). What is the thalamus in zebrafish? *Front. Neurosci.* 6, 64–64. doi: 10.3389/fnins.2012.00064
- Mueller, T., Vernier, P., and Wullimann, M. F. (2006). A phylotypic stage in vertebrate brain development: GABA cell patterns in zebrafish compared with mouse. *J. Comp. Neurol.* 494, 620–634. doi: 10.1002/cne.20824
- Mueller, T. W., and Wullimann, M. F. (2015). *Atlas of Early Zebrafish Brain Development: A Tool for Molecular Neurogenetics*. Boston, MA: Elsevier.
- Mundell, N. A., Beier, K. T., Pan, Y. A., Lapan, S. W., Goz Ayturk, D., Berezovskii, V. K., et al. (2015). Vesicular stomatitis virus enables gene transfer and transsynaptic tracing in a wide range of organisms. *J. Comp. Neurol.* 523, 1639–1663. doi: 10.1002/cne.23761
- Muto, A., Ohkura, M., Abe, G., Nakai, J., and Kawakami, K. (2013). Real-time visualization of neuronal activity during perception. *Curr. Biol.* 23, 307–311. doi: 10.1016/j.cub.2012.12.040
- Oh, S. W., Harris, J. A., Ng, L., Winslow, B., Cain, N., Mihalas, S., et al. (2014). A mesoscale connectome of the mouse brain. *Nature* 508, 207–214. doi: 10.1038/nature13186
- Orger, M. B., and de Polavieja, G. G. (2017). Zebrafish behavior: opportunities and challenges. *Annu. Rev. Neurosci.* 40, 125–147. doi: 10.1146/annurev-neuro-071714-033857
- Randlett, O., Wee, C. L., Naumann, E. A., Nnaemeka, O., Schoppik, D., Fitzgerald, J. E., et al. (2015). Whole-brain activity mapping onto a zebrafish brain atlas. *Nat. Methods* 12, 1039–1046. doi: 10.1038/nmeth.3581
- Robles, E., Laurell, E., and Baier, H. (2014). The retinal projectome reveals brain-area-specific visual representations generated by ganglion cell diversity. *Curr. Biol.* 24, 2085–2096. doi: 10.1016/j.cub.2014.07.080
- Rohlfing, T., and Maurer, C. R. (2003). Nonrigid image registration in shared-memory multiprocessor environments with application to brains, breasts, and bees. *IEEE Trans. Inform. Technol. Biomed.* 7, 16–25. doi: 10.1109/TITB.2003.808506
- Sakai, C., Ijaz, S., and Hoffman, E. J. (2018). Zebrafish models of neurodevelopmental disorders: past, present, and future. *Front. Mol. Neurosci.* 11:294. doi: 10.3389/fnmol.2018.00294
- Sato, T., Hamaoka, T., Aizawa, H., Hosoya, T., and Okamoto, H. (2007). Genetic single-cell mosaic analysis implicates ephrinB2 reverse signaling in projections from the posterior tectum to the hindbrain in zebrafish. *J. Neurosci.* 27, 5271–5279. doi: 10.1523/JNEUROSCI.0883-07.2007
- Satou, C., Kimura, Y., Hirata, H., Suster, M. L., Kawakami, K., and Higashijima, S. (2013). Transgenic tools to characterize neuronal properties of discrete populations of zebrafish neurons. *Development* 140, 3927–3931. doi: 10.1242/dev.099531
- Spickler, A. R. (2016). *Vesicular Stomatitis*. Available online at: <http://www.cfsph.iastate.edu/DiseaseInfo/factsheets.php> (accessed July 16, 2019).
- Stuermer, C. A. (1988). Retinotopic organization of the developing retinotectal projection in the zebrafish embryo. *J. Neurosci.* 8, 4513–4530. doi: 10.1523/JNEUROSCI.08-12-04513.1988
- Svara, F. N., Kornfeld, J., Denk, W., and Bollmann, J. H. (2018). Volume EM reconstruction of spinal cord reveals wiring specificity in speed-related motor circuits. *Cell Rep.* 23, 2942–2954. doi: 10.1016/j.celrep.2018.05.023
- Swanson, L. W., and Lichtman, J. W. (2016). From cajal to connectome and beyond. *Annu. Rev. Neurosci.* 39, 197–216. doi: 10.1146/annurev-neuro-071714-033954
- Thomas, D. C., Brewer, C. B., and Roth, M. G. (1993). Vesicular stomatitis virus glycoprotein contains a dominant cytoplasmic basolateral sorting signal critically dependent upon a tyrosine. *J. Biol. Chem.* 268, 3313–3320.
- Thyme, S. B., Pieper, L. M., Li, E. H., Pandey, S., Wang, Y., Morris, N. S., et al. (2019). Phenotypic landscape of schizophrenia-associated genes defines candidates and their shared functions. *Cell* 177, 478–491.e420. doi: 10.1016/j.cell.2019.01.048
- Vishwanathan, A., Daie, K., Ramirez, A. D., Lichtman, J. W., Aksay, E. R. F., and Seung, H. S. (2017). Electron microscopic reconstruction of functionally identified cells in a neural integrator. *Curr. Biol.* 27, 2137–2147.e2133. doi: 10.1016/j.cub.2017.06.028
- Wanner, A. A., Genoud, C., Masudi, T., Siksou, L., and Friedrich, R. W. (2016). Dense EM-based reconstruction of the interglomerular projectome in the zebrafish olfactory bulb. *Nat. Neurosci.* 19, 816–825. doi: 10.1038/nn.4290
- Watabe-Uchida, M., Zhu, L., Ogawa Sachie, K., Vamanrao, A., and Uchida, N. (2012). Whole-brain mapping of direct inputs to midbrain dopamine neurons. *Neuron* 74, 858–873. doi: 10.1016/j.neuron.2012.03.017
- Wickersham, I. R., Lyon, D. C., Barnard, R. J., Mori, T., Finke, S., Conzelmann, K. K., et al. (2007). Monosynaptic restriction of transsynaptic tracing from single, genetically targeted neurons. *Neuron* 53, 639–647. doi: 10.1016/j.neuron.2007.01.033
- Wickersham, I. R., Sullivan, H. A., and Seung, H. S. (2013). Axonal and subcellular labelling using modified rabies viral vectors. *Nat. Commun.* 4:2332. doi: 10.1038/ncomms3332
- Wilson, C. A., High, S. K., McCluskey, B. M., Amores, A., Yan, Y.-I., Titus, T. A., et al. (2014). Wild sex in zebrafish: loss of the natural sex determinant in domesticated strains. *Genetics* 198, 1291–1308. doi: 10.1534/genetics.114.169284
- Yang, B., Treweek, J. B., Kulkarni, R. P., Deverman, B. E., Chen, C. K., Lubeck, E., et al. (2014). Single-cell phenotyping within transparent intact tissue through whole-body clearing. *Cell* 158, 945–958. doi: 10.1016/j.cell.2014.07.017
- Yee, J. K., Miyanoohara, A., LaPorte, P., Bouic, K., Burns, J. C., and Friedmann, T. (1994). A general method for the generation of high-titer, pantropic retroviral vectors: highly efficient infection of primary hepatocytes. *Proc. Natl. Acad. Sci. U.S.A.* 91, 9564–9568. doi: 10.1073/pnas.91.20.9564
- Zhang, B. B., Yao, Y. Y., Zhang, H. F., Kawakami, K., and Du, J. L. (2017). Left habenula mediates light-preference behavior in zebrafish via an asymmetrical visual pathway. *Neuron* 93, 914–928.e914. doi: 10.1016/j.neuron.2017.01.011
- Zhu, P., Narita, Y., Bundschuh, S. T., Fajardo, O., Schärer, Y. P., Chattopadhyaya, B., et al. (2009). Optogenetic dissection of neuronal circuits in zebrafish using viral gene transfer and the tet system. *Front. Neural Circuits* 3:21. doi: 10.3389/neuro.04.021.2009
- Zingg, B., Chou, X. L., Zhang, Z. G., Mesik, L., Liang, F., Tao, H. W., et al. (2017). AAV-mediated anterograde transsynaptic tagging: mapping corticocollicular input-defined neural pathways for defense behaviors. *Neuron* 93, 33–47. doi: 10.1016/j.neuron.2016.11.045

Conflict of Interest: The authors declare that the research was conducted in the absence of any commercial or financial relationships that could be construed as a potential conflict of interest.

Copyright © 2020 Ma, Kler and Pan. This is an open-access article distributed under the terms of the Creative Commons Attribution License (CC BY). The use, distribution or reproduction in other forums is permitted, provided the original author(s) and the copyright owner(s) are credited and that the original publication in this journal is cited, in accordance with accepted academic practice. No use, distribution or reproduction is permitted which does not comply with these terms.



Neural Correlates of Learning Pure Tones or Natural Sounds in the Auditory Cortex

Ido Maor^{1,2}, Ravid Shwartz-Ziv², Libi Feigin², Yishai Elyada², Haim Sompolsky^{2,3} and Adi Mizrahi^{1,2*}

¹ Department of Neurobiology, Alexander Silberman Institute of Life Sciences, The Hebrew University of Jerusalem, Jerusalem, Israel, ² The Edmond and Lily Safra Center for Brain Sciences, The Hebrew University of Jerusalem, Jerusalem, Israel, ³ The Racah Institute of Physics, The Hebrew University of Jerusalem, Jerusalem, Israel

OPEN ACCESS

Edited by:

David J. Margolis,
Rutgers, The State University of New
Jersey, United States

Reviewed by:

Tania Rinaldi Barkat,
University of Basel, Switzerland
Sarah L. Pallas,
University of Massachusetts Amherst,
United States

*Correspondence:

Adi Mizrahi
Mizrahi.adi@mail.huji.ac.il

Received: 23 September 2019

Accepted: 17 December 2019

Published: 28 January 2020

Citation:

Maor I, Shwartz-Ziv R, Feigin L,
Elyada Y, Sompolsky H and
Mizrahi A (2020) Neural Correlates of
Learning Pure Tones or Natural
Sounds in the Auditory Cortex.
Front. Neural Circuits 13:82.
doi: 10.3389/fncir.2019.00082

Associative learning of pure tones is known to cause tonotopic map expansion in the auditory cortex (ACx), but the function this plasticity sub-serves is unclear. We developed an automated training platform called the “Educage,” which was used to train mice on a go/no-go auditory discrimination task to their perceptual limits, for difficult discriminations among pure tones or natural sounds. Spiking responses of excitatory and inhibitory parvalbumin (PV⁺) L2/3 neurons in mouse ACx revealed learning-induced overrepresentation of the learned frequencies, as expected from previous literature. The coordinated plasticity of excitatory and inhibitory neurons supports a role for PV⁺ neurons in homeostatic maintenance of excitation–inhibition balance within the circuit. Using a novel computational model to study auditory tuning curves, we show that overrepresentation of the learned tones does not necessarily improve discrimination performance of the network to these tones. In a separate set of experiments, we trained mice to discriminate among natural sounds. Perceptual learning of natural sounds induced “sparsening” and decorrelation of the neural response, consequently improving discrimination of these complex sounds. This signature of plasticity in A1 highlights its role in coding natural sounds.

Keywords: auditory, mice, automated training, interneurons, perceptual learning

INTRODUCTION

Learning is accompanied by plastic changes in brain circuits. This plasticity is often viewed as substrate for improving computations that sub-serve learning and behavior. A well-studied example of learning-induced plasticity is following perceptual learning where cortical representations change toward the learned stimuli (Gilbert et al., 2001; Roelfsema and Holtmaat, 2018). Whether such changes improve discrimination has not been causally tested and remains debated, and the mechanisms of change are still largely unknown.

Perceptual learning is an implicit form of lifelong learning during which perceptual performance improves with practice (Gibson, 1969). Extensive psychophysical research on perceptual learning tasks led to a general agreement on some attributes of this type of learning (Hawkey et al., 2004). For example, perceptual learning has been shown to be task specific and poorly generalized to other senses or tasks. It is also largely agreed upon that gradual training is essential for

improvement (Lawrence, 1952; Ramachandran and Braddick, 1973; Ball and Sekuler, 1987; Berardi and Fiorentini, 1987; Karni and Sagi, 1991; Irvine et al., 2000; Wright and Fitzgerald, 2001; Ahissar and Hochstein, 2004; Ericsson, 2006; Kurt and Ehret, 2010). Given the specificity observed at the behavioral level, functional correlates of perceptual learning are thought to involve neural circuits as early as primary sensory regions (Gilbert et al., 2001; Schoups et al., 2001). In auditory learning paradigms, changes are already observed at the level of primary auditory cortex (Weinberger, 2004). Learning to discriminate among tones results in tonotopic map plasticity toward the trained stimulus (Recanzone et al., 1993; Rutkowski and Weinberger, 2005; Polley et al., 2006; Bieszczad and Weinberger, 2010; reviewed in Irvine, 2017). Notably, however, not all studies could replicate the learning-induced changes in the tonotopic map (Brown et al., 2004). Furthermore, artificially induced map plasticity was shown to be unnecessary for better discrimination performances *per se* (Talwar and Gerstein, 2001; Reed et al., 2011). Our understanding of the mechanisms underlying auditory cortex plasticity remains rudimentary, let alone for more natural stimuli beyond pure tones.

To gain understanding of learning-induced plasticity at single neuron resolution, animal models have proven very useful. Mice, for example, offer the advantage of a rich genetic experimental toolkit to study neurons and circuits with high efficiency and specificity (Luo et al., 2018). Historically, the weak aspect of using mice as a model was its limited behavioral repertoire to learn difficult tasks. However, in the past decade, technical difficulties to train mice to their limits have been steadily improving with increasing number of software and hardware tools to probe mouse behavior in high resolution (de Hoz and Nelken, 2014; Egnor and Branson, 2016; Murphy et al., 2016; Aoki et al., 2017; Francis and Kanold, 2017; Krakauer et al., 2017; Cruces-Solis et al., 2018; Erskine et al., 2018). Here, we developed our own experimental system for training groups of mice on an auditory perceptual task—an automatic system called the “Educage.” The Educage is a simple affordable system that allows efficient training of several mice simultaneously. Here, we used the system to train mice to discriminate among pure tones or complex sounds.

A1 is well known for its tonotopic map plasticity following simple forms of learning in other animal models (Irvine, 2017). An additional interest in primary auditory cortex is its increasing recognition as a brain region involved in coding complex sounds (Bizley and Cohen, 2013; Kuchibhotla and Bathellier, 2018). We thus asked what are the changes single neurons undergo following training to discriminate pure tones or natural stimuli. We describe distinct changes in the long-term stimulus representations by L2/3 neurons of mice following perceptual learning and assess how these contribute to information processing by local circuits. Using two-photon targeted electrophysiology, we also describe how L2/3 parvalbumin-positive neurons change with respect to their excitatory counterparts. Our work provides a behavioral, physiological, and computational foundation to questions of auditory-driven plasticity in mice, from pure tones to natural sounds.

MATERIALS AND METHODS

Animals

A total of $n = 88$, 10- to 11-week-old female mice were used in this work as follows. Forty-four mice were C57BL/6 mice and 44 mice were a crossbreed of PV-Cre mice and tdTomato reporter mice (PV \times Ai9; Hippenmeyer et al., 2005; Madisen et al., 2010). All experiments were approved by the Hebrew University's IACUC.

Behavioral Setup

The “Educage” is a small chamber ($10 \times 10 \times 10$ cm), opening on one end into a standard animal home cage where mice can enter and exit freely (Figure 1A and Supplementary Figure 1a). On the other end, the chamber contains the hardware that drives the system, hardware for identifying mice and measuring behavioral performance. Specifically, at the port entrance there is a coil radio antenna (ANTC40 which connected to LID665 stationary decoder; Dorset) followed by infrared diodes used to identify mice individually and monitor their presence in the port. This port is the only access to water for the mice. Water is delivered *via* a solenoid valve (VDW; SMC) allowing precise control of the water volume provided on each visit. Water is delivered via a water spout, which is also a lickometer (based on 1 microampere current). An additional solenoid valve is positioned next to the water spout in order to deliver a mild air puff as a negative reinforcement, if necessary. For sound stimulation, we positioned a speaker (ES1; TDT), at the center of the top wall of the chamber. Sound was delivered to the speaker at 125 kHz sampling rate *via* a driver and a programmable attenuator (ED1, PA5; TDT). For high-speed data acquisition, reliable control, on-board sound delivery, and future flexibility, the system was designed via a field programmable gate array (FPGA) module and a real-time operating system (RTOS) module (CompactRIO controller; National Instruments). A custom-made A/D converter was connected to the CompactRIO controller, mediated signal from infrared diodes and lickometer and controlled the valves. A custom code was written in Labview to allow an executable user-friendly interface with numerous options for user-input and flexibility for designing custom protocols. All software and hardware design are freely available for download at <https://github.com/MizrahiTeam/Educage>.

Training Paradigm

Prior to the training, each mouse was implanted, under light and very short period of isoflurane anesthesia, with a radio frequency identification (RFID; Trovan) chip under its scruff. RFID chips allow identification of mice individually, which is then used by the system to control the precise stimulus delivery and track behavioral performance, on a per-mouse basis. Food and water were provided *ad libitum*. While access to water was only in the Educage, mice could engage the water port without restriction. Thus, mice were never deprived of food or water. At the beginning of each experiment, RFID-tagged mice were placed in a large home cage that was connected to the Educage. Before training, we removed the standard water bottle

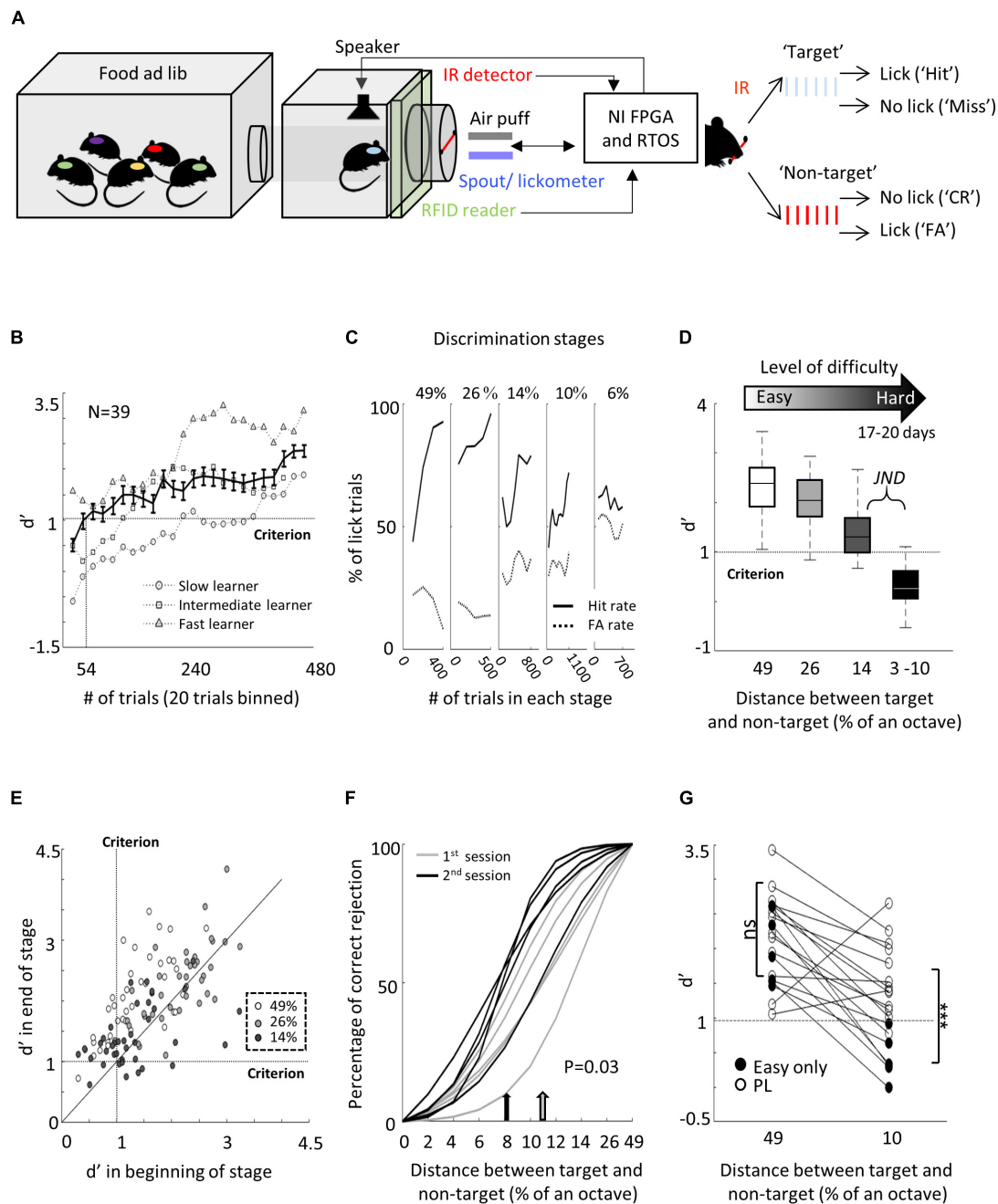


FIGURE 1 | Perceptual learning in the "Educage." **(A)** Left: Schematic design of the "Educage" system and its components. Colored ovals on the back of each mouse represent the different radio frequency identification (RFID) chip implanted prior to the experiment, which allows identification of mice individually. For high-speed data acquisition, system control, on-board sound delivery, and future flexibility, the system was designed via a field programmable gate array (FPGA) module and a real-time operating system (RTOS) module. Right: Schematic representation of the go/no-go auditory discrimination task. CR, correct rejection; FA, false alarm. **(B)** d' values of three representative mice and the population average \pm s.e.m. for the first stage of discrimination. Learning criterion is represented as dashed line ($d' = 1$). **(C)** Lick responses to the target tone (solid line) and non-target tone (dashed line) of one representative mouse along different discrimination stages. Proportions of lick responses were calculated over 100 trials/bin. This mouse improved his discrimination (hit rate went up and FA rate went down) within a stage but his discrimination deteriorated as task became more difficult. **(D)** Population average d' values for the different discrimination stages. $N = 39$ mice (mean \pm s.e.m.). Shades denote the level of difficulty (from 49% to 4–10% octave apart). **(E)** Individual d' values at the end of each level as a function of d' in the beginning of that level. Shades denote the level of difficulty. Learning criterion represented as dashed lines ($d' = 1$). **(F)** Normalized psychometric curves of five mice calculated from the first (light curves) and the second (dark curves) 14%/octave session. Light and dark arrows indicate average decision boundaries in the first and second sessions respectively (Mann-Whitney U -test on criteria: $p = 0.03$). **(G)** d' values in easy (49%/octave) and more difficult (10%/octave) discrimination stages of individual mice from the "Easy only" group (filled circles) and from the perceptual learning group (blank circles). d' values are significantly different between groups only for the hard discrimination level (Mann-Whitney U test: $***p < 0.001$).

from the home cage. Mice were free to explore the Educage and drink the water at the behavioral port. Every time a mouse entered the behavioral port, it was identified individually by the antenna and the infrared beam and a trial was initiated. Before learning, any entry to the port immediately resulted in a drop of water, but no sound was played. Following 24 h of exploration and drinking, mice were introduced for the first time to the “target” stimulus—a series of six 10-kHz pure tones (100 ms duration, 300 ms interval; 3 ms on and off linear ramps; 62 dB SPL) played every time the mouse crossed the IR beam. To be rewarded with water, mice were now required to lick the spout during the 900-ms response window. This stage of operant conditioning lasted for 2–3 days until mice performed at >70% hit rates.

We then switched the system to the first level of discrimination when mice learned to identify a non-target stimulus (a 7.1 kHz pure tone series at 62 dB SPL) from the already known target stimulus (i.e., tones separated by 49%/octave). Thus, on each trial, one of two possible stimuli were played for 2.1 s—either a target tone or a non-target tone. Mice were free to lick the water spout anytime, but for the purpose of evaluating mouse decisions, we defined a response window and counted the licking responses only within 900 ms after the sound terminated. Target tones were played at 70% probability and non-target tones were played at 30% probability, in a pseudorandom sequence. A “lick” response to a target was rewarded with a water drop (15 μ l) and considered as a “Hit” trial. A “no lick” response to a target sound was considered as a “Miss” trial. A lick response to the non-target was considered a “False Alarm” (FA) trial, which was negatively reinforced by a mild air puff (60 PSI; 600 ms) followed by a 9-s “timeout.” A “no lick” response to the non-target was considered a correct rejection (CR) and was not rewarded.

Once mice learned the easy discrimination (reached 70% correct ratio), we switched the system to the second discrimination stage. Here, we increased task difficulty by changing the non-target tone to 8.333 kHz, thus decreasing the inter tone distance to 26%/octave. In each training stage, only one pair of stimuli was presented. Then, at the following stage, the inter tone distance was further decreased to 14%/octave and then down to 6%/octave. This last transition was often done in a gradual manner ($\gg 12\%$ /octave $\gg 10\%$ /octave $\gg 8\%$ /octave $\gg 6\%$ /octave). In some of the animals ($n = 25$), we trained mice to their just noticeable difference (JND) and then changed the task back to an easier level. In order to extract psychometric curves, for some of the mice ($n = 5$), we played “catch trials” during the first and second sessions of the 14%/octave discrimination stages. In catch trials, different tones spanning the frequency range of the whole training (7–10 kHz) were presented to the animals in low probability (6% of the total number of sounds), and were neither negatively nor positively reinforced. We have recorded from 21 mice that underwent the behavioral training. Their discriminability indexes in the 49, 26, and 14% octave discrimination levels were: 2.4 ± 0.8 , 1.9 ± 0.6 , and 1.4 ± 0.5 , respectively.

For the vocalizations task, we used playback of pups’ wriggling calls (WC) as the target stimulus. These vocalizations were

recorded with a one-quarter-inch microphone (Brüel and Kjær) from P4–P5 PV \times Ai9 pups ($n = 3$), sampled at 500 kHz, and identified offline (Digidata 1322A; Molecular Devices). As the non-target stimulus, we used manipulations of the WC. During the first stage of the operant learning, mice learned to discriminate between WC and a fully reversed version of this call. Then, the second manipulation on the non-target stimulus was a gradual change of the frequency modulation (FM) of all but the last syllable in the call while leaving the temporal structure of the full call intact. To manipulate the syllable FM, we used a dynamic linear FM ramp. This operation multiplies each sampling interval within the syllable by a dynamic speeding factor, which changed according to the relative distance from the start and end of the syllable, and generated a new waveform by interpolation from the original waveform. For example, for a 0.6 speeding factor, the beginning of each syllable was slower by a factor of 0.4 while the end of each syllable accelerated by a factor of 0.4. The range of sound modulation used here was 0.66–0.9. A value of 0.66 is away from the WC; 0.9, similar to the WC; and 1, exactly the same as the WC. The basic task design for the non-target sound was as follows: Reverse $\gg 0.66 \gg 0.81 \gg 0.9$.

Surgical Procedure

Mice were anesthetized with an intraperitoneal injection of ketamine and medetomidine (0.80 and 0.65 mg/kg, respectively) and a subcutaneous injection of Carprofen (0.004 mg/g). Additionally, dextrose-saline was injected to prevent dehydration. Experiments lasted up to 8 h. The depth of anesthesia was assessed by monitoring the pinch withdrawal reflex, and ketamine/medetomidine was added to maintain it. The animal’s rectal temperature was monitored continuously and maintained at $36 \pm 1^\circ\text{C}$. For imaging and recording, a custom-made metal pin was glued to the skull using dental cement and connected to a custom stage to allow precise positioning of the head relative to the speaker (facing the right ear). The muscle overlying the left auditory cortex was removed, and a craniotomy ($\sim 2 \times 2$ mm) was performed over A1 (coordinates, 2.3 mm posterior and 4.2 mm lateral to bregma) as described previously (Stiebler et al., 1997; Cohen et al., 2011; Maor et al., 2016).

Imaging and Electrophysiology

Cell-attached recordings were obtained using targeted patch-clamp recording by a previously described procedure (Margrie et al., 2003; Cohen and Mizrahi, 2015; Maor et al., 2016). For visualization, the electrode was filled with a green fluorescent dye (Alexa Flour-488; 50 μ M). Imaging of A1 was performed using an Ultima two-photon microscope from Prairie Technologies equipped with a $16 \times$ water-immersion objective lens (0.8 numerical aperture; CF175; Nikon). Two-photon excitation at wavelength of 930 nm was used in order to visualize both the electrode, filled with Alexa Flour-488, and PV⁺ somata, labeled with tdTomato (DeepSee femtosecond laser; Spectraphysics). The recording depths of cell somata were restricted to subpial depths of 180–420 μ m, documented by the multiphoton imaging. Spike waveform analysis was performed on all recorded cells, verifying that tdTomato+ cells in L2/3 had faster/narrower

spikes relative to tdTomato-negative (tdTomato-) cells (see also Cohen and Mizrahi, 2015).

Auditory Stimuli

The auditory protocol comprised 18–24 pure tones (100 ms duration, 3 ms on and off linear ramps) logarithmically spaced between 3 and 40 kHz and presented at four sound pressure levels (72–42 dB SPLs). Each stimulus/intensity combination was presented 10–12 times at a rate of 1.4 Hz. The vocalizations protocol comprised the playback of pups' wriggling calls (WC) and three additional FM calls, presented at 62 dB SPL for 16 repetitions.

Behavioral Data Analysis

To evaluate behavioral performance, we calculated, for different time bins (normally 20 trials), Hit and FA rates, which are the probability to lick in response to the target and non-target tones, respectively. In order to compensate for the individual bias, we used a measure of discriminability from signal detection theory— d -prime (d'). d' is defined as the difference between the normal inverse cumulative distribution of the "Hit" and FA rates, $d' = z(\text{hit}) - z(\text{FA})$ (Nevin, 1969). d' for each discrimination stage was calculated based on trials from the last 33% of the indicated stage. Psychometric curves were extracted based on mouse performance in response to the catch trials. By fitting a sigmoidal function to these curves, we calculated decision boundaries as the inflection point of each curve. Detection time was calculated for each mouse individually, by determining the time in which lick patterns in the correct reject vs. the hit trials diverged (i.e., the time when significance levels crossed $p < 0.001$ in a two-sample t -test).

Data Analysis—Electrophysiology

Data analysis and statistics were performed using custom-written code in MATLAB (MathWorks). Spikes were extracted from raw voltage traces by thresholding. Spike times were then assigned to the local peaks of suprathreshold segments and rounded to the nearest millisecond. For each cell, we obtained peri-stimulus time histogram (PSTH) and determined the response window as the 100 ms following stimulus onset that evoked the maximal response integral. Only neurons that had tone-evoked response ($p < 0.05$; two sample t -test) were included in our dataset. Based on this response window, we extracted the cell's tuning curve and frequency-response area (FRA). Evoked firing rate was calculated as the average response to all frequencies that evoked a significant response. Firing rate in the training band was calculated as the response to frequencies inside the training band (7–10 kHz), averaged across all intensities. Best frequency (BF) of each cell was determined as the tone frequency that elicited the strongest responses averaged across all intensities. The selectivity of the cell is the % of all frequency-intensity combinations that evoked significant response (determined by a two-sample t -test followed by Bonferroni correction). Pairwise signal correlations (r_{sc}) were calculated as Pearson correlation between FRA's matrices of neighboring cells ($<250 \mu\text{m}$ apart; Maor et al., 2016). The spontaneous firing rate of the cell was calculated based on the 100 ms preceding each stimulus presentation. Response latency

is the time point after stimulus onset at which the average spike count reached maximum.

Statistical Model Based on the Independent Basis Functions (IBF) Method

Since the measured responses before and after learning are not from the same cells, we cannot estimate the changes of individual tuning curves due to learning. Instead, we must rely on estimated learning-induced changes in the *ensemble* of single-neuron responses. Our goal, therefore, was to build a statistical model of single-neuron tuning curves before and after learning. The models were based on the statistics of each experimental group separately and used to estimate the learning-induced changes in the population of responses in each condition. Furthermore, we used this model as a generative model that allowed us to generate a large number of "model neurons" with statistically similar response properties as the measured ones.

In principle, one could use a parametric model, by fitting each observed tuning curve to a specific shape of functions (e.g., Gaussian tuning curves). However, since the tuning curves of neurons to tone frequencies do not have symmetric "Gaussian" shapes, and some are bimodal, fitting them to a parametric model has not been successful. Instead, we chose to model each single neuron response as a weighted sum of a small set of orthogonal basis functions.

$$r_i(f) = \sum_{l=1}^K a_{il}^i g_l(f) \quad (1)$$

Here, $r_i(f)$ is the firing rate (i.e., the trial-averaged spike count) of the i th neuron in response to the stimulus with frequency f ; K is the number of orthogonal basis functions denoted by $g_l(f)$ (dependencies in f are in log scale). In order to determine the basis functions and the coefficients, a_{il}^i , we performed singular value decomposition (SVD) of the matrix of the measured neuronal firing rates for the 18 values of f . Our model (1) uses a subset of the K modes with the largest singular values (the determination of K is described below). The SVD yields the coefficients $a_{il, data}^i$ for the N observed neurons and (2) smoothes the resultant SVD f -dependent vectors using a simple "moving average" technique to generate the basis functions, $g_l(f)$. (3) Importantly, to use the SVD as a generative model, for each l , we compute the histogram of the N $a_{il, data}^i$ coefficients. To generate "new neurons," we sample each coefficient independently from the corresponding histogram. In other words, we approximate the joint distribution of the coefficients by a factorized distribution. This allowed us to explore the effect of changing the number of neurons that downstream decoders use in order to perform the perceptual task.

Model (1) describes the variability of the population responses to the stimulus, in terms of tuning curves of the trial averages firing rates. Additional variability in the data is the single trial spike count. We model these as independent Poisson random variables with means given by $r_i(f)$. Since neurons are not simultaneously recorded, we do not include noise correlations in the model. We performed this procedure for the *naïve*

and *expert* measured responses separately, so that both the basis functions and the coefficient histograms are evaluated for the two conditions separately. Note that we do not make Gaussian assumptions about the coefficient histograms. In fact, the observed histograms are in general far from Gaussian.

The Choice of Number of Basis Functions

Due to a limited number of trials that we sampled for each neuron, taking a large value of K can result in overfitting the model to the noise caused by the finite number of trials. To estimate the optimal number of basis functions, we evaluated the percentage of response firing rate variability of the population (i.e., the fraction of the sum of the squared SVD eigenvalues) as a function of K . We also evaluated the parameters of model (1) based on a subset of trials and checked how well it accounts for the observed tuning curves that are calculated from the test trials. We took K that produces the smallest test error and saturated the fractional variance.

We used model (1) with the above choice of K in order to evaluate the discrimination ability of the population of A1 neurons, by creating an *ensemble* of single-neuron responses for the naïve and expert conditions. To generate the model neurons, we sampled the coefficients of the basis function independently from the corresponding histogram of the measured neurons and used these neurons for the calculations depicted below.

Fisher Information

We calculated the Fisher Information (FI) for each condition (naïve vs. expert) using our model (1). FI measure bounds the mean squared error of an (unbiased) estimator of the stimulus from the noisy single trial neuronal responses. When the neuronal population is large (and they are noise-independent) FI also determines the discriminability d' of a maximum likelihood discriminator between two nearby values of the stimulus (Seung and Sompolinsky, 1993). Under the above Poisson assumption, the FI for the i th neuron is equal to $I_i = \frac{r'_i(f)^2}{r_i(f)}$, where $r'_i(f)$ is the derivative of the firing rate with respect to the stimulus value f . The total FI is the sum of the FIs of individual neurons (Seung and Sompolinsky, 1993). This has been evaluated in both naïve and expert conditions. Note that the FI are functions of the stimulus value f , around which the discrimination task is performed.

Discrimination by Linear Readout

We applied a linear decoder to assess the ability to discriminate between nearby stimuli on the basis of the neuronal population responses. We trained a support vector machine (SVM) with a linear kernel, which finds an “optimal” linear classifier that discriminates between two nearby frequencies on the basis of single-trial vectors of spike counts generated with our generative model (1) and Poisson variability. We then evaluated the probability of classification errors to test trials, in both naïve and expert conditions. Since our training set is not linearly separable, we used SVM with slack variables (Vapnik, 1998), which incorporates a “soft” cost for classification errors. Each classification was iterated a maximum 500 times (or until

converged). In each iteration, 16 trials were used for training the classifier and four trials were used to test the decoder accuracy. Classification performance of the decoder was tested separately for discrimination between nearby frequencies which lay inside the training band or near the training band (0.4396 octave apart).

Data Analysis—Vocalization Responses

Similarity of response to different vocalizations was calculated as Pearson correlation between the PSTHs of the different stimuli. To quantify lifetime sparseness, we used the following measure: $S = (1 - [(\sum r_i/n)2/\sum (r_i^2/n)])/[1 - (1/n)]$, where r_i is the response to the i th syllable in the original vocalization (averaged across trials) and n is the number of syllables. Values of S near 0% indicate a dense code, and values near 100% indicate a sparse code (Vinje and Gallant, 2000). Population sparseness was calculated as 100—the percent of cells that evoked a significant response to each syllable in the call (Willmore and Tolhurst, 2001). Classification of vocalization identity based on population activity was determined using the SVM decoder with a linear kernel and slack variables. The decoder was tested for its accuracy to differentiate between responses to two different vocalizations. The input to the SVM consisted of the spike count of each neuron in the syllable response window. The same number of neurons (37) was used in both groups to avoid biases. We then evaluated the probability of classification errors to test trials, using leave-one-out cross-validation. Each classification was iterated 1000 times. In each iteration, 15 trials were used for training the classifier and one trial was used to test decoder accuracy. The number of syllables utilized in the decoder was increased cumulatively.

Statistical Analysis

All statistical analysis was performed with MATLAB (Mathworks). Rank-sum test was used for comparison unless otherwise noted. In cases where the same data sample was used for multiple comparisons, we used the Holm-Bonferroni correction to adjust for the increased probability of Type I error. Statistical significance was defined as $p < 0.05$.

Code Accessibility

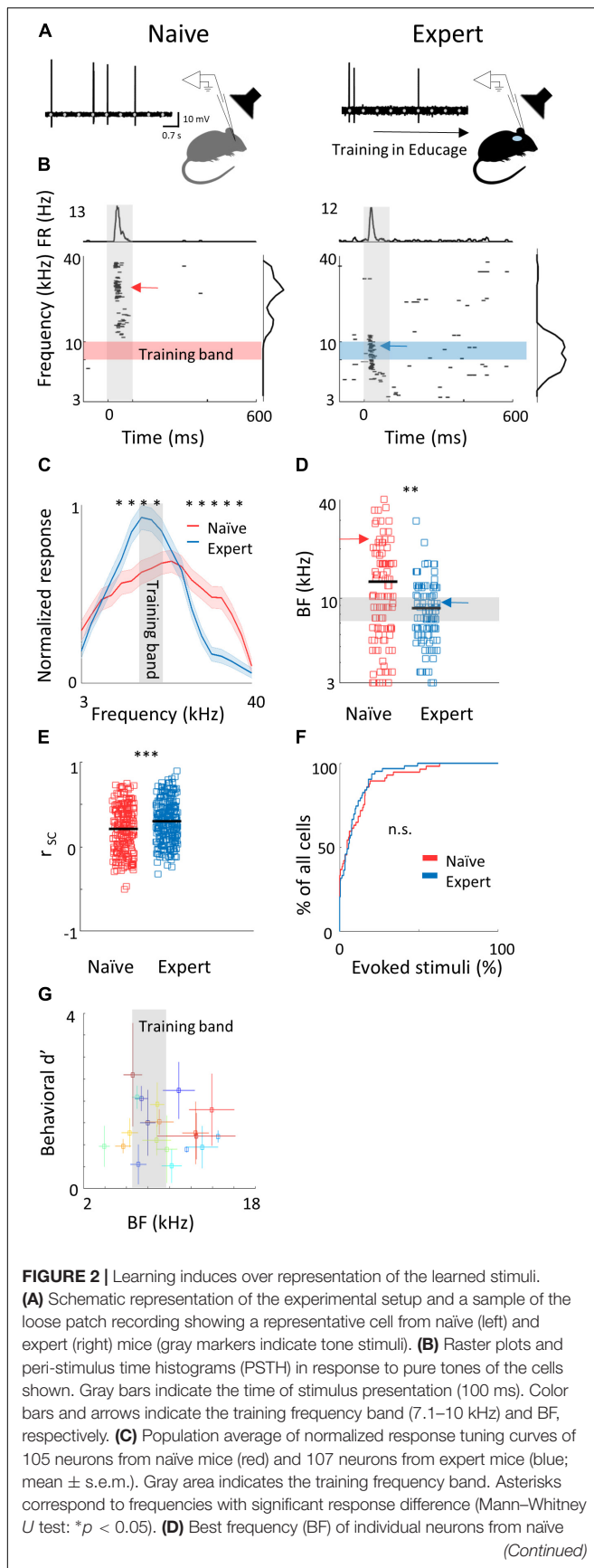
All software and hardware design for the Educage system are available for download at <https://github.com/MizrahiTeam/Educage>.

Codes used for data analysis are available from the corresponding author upon request.

RESULTS

Behavior—Discrimination of Pure Tones

To study perceptual learning in mice, we developed a behavioral platform named the “Educage” (all software and hardware design are freely available for download at <https://github.com/MizrahiTeam/Educage>). The Educage is an automated home-cage training apparatus designed to be used simultaneously with several mice (up to 8 animals). One advantage of the Educage over other procedures is that human interference is brought

**FIGURE 2 |** Continued

mice (red markers) and expert mice (blue markers; Mann–Whitney U test: $**p < 0.01$). Arrows indicate the neurons shown in **(B)**. **(E)** Pairwise signal correlations (r_{sc}) values between all neighboring neuronal pairs in naive (red) and expert (blue) mice. Neurons in expert mice have higher r_{sc} (Mann–Whitney U test: $***p < 0.001$). **(F)** Cumulative distribution of response selectivity in naive (red) and expert (blue) mice. Response selectivity was determined as the % of all frequency–intensity combinations that evoked a significant response. Distributions are not significantly different (Kolmogorov–Smirnov test; $p = 0.69$). **(G)** Mean BF of the neurons recorded in each mouse and its behavioral d' (during the 14% octave discrimination) shows no clear pattern of change with respect to mouse performance (mean \pm std across trials; $r^2 = -0.05$, $p = 0.7$).

to minimum and training efficiency increases. The “Educage” is a small modular chamber ($10 \times 10 \times 10$ cm), opening on one end into a standard animal home cage where mice can enter and exit freely (Figure 1A). On its other end, the chamber contains the hardware that drives the system, hardware for identifying mice and measuring behavioral performance (Figure 1A and Supplementary Figure 1, see section “Materials and Methods”). Mice were free to engage the behavioral port at their own will, where they consume all of their water intake. Following habituation, mice were trained on a go/no-go auditory discrimination task to lick in response to a target tone (a series of 10 kHz pure tones) and withhold licking in response to the non-target tone. A “lick” response to a target was rewarded with a water drop ($15 \mu\text{l}$) and considered as a “Hit” trial. A “no lick” response to a target sound was considered as a “Miss” trial. A lick response to the non-target was considered a “False Alarm” (FA) trial, which was negatively reinforced by a mild air puff (60 PSI; 600 ms) followed by a 9-s “timeout.” A “no lick” response to the non-target was considered a correct rejection (CR) and was not rewarded (Figure 1A). On average, mice performed 327 ± 71 trials per day, mainly during dark hours (Supplementary Figure 1b).

The initial level of learning was to identify a non-target stimulus (a series of 7.1 kHz pure tones) from the 10 kHz target stimulus (Figure 1A right and Supplementary Movie 1). These stimuli are separated by 49% of an octave and are perceptually easily separated by mice. Discrimination performances were evaluated using d' —a measure that is invariant to individual bias (Nevin, 1969). Despite the simplicity of the task, behavioral performance varied widely between mice (Figure 1B and Supplementary Figure 1c). On average, it took mice 54 ± 38 trials to cross our criterion of learning, which was set arbitrarily at $d' = 1$ (Figure 1B; dotted line), and gradually increased to plateau at $d' = 2.35 \pm 0.64$ (Figure 1D). To extend the task to more challenging levels, we gradually increased task difficulty by changing the non-target tone closer to the target tone. The target tone remained constant at 10 kHz throughout the experiment and only the non-target stimulus changed. The lowest distance used between target and non-target was 3%/octave (9.6 kHz vs. 10 kHz). A representative example from one mouse’s performance in the Educage throughout a complete experiment is shown in Figure 1C. The JND for each mouse was determined when mice could no longer discriminate (e.g., the

JND of the mouse shown in **Figure 1C** was determined between 6 and 10%/octave). The range of JNDs was 3–14%/octave and averaged $8.6 \pm 4.7\%$ /octave. These values of JND are typical for frequency discrimination in mice (Ehret, 1975; de Hoz and Nelken, 2014). Most mice improved their performance with training (**Figures 1E,F**), showing improved perceptual abilities along the task. The duration to reach JND varied as well, ranging 3069 ± 1099 trials (14 ± 3 days). Detection times, defined as the time in which lick patterns in the correct reject trials diverged from the lick patterns of the hit trials, increased monotonically by ~ 177 ms for each step of task difficulty, demonstrating the increased perceptual load during the harder tasks (**Supplementary Figure 1d**).

To show that gradual training is necessary for perceptual learning (Ahissar and Hochstein, 2004; Ericsson, 2006; Kurt and Ehret, 2010), we trained groups of littermate mice on different protocols simultaneously. In one group of mice, we used a standard protocol and the animals were trained on the gradually increasing task difficulty described above. Simultaneously, in the second group of mice—termed “easy only”—animals were trained continuously on the easy task. Although both groups of mice trained together, only the mice that underwent gradual training were able to perform the hard task (**Figure 1G**). Taking together, these data demonstrate the efficiency of the Educage to train groups of mice to become experts in discriminating between a narrowband of frequencies in a relatively short time and with minimal human intervention.

Representation of Pure Tones in L2/3 Neurons Following Perceptual Learning

To evaluate cortical plasticity following perceptual learning, we compared how pure tones are represented in A1 of expert mice, trained to discriminate between narrowband frequencies, and age-matched naive mice who were never introduced to these sounds. We used *in vivo* loose patch recording of L2/3 neurons in anesthetized mice to record tone-evoked spiking activity in response to 3–40 kHz pure tones (**Figures 2A,B** and **Table 1**). We targeted our recording electrode to the center of A1 based on previously validated stereotactic coordinates (Maor et al., 2016). Response latencies further support that our recordings are from primary auditory cortex (range of minimal latencies: 20–44 ms; mean \pm sd: 30 ± 6 ms). Loose patch recording enables superb spatial resolution, is not biased to specific cell types, and has high signal-to-noise ratio for spike detection. However, one

caveat of this technique is a potential bias of recording sites along the tonotopic axis. In order to overcome it, we measured from neurons in a large number of animals, such that possible biases are likely averaged out. In naive mice, responses were highly heterogeneous, with best frequencies covering a significant frequency range, as expected from the heterogeneous functional microarchitecture of L2/3 neurons in A1 (**Figures 2C,D**; $n = 105$ neurons, $n = 22$ mice, red). In expert mice, best frequencies of tuning curves were biased toward the frequencies that were presented during learning (**Figures 2C,D**; $n = 107$ neurons, $n = 20$ mice, blue). These data show, as expected from previous literature, that learned frequencies in A1 become overrepresented at least as measured by the neuron's best frequency (BF). We next showed that this overrepresentation was specific to the learned tone by training mice on 4 kHz as the target tone and recording neurons in a similar manner to the abovementioned experiment. Indeed, L2/3 neurons in A1 of mice training on 4 kHz showed BF shifts toward 4 kHz (**Supplementary Figure 2a**). These results are largely consistent with previous studies in monkeys, cats, rats, and gerbils (reviewed in Irvine, 2017), extending this phenomenon of learning-induced changes in tuning curves to the mouse, to L2/3 neurons and to local circuits.

To study neuronal changes further, we analyzed response dynamics. Temporal responses to the trained frequencies were only slightly different between naive and expert mice. Specifically, average spiking responses were slightly but significantly faster and stronger in experts (**Supplementary Figure 2b** and **Table 1**). In addition, we recorded the responses to pure tones at different intensities and constructed frequency response areas (**Supplementary Figure 2c**). The average pairwise signal correlation of neighboring neurons, calculated from these frequency response areas, was high in naive mice (0.2 ± 0.28) but even higher in experts (0.3 ± 0.24 ; **Figure 2E**). Notably, the increased signal correlation was not an artifact of differences in response properties between naive and expert group (**Supplementary Figure 2d**) but reflected true similarity in receptive fields (**Supplementary Figure 2e**). Thus, the basal level of functional heterogeneity in A1 (Bandyopadhyay et al., 2010; Rothschild et al., 2010; Maor et al., 2016) is reduced following learning. This learning-induced increase in functional homogeneity of the local circuit, emphasizes the kind of shift that local circuits undergo. Since neurons in expert mice did not have wider response areas (**Figure 2F** and **Table 1**), our data suggests that neurons shifted their response properties toward the learned tones at the expense of frequencies outside the training band.

TABLE 1 | Learning-induced physiological changes.

Group	Animals (n)	Cells (n)	BF (kHz)	Spontaneous spike rate (Hz)	Evoked firing rate in BF (Hz)	FR in T.B. (Hz)	Response latency (ms)	Selectivity (% of all stimuli)	“Lifetime sparseness” (%)
Naive	22	105	11.3 ± 8.4	0.45 ± 0.58	15.5 ± 5.3	3.4 ± 5	35.2 ± 8.7	9.7 ± 13.9	88 ± 1
Expert	20	107	8.6 ± 4	0.59 ± 0.65	13.2 ± 3.4	4.2 ± 4	32.6 ± 9.7	8.5 ± 9.9	88 ± 1
Rank-sum test			0.004	0.06	0.01	0.02	0.007	0.58	0.35

A summary table of the complete dataset of recordings from excitatory neurons in naive and expert mice after perceptual learning of pure tones. Columns show different parameters of the dataset or property tested. The third row shows the statistical *p*-value between naive and experts using a Mann–Whitney *U* test. T.B., Training Band.

Finally, the representation of sounds by the neuronal population was not clearly related to behavioral performance of individual mice (**Figure 2G**), raising the possibility that changes in BF are not necessarily related to better performance. Alternatively, the full breadth of the tuning curve is not faithfully reflected in the BF alone and a more detailed analysis of the tuning curves is necessary.

A Generative Model of A1 Population Responses to Pure Tones

To what extent does overrepresentation of a learned stimulus sub-serve better discrimination by the neural population? To answer this question, we built a statistical model of tuning curves of neurons in A1 using six basis functions (**Supplementary Figures 3a–f**) that correspond to the six largest SVD vectors of the population responses (IBF method; see section Materials and Methods). In **Figure 3A**, we show two representative examples of tuning curves and their reconstruction by our model. In contrast to Gaussian fits used previously (Vapnik, 1998; Briguglio et al., 2018), our model captures the salient features of the shape of the auditory tuning curves (asymmetry, multimodality), yet also smoothed the *raw* response vectors to reduce overfitting due to finite sampling.

In order to choose the appropriate number of basis functions, we determined the minimal number of basis functions that achieves good performance in reconstructing test single trial responses. In **Figure 3B**, we show the fraction of explained variance as a function of the number of basis functions, K . For both the naïve and expert groups, the explained variance reaches above 96% after five basis functions. **Figure 3C** shows the mean square error (MSE) on the unseen trials as a function of K in data from both the naïve and expert animals. The MSE exhibits a broad minimum for K in a range between 6 and 13. Interestingly, both naïve and experts achieve roughly the same MSE values, although for experts, the MSE values at both low and large values of K are considerably larger than that of the naïve. Taken together, we conclude that for these conditions, six basis functions are the appropriate number and we used this value for our calculations.

Based on the IBF method described above, we generated a population of tuning curves (500 “new neurons”) and estimated their total FI (see section Materials and Methods). **Figure 3D** shows the FI as a function of the stimulus f for both the naïve and expert conditions. Surprisingly, the FI of the neurons from expert animals was enhanced relative to the naïve group, but only for stimuli at both flanks of the training band. Importantly, the FI within the band of the trained frequencies remained unchanged (**Figure 3D**, within the black lines). The same result holds true for a performance of a SVM classifier. Using SVM to separate any two frequencies that are 0.2198 octave apart, discriminability (d') values derived from the classifier's error show similar results to the FI (**Figure 3E**; Seung and Sompolinsky, 1993). The value of d' is larger in the expert groups as compared to the naïve but only outside the training band, whereas within the band, discriminability is not improved (or even slightly compromised).

The results shown in **Figure 3** do not change qualitatively if we use our SVD model for the recorded neurons, as opposed

to newly modeled neurons, nor if we compute discriminability index directly from the neuronal firing rates (**Supplementary Figure 3g**). One advantage of having a generative model for the population responses is that we can generate an unlimited number of trials and tuning curves. We took advantage of this to explore whether the results of the FI and SVM change with population size. To answer this question, we evaluated the mean discrimination performance (over test neurons) as a function of the number of sampled cells, N , which increases as expected. Consistent with the results of the SVM, the performances in the naïve and expert groups are similar with slight tendency for a higher accuracy in the naïve population at large N s (**Figure 3F**). In contrast, for frequencies near the training band, the accuracy is substantially larger in the expert than in the naïve group for virtually all N (**Figure 3G**). Thus, it seems that learning-induced changes in tuning curves do not improve discriminability of the learned stimuli.

Perceptual Learning of Natural Sounds

Natural sounds are characterized by rich spectro-temporal structures with frequency and amplitude modulations over time (Mizrahi et al., 2014). Discrimination of such complex stimuli could be different from that of pure tones. Thus, we next designed a task similar to that with the pure tones but using mouse vocalizations as the training stimuli. We used playback of pups' wriggling calls (WC) as the target stimulus (**Figure 4A**, top). As the non-target stimuli, we used frequency modulations of the WC, a manipulation that allowed us to morph one stimulus to another by a continuous metric (**Figure 4A**). The range of sound modulation used here was indexed as a “speeding factor” (see section “Materials and Methods” for details). In short, a modulation factor of 0.66 affected the original WC more than a modulation factor of 0.9 did, and is therefore easier to discriminate (**Figure 4B**). To reach perceptual limits, we trained mice gradually, starting with an easy version of the task (WC vs. a temporally reversed version of the WC) and then gradually to modulated calls starting at 0.66 modulation. Once mice reached $> 80\%$ hit rates, we changed the non-target stimulus to more difficult stimuli until mice could no longer discriminate (**Figure 4C**). Mice ($n = 9$) learned the easy task, i.e., discriminating WC from a 0.66 modulated call, with average d' values of 2.5 ± 0.4 (**Figure 4D**). On average, mice could only barely discriminate between a WC and its 0.9 modulation (d' at 0.9 was 1 ± 0.8 ; **Figure 4D**). While these discrimination values were comparable to the performance of pure tones, detection times were substantially slower (**Supplementary Figure 4a**). For similar d' values, discriminating between the vocalizations took 300–1000 ms longer as compared to the pure tone tasks (**Figure 4E**). In addition, learning curves were slower for the vocalization task as compared to the pure tones task. The average number of trials to reach $d' = 1$ for vocalizations was 195 trials, more than three times longer as compared with pure tones (compare **Supplementary Figure 4b** and **Figure 1B**, respectively). These differences may arise from the difference in the delay, inter-syllable interval, and temporal modulation of each stimulus type, which we did not further explore. Taken together, these behavioral results demonstrate a

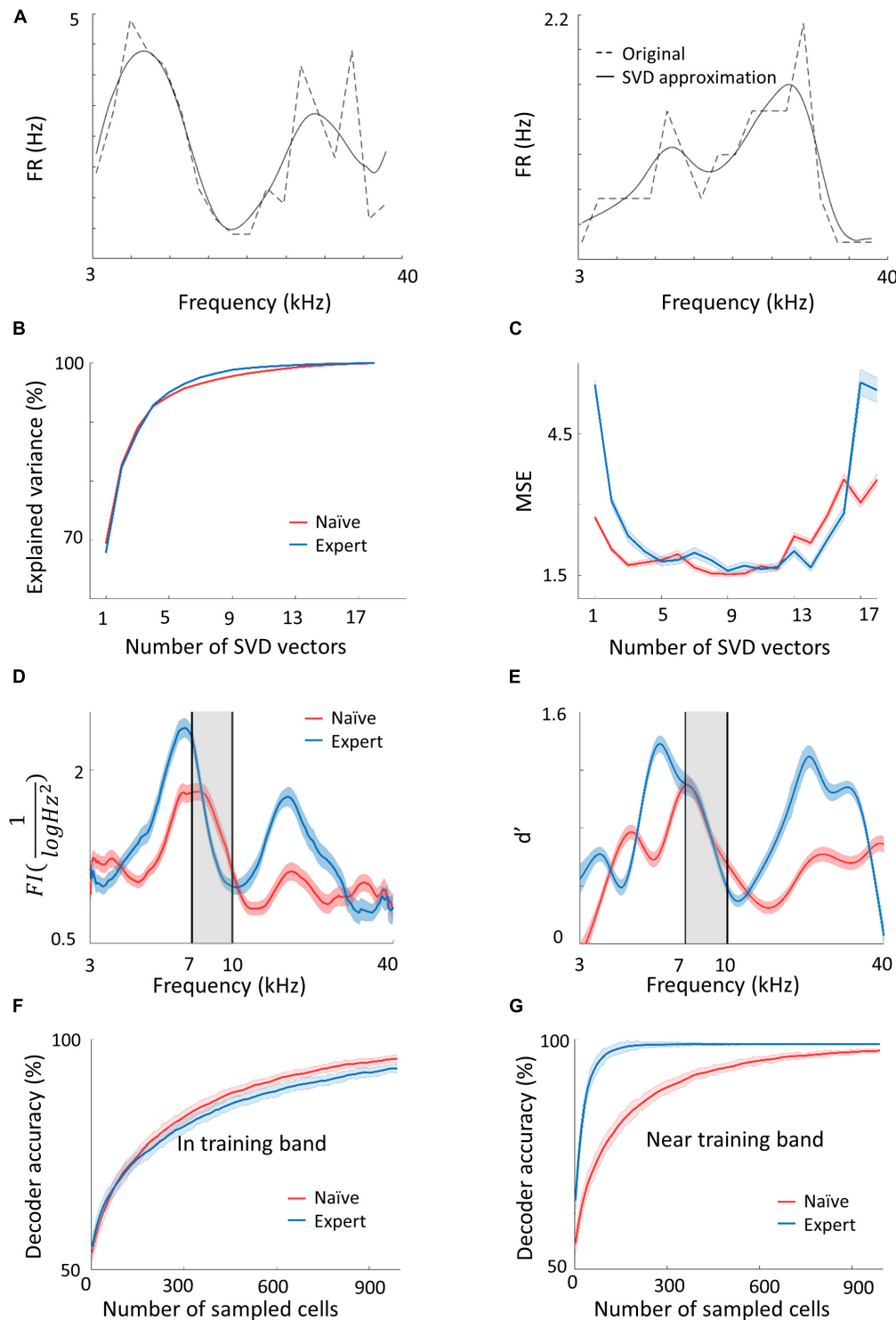


FIGURE 3 | Plasticity in A1 does not improve the discrimination of the learned tones. **(A)** Two representative examples of tuning curves of neurons recorded in A1. Average spike rates and the SVD approximation of the particular curves are shown in dashed and solid lines respectively. Note that although the SVD approximation is smooth, it captures the irregular dynamics (i.e., non-Gaussian) of the tuning curves. **(B,C)** The explained variance and error as a measure of the number of SVD vectors used in the model. **(D)** Fisher Information calculated from the tuning curves of both populations along the frequency dimension. Note the increased FI for the expert neurons in the flanks of the training band but not within it (gray band). **(E)** Discriminability (d') of SVM decoder along the range of frequencies. Pairwise comparison along the continuum is performed for frequencies 0.2198 octave apart. In accordance with d' , the decoder does not perform better in the training band (gray shade). **(F,G)** Classification performance of the decoder as a function of the number of neurons in the model. In the training band **(F)**, the performance is similar for both naïve and expert mice. Outside the training band (0.4396 octave apart; **G**) performance improved rapidly in the expert mice.

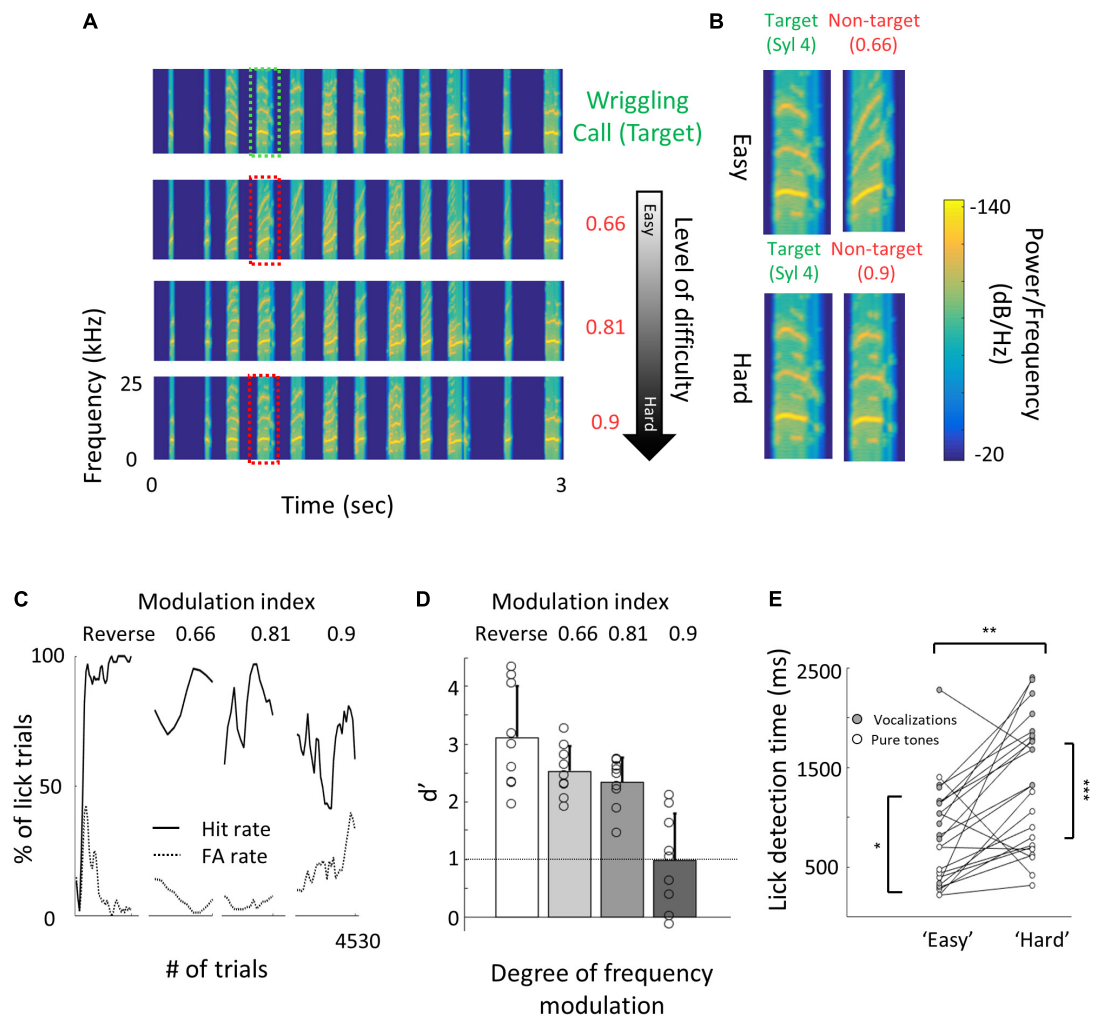


FIGURE 4 | Perceptual learning of vocalizations. **(A)** Spectrograms of the wriggling call (WC, “target” stimulus, top panel) and the manipulated WC’s (“non-target” stimuli, bottom panels). **(B)** Enlargement of the spectrogram’s 4th syllable of the target WC and the manipulated calls. Top, a large manipulation (speeding factor, 0.66), which is perceptually easy to discriminate from the WC. Bottom, a minor manipulation (speeding factor, 0.9), which is perceptually closer to the WC. **(C)** Lick responses to the target tone (solid line) and non-target tone (dashed line), binned over 50 trials, of one representative mouse along the different discrimination stages. The task of the first stage was to discriminate between WC vs. reversed playback of the call (“Reverse”). The following stages are different degrees of call modulation. Titles correspond to the speeding factors used for the non-target stimulus. **(D)** Population average d' values for the different discrimination levels. $N = 9$ mice (mean \pm s.e.m). Shades denote the level of difficulty. **(E)** Comparison between detection times during the easy and difficult stages of pure tone (blank circles) and vocalizations (filled circles) discrimination tasks. Detection times are significantly different between all groups (Mann–Whitney U test: * $p < 0.05$, ** $p < 0.01$, *** $p < 0.001$).

gradual increase in perceptual difficulty using a manipulation of a natural sound.

Sparser Response in L2/3 Neurons Following Perceptual Learning of Natural Sounds

To study the neural correlates in A1 that follow natural sound discrimination, we recorded L2/3 neurons in response to the learned stimuli (**Figure 5A**), expecting increased representation of these particular stimuli (e.g., that more neurons will respond to the calls or that firing rates will increase). Surprisingly, we did not find an increase in the representation of the

learned stimuli. The fraction of cells responding to the trained vocalization remained constant (**Supplementary Figure 5a**) as well as the evoked firing rate for the preferred vocalization or the preferred syllable within a vocalization (**Table 2**). Instead, representation in expert mice became sparser. Here, we measured the “lifetime sparseness” (Vinje and Gallant, 2000; Willmore and Tolhurst, 2001) of each neuron to determine how selective its responses is to a given syllable. Sparse representation can be a result of having a smaller fraction of neurons responding to a given stimulus and/or a decrease responsiveness in the call. We found that the population of neurons in expert mice were sparser (**Figure 5B**; Naïve: $45\% \pm 20\%$; Expert: $64\% \pm 15\%$; $p < 0.001$), even

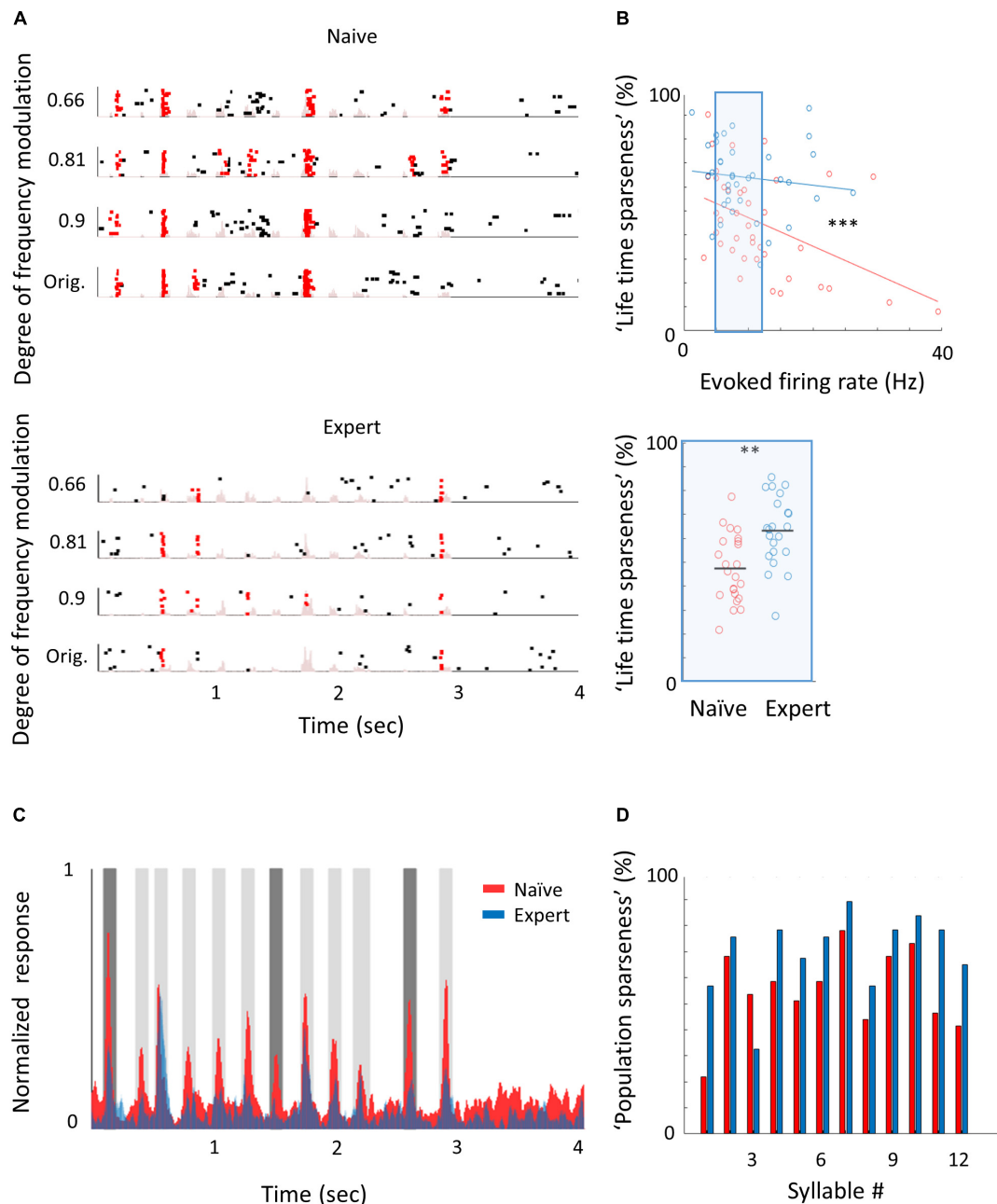


FIGURE 5 | Learning complex sounds induces “sparsening.” **(A)** Representative examples of raster plots in response to 4 modulated wriggling calls from naïve (top) and expert (bottom) mice. Red lines indicate spikes in response windows that are significantly above baseline. The stimulus power spectrum shown in light pink in the background. **(B)** Top: Scatter plot of “lifetime sparseness” (along the vocalization, see methods) and evoked firing rate for individual neurons from naïve (red circles) and expert (blue circles) mice. Sparseness is significantly higher in the expert group (Mann–Whitney U test; *** $p < 0.001$). The middle range of firing rate distribution (0.5 SD below and above the median) is indicated as a blue rectangle. Bottom: Lifetime sparseness for all cells from the middle range of the distribution shows significant difference between the groups (Mann–Whitney U test; ** $p = 0.001$). **(C)** Average normalized PSTHs calculated from all neurons in response to the original WC. Data are shown overlaid for naïve (red) and expert (blue) mice. In expert mice, only syllables 1, 7, and 11 evoked significantly weaker responses as compared to naïve mice (dark gray bars, Mann–Whitney U test followed by Bonferroni correction; $p = 0.03, 0.001, 0.03$). **(D)** Population sparseness (% of cells that evoked a significant evoked response to a given syllable) of all neurons in naïve (red) and expert (blue) for the different syllables in the call.

regardless of their evoked firing rate (**Figure 5B**; Naïve: $47\% \pm 14\%$; Expert: $63\% \pm 15\%$; $p = 0.001$). Increased sparseness was not apparent following pure tone learning (**Table 1**). Sparseness was also evident from the average population

response to the vocalization (**Figure 5C**). Nearly all syllables had weaker responses, three of which were statistically weaker (**Figure 5C**, dark gray bars). Moreover, the population sparseness (Willmore and Tolhurst, 2001), derived from the fraction of

TABLE 2 | Vocalization learning-induced physiological changes.

Group	Animals (n)	Cells (n)	Spontaneous firing rate (Hz)	Evoked firing rate (Hz)	Response latency (ms)	Response selectivity (% of evoked stimuli)	Fano-Factor
Naïve	8	41	1.8 ± 2.9	7.7 ± 5.9	36 ± 11	25.5 ± 21.6	1 ± 0.45
Expert	6	37	0.78 ± 0.74	6.7 ± 3.6	43 ± 13	15.4 ± 11	1.1 ± 0.35
Rank-sum test			$p = 0.1$	$p = 0.6$	$p = 0.02$	$p = 0.05$	$p = 0.12$

A summary table of the complete dataset of recordings from excitatory neurons in naïve and expert mice after perceptual learning of vocalizations. Columns show different parameters of the dataset or property tested. The third row shows the statistical p -value between naïve and experts using a Mann–Whitney U test.

active neurons at any time, was higher in expert animals for almost all syllables in the call (**Figure 5D**; Naïve: $55 \pm 16\%$; Expert: $70 \pm 15\%$; $p = 0.026$). Notably, the smaller fraction of responses was not just an apparent sparseness due to increase in trial-to-trial variability, as reliability of responses by neurons in the expert group remained similar to reliability of responses in the naïve group (**Table 2**). Thus, “sparsening” of A1 responses is a main feature of plasticity following learning to discriminate complex sounds.

We next asked whether the “sparsening” described above bears more information to the learned stimulus. We analyzed population responses by including all neurons from all mice as if they are a single population (naïve: $n = 41$ neurons from 8 mice; expert: $n = 37$ neurons from 6 mice). We calculated the Pearson correlation of the population response to all responses in a pairwise manner (**Figure 6A** and **Supplementary Figure 5b**). As compared to naïve mice, the absolute levels of correlations in expert mice were significantly lower for nearly all pairs of comparisons (**Figure 6A**, asterisks). As expected, weaker modulations of the call and, hence, high similarity among stimuli, were expressed as higher correlations in the neuronal responses (**Figure 6B**). The pairs of stimuli that mice successfully discriminated in the behavior (0.66 vs. the original WC and 0.81 vs. the original WC) had significantly lower correlation in the expert mice (**Figure 6B**, rank sum test, $p < 0.05$). Responses to the more similar stimuli that were near perceptual thresholds (i.e., 0.9 vs. the original WC) were lower in expert mice, but not significantly (**Figure 6B**, rank sum test, $p > 0.05$). This reduced correlation suggested that plasticity in A1 supports better discrimination among the learned natural stimuli. Indeed, a SVM decoder performed consistently better in expert mice, discriminating more accurately the original WC from the manipulated ones (**Figure 6C**). As expected, the decoder performance monotonically increased when utilizing the responses to more syllables in the call. However, in the expert mice, performances reached a plateau already halfway through the call, suggesting that neuronal responses to the late part of the call carried no additional information useful for discrimination. Similarly, the correlation of the population responses along the call shows that responses were separated already following the first syllable, but that the lowest level of the correlation was in the 5th to 7th syllable range, which then rapidly recovered by the end of the call (**Supplementary Figure 5c**). These findings are also consistent with the behavioral performance of the mice as decisions are made within the first 1.5 s of the trial (corresponding to the first seven syllables of the call).

Specifically, the head of the mouse is often retracted by the time the late syllables are played (**Figure 4E**). Taken together, “sparser” responses improve neural discrimination of learned natural sounds.

Learning-Induced Plasticity of Parvalbumin Neurons

The mechanisms responsible for the learning-induced changes are currently unknown. We used mouse genetics and two-photon targeted patch to ask whether local inhibitory neurons could contribute to the observed plasticity we describe above. To this end, we focused only on parvalbumin inhibitory (PV⁺) interneurons as they are the most abundant inhibitory cell type with the strongest direct silencing effect on pyramidal cells (Avermann et al., 2012; Hu et al., 2014). In addition, recent evidence points to their role in a variety of learning-related plasticity processes (Letzkus et al., 2011; Wolff et al., 2014; Kaplan et al., 2016; Lagler et al., 2016; Goel et al., 2017; Lee et al., 2017). Here, we probe the role of inhibition in perceptual learning by measuring learning-induced plasticity in the response properties of the PV⁺ neurons. We trained PV⁺-Cre x Ai9 mice (i.e., mice with PV⁺ neurons expressing tdTomato) in the Educage and then patched single neurons under visual guidance (**Figure 7A**; Cohen and Mizrahi, 2015; Maor et al., 2016). In order to increase the sample of PV⁺ neurons, we used targeted patch and often patched both PV⁺ and PV[−] neurons in the same mice. PV[−] neurons were used as proxy for excitatory neurons (these neurons were also included in the analysis shown in **Figures 2–6**). All the TdTomato⁺ neurons that we patched were also verified as having a fast spike shape (**Figure 7A**), a well-established electrophysiological signature of PV⁺ cells, while PV[−] neurons verified as having regular spike shape. PV⁺ neurons had response properties different from PV[−] neurons in accordance with our previous work (Maor et al., 2016). For example, PV⁺ neuron responses were stronger and faster to both pure tones and natural sounds (**Figures 7B,C** and **Table 3**; see also Maor et al., 2016).

Following pure tone learning, PV⁺ neurons also changed their response profile. On average, the BF of PV⁺ neurons shifted toward the learned frequencies, similar to what we described for PV[−] neurons (**Figures 8A,B**). This result is consistent with recent evidence from the visual cortex showing increased selectivity of PV⁺ to trained stimuli following learning (Khan et al., 2018). The shift in tuning curves of PV⁺ neurons was also accompanied by a significant widening of their receptive fields, unlike the PV[−] population (**Supplementary Figure 6a**). When we compared the

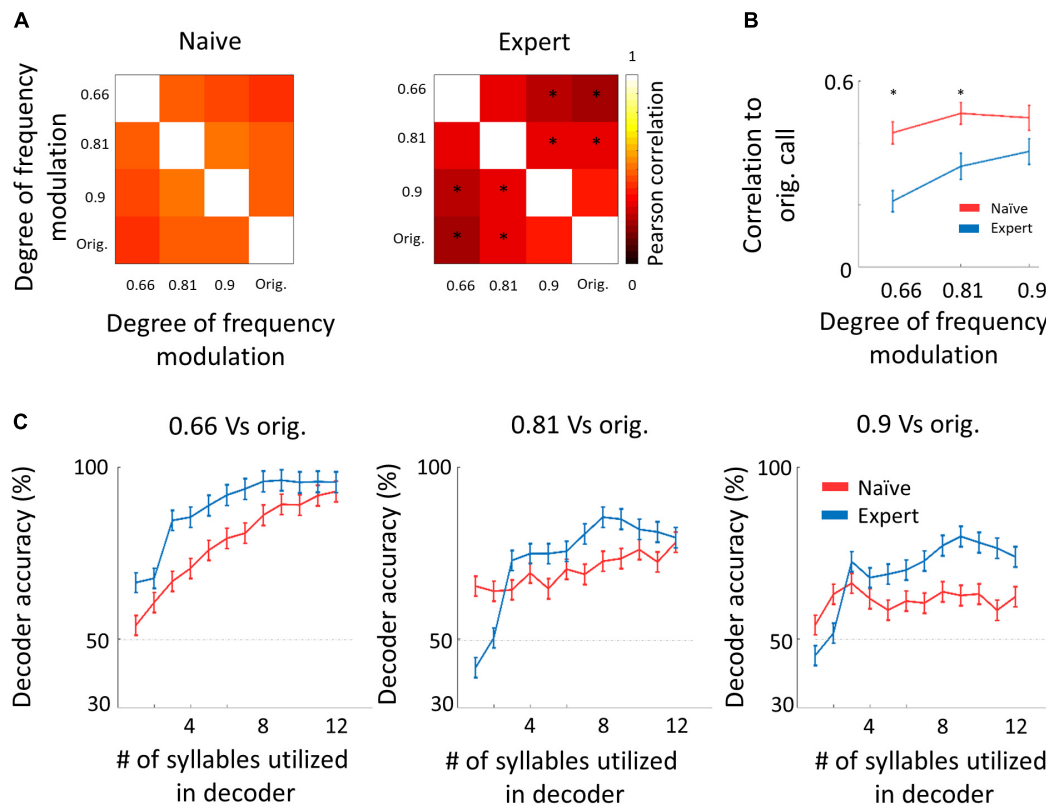


FIGURE 6 | Decorelation improves coding. **(A)** Matrices describing the average response similarity of individual neurons between all combinations of stimuli in naïve (left) and expert (right) mice. Each pixel indicates the average Pearson correlation value calculated from all syllables' evoked spike rate from all neurons to two different calls. Neurons from expert mice have lower correlation between responses to different modulated calls (asterisks indicate significant differences between naïve and expert groups; Mann–Whitney U test followed by Bonferroni correction: $*p < 0.05$). **(B)** Pearson correlation between responses to modulated WCs and responses to the original WC in naïve (red) and expert (blue) mice (mean \pm s.e.m.). Correlations are significantly different in the 0.66 and 0.81 modulation (Mann–Whitney U test: $*p < 0.05$). **(C)** Classification performance of a support vector machine (SVM) decoder. The decoder was tested for its accuracy to differentiate between the modulated WC stimuli against the original WC. The performance of the decoder is shown for neurons from the naïve (red) and expert (blue) groups. Decoder performance is plotted separately for the three different pairs of stimuli. Each point in each graph shows the number of syllables the decoder was trained on and allowed to use. Error bars are SEM for 1000 repetitions of leave-one-out cross-validation.

BFs of PV[−] and PV⁺ neurons within the same brain (within 250 microns of each other), we found that excitatory and inhibitory neurons became more functionally homogeneous as compared to naïve mice (**Figure 8C**). As both neuronal groups show similar trends in the shift of their preferred frequencies, we rule out a simple scenario whereas parvalbumin neurons increase their responses in the sidebands of the learning frequency. In other words, plasticity does not seem to be induced by lateral inhibition *via* parvalbumin neurons, but rather maintains a strict balance between excitation and inhibition, regardless of whether they are naïves or experts (Wehr and Zador, 2003; Zhou et al., 2014). Note that the peak of the PV⁺ population response and their BF distribution was on the outskirts of the training band, rather than within it (compare **Figures 8A,B** with **Figures 2C,D**), and concomitantly, the slope of the population responses at the trained frequency band increased due to learning (**Figure 8A**). To assess the computational effect of the plasticity in the inhibitory neurons' responses, we have applied on their responses the same d' and FI calculated for the PV[−] neurons

(**Figures 8D,E**). Overall, the discrimination performance of the two cell populations (when equalized in size) is similar. However, the PV⁺ population shows a significant learning related increase in tone discrimination performance by these cells within the training band (**Figures 8D,E**) in contrast to the results for PV[−] neurons (**Figures 3D,E**). This result is consistent with the abovementioned increase in their response slopes in the trained frequency.

Following natural sound learning, we found no significant changes in basic response properties of the PV⁺ neurons (**Table 3**), or in the degree of sparseness of their representation of the learned vocalizations (**Supplementary Figure 6b**). The relationship between the responses of PV⁺ and their PV[−] neighbors remained constant as reflected in the similar slopes of the functions describing PV[−] firing versus PV⁺ firing (**Supplementary Figure 6c**). This result suggests that the excitation–inhibition balance, as reflected in the responses of PV[−] versus PV⁺, remains. In PV⁺ neurons, the temporal correlation along the call as well as the decoding performance

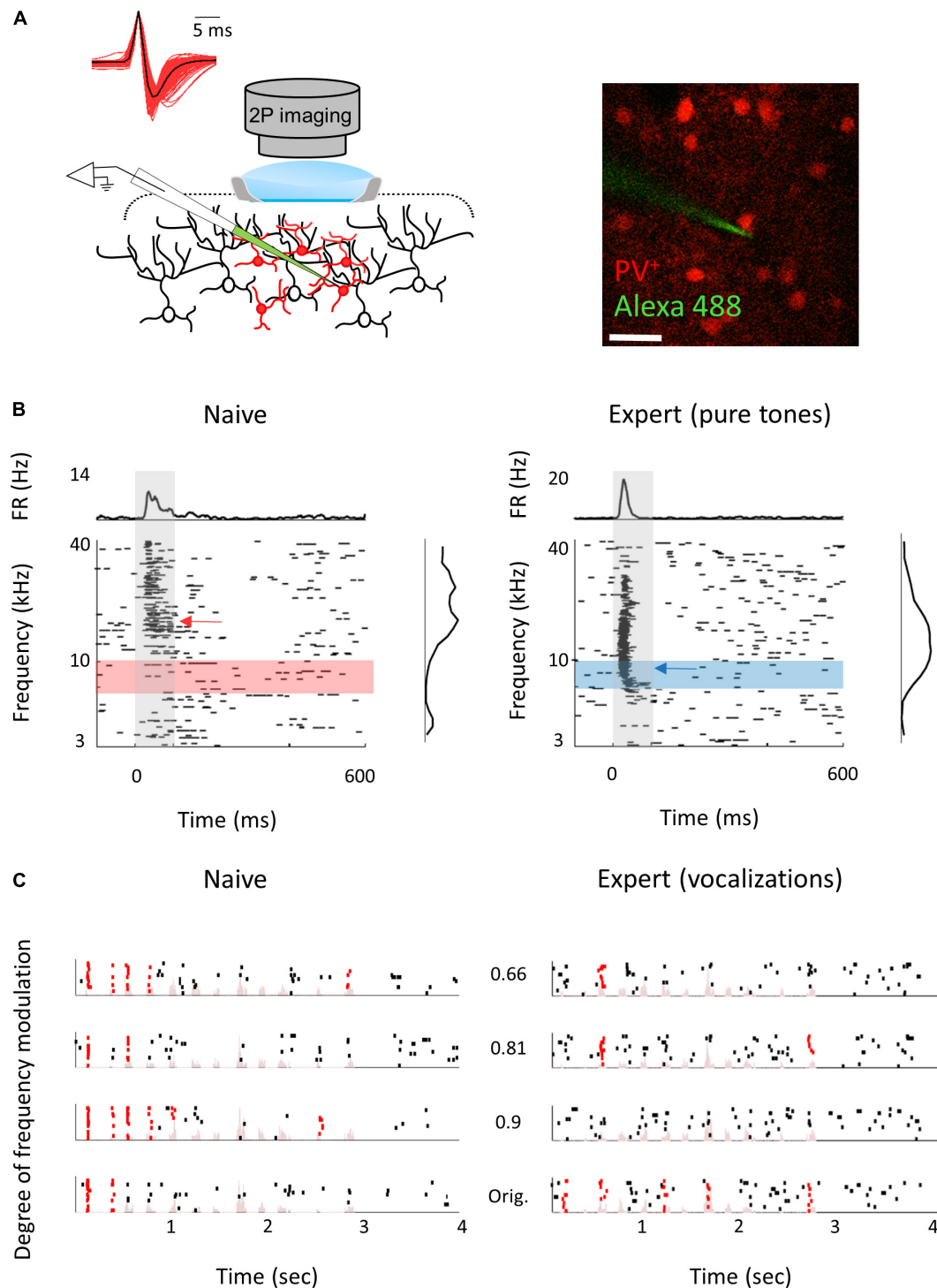


FIGURE 7 | Response properties of PV⁺ neurons. **(A)** Left: Schematic representation of the experimental setup for two-photon targeted patch and average spike waveform of 203 PV⁺ neurons. Right: Representative two-photon micrograph (projection image of 120 microns) of tdTomato+ cells (red) and the recording electrode (Alexa Fluor-488, green). **(B)** Raster plots and peri-stimulus time histograms (PSTH) in response to pure tones of a representative PV⁺ neuron from naïve (left) and expert (right) mice. Gray bars indicate the time of stimulus presentation (100 ms). Color bars and arrows indicate the training frequency band (7.1–10 kHz) and BF, respectively. **(C)** Representative examples of raster plots from PV⁺ neurons in response to four modulated wriggling calls from naïve (left) and expert (right) mice. Red lines indicate spikes in response windows that are significantly above baseline. Stimulus power spectrum shown in light pink in the background.

TABLE 3 | Physiological changes in PV⁺ neurons.

Group	Animals (n)	Cells (n)	BF (kHz)	Spontaneous firing rate (Hz)	Evoked firing rate in BF (Hz)	FR in training band (Hz)	Response latency (ms)	Response selectivity (% of evoked stimuli)
Naïve FS PT	21	120	16.2 ± 10.4	2.2 ± 2.1	21 ± 9	9.2 ± 9	31.1 ± 6.7	17 ± 17
Expert FS PT	18	83	11.8 ± 8.1	1.7 ± 1.8	22 ± 10	11.9 ± 10	33.2 ± 9.3	25 ± 18
Rank-sum test			0.006	0.05	0.7	0.02	0.2	<0.001
Naïve FS vocalizations	6	17		4 ± 3.7	14.3 ± 10.8		31.5 ± 8.6	27 ± 14.9
Expert FS vocalizations	5	18		3.4 ± 3.9	14.9 ± 12.9		32 ± 8	25.6 ± 15.6
Rank-sum test				0.4	0.97		1	0.72

A summary table of the complete dataset of recordings from PV neurons in naïve and expert mice after perceptual learning of pure tones (rows 1 and 2) and vocalizations (rows 4 and 5). Columns show different parameters of the dataset or property tested. The white color row shows the statistical *p* value between naïve and experts using a Mann–Whitney *U* test for each group separately.

from these neurons showed changes that are qualitatively similar to their PV[−] counterparts, but the data across the population were noisier (**Figures 8F,G** and **Supplementary Figure 6d**) perhaps due to the smaller sample of the PV⁺ dataset.

DISCUSSION

Plasticity in Frequency Tuning Following Perceptual Learning

Shifts in the average stimulus representation toward the learned stimuli are not a new phenomenon. Similar findings were observed in numerous studies, multiple brain areas, animal models, and sensory systems, including in auditory cortex (Karni and Sagi, 1991; Buonomano and Merzenich, 1998; Weinberger, 2004). In fact, the model of learning-induced plasticity in A1, also known as tonotopic map expansion, is an exemplar in neuroscience (Bakin and Weinberger, 1990; Recanzone et al., 1993; Rutkowski and Weinberger, 2005; but see Crist et al., 2001; Ghose et al., 2002; Kato et al., 2015). Although we did not measure tonotopic maps, our results support the observations of others that tuning curves are plastic in primary sensory cortex. Specifically, we show here an average shift in the tuning of L2/3 neurons in A1 in mice.

Since we sampled only a small number of neurons, our observations cannot be inferred as direct evidence for tonotopic map expansion. Rather, our data emphasize that plastic shifts occur in local circuits (**Figure 2E**). Given that neurons in A1 are functionally heterogeneous within local circuits (Maor et al., 2016), any area in A1 that represents a range of frequencies prior to learning could become more frequency-tuned once learned. Such a mechanism allows a wide range of modifications within local circuits to enable increased representation of the learned stimuli without necessarily perturbing gross tonotopic order. One advantage of local circuit heterogeneity is that it allows circuits to maintain a dynamic balance between plasticity and stability (Mermillod et al., 2013).

It is often assumed that the learning-induced changes in tuning properties improve the accuracy of coding of the trained stimuli. In particular, perceptual learning theory predicts that sharpening the slope of the tuning curves improves the discriminability of the relevant stimuli

(Seung and Sompolinsky, 1993). However, the observed increased representation of the BFs toward the training band in expert mice may not increase over all tuning slopes and may even decrease them, especially since the slopes tend to be small at the BFs. A closer look at the tuning curves in A1 shows that they are often irregular with multiple slopes and peaks (i.e., not having simple unimodal Gaussian shapes). Furthermore, the learning-induced changes in the ensemble of tuning curves are not limited to shifting the BF; hence, a more quantitative approach was required to assess the consequences of the observed learning-induced plasticity on discrimination accuracy. Our new, SVD-based, generative model (**Figure 3**) allowed us to assess the combined effects of changes in BFs as well as other changes in the shapes of the tuning curves. Surprisingly, both FI analysis and estimated classification errors of an optimal linear classifier show that learning-induced changes in tuning curves do not improve tone discriminability at trained values. This conclusion is consistent with previous work on the effect of exposure to tones during development that has been argued to decrease tone discriminability for similar reasons (Han et al., 2007). However, in that work, the functional effect of tuning curve changes was consistent with an observed impaired behavioral performance, suggesting that plasticity in A1 sub-serves discrimination behavior. In contrast, the stable (or even reduced) accuracy in the coding of the trained frequency we observed occurs despite the improved behavioral performance after training. To test whether behavioral performances of individual mice are correlated with coding accuracy, we plotted neuronal *d'* with behavioral *d'* on a mouse by mouse basis. Although we recorded high *d'* values in the few mice that performed particularly well, we did not find a significant correlation between these two measures across mice (**Supplementary Figure 7a**). Mice with similar neuronal *d'* values often differed as much as twofold in their behavioral performance (**Supplementary Figures 7a,b**).

One possibility for the observed changes in the tuning of pure tones in A1 are the result of unsupervised Hebbian learning induced by overexposure to the trained tones during the training period, similar to the reported results in early overexposure (Han et al., 2007). Unsupervised learning signals are not driven by task-related reward and punishment *per se* and may increase representation rather than discriminability. Increased representation of trained stimuli may lead to improved

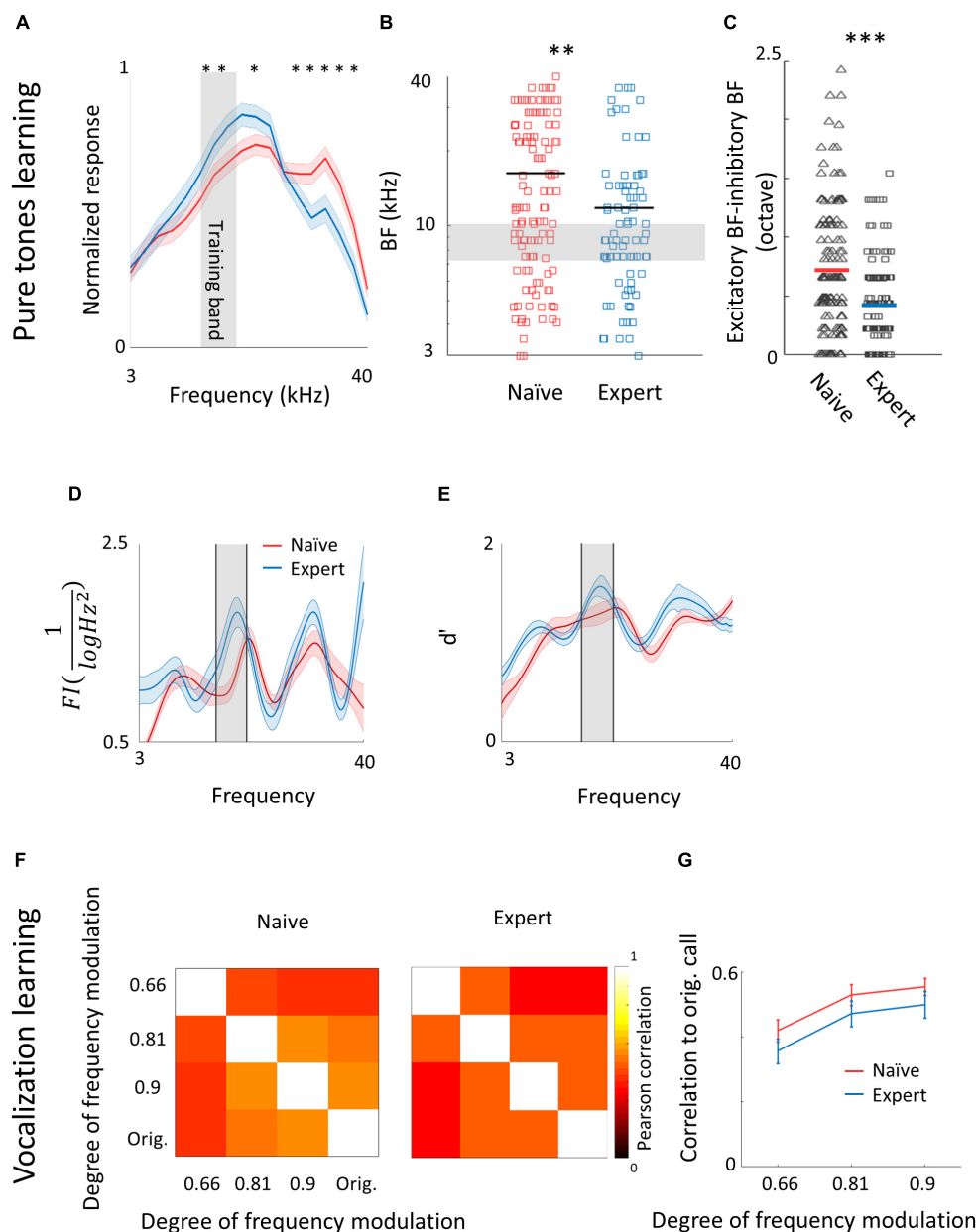


FIGURE 8 | Plasticity of PV⁺ neurons after learning. **(A)** Population average of normalized response tuning curves of $n = 120$ PV⁺ neurons from naïve mice (red) and 83 PV⁺ neurons from expert mice (blue; mean \pm s.e.m). Gray area indicates the training frequency band. Asterisks correspond to frequencies with significant response difference (Mann–Whitney U test: $*p < 0.05$). **(B)** Best frequency (BF) of individual PV⁺ neurons from naïve mice (red) and expert mice (blue; Mann–Whitney U test: $**p < 0.01$). **(C)** Average distance in BF between PV⁻ and PV⁺ neurons from the same penetration sites. Distances were significantly smaller in expert mice (Mann–Whitney U test: $***p < 0.001$). **(D)** Fisher Information calculated from the tuning curves of PV⁺ neurons **(E)** Discriminability (d') of SVM decoder along the range of frequencies. **(F)** Matrices describing the average response similarity of individual PV⁺ neurons between all combinations of different stimuli in naïve (left) and expert (middle) mice. Each pixel indicates the average Pearson correlation value calculated from all syllables evoked spike rate from all neurons to two different calls. There was no significant difference between correlations of responses to different modulated calls in naïve and expert mice (Mann–Whitney U test, $p > 0.05$). **(G)** Pearson correlation between responses to modulated WCs versus the responses to the original WCs in naïve (red) and expert (blue) mice (mean \pm s.e.m). Correlations are not significantly different for all comparisons (Mann–Whitney U test: $p = 0.4, 0.5, 0.5$).

discriminability to untrained tones, as observed experimentally. Both reward and punishment can drive associative learning and do so *via* non-overlapping neuronal pathways (Cohen and Blum, 2002; Seymour et al., 2007). Here, we used both reward and punishment to drive mice to their perceptual

limits. Fear conditioning has been shown to induce receptive field plasticity along the auditory pathway (Diamond and Weinberger, 1986; Kim and Cho, 2017), but so did positive reinforcement (Rutkowski and Weinberger, 2005). More recently, David et al. (2012) showed that positive and negative

reinforcements drive cortical plasticity in opposite directions—negative reinforcement boosts but positive reinforcement reduces responses of the target frequency (David et al., 2012). Notably, if both mechanisms act simultaneously, as it is in our case, it would be difficult to tease out their individual contribution to discrimination. In our data, the FI of expert mice peaked near 7 kHz (**Figure 3D**), leading us to speculate that aversion effects may have predominated. Indeed, the effects of the negative reinforcement on mouse behavior were strong. Specifically, following non-target stimuli (both FA and CR trials), mice returned back to the home cage and initiated their next trial only > 100 s later (**Supplementary Figure 7c**). Thus, we speculate that both unsupervised learning and the negative reinforcement may have affected cortical responses to pure tones.

Our protocol to push mice to their limits thus involves several processes acting simultaneously. The relative contribution of each—unsupervised learning or supervised learning (positive or negative)—utilized to drive the behavior and its resultant neural correlate remains to be elucidated.

Plasticity Following Natural Sounds Learning

Unlike pure tones, learning-induced changes in A1 improved the discriminability of learned natural sounds. Although auditory cortex is organized tonotopically, it may not be critical for processing simple sounds, as these stimuli are accurately represented in earlier stages in the auditory hierarchy (Nelken, 2004; Mizrahi et al., 2014). While the causal relationships between A1 and pure tones discrimination are still debatable (Ohl et al., 1999; LeDoux, 2000; Weible et al., 2014; O'Sullivan et al., 2019), the role of A1 in processing and decoding complex sounds is becoming increasingly more evident (Letzkus et al., 2011; Ceballos et al., 2019).

Neurons in A1 respond to sounds in a non-linear fashion (Bathellier et al., 2012; Harper et al., 2016; Angeloni and Geffen, 2018). These can be selective to harmonic content that are prevalent in vocalizations (Feng and Wang, 2017). Other neurons show strong correlations to global stimulus statistics (Theunissen and Elie, 2014). Furthermore, A1 neurons are sensitive to the fine-grained spectrotemporal environments of sounds, expressed as strong gain modulation to local sound statistics (Williamson et al., 2016), as well as to sound contrast and noise (Rabinowitz et al., 2011, 2013). These features (harmonics, globally and locally rich statistics, and noise), as well as other unique attributes such as frequency range, amplitude modulations, frequency modulations, inter syllable interval and duration variability, are well represented in the WCs. Importantly, WCs have been shown to drive strong responses in mouse A1 (Maor et al., 2016; Tasaka et al., 2018). Which of these particular sensitivities changes after perceptual learning and what is the contribution of the different attributes to the plasticity observed following vocalization learning is not yet known. However, one expression of this plasticity can be the increased sparse sound representation we found here (**Figure 5**). Sparseness can take different forms (Barth and Poulet, 2012). Here, sparseness was expressed as reduced number of neurons in the network that respond to any of

the 12 syllables played (**Figures 5B–D**). Such increase could arise from disparate mechanisms, and changes in the structure of local inhibition was one suspect that we tested (Froemke, 2015).

Inhibitory Plasticity Follows Excitatory Plasticity

Cortical inhibitory neurons are central players in many forms of learning (Kullmann et al., 2012; Hennequin et al., 2017; Sprekeler, 2017). Inhibitory interneurons have been implicated as important for experience-dependent plasticity in the developing auditory system (Hensch, 2005), during fear learning in adulthood (Letzkus et al., 2011; Courtin et al., 2014), and following injury (Resnik and Polley, 2017). Surprisingly, however, and despite the numerous studies on parvalbumin neurons, we could not find any references in the literature of recordings from parvalbumin neurons after auditory perceptual learning. Two simple (non-mutually exclusive) hypotheses are naively expected. One is that plasticity in inhibitory neurons is a negative mirror of the plasticity in excitatory neurons. This would predict that inhibitory neurons would increase their responses to the stimuli for which responses of excitatory neurons are downregulated, as found in the plasticity of somatostatin expressing (SOM) neurons following passive sound exposure (Kato et al., 2015), or in multisensory plasticity in mothers (Cohen and Mizrahi, 2015). The second is that inhibitory neurons enhance their response to “lateral” stimuli, thus enhancing selectivity to the trained stimulus, as suggested by the pattern of maternal-related plasticity to pup calls (Galindo-Leon et al., 2009). Our study provides a first test of these hypotheses in the context of perceptual learning. We found no evidence for these scenarios. Instead, a common motif in the local circuit was that parvalbumin neurons changed in a similar manner to their excitatory counterparts. These results are in line with the observation that PV neurons in V1 following visual discrimination task become as selective as their pyramidal neighbors (Khan et al., 2018).

The cortex hosts several types of inhibitory cells (Hattori et al., 2017; Zeng and Sanes, 2017), presumably serving distinct roles. While PV neurons are considered a rather homogeneous pool of neurons based on molecular signature, their role in coding sounds is not (Seybold et al., 2015; Phillips and Hasenstaub, 2016). In the visual cortex, PV⁺ cells' activity (and presumably its plasticity) was correlated with stimulus-specific response potentiation but not in ocular dominance plasticity (Kaplan et al., 2016), again suggesting that PV⁺ neurons are not necessarily involved in all forms of experience-dependent plasticity. Inhibitory neurons have been suggested to play a key role in enhancing the detection of behaviorally significant vocalization by lateral inhibition (Galindo-Leon et al., 2009). But recent imaging data argue that somatostatin interneurons rather than PV⁺ interneurons govern lateral inhibition in A1 (Kato et al., 2017). Our results are also consistent with the observation that in contrast to the SOM neurons, the changes in responses following sound exposure are similar in PV⁺ and pyramidal neurons (Kato et al., 2015; Khan et al., 2018). To what extent somatostatin or other interneurons subtypes

contribute to excitatory plasticity after auditory perceptual learning remains to be studied.

DATA AVAILABILITY STATEMENT

The datasets generated for this study are available on request to the corresponding author.

ETHICS STATEMENT

The animal study was reviewed and approved by the Hebrew University's IACUC.

AUTHOR CONTRIBUTIONS

IM and AM designed the experiments. RS-Z and HS analyzed data. LF conducted the experiments. YE constructed the vocalization stimuli and software for their delivery. IM conducted the experiments and analyzed the data. IM, HS, and AM wrote the manuscript.

REFERENCES

- Ahissar, M., and Hochstein, S. (2004). The reverse hierarchy theory of visual perceptual learning. *Trends Cogn. Sci.* 8, 457–464. doi: 10.1016/j.tics.2004.08.011
- Angeloni, C., and Geffen, M. N. (2018). Contextual modulation of sound processing in the auditory cortex. *Curr. Opin. Neurobiol.* 49, 8–15. doi: 10.1016/j.conb.2017.10.012
- Aoki, R., Tsubota, T., Goya, Y., and Benucci, A. (2017). An automated platform for high-throughput mouse behavior and physiology with voluntary head-fixation. *Nat. Commun.* 8:1196. doi: 10.1038/s41467-017-01371-0
- Avermann, M., Tomm, C., Mateo, C., Gerstner, W., and Petersen, C. C. (2012). Microcircuits of excitatory and inhibitory neurons in layer 2/3 of mouse barrel cortex. *J. Neurophysiol.* 107, 3116–3134. doi: 10.1152/jn.00917.2011
- Bakin, J. S., and Weinberger, N. M. (1990). Classical conditioning induces CS-specific receptive field plasticity in the auditory cortex of the guinea pig. *Brain Res.* 536, 271–286. doi: 10.1016/0006-8993(90)90035-a
- Ball, K., and Sekuler, R. (1987). Direction-specific improvement in motion discrimination. *Vis. Res.* 27, 953–965. doi: 10.1016/0042-6989(87)90011-3
- Bandyopadhyay, S., Shamma, S. A., and Kanold, P. O. (2010). Dichotomy of functional organization in the mouse auditory cortex. *Nat. Neurosci.* 13, 361–368. doi: 10.1038/nn.2490
- Barth, A. L., and Poulet, J. F. (2012). Experimental evidence for sparse firing in the neocortex. *Trends Neurosci.* 35, 345–355. doi: 10.1016/j.tins.2012.03.008
- Bathellier, B., Ushakova, L., and Rumpel, S. (2012). Discrete neocortical dynamics predict behavioral categorization of sounds. *Neuron* 76, 435–449. doi: 10.1016/j.neuron.2012.07.008
- Berardi, N., and Fiorentini, A. (1987). Interhemispheric transfer of visual information in humans: spatial characteristics. *J. Physiol.* 384, 633–647. doi: 10.1113/jphysiol.1987.sp016474
- Bieszczad, K. M., and Weinberger, N. M. (2010). Representational gain in cortical area underlies increase of memory strength. *Proc. Natl. Acad. Sci. U.S.A.* 107, 3793–3798. doi: 10.1073/pnas.1000159107
- Bizley, J. K., and Cohen, Y. E. (2013). The what, where and how of auditory-object perception. *Nat. Rev. Neurosci.* 14, 693–707. doi: 10.1038/nrn3565
- Briguglio, J. J., Aizenberg, M., Balasubramanian, V., and Geffen, M. N. (2018). Cortical neural activity predicts sensory acuity under optogenetic manipulation. *J. Neurosci.* 38, 2094–2105. doi: 10.1523/JNEUROSCI.2457-17.2017

FUNDING

This work was supported by an ERC consolidators grant to AM (#616063), ISF grant to AM (#224/17), and by Gatsby Charitable Foundation.

ACKNOWLEDGMENTS

We thank Israel Nelken and Livia de Hoz for help in setting up the initial behavioral experiments. We thank Yoni Cohen, David Pash, and Joseph Jubran for writing the software code of the Educage. We also thank Yonatan Loewenstein, Merav Ahissar, and the Mizrahi lab members for comments on the manuscript. This manuscript has been released as a pre-print at bioRxiv; doi: 10.1101/273342.

SUPPLEMENTARY MATERIAL

The Supplementary Material for this article can be found online at: <https://www.frontiersin.org/articles/10.3389/fncir.2019.00082/full#supplementary-material>

- Brown, M., Irvine, D. R., and Park, V. N. (2004). Perceptual learning on an auditory frequency discrimination task by cats: association with changes in primary auditory cortex. *Cereb. Cortex* 14, 952–965. doi: 10.1093/cercor/bhh056
- Buonomano, D. V., and Merzenich, M. M. (1998). Cortical plasticity: from synapses to maps. *Annu. Rev. Neurosci.* 21, 149–186. doi: 10.1146/annurev.neuro.21.1.149
- Ceballo, S., Piwkowska, Z., Bourg, J., Daret, A., and Bathellier, B. (2019). Targeted cortical manipulation of auditory perception. *Neuron* 104, 1168.e4–1179.e4. doi: 10.1016/j.neuron.2019.09.043
- Cohen, J. D., and Blum, K. I. (2002). Reward and decision. *Neuron* 36, 193–198. doi: 10.1016/s0896-6273(02)00973-x
- Cohen, L., and Mizrahi, A. (2015). Plasticity during motherhood: changes in excitatory and inhibitory layer 2/3 neurons in auditory cortex. *J. Neurosci.* 35, 1806–1815. doi: 10.1523/JNEUROSCI.1786-14.2015
- Cohen, L., Rothschild, G., and Mizrahi, A. (2011). Multisensory integration of natural odors and sounds in the auditory cortex. *Neuron* 72, 357–369. doi: 10.1016/j.neuron.2011.08.019
- Courtin, J., Chaudun, F., Rozeske, R. R., Karalis, N., Gonzalez-Campo, C., Wurtz, H., et al. (2014). Prefrontal parvalbumin interneurons shape neuronal activity to drive fear expression. *Nature* 505, 92–96. doi: 10.1038/nature12755
- Crist, R. E., Wu, L., and Gilbert, C. D. (2001). Learning to see: experience and attention in primary visual cortex. *Nat. Neurosci.* 4, 519–525. doi: 10.1038/87470
- Cruces-Solis, H., Jing, Z., Babaev, O., Rubin, J., Gur, B., Krueger-Burg, D., et al. (2018). Auditory midbrain coding of statistical learning that results from discontinuous sensory stimulation. *PLoS Biol.* 16:e2005114. doi: 10.1371/journal.pbio.2005114
- David, S. V., Fritz, J. B., and Shamma, S. A. (2012). Task reward structure shapes rapid receptive field plasticity in auditory cortex. *Proc. Natl. Acad. Sci. U.S.A.* 109, 2144–2149. doi: 10.1073/pnas.1117717109
- de Hoz, L., and Nelken, I. (2014). Frequency tuning in the behaving mouse: different bandwidths for discrimination and generalization. *PLoS One* 9:e91676. doi: 10.1371/journal.pone.0091676
- Diamond, D. M., and Weinberger, N. M. (1986). Classical conditioning rapidly induces specific changes in frequency receptive fields of single neurons in secondary and ventral ectosylvian auditory cortical fields. *Brain Res.* 372, 357–360. doi: 10.1016/0006-8993(86)91144-3
- Egnor, S. E., and Branson, K. (2016). Computational analysis of behavior. *Annu. Rev. Neurosci.* 39, 217–236. doi: 10.1146/annurev-neuro-070815-013845

- Ehret, G. (1975). Frequency and intensity difference limens and nonlinearities in the ear of the housemouse (*Mus musculus*). *J. Comp. Physiol.* 102, 321–336. doi: 10.1007/bf01464344
- Ericsson, K. A. (2006). The influence of experience and deliberate practice on the development of superior expert performance. *Camb. Handb. Expert. Expert Perform.* 38, 685–705.
- Erskine, A., Bus, T., Herb, J. T., and Schaefer, A. T. (2018). AutoMouse: high throughput automated operant conditioning shows progressive behavioural impairment with graded olfactory bulb lesions. *bioRxiv* doi: 10.1101/291815 [Preprint].
- Feng, L., and Wang, X. (2017). Harmonic template neurons in primate auditory cortex underlying complex sound processing. *Proc. Natl. Acad. Sci. U.S.A.* 114, E840–E848. doi: 10.1073/pnas.1607519114
- Francis, N. A., and Kanold, P. O. (2017). Automated operant conditioning in the mouse home cage. *Front. Neural Circ.* 11:10. doi: 10.3389/fncir.2017.00010
- Froemke, R. C. (2015). Plasticity of cortical excitatory-inhibitory balance. *Annu. Rev. Neurosci.* 38, 195–219. doi: 10.1146/annurev-neuro-071714-034002
- Galindo-Leon, E. E., Lin, F. G., and Liu, R. C. (2009). Inhibitory plasticity in a lateral band improves cortical detection of natural vocalizations. *Neuron* 62, 705–716. doi: 10.1016/j.neuron.2009.05.001
- Ghose, G. M., Yang, T., and Maunsell, J. H. (2002). Physiological correlates of perceptual learning in monkey V1 and V2. *J. Neurophysiol.* 87, 1867–1888. doi: 10.1152/jn.00690.2001
- Gibson, E. J. (1969). *Principles of Perceptual Learning and Development*. New York, NY: Appleton-Century-Crofts.
- Gilbert, C. D., Sigman, M., and Crist, R. E. (2001). The neural basis of perceptual learning. *Neuron* 31, 681–697. doi: 10.1016/s0896-6273(01)00424-x
- Goel, A., Cantu, D., Guilfoyle, J., Chaudhari, G. R., Newadkar, A., Todisco, B., et al. (2017). Impaired perceptual learning in Fragile X syndrome is mediated by parvalbumin neuron dysfunction in V1 and is reversible. *bioRxiv* doi: 10.1101/217414 [Preprint].
- Han, Y. K., Kover, H., Insanally, M. N., Semerdjian, J. H., and Bao, S. (2007). Early experience impairs perceptual discrimination. *Nat. Neurosci.* 10, 1191–1197. doi: 10.1038/nn1941
- Harper, N. S., Schoppe, O., Willmore, B. D., Cui, Z., Schnupp, J. W., and King, A. J. (2016). Network receptive field modeling reveals extensive integration and multi-feature selectivity in auditory cortical neurons. *PLoS Comput. Biol.* 12:e1005113. doi: 10.1371/journal.pcbi.1005113
- Hattori, R., Kuchibhotla, K. V., Froemke, R. C., and Komiyama, T. (2017). Functions and dysfunctions of neocortical inhibitory neuron subtypes. *Nat. Neurosci.* 20, 1199–1208. doi: 10.1038/nn.4619
- Hawkey, D. J., Amitay, S., and Moore, D. R. (2004). Early and rapid perceptual learning. *Nat. Neurosci.* 7, 1055–1056. doi: 10.1038/nn1315
- Hennequin, G., Agnes, E. J., and Vogels, T. P. (2017). Inhibitory plasticity: balance, control, and codependence. *Annu. Rev. Neurosci.* 40, 557–579. doi: 10.1146/annurev-neuro-072116-031005
- Hensch, T. K. (2005). Critical period plasticity in local cortical circuits. *Nat. Rev. Neurosci.* 6, 877–888. doi: 10.1038/nrn1787
- Hippenmeyer, S., Vrieseling, E., Sigrist, M., Portmann, T., Laengle, C., Ladle, D. R., et al. (2005). A developmental switch in the response of DRG neurons to ETS1 transcription factor signaling. *PLoS Biol.* 3:e159. doi: 10.1371/journal.pbio.0030159
- Hu, H., Gan, J., and Jonas, P. (2014). Fast-spiking, parvalbumin+ GABAergic interneurons: from cellular design to microcircuit function. *Science* 345:1255263. doi: 10.1126/science.1255263
- Irvine, D. R. (2017). Plasticity in the auditory system. *Hear. Res.* 362, 61–73. doi: 10.1016/j.heares.2017.10.011
- Irvine, D. R., Martin, R. L., Klimkeit, E., and Smith, R. (2000). Specificity of perceptual learning in a frequency discrimination task. *J. Acoust. Soc. Am.* 108, 2964–2968. doi: 10.1121/1.1323465
- Kaplan, E. S., Cooke, S. F., Komorowski, R. W., Chubykin, A. A., Thomazeau, A., Khibnik, L. A., et al. (2016). Contrasting roles for parvalbumin-expressing inhibitory neurons in two forms of adult visual cortical plasticity. *eLife* 5:e11450. doi: 10.7554/eLife.11450
- Karni, A., and Sagi, D. (1991). Where practice makes perfect in texture discrimination: evidence for primary visual cortex plasticity. *Proc. Natl. Acad. Sci. U.S.A.* 88, 4966–4970. doi: 10.1073/pnas.88.11.4966
- Kato, H. K., Asinof, S. K., and Isaacson, J. S. (2017). Network-level control of frequency tuning in auditory cortex. *Neuron* 95, 412.e4–423.e4. doi: 10.1016/j.neuron.2017.06.019
- Kato, H. K., Gillet, S. N., and Isaacson, J. S. (2015). Flexible sensory representations in auditory cortex driven by behavioral relevance. *Neuron* 88, 1027–1039. doi: 10.1016/j.neuron.2015.10.024
- Khan, A. G., Poort, J., Chadwick, A., Blot, A., Sahani, M., Mrsic-Flogel, T. D., et al. (2018). Distinct learning-induced changes in stimulus selectivity and interactions of GABAergic interneuron classes in visual cortex. *Nat. Neurosci.* 21, 851–859. doi: 10.1038/s41593-018-0143-z
- Kim, W. B., and Cho, J.-H. (2017). Encoding of discriminative fear memory by input-specific LTP in the amygdala. *Neuron* 95, 1129.e5–1146.e5. doi: 10.1016/j.neuron.2017.08.004
- Krakauer, J. W., Ghazanfar, A. A., Gomez-Marin, A., MacIver, M. A., and Poeppel, D. (2017). Neuroscience needs behavior: correcting a reductionist bias. *Neuron* 93, 480–490. doi: 10.1016/j.neuron.2016.12.041
- Kuchibhotla, K., and Bathellier, B. (2018). Neural encoding of sensory and behavioral complexity in the auditory cortex. *Curr. Opin. Neurobiol.* 52, 65–71. doi: 10.1016/j.conb.2018.04.002
- Kullmann, D. M., Moreau, A. W., Bakiri, Y., and Nicholson, E. (2012). Plasticity of inhibition. *Neuron* 75, 951–962. doi: 10.1016/j.neuron.2012.07.030
- Kurt, S., and Ehret, G. (2010). Auditory discrimination learning and knowledge transfer in mice depends on task difficulty. *Proc. Natl. Acad. Sci. U.S.A.* 107, 8481–8485. doi: 10.1073/pnas.0912357107
- Lagler, M., Ozdemir, A. T., Lagoun, S., Malagon-Vina, H., Borhegyi, Z., Hauer, R., et al. (2016). Divisions of identified parvalbumin-expressing basket cells during working memory-guided decision making. *Neuron* 91, 1390–1401. doi: 10.1016/j.neuron.2016.08.010
- Lawrence, D. H. (1952). The transfer of a discrimination along a continuum. *J. Comp. Physiol. Psychol.* 45, 511–516. doi: 10.1037/h0057135
- LeDoux, J. E. (2000). Emotion circuits in the brain. *Annu. Rev. Neurosci.* 23, 155–184. doi: 10.1146/annurev-neuro.23.1.155
- Lee, K., Holley, S. M., Shobe, J. L., Chong, N. C., Cepeda, C., Levine, M. S., et al. (2017). Parvalbumin interneurons modulate striatal output and enhance performance during associative learning. *Neuron* 93, 1451.e4–1463.e4. doi: 10.1016/j.neuron.2017.02.033
- Letzkus, J. J., Wolff, S. B., Meyer, E. M., Tovote, P., Courtin, J., Herry, C., et al. (2011). A disinhibitory microcircuit for associative fear learning in the auditory cortex. *Nature* 480, 331–335. doi: 10.1038/nature10674
- Luo, L., Callaway, E. M., and Svoboda, K. (2018). Genetic dissection of neural circuits: a decade of progress. *Neuron* 98, 256–281. doi: 10.1016/j.neuron.2018.03.040
- Madisen, L., Zwingman, T. A., Sunken, S. M., Oh, S. W., Zariwala, H. A., Gu, H., et al. (2010). A robust and high-throughput Cre reporting and characterization system for the whole mouse brain. *Nat. Neurosci.* 13, 133–140. doi: 10.1038/nn.2467
- Maor, I., Shalev, A., and Mizrahi, A. (2016). Distinct spatiotemporal response properties of excitatory versus inhibitory neurons in the mouse auditory cortex. *Cereb. Cortex* 26, 4242–4252. doi: 10.1093/cercor/bhw266
- Margrie, T. W., Meyer, A. H., Caputi, A., Monyer, H., Hasan, M. T., Schaefer, A. T., et al. (2003). Targeted whole-cell recordings in the mammalian brain *in vivo*. *Neuron* 39, 911–918. doi: 10.1016/j.neuron.2003.08.012
- Mermillod, M., Bugaiska, A., and Bonin, P. (2013). The stability-plasticity dilemma: investigating the continuum from catastrophic forgetting to age-limited learning effects. *Front. Psychol.* 4:504. doi: 10.3389/fpsyg.2013.00504
- Mizrahi, A., Shalev, A., and Nelken, I. (2014). Single neuron and population coding of natural sounds in auditory cortex. *Curr. Opin. Neurobiol.* 24, 103–110. doi: 10.1016/j.conb.2013.09.007
- Murphy, T. H., Boyd, J. D., Bolaños, F., Vanni, M. P., Silasi, G., Haupt, D., et al. (2016). High-throughput automated home-cage mesoscopic functional imaging of mouse cortex. *Nat. Commun.* 7:11611. doi: 10.1038/ncomms11611
- Nelken, I. (2004). Processing of complex stimuli and natural scenes in the auditory cortex. *Curr. Opin. Neurobiol.* 14, 474–480. doi: 10.1016/j.conb.2004.06.005
- Nevin, J. A. (1969). Signal detection theory and operant behavior: a review of David M. Green and John A. Swets' Signal detection theory and psychophysics I. *J. Exp. Anal. Behav.* 12, 475–480. doi: 10.1901/jeab.1969.12-475
- Ohl, F. W., Wetzels, W., Wagner, T., Rech, A., and Scheich, H. (1999). Bilateral ablation of auditory cortex in Mongolian gerbil affects discrimination of frequency modulated tones but not of pure tones. *Learn. Mem.* 6, 347–362.
- O'Sullivan, C., Weible, A. P., and Wehr, M. (2019). Auditory cortex contributes to discrimination of pure tones. *eNeuro* 6:ENEURO.340-19.2019. doi: 10.1523/ENEURO.0340-19.2019

- Phillips, E. A., and Hasenstaub, A. R. (2016). Asymmetric effects of activating and inactivating cortical interneurons. *eLife* 5:e18383. doi: 10.7554/eLife.18383
- Polley, D. B., Steinberg, E. E., and Merzenich, M. M. (2006). Perceptual learning directs auditory cortical map reorganization through top-down influences. *J. Neurosci.* 26, 4970–4982. doi: 10.1523/jneurosci.3771-05.2006
- Rabinowitz, N. C., Willmore, B. D., King, A. J., and Schnupp, J. W. (2013). Constructing noise-invariant representations of sound in the auditory pathway. *PLoS Biol.* 11:e1001710. doi: 10.1371/journal.pbio.1001710
- Rabinowitz, N. C., Willmore, B. D., Schnupp, J. W., and King, A. J. (2011). Contrast gain control in auditory cortex. *Neuron* 70, 1178–1191. doi: 10.1016/j.neuron.2011.04.030
- Ramachandran, V., and Braddick, O. (1973). Orientation-specific learning in stereopsis. *Perception* 2, 371–376. doi: 10.1068/p020371
- Recanzone, G. H., Schreiner, C. E., and Merzenich, M. M. (1993). Plasticity in the frequency representation of primary auditory cortex following discrimination training in adult owl monkeys. *J. Neurosci.* 13, 87–103. doi: 10.1523/jneurosci.13-01-00087.1993
- Reed, A., Riley, J., Carraway, R., Carrasco, A., Perez, C., Jakkamsetti, V., et al. (2011). Cortical map plasticity improves learning but is not necessary for improved performance. *Neuron* 70, 121–131. doi: 10.1016/j.neuron.2011.02.038
- Resnik, J., and Polley, D. B. (2017). Fast-spiking GABA circuit dynamics in the auditory cortex predict recovery of sensory processing following peripheral nerve damage. *eLife* 6:e21452. doi: 10.7554/eLife.21452
- Roelfsema, P. R., and Holtmaat, A. (2018). Control of synaptic plasticity in deep cortical networks. *Nat. Rev. Neurosci.* 19, 166–180. doi: 10.1038/nrn.2018.6
- Rothschild, G., Nelken, I., and Mizrahi, A. (2010). Functional organization and population dynamics in the mouse primary auditory cortex. *Nat. Neurosci.* 13, 353–360. doi: 10.1038/nn.2484
- Rutkowski, R. G., and Weinberger, N. M. (2005). Encoding of learned importance of sound by magnitude of representational area in primary auditory cortex. *Proc. Natl. Acad. Sci. U.S.A.* 102, 13664–13669. doi: 10.1073/pnas.0506838102
- Schoups, A., Vogels, R., Qian, N., and Orban, G. (2001). Practising orientation identification improves orientation coding in V1 neurons. *Nature* 412, 549–553. doi: 10.1038/35087601
- Seung, H. S., and Sompolsky, H. (1993). Simple models for reading neuronal population codes. *Proc. Natl. Acad. Sci. U.S.A.* 90, 10749–10753. doi: 10.1073/pnas.90.22.10749
- Seybold, B. A., Phillips, E. A., Schreiner, C. E., and Hasenstaub, A. R. (2015). Inhibitory actions unified by network integration. *Neuron* 87, 1181–1192. doi: 10.1016/j.neuron.2015.09.013
- Seymour, B., Daw, N., Dayan, P., Singer, T., and Dolan, R. (2007). Differential encoding of losses and gains in the human striatum. *J. Neurosci.* 27, 4826–4831. doi: 10.1523/jneurosci.0400-07.2007
- Sprekeler, H. (2017). Functional consequences of inhibitory plasticity: homeostasis, the excitation-inhibition balance and beyond. *Curr. Opin. Neurobiol.* 43, 198–203. doi: 10.1016/j.conb.2017.03.014
- Stiebler, I., Neulist, R., Fichtel, I., and Ehret, G. (1997). The auditory cortex of the house mouse: left-right differences, tonotopic organization and quantitative analysis of frequency representation. *J. Comp. Physiol. A* 181, 559–571. doi: 10.1007/s003590050140
- Talwar, S. K., and Gerstein, G. L. (2001). Reorganization in awake rat auditory cortex by local microstimulation and its effect on frequency-discrimination behavior. *J. Neurophysiol.* 86, 1555–1572. doi: 10.1152/jn.2001.86.4.1555
- Tasaka, G.-I., Guenther, C. J., Shalev, A., Gilday, O., Luo, L., and Mizrahi, A. (2018). Genetic tagging of active neurons in auditory cortex reveals maternal plasticity of coding ultrasonic vocalizations. *Nat. Commun.* 9:871. doi: 10.1038/s41467-018-03183-2
- Theunissen, F. E., and Elie, J. E. (2014). Neural processing of natural sounds. *Nat. Rev. Neurosci.* 15, 355–366. doi: 10.1038/nrn3731
- Vapnik, V. (1998). *Statistical Learning Theory*. New York, NY: Wiley.
- Vinje, W. E., and Gallant, J. L. (2000). Sparse coding and decorrelation in primary visual cortex during natural vision. *Science* 287, 1273–1276. doi: 10.1126/science.287.5456.1273
- Wehr, M., and Zador, A. M. (2003). Balanced inhibition underlies tuning and sharpens spike timing in auditory cortex. *Nature* 426, 442–446. doi: 10.1038/nature02116
- Weible, A. P., Liu, C., Niell, C. M., and Wehr, M. (2014). Auditory cortex is required for fear potentiation of gap detection. *J. Neurosci.* 34, 15437–15445. doi: 10.1523/JNEUROSCI.3408-14.2014
- Weinberger, N. M. (2004). Specific long-term memory traces in primary auditory cortex. *Nat. Rev. Neurosci.* 5, 279–290. doi: 10.1038/nrn1366
- Williamson, R. S., Ahrens, M. B., Linden, J. F., and Sahani, M. (2016). Input-specific gain modulation by local sensory context shapes cortical and thalamic responses to complex sounds. *Neuron* 91, 467–481. doi: 10.1016/j.neuron.2016.05.041
- Willmore, B., and Tolhurst, D. J. (2001). Characterizing the sparseness of neural codes. *Netw. Comput. Neural Syst.* 12, 255–270. doi: 10.1088/0954-898x/12/3/302
- Wolff, S. B., Gründemann, J., Tovote, P., Krabbe, S., Jacobson, G. A., Müller, C., et al. (2014). Amygdala interneuron subtypes control fear learning through disinhibition. *Nature* 509, 453–458. doi: 10.1038/nature13258
- Wright, B. A., and Fitzgerald, M. B. (2001). Different patterns of human discrimination learning for two interaural cues to sound-source location. *Proc. Natl. Acad. Sci. U.S.A.* 98, 12307–12312. doi: 10.1073/pnas.211220498
- Zeng, H., and Sanes, J. R. (2017). Neuronal cell-type classification: challenges, opportunities and the path forward. *Nat. Rev. Neurosci.* 18, 530–546. doi: 10.1038/nrn.2017.85
- Zhou, M., Liang, F., Xiong, X. R., Li, L., Li, H., Xiao, Z., et al. (2014). Scaling down of balanced excitation and inhibition by active behavioral states in auditory cortex. *Nat. Neurosci.* 17, 841–850. doi: 10.1038/nn.3701

Conflict of Interest: The authors declare that the research was conducted in the absence of any commercial or financial relationships that could be construed as a potential conflict of interest.

Copyright © 2020 Maor, Schwartz-Ziv, Feigin, Elyada, Sompolsky and Mizrahi. This is an open-access article distributed under the terms of the Creative Commons Attribution License (CC BY). The use, distribution or reproduction in other forums is permitted, provided the original author(s) and the copyright owner(s) are credited and that the original publication in this journal is cited, in accordance with accepted academic practice. No use, distribution or reproduction is permitted which does not comply with these terms.



Common Principles in Functional Organization of VIP/Calretinin Cell-Driven Disinhibitory Circuits Across Cortical Areas

Alexandre Guet-McCreight^{1,2}, Frances K. Skinner^{1,2,3*} and Lisa Topolnik^{4,5*}

¹ Krembil Brain Institute - Division of Clinical and Computational Neuroscience, Krembil Research Institute, University Health Network, Toronto, ON, Canada, ² Department of Physiology, University of Toronto, Toronto, ON, Canada, ³ Department of Medicine (Neurology), University of Toronto, Toronto, ON, Canada, ⁴ Department of Biochemistry, Microbiology and Bio-informatics, Laval University, Québec, QC, Canada, ⁵ Neuroscience Axis, CHU de Québec Research Center (CHUL), Québec, QC, Canada

OPEN ACCESS

Edited by:

Qian-Quan Sun,
University of Wyoming, United States

Reviewed by:

Xiaoming Jin,
Indiana University, Purdue University
Indianapolis, United States
Jochen Ferdinand Staiger,
University of Göttingen, Germany

*Correspondence:

Frances K. Skinner
frances.skinner@uhnresearch.ca
Lisa Topolnik
Lisa.Topolnik@bcm.ulaval.ca

† These authors share
senior authorship

Received: 20 February 2020

Accepted: 04 May 2020

Published: 09 June 2020

Citation:

Guet-McCreight A, Skinner FK and
Topolnik L (2020) Common Principles
in Functional Organization of
VIP/Calretinin Cell-Driven Disinhibitory
Circuits Across Cortical Areas.
Front. Neural Circuits 14:32.
doi: 10.3389/fncir.2020.00032

In the brain, there is a vast diversity of different structures, circuitries, cell types, and cellular genetic expression profiles. While this large diversity can often occlude a clear understanding of how the brain works, careful analyses of analogous studies performed across different brain areas can hint at commonalities in neuronal organization. This in turn can yield a fundamental understanding of necessary circuitry components that are crucial for how information is processed across the brain. In this review, we outline recent *in vivo* and *in vitro* studies that have been performed in different cortical areas to characterize the vasoactive intestinal polypeptide (VIP)- and/or calretinin (CR)-expressing cells that specialize in inhibiting GABAergic interneurons. In doing so, we make the case that, across cortical structures, interneuron-specific cells commonly specialize in the synaptic disinhibition of excitatory neurons, which can ungate the integration and plasticity of external inputs onto excitatory neurons. In line with this, activation of interneuron-specific cells enhances animal performance across a variety of behavioral tasks that involve learning, memory formation, and sensory discrimination, and may represent a key target for therapeutic interventions under different pathological conditions. As such, interneuron-specific cells across different cortical structures are an essential network component for information processing and normal brain function.

Keywords: hippocampus, cerebral cortex, vasoactive intestinal polypeptide, interneuron, microcircuit, disinhibition, behavior

INTRODUCTION

Interneuron-specific (I-S) cells are inhibitory interneurons that are specialized to primarily target other interneurons. Most often they are identified via expression of vasoactive intestinal polypeptide [VIP; a neuropeptide that was initially localized in gastrointestinal nerves and ventromedial hypothalamus (Larsson et al., 1976)], and calretinin [CR; a calcium-binding protein (Rogers, 1987)]. Some CR+ cells and VIP+ cells in hippocampus and cortex also express serotonin (5HT) receptor mRNA, including 5HT₂, 5HT_{3A} receptor (Lee et al., 2010; Tremblay et al., 2016; Prönnke et al., 2019) and 5HT₆ receptor (Helboe et al., 2015). As well, VIP has been shown to modulate the effects of 5HT (Rostene et al., 1983). There is also some indication that some

CR+ cells in hippocampus express corticotropin-releasing hormone (Gunn et al., 2019). In RNA sequencing datasets obtained from human middle temporal gyrus, VIP+ cells possess the richest diversity in transcriptomically-defined types when compared to non-VIP+ cells (Hodge et al., 2019). Specifically, in this study VIP+ cells were grouped into 21 different clusters. Notably, homologies in expression patterns were found in mouse visual cortex and lateral motor cortex, suggesting similar richness in VIP+ cell diversity across species and brain areas (Hodge et al., 2019). However, this may depend on the clustering method that one uses and the region being studied, since in a different RNA sequencing study conducted in the CA1 hippocampus, a smaller number of VIP+ cell clusters was found (Harris et al., 2018).

Importantly, some VIP+ cells, such as cholecystokinin co-expressing (CCK+) basket cells, primarily target excitatory cells, though they make up an apparently smaller fraction of VIP+ cells compared to I-S cells (Hajos et al., 1996; Kawaguchi and Kubota, 1996; Somogyi et al., 2004; Wang et al., 2004; Bezaire and Soltesz, 2013; Harris et al., 2018). Therefore, here we describe I-S cells generally as cells that preferentially inhibit other GABAergic interneurons. I-S cells, by this definition, have been described using imaging and electrophysiology techniques in several areas of the brain, including hippocampus (Gulyás et al., 1992, 1996; Acsády et al., 1996a,b; Tyan et al., 2014), frontal areas (Kawaguchi and Kubota, 1996, 1997; Pi et al., 2013), somatosensory cortex (Caputi et al., 2009; Lee et al., 2013; Prönnke et al., 2015), and visual cortex (Hajos et al., 1988; Zilles et al., 1991; Pfeiffer et al., 2013). In this review we will highlight similarities in I-S cells that exist across these cortical areas.

In recent years, I-S cells with similar properties across several cortical areas have been characterized at multiple levels experimentally and inspired computational modeling work. Most commonly, I-S cells in various cortical areas have been studied *in vivo* through calcium imaging of VIP+ cells. This method of study alone however does not sufficiently distinguish VIP+ I-S cells from VIP+ non-I-S cells (i.e., such as VIP+ basket cells). As such, these studies can often lump together cells that inhibit pyramidal cells with those that disinhibit pyramidal cells. On the other hand, there has been much *in vitro* characterization work to complement the data obtained *in vivo*. In this review, we summarize previous work that has investigated and characterized the recruitment and impact of I-S cells found in various cortical areas of the brain. Ultimately, obtaining common principles in how disinhibitory I-S cells across cortical regions are involved in network computations will help inform disinhibitory strategies through which information is processed across the cortex.

HIPPOCAMPAL FORMATION

Characterization of interneurons in the hippocampal CA1 area (Freund and Buzsáki, 1996; Klausberger and Somogyi, 2008; Bezaire and Soltesz, 2013; Pelkey et al., 2017) has highlighted nuances in different forms of inhibitory control over inhibitory neurons beyond I-S cells (Chamberland and Topolnik, 2012). Based on synaptic density analysis, interneurons receive a substantial amount of inhibition relative to excitation (Gulyás

et al., 1999), similar to pyramidal cells (Megias et al., 2001). As such, inhibition of inhibition can arise through several types of circuits, one of which is simply from the inhibitory neurons that target other inhibitory interneurons in addition to targeting pyramidal cells (Chamberland and Topolnik, 2012). Some examples include connections of neurogliaform cells to other inhibitory interneurons (Armstrong et al., 2012), basket cell connections to other basket cells (Cobb et al., 1997; Karson et al., 2009), recurrent connections between oriens lacunosum moleculare (OLM) and bistratified cells (Leão et al., 2012), and various OLM cell connections to interneuron dendrites in stratum lacunosum moleculare (SLM) (Katona et al., 1999). Inhibitory neurons in CA1 also receive long-range projecting GABAergic inputs (Chamberland and Topolnik, 2012). These include GABAergic projections from medial septum onto inhibitory interneurons in stratum oriens/alveus (SO/A) (Freund and Antal, 1988) and GABAergic projections from entorhinal cortex onto SLM interneurons (Melzer et al., 2012). In particular, axonal boutons from GABAergic medial septal projections form close appositions to PV+, CR+, calbindin-expressing (CB+), and CCK+ somata and dendrites, among others (Unal et al., 2015). Together with excitatory projections from entorhinal cortex and medial septum, this unveils a feedforward disinhibitory circuitry of specific CA1 pyramidal cell morphological compartments.

In the hippocampus, most I-S cells (19.4% of the interneuron population) express VIP, although some CCK+ basket cells (9.4% of the interneuron population) also express VIP—calculated in Bezaire and Soltesz (2013) according to Fuentealba et al. (2010) [though see Lorén et al. (1979), Köhler (1982), Léránth et al. (1984), Miettinen et al. (1992), Hajos et al. (1996), Tricoire et al. (2011)] for additional immunohistochemistry work investigating distribution densities of VIP+ cell types in hippocampus]. In the hippocampal CA1 area, I-S cells are divided into three types [I-S1, I-S2, and I-S3; Acsády et al. (1996a,b), Gulyás et al. (1996), Chamberland and Topolnik (2012), Tyan et al. (2014), Francavilla et al. (2015); **Table 1**], as well as a long-range projecting cell type that innervates the subiculum in addition to the hippocampal area CA1 (Francavilla et al., 2018). Because CCK+ basket cells also express VIP, isolation and manipulation of I-S cells is not straightforward, since results can possibly be contaminated with cells that input directly to pyramidal cells [e.g., see Pi et al. (2013), Fu et al. (2014), Pfeiffer and Foster (2015), Karnani et al. (2016a), Garcia-Junco-Clemente et al. (2017), Turi et al. (2019)]. Along these lines, combinatorial genetic-viral targeting methods could help further disambiguate I-S from non-I-S cell types (He et al., 2016).

The first type of I-S cells in the CA1, interneuron-specific 1 (I-S1) cells, have somata located in SO/A, pyramidal (SP), and radiatum (SR), express CR, and do not commonly express VIP (Klausberger and Somogyi, 2008; Chamberland and Topolnik, 2012; Harris et al., 2018) (**Table 1**). These primarily target CB+ cells, VIP+ basket cells, and CR+ cells, while at the same time avoiding PV+ basket and axo-axonic cells (Gulyás et al., 1996). Additionally, I-S1 cells are found to form dendro-dendritic and axo-dendritic connections with themselves with some indication of gap junction connections (Gulyás et al., 1996). The second

TABLE 1 | Hippocampal CA1 I-S cell types.

I-S cell type	Somatic location	Dendritic profile	Axonal profile	Expression profile	Synaptic targets	
I-S1 cell	SO/A	SO/A	SO/A	VIP-/CR+	I-S1 cells	
	SP	SP	SP		CB+ cells	
	SR	SR	SR		VIP+ basket cells	
		SLM	SLM		CR+ cells	
I-S2 cell	SR	SR	SR	VIP+/CR-	CB+ cells in SR	
	SLM	SLM	SLM		VIP+ cells in SR	
					VIP+/CCK+ basket cells	
I-S3 cell	SR	SR	SP	VIP+/CR+	OLM cells	
	SP	SLM	SO/A	Penk+	Bistratified cells	
	SO/A	SP		substance P receptor +	Basket cells	
		SO/A		mGluR1 α +	Axo-axonic cells	
				COUP-TFII+	SO/A cells	
VIP-LRP cell	SO/A	SO/A	Subiculum	NOS+		
				VIP+/CR+-	CA1: OLM cells	
	SP	SP		M2R+	Bistratified cells	
	SR	SR		CB+	CCK+ basket cells	
	SLM	SLM		SR	CCK-	SC-associated cells
					NOS-	Subiculum:
					SOM-	Pyramidal cells Interneurons

SO/A, Stratum Oriens/Alveus; SP, Stratum Pyramidale; SR, Stratum Radiatum; SLM, Stratum Lacunosum Moleculare; SC, Schaffer-Collateral; (+), expressing; (-), non-expressing; (+-), conditionally-expressing.

type, interneuron-specific 2 (I-S2) cells, have somata present near the SR and SLM border, and express VIP, but not CR (Klausberger and Somogyi, 2008; Chamberland and Topolnik, 2012; Harris et al., 2018) (**Table 1**). These cells have different morphologies with axons that target CB+ and VIP+ cells in SR, including VIP+/CCK+ basket cells (Acsády et al., 1996a,b; Chamberland and Topolnik, 2012). Though I-S1 and I-S2 cells are thought to be VIP-/CR+ and VIP+/CR-, respectively, it is worth noting that more recently obtained transcriptomics data suggests a more nuanced expression profile (Harris et al., 2018). When clustering cell types according to transcriptomic expression profiles, it is observed that I-S1 cells (i.e., traditionally VIP-/CR+) show some expression of *VIP* and I-S2 cells (i.e., traditionally VIP+/CR-) show some expression of *Calb2* (i.e., the gene that codes for CR) genes relative to non-I-S cells (Harris et al., 2018). It is only when compared to each other, that these expression levels appear relatively low.

The third type (**Table 1**), are the interneuron-specific 3 (I-S3) cells, which co-express VIP and CR. These interneurons have cell bodies mostly within the SP and SR, with dendrites extending to SLM, and axons arborizing in the SO/A (Acsády et al., 1996a,b; Chamberland et al., 2010) (**Table 1**). Together with CR, I-S3 cells may co-express other neurochemical markers such as proenkephalin (Penk), substance P receptor, metabotropic glutamate receptor 1a (mGluR1 α), COUP transcription factor 2 (COUP-TFII), and nitric oxide synthase (NOS) (Freund and Buzsáki, 1996; Blasco-Ibáñez et al., 1998; Ferraguti et al., 2004; Fuentealba et al., 2010; Tricoire et al., 2010). Electrophysiological characterization shows that I-S3 cells exhibit a high input

resistance with irregular or regular spiking firing pattern (Chamberland et al., 2010; Tyan et al., 2014; Guet-McCreight et al., 2016). Also, it is known from dendritic calcium imaging experiments in combination with computational modeling that voltage-gated channels can be present in proximal dendrites of I-S3 cells (Guet-McCreight et al., 2016). In particular, there are proximal dendritic distributions of kinetically fast Kv3.1 channel subunits, which was confirmed using immunohistochemical analysis (Guet-McCreight et al., 2016). Furthermore, I-S3 cell distal dendrites receive excitatory input from entorhinal cortex via the temporoammonic pathway, while the proximal dendrites receive excitatory input from CA3 via the Schaffer collateral pathway (Luo et al., 2020). As well, a proportion of inhibitory inputs onto I-S3 cells are from I-S1, I-S2, and other I-S3 cells (Luo et al., 2020). I-S3 cells primarily form synapses onto SOM+ and mGluR1 α + OLM cells in SO/A (Chamberland et al., 2010; Tyan et al., 2014; Francavilla et al., 2015), but also contact bistratified cells, basket cells, putative axo-axonic cells, and various other SO/A interneuron types (Tyan et al., 2014). Compared to medial septal input to OLM cells, inhibitory currents generated by I-S3 cell input are smaller amplitude and have a slower time course (Chamberland et al., 2010). Despite this, optogenetic activation of CR+ cells, which includes the I-S1 and I-S3 cell types, at 5 and 10 Hz frequencies is sufficient to control the spike timing of OLM cells and to pace their activity at theta frequency (Tyan et al., 2014). Calcium imaging of activity of putative I-S3 cells *in vivo* showed that these cells tend to spike toward the end of theta-run epochs (Luo et al., 2020). Putative I-S3 cells in this study were identified through expression of VIP, somata located near the SP

and SR border, and small somatic diameters (i.e., to distinguish them from VIP+/CCK+ basket cells, which have larger somatic diameters). Together with computational modeling and spike extraction analysis, it was found that I-S3 cells spike toward the rising to peak phases of theta waves, depending on the strengths of inputs from CA3 and entorhinal cortex (Luo et al., 2020). This capacity for phasic modulation suggests the involvement of I-S3 cells in the encoding and retrieval of information that occurs at distinct phases of theta waves (Siegle and Wilson, 2014). The VIP+/CR+ cells (i.e., putative I-S3 cells) that synapse onto SOM+ cells, including OLM cells, contain the $\alpha 5$ GABA_A receptor ($\alpha 5$ -GABA_AR). Interestingly, inhibiting $\alpha 5$ -GABA_AR at these synapses can modulate anxiety-like behaviors, with a possible impact on memory representations in the ventral hippocampus (Magnin et al., 2019).

In addition to the three I-S cell types described above, it is also worth mentioning a recently characterized long-range projecting (LRP) VIP cell type found in CA1 SO/A, with axons projecting to subiculum as well as to local interneurons in CA1 (Francavilla et al., 2018; Luo et al., 2019). VIP-LRP cells can have soma located in different CA1 layers, express muscarinic receptor 2 (M2R), and CB, and test negative for CCK and SOM (Table 1). In some cases, VIP-LRP cells with somata located in SP, SR, or SLM tested positive for Penk or CR suggesting further diversity, though the co-expression profiles of these markers in this cell type remain unknown. In the subiculum, VIP-LRP cells target both pyramidal cells and interneurons indiscriminately, while in the CA1, they target OLM, bistratified, and CCK+ basket cells and Schaffer-Collateral-associated cells. They are also electrically coupled with each other, but this mostly generates asynchronous spiking between pairs when depolarized past threshold using sinusoidal current injections. Further analysis revealed that this was because of low pass filtering properties which favored the conduction of slow after-spike hyperpolarizations, while attenuating the transfer of fast action potentials between electrically coupled cells. *In vivo*, these cells have elevated activity outside of theta-run periods, which could correspond with theta-off cells (Buzsáki et al., 1983; Colom and Bland, 1987). As well, they do not show activation during sharp wave-associated ripples. Although the inputs to these cells have not yet been characterized electrophysiologically, it is possible that they receive inhibitory input from I-S3 cells, since the somata of VIP-LRP cells were often decorated by VIP+ and CR+ axonal boutons (Francavilla et al., 2018). Though previous studies of I-S cells in hippocampus have generally classified I-S cells into these four types, a more recent transcriptomics study has also revealed a larger diversity of I-S cells in the CA1 area, with at least 8 transcriptomically-defined clusters [Harris et al. (2018); I-S1: 3 clusters; I-S2: 2 clusters; I-S3: 3 clusters]. Altogether, the characterization of I-S cell types in hippocampal CA1 area has highlighted a vast array of different cell types that are likely to enrich the mechanisms dedicated to information processing in this cortical area.

Notably, there are not many studies to date that have examined different types of hippocampal CA1 I-S cells *in vivo* during active learning. However, there is a recent calcium imaging study looking at the activity of VIP+ cells in CA1 during head-restricted behavior (Turi et al., 2019), though this

does not disentangle I-S cell types (Acsády et al., 1996a) from VIP+/CCK+ basket cells (Klausberger and Somogyi, 2008; Tyan et al., 2014; Francavilla et al., 2018; Luo et al., 2020). In this study, CA1 VIP+ cells exhibit a state-dependent disinhibition of pyramidal cells, which supports learning of reward site locations (Turi et al., 2019). During head-fixed locomotion, VIP+ cells were divided based on their activity pattern into those that are positively modulated by velocity, and those that are negatively modulated by velocity. Negatively velocity-modulated VIP+ cells exhibited activity either before or after running epochs, or both. Introduction of a spatially-guided reward learning task modulated the numbers of cells which falls into these functionally-defined VIP+ cell types. Interestingly, optogenetically suppressing VIP+ cell activity during this task led to an impairment in learning of the reward location and a decrease in the localization of pyramidal cell place fields near to the reward site, suggesting a role for VIP+ cells in learning the reward location and sharpening the memory representation. A network model further predicted that this sharpening of memory representation was due to the contribution of VIP+/CR+ cells, and not of VIP+/CCK+ basket cells (Turi et al., 2019). In line with this finding, another study found that chemogenetic silencing of CA1 VIP+ cells impairs spatial learning (Magnin et al., 2019). Together, these studies suggest an important role of I-S cells in learning and memory (Figure 1A).

FRONTAL AREAS

The spatial localization of I-S cells in frontal cortical areas can be extrapolated from the immunohistochemical studies that focused on the location of VIP+ cells. In rats, VIP+/CR+ cells show spatial distributions in layers II/III (i.e., 71% of CR+ cells are also VIP+) and layers V/VI (i.e., 94% of CR+ cells are also VIP+) (Kawaguchi and Kubota, 1997; Kawaguchi and Kondo, 2002). Smaller CCK+ cells tend to also be VIP+ and appear to be distributed similarly to VIP+/CR+ cells (Kawaguchi and Kubota, 1997). As well, some cells in layers II/III are immunoreactive for either VIP (i.e., 43% of VIP+ cells) or CR (i.e., 29% of CR+ cells), but not both (Kawaguchi and Kubota, 1997), similar to what is seen for hippocampal I-S1 and I-S2 cells. Further, VIP+ cells in frontal cortex, as classified based on their morphology, include bipolar cells, double bouquet cells, small basket cells, and arcade cells, of which small basket cells have rounder somata and smaller somatic diameters (Kawaguchi and Kubota, 1996; Kawaguchi and Kondo, 2002; Wang et al., 2002). In human frontal and temporal cortices, VIP+ cells can be found across all layers (Ong and Garey, 1991). In particular, VIP+ cells with small somatic diameters are located mostly in layers I and IV, whereas VIP+ cells with moderate somatic diameters are more numerous and more densely packed in layers II/III (Ong and Garey, 1991).

Notably, as far back as 2004, I-S cells were included in a network model of prefrontal cortex in order to make predictions on the neuronal operations that support working memory (Wang et al., 2004). Here, I-S cells were proposed to contribute to working memory by suppressing the dendrite-targeting

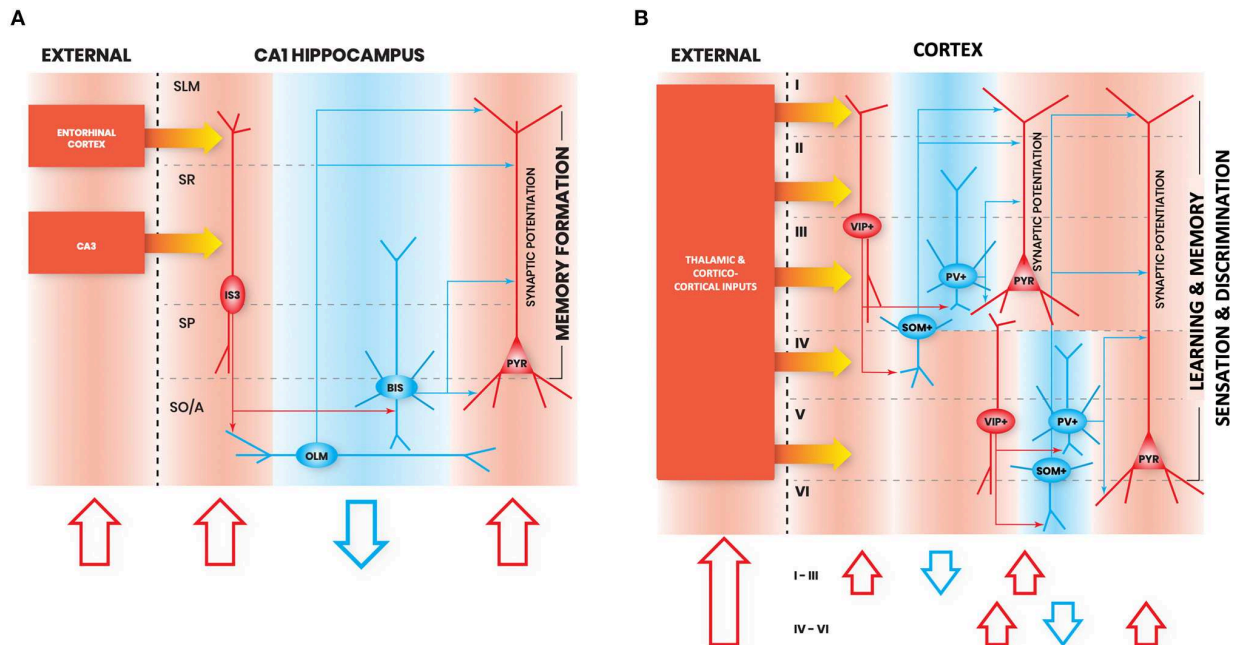


FIGURE 1 | Interneuron-specific cell circuitry across cortical areas allows disinhibition and synaptic potentiation of pyramidal cells via external inputs. In these schematic figures, we highlight the commonalities in I-S circuitry across **(A)** CA1 hippocampus, and **(B)** neocortex. We chose to provide illustrations for these brain regions because enough details on I-S cell circuitry in these areas have been reported in the literature. Red shapes denote increased neural activation, and blue shapes denote decreased neural activation. The flow of each schematic is the following: increased activation of excitation from external inputs (1st red arrow) increases activation of I-S cells (2nd red arrow), which decreases activity of other local SOM+ and PV+ cell types (blue arrow), and allows an increase in gain in pyramidal cells (3rd red arrow). In principle, this can be generalized as the basic mechanism through which activation of I-S cells in different brain areas can lead to enhancements in learning, memory, and sensory discrimination. SO/A, Stratum Oriens/Alveus; SP, Stratum Pyramidale; SR, Stratum Radiatum; SLM, Stratum Lacunosum Moleculare; PYR, Pyramidal neuron.

interneuron activity during sensory inputs, thus creating inverted sensory tuning curves in dendrite-targeting interneurons. Otherwise, dendrite-targeting interneurons provided resistance against distracting stimuli through elevated spontaneous activity. This pathway gating/ungating roles of I-S cells is further reviewed in Wang and Yang (2018).

Similar to I-S3 cells in CA1, VIP+ cells in auditory and medial prefrontal cortices primarily inhibit SOM+ cells, as well as a fraction of PV+ cells (Pi et al., 2013). A small percentage also contact pyramidal cells, which could represent an overlap with non-I-S VIP+ cells. *In vivo*, VIP+ cells in these areas are strongly but transiently activated following punishments in a go/no-go auditory discrimination task, and show a weaker but sustained response during rewards (Pi et al., 2013). Also, VIP+ cells are similar to pyramidal cells in that they exhibit responses during both go and no-go trials, while SOM+ and PV+ cells exhibit a response bias toward go trials (Kamigaki, 2019a).

In dorsomedial prefrontal cortex (also reviewed in Kamigaki, 2019a,b), activation of PV+ or SOM+ cells during this type of go/no-go task impairs performance, while activation of VIP+ cells enhances performance (Kamigaki and Dan, 2017). Similar findings were seen in a delayed two-alternative forced-choice task, which suggests an importance for VIP+ cell activation in enhancing short-term memory retention (Kamigaki and Dan, 2017). In addition, disinhibition through activation of VIP+

cells in prefrontal cortex enhances theta rhythm synchrony and communication from hippocampus to prefrontal cortex (Lagler et al., 2016; Lee et al., 2019). For example, in an elevated plus maze task, animals display avoidance of the open arm component of the maze, and this is accompanied with VIP+ cell activation and disinhibition of responses to hippocampal inputs, which can carry anxiety related-information (Lee et al., 2019). Correspondingly, inhibition of VIP+ cells leads to reduced open arm avoidance when there is theta synchrony between the two regions. During a different and more complex cue-matching-to-place task, the activity of PV+ basket cells in the prelimbic area of the prefrontal cortex forms neural ensembles that are either activated or suppressed at different stages of the task, thus allowing “multi-layered cognitive computations” (Lagler et al., 2016). More specifically, the activation or suppression of individual basket cells is correlated to the amount of VIP+ cell inputs that they receive.

In frontal association cortex *in vivo*, feedforward inhibition from VIP+ cells creates a pull-push circuitry, alternatively to the classical push-pull circuitry that can be generated through feedforward excitation (Garcia-Junco-Clemente et al., 2017). This is observed since VIP+ cells in this brain area make both direct connections to pyramidal cells in addition to connections to SOM+ cells. Without further characterization of VIP+ cell types in this brain area however, it is difficult to say whether this

arises from VIP+ cell uniqueness in frontal association cortex, or different I-S and non-I-S VIP+ cell types.

In summary, from work done in frontal areas, it is clear that I-S cells are involved in enhancing learning and memory discrimination, are recruited during theta rhythms, and primarily target SOM+ cells, but also PV+ cells (i.e., similar to hippocampal CA1 I-S3 cells; **Figures 1A,B**). Further characterization of VIP+ cell types in frontal areas is needed to distinguish how much I-S cell types in these areas contact pyramidal cells, compared to non-I-S VIP+ cells.

SOMATOSENSORY CORTEX

In the somatosensory barrel cortex, VIP+ cell dendrites often exhibit bipolar or tufted morphologies and span across cortical layers and columns (Bayraktar et al., 2000; Prönnke et al., 2015). Particularly, in layer IV, VIP+ and SOM+ cells, but not PV+ cells, show a higher density within intercolumnar septal areas (Bayraktar et al., 2000; Almási et al., 2019). Moreover, different VIP+ cell morphologies can be found across all layers in barrel cortex, though they exhibit a higher density in layers II/III (Prönnke et al., 2015; Almási et al., 2019). In a study of CR+ cells spanning across cortex, it was also found that CR is generally expressed in bipolar and multipolar cells (Caputi et al., 2009). While both preferentially target other interneurons, electrophysiological characterization of these cells in barrel cortex demonstrated key excitability and synaptic differences—most notably the existence of asymmetric electrical connections between multipolar CR+ cells and multipolar PV+ cells (Caputi et al., 2009).

Also in the somatosensory barrel cortex, VIP+ cells receive inputs from the primary vibrissal motor cortex pyramidal cells, and preferentially inhibit SOM+ cells (Lee et al., 2013). This highlights another cortical disinhibitory circuitry, where during whisking behavior *in vivo*, VIP+ cells show enhanced activation, while SOM+ cells reduce their activity (Gentet et al., 2012; Lee et al., 2013; Yu et al., 2019). This finding was both layer-specific (i.e., VIP+ cells in layers II/III) and behavior-dependent, where it was specifically observed during active wakefulness voluntary whisking (Yu et al., 2019). When tested in a goal-directed behavioral context where mice were actively attempting to localize an object, whisker touch events slightly suppressed VIP+ cells, with an immediate activation of fast spiking cells and a delayed activation of SOM+ and excitatory cells (Yu et al., 2019). VIP+ cells have also been shown to contact CB+ cells (Staiger et al., 2004) as well as PV+ cells (Dávid et al., 2007), where higher densities of VIP+ cell inputs to PV+ cells were associated with higher densities of excitatory inputs. Axon terminals from VIP+ cells in somatosensory cortex also highly express mGluR7a, a metabotropic glutamate receptor, which can be expressed in axon terminals that contact SOM+ and PV+ cells (Dalezios et al., 2002). As well, VIP+ cells can also target excitatory cells (Zhou et al., 2017), though it is unknown if this is due to different VIP+ cell types, or specialized layer-specific connections across the cortical layers of barrel cortex. In addition to inputs from the primary vibrissal motor cortex, VIP+ cells in somatosensory

barrel cortex generally also receive inputs from thalamus, and other cortical areas [i.e., proportionally more inputs than other inhibitory cell types receive; Wall et al. (2016)], in a spatially-specific way (Sohn et al., 2016; Almási et al., 2019). For example, when preferentially stimulating either the layer IV-projecting first-order ventral posterior medial thalamic nucleus or the layer I and V-projecting higher-order posterior thalamic nucleus, VIP+ cells are more broadly activated across layers when compared to the excitatory cells, PV+ cells, and SOM+ cells (Sermet et al., 2019). This is consistent with their bipolar dendritic arbors, which span across layers and can allow VIP+ cells to receive inputs that arrive to different cortical layers. In line with this, cortico-cortical and thalamo-cortical inputs in barrel cortex preferentially target the distal dendritic compartments of VIP+ cells (Sohn et al., 2016). Likewise, SOM+ cell inhibitory inputs also preferentially target distal dendritic compartments of VIP+ cells, while PV+ cell inhibitory inputs target the perisomatic compartments of VIP+ cells (Sohn et al., 2016). Higher-order thalamic inputs to VIP+ cells in particular are critical to the induction of LTP in disinhibited layers II/III pyramidal cells during whisker stimulation (Williams and Holtmaat, 2019).

Furthermore, following the study of Lee et al. (2013), it was found that the activity of SOM+ cells in barrel cortex during whisking depends highly on the cortical layer and the SOM+ cell morphology (Muñoz et al., 2017). In particular, some whisking-suppressed SOM+ cells presumably receive stronger inhibition from VIP+ cells during whisking, which, when removed, causes a reversal in their responses to whisking behavior. Blocking cholinergic receptors with bath application of atropine further highlights a state-dependent response, since all SOM+ cells become suppressed during whisking following this manipulation (Muñoz et al., 2017). In barrel cortex, there are also some data on the synaptic inputs by VIP+ and PV+ cells onto Martinotti cells, a SOM+ cell type that is analogous to OLM cells in the hippocampus (Walker et al., 2016). Specifically, Martinotti cells receive a stronger inhibition from PV+ cells. As well, PV+ cell inputs show a frequency-invariant short-term depression, while VIP+ cell inputs exhibit short-term facilitation. This suggests two temporally-specific modes of control over Martinotti cell spiking that can coordinate the disinhibition of pyramidal cells.

In barrel cortex and entorhinal cortex *in vitro*, VIP+ cells also show differential activation according to brain states (Neske et al., 2015; Neske and Connors, 2016). While PV+ cell activity is dominant during up states, there is also considerable spiking from SOM+ and VIP+ cells in barrel cortex, though spiking from these cells during up states is considerably smaller in the entorhinal cortex (Neske et al., 2015). Surprisingly, while optogenetic silencing of SOM+ cells enhances pyramidal cell excitability during up states, optogenetic activation or silencing of VIP+ cells in barrel cortex does not have any effect on pyramidal cell spiking (Neske and Connors, 2016). This suggests the existence of dynamically modulated states where VIP+ cells will not significantly impact network activity, despite their inhibitory connections to SOM+ cells.

VIP+ cells in barrel cortex are also extensively characterized *in vitro* (Prönnke et al., 2015). This work demonstrates the existence of layer-specific distributions of VIP+ cell

morphologically-defined types as well as a variety of different electrophysiologically-defined types, which do not necessarily map onto each other (Prönneke et al., 2015). In fact, a large diversity of different neuronal types could be present in the VIP+ cell population in barrel cortex. Furthermore, certain VIP+ cells in barrel cortex are sensitive to depolarization-inducing neuromodulation from acetylcholine or serotonin, which can effectively switch their firing patterns (Prönneke et al., 2019). Similarly, in auditory cortex, VIP+ cells are very sensitive to nicotinic neuromodulation, where bath application of nicotine can induce large depolarizations in VIP+ cells, with consequential weak depolarizations in pyramidal cells (Askeew et al., 2019).

In summary, similar to I-S cells in other areas, I-S cells in somatosensory cortex appear to also primarily target SOM+ cells. Particularly, they target Martinotti cells, which exhibit properties similar to OLM cells, the primary synaptic target of I-S3 cells in the hippocampus. As well, I-S cells in somatosensory cortex receive spatially organized inputs, which appears to be the case for I-S cells in other areas as well. Altogether, given the similarities in activation and circuitry between I-S cells across different cortical areas, it appears that they may provide similar contributions to network function, such as induction of synaptic plasticity in pyramidal cells during behavior (Figure 1B).

VISUAL CORTIX

In visual cortex, VIP+ cells have somata located in layers II/III, with dendrites distributed in layers I and II, and axons innervating layers I/II, IV, and VI (Hajós et al., 1988; Zilles et al., 1991; Ji et al., 2016). Notably, in both visual and auditory cortices, despite a higher somatic density in layers II/III, only VIP+ cells with somata in layer IV are likely innervated by thalamocortical inputs (Ji et al., 2016), which may be due to differences in laminar dendritic branching patterns between layers II/III and layer IV VIP+ cells or electrotonic distances from soma.

Furthermore, in visual cortex, the activity patterns of VIP+ cells *in vivo* are similar to PV+ cells in that they exhibit strong intra-population coupling (Knoblich et al., 2019). Similar to other areas, visual cortical VIP+ and SOM+ cells inhibit each other bidirectionally, and both SOM+ and VIP+ cells receive non-overlapping inputs from layers II/III pyramidal cells (Pfeffer et al., 2013; Karnani et al., 2016a,b). Moreover, ErbB4 (i.e., a tyrosine kinase receptor associated with signaling factor Neuregulin-1) in VIP+ cells regulates these connections throughout development (Batista-Brito et al., 2017). Specifically, ErbB4 regulates both VIP+ cell targeting of SOM+ cells, as well as excitatory synaptic targeting of VIP+ cells (Batista-Brito et al., 2017). In fact, abolishing ErbB4 in VIP+ cells alters network dynamics and leads to a loss in visual response selectivity and impaired sensory learning (Batista-Brito et al., 2017). *In vivo*, locomotion enhances VIP+ cell activation, which causes an increase in gain in visual responses (Fu et al., 2014), and modulation of cortical plasticity (Fu et al., 2015). This occurs through inputs from the basal forebrain to VIP+ cells, and

is independent of visual stimulation (Fu et al., 2014). This disinhibitory circuitry is context-dependent where during visual stimulation, all of VIP+, PV+, and SOM+ cells in layers II/III and IV show locomotion-associated activation. This indicates that SOM+ cells are activated by visual stimulation during movement, despite inhibition from VIP+ cells (Pakan et al., 2016). In darkness, VIP+ and PV+ cells remain locomotion-associated, while SOM+ cells become silent.

VIP+ cells in visual cortex *in vivo* are also active during non-locomotion, visual stimulation, and under anesthesia (Jackson et al., 2016). Specifically, two-photon calcium imaging has shown that VIP+ cell activity correlates most with the activity of pyramidal cells, and plays a causal role in generating states of high excitatory activity (Jackson et al., 2016). More specifically, suppression of VIP+ cells leads to a reduction of spontaneous excitatory network activity across different behavioral states (Jackson et al., 2016). This directly plays a role in visual spatial frequency tuning of pyramidal cells, where activation of VIP+ cells generates responses to higher visual spatial frequencies and inactivation of VIP+ cells generates responses to lower visual spatial frequencies (Ayzenshtat et al., 2016). During visual stimulation, VIP+ cells also respond differently to novel vs. familiar images (Garrett et al., 2020). While they become activated during novel images, they are suppressed during familiar images. As well, VIP+ cell activation ramps up when expected visual stimuli are omitted during sequences of visual stimuli (Garrett et al., 2020). Similarly, activation of VIP+ cells during visual stimulation (i.e., using a contrast drifting Gabor stimulus) enhances contrast detection, whereas activation of PV+ or SOM+ cells during the visual stimulation reduces contrast detection (Cone et al., 2019).

Interestingly, VIP+ cells in visual cortex following animal exposure to light exhibit a high expression of insulin like growth factor 1 (IGF1), an experience-regulated gene (Mardinly et al., 2016), which is in contrast to PV+ and SOM+ cells. Overexpression of IGF1 also promotes inhibitory inputs to VIP+ cells, thus reducing their activity, and, accordingly, the disinhibition of pyramidal cells. Additionally, when testing ocular dominance plasticity, knocking down IGF1 increases disinhibition and enhances visual acuity in an experience-dependent manner (Mardinly et al., 2016).

Visual acuity is also potentially modulated by inputs from the cingulate area in frontal cortex, which improves visual discrimination via strong connections to VIP+ cells in visual cortex, in addition to contacting PV+ cells, SOM+ cells, and pyramidal cells (Zhang et al., 2014). Particularly, focal layer-specific activation of cingulate area axons in visual cortex leads to SOM+ cell-mediated surround suppression and VIP+ cell-mediated center facilitation (i.e., disinhibition) (Zhang et al., 2014). Based on computational modeling work, these types of connectivity mechanisms can sharpen and enhance visual responses for optimal encoding of visual stimuli (Lee and Mihalas, 2017; Lee et al., 2017). Moreover, VIP+ cells *in vivo* possess vertically elongated axons with narrow spatial layouts that allow lateral disinhibition of pyramidal cells, which can generate local transient holes in the blanket of inhibition in visual cortex (Karnani et al., 2014, 2016a).

In visual cortex, there is also some indication that VIP+ cells may be involved in associative learning through long-range top-down projections from the retrosplenial cortex (Makino and Komiyama, 2015). Here it was shown that retrosplenial inputs to layers II/III pyramidal cells become enhanced during a visually-guided active avoidance task, where mice are trained to run on a treadmill when they see a drifting grating stimulus with particular orientation. Comparatively, bottom-up pyramidal cell projections from layer IV and SOM+ cell projections from layers II/III (i.e., which gate retrosplenial inputs) become weaker over the course of this task. Both retrosplenial inactivation and SOM+ cell activation were sufficient to reverse the learning-related changes in layers II/III. Although no changes in VIP+ cell activation were observed throughout this task, it is nonetheless possible that VIP+ cells are entrained by retrosplenial inputs to suppress SOM+ cells, which would ungate retrosplenial inputs to layers II/III pyramidal cells. This, however, remains to be tested directly.

Once again, like I-S cells in the hippocampus, frontal areas, and somatosensory cortex, I-S cells in visual cortex exhibit similar morphological properties and primarily target SOM+ cells. Similar to I-S cells in other areas, visual cortical I-S cell activation contributes through enhancement of sensory discrimination and by promoting plasticity mechanisms, which, again, suggests similar roles for I-S cells across cortical areas (**Figure 1B**).

MOTOR CORTEX

VIP+ cell morphological and electrophysiological characterization has also been performed in the motor cortex. Here I-S cells also tend to have bipolar morphologies with irregular spiking activity and local intracortical glutamatergic inputs from pyramidal cells (Cauli et al., 1997; Porter et al., 1998). They are further characterized as two distinct populations, based on differences in burst duration, and expression of CR and choline acetyltransferase.

In motor cortex, VIP+ cells are also involved in motor skill learning (Adler et al., 2019). In this study, mice were trained to run forwards or backwards at fixed speeds on a treadmill, effectively changing their gait patterns such that they run with a structured pattern. During this motor learning, layers II/III pyramidal cells exhibited sequential activation patterns across the population that are shifted compared to normal treadmill running—a finding that was dependent on the presence of CaMKII-mediated synaptic plasticity (Adler et al., 2019). SOM+ cells, on the other hand, exhibited diverse responses where they would become enhanced, suppressed, or unchanged at the onset of forward and backward running. As well, their responses to either forward or backward running was not indicative of what their response would be in the opposite case. Interestingly, activation of SOM+ cells suppressed both the temporal shift in the sequential activation of pyramidal cells as well as motor learning. Conversely, suppressing SOM+ cells during new learning de-stabilized previously learned motor skills (i.e., when switching from a forward running to backward running learning paradigm). Further tests revealed that VIP+

cells, which become activated during both forward and backward running, are necessary for the shifted sequential pyramidal cell activation patterns and motor learning to occur, but not necessary for preserving previously learned motor skills. Altogether, Adler et al. (2019) provides a clear demonstration of how VIP+ cells can inhibit SOM+ cells, causing disinhibition in pyramidal cells and allowing synaptic plasticity and learning to occur.

BASOLATERAL AMYGDALA

Although it is not a part of cerebral cortex, certain commonalities also exist with VIP+ cells located in the basolateral amygdala. In this area, VIP+ cells have been classified as either I-S or cannabinoid-expressing basket cells (Rhomberg et al., 2018). Additionally, three types of activity patterns are observed when recording from I-S cells, based on the number of spikes observed upon depolarization. Here, I-S cells primarily target other I-S cells, CCK+ basket cells, and neurogliaform cells. I-S cells themselves receive a dense inhibition, of which only a small proportion is from other I-S cells (Rhomberg et al., 2018). Though connections to SOM+ or PV+ cells were not tested in this study, other studies showed that VIP+ cells target CB+ cells, which include SOM+, PV+, and CCK+ cells (Muller et al., 2003; Krabbe et al., 2018). More recently, deep-brain calcium imaging and optogenetic experiments have demonstrated the involvement of the basolateral amygdala VIP+ cells in associative learning (Krabbe et al., 2019). More specifically, these cells were activated by aversive stimuli, were modulated by expectations, and were necessary for the induction of synaptic plasticity and learning to occur. Moreover, VIP+ cell contribution to circuit function is achieved through innervation of SOM+ and PV+ cells, which allows disinhibition of projecting neurons in basolateral amygdala (Krabbe et al., 2019). Overall, this circuitry motif and functional role are similar to the VIP+ cell circuitry and function seen in other brain areas.

I-S CELLS AS A CLINICAL TARGET?

Given their specialized connectivity, disinhibitory control, and potentially beneficial effects on learning and memory, it is worth considering I-S cells as potential targets in clinical studies. As such in this section we will give an overview of some studies that have already investigated I-S cells in various neuropathologies and clinical contexts.

In the CA1 hippocampus, I-S3 cells have been studied in the context of status epilepticus using a mouse model of temporal lobe epilepsy, where these cells showed altered dendritic morphologies and passive membrane properties, and provided a lower inhibition to their postsynaptic targets (David and Topolnik, 2017). Although I-S3 cell densities were preserved in this study, it has been shown in human dentate gyrus that densities of CR+ cells are reduced in epilepsy (Maglóczy et al., 2000). Furthermore, hippocampal CR+ cells have altered morphologies and connectivity to a degree which depends on the severity of the temporal lobe epilepsy (Tóth et al.,

2010; Thom et al., 2012). In another mouse model of epilepsy desynchronization of interneuron firing between regions CA1 and dentate gyrus lead to destabilization of CA1 place cell Shuman et al. (2020). As well, in an optogenetically-induced epilepsy model, it is observed that different motor cortex neuron types follow different trajectories throughout a seizure (Khoshkhoo et al., 2017). While PV+, SOM+, and VIP+ cells all become activated at the onset of a seizure, pyramidal cells exhibit a delay in activation. As well, PV+ and SOM+ cells exhibit a gradual increase in activation throughout the seizure, while VIP+ cell activation peaks near the mid-point of seizures. Interestingly, optogenetic inhibition of VIP+ cells consistently disrupts seizure onset, and reduces the duration of seizures, which highlights VIP+ cells as a potential neuromodulatory target for seizure control (Khoshkhoo et al., 2017). Along these lines, VIP+ cells, alongside PV+ and SOM+ cells in motor cortex, are known to be manipulable through brain machine interfacing (Mitani et al., 2018).

Somatosensory cortex VIP+ cells have also been studied in a mouse model of neuropathic pain. Specifically, VIP+ cells are over-active during neuropathic pain, which parallels the activity of pyramidal cells, but is in contrast to a reduced activity of PV+ and SOM+ cells (Cichon et al., 2017). This combination of effects therefore leans in favor of pyramidal cell hyperexcitability through disinhibition. Moreover, activation of SOM+ cells was sufficient for suppressing pyramidal cell hyperactivity and reversing symptoms of neuropathic pain.

VIP+ cells can also contribute to the pathogenesis of Dravet syndrome, a neurodevelopmental disorder associated with a loss of functional variants of the gene *SCN1A* that encodes for the Nav1.1 channel subunits (Goff and Goldberg, 2019). More specifically, a mouse model of Dravet syndrome (*Scn1a*^{+/-}) had previously been associated with a loss of excitability in PV+ and SOM+ cells, which both express Nav1.1 (Yu et al., 2006; Ogiwara et al., 2007; Tai et al., 2014; De Stasi et al., 2016; Favero et al., 2018). In addition, in *Scn1a*^{+/-} mouse somatosensory and visual cortices, VIP+ cells that displayed irregular spiking, but not those that displayed continuous adapting spiking, were found to exhibit reductions in gain (Goff and Goldberg, 2019). Notably, the irregular spiking firing pattern did not coincide with whether VIP+ cells co-expressed CR or CCK, nor with whether the morphology was bipolar vs. multipolar. These irregular spiking VIP+ cells were also found to express Nav1.1, which explains their involvement in the pathogenesis, and the irregular spiking pattern was dependent on the activation of the M-type potassium channels (Goff and Goldberg, 2019).

CR+ cells have also been studied in the context of an Alzheimer's disease mouse model where decreased numbers were reported and, in parallel, increased amyloid beta deposits were observed within the axonal fields of CR+ cells (Baglietto-Vargas et al., 2010). These were distinguished from other Cajal-Retzius cells, which also express CR but did not show decreased numbers. However, reduced densities of CR+ cells have not been observed in human dentate gyrus or entorhinal cortex, and these do not appear to co-localize with neurofibrillary tangles, nor their axonal fields with amyloid beta plaques (Brion and Résibois, 1994). On the other hand, CR+ cells in this study did exhibit

reduced dendritic trees and dystrophic fibers in subjects with Alzheimer's disease (Brion and Résibois, 1994). During aging, there is also a down-regulation of genes associated with synaptic transmission in SOM+ and VIP+ cells in human frontal cortex, suggesting age-dependent changes in the functionality of this circuitry (French et al., 2017). As such, stimulating this circuitry (e.g., pharmacologically exciting VIP+ cells) could be a viable option for targeting age-related changes in cognition, such as learning and memory.

SUMMARY AND CONCLUSIONS

Overall, it is clear from this body of literature that I-S cells across cortex share many common principles in their organization, and I-S cell types may be particularly diverse. We highlight this with the illustrations shown in **Figure 1**. Of course, much more information on the detailed I-S circuitry organization is currently available for CA1 hippocampus when compared to other cortical areas, which often characterize cell types through neurochemical marker expression alone. Amongst commonalities we note the tendency of I-S cells to have vertical bipolar-shaped morphologies with dendrites that project across layers. This allows them to receive inputs from multiple layer-specific external projections. We also indicate commonalities in their preferential targeting of SOM+ cells (and PV+ cells to a lesser extent), as well as their ability to disinhibit pyramidal cells through this circuitry, which may create a window for synaptic plasticity to occur. Altogether, these features allow I-S cells across cortex to perform a wide array of different cortical computations during behavior. Because of their common ability to effectively gate synaptic plasticity in pyramidal cells across cortical structures, I-S cells in cortex offer an interesting therapeutic target for neuromodulation by using drugs that specifically modulate the excitability of I-S cells. For example, we can study how global enhancement or suppression of I-S cell activity across the cortex might impact behavior. Along these lines, since similar analogous circuitries exist across the cortex, it seems that I-S cells in general play a role in learning and sensory tuning of pyramidal cell receptive fields. As such, activation of I-S cells across cortical structures *in vivo* offers a target for globally enhancing performance on memory-related tasks.

It is important to note that VIP+ cells exhibit a large diversity in transcriptomic, morphological and physiological properties (Prönnke et al., 2015; Harris et al., 2018; Gouwens et al., 2019; Hodge et al., 2019), which so far made the definition of cell types largely impossible. While I-S cells exhibit commonalities across different cortical structures, these cells might thus still exhibit local differences in functional roles and contributions to network activity. Moreover, different balances of I-S vs. non-I-S VIP+ cells across different brain areas could give the appearance of different region-specific functional contributions to circuit function *in vivo*, when in fact it only appears this way because I-S cells are not sufficiently isolated from non-I-S cells when VIP+ cells are targeted (e.g., CCK+/VIP+ basket cells). Further classification studies based on transcriptomic and morphological characteristics in relation to synaptic connectivity (i.e., inputs and

outputs) across different cortical areas would help to elucidate these aspects of I-S cell diversity.

Another aspect to highlight from these studies is that I-S cells from any particular region appear to receive a mixture of inputs from different distant regions. It has already been postulated (Wang and Yang, 2018), and demonstrated in a model (Yang et al., 2016), that the reason for this is because I-S cells can gate particular external pathways and allow flexible switching between information arriving from different external structures. As such, without I-S cell contributions to circuit function throughout the brain, it is possible that information would not be properly routed during behavioral tasks where integration of different types of sensory stimuli are relevant. This is particularly relevant in Lagler et al. (2016) where basket cell activation during a complex behavioral task was dependent on the level of I-S cell activation, suggesting the existence of complex learned disinhibitory pathways.

To conclude, we present in this review compelling evidence indicating that I-S cells across different cortical areas share many morphological, physiological, and connectivity features, which allows them to contribute in similar ways to network function. As such, we highlight that I-S cells across cortex are a crucial network component that is

necessary for supporting sensory discrimination, learning, and memory formation.

AUTHOR CONTRIBUTIONS

AG-M: conceptualization, visualization, writing—original draft preparation, and writing—review and editing. FS and LT: project administration, resources, supervision, and writing—review and editing.

FUNDING

This research was supported by the Natural Sciences and Engineering Research Council of Canada (NSERC): Discovery Grants (RGPIN-2016-06182) to FS and (342292-2012-RGPIN) to LT, Graduate Scholarship (CGSD2 - 504375 - 2017) to AG-M, and by the Canadian Institutes of Health Research (CIHR) Operating Grants (Grants #MOP-137072 and MOP-142447) to LT.

ACKNOWLEDGMENTS

We would like to offer special thanks to Dimitry Topolnik for the preparation of the schematics shown in **Figure 1**.

REFERENCES

- Acsády, L., Arabadzisz, D., and Freund, T. F. (1996a). Correlated morphological and neurochemical features identify different subsets of vasoactive intestinal polypeptide-immunoreactive interneurons in rat hippocampus. *Neuroscience* 73, 299–315. doi: 10.1016/0306-4522(95)00610-9
- Acsády, L., Görös, T. J., and Freund, T. F. (1996b). Different populations of vasoactive intestinal polypeptide-immunoreactive interneurons are specialized to control pyramidal cells or interneurons in the hippocampus. *Neuroscience* 73, 317–334. doi: 10.1016/0306-4522(95)00609-5
- Adler, A., Zhao, R., Shin, M. E., Yasuda, R., and Gan, W.-B. (2019). Somatostatin-expressing interneurons enable and maintain learning-dependent sequential activation of pyramidal neurons. *Neuron* 102, 202–216.e7. doi: 10.1016/j.neuron.2019.01.036
- Almási, Z., Dávid, C., Witte, M., and Staiger, J. F. (2019). Distribution patterns of three molecularly defined classes of GABAergic neurons across columnar compartments in mouse barrel cortex. *Front. Neuroanat.* 13:45. doi: 10.3389/fnana.2019.00045
- Armstrong, C., Krook-Magnuson, E., and Soltesz, I. (2012). Neurogliaform and ivy cells: a major family of nNOS expressing GABAergic neurons. *Front. Neural Circuits* 6:23. doi: 10.3389/fncir.2012.00023
- Askew, C. E., Lopez, A. J., Wood, M. A., and Metherate, R. (2019). Nicotine excites VIP interneurons to disinhibit pyramidal neurons in auditory cortex. *Synapse* 73:e22116. doi: 10.1002/syn.22116
- Ayzenshtat, I., Karnani, M. M., Jackson, J., and Yuste, R. (2016). Cortical control of spatial resolution by VIP+ interneurons. *J. Neurosci.* 36, 11498–11509. doi: 10.1523/JNEUROSCI.1920-16.2016
- Baglietto-Vargas, D., Moreno-Gonzalez, I., Sanchez-Varo, R., Jimenez, S., Trujillo-Estrada, L., Sanchez-Mejias, E., et al. (2010). Calretinin interneurons are early targets of extracellular amyloid- β pathology in PS1/A β PP Alzheimer mice hippocampus. *J. Alzheimers Dis.* 21, 119–132. doi: 10.3233/JAD-2010-100066
- Batista-Brito, R., Vinck, M., Ferguson, K. A., Chang, J. T., Laubender, D., Lur, G., et al. (2017). Developmental dysfunction of VIP interneurons impairs cortical circuits. *Neuron* 95, 884–895.e9. doi: 10.1016/j.neuron.2017.07.034
- Bayraktar, T., Welker, E., Freund, T. F., Zilles, K., and Staiger, J. F. (2000). Neurons immunoreactive for vasoactive intestinal polypeptide in the rat primary somatosensory cortex: morphology and spatial relationship to barrel-related columns. *J. Comp. Neurol.* 420, 291–304. doi: 10.1002/(SICI)1096-9861(20000508)420:3h291::AID-CNE2i3.0.CO;2-H
- Bezaire, M. J., and Soltesz, I. (2013). Quantitative assessment of CA1 local circuits: knowledge base for interneuron-pyramidal cell connectivity. *Hippocampus* 23, 751–785. doi: 10.1002/hipo.22141
- Blasco-Ibáñez, J. M., Martínez-Guijarro, F. J., and Freund, T. F. (1998). Enkephalin-containing interneurons are specialized to innervate other interneurons in the hippocampal CA1 region of the rat and guinea-pig. *Eur. J. Neurosci.* 10, 1784–1795. doi: 10.1046/j.1460-9568.1998.00190.x
- Brion, J. P., and Résibois, A. (1994). A subset of calretinin-positive neurons are abnormal in Alzheimer's disease. *Acta Neuropathol.* 88, 33–43. doi: 10.1007/BF00294357
- Buzsáki, G., Lai-Wo, S. L., and Vanderwolf, C. H. (1983). Cellular bases of hippocampal EEG in the behaving rat. *Brain Res. Rev.* 6, 139–171. doi: 10.1016/0165-0173(83)90037-1
- Caputi, A., Rozov, A., Blatow, M., and Monyer, H. (2009). Two calretinin-positive GABAergic cell types in layer 2/3 of the mouse neocortex provide different forms of inhibition. *Cereb. Cortex* 19, 1345–1359. doi: 10.1093/cercor/bhn175
- Cauli, B., Audinat, E., Lambolez, B., Angulo, M. C., Ropert, N., Tsuzuki, K., et al. (1997). Molecular and physiological diversity of cortical nonpyramidal cells. *J. Neurosci.* 17, 3894–3906. doi: 10.1523/JNEUROSCI.17-10-03894.1997
- Chamberland, S., Salesse, C., Topolnik, D., and Topolnik, L. (2010). Synapse-specific inhibitory control of hippocampal feedback inhibitory circuit. *Front. Cell. Neurosci.* 4:130. doi: 10.3389/fncel.2010.00130
- Chamberland, S., and Topolnik, L. (2012). Inhibitory control of hippocampal inhibitory neurons. *Front. Neurosci.* 6:165. doi: 10.3389/fnins.2012.00165
- Cichon, J., Blanck, T. J. J., Gan, W.-B., and Yang, G. (2017). Activation of cortical somatostatin interneurons prevents the development of neuropathic pain. *Nat. Neurosci.* 20, 1122–1132. doi: 10.1038/nn.4595
- Cobb, S. R., Halasy, K., Vida, I., Nyiri, G., Tamás, G., Buhl, E. H., et al. (1997). Synaptic effects of identified interneurons innervating both interneurons and pyramidal cells in the rat hippocampus. *Neuroscience* 79, 629–648. doi: 10.1016/S0306-4522(97)00055-9

- Colom, L. V., and Bland, B. H. (1987). State-dependent spike train dynamics of hippocampal formation neurons: evidence for theta-on and theta-off cells. *Brain Res.* 422, 277–286. doi: 10.1016/0006-8993(87)90934-6
- Cone, J. J., Scantlen, M. D., Histed, M. H., and Maunsell, J. H. R. (2019). Different inhibitory interneuron cell classes make distinct contributions to visual contrast perception. *eNeuro* 6:ENEURO.0337-18.2019. doi: 10.1523/ENEURO.0337-18.2019
- Dalezios, Y., Luján, R., Shigemoto, R., Roberts, J. D. B., and Somogyi, P. (2002). Enrichment of mGluR7a in the presynaptic active zones of GABAergic and Non-GABAergic terminals on interneurons in the rat somatosensory cortex. *Cereb. Cortex* 12, 961–974. doi: 10.1093/cercor/12.9.961
- Dávid, C., Schleicher, A., Zuschratter, W., and Staiger, J. F. (2007). The innervation of parvalbumin-containing interneurons by VIP-immunopositive interneurons in the primary somatosensory cortex of the adult rat. *Eur. J. Neurosci.* 25, 2329–2340. doi: 10.1111/j.1460-9568.2007.05496.x
- David, L. S., and Topolnik, L. (2017). Target-specific alterations in the VIP inhibitory drive to hippocampal GABAergic cells after status epilepticus. *Exp. Neurol.* 292, 102–112. doi: 10.1016/j.expneurol.2017.03.007
- De Stasi, A. M., Farisello, P., Marcon, I., Cavallari, S., Forli, A., Vecchia, D., et al. (2016). Unaltered network activity and interneuronal firing during spontaneous cortical dynamics *in vivo* in a mouse model of severe myoclonic epilepsy of infancy. *Cereb. Cortex* 26, 1778–1794. doi: 10.1093/cercor/bhw002
- Favero, M., Sotuyo, N. P., Lopez, E., Kearney, J. A., and Goldberg, E. M. (2018). A transient developmental window of fast-spiking interneuron dysfunction in a mouse model of dravet syndrome. *J. Neurosci.* 38, 7912–7927. doi: 10.1523/JNEUROSCI.0193-18.2018
- Ferraguti, F., Cobden, P., Pollard, M., Cope, D., Shigemoto, R., Watanabe, M., et al. (2004). Immunolocalization of metabotropic glutamate receptor 1α (mGluR1α) in distinct classes of interneuron in the CA1 region of the rat hippocampus. *Hippocampus* 14, 193–215. doi: 10.1002/hipo.10163
- Francavilla, R., Luo, X., Magnin, E., Tian, L., and Topolnik, L. (2015). Coordination of dendritic inhibition through local disinhibitory circuits. *Front. Synap. Neurosci.* 7:5. doi: 10.3389/fnsyn.2015.00005
- Francavilla, R., Villette, V., Luo, X., Chamberland, S., Munoz-Pino, E., Camire, O., et al. (2018). Connectivity and network state-dependent recruitment of long-range VIP-GABAergic neurons in the mouse hippocampus. *Nat. Commun.* 9:5043. doi: 10.1038/s41467-018-07162-5
- French, L., Ma, T., Oh, H., Tseng, G. C., and Sibille, E. (2017). Age-related gene expression in the frontal cortex suggests synaptic function changes in specific inhibitory neuron subtypes. *Front. Aging Neurosci.* 9:162. doi: 10.3389/fnagi.2017.00162
- Freund, T. F., and Antal, M. (1988). GABA-containing neurons in the septum control inhibitory interneurons in the hippocampus. *Nature* 336, 170. doi: 10.1038/336170a0
- Freund, T. F., and Buzsáki, G. (1996). Interneurons of the hippocampus. *Hippocampus* 6, 347–470. doi: 10.1002/(SICI)1098-1063(1996)6:4<347::AID-HIPO1i3.0.CO;2-I
- Fu, Y., Kaneko, M., Tang, Y., Alvarez-Buylla, A., and Stryker, M. P. (2015). A cortical disinhibitory circuit for enhancing adult plasticity. *eLife* 4:e05558. doi: 10.7554/eLife.05558
- Fu, Y., Tucciarone, J., Espinosa, J. S., Sheng, N., Darcy, D., Nicoll, R., et al. (2014). A cortical circuit for gain control by behavioral state. *Cell* 156, 1139–1152. doi: 10.1016/j.cell.2014.01.050
- Fuentealba, P., Klausberger, T., Karayannis, T., Suen, W. Y., Huck, J., Tomioka, R., et al. (2010). Expression of COUP-TFII nuclear receptor in restricted GABAergic neuronal populations in the adult rat hippocampus. *J. Neurosci.* 30, 1595–1609. doi: 10.1523/JNEUROSCI.4199-09.2010
- Garcia-Junco-Clemente, P., Ikrar, T., Tring, E., Xu, X., Ringach, D. L., and Trachtenberg, J. T. (2017). An inhibitory pull-push circuit in frontal cortex. *Nat. Neurosci.* 20, 389–392. doi: 10.1038/nn.4483
- Garrett, M., Manavi, S., Roll, K., Ollerenshaw, D. R., Groblewski, P. A., Ponvert, N. D., et al. (2020). Experience shapes activity dynamics and stimulus coding of VIP inhibitory cells. *eLife* 9:e50340. doi: 10.7554/eLife.50340
- Gentet, L. J., Kremer, Y., Taniguchi, H., Huang, Z. J., Staiger, J. F., and Petersen, C. C. H. (2012). Unique functional properties of somatostatin-expressing GABAergic neurons in mouse barrel cortex. *Nat. Neurosci.* 15, 607–612. doi: 10.1038/nn.3051
- Goff, K. M., and Goldberg, E. M. (2019). Vasoactive intestinal peptide-expressing interneurons are impaired in a mouse model of Dravet syndrome. *eLife* 8:e46846. doi: 10.7554/eLife.46846
- Gouwens, N. W., Sorensen, S. A., Berg, J., Lee, C., Jarsky, T., Ting, J., et al. (2019). Classification of electrophysiological and morphological neuron types in the mouse visual cortex. *Nat. Neurosci.* 22, 1182–1195. doi: 10.1038/s41593-019-0417-0
- Guet-McCreight, A., Camiré, O., Topolnik, L., and Skinner, F. K. (2016). Using a semi-automated strategy to develop multi-compartment models that predict biophysical properties of interneuron-specific 3 (IS3) cells in hippocampus. *eNeuro* 3:ENEURO.0087-16.2016. doi: 10.1523/ENEURO.0087-16.2016
- Gulyás, A. I., Hájos, N., and Freund, T. F. (1996). Interneurons containing calretinin are specialized to control other interneurons in the rat hippocampus. *J. Neurosci.* 16, 3397–3411
- Gulyás, A. I., Megias, M., Emri, Z., and Freund, T. F. (1999). Total number and ratio of excitatory and inhibitory synapses converging onto single interneurons of different types in the CA1 area of the rat hippocampus. *J. Neurosci.* 19, 10082–10097
- Gulyás, A. I., Miettinen, R., Jacobowitz, D. M., and Freund, T. F. (1992). Calretinin is present in non-pyramidal cells of the rat hippocampus—I. A new type of neuron specifically associated with the mossy fibre system. *Neuroscience* 48, 1–27. doi: 10.1016/0304-4522(92)90334-X
- Gunn, B. G., Sanchez, G. A., Lynch, G., Baram, T. Z., and Chen, Y. (2019). Hyperdiversity of CRH interneurons in mouse hippocampus. *Brain Struct. Funct.* 224, 583–598. doi: 10.1007/s00429-018-1793-z
- Hájós, F., Zilles, K., Schleicher, A., and Kálmán, M. (1988). Types and spatial distribution of vasoactive intestinal polypeptide (VIP)-containing synapses in the rat visual cortex. *Anat. Embryol.* 178, 207–217. doi: 10.1007/bf00318224
- Hájós, N., Acsády, L., and Freund, T. F. (1996). Target selectivity and neurochemical characteristics of VIP-immunoreactive interneurons in the rat dentate gyrus. *Eur. J. Neurosci.* 8, 1415–1431. doi: 10.1111/j.1460-9568.1996.tb01604.x
- Harris, K. D., Hochgerner, H., Skene, N. G., Magno, L., Katona, L., Gonzales, C. B., et al. (2018). Classes and continua of hippocampal CA1 inhibitory neurons revealed by single-cell transcriptomics. *PLoS Biol.* 16:e2006387. doi: 10.1371/journal.pbio.2006387
- He, M., Tucciarone, J., Lee, S., Nigro, M. J., Kim, Y., Levine, J. M., et al. (2016). Strategies and tools for combinatorial targeting of GABAergic neurons in mouse cerebral cortex. *Neuron* 91, 1228–1243. doi: 10.1016/j.neuron.2016.08.021
- Helboe, L., Egebjerg, J., and de Jong, I. E. M. (2015). Distribution of serotonin receptor 5-HT6 mRNA in rat neuronal subpopulations: a double *in situ* hybridization study. *Neuroscience* 310, 442–454. doi: 10.1016/j.neuroscience.2015.09.064
- Hodge, R. D., Bakken, T. E., Miller, J. A., Smith, K. A., Barkan, E. R., Graybiel, L. T., et al. (2019). Conserved cell types with divergent features in human versus mouse cortex. *Nature* 573, 61–68. doi: 10.1038/s41586-019-1506-7
- Jackson, J., Ayzenshtat, I., Karnani, M. M., and Yuste, R. (2016). VIP+ interneurons control neocortical activity across brain states. *J. Neurophysiol.* 115, 3008–3017. doi: 10.1152/jn.01124.2015
- Ji, X.-Y., Zingg, B., Mesik, L., Xiao, Z., Zhang, L. I., and Tao, H. W. (2016). Thalamic innervation pattern in mouse auditory and visual cortex: laminar and cell-type specificity. *Cereb. Cortex* 26, 2612–2625. doi: 10.1093/cercor/bhv099
- Kamigaki, T. (2019a). Dissecting executive control circuits with neuron types. *Neuroscience Research* 141, 13–22. doi: 10.1016/j.neures.2018.07.004
- Kamigaki, T. (2019b). Prefrontal circuit organization for executive control. *Neuroscience Research* 140, 23–36. doi: 10.1016/j.neures.2018.08.017
- Kamigaki, T., and Dan, Y. (2017). Delay activity of specific prefrontal interneuron subtypes modulates memory-guided behavior. *Nat. Neurosci.* 20, 854–863. doi: 10.1038/nn.4554
- Karnani, M. M., Agetsuma, M., and Yuste, R. (2014). A blanket of inhibition: functional inferences from dense inhibitory connectivity. *Curr. Opin. Neurobiol.* 26, 96–102. doi: 10.1016/j.conb.2013.12.015
- Karnani, M. M., Jackson, J., Ayzenshtat, I., Sichani, A. H., Manoocheri, K., Kim, S., et al. (2016a). Opening holes in the blanket of inhibition: localized lateral disinhibition by VIP interneurons. *J. Neurosci.* 36, 3471–3480. doi: 10.1523/JNEUROSCI.3646-15.2016

- Karnani, M. M., Jackson, J., Ayzenshtat, I., Tucciarone, J., Manoocheri, K., Snider, W. G., et al. (2016b). Cooperative subnetworks of molecularly similar interneurons in mouse neocortex. *Neuron* 90, 86–100. doi: 10.1016/j.neuron.2016.02.037
- Karson, M. A., Tang, A.-H., Milner, T. A., and Alger, B. E. (2009). Synaptic cross talk between perisomatic-targeting interneuron classes expressing cholecystokinin and parvalbumin in hippocampus. *J. Neurosci.* 29, 4140–4154. doi: 10.1523/JNEUROSCI.5264-08.2009
- Katona, I., Acsády, L., and Freund, T. F. (1999). Postsynaptic targets of somatostatin-immunoreactive interneurons in the rat hippocampus. *Neuroscience* 88, 37–55. doi: 10.1016/S0306-4522(98)00302-9
- Kawaguchi, Y., and Kondo, S. (2002). Parvalbumin, somatostatin and cholecystokinin as chemical markers for specific GABAergic interneuron types in the rat frontal cortex. *J. Neurocytol.* 31, 277–287. doi: 10.1023/A:1024126110356
- Kawaguchi, Y., and Kubota, Y. (1996). Physiological and morphological identification of somatostatin- or vasoactive intestinal polypeptide-containing cells among GABAergic cell subtypes in rat frontal cortex. *J. Neurosci.* 16, 2701–2715. doi: 10.1523/JNEUROSCI.16-08-027.01.1996
- Kawaguchi, Y., and Kubota, Y. (1997). GABAergic cell subtypes and their synaptic connections in rat frontal cortex. *Cereb. Cortex* 7, 476–486. doi: 10.1093/cercor/7.6.476
- Khoshkhoo, S., Vogt, D., and Sohal, V. S. (2017). Dynamic, cell-type-specific roles for GABAergic interneurons in a mouse model of optogenetically inducible seizures. *Neuron* 93, 291–298. doi: 10.1016/j.neuron.2016.11.043
- Klausberger, T., and Somogyi, P. (2008). Neuronal diversity and temporal dynamics: the unity of hippocampal circuit operations. *Science* 321, 53–57. doi: 10.1126/science.1149381
- Knoblich, U., Huang, L., Zeng, H., and Li, L. (2019). Neuronal cell-subtype specificity of neural synchronization in mouse primary visual cortex. *Nat. Commun.* 10:2533. doi: 10.1038/s41467-019-10498-1
- Köhler, C. (1982). Distribution and morphology of vasoactive intestinal polypeptide-like immunoreactive neurons in regio superior of the rat hippocampal formation. *Neurosci. Lett.* 33, 265–270. doi: 10.1016/0304-3940(82)90382-2
- Krabbe, S., Gründemann, J., and Lüthi, A. (2018). Amygdala inhibitory circuits regulate associative fear conditioning. *Biol. Psychiatry* 83, 800–809. doi: 10.1016/j.biopsych.2017.10.006
- Krabbe, S., Paradiso, E., d'Aquin, S., Bitterman, Y., Courtin, J., Xu, C., et al. (2019). Adaptive disinhibitory gating by VIP interneurons permits associative learning. *Nat. Neurosci.* 22, 1834–1843. doi: 10.1038/s41593-019-0508-y
- Lagler, M., Ozdemir, A. T., Lagoun, S., Malagon-Vina, H., Borhegyi, Z., Hauer, R., et al. (2016). Divisions of identified parvalbumin-expressing basket cells during working memory-guided decision making. *Neuron* 91, 1390–1401. doi: 10.1016/j.neuron.2016.08.010
- Larsson, L. I., Fahrenkrug, J., Muckadell, O. S. D., Sundler, F., Håkanson, R., and Rehfeld, J. R. (1976). Localization of vasoactive intestinal polypeptide (VIP) to central and peripheral neurons. *Proc. Natl. Acad. Sci. U.S.A.* 73, 3197–3200. doi: 10.1073/pnas.73.9.3197
- Leão, R. N., Mikulovic, S., Leão, K. E., Munguba, H., Gezelius, H., Enjin, A., et al. (2012). OLM interneurons differentially modulate CA3 and entorhinal inputs to hippocampal CA1 neurons. *Nat. Neurosci.* 15, 1524–1530. doi: 10.1038/nn.3235
- Lee, A. T., Cunliff, M. M., See, J. Z., Wilke, S. A., Luongo, F. J., Ellwood, I. T., et al. (2019). VIP interneurons contribute to avoidance behavior by regulating information flow across hippocampal-prefrontal networks. *Neuron* 102, 1223–1234.e4. doi: 10.1016/j.neuron.2019.04.001
- Lee, J. H., Koch, C., and Mihalas, S. (2017). A computational analysis of the function of three inhibitory cell types in contextual visual processing. *Front. Comput. Neurosci.* 11:28. doi: 10.3389/fncom.2017.00028
- Lee, J. H., and Mihalas, S. (2017). Visual processing mode switching regulated by VIP cells. *Sci. Rep.* 7:1843. doi: 10.1038/s41598-017-01830-0
- Lee, S., Hjerling-Leffler, J., Zagha, E., Fishell, G., and Rudy, B. (2010). The largest group of superficial neocortical GABAergic interneurons expresses ionotropic serotonin receptors. *J. Neurosci.* 30, 16796–16808. doi: 10.1523/JNEUROSCI.1869-10.2010
- Lee, S., Kruglikov, I., Huang, Z. J., Fishell, G., and Rudy, B. (2013). A disinhibitory circuit mediates motor integration in the somatosensory cortex. *Nat. Neurosci.* 16, 1662–1670. doi: 10.1038/nn.3544
- Léránth, C., Frotscher, M., Tömböl, T., and Palkovits, M. (1984). Ultrastructure and synaptic connections of vasoactive intestinal polypeptide-like immunoreactive non-pyramidal neurons and axon terminals in the rat hippocampus. *Neuroscience* 12, 531–542. doi: 10.1016/0306-4522(84)90071-X
- Lorén, I., Emson, P. C., Fahrenkrug, J., Björklund, A., Alumets, J., Håkanson, R., et al. (1979). Distribution of vasoactive intestinal polypeptide in the rat and mouse brain. *Neuroscience* 4, 1953–1976. doi: 10.1016/0306-4522(79)90068-X
- Luo, X., Guet-McCreight, A., Villette, V., Francavilla, R., Marino, B., Chamberland, S., et al. (2020). Synaptic mechanisms underlying the network state-dependent recruitment of VIP-expressing interneurons in the CA1 hippocampus. *Cereb. Cortex* 30, 3667–3685. doi: 10.1093/cercor/bhz334
- Luo, X., Muñoz-Pino, E., Francavilla, R., Vallée, M., Droit, A., and Topolnik, L. (2019). Transcriptomic profile of the subiculum-projecting VIP GABAergic neurons in the mouse CA1 hippocampus. *Brain Struct. Funct.* 224, 2269–2280. doi: 10.1007/s00429-019-01883-z
- Maglóczy, Z., Wittner, L., Borhegyi, Z., Halász, P., Vajda, J., Cziráj, S., et al. (2000). Changes in the distribution and connectivity of interneurons in the epileptic human dentate gyrus. *Neuroscience* 96, 7–25. doi: 10.1016/S0306-4522(99)00474-1
- Magnin, E., Francavilla, R., Amalyan, S., Gervais, E., David, L. S., Luo, X., et al. (2019). Input-specific synaptic location and function of the $\alpha 5$ GABAA receptor subunit in the mouse CA1 hippocampal neurons. *J. Neurosci.* 39, 788–801. doi: 10.1523/JNEUROSCI.0567-18.2018
- Makino, H., and Komiyama, T. (2015). Learning enhances the relative impact of top-down processing in the visual cortex. *Nat. Neurosci.* 18, 1116–1122. doi: 10.1038/nn.4061
- Mardinly, A. R., Spiegel, I., Patrizi, A., Centofante, E., Bazinet, J. E., Tzeng, C. P., et al. (2016). Sensory experience regulates cortical inhibition by inducing IGF1 in VIP neurons. *Nature* 531, 371–375. doi: 10.1038/nature17187
- Megias, M., Emri, Z., Freund, T. F., and Gulyás, A. I. (2001). Total number and distribution of inhibitory and excitatory synapses on hippocampal CA1 pyramidal cells. *Neuroscience* 102, 527–540. doi: 10.1016/S0306-4522(00)00496-6
- Melzer, S., Michael, M., Caputi, A., Eliava, M., Fuchs, E. C., Whittington, M. A., et al. (2012). Long-range-projecting GABAergic neurons modulate inhibition in hippocampus and entorhinal cortex. *Science* 335, 1506–1510. doi: 10.1126/science.1217139
- Miettinen, R., Gulyás, A. I., Baimbridge, K. G., Jacobowitz, D. M., and Freund, T. F. (1992). Calretinin is present in non-pyramidal cells of the rat hippocampus—II. Co-existence with other calcium binding proteins and gaba. *Neuroscience* 48, 29–43. doi: 10.1016/0306-4522(92)90335-Y
- Mitani, A., Dong, M., and Komiyama, T. (2018). Brain-computer interface with inhibitory neurons reveals subtype-specific strategies. *Curr. Biol.* 28, 77–83.e4. doi: 10.1016/j.cub.2017.11.035
- Muller, J. F., Mascagni, F., and McDonald, A. J. (2003). Synaptic connections of distinct interneuronal subpopulations in the rat basolateral amygdalar nucleus. *J. Comp. Neurol.* 456, 217–236. doi: 10.1002/cne.10435
- Muñoz, W., Tremblay, R., Levenstein, D., and Rudy, B. (2017). Layer-specific modulation of neocortical dendritic inhibition during active wakefulness. *Science* 355, 954–959. doi: 10.1126/science.aag2599
- Neske, G. T., and Connors, B. W. (2016). Distinct roles of SOM and VIP interneurons during cortical up states. *Front. Neural Circuits* 10:52. doi: 10.3389/fncir.2016.00052
- Neske, G. T., Patrick, S. L., and Connors, B. W. (2015). Contributions of diverse excitatory and inhibitory neurons to recurrent network activity in cerebral cortex. *J. Neurosci.* 35, 1089–1105. doi: 10.1523/JNEUROSCI.2279-14.2015
- Ogiwara, I., Miyamoto, H., Morita, N., Atapour, N., Mazaki, E., Inoue, I., et al. (2007). Nav1.1 Localizes to axons of parvalbumin-positive inhibitory interneurons: a circuit basis for epileptic seizures in

- mice carrying an *Scn1a* gene mutation. *J. Neurosci.* 27, 5903–5914. doi: 10.1523/JNEUROSCI.5270-06.2007
- Ong, W. Y., and Garey, L. J. (1991). Distribution of GABA and neuropeptides in the human cerebral cortex. A light and electron microscopic study. *Anat. Embryol.* 183, 397–413. doi: 10.1007/bf00196841
- Pakan, J. M., Lowe, S. C., Dylida, E., Keemink, S. W., Currie, S. P., Coutts, C. A., et al. (2016). Behavioral state modulation of inhibition is context-dependent and cell type specific in mouse visual cortex. *eLife* 5:e14985. doi: 10.7554/eLife.14985
- Pelkey, K. A., Chittajallu, R., Craig, M. T., Tricoire, L., Wester, J. C., and McBain, C. J. (2017). Hippocampal GABAergic inhibitory interneurons. *Physiol. Rev.* 97, 1619–1747. doi: 10.1152/physrev.00007.2017
- Pfeffer, C. K., Xue, M., He, M., Huang, Z. J., and Scanziani, M. (2013). Inhibition of inhibition in visual cortex: the logic of connections between molecularly distinct interneurons. *Nat. Neurosci.* 16, 1068–1076. doi: 10.1038/nn.3446
- Pfeiffer, B. E., and Foster, D. J. (2015). Autoassociative dynamics in the generation of sequences of hippocampal place cells. *Science* 349, 180–183. doi: 10.1126/science.aaa9633
- Pi, H.-J., Hangya, B., Kvitsiani, D., Sanders, J. I., Huang, Z. J., and Kepecs, A. (2013). Cortical interneurons that specialize in disinhibitory control. *Nature* 503, 521–524. doi: 10.1038/nature12676
- Porter, J. T., Cauli, B., Staiger, J. F., Lambolez, B., Rossier, J., and Audinat, E. (1998). Properties of bipolar VIPergic interneurons and their excitation by pyramidal neurons in the rat neocortex. *Eur. J. Neurosci.* 10, 3617–3628.
- Prönneke, A., Scheuer, B., Wagener, R. J., Möck, M., Witte, M., and Staiger, J. F. (2015). Characterizing VIP neurons in the barrel cortex of VIPcre/tdtomato mice reveals layer-specific differences. *Cereb. Cortex* 25, 4854–4868. doi: 10.1093/cercor/bhv202
- Prönneke, A., Witte, M., Möck, M., and Staiger, J. F. (2019). Neuromodulation leads to a burst-tonic switch in a subset of VIP neurons in mouse primary somatosensory (barrel) cortex. *Cereb. Cortex* doi: 10.1093/cercor/bhz102
- Rhomberg, T., Rovira-Esteban, L., Vikór, A., Paradiso, E., Kremser, C., Nagy-Pál, P., et al. (2018). Vasoactive intestinal polypeptide-immunoreactive interneurons within circuits of the mouse basolateral amygdala. *J. Neurosci.* 38, 6983–7003. doi: 10.1523/JNEUROSCI.2063-17.2018
- Rogers, J. H. (1987). Calretinin: a gene for a novel calcium-binding protein expressed principally in neurons. *J. Cell Biol.* 105, 1343–1353. doi: 10.1083/jcb.105.3.1343
- Rostene, W. H., Fischette, C. T., and McEwen, B. S. (1983). Modulation by vasoactive intestinal peptide (VIP) of serotonin receptors in membranes from rat hippocampus. *J. Neurosci.* 3, 2414–2419. doi: 10.1523/JNEUROSCI.03-12-02414.1983
- Sermet, B. S., Truschow, P., Feyerabend, M., Mayrhofer, J. M., Oram, T. B., Yizhar, O., et al. (2019). Pathway-, layer- and cell-type-specific thalamic input to mouse barrel cortex. *eLife* 8:e52665. doi: 10.7554/eLife.52665
- Shuman, T., Aharoni, D., Cai, D. J., Lee, C. R., Chavlis, S., Page-Harley, L., et al. (2020). Breakdown of spatial coding and interneuron synchronization in epileptic mice. *Nat. Neurosci.* 23, 229–238. doi: 10.1038/s41593-019-0559-0
- Siegle, J. H., and Wilson, M. A. (2014). Enhancement of encoding and retrieval functions through theta phase-specific manipulation of hippocampus. *eLife* 3:e03061. doi: 10.7554/eLife.03061
- Sohn, J., Okamoto, S., Kataoka, N., Kaneko, T., Nakamura, K., and Hioki, H. (2016). Differential inputs to the perisomatic and distal-dendritic compartments of VIP-positive neurons in layer 2/3 of the mouse barrel cortex. *Front. Neuroanat.* 10:124. doi: 10.3389/fnana.2016.00124
- Somogyi, J., Baude, A., Omori, Y., Shimizu, H., Mestikawy, S. E., Fukaya, M., et al. (2004). GABAergic basket cells expressing cholecystokinin contain vesicular glutamate transporter type 3 (VGLUT3) in their synaptic terminals in hippocampus and isocortex of the rat. *Euro. J. Neurosci.* 19, 552–569. doi: 10.1111/j.0953-816X.2003.03091.x
- Staiger, J. F., Masanneck, C., Schleicher, A., and Zuschratter, W. (2004). Calbindin-containing interneurons are a target for VIP-immunoreactive synapses in rat primary somatosensory cortex. *J. Comp. Neurol.* 468, 179–189. doi: 10.1002/cne.10953
- Tai, C., Abe, Y., Westenbroek, R. E., Scheuer, T., and Catterall, W. A. (2014). Impaired excitability of somatostatin- and parvalbumin-expressing cortical interneurons in a mouse model of Dravet syndrome. *Proc. Natl. Acad. Sci. U.S.A.* 111, E3139–E3148. doi: 10.1073/pnas.1411131111
- Thom, M., Liagkouras, I., Martinian, L., Liu, J., Catarino, C. B., and Sisodiya, S. M. (2012). Variability of sclerosis along the longitudinal hippocampal axis in epilepsy: a post mortem study. *Epilepsy Res.* 102, 45–59. doi: 10.1016/j.eplepsyres.2012.04.015
- Tóth, K., Eross, L., Vajda, J., Halász, P., Freund, T. F., and Maglóczy, Z. (2010). Loss and reorganization of calretinin-containing interneurons in the epileptic human hippocampus. *Brain* 133, 2763–2777. doi: 10.1093/brain/awq149
- Tremblay, R., Lee, S., and Rudy, B. (2016). GABAergic interneurons in the neocortex: from cellular properties to circuits. *Neuron* 91, 260–292. doi: 10.1016/j.neuron.2016.06.033
- Tricoire, L., Pelkey, K. A., Daw, M. I., Sousa, V. H., Miyoshi, G., Jeffries, B., et al. (2010). Common origins of hippocampal ivy and nitric oxide synthase expressing neurogliaform cells. *J. Neurosci.* 30, 2165–2176. doi: 10.1523/JNEUROSCI.5123-09.2010
- Tricoire, L., Pelkey, K. A., Erkkila, B. E., Jeffries, B. W., Yuan, X., and McBain, C. J. (2011). A blueprint for the spatiotemporal origins of mouse hippocampal interneuron diversity. *J. Neurosci.* 31, 10948–10970. doi: 10.1523/JNEUROSCI.0323-11.2011
- Turi, G. F., Li, W.-K., Chavlis, S., Pandi, I., O'Hare, J., Priestley, J. B., et al. (2019). Vasoactive intestinal polypeptide-expressing interneurons in the hippocampus support goal-oriented spatial learning. *Neuron* 101, 1150–1165.e8. doi: 10.1016/j.neuron.2019.01.009
- Tyan, L., Chamberland, S., Magnin, E., Camiré, O., Francavilla, R., David, L. S., et al. (2014). Dendritic inhibition provided by interneuron-specific cells controls the firing rate and timing of the hippocampal feedback inhibitory circuitry. *J. Neurosci.* 34, 4534–4547. doi: 10.1523/JNEUROSCI.3813-13.2014
- Unal, G., Joshi, A., Viney, T. J., Kis, V., and Somogyi, P. (2015). Synaptic targets of medial septal projections in the hippocampus and extrahippocampal cortices of the mouse. *J. Neurosci.* 35, 15812–15826. doi: 10.1523/JNEUROSCI.2639-15.2015
- Walker, F., Möck, M., Feyerabend, M., Guy, J., Wagener, R. J., Schubert, D., et al. (2016). Parvalbumin- and vasoactive intestinal polypeptide-expressing neocortical interneurons impose differential inhibition on Martinotti cells. *Nat. Commun.* 7:13664. doi: 10.1038/ncomms13664
- Wall, N. R., Parra, M. D. L., Sorokin, J. M., Taniguchi, H., Huang, Z. J., and Callaway, E. M. (2016). Brain-wide maps of synaptic input to cortical interneurons. *J. Neurosci.* 36, 4000–4009. doi: 10.1523/JNEUROSCI.3967-15.2016
- Wang, X.-J., Tegnér, J., Constantinidis, C., and Goldman-Rakic, P. S. (2004). Division of labor among distinct subtypes of inhibitory neurons in a cortical microcircuit of working memory. *Proc. Natl. Acad. Sci. U.S.A.* 101, 1368–1373. doi: 10.1073/pnas.0305337101
- Wang, X.-J., and Yang, G. R. (2018). A disinhibitory circuit motif and flexible information routing in the brain. *Curr. Opin. Neurobiol.* 49, 75–83. doi: 10.1016/j.conb.2018.01.002
- Wang, Y., Gupta, A., Toledo-Rodriguez, M., Wu, C. Z., and Markram, H. (2002). Anatomical, physiological, molecular and circuit properties of nest basket cells in the developing somatosensory cortex. *Cereb. Cortex* 12, 395–410. doi: 10.1093/cercor/12.4.395
- Williams, L. E., and Holtmaat, A. (2019). Higher-order thalamocortical inputs gate synaptic long-term potentiation via disinhibition. *Neuron* 101, 91–102.e4. doi: 10.1016/j.neuron.2018.10.049
- Yang, G. R., Murray, J. D., and Wang, X.-J. (2016). A dendritic disinhibitory circuit mechanism for pathway-specific gating. *Nat. Commun.* 7, 1–14. doi: 10.1038/ncomms12815
- Yu, F. H., Mantegazza, M., Westenbroek, R. E., Robbins, C. A., Kalume, F., Burton, K. A., et al. (2006). Reduced sodium current in GABAergic interneurons in

- a mouse model of severe myoclonic epilepsy in infancy. *Nat. Neurosci.* 9, 1142–1149. doi: 10.1038/nn1754
- Yu, J., Hu, H., Agmon, A., and Svoboda, K. (2019). Recruitment of GABAergic interneurons in the barrel cortex during active tactile behavior. *Neuron* 104, 412–427.e4. doi: 10.1016/j.neuron.2019.07.027
- Zhang, S., Xu, M., Kamigaki, T., Do, J. P. H., Chang, W.-C., Jenvay, S., et al. (2014). Long-range and local circuits for top-down modulation of visual cortex processing. *Science* 345, 660–665. doi: 10.1126/science.1254126
- Zhou, X., Rickmann, M., Hafner, G., and Staiger, J. F. (2017). Subcellular targeting of VIP boutons in mouse barrel cortex is layer-dependent and not restricted to interneurons. *Cerebral Cortex* 27, 5353–5368. doi: 10.1093/cercor/bhx220
- Zilles, K., Kálmán, M., Hajós, F., and Schleicher, A. (1991). Developmental gradients of vasoactive intestinal polypeptide (VIP)-containing neurons in the rat visual cortex detected by image analysis. *Dev. Brain Res.* 60, 137–144. doi: 10.1016/0165-3806(91)90042-H
- Conflict of Interest:** The authors declare that the research was conducted in the absence of any commercial or financial relationships that could be construed as a potential conflict of interest.

Copyright © 2020 Guet-McCreight, Skinner and Topolnik. This is an open-access article distributed under the terms of the Creative Commons Attribution License (CC BY). The use, distribution or reproduction in other forums is permitted, provided the original author(s) and the copyright owner(s) are credited and that the original publication in this journal is cited, in accordance with accepted academic practice. No use, distribution or reproduction is permitted which does not comply with these terms.

Advantages of publishing in Frontiers



OPEN ACCESS

Articles are free to read
for greatest visibility
and readership



FAST PUBLICATION

Around 90 days
from submission
to decision



HIGH QUALITY PEER-REVIEW

Rigorous, collaborative,
and constructive
peer-review



TRANSPARENT PEER-REVIEW

Editors and reviewers
acknowledged by name
on published articles

Frontiers

Avenue du Tribunal-Fédéral 34
1005 Lausanne | Switzerland

Visit us: www.frontiersin.org

Contact us: frontiersin.org/about/contact



REPRODUCIBILITY OF RESEARCH

Support open data
and methods to enhance
research reproducibility



DIGITAL PUBLISHING

Articles designed
for optimal readership
across devices



FOLLOW US

@frontiersin



IMPACT METRICS

Advanced article metrics
track visibility across
digital media



EXTENSIVE PROMOTION

Marketing
and promotion
of impactful research



LOOP RESEARCH NETWORK

Our network
increases your
article's readership